An Unsteady Hydrodynamic Model for Tidal Current Turbines

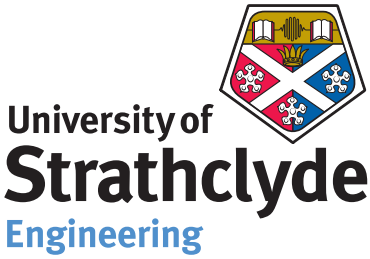

Tom Ruaridh McCombes
BEng (Hons) MSc CEng MIMechE
Department of Mechanical and Aerospace Engineering
University of Strathclyde

A thesis presented in fulfilment of the
requirements for the degree of

Doctor of Philosophy

2014

Statement of Originality

This thesis is the result of the author's original research. It has been composed by the author and has not been previously submitted for examination which has led to the award of a degree.

Signed: Date:

This thesis was typeset in LaTeX 2_ε using Eclipse. Figures were drawn using Inkscape, all 2-D and most 3-D plots were produced using Matlab, and some 3-D graphics were made using ParaView. The method was implemented using C++ with the GNU Compiler Collection and programmed in NetBeans. Results were generated using Mac OSX and openSUSE GNU/Linux systems.

Acknowledgements

I would like to express appreciation to my supervisors Cameron Johnstone and Andy Grant for the years of support and guidance they have given me, and for staying the course. They have consistently believed in me and this work – even when I have not – and have provided me with both pointed direction and carte blanche as I've needed it.

I must also thank the past and present students and staff in ESRU for their guidance and forbearance, in particular Gary Connor, Stephanie Ordonez-Sanchez and Sam Rose whose brains I have regularly picked and who have helped bear the load on many an occasion.

Thanks too to the friends I have made along the way, in particular those with whom long discussions have led to new insights or bafflement – Peter Johnson, Gareth Gretton and João Baltazar – and my INOREan cohort Miguel Lopes, Helen Bailey, Sarah Caraher, Lander Victor, Angus Vantoch-Wood, Mairéad Atcheson and Julien Cretel. Special thanks to those friends whose support and guidance has been more. . . philosophical: Florent Guinot and Lucia Margheritini. I could write a list of names of those who I should thank for their various direct and indirect contributions (and it would be extensive) however, I'm sure I would miss many who deserve inclusion and perhaps include some who don't – so I won't.

My thanks go to my "civilian" friends and my family who I've treated appallingly throughout, who – when not being a hermit – I've abused with my poor moods and bored with my single topic of conversation. Those days are done! I ought to thank Lindsay Finnie who, although she doesn't know it yet, is going to proof-read my thesis.

Finally, more thanks than I can bestow go to my best friend and partner, Ruth Hind, who has been my PhD widow for the best part of a decade now. She has pretty much enabled the whole thing: she kept me from plumbing the very depths during the darkest days, and helped me see the bright side otherwise. I promise I'll make it up to you!

Abstract

Due to concerns about the impacts of carbon emissions on the environment, the security of supply of electricity and the likelihood of achieving “peak-oil” in the near future, governments have legislated to reduce reliance on fossil fuels. An attractive alternative is power obtained from tidal currents, and the coast of the British Isles is especially hydraulically active.

Tidal energy converters typically resemble wind turbines however, unlike wind turbines, they are expected to operate in an environment which is singularly hostile, and will also be expected to generate power in non-ideal operating conditions.

This thesis is concerned with the ability to model individual and groups of tidal devices including their mutual interactions. The ability to capture unsteady inflow conditions at realistic array spacing requires preservation of turbine wakes over a sufficiently large range at spatial resolutions and over time durations which are not feasible using standard computational fluid dynamics software. This thesis has combined methodologies developed for helicopter wake modelling with techniques used in naval architecture for modelling thick maritime propellers into a computational tool. The particular formulation of the Navier-Stokes equations employed allows the determination of the unsteady pressure and force distributions on a turbine rotor due to the effects of a neighbouring device, even if it is operating some significant distance upstream.

The constituents of the method of this thesis are developed and applied to “proof-of-principle” studies. These include flow past static and oscillating 2-D aerofoils and past a 3-D wing, wind turbine and tidal turbine configuration. The results from these studies demonstrate that the model is convergent and capable of capturing the time dependant forces on these devices, and by comparison with analytical or experimental results, or via inter-model comparison begins the process of calibration and validation of the model. The method is then applied to flow past groups of turbines in various array configurations, and a coaxial, contra-rotating device.

The outcome of this work is a decision making tool which can be used to improve success and reduce risk in tidal power array planning, optimise device configurations and is translatable back into rotorcraft or naval architecture usage.

Contents

List of Figures

List of Tables

List of Symbols

Abbreviations and Acronyms

1-D ..... One-Dimensional, used throughout.
2-D ..... Two-Dimensional, used throughout.
3-D ..... Three-Dimensional, used throughout.
AD ..... Alternating Dimension (splitting), page 74.
ADCP ..... Acoustic Doppler Current Profiler, page 9.
ADV ..... Acoustic Doppler Velocimetry, page 11.
AIAA ..... American Institute of Aeronautics and Astronautics (US), page 230.
AR ..... Aspect-Ratio (wing) $AR = b^2/S$, used throughout.
ASME ..... American Society of Mechanical Engineers (US), page 230.
BC, BCs ..... Boundary Condition(s), used throughout.
BEM ..... Boundary-Element Method, page 99.
BEMT ..... Blade-Element/Momentum Theory, page 16.
BERP ..... British Experimental Rotor Programme, page 216.
BERR ..... (Department of) Business, Enterprise and Regulatory Reform (UK), page 1.
BL ..... Boundary Layer, used throughout.
BVI ..... Blade/Vortex Interaction, used throughout.
cf. ..... *confer*, Latin: bring together, read "compare", used throughout.
CFD ..... Computational Fluid Dynamics, page 7.
CFL ..... Courant-Friedrichs-Lewy condition, related to Courant number $C = u\Delta t/h$, used throughout.
CO_2 ..... Carbon dioxide, page 1.
CoRMaT ..... COntra-Rotating MArine Turbine.
CPU ..... Central Processing Unit, used throughout.
DECC ..... Department of Energy & Climate Change (UK), page 1.
DTI ..... Department of Trade and Industry (UK), page 4.
DTRC ..... David Taylor Research Center, page 216.
e.g. ..... *exempli gratia*, Latin: for the sake of example, read "for example", used throughout.
EMEC ..... European Marine Energy Centre, page 2.
ESRU ..... Energy Systems Research Unit (University of Strathclyde).
etc. ..... *et cetera*, Latin: and other things, read "and so on", used throughout.
EU ..... European Union, page 1.
FEA ..... Finite-Element Analysis, page 104.
FFT ..... Fast-Fourier transform, page 48.
FISHPACK, FISHPACK90 Efficient FORTRAN Subprograms for the Solution of Separable Elliptic Partial Differential Equations, page 48.
FMM ..... Fast-Multipole Method, used throughout, introduced, page 50.
FORTRAN ..... The IBM Mathematical FORmula TRANslating System, page 50.
FVM ..... Finite-Volume Method, page 61.
GCI ..... Grid convergence index, used throughout, see Appendix A.3.1.
GDP ..... Gross Domestic Product, page 1.
GL ..... Germanischer Lloyd, a classification society.

GPU ..... Graphics Processing Unit, used throughout.
GW, GWh ..... Gigawatt (power), gigawatt-hour (energy), page 2.
TW, TWh ..... Terawatt (power), terawatt-hour (energy), page 1.
HAWTDAWG .... HORIZONTAL AXIS WIND TURBINE DIRECTLY ALLOCATED WAKE GEOMETRY, a vortex wake model , page 17.
HPC ..... High Performance Computer/Computing, used throughout.
i.e. ..... *id est*, Latin: that is, read "that is (to say)", used throughout.
IC, ICs ..... Initial Condition(s), used throughout.
ITTC ..... International Towing Tank Conference.
JONSWAP ..... Joint North Sea Wave Project.
kW, kWh ..... Kilowatt (power), kilowatt-hour (energy), page 2.
LDA ..... Laser Doppler Anemometry, page 11.
LES ..... Large Eddy Simulation, page 68.
LHS ..... Left Hand Side, used throughout.
m ..... Metres, SI unit of length.
MPI ..... Message Passing Interface, used throughout.
MUDPACK ..... Multigrid Software for Elliptic Partial Differential Equations.
MUSCL ..... Monotone Upstream-centred Schemes for Conservation Laws see Eq. (3.52), page 63.
MW, MWh ..... Megawatt (power), megawatt-hour (energy), page 4.
NACA ..... National Advisory Committee for Aeronautics (US), used throughout.
NASA ..... National Aeronautics and Space Administration (US), used throughout.
NPARC ..... National Program for Applications-Orientated Research in CFD (US), page 232.
NREL ..... National Renewable Energy Laboratory (US), used throughout.
NS ..... Navier-Stokes (equations), see Eqs. (1.2), page 14.
NURBS ..... Non-Uniform, Rational B-Spline, page 39.
ODE ..... Ordinary Differential Equation, used throughout.
$\mathcal{O}(\ldots)$ ..... Order (of magnitude), used throughout.
Pa ..... Pascal, SI unit of pressure.
PALISUPAN ..... "PARALLEL LIFTING SURFACE PANEL – a panel code, page 104.
PDE ..... Partial Differential Equation, used throughout.
PIC ..... Particle-In-Cell, page 47.
PISO ..... Pressure Implicit with Split Operator, page 67.
PIV ..... Particle Image Velocimetry, page 11.
PL ..... Piecewise-Linear (limiter), page 85.
PR ..... Polynomial-Ratio (limiter), page 85.
PSE ..... Particle-Strength-Exchange, page 35.
PTO ..... Power-Take-Off (subsystem), page 6.
QSLE ..... Quasi-Static Lift Equation, see Eq. (6.16), page 170.
QUICK ..... Quadratic Upwind Interpolation for Convective Kinematics, see Eq. (3.36), page 81.
RANS ..... Reynolds-averaged Navier-Stokes (equations), page 62.
RBF ..... Radial Basis Function, page 37.
R&D ..... Research and Development.
Re ..... Reynolds number, used throughout.
RHS ..... Right Hand Side, used throughout.
RSM ..... Reynolds Stress Modelling, page 65.

s ..... Seconds, SI unit of time.
SERG ..... Sustainable Energy Research Group (University of Southampton).
SHASTA ..... SHarp And Smooth Transport Algorithm, page 63.
SIMPLE ..... Semi-Implicit Method for Pressure-Linked Equations, page 67.
SPH ..... Smoothed Particle Hydrodynamics, page 45.
std ..... Sample standard deviation, page 141.
SWSS ..... Symmetrically Weighted Sequential Splitting, page 74.
TSR ..... Tip-Speed Ratio, $\lambda = \Omega R/U_\infty$, used throughout.
TV, TVD ..... Total Variance, Total Variance Diminishing, see Eq. (3.41), page 82.
UAE ..... NREL Unsteady Aerodynamics Experiment, used throughout.
UMIST ..... Upstream Monotonic Interpolation for Scalar Transport, see Eq. (3.52), page 87.
UNIDO ..... United Nations Industrial Development Organisation, page 5.
USLE ..... Unsteady Lift Equation, see Eq. (6.21), page 172.
VIC ..... Vortex-in-cell, page 47.
VLM ..... Vortex Lattice Method, page 105.
VN ..... von Neumann condition, page 88.
VRM ..... Vortex Redistribution Method, page 36.
VTM ..... VORTICITY TRANSPORT MODEL, page 107.
w.r.t. ..... with respect to, used throughout.

Greek Symbols

α ..... Angle of incidence [° *or* rad].
β ..... Sideslip angle [° *or* rad], page 216.
Δ ..... A finite-difference or element.
δ ..... Boundary-layer thickness, page 111.
δ ..... Core radius [m] – also σ.
$\delta(\ldots)$ ..... Delta function, page 114.
ϵ ..... Turbulence dissipation rate [$\mathrm{J\,kg^{-1}\,s^{-1}}$], page 65.
η, $\boldsymbol{\eta}$ ..... One of local coordinate directions $[\xi, \eta, n]$, basis vector of the same, page 125.
Γ ..... Circulation strength [$\mathrm{m^2\,s^{-1}}$], see Eq. (2.3), page 29.
Γ ..... Diffusion coefficient in Eq. (3.1), page 69.
λ ..... Tip-Speed Ratio, TSR, $\lambda = \Omega R/u_\infty$, used throughout.
μ ..... Dipole (singularity) strength, page 116.
μ ..... Helicopter rotor advance ratio [1], page 216.
μ_0 ..... Permeability of free space [$\mathrm{H\,m^{-1}}$] , page 29.
μ_t ..... Turbulence/eddy viscosity [Pa s], page 65.
∇ ..... Del vector differential operator.
∇^2 ..... Laplacian differential operator.
∇f ..... Gradient of scalar field f.
$\nabla \boldsymbol{f}$ ..... Tensor derivative of vector field $\boldsymbol{f}$.
$\nabla \cdot \boldsymbol{f}$ ..... Divergence of vector field $\boldsymbol{f}$.
$\nabla \times \boldsymbol{f}$ ..... Curl of vector field $\boldsymbol{f}$.
ν ..... Fluid kinematic viscosity [$\mathrm{m^2\,s^{-1}}$].
$\boldsymbol{\omega}$ ..... Vorticity vector [$\mathrm{s^{-1}}$].
ω ..... Specific dissipation rate [$\mathrm{s^{-1}}$], page 65.
Ω, $\boldsymbol{\Omega}$ ..... Rotorspeed (in TSR), angular velocity vector, both [$\mathrm{rad\,s^{-1}}$], used through-

out.

Ω, $\partial\Omega$ ..... Domain volume, domain boundary surface, page 48.

$\phi(\ldots)$ ..... Radial basis function, page 43.

ϕ ..... A scalar transport variable in Eq. (3.1), page 69.

ϕ, φ ..... Velocity perturbation potential $[\mathrm{m}^2\,\mathrm{s}^{-1}]$, see Eq. (4.1), page 109.

Ψ ..... Turbine yaw angle, taken about body z-axis, relating inflow velocity vector with body x-axis [° *or* radian].

ρ ..... Fluid density $[\mathrm{kg}\,\mathrm{m}^{-3}]$.

σ ..... Rotor solidity, in Eqs. (8.1) and (8.2), page 208.

σ ..... Core radius [m] – also δ.

σ ..... Source (singularity) strength, page 116.

$\boldsymbol{\tau}$ ..... Reynolds stress tensor $[\mathrm{m}^2\,\mathrm{s}^{-2}]$, page 65.

ξ, $\boldsymbol{\xi}$ ..... One of local coordinate directions $[\xi, \eta, n]$, basis vector of the same, page 125.

$\zeta(u)$ ..... Gaussian core projection function in u, page 44.

Subscripts

$\oint_C$ ..... Circuit integral.

$\iint_S$ ..... Surface integral.

$\int_V$ ..... Volume integral.

C_d, C_D ..... Drag coefficient (2-D), (3-D).

C_l, C_L ..... Lift coefficient (2-D), (3-D).

C_P ..... Power coefficient, note uppercase.

C_p ..... Pressure coefficient, note lowercase.

C_T ..... Thrust coefficient.

$[\ldots]_\infty$ ..... $[\ldots]$ evaluated at infinity, in the freestream.

$[\ldots]_{\mathrm{n,s,e,w,t,b,N,S,E,W,T,B}}$ $[\ldots]$ on north, south, east, west, top, bottom faces (lowercase) or neighbours (uppercase).

$[\ldots]_P$ ..... $[\ldots]$ at field point P.

Roman Letters

$\mathbf{A}, \mathbf{B}, \mathbf{C}, \mathbf{D}$ ..... Coefficient matrices for a linear system of equations. Typically BEM influence matrices..

A ..... Area $[\mathrm{m}^2]$.

a ..... Wave amplitude [m], page 222.

a, a' ..... Axial and tangential induction factors, respectively, [1]. See Eqs. (8.1) and (8.2), page 208.

$\boldsymbol{B}$ ..... Magnetic B-field [T] , page 29.

b ..... Span (wing) [m], used throughout.

c ..... Chord (aerofoil/wing) [m], used throughout.

C ..... Courant number, $C = u\Delta t/h$, used throughout.

d ..... Mean water depth [m], page 222.

$\mathrm{d}F$, $\mathrm{d}S$ ..... Single blade-element axial and tangential force contributions, respectively, [N]. See Eqs. (8.1) and (8.2), page 208.

$\mathbb{G}(\ldots)$ ..... Kernel function.

g ..... Gravity $[9.806\,65\,\mathrm{m}\,\mathrm{s}^{-2}]$.

h ..... Cell side length, used throughout.

H_s ..... Significant wave height [m].
i, j ..... A general index or counter.
$\boldsymbol{J}$ ..... Total current density [$\mathrm{A\,m^{-1}}$] , page 29.
J ..... Marine rotor advance ratio [1], page 216.
k ..... Turbulent kinetic energy [$\mathrm{J\,kg^{-1}}$], page 65.
k ..... Wavenumber [$\mathrm{m^{-1}}$], page 222.
$\boldsymbol{l}, \Delta\boldsymbol{l}$ ..... Line segment, finite line segment.
L ..... A characteristic length scale [m].
$M_4'(u)$ ..... third-order projection function in u, see Eq. (2.24), page 45.
m, n ..... Counters [1].
M_x ..... In-plane blade root bending moment[N m], page 222.
M_y ..... Out-of-plane blade root bending moment[N m], page 222.
$n, \boldsymbol{n}$ ..... One of local coordinate directions $[\xi, \eta, n]$, basis vector of the same, unit normal vector, page 125.
P ..... Power [W].
p ..... An index or counter of vortex particles.
p ..... Pressure [Pa].
$\mathbb{R}$ ..... Real number, used throughout.
$r, R, \boldsymbol{R}$ ..... Distance or radius (scalar), displacement (vector) [m].
S ..... Planform area (wing/blade), swept-area (rotor), inflow area of hydrodynamic subsystem (general device) [$\mathrm{m^2}$], used throughout.
$S, \boldsymbol{S}$ ..... Surface, in terms of surface normal (unit) vector.
$S_{[\ldots]}$ ..... $[\ldots]$ computational domain boundary.
T ..... A characteristic time scale [s].
t ..... Time, in seconds [s].
T_z ..... Wave zero up-crossing period [s].
$\boldsymbol{u}$ ..... Fluid velocity vector [$\mathrm{m\,s^{-1}}$].
U ..... A characteristic velocity [$\mathrm{m\,s^{-1}}$].
u ..... $\boldsymbol{i}$ velocity component [$\mathrm{m\,s^{-1}}$].
V ..... A characteristic velocity [$\mathrm{m\,s^{-1}}$].
V ..... Volume [$\mathrm{m^3}$].
v ..... $\boldsymbol{j}$ velocity component [$\mathrm{m\,s^{-1}}$].
v ..... Resultant axial inflow velocity [$\mathrm{m\,s^{-1}}$], in Eq. (8.1), page 208.
v_{mean} ..... Mean velocity [$\mathrm{m\,s^{-1}}$].
w ..... $\boldsymbol{k}$ velocity component [$\mathrm{m\,s^{-1}}$].
w ..... Resultant rotational inflow velocity [$\mathrm{m\,s^{-1}}$], in Eq. (8.2), page 208.
$\boldsymbol{x}$ ..... Position vector [m].

Superscripts and Accents

$\overline{[\ldots]}$ ..... Volume integral average of $[\ldots]$.
$\underline{[\ldots]}$ ..... $[\ldots]$ in dimensionless form, $[\ldots]$ in local (non-global) coordinates.
$\dot{[\ldots]}$ ..... Time derivative of $[\ldots]$.

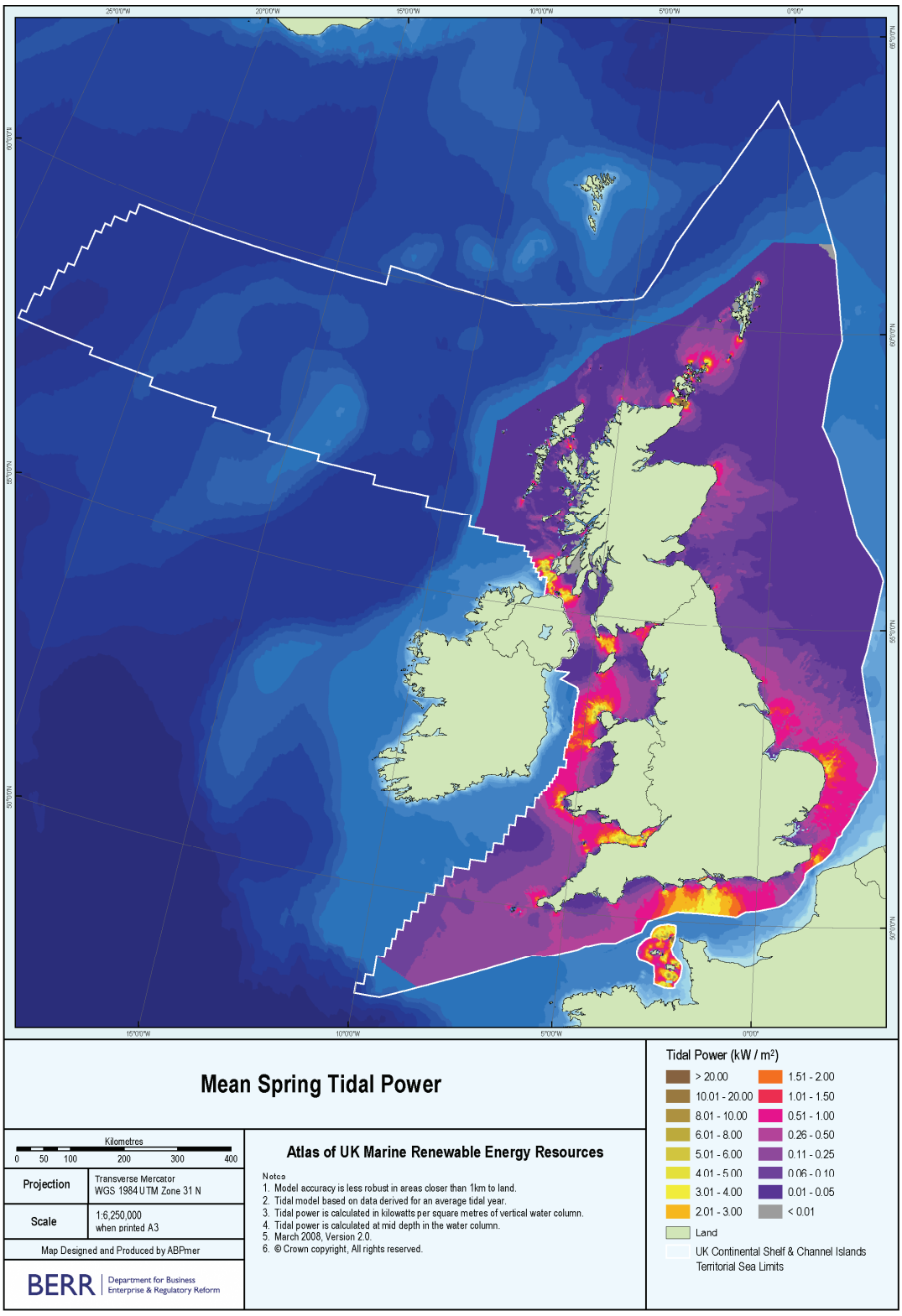

Figure 1.1: Mean spring tide velocity contours. The UK has an estimated potential of 18 TW h to 20 TW h tidal stream power generation per annum. From BERR (2008).

1

Introduction and Historical Review

1.1 A Rationale for Tidal Energy

Rising oil prices, scientific consensus on anthropogenic climate change, and public acceptance of renewable energy are driving governmental desires to appear "green", allowing – despite strong criticism in the lay press to the contrary – offshore renewables to become economically viable. The EU has set binding targets requiring that 20 % of EU power generation is from renewable sources by 2020 – part of the "20-20-20" targets, alongside emissions and efficiency targets. In Britain – and at the time of writing – these have been translated by the Coalition Government as a 15 % renewable energy contribution to energy supply, and by the Scottish Government as a somewhat more ambitious 100 % renewables contribution to electricity supply along with a 42 % CO_2 reduction agenda. It is estimated by the Carbon Trust (Black & Veatch, 2005, 2011) and Savage (2007) that 18 TW h to 20 TW h per year may be extracted from tidal sites around the British Isles accounting for approximately 6 % of UK national demand at 2011 levels (DECC, 2012), and potentially considerably more according to Salter (2009) – see Fig. 1.1. The Carbon Trust estimates that UK resources account for approximately 25 % of European and 10 % of globally accessible tidal resources and will account for around 22 % of the global market in marine renewables between 2010–2050, estimated at about £93 bn for the global tidal market and hence £5 bn for UK GDP. Scotland in particular features significant stretches of hydraulically dynamic coastline – see Fig. 1.2 – in the inner Hebrides: the Sound of Islay and the Gulf of Corryvreckan; the Grey Dogs between Scarba and Lunga; as well as the Dorus Mòr at the Sound of Jura and Kyle Rhea between Skye and Lochalsh. To the north there is the Pentland Firth and the Orkney archipelago with the European Marine Energy Centre (EMEC) Falls of Warness test site off the small island of Eday, and to the south strong flows around the Mulls of Kintyre and Galloway.

Compared to wave energy converters, tidal power devices are relatively mature. Although to date only a handful of devices have been successfully deployed at or near to full prototype scale (a selection are identified below), IEA Blue Map scenarios predict global

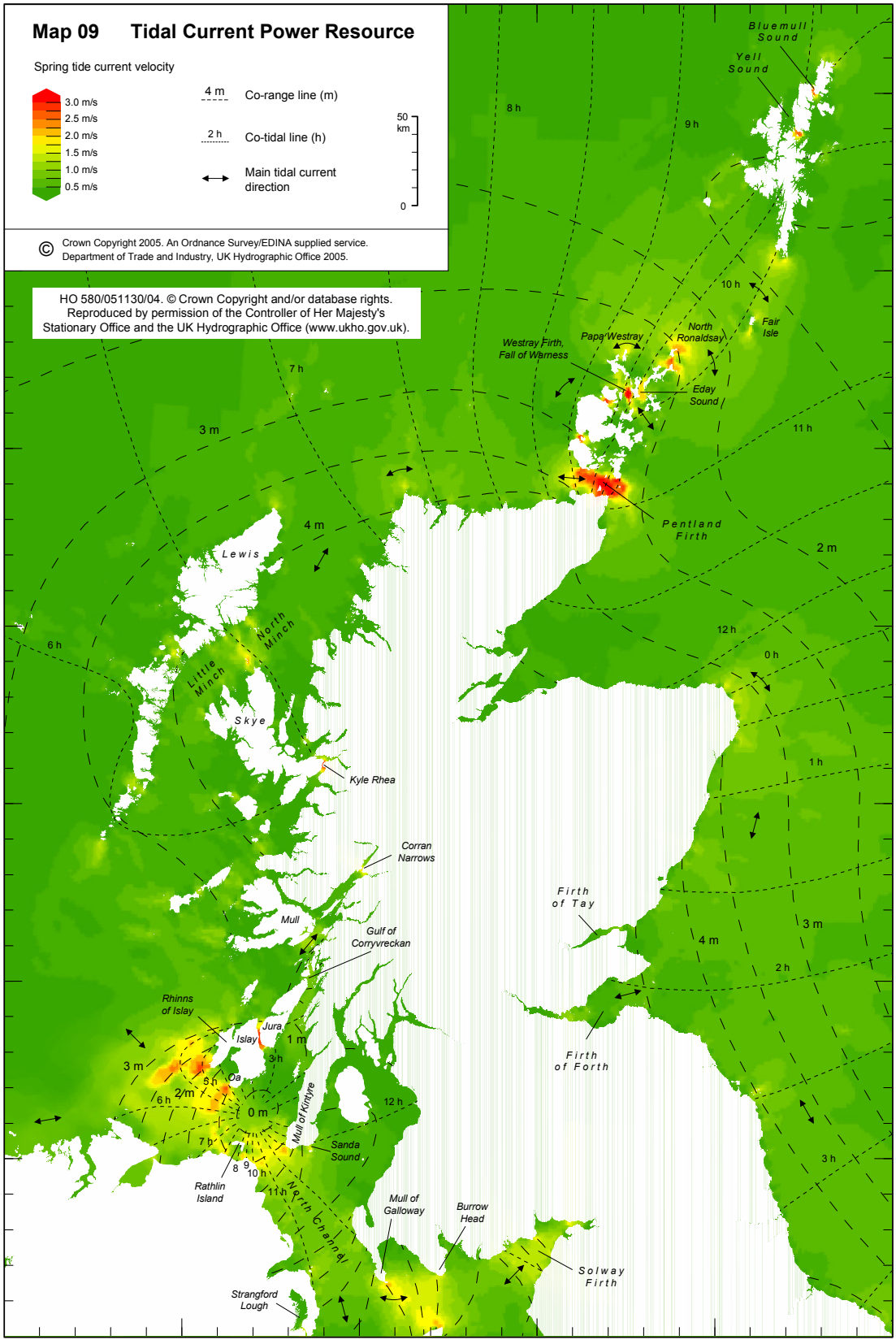

Figure 1.2: Mean spring tide velocity contours. Scotland detail, from the Scottish Executive (2006).

tidal deployment in the region of 52 GW (from Carbon Trust – assuming tidal stream is 20 % of tidal power, the rest being tidal range, and a capacity factor of 30 %) by 2050.

1.2 Tidal Devices

1.2.1 Principles of Operation

The power available in a tidal flow is due to the kinetic energy of the moving water. Assuming a mass density of $1000\,\mathrm{kg\,m^{-3}}$, a parcel of fluid of one cubic metre with a mean bulk flow speed of $1\,\mathrm{m\,s^{-1}}$ maintains 500 J of kinetic energy until its speed changes. At $2\,\mathrm{m\,s^{-1}}$ this increases to 2000 J and at $4\,\mathrm{m\,s^{-1}}$ to 8000 J. If a surface in the flow is such that in a $1\,\mathrm{m\,s^{-1}}$ flow, $1\,\mathrm{m^3}$ (or more strictly, 1000 kg) of water per second passes through it, then the kinetic energy flux through that surface is $500\,\mathrm{J\,s^{-1}}$ or 500 W. Similarly, increasing the velocity and keeping the area constant, over one second at $2\,\mathrm{m\,s^{-1}}$ this is 2000 kg thus 4 kW and at $4\,\mathrm{m\,s^{-1}}$ it is 4000 kg and 32 kW. Available power in a fluid flow is given by the flow kinetic energy (passing through a reference area) over a reference time scale. The simple formula for this is

$$P = \frac{\text{kinetic energy}}{\text{time}} = \frac{1}{2t}mu^2 = \frac{1}{2t}(\rho A u t)u^2 = \frac{1}{2}\rho u^3 A. \tag{1.1}$$

Assuming a fixed density, the power available scales with velocity cubed and linearly with area. If area is expressed in terms of radius, power scales quadratically with radius.

This is the available power. In order to use this, the energy must be converted into a usable form. In general, this will be a rotational shaft power – a torque times an angular velocity – to use with a generator, although it can also be converted to hydraulic power – a pressure times a volumetric flow rate. These energy conversion steps can never be lossless, and this includes the primary conversion where the working fluid meets the hydrodynamic interface. According to Betz's law (see e.g. Hansen, 2007), the maximum available power that can be captured by a device in open flow is 16/27 of that available, or about 59.3 %. This number, known as the Betz limit, is attained only for a hypothetical device under certain conditions (no hub, no drag, no wake, no heat loss, no radial flow), all of which serve to increase the power captured to this value, and are all more or less invalid in real world cases. The main physical interpretation for this limit is that above this value, the device would be slowing so much fluid down that upstream fluid due to pass through the device's primary hydrodynamic interface would bypass around the outside and power production would fall. Therefore the efficiency of an isolated device can never exceed the Betz limit, however, Garrett and Cummins (2007), then later Nishino and Willden (2012) and Vennell

(2013) have shown that there is an optimal array layout that, due to local blockage effects, may theoretically increase the overall hydrodynamic subsystem performance of arrays of devices in channels to above the Betz efficiency limit. The hydrodynamic efficiency of the device is expressed as a power coefficient, which is the ratio of power captured by the hydrodynamic subsystem to the available power to the device.

1.2.2 Hydrodynamic Subsystems

Unlike wind energy, there is as yet no standard form of a tidal energy converter, however, axial-flow turbines appear to be the dominant configuration. Excepting Venturi systems and those relying on tidal range – e.g. barrages or lagoons – principles of operation for all devices are broadly similar (and even those omitted operate along the same hydrodynamic basis).

1.2.2.1 Axial-flow Turbines

Similarly to wind turbines, these rotors generate a torque on a central or concentric shaft using the reactive hydrodynamic forces on a set of radial blades. Effective and efficient operation requires that the flow impinges on the rotor-plane orthogonally – any deviation from truly axial-flow results in a reduction in efficiency and an increase in cyclical loading that can lead to fatigue damage. The pitch of the blades can be fixed; in that case blade stall prevents the rotor from over-speeding at the expense of increased thrust, or the pitch can be controlled so that the blades can be feathered to reduce the possibility of overloading the power-train. Pitch control is also useful in optimising the performance of the device over the entire tidal cycle.

Extensions and Variations Contra-rotating, coaxial rotors such as the Nautricity CoR-MaT system, developed at the University of Strathclyde by Clarke *et al.* (2007), use a second downstream rotor system to provide a counter-torque, with the objective being reduction of mooring requirements. The system also provides some incremental increase in efficiency over a single rotor, and a possible reduction in downstream swirl might mitigate environmental impact. Ducted turbines, such as the Rotech Tidal Turbine developed by Lunar Energy (see Lunar Energy Ltd., 2012), employ a flow augmentation system that boosts performance at the rotor by increasing the volume of water entering the hydrodynamic subsystem. This increases the velocity, reduces or eliminates the bypass flow at the rotor and possibly tunes the rotor exhaust pressure field allowing the rotor to operate at greater than the Betz limit. However, the device as a whole does not (and cannot) exceed the limit.

(a) MCT SeaGen dual 600 kW turbines at Strangford Lough, Northern Ireland, UK (Siemens press picture, copyright Siemens AG, Munich/Berlin)

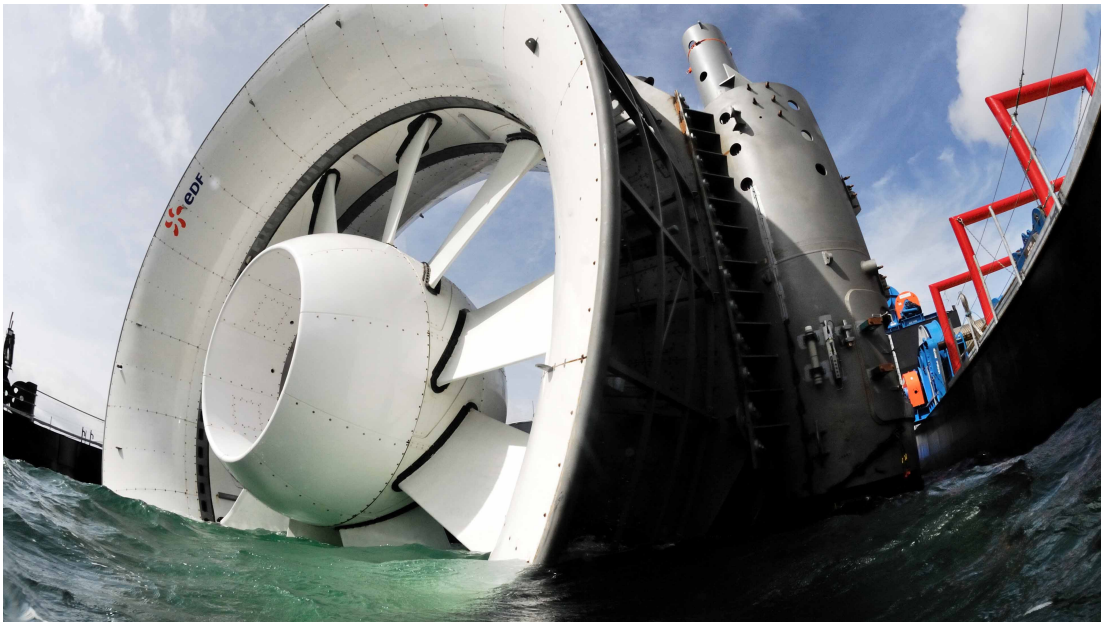

(b) OpenHydro turbine for deployment at Paimpol-Brèhat in Brittany, France (from DCP Strategic Communication Ltd, 2012)

Figure 1.3: Prominent examples of deployed large-scale axial-flow turbine configurations.

Examples Prominent examples of axial-flow turbines include Hammerfest Strøm, whose grid connected 300 kW HS300 turbine was deployed at Kvalsund in Northern Norway between 2003-09 (see Hammerfest Strøm AS, 2012) and who have installed a 300 kW device at EMEC. Aspirations include deployment of a commercial array in the Sound of Islay. Marine Current Turbines Ltd. – now a fully owned subsidiary of Siemens – have deployed a single-rotor, rheostat loaded 300 kW turbine named SeaFlow (see DTI, 2005a; Fraenkel, 2007) and a grid connected 1.2 MW dual-rotor system named SeaGen (see Fraenkel, 2010, and Fig. 1.3a). The devices were installed in the Bristol Channel in 2003 and Strangford Lough in 2008 respectively. Aspirations include development of multi-rotor systems and installation at sites in Nova Scotia (Bay of Fundy). Versions of the OpenHydro turbine (see OpenHydro Group Ltd., 2012), an axial-flow variant with an open centre (i.e. no hub, and a "rim-drive" generator – see Fig. 1.3b) have been installed at EMEC since 2006. Aspirations include installation at sites in the Channel Islands.

1.2.2.2 Cross-flow Turbines

Cross-flow rotor-systems use a number of rotor-blades arranged in a circle whose individual axis and shared axis of rotation are orthogonal to the fluid flow. Because the blades rotate through the flow, the geometric pitch angle rotates through 360°, and thus there are large excursions in local angle of attack during a revolution. Although in simple devices the pitch of the blades can be fixed, more sophisticated devices seek to reduce this "ripple" by applying pitch control by some active or passive system. Even with pitch control the local flowfield is highly unsteady because, during the downstream pass of the revolution, blades have to cut through the wake due to the upstream pass. This thesis differentiates between (and does not consider) impulse turbines such as the Savonius rotor and reaction turbines, such as the Darrieus type.

Extensions and Variations Excluding pitch regulation, the two-dimensional form of cross-flow turbines is fairly consistent, exceptions being where the path taken by the blades is not circular (although it could be argued that these represent translating foil devices). In three dimensions, the extruded shape of the blades can vary: common forms are the "Gyromill" or H-bar with straight blades joined at the tips or middle; *troposkein* or "egg-beater" shaped blades such as the Darrieus rotor; or helical blades as in the Gorlov design. Gyromill shapes are easy to construct and pitch regulate; Darrieus have better stress distribution by moving mass towards the axis; and Gorlov rotors can reduce torque ripple since some section of the rotor is always at each azimuth. As with axial-flow turbines, performance enhancement

(a) Kobold ENERMAR 160 kW turbine as deployed in the Straits of Messina, Italy (from Ponte di Archimede International S.p.A., 2012)

(b) Uppsala University Söderfors 30 kW turbine as deployed in the Dalälven river, Sweden (from von Schultz, 2013)

Figure 1.4: Examples of cross-flow turbine configurations.

can be attained by placing the turbine in a flow augmenting duct.

Examples In 2001, the Italian company Ponte di Archimede installed the 160 kW Kobold ENERMAR H-bar pitch regulated cross-flow turbine in the Straits of Messina (see Ponte di Archimede International S.p.A., 2012, and Fig. 1.4a). The device is currently used as a proof-of-concept research device for the University of Naples. Aspirations for the device include deployment as a 150 kW device in rural Indonesia as part of a UNIDO project, and deployment of an array of 4 devices at EMEC under the BlueTEC brand (name change due to project partners Bluewater group). Most other examples of cross-flow turbines belong to university research groups, e.g. the design of Salter and Taylor (2007) at the University of Edinburgh or the Söderfors Project turbine at Uppsalla University, described in Yuen *et al.* (2009) and shown in Fig. 1.4b.

1.2.2.3 Translating and Oscillating Hydrofoils

If the concept of cross-flow turbines is generalised so that the blades (or their axis) do not necessarily transcribe a circular path around a hub, the result is a translating or oscillating hydrofoil system. In a typical translating hydrofoil system, rows of blades are constructed by mounting blades at the tips to a guide track or cable – rather like a Venetian blind. The blades then pass through the flow before being guided back to form a circuit. The main difference between this and a turbine is that the blade path is often flexible rather than fixed as in a turbine design. An oscillating foil can be considered a specific case of a pitch regulated cross-flow turbine in that the foil only passes through a limited arc before returning. The foil is affixed by an articulated mount to a pivoted or sliding armature, and either oscillates linearly or in an arc around a central point due to the lift on the foil. In oscillating devices, power-take-off can be achieved by actuating a hydraulic circuit or direct driving a generator. In translating devices, power-take-off can be by driving a generator attached to a sprocket, or similar, driven by the cable/chain.

Translating and oscillating foil based tidal power concepts are particularly rare by comparison with “traditional” turbine configurations and as such their configurations are rather distinct.

Examples The 150 kW Engineering Business Stingray device is the earliest major deployment of an oscillating or translating foil device (see DTI, 2005b, and Fig. 1.5a). The device was installed in the Yell Sound off Shetland between 2002 and 2003. At the time of writing, there is no development activity on the device. A related concept is the Pulse Stream

(a) Engineering Business Stingray 150 kW prototype (image courtesy Engineering Business Ltd, from Mueller and Wallace, 2008)

(b) PulseTidal 100 kW PS100 prototype (from Pulse Tidal Ltd., 2012)

Figure 1.5: Prominent examples of oscillating foil configurations.

oscillating foil device, as described in Paish, Giles and Panahandeh (2010). A consortium including Pulse and IT Power installed the 100 kW grid connected PS100 prototype in the Humber in 2009 (see Pulse Tidal Ltd., 2012, and Fig. 1.5b). Aspirations include development and deployment of a 1.2 MW full-scale demonstrator device. A less mature concept is the BioSTREAM device, described in Kloos, Gonzalez and Finnigan (2009), which is under development by BioPower Systems. As of 2011, the development of the BioSTREAM tidal device had focussed on the PTO subsystem (see Kloos, Benitez and Gonzalez, 2011), and the hydrodynamic subsystem appears to be a broadly biomimetic representation of a lunate fin mounted on an articulated arm. Aspirations for the device include installation of a 250 kW prototype off Tasmania.

Few translating foil concepts have been reported. Holmes and Devaney (2011) describes the Tidal Flyer device, which has been tested at small scale in wind tunnels and a flume. Tidal Flyer consists of a number of flexible sails that self-align to the flow as they travel around a pre-defined track. A similar, but more mature concept is the Tidal Sails device that has been sea-trialled at small scale (see Tidal Sails AS, 2012). At the time of writing, it is fair to say that both these devices are very much at a pre-commercial, concept appraisal development stage.

1.3 Flow Physics for Tidal Devices

Scaling Issues and the Requirement for Numerical Modelling Experimental testing is governed by the laws of similitude. These are expressions for:

1. Geometric similitude – where the device is a geometric scale model;
2. Kinematic similitude – where device and fluid velocities are also scaled; and
3. Dynamic similitude – where in addition to geometry and velocities, forces are scaled.

To describe geometric scaling, a scale factor such as $s = 30$ for $1/30^{\text{th}}$ scale is used to scale the lengths of device components such that all length scale ratios between the model and the prototype are equal. For kinematic scaling, velocity ratios are held constant, giving rise to kinematic parameters such as tip-speed ratio (TSR, λ), which is used to match full-scale and model velocities. For dynamic scaling, the ratios of forces between full and model scales are constant, giving rise to the dynamic scaling laws e.g. the Reynolds number (ratio of inertial to viscous forces) or Froude number (ratio of inertial to gravitational forces) that are typically used in experimental fluid dynamics with tidal turbines. The relevance of the

Froude law scaling in the absence of a free-surface is questionable, since the Froude number is indicative of the relative importance of the effects of gravity. Unfortunately, when testing tidal devices it is particularly difficult to achieve Reynolds number matching (without running at exceptionally high velocities, or using mercury as the working fluid), and so the Froude scaling is often applied. It is also well known that in practical experiments it is generally impossible to match more than a single force ratio (without resorting to a $s = 1$ scale model). In these scenarios, it is generally accepted that a kinematic relation will be used and the experiment will form part of a chain of increasing size experiments as the device matures.

In addition to scaling issues due to the flow physics, there are issues in that different subsystems of the device scale according to differing length/time laws: for example for Froude scaling power scales with $s^{3.5}$ and velocity with $\sqrt{s}$; with Reynolds scaling power scales with s^5, whereas velocity scales with s. This means that it is often exceedingly difficult to manufacture scaled PTO and control subsystems for model testing, and therefore in practice a proxy is used, e.g. a rheostatic dump load or brake, or the subsystem is simply absent. Similarly, hydrodynamic subsystems at small scales are often replaced by proxies, for example porous meshes or – ideally – low Reynolds number rotors (that bear very little similarity to the geometry of the full scale device), so that the scale effects of the device on the flow, rather than the flow on the device, can be modelled experimentally.

Numerical modelling does not suffer from scaling issues, and since the model can be run at both small and full scale. Results from computational fluid dynamics (CFD) analysis can be used to both inform the development of tidal power devices when moving from smaller to larger scale, and shed light on and explain the mechanisms of fluid dynamics and device behaviour observed during experimental testing. There are of course a number of phenomena which are particularly challenging to model using CFD.

1.3.1 Macro-scale Hydrodynamics

The hydrodynamics of tidal energy converters share numerous similarities with the aerodynamics of wind turbines. There are some notable differences due to differences in properties between liquid and gas mixtures and also between global flow conditions. Some issues that have been identified as particularly important or challenging to capture using computational methods are listed below.

Large scale hydrodynamics affecting tidal turbines are particularly difficult to account for using computational methods, since the range of scales requiring resolution ranges from below a metre to the order of kilometres. While the most obvious macroscopic hy-

drodynamic issues are the inclusion of and proximity to a free-surface, there are various others also.

1.3.1.1 Met-ocean Conditions and Wave/Device Interactions

Tidal currents are often assumed to be bi-directional, with the flood and ebb tides being equal and opposite. This is generally not the case. Tidal currents in one direction can deviate by as much as 35° from the expected reverse direction, as shown in results of analysis at Portland Bill in the UK (Blunden and Bahaj, 2006), and as such, a device might spend some considerable portion of the tidal cycle in yaw, with consequentially reduced power output (according to the commonly applied geometric ready-reckoner, a yaw misalignment angle of Ψ results in a reduced power output of $P = P_{\text{aligned}} \cos^3 \Psi$) and increased fatigue loading. In addition to the regular ebb and flood of the tidal currents, tidal devices are expected to operate where weather conditions have a significant effect. It is probable that access to devices will be significantly limited due to infrequent and short safe operating windows, e.g. when significant wave height is below 50 cm. Because of this, devices must be built in such a manner that they are robust and reliable, rather than optimised perfectly, and this will entail simplifications, such as perhaps being unable to yaw into the flow, or being fixed pitch. Therefore it is likely that devices might spend substantial periods in off-design conditions and being able to adequately capture the effect of these and account for it is essential during any device development. Met-ocean conditions can effect device performance directly, for example by pressure and temperature changes, surge or changes in the turbulent environment due to waves, and indirectly, by changing the sediment transport conditions and nutrient levels, modifying the turbidity of the water-column and the likelihood of biofouling. Unlike wind turbines, tidal turbines operate in conditions that are notionally predictable. However, as much as the background tidal velocity might be calculable, it is much more difficult to predict for the influence of wave or wind driven currents without direct measurement on site, for example as described in Abonnel *et al.* (2005) for Nord-Cotentin in the north of France, Norris and Droniou (2007) for the EMEC Falls of Warness test site, and Guinot and le Boulleuec (2008) close to Brèhat island in Brittany, France, or recourse to non-deterministic modelling. Abonnel *et al.* used a combination of wave-buoy and ADCP measurements of water surface elevation – taken every 3 seconds – and flow velocity measurements at 1 m intervals from the seabed and report high frequency "flickering" in power as a result of wave interactions when compared with predictions from a numerical model. Norris and Droniou state – somewhat optimistically – that the wave induced current fluctuations penetrate 15 m down, while the seabed boundary layer pene-

(a) From EWEA (2012)

(b) From SUPERGEN Wind (2009)

Figure 1.6: Horns Rev offshore wind farm wake images.

trates 28 m up in a 45 m water column, leaving only 13 m of relatively quiescent flow. This is obtained from the contour (representing the crossing bins) of a “turbulence penetration parameter" equal to a $\pm 1\,\mathrm{m\,s^{-1}}$ fluctuation over a 10 s ADCP sample. In actuality, reduced magnitude wave effects can in fact be seen to penetrate far deeper than this and can have serious effects: Guinot and le Boulleuec (2008) use ADCP to record velocity shear of up to $10\,\mathrm{cm\,s^{-1}\,m^{-1}}$and fluctuations of $\pm 0.2\,\mathrm{m\,s^{-1}}$, which would result in substantial deviations from mean flow over a typical rotor diameter.

1.3.1.2 Boundary Effects and Wake Interactions in Arrays

Unlike wind turbines, tidal devices operate in a flow regime bounded on two or more sides. Since tidal devices are presently limited to shallow water (depth less than about 50 m due to cost restrictions associated with operating in deep water) the vertical expansion of the device wake is limited by proximity to both the water surface and the seabed. Generally, horizontal wake expansion is unlikely to be limited by proximity to flow boundaries except where the device is placed in an artificially narrow channel, for example at the Tidal Testing Centre at Den Oever in the Netherlands (TTC, 2012), where devices are trialled in a sluice gate in the dyke used to separate the Waddenzee and the IJsselmeer. The wakes from adjacent devices in arrays will produce interference in and alteration of the wake development. In laboratory conditions, for example tow-tanks and flumes, horizontal and vertical wake expansion are restricted by both facility walls and the free-surface if present. In general, device modelling using computational methods is absent of free-surface or other boundaries. The effect of flow boundaries can be positive – with device performance increased because of the flow acceleration caused by the device blockage in a narrow channel – and negative, where wake under-expansion reduces power and increases thrust compared to an isolated rotor.

The famous images of the wakes of the Horns Rev array of wind turbines, Fig. 1.6, indicates the longevity of the wakes in free atmospheric flow (unbounded, low turbulence). Unlike wind turbine wakes, the behaviour of marine turbine wakes will be strongly influenced by the flow boundaries, and it is possible that they might persist for considerably further than an equivalent wind turbine wake that is able to recover momentum from fluid above it. Turbine wakes, wind or tidal, reduce the potential power output of downstream rotors.

Blockage Full scale tidal devices may produce beneficial local impacts somewhat related to their apparent blockage of the tidal flow. Analytical models have been developed to

explore the upper limit of power extraction utilising the entire (in Garrett and Cummins, 2007) and partial (in Nishino and Willden, 2012) areas of a channel flow in the absence of a free-surface, and found it to be somewhat higher than the Betz limit (Nishino and Willden give an efficiency of around 0.8 for the entire channel). Whelan, Graham and Peiró (2009) expanded the Garrett and Cummins model to include a free surface and Vennell (2013) included a feedback mechanism to alter the channel velocity as a result of the array. The theoretical maximum power generation from a bounded hydraulic flow is due to the blockage effects generating a head-loss and commensurate velocity reduction. As blockage (equivalently extracted power) increases, the reduction in velocity decreases the power available to all devices as additional devices are installed. Above a certain maximum power blockage, the amount of power decreases with the cube of the velocity, until the case where the channel is completely blocked. In real world situations, this would generally be unlikely as – excepting barrage type arrangements – bypass flows would skirt the region where maximum power was extracted. This array would also be an environmental and economic disaster. For further discussion and analysis on available power and blockage subject, the interested reader is directed to Bryden *et al.* (2007), Iyer (2012) and Malki *et al.* (2013).

In experimental testing, flow boundaries exist in the walls of the tow-tank, flume or wind tunnel. It has long been observed that blockage effects can alter experimental readings (in the same way as in channel flows), and a range of correction methodologies exist. These encompass the Glauert (1926) thrust corrections for propellers, the Maskell (1963) correction for bluff bodies and the Barnsley and Wellicome (1992) and Sørensen and Mikkelsen methods (in Mikkelsen, 2003) for wind turbines. The International Towing Tank Conference (ITTC) Recommended Procedures and the EquiMar protocols provide guidance on corrections for tank testing turbines where free-surface effects can be neglected, and Whelan, Graham and Peiró (2009) proposes a Froude number correction for tidal turbine tests near a free-surface.

In all cases, the objective of correcting experimental results is to remove the idiosyncrasies of the facility (and often method) used from the results in order that they are as generally applicable as possible. Computational methods are slightly different. Due to the varying fidelity with which algebraic and numerical models approximate the flow physics, computer models are often calibrated and can also be "corrected" to better mimic experimental results. Examples are free-surface and blockage corrections for blade-element methods in Buckland (2013), or modelling facility walls directly in CFD, e.g. O'Doherty *et al.* (2009). The model developed herein is capable of capturing flow boundaries (either

via the boundary-element method, an Eulerian CFD method, or through vortex method approach based on treating boundaries as reflective surfaces – see Chapter 9 for discussion), however, in this thesis, results are presented for unbounded flows. This choice was taken to avoid additional complexity and overhead in preparing runs, generating data and analysing results. It also allows an opportunity to present the results obtained from the model in the simplest possible manner (in the spirit of the elemental validation steps in Appendix A.3.2). This rationale was aligned with the understanding that experimental results used in the validation cases are already corrected so the represent (as best as possible) free-stream conditions.

1.3.2 Smaller-scale Hydrodynamics

Close to the rotor, flow structures and interactions occur at much smaller scales. Even in experiments carried out “in-the-dry," it is difficult to obtain information other than pressure measurements. Intrusive measurements in air (hot-wire/hot-film anemometry) can provide very high-frequency, high-sensitivity three-dimensional velocity measurements, but only in a single location in the flow. Mounting the probe on a jig and phase-locking with a rotor can obtain time-averaged point-wise measurements of three-dimensional flowfields, but this method is slow and subject to experimental variation. Non-intrusive measurements, using laser-doppler anemometry (LDA) can also give point-wise measurements of a three-dimensional flowfield, but with the added problems associated with working with lasers. Particle-image-velocimetry (PIV) can provide “slices" of two- and three-dimensional velocities, including some measurement of time dependency, but again is limited due to the use of laser illumination. All methods require some statistical ensemblage of measurements and post-processing to remove low-quality results. In “wet” experiments, additions to these methods exist. Acoustic Doppler velocimetry (ADV) can be used alongside LDA, for example, and replaces the laser beams with sound pulses. However, this is still a point measurement. In general, techniques that are difficult to implement in-the-dry are significantly more difficult in-the-wet, and this translates into additional time and cost. This is especially so for sea-trials. Perhaps for these reasons, there is an apparent dearth in the literature of experimental data for flowfields in close proximity to tidal devices. Because of this, a large portion of the experimental fluid dynamics results of tidal devices is directly translated from wind-turbines or from naval propellers, and in general, tidal tests focus on systems performance or “large-scale” effects using small-scale rotors or proxies.

1.3.2.1 Three-dimensional and Transient Effects on Turbine Rotors

When describing the performance of an aero- or hydrodynamic shape it is typical to do so using coefficients based on the assumption of two-dimensional flow. In the context of a wing, this implies that the wing is of infinite length, and is thus useful in that quantities can be obtained "per-unit-length" etc. However, real wings are three-dimensional, and for various reasons lift is not constant along them, primarily since a relatively low pressure region generated on the lifting surface sucks higher pressure fluid around the tips of the wing. This generates a down-wash on the suction side, reduces lift towards the tips, and is responsible for the creation of rotating tip-vortices.

Turbine rotors are more complex still. In addition to the roll-off of lift at blade tips, turbine rotor blade boundary-layers are subject to Coriolis and centripetal accelerations due to experiencing the inflow in a rotating reference frame. This further modifies the boundary-layer from the two-dimensional ideal case (see Hansen *et al.*, 2006, for a discussion based on wind turbine aerodynamics).

Axial-flow turbine rotors in yaw or operating in tower-shadow and all cross-flow turbine rotors are subject to periodic inflow angle excursions that can set up complex three-dimensional flow-structures. Separation (and static stall) can be delayed and dynamic stall occurs when vortices are repeatedly shed from the leading edge and convect back over the upper and lower surfaces. This can significantly increase the local forces and moments.

Turbine rotor blades operating in velocity shear will experience transient inflow angles, and as the blade rotates it will experience pressure pulses (1 bar for every 10 m travelled vertically), which can influence cavitation characteristics.

1.3.2.2 Local Wake Effects

Trailing vortices are formed behind lift generating surfaces (wings) due to vorticity formed by viscosity in boundary layers on the high pressure surfaces becoming drawn out in a spanwise direction and around the wing-tip towards the suction surface. The boundary layer vorticity, initially (and in two dimensions) aligned with the axis of the wing is – due to the highly three-dimensional flowfield at the tip – realigned and redistributed such that a coherent vortex emerges at the wing-tip. Since the momentum and viscosity of the fluid prohibit the spanwise flow from wrapping completely around the wing, the vortex "emerges" from the wing around the half-chord at moderate angles of attack (moving forward as α increases), developing further as more fluid is entrained. The vorticity in the trailing vortices accounts initially for around 50 % of the bound vorticity of the wing: the remaining is shed in a viscous wake along the separation line (notionally the trailing

edge) and is quickly drawn into the trailing wing-tip vortices. The wake can be considered a continuous sheet that is drawn into the structure of the trailing vortices with inboard vorticity being drawn into the outer regions of the trailing vortex, and outboard vorticity forming the core.

Tip vortices develop local areas of low pressure on surfaces they pass, and down-wash reduces the angle of attack and thus lift at blade tips. It is therefore possible to temporarily increase the local lift-coefficient above a static stall C_l due to the low pressure associated with a passing vortex, either from the blade itself (in dynamic stall), or from an upstream blade (blade/vortex interaction).

1.3.2.3 Cavitation

Cavitation is the phase change from liquid to gas states that normally occurs by heating to a boil, but can also be obtained by a reduction in pressure. It is thus clearly never an issue on wind turbines, or other rotors that solely operate in gasses. Cavitation can be replicated successfully in appropriate laboratory conditions by dropping the pressure in the facility. When the local pressure increases above the vapour pressure, cavitation bubbles collapse at the local sonic velocity resulting in shock-waves and noise (in a traditional undergraduate experiment, cavitating flow in a Venturi sounds like rice or small stones rather than water flowing through the pipe). This can cause erosion of the blade surface and typically results in pitting on ship propellers that are not designed to cavitate – certain types of propellers are designed to operate under full or partial cavitation. Noise due to cavitation is also an environmental concern. Super-cavitation occurs when a large low pressure region builds up over the surface of the rotor and extends into the wake (the tip vortices are amongst the lowest pressure regions of the flow).

Tip vortex cavitation is a regular occurrence on the Marine Current Turbines SeaGen rotor-system, with bubbles observed on the surface from the wake system (SUPERGEN Marine, 2010). Proximity to the surface, and resulting decrease in pressure, increases the likelihood of cavitation. Therefore, waves that reduce the clearance between the top of the turbine and the free-surface may have a significant impact.

Cavitation can be predicted by first calculating a cavitation number for a given condition, defined as the ratio of the pressure difference between total absolute and vapour pressures to the freestream dynamic pressure, and comparing it to the local pressure coefficient (itself the ratio of the difference between total absolute and local pressure to freestream dynamic pressure). A critical cavitation number determines when cavitation will occur: above this number the pressure is too high, and cavitation will not occur. When

a model predicts a pressure coefficient that is equal to or below the critical cavitation number, cavitation can be expected.

Cavitation inception in tidal turbine is explored experimentally in Bahaj *et al.* (2007), and modelling is performed using various methods, for example blade-element/momentum theory in Bahaj *et al.* (2007) and Buckland *et al.* (2013), or using a boundary element method in Baltazar and Falcão de Campos (2011).

1.3.2.4 Compressibility

Unlike the flow towards the tips of a large wind turbine, the fluid flow around a tidal device is considered incompressible (as long as bubbles are absent). To double the pressure from 1 bar to 2 bar, approximately 10 m of water depth is required. This will achieve a reduction to 50 % in the volume of air in a balloon, but only a 0.000 05 % reduction in volume of water. This is because air is considerably more compressible than water: the bulk modulus of air is approximately 1×10^5 Pa whereas that of water is around 2×10^9 Pa. At 4 km depth, and 400 bar pressure, water volume occupied by a given mass will decrease by 1.8 %.

1.4 The Navier-Stokes Equations

The Navier-Stokes (NS) equations can be used to describe and model viscous fluid flow and, for the idealised incompressible flow around a marine current turbine, they are the following partial differential equations (Batchelor, 1967):

$$\nabla \cdot \boldsymbol{u} = 0; \tag{1.2a}$$

$$\frac{\partial \boldsymbol{u}}{\partial t} + \boldsymbol{u} \cdot \nabla \boldsymbol{u} = \boldsymbol{g} - \frac{1}{\rho}\nabla p + \nu \nabla^2 \boldsymbol{u}. \tag{1.2b}$$

Eq. (1.2a): the Continuity equation. An equation that enforces the conservation of mass – mass can neither be created nor destroyed, and mass flowing into a region must be balanced by mass flowing away from the region – written in terms of the fluid velocity;
Eq. (1.2b): the Momentum equations. One per spatial dimension, which describe the evolution of the fluid by essentially stating that the acceleration of a mass of fluid depends on the forces acting on it and in particular forces due to pressure and viscosity.

The standard form of the Navier-Stokes equations is written in “primitive-variable" form, with velocity and pressure being the primitive variables. In three-dimensional flows this results in a set of four equations that must be solved for the x,y and z momentum (velocity) and also the pressure – for the purposes of this thesis, the viscosity is an inten-

sive property of the fluid, known from the outset and which remains constant. A potential problem encountered using the Navier-Stokes equations is that the pressure field and the velocity field form an under-determined system, as the pressure does not feature in the continuity equation. This means that it is not possible to arrive at a closed form solution of these equations and – except in a small number of special cases – an iterative procedure must be used. Another potential problem that is common to all forms of the Navier-Stokes equations is that they describe flow physics over a huge range of time and length scales, from massive flows whose scales are of the order of tens or hundreds of kilometres or higher, right down to turbulence at millimetre scale. This gives rise to the concept of separating the flow scales into either the very quickly fluctuating (and usually very small) turbulence scales and the large-scale bulk characteristics of the flow. Unfortunately, these scales are extremely interdependent, since energy tends to flow from large to small flow-features and the entire cascade must be captured. Methods where turbulence is modelled as a property are based on observations from physical experiments and exact, analytical solutions, and each type of turbulence model can yield a different result for the same problem.

1.5 Computational Methods for Tidal Devices

The following section outlines the predominant modelling methods for tidal power devices. These are primarily aimed towards turbines.

1.5.1 Actuator Disc and Blade-Element type Approaches

1.5.1.1 Actuator Disc (Momentum) Theory

The idea – which has been around for almost 150 years (Rankine, 1865; Froude, 1889) – uses an infinitely thin actuator disc to represent the rotor. The relationship between thrust and power can be derived and, by introducing an induction factor, expressions for rotor performance can be obtained. Two expressions exist: one each for axial and rotational effects. Momentum theory only considers the average performance of the rotor, under a number of strict simplifications. It is only when combined with a blade-element approach that it becomes useful as a design tool, however, the relations between overall rotor thrust, power and induction factor are applicable to any analysis (e.g. experimental or CFD results), and the ability to calculate the momentum change due to an actuator disc can be used as a momentum source/sink in CFD methodologies.

1.5.1.2 Blade-Element/Momentum Theory

The classic turbine rotor analysis method is based on a conjoining of Froude's momentum theory with extension to a combined blade-element/momentum theory (BEMT), originally for aircraft propellers (Glauert, 1926). A full description of the most basic BEMT can be found in e.g. Hansen (2007) but large numbers of modifications exist and common extensions can be found in e.g. Burton *et al.* (2011), amongst others.

BEMT improves the momentum theory analysis by considering the loading along the rotor blades as a function of the section characteristics of the rotor aerofoils. The method divides the rotor into a number of concentric annuli that are assumed independent of one-another. A force and momentum balance is performed over each annulus, using the induction factor obtained via momentum theory to calculate the local angle of attack and therefore the lift and drag from knowledge of the local section characteristics. An average of the wake and upstream velocities (obtained via momentum theory) is used to calculate the resultant velocity at the rotor, from which rotor force (and torque) is obtained, and then a momentum balance is applied. This process, although iterative, is exceptionally quick on modern computers, and relatively simple to program. As such, it remains the principal analysis method used in designing new rotors where optimisation routines – such as genetic algorithms – require analysis of a large population of potential rotors.

The principal shortcomings of the method are that it assumes azimuthally averaged inflow around the rotor – in other words it only provides a time averaged solution valid only for inflow parallel to the rotor axis. Various extensions have been proposed for including the effects of yaw (such as the cos-cubed adjustment described above), admitting certain temporal effects, and work has been undertaken to overcome this limitation using dynamic stall models, dynamic inflow models and wake modelling.

There is also a dependence on the availability of high quality section data, at the right Reynolds number, for the aerofoil sections of interest. This was highlighted in Coton, Wang and Galbraith (2002) with regards to the NREL UAE blind comparison exercise (Simms *et al.*, 2001). Extensions, e.g. those in Le Pape and Lecanu (2004) propose using CFD results to provide section data.

Finally, the method does not naturally provide any useful data about the effects of the turbine on the flowfield beyond far-field conditions obtained via momentum theory. Certainly temporal variation in flowfield is not obtained from the method without extension e.g. Chaney and Eggers (2002) or the potential flow wake inflow model HAWTDAWG added to the NREL code AeroDyn in Wang and Coton (2001). As with actuator disc models, steady-state output from BEMT can be coupled with CFD methods for wake and array

modelling, as in e.g. Harrison, Batten and Bahaj (2010) or Malki *et al.* (2013) – see Section 3.2.1.2 for further discussion. Prominent BEMT codes employed in analysis of tidal turbine rotors are the commercial code developed by GL Garrad Hassan – TIDALBLADED (Bossanyi, 2008), the open-source code developed by NREL – AERODYN (Moriarty and Hansen, 2005), and there are various university in-house codes, e.g. SWANBEMT developed at Swansea University (in Masters *et al.*, 2011; Buckland, 2013), SERG-TIDAL developed at Southampton University (in Batten *et al.*, 2007), and the various standard and coaxial BEMT codes developed at the University of Strathclyde (in e.g. Barltrop *et al.*, 2005; McCombes, Johnstone and Grant, 2011).

1.5.1.3 The (Double) Multi Stream-tube Method

The stream-tube method is a formulation of the BEMT for cross-flow devices. Various versions exist, with the earliest due to Strickland (1975), which considers the rotor modelled as a single actuator disc. Improved versions use two discs (Paraschivoiu, 1981); one for the upstream and one for the downstream blade passages – hence *double* multi stream-tube. As with BEMT, an iteration is performed on an induction factor, based on momentum considerations applied individually to a number of stream-tubes passing through the rotor.

1.5.2 Boundary-Element Methods

Boundary-Element Methods (BEMs), synonymous in this thesis with panel methods, solve the linearised flow equations obtained by neglecting viscosity and assuming small perturbations. The flow is described by the Laplace equation. This effectively translates the unsteady problem from an Eulerian, volumetric approach to a Lagrangian, surface orientated approach. The method – and its history, methodology and application – are discussed in Chapter 4, but the primary aspects of the model that are relevant to this thesis are in the way it handles wakes. In particular, the model can either be:

- a fixed-wake model, in that the wake is essentially fixed in advance of this calculation using, e.g. a screw-surface. This is clearly not predictive;
- a free-wake model, in that the wake is allowed to evolve freely over the calculation. This is problematic as the evolving wake becomes more and more unstable due to accumulation of errors; or
- a wake-relaxation model, which starts with a presumed wake shape, and relaxes it into a final position such would be accomplished if the wake were allowed to evolve. This mitigates – to a certain extent – the problems with the first two models, however

is not really an option for unsteady flows where, e.g. wakes and structures interact, or there are multiple strongly interacting wakes.

The wake geometry in any case can be represented by either panels, filaments or points. Prominent BEM codes used to model tidal turbines are introduced in Chapter 4.

1.5.3 Computational Fluid Dynamics

At the other end of the computational scale from BEMT, Computational Fluid Dynamics (CFD) methods are – in principle – able to fundamentally treat the vast majority of the pertinent flow physics. Practical CFD involves a solution to the Reynolds-averaged Navier-Stokes equations (RANS) discretised onto a volumetric computational mesh with suitable boundary conditions. This Eulerian basis does, however, pose a number of issues that currently limit the effectiveness of CFD in treating rotor fluid dynamics. Solid surfaces (e.g. blades) must be represented with sufficient detail to accommodate small-scale fluid phenomena, for example the near-field effects associated with the development of the boundary layer. On the other hand, sufficient evolution of the wake must be allowed to capture the major physics and prevent violation of the outflow boundary conditions. To model wakes correctly, it has been suggested that in order to fully resolve a tip vortex at least 15 points are required across the core (Dacles-Mariani *et al.*, 1995). Since the wake can persist many chord-lengths downstream this poses a dilemma: for a given finite computational outlay, resource (read cells/memory/CPU time) can either be clustered to capture the rotor flowfield or the wake. Generally the objective is the resolution of the rotor surface and associated shear layers, and this gives rise to very aggressive mesh sizing functions in order to capture a sufficient fluid domain in order to fully encapsulate the distant boundary conditions.

The most important challenge in rotor modelling is concerned with artificial (i.e. numerical) dissipation of the wake, and is a manifestation of the grid-based solution itself. The diffusion occurs due to the coupled facts that:

1. the grid must be a reasonable shape, preferably hexahedral to avoid too much interpolation, thus the surfaces of the elements are not necessarily aligned with the local velocities; and

2. the discretised governing equations themselves must be of sufficient accuracy to make the computation worthwhile.

The problems associated with Item 1 are intuitive and most significant: the transported variables are smeared spatially over the mesh due to an inability to translate small fea-

tures without distributing them between neighbouring cells – this is similar in cause and effect to the distortion of computer images which is observed when performing small rotations. This gives rise to problems associated with Item 2 that are a result of the fact that in order to reduce this effect, a higher-order discretisation scheme must be used. LeVeque (2002) describes the reasons for the artificial diffusion, i.e. the introduction of an erroneous Laplacian term in the modified equation (the equation actually solved when the solution to a PDE is sought by discretising on a finite-volume mesh). Comparison between the coefficients of this and the Newtonian viscosity will yield the relative impact of both – in one dimension for the first-order upwind scheme, the artificial viscosity coefficient is $\frac{1}{2}uh(1-C)$, where u is the local velocity, h is the cell spacing and C is the Courant number – essentially the ratio between the distance covered by a convected quantity during a time-step and the cell spacing. A $C > 1$ implies that a transported variable will skip over a computational cell during the time-step. Unless a numerical method is used where future values of transport variables are used as part of the solution strategy via simultaneous equations (known as an implicit method), this will result in an unstable scheme. The Courant number therefore provides an upper limit on time-step duration. Since the time-step is applied uniformly over cells with different h and C must be less than unity in all cells, the cell with the highest C determines the time-step length. This increases the number of time-steps globally and thus the number of applications of the artificial diffusion term. A similar analysis on higher order methods reveals nonzero coefficients on the third and other odd-order derivatives, equivalent to non-physical dispersion terms. Whereas dissipation results in amplitude errors, dispersion results in phase errors resulting in oscillations in the solution around discontinuities that must be damped via an additional artificial viscosity.

1.6 Purpose of this Thesis

Problem Statement The inflow to a tidal turbine is unsteady and three-dimensional. Of the various sources of this unsteady three-dimensional flowfield, the most important to capture if the device performance is to be adequately parameterised is due to the wake. However, traditional computational methods do not adequately capture the wake induced effects over the surfaces of a tidal device. This is because:

- Blade-element/momentum theory is steady-state/azimuthally averaged and contains no information on radial flow or wake development
- Boundary-element methods have difficulties in developing wakes because Lagrangian,

free-wake models result in “spaghettification” or sparsification of the wake and wake-relaxation methods are not unsteady

- Primitive-variable RANS CFD artificially smears the wake structure because it focusses resources away from the wake. If this wake is resolved simulations become prohibitively expensive.

Purpose of this Thesis The purpose of this thesis is to describe an improved engineering model that increases the predictive capability of boundary-element methods, specifically those used in modelling marine current turbines. The work seeks to address the issue of adequately modelling the wake generated by a tidal current turbine (or in fact any hydrodynamically similar device, e.g. propeller or hydrofoil) when the turbine itself is modelled in a boundary-element method framework. The abilities that are required to be addressed by the formulation of the proposed method are:

1. the ability to model fully three-dimensional bodies, that is bodies where the surface pressure distribution is required in order to calculate forces and moments on – in particular – turbine blades;

2. the ability to capture and preserve the wake due to the generation of lift by these bodies (bluff-body and viscous wakes are not considered); and

3. the ability to generate the large and complex flowfields associated with arrays of several devices.

To this end, a wake modelling strategy from the rotorcraft community has been adopted – although it is now seeing use in tidal turbine work – and coupled with a boundary-element method commonly used in the naval propeller community – again seeing use in tidal turbine work. This work builds on previous methods of wake modelling by extending the rotorcraft method to three-dimensional lifting bodies, rather than a solution based on lookup tables and lifting lines, and it extends the BEM methodology away from the traditional panel wake and less traditional “blob” wake methods.

The principal shortcomings of the rotorcraft method are that the differential in inflow across the surface of the blades is not captured since only the velocity at a single control point per blade element is used. Therefore, pitching moment excursions due to – for example – blade vortex interactions are not fully captured. The issues associated with the traditional BEM approach are that it is particularly difficult to ensure that the boundary conditions associated with the wake are satisfied, especially as the duration of the calculation increases since the wake shape cannot be known a priori. Free-wake methods – where

the evolution of the wake is calculated at each time-step – can become prohibitively costly due to the number of degrees of freedom, and methods such as wake relaxation are limited in both the complexity of the scenario, e.g. the number of wakes, as well as the number of wake elements.

The contribution of this work, therefore, is the development and analysis of the combined methodology of turbine and wake modelling described herein, the generation of performance metrics for the method in terms of applicability, and new results for problems that have not been addressed using other methods. In particular, the method by which the boundary-element method is coupled in both directions with the finite-volume method is a novel hybrid method with application of the vortex re-gridding strategy employed in mesh free and meshed vortex methods.

1.7 Structure of this Thesis

This expositional Chapter has identified the argument for renewable energy and elucidated the potential role tidal power might play fulfilling that requirement. The basic premise behind the main tidal power concepts has been described, with a brief explanation of their means of operation and their fluid dynamics. The Navier-Stokes equations governing fluid flow have been introduced. A perspective on the present approach to modelling tidal devices is given, followed with comparisons of methods and lessons from related fields and it concludes with a statement of intent for this thesis.

Chapter 2 describes the evolution and development of vortex models for fluid dynamics. The vorticity transport equations are introduced, and methods associated with vorticity flow solvers are discussed. Interpolation kernels and the means to recover the velocity from the vorticity field are discussed and a précis of the development of the methods most pertinent to this thesis is given.

Chapter 3 introduces RANS type finite-volume approaches to the tidal turbine modelling before presenting a finite-volume method for the unsteady Navier-Stokes equations in vorticity-velocity form. Subsequent sections describe particular issues associated with linearising and discretising the convection and diffusion terms for the general transport equation. Unsteady, high resolution, non-linear schemes are given for the vorticity transport equations in two- and three-dimensions.

Chapter 4 provides an overview of the history of boundary-element methods of the “panel-code" type, their use in fields related to tidal energy, and describes the mathematical formulation of the BEM in the proposed method. The theoretical justification and basis of utilising an inviscid model are given with a description of the approximations to the

surfaces that are used to describe the problem and their associated boundary conditions. The practical means of generating a unique (and “correct") solution to the boundary value problem are presented.

Chapter 5 describes the methodology of this thesis, including detail on the novel components introduced in Section 1.6, above. A brief description of the domain decomposition methods used in this work, and an implementation of the fast-multipole method to recover the velocity field is given. The performance of this portion of the method is crucial to the success of the method as a whole, since this represents the most costly part in terms of both computational overheads and errors, and these are evaluated for the method as applied.

Chapter 6 contains unit-tests and proof-of-concept studies in one- and two-dimensions for the proposed method. The performance in simple tests is analysed by comparison to analytical methods. One-dimensional test cases compare different diffusion and advection schemes for continuous and discontinuous initial data; two-dimensional tests examine the performance of difference schemes for multidimensional advection only problems using diagonal and rotating flow. The performance of the vorticity-transport solver in two-dimensions is examined in the absence of a boundary-element method by modelling the relaxation of a perturbed monopole into a tripole attractor, with comparison to results from the literature. The combined BEM/vorticity-solver is tested using a static hydrofoil, again with comparison to the literature. An oscillating foil is used to test the unsteady components of the model, with comparison to analytical results.

Chapter 7 contains unit-tests and proof-of-concept studies in three-dimensions. The solution of flows about non-lifting bodies tests the three-dimensional BEM component of the method in isolation. The flow about a static hydrofoil is modelled to test the combined three-dimensional BEM/vortex model, with comparison to experimental results from the literature. Finally, the flow about the NREL Phase VI and the flow about the Southampton University model turbine is presented, with experimental and inter-model comparisons, respectively.

Chapter 8 contains some exemplar cases in three-dimensions: the flow around several array configurations is presented and the performance of a coaxial, contra-rotating turbine is analysed.

Chapter 9 presents conclusions and recommendations for future work.

References

Abonnel, C., Achard, J.L., Archer, A., Buvat, C., Guittet, L., Lénès, A., Maître, T., Maniati, M., Peyrard, C., Renaud, T. and Violeau, D. (2005). “Some aspects of EDF modelling and testing activities, within its marine current energy research and development project.”

In "Proceedings of the 6th European Wave and Tidal Energy Conference (EWTEC2005)," Glasgow, Scotland.

Bahaj, A., Molland, A., Chaplin, J. and Batten, W. (2007). "Power and thrust measurements of marine current turbines under various hydrodynamic flow conditions in a cavitation tunnel and a towing tank." *Renewable Energy*, **32**(3): pp. 407–426.

Baltazar, J. and Falcão de Campos, J.A.C. (2011). "Hydrodynamic analysis of a horizontal axis marine current turbine with a boundary element method." *Journal of Offshore Mechanics and Arctic Engineering*, **133**(4).

Barltrop, N., Grant, A., Varyani, K.S. and Pham, X.P. (2005). "Wave-current interactions in marine current turbines." In "Proceedings of the 6th European Wave and Tidal Energy Conference (EWTEC2005)," Glasgow, Scotland.

Barnsley, M. and Wellicome, J. (1992). "Wind tunnel investigation of stall aerodynamics for a 1.0 m horizontal axis rotor." *Journal of Wind Engineering and Industrial Aerodynamics*, **39**(1–3): pp. 11–21.

Batchelor, G.K. (1967). *An Introduction to Fluid Dynamics*. Cambridge Univ Press.

Batten, W., Bahaj, A., Molland, A. and Chaplin, J. (2007). "Experimentally validated numerical method for the hydrodynamic design of horizontal axis tidal turbines." *Ocean Engineering*, **34**(7): pp. 1013–1020.

BERR (2008). "Atlas of UK marine renewable energy resources." Tech. rep., BERR.

Black & Veatch (2005). "Phase II UK tidal stream resource assessment." Tech. rep., The Carbon Trust.

Black & Veatch (2011). "UK tidal current resource & economics." Tech. rep., Carbon Trust.

Blunden, L.S. and Bahaj, A.S. (2006). "Initial evaluation of tidal stream energy resources at Portland Bill, UK." *Renewable Energy*, **31**(2): pp. 121–132.

Bossanyi, E.A. (2008). "GH Tidal Bladed Theory Manual." Tech. rep., Garrad Hassan and Partners, Ltd.

Bryden, I., Couch, S., Owen, A. and Melville, G. (2007). "Tidal current resource assessment." *Proceedings of the Institution of Mechanical Engineers, Part A: Journal of Power and Energy*, **221**(2): pp. 125–135.

Buckland, H. (2013). *Combined Current, Wave and Turbulent Flows and their Effects on Tidal Energy Devices*. Ph.D. thesis, Swansea University.

Buckland, H.C., Masters, I., Orme, J.A. and Baker, T. (2013). "Cavitation inception and simulation in blade element momentum theory for modelling tidal stream turbines." *Proceedings of the Institution of Mechanical Engineers, Part A: Journal of Power and Energy*, **227**(4): pp. 479–485.

Burton, T., Jenkins, N., Sharpe, D. and Bossanyi, E. (2011). *Wind Energy Handbook*. Wiley-Blackwell, London, 2nd edn.

Chaney, K. and Eggers, A.J. (2002). "Expanding wake induction effects on thrust distribution on a rotor disc." *Wind Energy*, **5**(2-3): pp. 213–226.

Clarke, J., Connor, G., Grant, A. and Johnstone, C. (2007). "Design and testing of a contra-rotating tidal current turbine." *Proceedings of the Institution of Mechanical Engineers, Part A: Journal of Power and Energy*, **221**(2): pp. 171–179.

Coton, F.N., Wang, T. and Galbraith, R.A.M. (2002). "An examination of key aerodynamic modelling issues raised by the NREL blind comparison." *Wind Energy*, **5**(2-3): pp. 199–212.

Dacles-Mariani, J., Zilliac, G.G., Chow, J.S. and Bradshaw, P. (1995). "Numerical/experimental study of a wingtip vortex in the near field." *AIAA Journal*, **33**(9): pp. 1561–1568.

DCP Strategic Communication Ltd (2012). "Bord Gáis and OpenHydro Awarded Lease to Develop Northern Ireland's First Tidal Energy Farm." Press Release on behalf of Tidal Ventures Ltd.

DECC (2012). "Digest of UK energy statistics, chapter 5." Tech. rep., DECC.

DTI (2005a). "Development, installation and testing of a large scale tidal current turbine." Tech. Rep. T/06/00210/00/REP; URN 05/1698, DTI.

DTI (2005b). "Stingray tidal stream energy device – Phase 3." Tech. Rep. T/06/00230/00/REP; URN 05/864, DTI.

EWEA (2012). URL `http://www.ewea.org`.

Fraenkel, P. (2007). "Marine current turbines: Pioneering the development of marine kinetic energy converters." *Proceedings of the Institution of Mechanical Engineers, Part A: Journal of Power and Energy*, **221**(2): pp. 159–169.

Fraenkel, P. (2010). "Development and testing of Marine Current Turbines' SeaGen 1.2MW tidal stream turbines." In "Proceedings of the 3rd International Conference on Ocean Energy (ICOE2010)," Bilbao, Spain.

Froude, R., E. (1889). "On the part played in propulsion by differences of fluid pressure." *Transactions of the Institution of Naval Architects*, **39**: p. 390.

Garrett, C. and Cummins, P.F. (2007). "The efficiency of a turbine in a tidal channel." *Journal of Fluid Mechanics*, **588**: pp. 243–251. ISSN 1469-7645. URL `http://journals.cambridge.org/article_S0022112007007781`.

Glauert, H. (1926). *The Elements of Airfoil and Airscrew Theory*. Cambridge University Press.

Guinot, F. and le Boulleuec, M. (2008). "Realistic marine flow conditions for current turbines studies." In "Proceedings of the 2nd International Conference on Ocean Energy (ICOE2008)," Brest, France.

Hammerfest Strøm AS (2012). URL `http://www.hammerfeststrom.com`.

Hansen, M.O.L., Sørensen, J.N., Voutsinas, S., Sørensen, N. and Madsen, H.A. (2006). "State of the art in wind turbine aerodynamics and aeroelasticity." *Progress in Aerospace Sciences*, **42**(10): pp. 285–330.

Hansen, M.O.L. (2007). *Aerodynamics of Wind Turbines*. Earthscan, London; Sterling, VA, 2nd edn.

Harrison, M.E., Batten, W.M.J. and Bahaj, A.S. (2010). "A blade element actuator disc approach applied to tidal stream turbines." In "Proceedings of the OCEANS Conference," Sydney, Australia.

Holmes, B. and Devaney, T. (2011). "Investigation of the fundamental operation of a novel tidal energy device at circa 1:16 scale Tidal Flyer Junior." In "Proceedings of the 9th European Wave and Tidal Energy Conference (EWTEC2011)," Southampton, England.

Iyer, A.S. (2012). *New methodologies and scenarios for evaluating tidal current energy potential*. Ph.D. thesis, The University of Edinburgh, Edinburgh, Scotland.

Kloos, G., Gonzalez, C.A. and Finnigan, T.D. (2009). "The bioSTREAM^{TM}tidal current energy converters." In "Proceedings of the 8th European Wave and Tidal Energy Conference (EWTEC2009)," Uppsala, Sweden.

Kloos, G., Benitez, Z. and Gonzalez, C.A. (2011). "The bioWAVE and bioSTREAM test unit." In "Proceedings of the 9th European Wave and Tidal Energy Conference (EWTEC2011)," Southampton, England.

Le Pape, A. and Lecanu, J. (2004). "3D Navier-Stokes computations of a stall-regulated wind turbine." *Wind Energy*, **7**(4): pp. 309–324.

LeVeque, R.J. (2002). *Finite Volume Methods for Hyperbolic Problems*. Cambridge texts in applied mathematics.

Lunar Energy Ltd. (2012). URL `http://www.lunarenergy.co.uk/`.

Malki, R., Williams, A., Croft, T., Togneri, M. and Masters, I. (2013). "A coupled blade element momentum – computational fluid dynamics model for evaluating tidal stream turbine performance." *Applied Mathematical Modelling*, **37**(5): pp. 3006–3020.

Maskell, E. (1963). "A theory of the blockage effects on bluff bodies and stalled wings in a closed wind tunnel." Tech. rep., Aeronautical Research Council, London.

Masters, I., Chapman, J., Orme, J. and Willis, M. (2011). "A robust blade element momentum theory model for tidal stream turbines including tip and hub loss corrections." *Proceedings of IMarEST - Part A - Journal of Marine Engineering and Technology*, **10**(1): pp. 25–35.

McCombes, T., Johnstone, C. and Grant, A. (2011). "Navier-Stokes modelling for contra-rotating tidal turbines." In "Proceedings of the 9th European Wave and Tidal Energy Conference (EWTEC2011)," Southampton, England.

Mikkelsen, R. (2003). *Actuator Disc Methods Applied to Wind Turbines*. Ph.D. thesis, Technical University of Denmark.

Moriarty, P. and Hansen, A. (2005). "AeroDyn theory manuals." Tech. Rep. NREL/TP-50-36881, NREL.

Mueller, M. and Wallace, R. (2008). "Enabling science and technology for marine renewable energy." *Energy Policy*, **36**(12): pp. 4376–4382.

Nishino, T. and Willden, R.H.J. (2012). "The efficiency of an array of tidal turbines partially blocking a wide channel." *Journal of Fluid Mechanics*, **708**: pp. 596–606.

Norris, J.V. and Droniou, E. (2007). "Update on EMEC activities, resource description, and characterisation of wave-induced velocities in a tidal flow." In "Proceedings of the 7th European Wave and Tidal Energy Conference (EWTEC2007)," Porto, Portugal.

O'Doherty, D., Mason-Jones, A., O'Doherty, T. and Byrne, C. (2009). "Experimental and computational analysis of a model horizontal axis tidal turbine." In "Proceedings of the 8th European Wave and Tidal Energy Conference (EWTEC2009)," Uppsala, Sweden.

OpenHydro Group Ltd. (2012). URL `http://www.openhydro.com/home.html`.

Paish, M., Giles, J. and Panahandeh, B. (2010). "The pulse stream concept, and the development of the pulse stream commercial demonstrator." In "Proceedings of the 3rd International Conference on Ocean Energy (ICOE2010)," Bilbao, Spain.

Paraschivoiu, I. (1981). "Double-multiple streamtube model for darrieus wind turbines." In R. W. Thresher (ed.), "Wind Turbine Dynamics," pp. 19–25.

Ponte di Archimede International S.p.A. (2012). URL http://www.pontediarchimede.com/.

Pulse Tidal Ltd. (2012). URL http://www.pulsetidal.com.

Rankine, W., J.M. (1865). "On the mechanical principles of the action of propellers." *Transactions of the Institution of Naval Architects*, **6**: pp. 13–39.

Salter, S. and Taylor, J. (2007). "Vertical-axis tidal-current generators and the Pentland Firth." *Proceedings of the Institution of Mechanical Engineers, Part A: Journal of Power and Energy*, **221**(2): pp. 181–199.

Salter, S. (2009). "Correcting the under-estimate of the tidal-stream resource of the Pentland Firth." In "Proceedings of the 8th European Wave and Tidal Energy Conference (EWTEC2009)," Uppsala, Sweden.

Savage, A. (2007). "Tidal Power in the UK - Tidal technologies overview." Tech. Rep. 19495 C055i2, Sustainable Development Commission.

Simms, D., Schreck, S., Hand, M. and Fingersh, L.J. (2001). "NREL Unsteady Aerodynamics Experiment in the NASA-Ames wind tunnel: A comparison of predictions to measurements." Tech. Rep. NREL/TP-500-29494, NREL.

Strickland, J. (1975). "The Darrieus turbine: A performance prediction model using multiple streamtubes." Tech. Rep. SAND75-0431, Sandia National Laboratory.

SUPERGEN Marine (2010). *SUPERGEN Marine Doctoral Training Workshop Course Materials*. Edinburgh University.

SUPERGEN Wind (2009). "Research monograph." Tech. rep., SUPERGEN Wind Energy Technologies Consortium.

the Scottish Executive (2006). "Matching renewable electricity generation with demand." Tech. rep., The Scottish Executive.

Tidal Sails AS (2012). URL http://tidalsails.com/.

TTC (2012). URL http://www.tidaltesting.nl.

Vennell, R. (2013). "Exceeding the Betz limit with tidal turbines." *Renewable Energy*, **55**(0): pp. 277–285.

von Schultz, C. (2013). "Sänker långsamt kraftverk i Dalälven." Newspaper article in Ny Teknik. URL http://www.nyteknik.se/nyheter/energi_miljo/vattenkraft/article3651848.ece.

Wang, T. and Coton, F.N. (2001). "A high resolution tower shadow model for downwind wind turbines." *Journal of Wind Engineering and Industrial Aerodynamics*, **89**(10): pp. 873–892.

Whelan, J.I., Graham, J.M.R. and Peiró, J. (2009). "A free-surface and blockage correction for tidal turbines." *Journal of Fluid Mechanics*, **624**: pp. 281–291. ISSN 1469-7645.

Yuen, K., Lundin, S., Grabbe, M., Lalander, E., Goude, A. and Leijon, M. (2009). "The Söderfors Project: Construction of an experimental hydrokinetic power station." In "Proceedings of the 8th European Wave and Tidal Energy Conference (EWTEC2009)," Uppsala, Sweden.

2

Vortex Methods for Modelling Two- and Three-Dimensional Fluid Flow

2.1 Introduction

Vortex methods are a mature and established computational fluid dynamics approach, to the extent that there are several books on the subject (e.g. those of Cottet and Koumoutsakos, 2000; Majda and Bertozzi, 2001) and there have been a number of review papers (spanning Leonard, 1980; Koumoutsakos, 2005 or Winckelmans *et al.* 2005). Vortex models have gone from just about being able to model sheet rollup in two dimensions to billion-particle simulations of aircraft wakes in three dimensions, and this rise can be attributed to a combination of a concerted effort to establish a theoretical basis for the models, coupled to an exponential rise in computational capability.

2.1.1 The Vorticity Transport Equations

Instead of describing the fluid flow in terms of the linear momentum of fluid elements, an alternative is the vorticity form of the Navier-Stokes equations. These describe the flow by considering the amount of rotation undergone by small parcels of fluid. The vorticity-velocity form of the Navier-Stokes equations, rather than the pressure-velocity form described in Section 1.4, is obtained by taking the curl (applying a particular mathematical transform) to the primitive-variable form of the equations (Eqs. 1.2). This process is mathematically exact and, according to a number of identities, results in equations describing the fluid flow as follows:

$$\nabla \cdot \boldsymbol{u} = 0; \tag{2.1a}$$

$$\boldsymbol{\omega} = \nabla \times \boldsymbol{u}; \tag{2.1b}$$

$$\frac{\partial \boldsymbol{\omega}}{\partial t} + (\boldsymbol{u} \cdot \nabla)\,\boldsymbol{\omega} = (\boldsymbol{\omega} \cdot \nabla)\,\boldsymbol{u} + \nu \nabla^2 \boldsymbol{\omega}; \tag{2.1c}$$

$$\nabla^2 \boldsymbol{u} = -\nabla \times \boldsymbol{\omega}. \tag{2.1d}$$

Eq. (2.1a): the continuity equation. A mass conservation equation, as in Section 1.4.

Eq. (2.1b): the definition of vorticity. The relationship defining the vorticity field in terms of curl of the velocity field (i.e. a description of the mathematical transform).

Eq. (2.1c): the vorticity transport equations. One (in two dimensions) or three (in three dimensions) equations describing the evolution of the vorticity field, essentially that the spatial and temporal acceleration of vorticity carried (convected) by the fluid is determined by the velocity and forces acting on the fluid, and in particular those due to viscosity (in two and three dimensions) and the conservation of angular momentum (in three dimensions only, known as the "tilting" or "stretching" term).

Eq. (2.1d): the Poisson equation. This relates the velocity and vorticity. The vorticity-transport equations are solved when a means of inverting this expression is combined with the other equations, resulting in a description of the velocity in the flow in terms of the vorticity field.

2.1.2 Rationale

The advantages of the vorticity-velocity form of the Navier-Stokes equations are well documented, e.g. Speziale (1987), Gharakhani (1997) and Brown and Line (2005). The most often cited advantages are:

- the vorticity-velocity form of Navier-Stokes eliminates the requirement for solution of a pressure Poisson equation and inherently satisfies the continuity equation: the only flow variables are velocity and vorticity;
- the evolution of vorticity in the flow can be tracked in a Lagrangian manner, so that computational resources are automatically focussed on regions of interest in a dynamic, solution dependant manner; and
- using appropriate tools and methods, convection can be modelled with minimal artificial diffusion.

However, there are also some significant shortcomings:

- boundary conditions are difficult to implement, especially in three dimensions;

- the vorticity form of the Navier-Stokes equations still requires a means of capturing or modelling turbulence when used to simulate multi-scale flows;
- calculating the velocity field due to a vorticity field is notoriously time-consuming if done directly, and inexact and difficult otherwise;
- if a Lagrangian method is used and the distribution of markers is irregular, it becomes challenging to calculate the gradients of vorticity and velocity; and
- vortex methods using Lagrangian methods are only convergent if their representation of the vorticity field is smooth: this minimally requires that the elements overlap.

2.1.3 Biot-Savart Law to Recover Velocity

Recalling (from high-school physics) Ampere's law for electromagnetics, written in differential form as $\nabla \times \boldsymbol{B} = \mu_0 \boldsymbol{J}$, and observing its similarity to the definition of vorticity as the curl of the velocity field, the Biot-Savart law can be co-opted to provide a Green's function solution for the velocity at $\boldsymbol{x}$ due to a distribution of vorticity in volume Ω:

$$\boldsymbol{u}(\boldsymbol{x}, t) = -\frac{1}{4\pi} \int_{\Omega} \frac{\boldsymbol{x} - \boldsymbol{y}}{|\boldsymbol{x} - \boldsymbol{y}|^3} \times \boldsymbol{\omega}(\boldsymbol{y}, t) \, \mathrm{d}\boldsymbol{y}. \tag{2.2}$$

2.1.4 Stokes' and Kelvin's Theorem

This thesis is concerned with vector fields, specifically the velocity field $\boldsymbol{u}(\boldsymbol{x}, t)$, which denotes the flow velocities in the computational domain, and the vorticity field $\boldsymbol{\omega}(\boldsymbol{x}, t)$, which is equal to the curl of the velocity field. A concept relating velocity and vorticity is that of circulation, denoted Γ, which is, broadly speaking, a measure of the amount of flow rotation about a point. Circulation is defined as the line integral of fluid velocity around a closed contour, and is related to the average vorticity over the enclosed area by Stokes' theorem and the mean value theorem:

$$\Gamma(t) = \oint_{C(t)} \boldsymbol{u}(\boldsymbol{x}, t) \cdot \mathrm{d}\boldsymbol{l} = \iint_{S(t)} \nabla \times \boldsymbol{u}(\boldsymbol{x}, t) \cdot \mathrm{d}\boldsymbol{S}. \tag{2.3}$$

So in the limiting case for an infinitesimally small area, i.e. a point,

$$\boldsymbol{\omega}(\boldsymbol{x}, t) = \frac{\mathrm{d}\Gamma}{\mathrm{d}\boldsymbol{S}} \equiv \frac{\Gamma}{\widehat{\boldsymbol{S}}(\boldsymbol{x}, t)} \delta(r), \tag{2.4}$$

where $\widehat{\boldsymbol{S}}(\boldsymbol{x}, t)$ is the unit vector normal to the enclosed surface and δ is the Dirac delta for the radial distance r from the point, perpendicular to the surface normal $\boldsymbol{S}$. In other words,

the vorticity at a point can be parameterised using the perpendicular to the infinitesimal "area" of the point giving an axis for the circulation associated with the point.

Kelvin's theorem states

$$\frac{\partial \Gamma}{\partial t} + \boldsymbol{u} \cdot \nabla \Gamma = 0, \tag{2.5}$$

which, when cast into a Lagrangian framework (a method where the convection term is dealt with using Lagrangian markers), implies that the circulation associated with a marker will remain constant in time.

There are three essential components to every vortex dynamics model

1. a discrete representation of the vorticity, capable of tracking the vorticity in space,
2. an adaptive method to maintain the spatial resolution as simulation time advances, and
3. a quadrature scheme for evaluating the Biot-Savart integral.

The remainder of this chapter is split into three sections, addressing these in turn.

2.2 Hybrid (Meshed) Models

Meshed Lagrangian models are only meshed in the sense that at certain stages in the calculation various parameters of the Lagrangian markers are transferred onto a mesh to facilitate either a calculation, such as approximating a gradient by finite-differences, or to allow re-distribution of the parameters of the underlying markers. Hybrid models use a combination of vorticity field representation by Lagrangian markers and an Eulerian mesh which tracks the marker distribution. The objective of this method is to reduce the errors introduced by the increasing distortion and irregularity in the spacing and location of the Lagrangian markers. The method is used to re-initialise the Lagrangian model. By first subsuming the Lagrangian vorticity field onto the mesh , then redistributing it back onto a new set of more evenly distributed markers, the model can perform more efficiently in terms of convergence, accuracy and overhead. Additional advantages of a meshed model are that the diffusion and stretching terms can be calculated "on-the-mesh" and that velocity field calculation can be done via Poisson solvers, but with the accompanying disadvantage that the mesh must then contain the whole domain, and boundary conditions must be specified.

2.2.1 Finite-Volume Models

2.2.1.1 Two Dimensions

There are a small number of two-dimensional finite-volume vorticity transport methods. Qian and Vezza (2001) produced a finite-volume method for flow around a circular cylinder. The method comprised a FV solver using central- and upwind-difference reconstruction depending on the cell Reynolds number. The velocity was calculated using a Laurent expansion along with a quadtree domain decomposition. Boundary conditions used vorticity source terms with "diffusion" through solid surfaces required to enforce zero surface flow velocity.[1]

2.2.1.2 Three Dimensions

Li and Vezza (2008) use a hybrid method consisting of a hexahedral cell core with a vortex sheet boundary to simulate the low Reynolds number flow past a sphere. Vorticity flux is emitted from the vortex sheet to satisfy the no-slip condition, and is transported using a finite-volume solver, using the fast-multipole method of Draghicescu and Draghicescu (1995) for velocity evaluation. The finite-volume method in this case uses the QUICK scheme for the convection term and a central-difference calculation of the diffusion term, however, there is no mention of how the tilting/stretching term is dealt with. As with the two-dimensional method of Qian and Vezza (2001), there is a vorticity flux through the face of a finite-volume cell which is adjacent to a solid boundary (in this case a sphere rather than a cylinder).

2.3 Mesh-free Vortex Models

Mesh-free methods attempt to model continua using a finite set of markers (e.g. points, filaments, surfaces, polyhedra, etc.). These markers store the governing variables' properties of the continuum at their location. The distribution of the markers can track the evolution of the flow in a Lagrangian manner and as such, mesh-free methods are extremely well suited to modelling convection dominated flows: the significant advantage of these methods is that variable values are not artificially diffused during convection. The disadvantages are that the evolution is generally dependant on the location and variables of the marker: it is frequently required to compute interactions between markers in order to, for example, modify marker strength due to diffusion or compute forces and fields due to

[1] In vortex methods, either no-slip or no-penetration conditions can be used to specify vorticity flux, and they are equivalent: specifying one automatically fulfils the other.

all markers. These both entail either an n-body interaction – where the motion of each "body" is dependant on the position and strength of every other body – or the requirement to determine the location of a subset of markers whose proximity to a given marker entails their inclusion in a truncated calculation. Related issues are that locations of markers themselves can become concentrated or distorted such that either new markers must be introduced in developing regions of interest or where the marker distributions has become especially sparse. Identifying sparse or overcrowded regions and redistributing vorticity to regularise them entails increasing storage and CPU usage.

In their review paper on general mesh-free particle methods, Li and Lui (2004) note the obvious advantages of a mesh-free model, of which the most relevant to the present thesis are:

1. they can model high strain flows with large deformations;
2. easy linking with practical geometries since no mesh is required;
3. they are highly adaptive, with the ability to focus resource on interesting regions in the flow; and
4. they can provide multi-scale models for fluid flow.

2.3.1 Particle/Blob Models

2.3.1.1 Premise

Particle methods use either singular points in an atomistic "vorton" method, or a point with an attached volume represented by e.g. a radial basis function – often referred to as a "blob". In two-dimensional models, particles are vortex filaments which are infinitely long in both out-of-plane directions; in three-dimensional models their influence is that of a unit length vortex filament, but they are interpreted and modelled as being infinitesimally short. Each particle is free to move and has both a location and a circulation strength, vorticity, or strength per unit volume associated with it.

2.3.1.2 History

Vortex particle methods are the oldest practical and the most intuitive two-dimensional discretisation of a vorticity field. In three dimensions, filament methods hold these distinctions e.g. Prandtl lifting-line theory. A vortex particle discretisation was proposed in the early 20^{th} century by Low (1928) and implemented to an extent the following decade by Rosenhead (1930), who used a vortex particle method based on a de-singularised point vortex

to model the roll up of double rows of vortices. Leonard (1980) splits particle methods into those using points (as in Rosenhead) and those using blobs. The primary distinction is that a point vortex is a singularity whereas the blob is de-singularised or smoothed and thus has a finite core strength. The type of de-singularisation can be a simple cutoff after a certain distance, as in Chorin *et al.* (1978), or regularisation using a smoothing parameter giving, for example, the Rosenhead-Moore kernel as in Moore and Saffman (1972), or more usually a smooth cutoff function. A blob method for the two-dimensional Euler equations due to Chorin and Bernard (1973) uses a smoothed kernel to de-singularise the vortex. The work of Beale and Majda (1982a,b) extended the Lagrangian blob concept to three dimensions. (Leonard 1980 and Chorin 1980 extended it to three dimensions using filaments and Anderson and Greengard 1985 later extended it to three dimensions using differentiation on a mesh for the gradients. Neither of these are both mesh-free and particle methods, and both are discussed in the sequel).

From a vortex dynamics perspective, if a smooth vorticity field is desired then the cores of the point vortices must overlap. If this is the case, Beale (1986) has proven that the method is convergent.

2.3.1.3 Representation of Flow Physics

Following Beale and Majda (1982a), an approximation of a vorticity field in terms of a set of n particles is

$$\boldsymbol{\omega}(\boldsymbol{x}) \approx \sum_{p}^{n} \boldsymbol{\omega}_p \delta\left(\boldsymbol{x} - \boldsymbol{x}_p\right), \tag{2.6}$$

where the strength $\boldsymbol{\omega}_p$ of particle p is the local vorticity over the volume of the particle v_p and δ is the Dirac delta (which can be replaced by a smooth cutoff function such as a Gaussian or alternative kernel). Conservation is enforced by keeping the particle strength constant except where changes are required by diffusion or stretching. The Lagrangian form of the vorticity transport equation (Eq. 2.1c) is

$$\frac{\mathrm{d}\boldsymbol{x}_p}{\mathrm{d}t} = \boldsymbol{u}(\boldsymbol{x}_p, t), \tag{2.7a}$$

$$\frac{\partial \boldsymbol{\omega}}{\partial t} = \boldsymbol{\omega}_p \cdot \nabla \boldsymbol{u}(\boldsymbol{x}_p, t) + \nu \nabla^2 \boldsymbol{\omega}(\boldsymbol{x}_p, t). \tag{2.7b}$$

The particles are directly convected through the domain due to integration of the system of autonomous ordinary differential equations (Eqs. 2.7) in either a single calculation, or by splitting the equations, for example, in two dimensions into convection and diffusion steps:

$$\text{Convection:} \begin{cases} \dfrac{\mathrm{d}\boldsymbol{x}_p}{\mathrm{d}t} = \boldsymbol{u}(\boldsymbol{x}_p, t); \\ \dfrac{\partial \boldsymbol{\omega}}{\partial t} = 0. \end{cases} \tag{2.8a}$$

$$\text{Diffusion:} \begin{cases} \dfrac{\mathrm{d}\boldsymbol{x}_p}{\mathrm{d}t} = 0; \\ \dfrac{\partial \boldsymbol{\omega}}{\partial t} = \nu \nabla^2 \boldsymbol{\omega}(\boldsymbol{x}_p, t). \end{cases} \tag{2.8b}$$

2.3.1.4 Biot-Savart Expression

The velocity field through which the particles move is obtained following a Biot-Savart summation:

$$\boldsymbol{u}(\boldsymbol{x}) = \frac{1}{4\pi} \sum_{p}^{n} \frac{\boldsymbol{\omega}_p(\boldsymbol{x}_p) \times (\boldsymbol{x} - \boldsymbol{x}_p)}{\nu_p \left| \boldsymbol{x} - \boldsymbol{x}_p \right|^3} + \nabla \phi(\boldsymbol{x}). \tag{2.9}$$

This is in essence a discrete quadrature of the integral form of the Biot-Savart law, carried out using the particle locations as quadrature points. Fast methods can be substituted in to replace the Biot-Savart summation as it represents an n-body problem, as discussed in Section 2.5. The locations $\boldsymbol{x}$ of the particles are updated using a time-integrator, e.g. Euler, or more optimally Runge-Kutta or Adams-Bashforth-Moulton time-stepping, and the evolution of the particle strengths is updated according to diffusion and tilting/stretching terms in the Lagrangian transport equation. The convection, diffusion and (in three dimensions) stretching steps are performed separately at each time-step.

2.3.1.5 Modelling Diffusion

Calculating the diffusion term in particle methods is problematic. The most common methods include the following:

Random walk method Introduced by Chorin (1973), the random walk uses particles of fixed shape, and adds random jumps to the convection step to simulate diffusion. The method is easy to implement but shows low convergence according to Cottet and Koumoutsakos (2000), whose analysis shows that a very large number of particles are required for convergence since overlapping particle cores are required.

Core spreading Leonard (1980) suggested that the core radius is permitted to change in time according to a two-dimensional solution of the Navier-Stokes equations, which

in the absence of velocity is

$$\frac{\partial \boldsymbol{\omega}}{\partial t} = \nu \nabla^2 \boldsymbol{\omega}. \tag{2.10}$$

An initial Gaussian distribution of vorticity, centered at $\boldsymbol{x}_c$ at t_0,

$$\boldsymbol{\omega}\left(\boldsymbol{x}, t_0\right) = \exp\left(-\frac{\left(\boldsymbol{x} - \boldsymbol{x}_c\right)^2}{4\nu t_0}\right), \tag{2.11}$$

is allowed to diffuse. The change in radius of the blob is obtained from the time evolution, given analytically by

$$\boldsymbol{\omega}\left(\boldsymbol{x}, t\right) = \sqrt{\left(\frac{t}{t_0}\right)} \exp\left(-\frac{\left(\boldsymbol{x} - \boldsymbol{x}_c\right)^2}{4\nu t_0}\right). \tag{2.12}$$

Greengard (1985) argues that this method is incorrect, stating that "vorticity is correctly diffused, but incorrectly convected, even in the limit of infinitely many vortices". Greengard states that using a splitting method (cf. Eqs. 2.8), where the Euler equations are first solved exactly followed by an exact solution of the diffusion equation, the core spreading method can be utilised.

Core spreading has been "resurrected" by Rossi (1996) in a method whereby blobs whose radii have exceeded some threshold are split into a number of smaller blobs. Similarly, the method of Huang, Su and Chen (2009) seeks to improve the method whereby weaker and closely packed new blobs are re-captured. Barba, Leonard and Allen (2005b) also uses a core spreading method in a model which is entirely mesh free.

Diffusion velocity method Due to Ogami and Akamatsu (1991) and Strickland, Kempka and Wolfe (1996) for two-dimensional vortex flows and Grant and Marshall (2005) for three dimensions, this method attempts to retain the character of the inviscid flow models (i.e. the attributes of Helmholtz's vortex laws – see Section 4.3.1.1) whilst simulating viscosity. An additional diffusion velocity field is superimposed on that obtained from the Poisson relation. The velocity at each time-step is also based on the gradients of the vorticity field as well the kinematic viscosity and the inverse of the vorticity magnitude – to avoid problems, the method must be modified as the vorticity tends to zero.

Particle-strength-exchange (PSE) The PSE method is due to the Degond and Mas-Gallic (1989) correction for a core radius.

Similar to the discrete Biot-Savart summation, this is effectively a discretised quadrature of the integral form of the the Laplacian, using the particle locations as quadra-

ture points. The classical PSE is known to tend towards at best second-order accuracy as the ratio of the characteristic particle/stencil displacement h to the core radius diminishes, and the quality of the quadrature is strongly dependant on the underlying distribution of particles – as they become less homogeneous, the approximation of the Laplacian degrades. The PSE and the core spreading method can be combined, increasing accuracy and convergence (Cottet and Koumoutsakos, 2000), and by improving the quality of the discretisation functions. As a counter example, Poncet (2006) has improved accuracy to second-order in terms of only h, i.e. removing the convergence dependency on core radius and allowing simplified models which use constant radius blobs.

Vortex redistribution method (VRM) The method of Shankar and van Dommelen (1996) is similar to the PSE – a set of linear equations is solved to determine how much vorticity is transferred to available nearby particles. If no solution can be found due to a paucity of nearby particles, new particles are added until the equations can be solved, and the order of the approximation can be (in theory) arbitrarily high.

Fishelov's method Fishelov (1990) suggested that an explicit differentiation of the kernel function for the vorticity can provide a high accuracy approximation of the Laplacian. Nordmark (1996) used this method in two dimensions, and found that as long as the kernel function is of high order, and re-gridding has been used to ensure the distribution of particles is homogeneous, Fishelov's method was highly accurate.

Grid-based methods for example Lu and Ross (1991): the particle strengths are interpolated onto an overlying mesh, and the Laplacian is differentiated using grid node values. The diffusion time derivative is subsequently interpolated back onto the underlying particles or onto a new set. Either way, this is not a mesh-free method.

2.3.1.6 Tilting/Stretching

For three-dimensional flows using particle methods, obtaining a good approximation the stretching/tilting term is less problematic than approximating the Laplacian; however, to do it efficiently without resorting to a naïve brute-force velocity field differentiation is more difficult. Some of the more common methods include:

Fully grid-free The tilting/stretching term is obtained directly from the gradients of the smoothed Biot-Savart sum e.g. Anderson and Greengard (1985), Beale (1986) and Fishelov (1990); and

Grid-based methods Marshall and Grant (1996) calculate the velocity on a mesh then use the mesh with finite-difference methods to differentiate it.

There appears to be scant literature (by comparison with diffusion) on implementations of the tilting/stretching term for any vorticity formulation.

2.3.1.7 Specific Limitations and Extensions

The resolution is dependant on the scale of the vortex particles, which are generally significantly greater than the Kolmogorov micro-scale, and as such a dichotomy arises: to ensure a convergent method blobs must be sufficiently close together that they overlap, but the highly shearing flows commonly encountered in engineering problems create length scales such that huge numbers of particles would thus be required. In these circumstances, typically a hybrid mesh/particle method is required to ensure stability. A hybrid particle/mesh model uses an occasional re-initialisation or "re-gridding" of the vortex elements to better redistribute an inhomogeneous distribution of the particles. Because the particles are interpolated onto and then off the mesh every time-step, the model is no longer fully Lagrangian and can be artificially diffusive.

In general, most practical vortex methods seem to require this mesh-based regularisation. However, some counter-examples being totally mesh free are Barba, Leonard and Allen (2005a,b) [in Leitão, Alves and Duarte (2005)], a two-dimensional method which uses a RBF re-gridding strategy where the RBF can be modified allowing core spreading; and that of Stock and Gharakhani (2010) which uses a VRM.

As with all vortex methods, the ability to accurately recover the velocity field at and due to a high number of particles is hampered by the n^2 scaling of the Biot-Savart summation. Tree-codes and fast-multipole methods circumvent this to some degree, but introduce a level of approximation. Meshed methods require two sets of boundary conditions (one for vorticity, one for velocity) and on-mesh resolution of the entire domain for velocity calculation by solving a finite-difference form of the Poisson equation.

2.3.1.8 Notable Successes and Recent Work

Large particle count simulations of aircraft are becoming more common, especially with the availability of GPU architecture and massively parallel high performance computers. Chatelain *et al.* (2008) performed a 6 billion vortex particle direct numerical simulation of aircraft wakes using a hybrid particle/mesh model where the diffusion and stretching terms were computed on the mesh using fourth-order differences. Chatelain *et al.* (2011) and Backaert *et al.* (2011) present analysis on wind turbine rotors using the same

vortex method, with good results applied to the Tjæreborg 2MW wind turbine and the MEXICO experiment, but massive CPU outlay (2048 CPU days). Stock and Gharakhani (2010) model helicopter rotor wakes with long time preservation of the wake structure, although this paper primarily appears to be more of a "proof-of-concept" study using a hybrid RANS/particle-wake model, and so does not contain any load data, but does compare velocity field results with experiments. Willis (2006) use a vortex method for aircraft wake modelling, and Maganga *et al.* (2008); Pinon *et al.* (2012) uses a basic vortex wake model on a tidal turbine.

2.3.1.9 Relevance to the Current Work

As mentioned in the introductory paragraphs of this Section, methods associated with particle/blob vortex methods are more-or-less general to the whole class of vortex methods. Although the method proposed in this thesis primarily uses a mesh-based discretisation, the mesh-free methods described apply directly to the intermediate steps proposed to marry up the finite-volume aspect of the code to the boundary-element method, and observations on the n^2 nature of vortex methods apply.

2.3.2 Filament Models

2.3.2.1 Premise

Filament models use straight or curved segments of vorticity supported by nodes which are convected and evolve in time. Because of the connection between nodes, modification of the filament strength due to stretching/tilting is accounted for very simply; although unless a core spreading technique is being employed, the diffusion calculation requires that local connectivity be recorded.

The concept of vortex filaments is a fundamental building block in inviscid boundary-element methods, from lifting-line theory to unsteady three-dimensional panel methods. Physically, filament methods are consistent with Helmholtz' vortex laws (see Section 4.3.1.1) and follow from Batchelor (1967), who wrote the following expression describing the evolution of a line segment $\Delta \boldsymbol{l}$ in a fluid

$$\frac{\partial \Delta \boldsymbol{l}}{\partial t} + (\boldsymbol{u} \cdot \nabla)\, \Delta \boldsymbol{l} = (\Delta \boldsymbol{l} \cdot \nabla)\, \boldsymbol{u}. \tag{2.13}$$

C.f. Eqs. (2.7) with $\nu \to 0$: in the limit of zero viscosity, a vortex filament will evolve as if it were a material line segment. Conceptually and mathematically, expressions for filaments are obtained by stretching a point, however, practically they are implemented by joining a

series of supporting nodes with straight or curved splines. It is the supporting nodes which are convected in time, with the filaments themselves being reconstructed based on the final position of their nodes.

The vorticity of a filament of circulation Γ, defined by the general arc of length s along $\boldsymbol{r}$ is given by

$$\boldsymbol{\omega}(\boldsymbol{x}) = \Gamma \int \delta \left[\boldsymbol{x} - \boldsymbol{r}\left(s'\right)\right] \frac{\partial \boldsymbol{r}}{\partial s'} \, \mathrm{d}s'. \tag{2.14}$$

Identifying the segment $\Delta\boldsymbol{l} = \boldsymbol{x}_2 - \boldsymbol{x}_1$ and defining its vorticity $\boldsymbol{\omega} = \Gamma\Delta\boldsymbol{l}$ allows the Lagrangian formulation

$$\frac{\mathrm{d}}{\mathrm{d}t}(\Gamma\Delta\boldsymbol{l}) = \Gamma\Delta\boldsymbol{l} \cdot \nabla\boldsymbol{u} \approx \Gamma\left[\boldsymbol{u}(\boldsymbol{x}_2) - \boldsymbol{u}(\boldsymbol{x}_1)\right], \quad \text{with} \tag{2.15}$$

$$\frac{\mathrm{d}\boldsymbol{x}_1}{\mathrm{d}t} = \boldsymbol{u}(\boldsymbol{x}_1, t) \quad \text{and} \quad \frac{\mathrm{d}\boldsymbol{x}_2}{\mathrm{d}t} = \boldsymbol{u}(\boldsymbol{x}_2, t).$$

Due to its constancy, the term Γ can be cancelled from both sides of Eq. (2.15). The vorticity transport equation (in the absence of viscosity) is thus satisfied to a first-order approximation by this discretisation. More accurate results (in terms of spatial accuracy along the filament rather than radial convergence) can be obtained by considering a higher-order reconstruction of the filament, e.g. using cubic splines (NURBS), etc.

2.3.2.2 Biot-Savart Expression

The integral form of the Biot-Savart law for the velocity induced by a vortex filament is given by

$$\boldsymbol{u} = \int_{\Delta l} \frac{\Gamma}{4\pi} \cdot \frac{\mathrm{d}\boldsymbol{l} \times \boldsymbol{r}}{|\boldsymbol{r}|^3}. \tag{2.16}$$

Since the vortex filament convects according to the location of its supporting nodes, a discrete analytical form of this can be written in for the straight-line segment between points $\boldsymbol{x}_1$ and $\boldsymbol{x}_2$ at displacements $\boldsymbol{r}_1$ and $\boldsymbol{r}_2$ from field point $\boldsymbol{x}_P$ as

$$\boldsymbol{u}(\boldsymbol{x}_P) = \frac{\Gamma}{4\pi} \cdot \frac{\boldsymbol{r}_1 \times \boldsymbol{r}_2}{\left|\boldsymbol{r}_1 \times \boldsymbol{r}_2\right|} \left(\boldsymbol{r}_2 - \boldsymbol{r}_1\right) \left(\hat{\boldsymbol{r}}_1 - \hat{\boldsymbol{r}}_2\right), \tag{2.17}$$

where $\hat{\boldsymbol{r}}_1$ and $\hat{\boldsymbol{r}}_2$ are unit vectors of position vectors to $\boldsymbol{x}_1$ and $\boldsymbol{x}_2$ from $\boldsymbol{x}_P$. Obviously this assumes a constant distribution of Γ along a straight line segment, and more elaborate expressions can be obtained for higher-order distributions in both axial and radial directions.

2.3.2.3 History

Two-dimensional vortex filament methods are the basis of the early boundary-element methods of Hess and Smith (1964). In these early models, vortex lines are shed from the trailing edge of an aerofoil and allowed to curl up and convect. However, in the context of this thesis, this approach is classified as a two-dimensional form of a vortex surface model; two-dimensional filament methods do not exist – they are simply blob methods where the blob velocity is calculated as if it were due to an out of plane vortex filament of $\pm\infty$ length.

Three-dimensional vortex methods using filaments, as pioneered in Rehbach (1977), rather than boundary-element methods using vortex filaments, have developed as a logical extension of boundary-element type methods using vortex lattices, which are themselves an extension of probably the oldest useful three-dimensional method for engineering calculations for lifting flows, Prandtl's lifting line theory. The original vortex methods used straight line segments, with a Biot-Savart integration along the line being provided based on a change of variables between the vector displacements of a field point from the line nodes to the angle subtended by the line at the field point. Higher-order methods using curved segments followed with either analytical Biot-Savart integration, e.g. Leishman (2002), or a curve supported on a number of intermediate nodes which became the quadrature points for a numerical integration, for example cubic in Ashurst and Meiburg (1988) as used for modelling deformation of shear layers. In general, it seems that straight or cubic filaments are the most common discretisation, and work tends to focus on improving accuracy by increasing the order of the kernel function (focussing on radial rather than axial convergence).

From a vortex dynamics point of view, filament methods – like particle methods – must model the flow using overlapping cores to obtain a smooth vorticity field. This can cause a number of issues, since it is significantly more difficult from an implementation perspective to regularise deformed distributions of filaments. However, the filament method has been proven convergent in Greengard (1986), although Winckelmans *et al.* (2005) states that low-order kernels are not convergent, and should only find use in "global vortex flow modelling" of e.g. aircraft wake vortices as in Leishman (2002), rather than in attempting to resolve detailed vorticity fields.

Other methods have emerged which use point storage of filament properties as particles, for example in modelling vortex sheet rollup in Lindsay and Krasny (2001). In this method, particles are formed or deleted along particularly stretched/compressed filaments.

2.3.2.4 Representation of Flow Physics

- Convection: the nodes defining the vortex filament are convected in the velocity field due to the vortex filaments. This may be calculated in a grid free manner using a (fast-multipole approximation to the) Biot-Savart summation, e.g. Winckelmans *et al.* (1996), or using a grid-based Poisson solver based on the VIC method, e.g. Couët, Buneman and Leonard (1981).

- Diffusion: vortex filament methods (except in the extreme case where vorticity field is modelled with a very high number of overlapping filaments) are essentially fully inviscid. An approximation to the effects of diffusion for a regularised vortex filament equivalent to a core spreading method is given in Leonard (1985), and Chorin (1990) provides a method to remove "hairpins" – small lengthscale disturbances in the discretised vorticity field – and later Fernandez *et al.* (1996) proposes an ad hoc vortex-surgery method, used to model the vortex collapse-reconnection process and join filaments when they come within a close proximity to one-another.

- Stretching: Eq. (2.5) contains no stretch/tilt term. Unlike particle/blob methods, as long as the filament length can change so that volume is maintained to conserve energy, the tilting/stretching term is intrinsically satisfied for constant circulation.

2.3.2.5 Specific Limitations

When filaments are used in bundles to allow high resolution discretisation of concentrated vorticity fields, in time they tend to drift apart reducing the resolution of the field representation. To circumvent this, additional filaments must be introduced by splitting existing tubes, or some other interpolations, in a manner similar to particle re-initialisation (Chorin and Hald, 1995; Zhou, 1997).

2.3.2.6 Notable Successes and Recent Work

Vortex filament methods with overlapping cores are used to represent vorticity fields rather than isolated vortices and have not enjoyed major uptake in engineering applications. Researchers seem to prefer to use three-dimensional particle methods for detailed field studies of wakes. Vortex filament methods using low-order cores are used to model large vortex systems using long isolated filaments, with each made up of hundreds of nodes. These models are really more in keeping with the ethos of the horseshoe vortex mode for the lifting line, and are used – by e.g. Winckelmans *et al.* (2005) – to model the evolution

and breakdown due to instability of aircraft wakes. Due to their simplicity, they often find use in computer graphics for games, e.g. Weißmann and Pinkall (2010).

2.3.2.7 Relevance to this Thesis

Vortex filaments play a crucial role in three-dimensional low-order panel methods. It is well known (see e.g. Voutsinas, 2006) that a dipole distribution (a solution to Laplace's equation) of order n is equivalent to a vortex distribution of order $n-1$. For example, a (bi)-linear dipole distribution over a surface element equates to a vortex either side of the surface and a constant vorticity over the surface. Similarly, a constant surface distribution of dipoles on a surface can be modelled as a collection of vortex filaments along its edges. In boundary-element methods using a Kutta condition, this allows an intuitive physical interpretation to the dipole wake panels generated by the models. In this thesis, this also allows integration of the dipole panels to provide vortex blobs which are then regularised onto a finite-volume mesh.

2.3.3 Surface Models

2.3.3.1 Premise

Surface models or vortex sheet models approximate a vortex sheet by a distribution of vorticity over a surface, rather than as a sheet-like collection of particles or filaments. In the context of vortex-dynamics methods, sheet models are principally used to model flows as free-shear layers, for example as observed at density interfaces and behind the sharp edge of an aerodynamic body in both two and three dimensions. Because of this, the most common use of vortex sheet models is in boundary-element methods. Vortex sheets are an attractive proposition for flow modelling due to their close approximation of physical reality: they are the only means by which a genuinely continuous vortical structure can be modelled. They are, however, awkward to implement by comparison with particle and filament based models, especially in three dimensions, and thus the evolution of vortex sheets is more often approximated by discretisation as surfaces essentially defined by particles or filaments. For this reason, vortex surfaces are not used in this thesis for three-dimensional work. In two-dimensional work where they are used to represent boundary surfaces and wakes, linear vortex panels are better than constant strength panels for a number of reasons. For a constant vortex panel, the self induced velocity at the centroid is zero and this results in a zero diagonal coefficient matrix. Further, the Kutta condition requires that the circulation on the upper and lower trailing edge panels sums to zero, removing these

from the system of equations: for n panels there are only $n-2$ independent equations and the problem is underspecified. Because of these factors, and also since the linear panel is simple to implement, the linear vortex surface panel is used.

2.3.3.2 Relevance

Two-dimensional surface models using linear vortex elements are used in this thesis to simulate aerofoils, as a proof-of-concept for the three-dimensional methods.

Three-dimensional surface models of vorticity are not particularly relevant to the work presented in this thesis, where only a first-order panel method is used effectively resulting in a filament based wake. Were the model extended to a higher-order (there are a number of compelling reasons for this, see Chapter 9) it would be more relevant.

2.4 Regularisation Kernels

The method proposed in this thesis comprises a boundary-element model for turbine surfaces and a finite-volume vorticity transport model for their wakes. The boundary-element model will generate wakes (as described in Chapter 4) so as to satisfy Kelvin's theorem, and these are used as a vorticity source in the finite-volume wake model. In order to couple the wake generated from the boundary-element side of the method to the finite-volume side, the wake circulation is integrated into vortices, regularised and ingested into the finite-volume mesh using interpolation kernels, rather than e.g. binning into the nearest cell, as this results in very discontinuous vorticity fields.

Given a distribution of wake vorticity defined by the position $\boldsymbol{x}_p$ and vorticity $\boldsymbol{\omega}_p$ of p vortex particles, the vorticity field at $\boldsymbol{x}$ is written as $\boldsymbol{\omega}(\boldsymbol{x}) = \sum_p \boldsymbol{\omega}_p \delta\left(\boldsymbol{x} - \boldsymbol{x}_p\right)$ where δ is the Dirac delta function. By introducing radial basis functions $\phi(x)$ on the grid in order to regularise the infinitesimal vortex points so they have an area in two dimensions or a volume in three dimensions, the mesh vorticity at cell i is obtained as

$$\boldsymbol{\omega}\left(\boldsymbol{x}_i\right) = \frac{1}{V_i} \sum_p \Gamma_p \phi\left(\boldsymbol{x}_p\right). \tag{2.18}$$

In order to ensure that the total circulation between the vortex and mesh is conserved, it is required that

$$\sum_i \boldsymbol{\omega}_i \Delta V_i = \sum_p \Gamma_p, \tag{2.19}$$

which requires that the distribution due to the kernel is normalised to unity, e.g.

$$\sum_i \phi(u) \equiv 1. \tag{2.20}$$

This means that the zeroth invariant – the overall vorticity – is conserved, and that the first invariant (linear impulse)

$$\sum_i \boldsymbol{x}_i \phi(u) \equiv \boldsymbol{x}, \tag{2.21}$$

and second invariant (angular impulse)

$$\sum_i \boldsymbol{x}_i^2 \phi(u) \equiv \boldsymbol{x}^2, \tag{2.22}$$

are conserved.

In these expressions $u = (\boldsymbol{x} - \boldsymbol{x}_i)/\sigma$ and is the distance in terms of e.g. cell spacings if $\sigma = h$ or core radii if σ is taken as a smoothing parameter. By respectively satisfying Eqs. (2.20) to (2.22), the interpolation of the wake vorticity onto the mesh will be of first, second and third-order accuracy (Ould-Salihi, Cottet and Hamraoui, 2000).

A commonly used interpolation kernel is a Gaussian core. The following n-dimensional core is given in two-dimensional form in Yokota and Barba (2011)

$$\zeta(u) = \frac{1}{\left(\sqrt{k\pi}\sigma\right)^n} \exp\left(-\frac{u^2}{k\sigma^2}\right), \tag{2.23}$$

where σ is the core radius and the constant k is chosen to be 2. The Gaussian kernel asymptotes towards zero and does not cutoff the interpolation after a finite number of cells, although after a radius of 6 cells in each direction the blob has decayed to $\mathcal{O}(10^{-6})$ of the original value. In two dimensions this equates to an area of 121 cells and in three dimensions a volume of 1331 cells. According to numerical experiments performed using Eqs. (2.20) to (2.22) – see Table 2.1 and Fig. 2.1 – the Gaussian core is second order accurate. If the only purpose is to calculate velocity on the mesh, then the associated dissipative error might be acceptable. In methods where the diffusion or stretch/compression terms are computed on a mesh, the accuracy is too low and Ould-Salihi, Cottet and Hamraoui (2000) recommend a higher-order kernel.

The method described in this thesis makes use of the M_4' kernel for transfer of the boundary-element method vortex circulation onto the finite-volume mesh. The M_4' kernel was originally devised for smoothed-particle hydrodynamics (SPH) in Monaghan (1985), and is characterised by highly accurate interpolation due to its ability to conserve total circulation and linear and angular impulse at low computational cost, and has thus found use throughout the vortex flow community for use when re-gridding or regularising the

Invariant		$\phi(u) = \zeta(u)$	$\phi(u) = M_4'(u)$	Exact
0	$\sum \phi(u)$	1.000	1.000	1.000
1	$\sum x\phi(u)$	-1.1808	-1.1808	-1.1808
2	$\sum x^2\phi(u)$	2.3943	1.3943	1.3943

Table 2.1: First three invariants as calculated in a numerical experiment interpolating a unit impulse test signal at $x = -1.1080$ using Gaussian (ζ) and M_4' interpolation kernels. Here $\sigma = 2$.

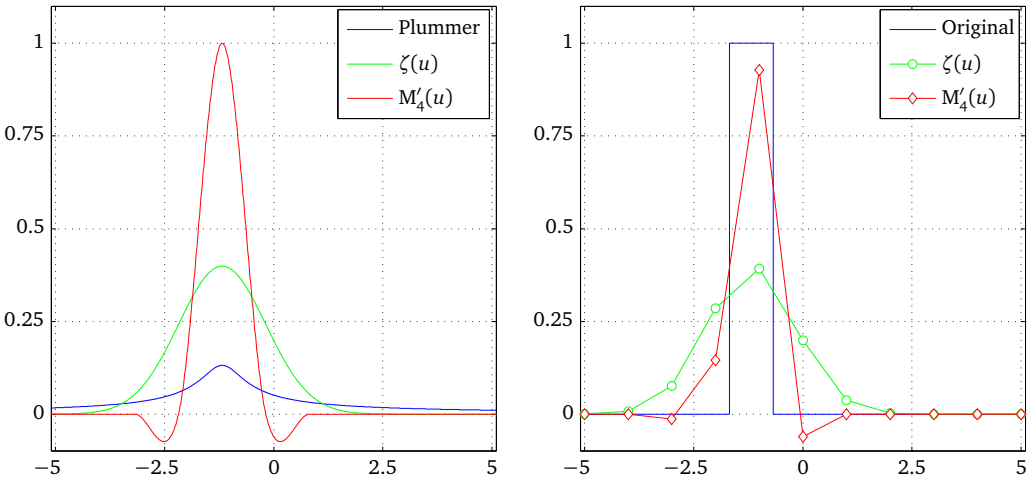

(a) Exact interpolating kernels

(b) Actual interpoland with $h = 1$

Figure 2.1: Interpolation Kernels for a unit pulse of radius 0.5 centred on an arbitrary $x = -1.1808$. Included in first plot is the Plummer potential, for illustration. Clearly it attenuates very slowly by comparison with even the Gaussian kernel.

blobs in particle methods. The kernel is given by the following cutoff function

$$M_4'(u) = \begin{cases} 1 - \frac{5}{2}u^2 + \frac{3}{2}u^3 & \text{if } 0 \leq u < 1 \\ \frac{1}{2}(1-u)(2-u)^2 & \text{if } 1 \leq u \leq 2 \\ 0 & \text{if u} > 2, \end{cases} \tag{2.24}$$

and redistributes the circulation of the blob onto 16 (in two dimensions) or 64 (in three dimensions) finite-volume cells. In numerical experiments, the M_4' kernel satisfies Eqs. (2.20) to (2.22), verifying its third-order accuracy. The very low cost (no transcendental function calls cf. the Guassian kernel) and high accuracy are the reasonable grounds for its use herein.

The contribution to a particular cell i due to the p^{th} vortex is obtained by combining the output of the interpolation kernels in each dimension, so if the kernel function is $\phi(\ldots)$, in three dimensions

$$\Delta\Gamma_i = \Gamma_p \phi\left(\frac{x_i - x_p}{h}\right)\phi\left(\frac{y_i - y_p}{h}\right)\phi\left(\frac{z_i - z_p}{h}\right). \tag{2.25}$$

This "sweeping" is slightly different from applying the ϕ based on radial displacement, which results in a violation of Eqs. (2.20) to (2.22).

See Voutsinas (2006) – projection functions for a good review.

2.4.1 Relevance

In the context of this thesis, vortex models can be divided into essentially Lagrangian vorticity transport models – where markers of dimension 0-3 (points, lines, surfaces and volumes) are tracked through a computational domain – and essentially Eulerian vorticity transport models, where the domain is discretised into two- or three-dimensional cells. Eulerian models operate by effectively fixing the markers in space and allowing their extensive properties to vary in time according to the governing equations. Lagrangian models are again sub-divided into those which are meshed and those which are mesh-free. The so-called meshed models use a grid only for certain stages of the calculation, and maintain the Lagrangian marker philosophy otherwise. Mesh-free models perform all calculations on and using only the markers. Eulerian models are assumed to be meshed.

Mesh-free methods, especially particle/blob methods (as filaments, surfaces and volumes are simply higher-order distributions of vorticity in space), can be thought of as a generalisation of flow modelling using vortex methods. A fully meshed model where even the flow which is free from vorticity is modelled on the grid is just a derived and spe-

cialised form of the model, and the general methods and definitions still apply. Because of this, and also the fact that the work of this thesis has been substantially influenced by the vortex particle/blob methods, without loss of generality the principles of vortex methods will be set out here using a mesh-free, particle method framework. The subsequent models (including those in this thesis) are specific implementations of the method, inheriting and extending the same conceptual and mathematical framework.

2.5 Vortex Model Velocity Calculation

One of the crucial components of a vortex model is a means of obtaining the velocity field due to the volumetric distribution of vorticity. Without this, the vorticity would convect only due to an underlying freestream velocity (if present), and diffuse.

2.5.1 Direct Calculation

A Green's function solution to the velocity field due to a vortex or group of vortices is obtained via an analogy between the electromagnetic field due to a current along a wire, and the velocity due to a vortex filament. Using a point-wise representation of the vorticity field, where the filament is compressed into a point, the Biot-Savart sum gives the velocity field at a field point P

$$\boldsymbol{u}(\boldsymbol{x}_P, t) = \frac{1}{4\pi} \sum_j^n \mathbb{K}(\boldsymbol{x}_P, \boldsymbol{y}_j) \times \boldsymbol{\omega}_j, \tag{2.26}$$

where the Biot-Savart kernel is

$$\mathbb{K}(\boldsymbol{x}_P, \boldsymbol{y}_j) = (-)\frac{\boldsymbol{R}}{|\boldsymbol{R}|^3} \tag{2.27}$$

and the negative sign in Eq. (2.27) is due to the anticommutative nature of the cross product. Direct calculation of the Biot-Savart sum is a non-starter except in very limited quantities where other methods are used, or in particularly low resolution cases. The Biot-Savart law for a vortex is singular in R: as $R \to 0$, the velocity$\to \infty$. This is mathematically due to a division by a very small number but is physically unrealistic. If the Biot-Savart kernel is modified to include a smoothing parameter, the singularity can be removed. A number of kernels can be used, i.e. those discussed previously, where the gradients approximate the Biot-Savart kernel. A particular example is to use the gradients of the Plummer potential (illustrated in Fig. 2.1a), known as the Rosenhead-Moore kernel, to replace the singular

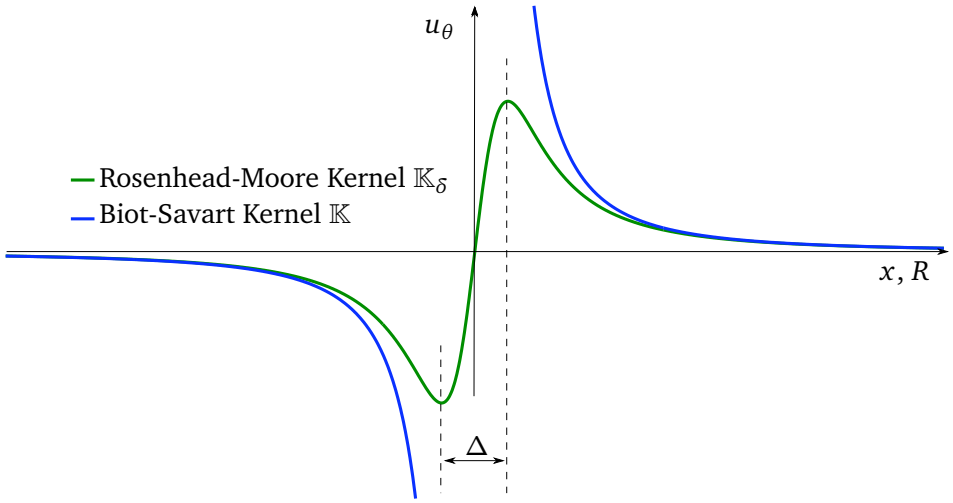

Figure 2.2: Tangential velocity due to smoothed Rosenhead-Moore and singular Biot-Savart kernels as a function of radius.

Biot-Savart kernel. The Plummer potential is

$$\phi_\delta = \frac{1}{\sqrt{|\boldsymbol{R}|^2 + \delta^2}} \tag{2.28}$$

and the gradients of which are

$$\mathbb{K}_\delta \equiv \nabla\phi_\delta = -\frac{\boldsymbol{R}}{\left(|\boldsymbol{R}|^2 + \delta^2\right)^{3/2}}. \tag{2.29}$$

A comparison between the smoothed Rosenhead-Moore and singular Biot-Savart kernels is presented in Fig. 2.2. The Biot-Savart kernel can be integrated over a control volume to give the velocity due to an area or volume rather than a point. Qian and Vezza (2001) provides two-dimensional expressions for a constant distribution of vorticity over arbitrary control volumes based on decomposing the area integration using Stokes' theorem to a summation of edge contributions. Similarly, Suh (2000) provides expressions for constant and linear distributions over two- and three-dimensional volumes, based on both Gauss's and Stokes' theorem. A modified version of the resulting expressions are used in Li and Vezza (2008) to calculate the near-field velocity due to cells, however, it is noted that the analytic expression for the distributions requires evaluation of a large number of transcendental functions per volume, resulting in an exceptionally costly velocity recovery. As a result of the cost of the direct velocity inversion, a number of alternatives have been proposed.

2.5.2 Fast-Poisson Solvers and the Vortex-in-Cell Method

2.5.2.1 History

The Particle-in-Cell (PIC) model was introduced by Harlow (1956). The idea was to represent mass as a particle and momentum/energy on a grid, then perform Eulerian grid evolution on the properties of particles in each cell; the later review on PIC in Harlow (1988) shows strong uptake by that time. Although the original method used a nearest-neighbour interpolation, later methods use smooth interpolation kernels for particle-mesh and mesh-particle transfer of data. The PIC technique is only first-order accurate in space. An extension of the PIC method is the vortex-in-cell (VIC) method, where the location and vorticity is represented as a particle, and the velocity is calculated using the grid. The VIC method uses a combination of grid-based and grid-free operations to approximate the Navier-Stokes equations. A particle method is used to model advection, and the diffusion (and stretching in three dimensions) terms are calculated using the results of interpolating

the newly advected vorticity distribution back onto the mesh. The VIC method is typically used along with a fast-Poisson solver for velocity inversion, and can be an efficient, and easily parallelised flow solver.

Fast-Poisson solvers are implemented as a discretised finite-difference expression for the LHS and RHS of the Poisson equation (Eq. 2.1d) written in matrix form. The solution of a system of m equations of the form $\mathbf{A}\boldsymbol{u} = \mathbf{B}\boldsymbol{\omega}$ is obtained on a cuboidal or rectangular domain Ω by specifying the Dirichlet/Neumann data for $\boldsymbol{u}$ on $\partial\Omega$, e.g. periodic or semi-periodic, etc. The linear algebra is generally an $\mathcal{O}(m^2)$ cost calculation when using elimination, but the method of cyclic-reduction improves this: the "fast" aspect comes from the use of FFT-type expansions for the LHS and RHS of the system of equations, used to eigen-decompose the problem into a number of block tridiagonal sub-matrices which are then solved (in parallel if desired). This is implemented in FISHPACK/FISHPACK90 (see Swarztrauber and Sweet, 1975, for original source). The method can be further accelerated by using a multi-grid meshing to calculate coarse solution estimates which are then used as input in a refined mesh. An example implementation of this algorithm is MUDPACK (see Adams, 1999). The main attraction of the method is the ease of implementing a parallel version of the solver, since distribution of work can be accomplished in a very straightforward manner using simple domain partitioning.

The immediate drawback of fast-Poisson solvers is the requirement for rectangular or cuboidal domains and the specification of the boundary conditions on $\partial\Omega$ in the normal direction of the surfaces. This is because of the requirement to represent the solution as a series of waves during the FFT process, and the domains must be filled with a uniform Cartesian mesh to obtain the required diagonal system. In the context of vortex methods, this can result in large volumes of empty cells, and the requirement to calculate the velocity (or velocity gradients) on the domain boundaries. Practical methods utilise a tree-code or fast-multipole method for the velocity boundary conditions, as used in Ould-Salihi, Cottet and Hamraoui (2000).

The cost of the method can be reduced to very close to $\mathcal{O}(m)$, although this m includes all of the empty padding elements, which will be subject to change if the domain is growing in time. However, the method is readily parallelised, the underlying discretisation can be of almost arbitrary order – typically second or fourth – and in certain flows, for example behind wings or turbines, the additional padding required can be marginal (this is known from experience since the marching-cubes isosurface calculation employed herein to analyse the results generated in later chapters does not accept sparse three-dimensional arrays, and as such cuboidal domains were generated. Only in very large domains, e.g.

long duration turbine simulations or multi-rotor simulations, did the padded domain become excessively memory hungry).

Fast-Poisson solvers have found use in vortex methods, especially those based on a vorticity-streamfunction Poisson equation rather than vorticity-velocity form. Vortex-in-cell methods typically use fast-Poisson solvers, and until the evolution of vortex fast-multipole methods, particle methods would also be regularised onto a mesh for velocity computation.

Relevant examples of fast-Poisson solvers in practical engineering fluid dynamics are the work of Brown (2000), which used cyclic reduction to compute the velocity field for the flow around helicopter rotor-systems, before replacing it with the fast-multipole method in later versions and Chatelain *et al.* (2008), which use a periodic fast-Poisson solver in a large parallel 6 billion vortex hybrid particle/mesh simulation of an aircraft wake.

2.5.3 Tree-codes and Fast-Multipole Methods

Alternatives to the fast-Poisson solver for n-body interactions are the related tree-code and fast-multipole methods. Originating in the Barnes and Hut (1986) tree-code for stellar dynamics, the method organises the bodies into a tree-structure by partitioning the distribution of bodies into clusters or "boxes". Multipole expansions – effectively Taylor series expansions for functions dependant on the radius (and perhaps spherical coordinate angles) between the evaluation point and the expansion centre – are taken around the centre of boxes, and used to compute long range interactions between distant boxes, that is boxes separated by a distance greater than some multiple of the characteristic size of the box. If the boxes are not well separated, nearby smaller sub-cluster interactions are evaluated. The method reduces the cost of the calculation to $\mathcal{O}(\log n)$ per body, and hence $\mathcal{O}(n \log n)$ for all bodies.

The fast-multipole method – originating with Greengard and Rokhlin (1987) – uses the idea of the tree-code, but expands it by summing interactions due to the various hierarchical levels of a recursive tree. A multipole method for two-dimensional vortex blobs is due to Draghicescu and Draghicescu (1995), who provide a Taylor expansion based method in two dimensions which relies on de-singularising the Biot-Savart kernel using a smoothing parameter – very much like the Rosenhead-Moore kernel. The method is then used with a recursive relation to calculate the Taylor coefficients and a quadtree to decompose the domain, and is used to model vortex sheet rollup. The analogous three-dimensional method is presented in Lindsay and Krasny (2001), again with application to vortex sheets represented by blobs. Lindsay and Krasny expand the Draghicescu and Draghicescu two-dimensional Biot-Savart method into three dimensions, providing the recursion relation

needed for fast calculation of the expansion coefficients to arbitrary orders.

2.5.3.1 Fast-Multipole Method

The fast-multipole method (FMM) is an algorithm for approximating the solution of an n-body problem. The algorithm has been ranked as one of the top ten most influential algorithms of the 20$^{\text{th}}$ Century by the Society of Industrial and Applied Mathematics (Cipra, 2000) (amongst such illustrious companions as the optimising FORTRAN compiler, the fast-Fourier transform, QR-factorisation and the Monte-Carlo method), and as with these, there is a staggering literature base on the method.

The FMM is used for accelerating the calculation of n-body interactions of the form

$$f\left(\boldsymbol{x}_i\right) = \sum_{j}^{n} c_j \mathbb{K}\left(\boldsymbol{x}_i, \boldsymbol{y}_j\right). \tag{2.30}$$

The objective with a fast-multipole method is to decompose the solution into near and far-field components

$$f\left(\boldsymbol{x}_i\right) = \sum_{j}^{n_{\text{near}}} c_j \mathbb{K}\left(\boldsymbol{x}_i, \boldsymbol{y}_j\right) + \sum_{k}^{n_{\text{far}}} c_k \mathbb{K}\left(\boldsymbol{x}_i, \boldsymbol{y}_k\right), \tag{2.31}$$

and to perform expansions to approximate the near- and far-field contribution, thus reducing the computational cost of the n-body evaluation. This is attained by expanding the kernel into isolated expressions for the source point and the field point.

The core components of the algorithm for the three-dimensional FMM used to calculate the velocity due to a discrete form of a vorticity field are due to Lindsay and Krasny (2001), and the expressions for reusing the moments of a cluster at that cluster's parent (moment-to-moment translations, M2M) and recycling the local velocity field expansion at a point to calculate the velocity field at a nearby point (local-to-local translation, L2L) are given in Brown and Line (2005), using the basic method of Cheng, Greengard and Rokhlin (1999). The process begins by first defining a distant group c of n_{c} vorticity containing elements (voxels, as in "volume elements", cf. pixel) whose centroid is located at $\boldsymbol{x}_{\text{c}}$, the centre of the parent voxel. Rendering the Biot-Savart kernel (Eq. 2.27) infinitely differentiable using the smoothing parameter δ results in a smoothed Biot-Savart kernel $\mathbb{K}_\delta$ which is equal to the gradients of the regularised Newtonian potential[2] (the Plummer potential) – see

[2] Or alternatively by using a smooth radial basis function – e.g. the gradients of the Gaussian interpolation kernel.

Fig. 2.2. The velocity due to the members of this cluster is then

$$4\pi \boldsymbol{u} = \sum_{j}^{n_c} \mathbb{K}_\delta \left(\boldsymbol{x}_i, \boldsymbol{y}_j \right) \times \boldsymbol{\omega}_j. \tag{2.32}$$

Lindsay and Krasny (2001) show that for the velocity induced at the i^{th} distant point $\boldsymbol{x}_i$ by a cluster of n_c vorticity containing cells at points $\boldsymbol{y}_j$ centred at $\boldsymbol{y}_c$, Eq. (2.32) can be written as a series expansion. Using multi-index notation

$$\begin{aligned} 4\pi \boldsymbol{u} \left(\boldsymbol{x}_i, \boldsymbol{y}_c \right) &= \sum_{\boldsymbol{k}=0}^{\infty} \frac{1}{\boldsymbol{k}!} \mathrm{D}_y^{\boldsymbol{k}} \mathbb{K}_\delta \left(\boldsymbol{x}_i, \boldsymbol{y}_c \right) \times \sum_{j}^{n_c} \left(\boldsymbol{y}_j - \boldsymbol{y}_c \right)^{\boldsymbol{k}} \boldsymbol{\omega}_j \\ &= \sum_{\boldsymbol{k}=0}^{\infty} \boldsymbol{a}_{\boldsymbol{k}} \left(\boldsymbol{x}_i, \boldsymbol{y}_c \right) \times \boldsymbol{m}_{\boldsymbol{k}} \left(\boldsymbol{y}_c \right), \end{aligned} \tag{2.33}$$

where $\mathrm{D}_y^{\boldsymbol{k}} \mathbb{K}_\delta$ is the $\boldsymbol{k}^{\text{th}}$ partial spatial derivative of $\mathbb{K}_\delta$ with respect to $\boldsymbol{y}$, and is evaluated at the source cluster centre $\boldsymbol{y}_c$ giving the local field expansion coefficient $\boldsymbol{a}_{\boldsymbol{k}}$. The cluster moment of vorticity $\boldsymbol{m}_{\boldsymbol{k}}$, is also evaluated about the cluster centre. In practice, the expansion is limited to a finite order $\|\boldsymbol{k}\| = p_{\max}$.

The velocity field is computed at the target cluster centre by performing the cross product of the vector elements of the $\boldsymbol{a}$ and $\boldsymbol{m}$ tensors. The main point here is that the source evaluation resulting in the cluster moments is dependant on the distribution of vorticity in the cluster, and can be performed as a single independent calculation valid for all evaluations of its cross product at field points.

The "fast" aspect of the FMM relies on the generation and subsequent reuse of expansions for the vorticity field and for the velocity field, and translation of the centres of these expansions. This is illustrated in Fig. 2.3. To obtain a correct approximation of the vorticity and velocity fields, the radii of convergence of these expansions must be observed. The following general expansions are used:

Multipole Expansion Define a far-field multipole expansion representing the integration or quadrature of the cluster of vortices centred at $\boldsymbol{x}_1$ and valid at a distant field point $\boldsymbol{y}$, lying in the domain of convergence Ω_1, which is exterior to a sphere of radius R_1 centred at $\boldsymbol{x}_1$. If the centre of the expansion is translated, for example to a new point $\boldsymbol{x}_2$, the domain of convergence of the translated expansion is exterior to a sphere of radius R_2, centred at $\boldsymbol{x}_2$, where the second sphere fully encloses the first: $R_2 > (|\boldsymbol{x}_1 - \boldsymbol{x}_2| + R_1)$. Now, since $R_2 > R_1$ and the nearest convergent point to the centre of the expansion must be at a greater radius, the size of the domain in which the multipole expansion is valid is diminished, but this is only very marginal and is

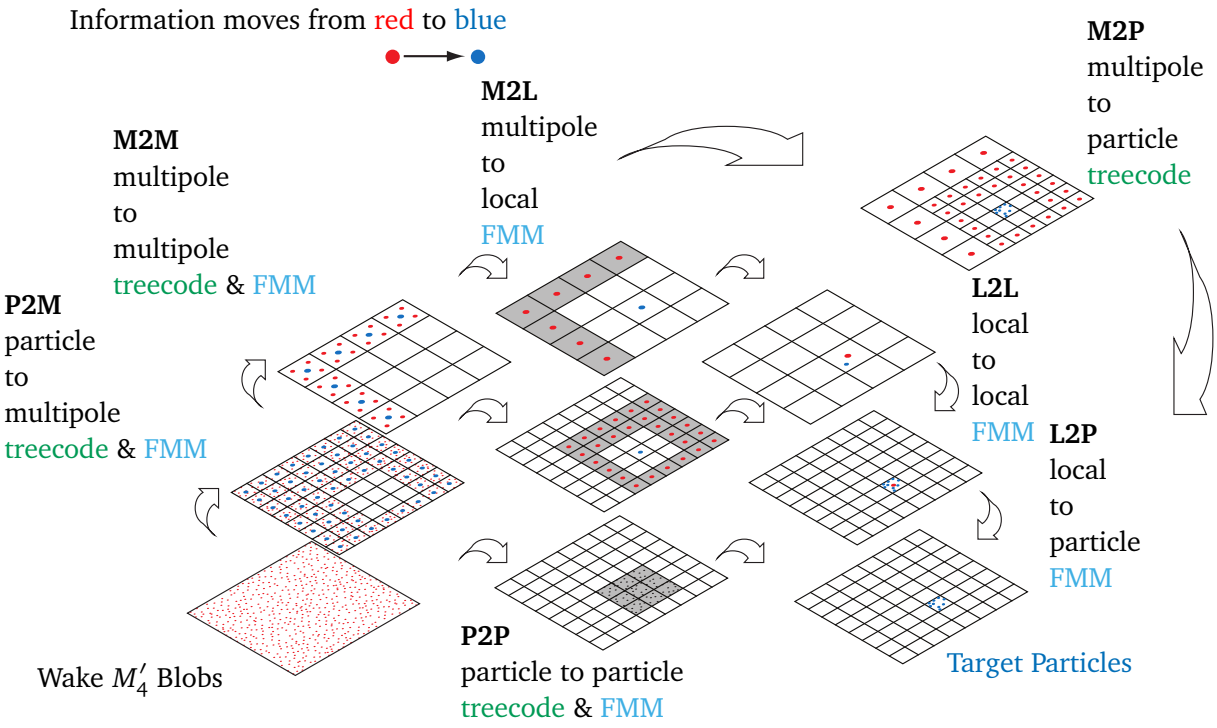

Figure 2.3: Radii of convergence for translated far-field expansions. Darker areas mark domain of convergence.

offset by the ability to translate the centres and combine the contributions of several expansions to a new a common centre representing a large number of vortices.

Local Expansion Define a local expansion of the velocity field which is centred around the point $\boldsymbol{x}_1$ and valid at field point $\boldsymbol{y}$ which lies in the domain of convergence, this time interior to a sphere of radius R_1 centred on $\boldsymbol{x}_1$. The centre of the expansion can be translated to a new point $\boldsymbol{x}_2$, as long as the centre of the resulting expansion is located within the domain of convergence of the first expansion. Similarly, the radius of convergence of the translated expansion is such that the domain of convergence of the second expansion is entirely contained by the domain of the first expansion. The region in which the expansion is convergent thus diminishes, however this is offset by the ability to use the initial expansion in a large number of interior expansions, which can be enriched with far-field/local interactions at a local, refined scale.

Multipole/Local Interactions The local expansion coefficients are computed using the multipole expansions. The domain of validity of the interaction is that which is exterior to the far-field multipole radius of convergence, and interior to the local expansion Taylor series radius of convergence. It clearly makes most sense to ensure that the local expansion domain is entirely exterior to that of the far-field domain. The FMM maintains this for radii of similar magnitude using a hierarchical domain decomposition.

The following vorticity specific expressions are used during the FMM expansion, where field points are denoted $\boldsymbol{x}$, sources are denoted $\boldsymbol{y}$ and the expansions are truncated at order p:

Multipole Expansion (ME) calculates the multipole moments due to a cluster of n sources at $\boldsymbol{y}_i$, each with vorticity $\boldsymbol{\omega}_i$, about some central point $\boldsymbol{y}_c$. This step entails retention of a finite number of terms of an infinite expansion, and thus results in a truncation error. The $\boldsymbol{k}^{\text{th}}$ term of the ME for the vorticity cluster is the cluster moment of vorticity

$$\boldsymbol{m}_{\boldsymbol{k}}\left(\boldsymbol{y}_c\right) = \sum_{i}^{n} \left(\boldsymbol{y}_i - \boldsymbol{y}_c\right)^{\boldsymbol{k}} \boldsymbol{\omega}_i. \tag{2.34}$$

Moment-to-moment translation (M2M) translates the cluster moments of vorticity from the j^{th} expansion centre $\boldsymbol{y}_j$ (dropping the subscript c for clarity) to a nearby location $\boldsymbol{y}$, where the contributions of a number of clusters are summed. M2M translation is exact within the domain of convergence, so a finite number of terms is required for translation and no further truncation error is introduced. The M2M translation is

accomplished using the multi-index binomial sum

$$\boldsymbol{m}_{\boldsymbol{k}}\left(\boldsymbol{y}\right)=\sum_{j}\sum_{\boldsymbol{n}=0}^{\boldsymbol{k}}\binom{\boldsymbol{n}}{\boldsymbol{k}}\left(\boldsymbol{y}-\boldsymbol{y}_{j}\right)\boldsymbol{m}_{\boldsymbol{k}-\boldsymbol{n}}\left(\boldsymbol{y}_{j}\right). \tag{2.35}$$

Local Expansion and moment-to-local translation (M2L) calculates the velocity field at the field point $\boldsymbol{x}$ due to the distant moments (calculated via either Eq. 2.34 or Eq. 2.35) at point $\boldsymbol{y}$. This step also uses a finite number of an infinite number of terms, and additional truncation error is introduced. The $\boldsymbol{k}^{\text{th}}$ Taylor coefficients (multiplied by the kernel derivatives),

$$\boldsymbol{a}_{\boldsymbol{k}}\left(\boldsymbol{x},\boldsymbol{y}\right)=\frac{1}{\boldsymbol{k}!}\mathrm{D}_{\boldsymbol{y}}^{\boldsymbol{k}}\mathbb{K}_{\delta}\left(\boldsymbol{x},\boldsymbol{y}\right), \tag{2.36}$$

are used to generate the $\boldsymbol{k}^{\text{th}}$ velocity field derivatives centred at $\boldsymbol{x}_{c}$,

$$\mathrm{D}_{\boldsymbol{x}}^{\boldsymbol{k}}\boldsymbol{u}\left(\boldsymbol{x}_{c}\right)=\sum_{\boldsymbol{n}=\boldsymbol{k}}^{p}(-1)^{\boldsymbol{n}}\frac{\boldsymbol{n}!}{(\boldsymbol{k}-\boldsymbol{n})!}\boldsymbol{a}_{\boldsymbol{n}}\left(\boldsymbol{x}_{c},\boldsymbol{y}\right)\times\boldsymbol{m}_{\boldsymbol{k}-\boldsymbol{n}}\left(\boldsymbol{y}\right). \tag{2.37}$$

Local-to-local translation (L2L) translates the centre of the local field expansion (obtained using Eq. 2.37) at the point $\boldsymbol{x}_{c}$ to another, nearby field point $\boldsymbol{x}$ (the kernel evaluation at $\boldsymbol{x}$ is simply the zeroth derivative). A finite number of terms is required for a L2L translation and thus no new truncation error is introduced as long as the new centre is within the domain of convergence of the original centre. The L2L used herein to translate the velocity field $\mathrm{D}_{\boldsymbol{x}}^{\boldsymbol{k}}\boldsymbol{u}\left(\boldsymbol{x}_{c}\right)$ is

$$\mathrm{D}_{\boldsymbol{x}}^{\boldsymbol{k}}\boldsymbol{u}\left(\boldsymbol{x}\right)=\sum_{\boldsymbol{k}=\boldsymbol{n}}^{p}\frac{\left(\boldsymbol{x}_{c}-\boldsymbol{x}\right)^{\boldsymbol{k}-\boldsymbol{n}}}{(\boldsymbol{k}-\boldsymbol{n})!}\mathrm{D}_{\boldsymbol{x}}^{\boldsymbol{k}}\boldsymbol{u}\left(\boldsymbol{x}_{c}\right). \tag{2.38}$$

Expansion for integral of kernel converts the field expansion at a particular location $\boldsymbol{x}$ to an evaluation of the kernel at a nearby field point $\boldsymbol{x}_{P}$. This step introduces no new truncation errors and for the present method is

$$\boldsymbol{u}\left(\boldsymbol{x}_{P}\right)=\sum_{\boldsymbol{k}=0}^{p}\frac{\left(\boldsymbol{x}_{P}-\boldsymbol{x}\right)}{\boldsymbol{k}!}\mathrm{D}_{\boldsymbol{x}}^{\boldsymbol{k}}\boldsymbol{u}\left(\boldsymbol{x}\right). \tag{2.39}$$

Sweeping up When kernel evaluations are required outside of the region where the expansions are valid, a direct Biot-Savart calculation can be performed.

Lindsay and Krasny (2001) prove that the gradients of this potential for an arbitrary source cluster distribution of vorticity can be found efficiently via recursion. In this case

the coefficients are obtained by solution of an expression of the form

$$\|\boldsymbol{k}\| R^2 b_{\boldsymbol{k}} - (2\|\boldsymbol{k}\| - 1) \sum_{i=1}^{3} (x_i - y_i)\, b_{\boldsymbol{k}-\boldsymbol{e}_i} + (\|\boldsymbol{k}\| - 1) \sum_{i=1}^{3} (x_i - y_i)\, b_{\boldsymbol{k}-2\boldsymbol{e}_i} = 0. \quad (2.40)$$

Once this is evaluated for all positive $\boldsymbol{k}$, where $\boldsymbol{e}_i$ is the i^{th} Cartesian basis vector, the Taylor coefficients $\boldsymbol{a}$ can then be reconstructed via

$$\boldsymbol{a}_{\boldsymbol{k}} = -\sum_{i=1}^{3} (k_i + 1)\, b_{\boldsymbol{k}+\boldsymbol{e}_i} \boldsymbol{e}_i. \quad (2.41)$$

The coefficients required for the FMM can be calculated analytically using recursion, as above, or directly using the following definitions. If the geometry of the cluster is fixed, the relationship between each cluster leaf and its parent is constant. This simplifies the process somewhat, allowing a linear superposition at the parent cluster centroid of the contributions of the moments of all leaves (and clusters) lower in the tree. This is done by simply obtaining in advance the coefficient multipliers then at runtime summing through the contributions to the moments. Recursive calculation has been eschewed in the method proposed in this thesis, since the coefficients only need to be calculated once per quad/octree level (or actually once per tree, then scaled for each level), similar to the method used in Barnes (1990).

The Biot-Savart kernel $\mathbb{K}_\delta$ is equal to the gradients $\nabla\mathbb{G}$ of the Newtonian potential

$$\mathbb{G}\left(\boldsymbol{x}_i, \boldsymbol{x}_j\right) = \begin{cases} \dfrac{1}{2\pi} \log\left(\left|\boldsymbol{x}_j - \boldsymbol{x}_i\right|\right) & \text{in 2-D} \\ \dfrac{1}{4\pi} \dfrac{1}{\left|\boldsymbol{x}_j - \boldsymbol{x}_i\right|} & \text{in 3-D,} \end{cases}$$

the denominator of which is regularised or de-singularised by the smoothing parameter δ for stability purposes, and to allow differentiation. This yields the multi-quadratic radial basis function $\phi_\delta\left(\boldsymbol{x}_i, \boldsymbol{x}_j\right) = \sqrt{\left|\boldsymbol{x}_j - \boldsymbol{x}_i\right|^2 + \delta^2}$. The FMM relies on a series expansion of the velocity potential in space. The coefficients of this expansion are multiplied by the gradients of the potential which, for the two-dimensional kernel, are presented in Table 2.2 for $\|\boldsymbol{k}\| < 4$. The three-dimensional kernel follows naturally.

2.5.3.2 Hierarchical Domain Decomposition

For the FMM (or FMM type method, e.g. based on Laurent expansions in two dimensions) to be effective, it requires a means of determining whether or not a particular group of vorticity containing cells should be treated as near or far-field when calculating the velocity at some point $\boldsymbol{x}$. A convenient means which is frequently used in analysis of vorticity and

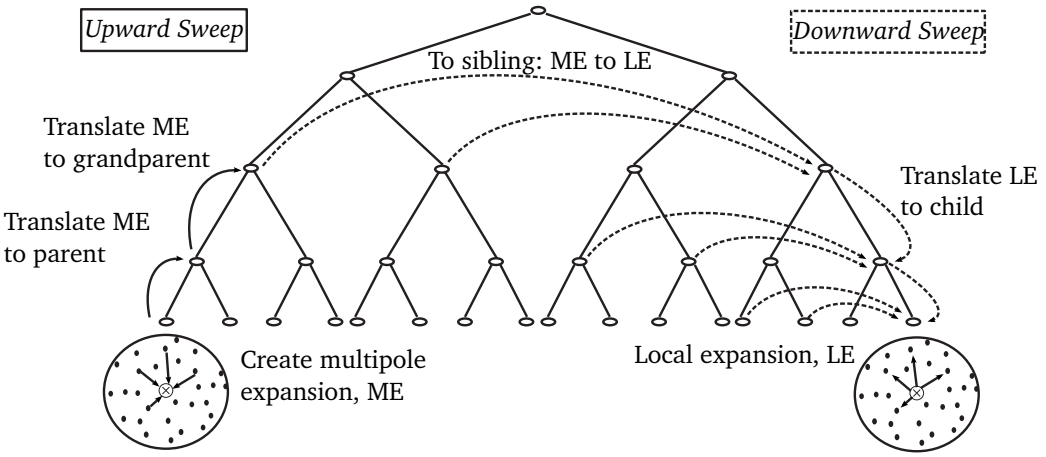

Figure 2.4: Fast-multipole method and tree-code data transfer directions. Taken from Cruz and Barba (2009).

Table 2.2: Two-dimensional derivatives $\frac{\partial^{m+n}\mathbb{G}}{\partial x^m \partial y^n}$ for $p_{\max} = 3$, where $\left|\boldsymbol{x}_j - \boldsymbol{x}_i\right| \equiv \sqrt{x^2+y^2+\delta^2}$.

		m			
		0	1	2	3
n	0	$\frac{\log\left(x^2+y^2+\delta^2\right)}{4\pi}$	$\frac{x}{2\pi\left(x^2+y^2+\delta^2\right)}$	$\frac{-x^2+y^2+\delta^2}{2\pi\left(x^2+y^2+\delta^2\right)^2}$	$\frac{x\left(x^2-3\left(y^2+\delta^2\right)\right)}{\pi\left(x^2+y^2+\delta^2\right)^3}$
	1	$\frac{y}{2\pi\left(x^2+y^2+\delta^2\right)}$	$-\frac{xy}{\pi\left(x^2+y^2+\delta^2\right)^2}$	$-\frac{y\left(-3x^2+y^2+\delta^2\right)}{\pi\left(x^2+y^2+\delta^2\right)^3}$	
	2	$\frac{x^2-y^2+\delta^2}{2\pi\left(x^2+y^2+\delta^2\right)^2}$	$-\frac{x\left(x^2-3y^2+\delta^2\right)}{\pi\left(x^2+y^2+\delta^2\right)^3}$		
	3	$\frac{-3x^2y+y^3-3y\delta^2}{\pi\left(x^2+y^2+\delta^2\right)^3}$			

other potential fields is using a tree based domain decomposition. The original vortex FMM proposed by Lindsay and Krasny used a tree structure with a rectangular/cuboidal zoning system where the voxels were constructed around clusters of vortex elements, and subdivided when the number of elements exceeded a particular threshold.

A more regular zonal decomposition is used in the two-dimensional work of Taylor and Vezza (1999) for vortex particles and three-dimensional work of Brown and Line (2005) for cells. These differ in the means by which resources are focussed. Similarly to Lindsay and Krasny, the method of Taylor and Vezza splits the quadtree voxels according to a threshold. The three-dimensional octree method of Brown and Line is the somewhat extreme case of flowfield decomposition with one vortex particle per voxel at the highest tree resolution. The differing decompositions reflect the differences in the methods themselves, in particular a fully Lagrangian vortex particle versus Eulerian finite-volume convection methods, and also the advantages that fully resolving the octree confer in terms of book-keeping and calculation reuse: the cost of additional storage in the full octree/quadtree is offset by the geometrically similar structure at each recursion level allowing functions and calculation results to simply be rescaled and reused.

2.6 Conclusions

General Remarks and Recap This chapter has discussed vortex methods. The advantages of modelling fluid flow using vortex methods were discussed, most notably the ability to convect with minimum artificial diffusion, and capture a large size range of flow-features. However, this comes at the expense of large numbers of elements which, due to the Lagrangian nature of the flow, can become irregularly distributed in high-shear flows. This entails re-gridding or re-initialisation by some means to ensure that there is overlap in the kernel functions representing the vortex cores. Additionally, the cost of computing the velocity field using the Biot-Savart law rises with the square of the number of elements.

The various means of discretising the vorticity were discussed, including their respective Biot-Savart implementations. The basic building blocks of a vortex model were described using examples from a particle/blob framework, but are generally applicable to a higher-order discretisation. The fundamental differences between a “meshed” and a “mesh-free” model were noted, and examples were given.

The method of this thesis is a “meshed” model – velocity and vorticity quantities are calculated on the mesh. Even the particle wake component of the boundary-element model is essentially a meshed model in that it is the regularisation of the particles onto the mesh which provides the source in the finite-volume framework.

The fast-multipole method was described. This provides the means by which the velocity field due to the vorticity field is recovered. The method reduces the computational cost of the method from $\mathcal{O}(n^2)$ for a direct calculation or $\mathcal{O}(n \log n)$ for a fast-Poisson calculation to a theoretical cost of $\mathcal{O}(n)$.

Impacts on this Thesis The vortex methods described are all used in this thesis:

- Vortex lines are used by the boundary-element method to model the thin shear layers in the wakes of tidal turbines. These are fixed circulation and are allowed to convect in a Lagrangian manner due to the local velocity field.
- Vortex blobs are used in intermediate steps between the lines and the meshed model. These are also of fixed vorticity, and convect in a Lagrangian manner.
- The regularisation kernels, in particular the M_4' kernel, are used to convert the vortex blobs into a meshed distribution of vorticity.
- Meshed vortex volumes are used in the finite-volume part of the method. The location of these is fixed while there is vorticity in the region, and their cores overlap so the method should be convergent on a smooth vorticity field. Instead of moving to convect the flow in a Lagrangian manner, their properties are transferred in an Eulerian manner.
- Biot-Savart expressions for all of the above are used, along with the fast-multipole method to recover the velocity field from the vorticity field in this thesis.

References

Adams, J.C. (1999). "Fortran code with OpenMP directives for shared memory parallelism." Tech. rep., NCAR.

Anderson, C. and Greengard, C. (1985). "On vortex methods." *SIAM Journal on Numerical Analysis*, **22**(3): pp. 413–440.

Ashurst, W.T. and Meiburg, E. (1988). "Three-dimensional shear layers via vortex dynamics." *Journal of Fluid Mechanics*, **189**: pp. 87–116.

Backaert, S., Chatelain, P., Winckelmans, G., Kern, S. and Koumoutsakos, P. (2011). "LES of wind turbine wakes and coarse scale aerodynamics using a Vortex Particle-Mesh method." In "Proceedings of the ERCOFTAC-Belgium Yearly Seminar 2011," von Karman Institute for Fluid Dynamics, Rhode-St-Genése, Belgium.

Barba, L.A., Leonard, A. and Allen, C.B. (2005a). "Advances in viscous vortex methods - meshless spatial adaption based on radial basis function interpolation." *International Journal for Numerical Methods in Fluids*, **47**(5): pp. 387–421.

Barba, L.A., Leonard, A. and Allen, C.B. (2005b). "Vortex method with meshless spatial adaption for accurate simulation of viscous, unsteady vortical flows." *International Journal for Numerical Methods in Fluids*, **47**(8-9): pp. 841–848.

Barnes, J. and Hut, P. (1986). "A hierarchical O(N log N) force-calculation algorithm." *Nature*, **324**: pp. 446–449.

Barnes, J.E. (1990). "A modified tree code: Don't laugh; it runs." *Journal of Computational Physics*, **87**(1): pp. 161–170.

Batchelor, G.K. (1967). *An Introduction to Fluid Dynamics*. Cambridge Univ Press.

Beale, J.T. (1986). "A convergent 3-D vortex method with grid-free stretching." *Mathematics of Computation*, **46**(174): pp. 401–424.

Beale, J.T. and Majda, A. (1982a). "Vortex methods I: Convergence in three dimensions." *Mathematics of Computation*, **29**(159): pp. 1–27.

Beale, J.T. and Majda, A. (1982b). "Vortex methods II: Higher order accuracy in two and three dimensions." *Mathematics of Computation*, **29**(159): pp. 29–52.

Brown, R. (2000). "Rotor wake modeling for flight dynamic simulation of helicopters." *AIAA Journal*, **38**(1): pp. 57–63.

Brown, R. and Line, A.J. (2005). "Efficient high-resolution wake modeling using the vorticity transport equations." *AIAA Journal*, **43**(7): pp. 1434–1443.

Chatelain, P., Bricteux, L., Backaert, S., Winckelmans, G., Kern, S. and Koumoutsakos, P. (2011). "Vortex particle-mesh methods with immersed lifting lines applied to the large eddy simulation of wind turbine wakes." In "Proceedings of the Wake Conference," Gotland University, Visby, Sweden.

Chatelain, P., Curioni, A., Bergdorf, M., Rossinelli, D., Andreoni, W. and Koumoutsakos, P. (2008). "Billion vortex particle direct numerical simulations of aircraft wakes." *Computer Methods in Applied Mechanics and Engineering*, **197**(13-16): pp. 1296–1304.

Cheng, H., Greengard, L. and Rokhlin, V. (1999). "A fast adaptive multipole algorithm in three dimensions." *Journal of Computational Physics*, **155**(2): pp. 468–498.

Chorin, A.J. and Hald, O.H. (1995). "Vortex renormalization in three space dimensions." *Physical Review B: Condensed Matter and Materials Physics*, **51**: pp. 11,969–11,972.

Chorin, A.J., Hughes, T.J.R., McCracken, M.F. and Marsden, J.E. (1978). "Product formulas and numerical algorithms." *Communications on Pure and Applied Mathematics*, **31**(2): pp. 205–256.

Chorin, A.J. (1973). "Numerical study of slightly viscous flow." *Journal of Fluid Mechanics*, **57**: pp. 785–796.

Chorin, A.J. (1980). "Vortex models and boundary layer instability." *SIAM Journal on Scientific and Statistical Computing*, **1**(1): pp. 1–21.

Chorin, A.J. (1990). "Hairpin removal in vortex interactions." *Journal of Computational Physics*, **91**(1): pp. 1–21.

Chorin, A.J. and Bernard, P.S. (1973). "Discretization of a vortex sheet, with an example of roll-up." *Journal of Computational Physics*, **13**(3): pp. 423–429.

Cipra, B.A. (2000). "The best of the 20$^{\text{th}}$ Century: Editors name top 10 algorithms." *SIAM News*, **33**.

Cottet, G. and Koumoutsakos, P. (2000). *Vortex methods: theory and practice*. Cambridge University Press.

Couët, B., Buneman, O. and Leonard, A. (1981). "Simulation of three-dimensional incompressible flows with a vortex-in-cell method." *Journal of Computational Physics*, **39**(2): pp. 305–328.

Cruz, F.A. and Barba, L.A. (2009). "Characterization of the accuracy of the fast multipole method in particle simulations." *International Journal for Numerical Methods in Engineering*, **79**(13): pp. 1577–1604.

Degond, P. and Mas-Gallic, S. (1989). "The weighted particle method for convection-diffusion equations, Part 1: The case of an isotropic viscosity." *Mathematics of Computation*, **53**(188): pp. 485–507.

Draghicescu, C.I. and Draghicescu, M. (1995). "A fast algorithm for vortex blob interactions." *Journal of Computational Physics*, **116**(1): pp. 69–78.

Fernandez, V.M., Zabusky, N.J., Liu, P. and Gerasoulis, A. (1996). "Filament surgery and temporal grid adaptivity extensions to a parallel tree code for simulation and diagnosis in 3D vortex dynamics." *ESAIM: Proceedings*, **1**: pp. 197–211.

Fishelov, D. (1990). "A new vortex scheme for viscous flows." *Journal of Computational Physics*, **86**: pp. 211–224.

Gharakhani, A. (1997). "A survey of grid-free methods for the simulation of 3-D incompressible flows in bounded domains." Tech. Rep. SAND97-2256, Sandia National Laboratory, US.

Grant, J. and Marshall, J. (2005). "Diffusion velocity for a three-dimensional vorticity field." *Theoretical and Computational Fluid Dynamics*, **19**: pp. 377–390.

Greengard, C. (1986). "Convergence of the vortex filament method." *Mathematics of Computation*, **47**: pp. 387–398.

Greengard, L. and Rokhlin, V. (1987). "A fast algorithm for particle simulations." *Journal of Computational Physics*, **73**(2): pp. 325–348.

Greengard, L. (1985). "The core spreading vortex method approximates the wrong equation." *Journal of Computational Physics*, **61**: pp. 345–348.

Harlow, F.H. (1956). "The Particle-in-Cell method for two dimensional hydrodynamic problems." Tech. Rep. Report No. LAMS-2082, Los Alamos Scientific Laboratory.

Harlow, F.H. (1988). "PIC and its progeny." *Computer Physics Communications*, **48**(1): pp. 1–10.

Hess, J. and Smith, A. (1964). "Calculation of nonlifting potential flow about arbitrary three dimensional bodies." *Journal of Ship Research*, **8**(2): pp. 22–44.

Huang, M.J., Su, H.X. and Chen, L.C. (2009). "A fast resurrected core-spreading vortex method with no-slip boundary conditions." *Journal of Computational Physics*, **228**: pp. 1916–1931.

Koumoutsakos, P. (2005). "Multiscale flow simulations using particles." *Annual Review of Fluid Mechanics*, **37**(1): pp. 457–487.

Leishman, J.G. (2002). "Challenges in modeling the unsteady aerodynamics of wind turbines." In "Proceedings of the 40th AIAA Aerospace Sciences Meeting and Exhibit Wind Energy Symposium," pp. 141–167. Reston, Reno, Nevada, USA.

Leitão, V., Alves, C. and Duarte, C. (2005). *Advances in meshfree techniques*, vol. 5 of *Computational methods in applied sciences*. Springer.

Leonard, A. (1980). "Vortex methods for flow simulation." *Journal of Computational Physics*, **37**: pp. 289–335.

Leonard, A. (1985). "Computing three-dimensional incompressible flows with vortex elements." *Annual Review of Fluid Mechanics*, **17**(1): pp. 523–559.

Li, S. and Lui, W.K. (2004). *Meshfree Particle Methods*. Springer Verlag.

Li, W. and Vezza, M. (2008). "A hybrid vortex method for the simulation of three-dimensional flows." *International Journal for Numerical Methods in Fluids*, **57**: pp. 31–45.

Lindsay, K. and Krasny, R. (2001). "A particle method and adaptive treecode for vortex sheet motion in three-dimensional flow." *Journal of Computational Physics*, **172**(2): pp. 879–907.

Low, A.R. (1928). "Postulates of hydrodynamics." *Nature*, **121**(3050): p. 576.

Lu, Z.Y. and Ross, T.J. (1991). "Diffusing-vortex numerical scheme for solving incompressible Navier-Stokes equations." *Journal of Computational Physics*, **95**: pp. 400–435.

Maganga, F., Pinon, G., Germain, G. and Rivoalen, E. (2008). "Numerical simulation of the wake of marine current turbines with a particle method." In "Proceedings of the 10th World Renewable Energy Congress (WRECX)," Glasgow, Scotland.

Majda, A.J. and Bertozzi, A.L. (2001). *Vorticity and Incompressible Flow*. Cambridge University Press.

Marshall, J.S. and Grant, J.R. (1996). "Penetration of a blade into a vortex core: vorticity response and unsteady blade forces." *Journal of Fluid Mechanics*, **306**: pp. 83–109.

Monaghan, J.J. (1985). "Particle method for hydrodynamics." *Computer Physics Reports*, **3**: pp. 71–124.

Moore, D.W. and Saffman, P.G. (1972). "The motion of a vortex filament with axial flow." *Philosophical Transactions of the Royal Society A: Mathematical, Physical and Engineering Sciences*, **272**: pp. 403–429.

Nordmark, H.O. (1996). "Deterministic high order vortex methods for the 2D Navier-Stokes equation with rezoning." *Journal of Computational Physics*, **129**: pp. 41–56.

Ogami, Y. and Akamatsu, T. (1991). "Viscous flow simulation using the discrete vortex model: the diffusion velocity method." In "Proceedings of the third international symposium on Computational fluid dynamics," pp. 433–441. Pergamon Press, Inc., Tarrytown, NY, USA.

Ould-Salihi, M.L., Cottet, G.H. and Hamraoui, M.E. (2000). "Blending finite-difference and vortex methods for incompressible flow computations." *SIAM Journal on Scientific Computing*, **22**: pp. 1655–1674.

Pinon, G., Mycek, P., Germain, G. and Rivoalen, E. (2012). "Numerical simulation of the wake of marine current turbines with a particle method." *Renewable Energy*, **46**(0): pp. 111–126.

Poncet, P. (2006). "Finite difference stencils based on particle strength exchange schemes for improvement of vortex methods." *Journal of Turbulence*, pp. 1–24.

Qian, L. and Vezza, M. (2001). "A vorticity-based method for incompressible unsteady viscous flows." *Journal of Computational Physics*, **172**: pp. 515–542.

Rehbach, C. (1977). "Numerical calculation of three-dimensional unsteady flows with vortex sheets." *La Recherche Aerospatiale* in French, pp. 289–298.

Rosenhead, L. (1930). "The spread of vorticity in the wake behind a cylinder." *Proceedings of the Royal Society of London A: Mathematical, Physical and Engineering Sciences*, **127**(806): pp. 590–612.

Rossi, L.F. (1996). "Resurrecting core spreading vortex methods: A new scheme that is both deterministic and convergent." *SIAM Journal on Scientific Computing*, **17**: pp. 370–397.

Shankar, S. and van Dommelen, L. (1996). "A new diffusion procedure for vortex methods." *Journal of Computational Physics*, **127**: pp. 88–109.

Speziale, C.G. (1987). "On the advantages of the vorticity-velocity formulation of the equations of fluid dynamics." *Journal of Computational Physics*, **73**(2): pp. 476–480.

Stock, M.J. and Gharakhani, A. (2010). "Modeling rotor wakes with a hybrid OVERFLOW-vortex method on a GPU cluster." In "Proceedings of the 28th AIAA Applied Aerodynamics Conference," .

Strickland, J.H., Kempka, S.N. and Wolfe, W.P. (1996). "Viscous diffusion of vorticity using the diffusion velocity concept." *ESAIM: Proceedings*, **1**: pp. 135–151.

Suh, J.C. (2000). "The evaluation of the Biot-Savart integral." *Journal of Engineering Mathematics*, **37**: pp. 375–395.

Swarztrauber, P. and Sweet, R. (1975). "Efficient FORTRAN subprograms for the solution of elliptic partial differential equations." Tech. rep., NCAR.

Taylor, I. and Vezza, M. (1999). "Calculation of the flow field around a square section cylinder undergoing forced transverse oscillations using a discrete vortex method." *Journal of Wind Engineering and Industrial Aerodynamics*, **82**(1-3): pp. 271–291.

Voutsinas, S.G. (2006). "Vortex methods in aeronautics: how to make things work." *International Journal of Computational Fluid Dynamics*, **20**(1): pp. 3–18.

Weißmann, S. and Pinkall, U. (2010). "Filament-based smoke with vortex shedding and variational reconnection." *ACM Transactions on Graphics*, **29**(4): pp. 115:1–115:12.

Willis, D.J. (2006). *An Unsteady, Accelerated, High Order Panel Method with Vortex Particle Wakes*. Ph.D. thesis, Massachusetts Institute of Technology.

Winckelmans, G., Cocle, R., Dufresne, L. and Capart, R. (2005). "Vortex methods and their application to trailing wake vortex simulations." *Comptes Rendus Physique*, **6**(4-5): pp. 467–486.

Winckelmans, G., Salmon, J., Warren, M., Leonard, A. and Jodoin, B. (1996). "Application of fast parallel and sequential tree codes to computing three-dimensional flows with the vortex element and boundary element methods." In "ESAIM: Proceedings," vol. 1, pp. 225–240.

Yokota, R. and Barba, L. (2011). "Comparing the treecode with FMM on GPUs for vortex particle simulations of a leapfrogging vortex rings." *Computers and Fluids*, **45**(1): pp. 155–161.

Zhou, H. (1997). "On the motion of slender vortex filaments." *Physics of Fluids*, **9**(4): pp. 970–981.

3

Finite-Volume Methods and Application to the Vorticity Transport Equations

3.1 Introduction

The finite-volume method (FVM) is another very well established computational methodology and is the basis for a very large number of commercial and public codes. Because of the volume of literature and availability of comprehensive textbooks on the subject, the first part of this chapter reviews very briefly a time-line of key developments in finite-volume methods relevant to the work of this thesis followed by a brief examination of the Reynolds-averaged Navier-Stokes equations in primitive-variable form, and their application to tidal power.

The second part of the chapter is concerned with the discretisation and representation of the equations governing the flow of an incompressible Newtonian fluid, using the Navier-Stokes equations in a vorticity-velocity formulation. In order to solve these numerically, they must first be represented in a computationally tractable form: the obvious candidate for achieving this end is the finite-volume method.

The finite-volume method has the advantage that it is – by virtue of its formulation – conservative. The equations are represented explicitly in terms of the flux into and out of control volumes and the domain is represented by integral values of flow quantities over the control volumes, unlike a purely finite-difference methodology whereby the fluid is represented by point-wise sampling over the domain. In other words, by virtue of the fact that the volume of the domain is split into sub-volumes and the face fluxes must be consistent between adjacent volumes, a quantity of a transport variable carried out of a volume must appear in its neighbour(s): conservation is enforced by the basis of the methodology.

The contents of this chapter are therefore split into four sections: a brief review followed by two theoretical and one practical sections. The first theoretical section deals with

the discretisation of the general transport equation in one to three space dimensions; the second deals with specific issues associated with the convection term; the final section describes the method as applied to the vorticity transport equations in two and three dimensions.

3.1.1 Premise

Computational Fluid Dynamics (CFD – that is, differential equations solved using numerical methods on some form of computational mesh, as opposed to approximations to fluid dynamics based on abstraction such as potential flow models) based on the finite-volume method solves the partial differential equations (PDEs) governing fluid flow on a domain tessellated into volumes. Volume integrals are converted to surface flux integrals using Gauss's theorem. Every finite-volume method contains the following constituents:

1. a PDE or system of PDEs describing the fluid flow;
2. a discretisation of a geometric representation of a physical problem into cells and representation in a computational domain, specifically including connecting faces between cells;
3. a point-wise storage of the volume averaged extensive properties of the fluid of interest at each cell; and
4. an approximation first to the parameter gradients and thus to the face fluxes due to convection/diffusion/etc. used to advance the solution.

From the most simple one-dimensional heat equation solution with 1 equation over 100 cells, to a three-dimensional Reynolds-averaged Navier-Stokes (RANS) simulation with 7 equations and billions of cells and free-surfaces etc., all models comprise these four major components.

3.2 Historical Development and Application to Tidal Power

The historical evolution of recognisable CFD probably started with Richardson, who attempted to model weather systems using differential equations in 1922 (without great success, although this was apparently a fault of the initial conditions rather than his method).[1]

[1] Richardson also neatly summarised the energy cascade in rhyming verse, and a thesis on vorticity would be remiss were it not included:

> Big whirls have little whirls that feed on their velocity,
> and little whirls have lesser whirls and so on to viscosity.

Courant, Friedrichs and Lewy (1928) provided a stability analysis of the convection equation, resulting in the Courant number. Thom (1933) manually computed the flow past a cylinder, repeated in Kawaguti (1953) using a desk calculator. Between the 1950s and 1980s there were significant developments in available computer power as well as some major theoretical advances, where the most relevant to this thesis are:

- Courant, Isaacson and Rees (1952) provide the CIR scheme that is an upwind biased finite-difference stencil – see Section 3.6.1. This paves the way for stable methods for discretising systems of equations.
- In Godunov (1959), it is proven that a numerical scheme that does not introduce oscillations near solution discontinuities (is monotonic) and has constant coefficients (is linear) can be at most first-order accurate when used to advance the linear advection equation. In the same paper the “upwind scheme” is presented that provides the least diffusive, lowest truncation error monotonic finite-volume method.
- Strang (1968) provides a second-order sub-time-stepping method for time marching convection and diffusion operators (and in fact dimensional operators too). This is discussed further in Section 3.4.
- Fromm (1968) provided a scheme that was second-order in both space and time, based on using an average of Lax-Wendroff and Beam-Warming fluxes. van Leer (1977) states that the method, though highly acclaimed, “appears to be used mainly by its inventor.”
- Boris and Book (1973) present a “Sharp And Smooth Transport Algorithm" – SHASTA – and develop a successful means of preserving monotonicity, namely *Flux Corrected Transport*, which paves the way for the concept of flux limiters. An anti-diffusive (correction) flux was applied after the solution was advanced using a first-order upwind scheme.
- The work of van Leer (1974) provides a slope limiter that is an average of the non-conservative limited versions of the Lax-Wendroff and Beam-Warming schemes, resulting in a conservative, limited version of Fromm’s scheme. The seminal van Leer (1979) MUSCL (Monotonic Upwind Schemes for Conservation Laws) provides explicit, monotonic schemes that are considerably more accurate than ordinary first-order upwind methods.
- Harten (1983) introduces the notion of *Total Variance Diminishing* (TVD) to characterise oscillation free schemes, and Harten’s theory provides the necessary and

sufficient conditions that a scheme is TVD and is used to construct flux limiter functions. A TVD scheme is one in which over time, maxima reduce, minima increase, and no new extrema are created, and Harten proves that a monotone scheme is TVD, and that a TVD scheme remains monotone.

- Sweby (1984) introduces flux limiters by adding the anti-diffusive flux to a conservative and stable first-order scheme. A class of limiters (into which the as yet unpublished minmod, superbee etc. slot) was proposed and investigated numerically. The main result of this paper was the TVD diagram for flux-limiter design.

- In Engquist, Osher and Somerville (1985), Roe (1985) publishes the minmod and superbee limiters (and calls van Leer's MUSCL "Ultimate Conservative Differencing Scheme" a mirage, "a dream city hovering in the distant haze"). He seeks a "high accuracy with guaranteed exclusion of non-physical oscillations or entropy-violating solutions."

3.2.1 Primitive Variable CFD

Reynolds-averaged Navier-Stokes (RANS) equations in pressure-velocity – "primitive variable" – form are the basis of most CFD; certainly the vast majority of practical engineering solutions obtained with commercial solvers. RANS equations are obtained by Reynolds decomposition of the exact instantaneous Navier-Stokes equations into a time-averaged and fluctuating component. The "time-averaging" is conceptual rather than real: it allows separation of the "unsteady" or "turbulent" component of the flow by assuming the time scales associated with turbulence are significantly faster than those associated with the bulk flow. Although "steady" CFD calculations are ignored in this review, as they are an abstract form of a time-marching method where the objective is to tend the time-derivatives towards zero, applying the Reynolds-averaging to the unsteady turbulent flowfield results in equations that may have steady, i.e. equilibrium, solutions. During a simulation, the transport variables themselves are *not* time averaged – except in the sense of the finite-volume integral averaging – but are taken as belonging to an ergodic process at each time-step for the purpose of the Reynolds (ensemble) averaging: the conceptual ensemble averaging returns a mean velocity for all the velocities over that volume of space-time.

The Reynolds stresses, $\tau_{ij} = \overline{u_i' u_j'}$ for dimensions i and j, are the only fluctuating terms that remains in the RANS equations after time-averaging and they are taken as representing turbulent velocity fluctuations. They must be approximated with a closure model, generally referred to as a turbulence model. Two major methods exist for RANS turbu-

lence modelling: Reynolds Stress Modelling (RSM) or an eddy viscosity model. The eddy viscosity model uses the Boussinesq hypothesis that states that the small scale momentum transfer due to the turbulent eddies is effectively isotropic and can thus be modelled as a form of viscosity. This is because turbulence mixes transported quantities in the flow causing fluctuations in the quantities. The Boussinesq approximation proposes a relation that defines τ in terms of the mean velocity gradients and the turbulent kinetic energy per unit mass k. Reynolds Stress Modelling treats each important term in τ with its own transport equation along with a scaling equation (generally for k). Turbulence models seek to close the RANS equations by arriving at a value for the eddy viscosity μ_t – which is appended to the Newtonian viscosity – or Reynolds stresses τ. This is based on calculated flow parameters and using the turbulent kinetic energy k in an empirical process dependant on a scaling equation (solving additional PDEs for k and also e.g. dissipation rate ϵ or specific dissipation rate ω) and not on the finite-volume mesh scale. This mesh scale independence means that the eddy viscosity does not tend to zero with increasing mesh density (an alternative to RANS is Large Eddy Simulation, where this is the raison d'étre – see Section 3.2.1.2). The resulting RANS solution is in essence a laminar solution where the transport variable fields are the Reynolds average of the turbulence fields, and there is an additional corrective diffusion to stabilise the model by damping out the small perturbations.

The most regularly used turbulence models are given in Table 3.1, where the number of equations is indicative of complexity and computational overhead. In the absence of a turbulence model, one obtains a so-called "laminar" RANS method, where the energy cascade effectively stops at the scale of the grid: if the grid and time scales were of the order of the Kolmogorov micro-scales, the method would qualify as a Direct Numerical Simulation as long as all length scales were correctly resolved.

Turbulence models suffer a number of deficiencies: two equation models (e.g. variations on $k-\epsilon$ and $k-\omega$) rely on being equilibrium turbulent flow – that rate of production and destruction are equal – in order to be able to calculate the turbulent dissipation ϵ from k. They also rely on the assumption of isotropic turbulence: RSM does not. As mentioned, eddy viscosity acts as an additional diffuser in a laminar simulation and is dependant on the nearby global flow rather than the availability of additional resolution on the mesh: RSM circumvents this. RSM introduces 5 additional transport variables (over 2 equation models) that must be solved – the computational overhead of achieving mesh independence with RSM simulations is exceedingly high; higher than attempting to resolve the larger-scale turbulence on the grid using a method such as Large Eddy Simulation.

Comparisons between a number of the turbulence models applied to tidal turbines can be found in Klaptocz *et al.* (2007) and Consul and Willden (2009), and in the general literature in, for example, Versteeg and Malalasekera (2007). A summary of observations regarding the applicability of the various models is that:

- The Spalart-Allmaras model is the lowest cost turbulence model but suffers from poor post-stall performance and an inability to support a bluff-body wake during transient cross-flow turbine simulations, as reported in Consul and Willden (2009). Consul and Willden also state that the model performs poorly at lower-than stall angles of attack. This somewhat contradicts advice given in ANSYS (2012) stating that the model should perform well in adverse pressure gradients, however, the advice does go on to state that the model poorly predicts the transition from a boundary layer to a free-shear layer due to a lack of length scales support, and this might be the root of the issue.

- $k-\epsilon$ variants perform better than Spalart-Allmaras, but at the cost of an additional equation. They represent probably the most often used turbulence model taken over all CFD calculations.

- $k-\omega$ variants perform better than $k-\epsilon$ close to solid boundaries with detached and recirculating flow due to adverse pressure gradients, for example on stalled aerofoils, but displays worse behaviour than the $k-\epsilon$ models in the freestream due to high sensitivity to inflow turbulence. To circumvent this, a coupled model that uses $k-\omega$ near the wall and switches to $k-\epsilon$ away from the wall is often used, and is apparently the most popular model in tidal turbine CFD analysis. However, in Batten, Harrison and Bahaj (2011) it is noted that the blending functions in the $k-\omega$ SST model (sub-shear transport model, as this is known) cause underprediction of eddy viscosity in turbine wakes, and hence the rate of wake recovery was reduced. Other examples of use for tidal devices are in Harrison *et al.* (2009); McSherry *et al.* (2011); Jo *et al.* (2011).

- Reynolds Stress Models take approximately 50 % to 60 % additional CPU per iteration, 15 % to 20 % additional memory and require more iterations than eddy-viscosity models (ANSYS, 2012) but this is rewarded with the ability to model highly swirling or stress driven flows, where turbulence is anisotropic. O'Doherty *et al.* (2009) uses the RSM as a benchmark for testing simpler models, and finds that although measurable, the differences between models are marginal.

Turbulence Model		
Model	Equations	Used By e.g.
Spalart-Allmaras	1	Klaptocz *et al.* (2007), Consul and Willden (2009)
$k-\epsilon$ variants	2	Masters *et al.* (2013)
$k-\omega$ variants	2	Harrison *et al.* (2009), Jo *et al.* (2011)
RSM	7	O'Doherty *et al.* (2011)

Table 3.1: The more prominent turbulence models. References are for work where the model is used on wind turbines or tidal devices. All models are fully described in Versteeg and Malalasekera (2007).

In addition to the closure problem, primitive variable RANS CFD requires a means of coupling the pressure and velocity fields. The issue is that given an initial condition for these fields, the momentum equations can be solved for velocity, but there is no pressure term in the continuity equation – there are too many unknowns for the number of equations. Various methods exist, e.g. SIMPLE, PISO and others (see Versteeg and Malalasekera, 2007), and they all iterate on the pressure and velocity fields until some arbitrary convergence criterion is met. A related requirement is that pressures cannot be specified simultaneously with velocities, due to their coupling in the Navier-Stokes equations. In situations where a particular flow velocity is desired at an inflow boundary, in order that there be no flow reversal, the domain must be resolved and the velocity and pressure solved at locations often some considerable distance away from regions of interest.

3.2.1.1 CFD Codes Used in Modelling Tidal Devices

There exist several commercial and a large number of in-house codes, where a subset are suitable for analysis of tidal turbines. The most prominent commercial codes are ANSYS FLUENT and CFX (accounting for 33 % and 22 % respectively of all CFD papers in EWTEC 2005-2011). Table 3.2 provides a breakdown of the code use in these conferences.

3.2.1.2 Applications and Extensions Relevant to Tidal Power

Actuator-Disc/RANS embeds an actuator-disc within a RANS CFD framework. The forces on the flow due to the actuator-disc are accommodated within the CFD model by inclusion of an additional momentum source/sink. In general, the thrust load on the actuator-disc is trimmed to a particular operating point, and the wake and upstream effects are modelled. Actuator-disc momentum theory is used to calculate the source term, and the turbine model can be easily parameterised using the $C_P - \lambda$ and $C_T - \lambda$ curves for the device feeding the thrust characteristics into the CFD code via, for example, a method based on Darcy's law or similar. Clearly, this model cannot incorporate effects due to individual blades, but there is an advantage in that the number of cells required is significantly lower than if a turbine rotor were to be fully meshed, and resources can be re-deployed in areas of interest [or large numbers of turbines can be modelled, as in the ANSYS WindModeller package ANSYS (2013)].

BEMT/RANS embeds a Blade Element/Momentum Theory (BEMT) model within a RANS framework, similarly to Actuator-Disc/RANS. Relevant examples of this include work in Malki *et al.* (2013) and that of Turnock *et al.* (2011), both used for modelling arrays of

Software		
Code & Occurrences	Example Capabilities & Applications	Reference
CFX (11)	3-D axial-flow turbine modelling – verification/validation studies	e.g. McSherry *et al.* (2011)
	Cross-flow turbines & aerofoil section analysis	e.g. Gretton *et al.* (2005; 2007; 2009; 2011)
	Actuator-disc/RANS modelling	e.g. Batten, Harrison and Bahaj (2011), Daly, Myers and Bahaj (2011)
	Meso-scale hydrodynamics	Jones *et al.* (2011)
FLUENT (17)	Analysis, design & optimisation of axial-flow turbines	e.g. O'Doherty *et al.* (2009), Mason-Jones *et al.* (2011)
	Devices operating in proximity to a free-surface	e.g. Couch, Sun and Bryden (2005), Consul, Willden and McIntosh (2011)
	Cross-flow turbines	e.g. Klaptocz *et al.* (2007), Consul and Willden (2009)
	Coaxial rotor systems	e.g. Clarke *et al.* (2007), O'Doherty *et al.* (2009)
	Arrays, wakes and meso-scale hydrodynamics	e.g. Bai, Spence and Dudziak (2009), Adams, Ranford and Livingston (2011)
	Ducted rotor systems	e.g. Belloni and Willden (2011)
	Oscillating hydrofoil systems	e.g. LES in Kloos, Gonzalez and Finnigan (2009)
CODE_SATURNE (1)	RANS of turbine including deforming free-surface	Gretton, Ingram and Bryden (2011)
OPENFOAM (3)	RANS/LES of arrays of axial-flow devices in three dimensions	Churchfield, Li and Moriarty (2011)
	Optimisation and analysis of axial-flow turbines	Ruopp, Ruprecht and Riedelbauch (2011)
PHYSICA (1)	3-D BEMT/RANS for individual & multiple axial-flow turbines	Malki *et al.* (2011)
SNL-EFDC (1)	Simulating porous disc flowfields	James *et al.* (2011)

tidal turbines and McIntosh, Fleming and Willden (2011) who use it for turbine design.

Large Eddy Simulation (LES) uses a low-pass filtering process rather than time or ensemble averaging to separate out the fast time scales in the governing equations. The largest energy containing eddies are resolved on the mesh, and the mesh can act like a box filter on length scales; alternatively a finer mesh can be used than the largest scale to be resolved, and a filtering kernel is applied to the governing equations. Processes whose scale is lower than that of the mesh or the filtering kernel are dealt with using a sub-grid-scale (SGS) model or the smallest resoluble eddies are allowed simply to dissipate due to the artificial viscosity. The results are a turbulence field made up of bulk flow and large-scale resolved eddies, and a modelled SGS correction. Since LES introduces a grid dependence into the actual PDEs being solved, mesh dependence studies are difficult except in the limiting case where it approaches a Direct Numerical Simulation. Successful LES is very grid intensive, especially when attempting to capture boundary layers. Because of this, a hybrid RANS/LES method known as Detached Eddy Simulation exists whereby RANS is used at the boundary layer, and the LES is used elsewhere (actually, LES is not always used elsewhere – Euler solutions can be employed in “padding" regions where there will be no turbulence, far away from regions of interest). Until recently, typical LES models of turbine rotors presently appeared to eschew resolving the blades themselves, utilising actuator disk/line models. For example, LES was used by Jimenez *et al.* (2007) to simulate wind turbine wakes with a model which used a drag force rather than explicitly model the rotor blades. The results showed rough qualitative agreement with experiment, especially in terms of τ. Calaf, Meneveau and Meyers (2010) use an actuator disk approach to model large arrays of wind turbines and Churchfield, Li and Moriarty (2011) performed an actuator line based analysis of the rotor/wake interaction between a group of three tidal turbines. Churchfield, Li and Moriarty report that the primary difficulty was in generating the background turbulent velocity field, in particular this paper utilised a field which was “recycled” until the desired characteristics were obtained. An unintended and undesirable coherent structure developed and was recirculated and stretched longitudinally throughout the length of the domain. Afgan *et al.* (2013) perform a comparison of LES and RANS CFD applied to a model tidal turbine including a fully resolved rotor. Both LES and RANS produce good agreement in global performance metrics (C_P and C_T) but RANS performance drops at $\lambda < 3$ where it underpredicts C_P. LES trumps RANS in resolving tip vortices and

Table 3.2*(facing page)*: Summary of finite-volume method RANS/LES based CFD codes used in European Wave and Tidal Energy Conferences for modelling tidal devices between 2005-2011.

their interaction with the turbine tower. Afgan *et al.* observe that the cost of each LES simulation is around 4.4 million CPU hours, by comparison each RANS run required 0.14 million CPU hours and the BEMT/RANS model of Malki *et al.* (2013) applied to the same rotor geometry required 30 CPU hours (although it is not apparent what clock speed the CPUs were).

Concluding remarks on RANS based CFD The take-home message from this subsection on RANS based CFD is that there is no universally applicable model setup. Each case must be considered individually and the coupled factors of model choice, mesh generation, boundary and initial condition parameterisation and so on must be performed based on the experience of the operator or existing best practices.

The competing requirements of the CFD mesh to simultaneously resolve the developing boundary layer – as well as retaining sufficient wake that appropriate boundary conditions may be applied downstream – are coupled with the fact that the entire domain must contain computational cells, even if they contain nothing of immediate interest. This is either treated directly at great cost, as in LES, or circumvented, as in actuator-disc, or BEMT RANS.

3.3 Discretisation of the General Transport Equation

The following sections will consider a passive scalar φ in 1-3 space dimensions, which is subject to convection due to the velocity field $\boldsymbol{u}(\boldsymbol{x},t)$ as well as diffusion. The evolution of φ given by the differential form of the general transport equation:

$$\frac{\partial\varphi(\boldsymbol{x},t)}{\partial t}+\nabla\cdot\boldsymbol{f}(\boldsymbol{x},t)=\nabla\cdot\left(\Gamma\nabla\varphi(\boldsymbol{x},t)\right), \tag{3.1}$$

where the convective flux function $\boldsymbol{f}(\boldsymbol{x},t)=\boldsymbol{u}(\boldsymbol{x},t)\varphi(\boldsymbol{x},t)$. This allows the derivation of the discretised form of the transport equations to proceed in a transport variable independent manner; later sections describe extension to the vorticity transport equations using these methodologies.

3.3.1 Integral Form of the General Transport Equation

Specifications of a finite-volume The present method only considers cubic finite-volumes, or cells, that are aligned to a right Cartesian coordinate system. This gives rise to the following properties:

1. Each volume has side length $\Delta x = \Delta y = \Delta z = h$ and the spacing between centroids of each volume is also h;

2. The face areas are unity, h and h^2 respectively for one-, two- and three-dimensional volumes;

3. The volumes of cells are thus h, h^2 and h^3 respectively.

The Imperial College compass notation (Versteeg and Malalasekera, 2007) is used since in the final implementation of the present method, cells are not stored in a contiguous array and may also not have neighbours. However, in unit tests in one- and two-dimensions, and also in the general literature (Hirsch, 1988; Toro, 1999; LeVeque, 2002), contiguous arrays of cells are used and so it often makes sense to refer to cell neighbours by their indices.

Consider a simply connected domain in one to three space dimensions tessellated with volumetric elements Ω and containing a distribution of an inert scalar φ. Define flow parallel to the axis system sharing the sign of those axes. In order to solve the transport equation in unsteady flow, the substantive derivative must be retained in its entirety during the discretisation process. A finite-volume integration is performed by defining the volume averaging of scalar quantity φ over the volume Ω and and subsequently over a time interval as

$$\int_{\Delta t}\int_{\Omega} \frac{\partial \varphi}{\partial t}\, \mathrm{d}V\, \mathrm{d}t + \int_{\Delta t}\int_{\Omega} \nabla \cdot \boldsymbol{f}\, \mathrm{d}V\, \mathrm{d}t = \int_{\Delta t}\int_{\Omega} \nabla \cdot \left(\Gamma \nabla \varphi\right)\, \mathrm{d}V\, \mathrm{d}t. \tag{3.2}$$

Using Gauss's theorem, the integral sum of the value of all sources and sinks within the control volume is equal to the flux through the surface of a control volume. So for the scalar field $\varphi(\boldsymbol{x}, t)$ and a divergence free velocity field $\boldsymbol{u}(\boldsymbol{x}, t)$ the convection term is

$$\int_{\Omega} \left[\boldsymbol{u} \cdot \left(\nabla \varphi\right) + \varphi \left(\nabla \cdot \boldsymbol{u}\right)\right]\, \mathrm{d}V = \int_{\partial\Omega} \boldsymbol{f} \cdot \mathrm{d}\boldsymbol{S}, \tag{3.3}$$

and the diffusion term is

$$\int_{\Omega} \nabla \cdot \left(\Gamma \nabla \varphi\right)\, \mathrm{d}V = \int_{\partial\Omega} \left(\Gamma \nabla \varphi\right) \cdot \mathrm{d}\boldsymbol{S}. \tag{3.4}$$

Dropping the integral subscripts for clarity, and substituting the RHSs of Eqs. (3.3) and (3.4) into Eq. (3.1) results in a more useful form of the general transport equation,

$$\iint \frac{\partial \varphi}{\partial t}\, \mathrm{d}V\, \mathrm{d}t + \iint \boldsymbol{f} \cdot \mathrm{d}\boldsymbol{S}\, \mathrm{d}t = \iint \left(\Gamma \nabla \varphi\right) \cdot \mathrm{d}\boldsymbol{S}\, \mathrm{d}t. \tag{3.5}$$

This can be written in words as

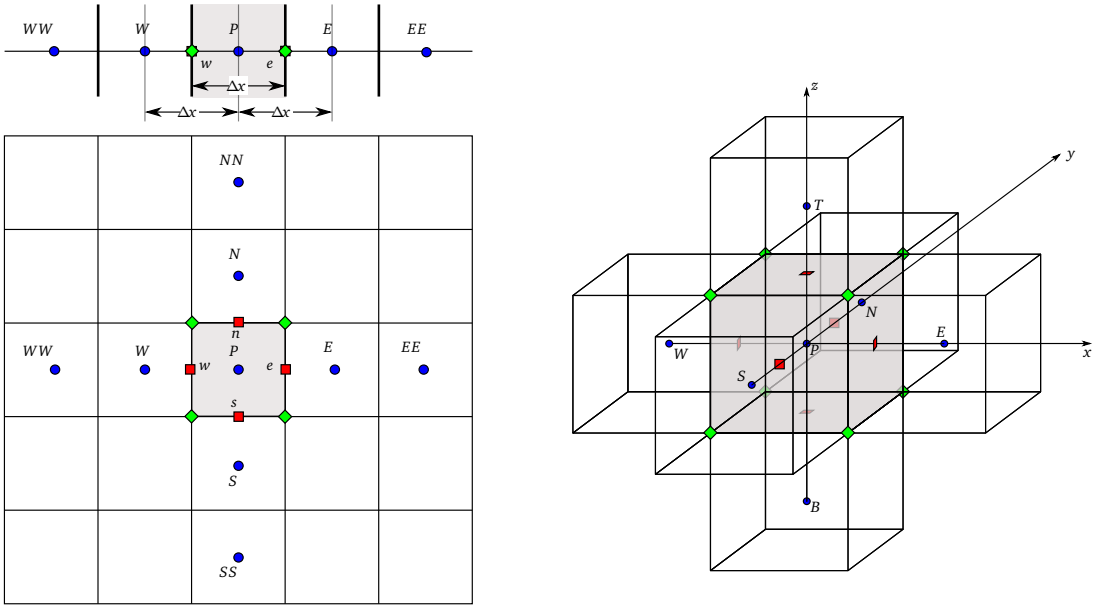

Figure 3.1: Properties of a cubic finite-volume cell in one dimension (top-left), two dimensions (bottom-left) and three dimensions (bottom-right). Blue dots (●) indicate location of cell averages; green rhombi (⧫) are where cell velocities are obtained; red squares (■) are where face fields and fluxes are calculated. For simplicity, only the nearest neighbours are shown in three dimensions, and cell dimensions are only indicated in one dimension.

Table 3.3: Properties of a cubic finite-volume cell: Imperial College compass subscripts.

			Neighbour					
			East	*West*	*North*	*South*	*Top*	*Bottom*
Cell	*Array*		*i+1,j,k*	*i-1,j,k*	*i,j+1,k*	*i,j-1,k*	*i,j,k+1*	*i,j,k-1*
	Compass		*N*	*S*	*E*	*W*	*T*	*B*
Face	*Array*		*i+1/2,j,k*	*i-1/2,j,k*	*i,j+1/2,k*	*i,j-1/2,k*	*i,j,k+1/2*	*i,j,k-1/2*
	Compass		*e*	*w*	*n*	*s*	*t*	*b*
	Normal	***i***	1	-1	0	0	0	0
		j	0	0	-1	1	0	0
		k	0	0	0	0	1	-1

$$\begin{array}{l}\text{Rate of change of } \varphi \\ \text{in } \Omega\end{array} + \begin{array}{l}\text{Rate of } \varphi \text{ convective flux out of } \Omega \\ \text{through } \partial\Omega\end{array} = \begin{array}{l}\text{Rate of } \varphi \text{ diffusion} \\ \text{into } \Omega \text{ through } \partial\Omega.\end{array}$$

This is the finite-volume form of the general transport equation. What remains is to find approximations to the integrals. A central tenet of the finite-volume method that aids in the approximation of Eq. (3.5) is that the value of φ "in" each volume is the volume integrated (and time averaged) value: $\varphi \equiv \overline{\varphi}$ – this is taken as read hereafter. This means that at time t the domain is represented by a number of sub-volumes that are piecewise constant in φ. It is the quality of the approximation to the face fields that will determine the success of the finite-volume scheme.

For each control volume P, the volume average of a quantity $[\ldots]$ is given by

$$\overline{[\ldots]}_P(t) = \frac{1}{\Delta V_P}\int_{\Delta V_P} [\ldots](\boldsymbol{x},t)\ \mathrm{d}V, \tag{3.6}$$

and so performing the time integration over Δt and the volume integration over ΔV_P, the time derivative on the LHS of Eq. (3.5) can be written as

$$\int_{\Delta t}\int_{\Delta V_P} \frac{\partial\varphi(\boldsymbol{x},t)}{\partial t}\ \mathrm{d}V\ \mathrm{d}t = \left(\overline{\varphi}_P(t+\Delta t) - \overline{\varphi}_P(t)\right)\Delta V_P. \tag{3.7}$$

The evolution of the volume and time averages of Eq. (3.5) is

$$\overline{\varphi}_P(t+\Delta t) = \overline{\varphi}_P(t) - \frac{1}{\Delta V}\iint \boldsymbol{f}(\boldsymbol{x},t)\cdot\mathrm{d}\boldsymbol{S}\ \mathrm{d}t + \frac{1}{\Delta V}\iint \left(\Gamma\nabla\varphi(\boldsymbol{x},t)\right)\cdot\mathrm{d}\boldsymbol{S}\ \mathrm{d}t, \tag{3.8}$$

where the RHS integrations are taken over the time-step Δt starting at t and over the surfaces of the sub-volume. This expression forms the basis of all numerical time integrators considered in this thesis. More advanced integrators, e.g. Runge-Kutta, Adams-Bashforth-Moulton or Strang splitting simply use intermediate time-steps that are all still advanced explicitly using this form of expression. Stability criteria in one dimension still apply to these sub-steps (through modification of e.g CFL conditions to use the sub-step Δt).

3.4 Time Evolution Strategies

3.4.1 Operator Addition

For one-dimensional flow, a method to utilise the Euler integration scheme is obtained by extending the volume integral averaging method to a volume containing a time dimension. Putting all spatial variables on the RHS and all temporal variables on the LHS results in

expressions of the form

$$\text{LHS:} \int_{\Delta t} \frac{\partial \varphi}{\partial t} \, \mathrm{d}t = \varphi(t + \Delta t) - \varphi(t) \quad \text{and} \tag{3.9a}$$

$$\text{RHS:} \int_{\Delta t} [\ldots] \; \mathrm{d}t = [\ldots] \, \Delta t, \tag{3.9b}$$

and therefore $\varphi(t + \Delta t) = \varphi(t) + [\ldots] \, \Delta t$.

The ellipsis in brackets indicate the volume averaged time derivatives – e.g. terms in Eq. (3.8) – as calculated due to convection and diffusion (and stretching for the vorticity transport equation) brought together. Truncation error analysis reveals that the leading error term is $\mathcal{O}(\Delta t)$ so the scheme is first-order in time.

In the scheme above, all of the finite-volume operations have been combined in the brackets to give a single time rate of change of the transport variable. This process is known as "operator addition", and each of the convection, diffusion and stretching terms is termed an operator. The operator addition method assumes that each operator is applied independently of the others – in other words is integrated simultaneously as an independent PDE using the same initial conditions. Operator addition is one method of coupling the various components of a scheme, however, it suffers in that it cannot guarantee a stable scheme, even if all operators are stable for the given cell conditions. It does have the advantage that – for "steady" problems where an equilibrium condition is exists – the operators can cancel allowing exactly zero time derivative; however, this is unlikely in the work of this thesis.

For two-dimensional flow, operator addition is used with an explicit forward Euler type step resulting in the expression

$$\varphi_P(t + \Delta t) = \varphi_P(t) + \frac{\Delta t}{\Delta x \Delta y} \left[\left(\left(d_\mathrm{e} - f_\mathrm{e} \right) - \left(d_\mathrm{w} - f_\mathrm{w} \right) \right) + \left(\left(d_\mathrm{n} - f_\mathrm{n} \right) - \left(d_\mathrm{s} - f_\mathrm{s} \right) \right) \right], \tag{3.10}$$

where the diffusive fluxes $d_{[\ldots]}$ and the convective fluxes $f_{[\ldots]}$ are calculated as described in later sections. This is first-order in time and up to second-order in space.

3.4.2 Fractional Step Methods

An alternative to the operator addition method are fractional step methods, or "operator splitting". The objective is to cover the time-step using a series of individual steps, each corresponding to application of a single operator, and each using the output of the previous. The advantages of this method is that different schemes can be used for each stage (in both time and space if desired) and the stability and accuracy of the scheme are only as bad as

the characteristics of the worst operator, allowing the use of high-resolution schemes with higher than first-order time marching in two and three dimensions.

Two explicit examples for the convection/diffusion equation are Lie splitting and Strang splitting.

3.4.2.1 Lie Splitting

Lie splitting – formally first-order (LeVeque, 2002) – uses the mean of the original and the solution advanced using the first operator (e.g. convection) over the complete time-step as the input to the second operator (e.g. diffusion), whose solution becomes that at the next time-step:

$$\frac{\varphi(t^*) - \varphi(t)}{\Delta t} = -(\boldsymbol{u} \cdot \nabla)\,\varphi(t); \tag{3.11a}$$

$$\frac{\varphi(t + \Delta t) - \varphi(t^*)}{\Delta t} = \Gamma \nabla^2 \left(\frac{\varphi(t^*) + \varphi(t)}{2} \right). \tag{3.11b}$$

Applied to convection-diffusion equations in one-dimension, this splitting is exact (as are all splittings, since the one-dimensional convection and diffusion operators commute). However, for non-commutative operators (e.g. multi-dimensional convection problems), taking a Taylor expansion of Eqs. (3.11a) and (3.11b) and substituting the expansion of Eq. (3.11a) into Eq. (3.11b) and subtracting from the expansion for the original problem reveals that Lie-splitting results in a leading splitting error of $\mathcal{O}(\Delta t^2)$.

3.4.2.2 Strang Splitting

Strang splitting – formally second-order (LeVeque, 2002) – advances the solution using the first operator over a half time-step to provide input to the second operator, which advances the solution over a complete step. The output of this is then used to advance the solution using the first operator again over a second half time-step:

$$\frac{\varphi(t^*) - \varphi(t)}{\Delta t/2} = -(\boldsymbol{u} \cdot \nabla)\,\varphi(t); \tag{3.12a}$$

$$\frac{\varphi(t^{**}) - \varphi(t^*)}{\Delta t} = \Gamma \nabla^2 \left(\frac{\varphi(t^*) + \varphi(t^{**})}{2} \right); \tag{3.12b}$$

$$\frac{\varphi(t + \Delta t) - \varphi(t^{**})}{\Delta t/2} = -(\boldsymbol{u} \cdot \nabla)\,\varphi(t^{**}). \tag{3.12c}$$

This approach can be written in a form of shorthand as e.g. *cddc*, for *convection, diffusion, diffusion, convection,* where the two diffusion steps are each taken over $2 \times \Delta t/2 = \Delta t$.

Multidimensional schemes can be obtained by writing the directional convection operations as x, y and z. In two dimensions, an *alternating dimension* (AD) Strang splitting might be *xyyx* or *yxxy*, and similarly in three dimensions *xyzzyx* and so on for any cyclical arrangement of operators. Clearly, the end results will be dependant on the starting operator. A potential issue with this form of the Strang splitting compared to the Lie splitting is that when applied to multidimensional flows, the integrations in the first dimension are performed over half time-steps that can result in increased artificial diffusion and thus reduced accuracy due to being conducted at Courant number $C \leq 1/2$. If the operators do not commute, the splitting error term in the AD scheme is $\mathcal{O}(\Delta t^3)$.

A better alternative is to use the *symmetrically weighted sequential splitting* (SWSS), which is essentially the arithmetic mean of solution results from two simultaneous but independent sequential Lie splittings, where each sub-integration is taken over the full time-step and the operators are applied in opposite directions. The truncation error term in the SWSS scheme is $\mathcal{O}(\Delta t^3)$.

This is analogous to a Runge-Kutta or a predictor/corrector scheme in that an Euler step predictor is used to supply the input to a trapezoidal step corrector resulting in (for the simplest case with only one operator) Heun's method. This yields solutions that are independent of the order of integrations. So, for example, a scheme for two-dimensional convection only is $(xy+yx)/2$ and for three-dimensional convection-diffusion $(dxyz+zyxd)/2$. SWSS and AD are both globally second-order accurate in time, and as long as the schemes used for each dimension are TVD, then the overall schemes are are stable (the concept of TVD does not make sense in higher than one dimension, since inflow from neighbouring cells can correctly cause local extrema) in two and three dimensions.

From the perspective of the method proposed in this thesis, the most important operator to get "right" is the convection term if a high-resolution method is to be obtained. The following Section identifies methods used to linearise and discretise this term. Later, the diffusion and tilt/stretch term will be addressed.

3.5 Convection Term

To begin linearising the convection term, consider Eq. (3.1) reduced to one dimension and written as the linear advection equation

$$\frac{\partial \varphi}{\partial t} + \frac{\partial f}{\partial x} = 0. \tag{3.13}$$

The flux function is now scalar, and Γ is set to zero. The linear advection equation is useful for demonstrating the performance of numerical schemes, as it ensures that all dissipation (amplitude) and dispersion (phase) errors in the solution are non-physical. Recalling Eq. (3.8) and noting that in one dimension ∇f and $\partial f/\partial x$ are equivalent, the convection term in isolation can be integration averaged over the control volume $x \in [x_\mathrm{w}, x_\mathrm{e}]$ as

$$\frac{1}{x_\mathrm{e} - x_\mathrm{w}} \int_{x_\mathrm{w}}^{x_\mathrm{e}} \frac{\partial f}{\partial x} \,\mathrm{d}x = \frac{1}{h} \int_{\partial\Omega} f \,\mathrm{d}S. \tag{3.14}$$

Noting that the faces of a control volume aligned with a right Cartesian axis system have the properties in Table 3.3, Eq. (3.14) can be written as

$$\frac{1}{h} \int_{\partial\Omega} f \,\mathrm{d}S \equiv \frac{1}{h} \left[\left(f_\mathrm{e} A_\mathrm{e}\right) - \left(f_\mathrm{w} A_\mathrm{w}\right) \right]. \tag{3.15}$$

In other words, using divergence theorem, the volume integral of the flux over the control volume Ω has been substituted with an evaluation of the flux through its faces $\partial\Omega$, which is evaluated at the boundaries of the cell. Eq. (3.15) can be expanded into three dimensions by various means, for example repeating the process with the additional space dimension to arrive at an operator addition approximation. So for a cubic control volume

$$\frac{1}{\Delta V} \int_{\partial\Omega} \boldsymbol{f} \cdot \mathrm{d}\boldsymbol{S} \equiv \frac{A}{\Delta V} \left[\left(f_\mathrm{e} - f_\mathrm{w}\right) + \left(g_\mathrm{n} - g_\mathrm{s}\right) + \left(h_\mathrm{t} - h_\mathrm{b}\right) \right]. \tag{3.16}$$

The convection integral is now discretised in space. Next, approximations for the face fluxes based on using the information obtained from the distribution of the volume averaged flow variables must be found.

The finite-volume methodology consists of approximating the solution of the face fields required by Eq. (3.15) by a piecewise constant distribution of the cell average values φ at time t. Given the flux functions are to be evaluated at the cell interfaces, but the cell averaged quantities "live" at the cell centres, a logical approximation might seem to be to use a central-difference between adjacent cell centred values, essentially averaging the values in neighbouring cells at the cell boundary.

3.5.1 Central-Differencing

The volume averaged quantities can be extrapolated to a face from the adjacent cell centres using a central-difference, so for example φ fields at the east and west faces of cell P can be approximated by

$$\varphi_\mathrm{e} \approx \varphi_P + \frac{\varphi_\mathrm{E} - \varphi_P}{\Delta x} \cdot \frac{h}{2} \quad \text{and} \quad \varphi_\mathrm{w} \approx \varphi_P + \frac{\varphi_P - \varphi_\mathrm{W}}{h} \cdot \frac{h}{2}; \tag{3.17 a,b}$$

which gives cell faces fluxes

$$f_{\mathrm{e}} = u_{\mathrm{e}} \left[\varphi_P + \frac{1}{2} \left(\varphi_{\mathrm{E}} - \varphi_P \right) \right]; \tag{3.18a}$$

$$f_{\mathrm{w}} = u_{\mathrm{w}} \left[\varphi_{\mathrm{W}} + \frac{1}{2} \left(\varphi_P - \varphi_{\mathrm{W}} \right) \right]. \tag{3.18b}$$

Substituting Eqs. (3.18) into the right hand side of Eq. (3.15) with the assumption of constant u and one-dimensional cells ($A = 1$) yields the following semi-discrete central-difference approximation

$$\frac{\mathrm{d}\varphi_P}{\mathrm{d}t} = -u \left[\frac{\varphi_{\mathrm{E}} - \varphi_{\mathrm{W}}}{2h} \right]. \tag{3.19}$$

The central-difference scheme is unstable at all CFL numbers and this results in unbounded error growth and thus unfortunately, this method – if applied directly to the convection term – is unusable due to its instability. This is demonstrated in Appendix A.1, and the following presents an analysis of more appropriate schemes.

3.6 Stable Differencing Schemes

The central scheme cannot be used, even though it is second-order accurate in space, due to its unstable error growth in time. Furthermore, Godunov's theorem asserts that for a linear scheme to be stable, it can be at most first-order accurate. Defining stability as the requirement that errors diminish in time, this can be stated as requiring that the solution of the scheme be monotone. Toro (1999) defines such a scheme as having the following property:

$$\forall P : \beta_P(t) \geq \alpha_P(t) \Longrightarrow \beta_P(t + \Delta t) \geq \alpha_P(t + \Delta t); \tag{3.20}$$

i.e. very slightly paraphrasing definition 13.5.1 in Toro:

> if two initial data functions $\beta(x, 0)$ and $\alpha(x, 0)$ (for Eq. 3.13) satisfy $\beta(x, 0) \geq \alpha(x, 0), \forall x$, then their corresponding solutions $\beta(x, t)$ and $\alpha(x, t)$ satisfy $\beta(x, t) \geq \alpha(x, t)$ for $t > 0$.

In other words, no new extrema will be introduced into the cell data as the solution is advanced – recall Harten's theorem (Section 3.2). New extrema appear as under- or over-shoots in the solution near sharp fronts. They then spread as wiggles and quickly pervade the entire domain. They are a result of the amplification of odd-order derivatives (dispersive terms) found in the modified equation – see Appendix A and e.g. the RHS of Eq. (A.3) – which are not present in the original equation. The artificial dispersion results in solution "waves" with different wavelengths propagating through the solution at different – and

incorrect – speeds.

3.6.1 Upwind Differencing

First-order schemes were specifically designed in order to overcome the issues associated with the stability of the discretisation. The first successful difference scheme, proposed in Courant, Isaacson and Rees (1952), was the aptly named CIR scheme, which provides a solution dependant first-order upwind finite-difference stencil whereby the direction of wave propagation at the boundary dictates the cells contained within the stencil. The solution replaces the transported variable field at the cell boundaries with the value of the cell average of the upwind cell at that boundary, discarding downwind variables. In other words, this method assumes the boundary value is either of the neighbouring cell values rather than an interpolation between them as in central-differences. Godunov (1959) provides a finite-volume version of the upwind scheme by calculating the time averaged flux values using solutions to the Riemann problems between cells. This method requires the use of a Riemann solver; however, when an approximate Riemann solver is used, or a linear transport equation is solved, the finite-volume analogue of the CIR scheme is recovered.

The Godunov scheme extends the upwind principle into a finite-volume scheme by considering an exact evaluation of the volume-averaged quantities over the control volume $\left[x_{\mathrm{w}}, x_{\mathrm{e}}\right] \times [t, t+\Delta t]$ giving the expression

$$\frac{\varphi_P(t+\Delta t) - \varphi_P(t)}{\Delta t} = -\frac{f_{\mathrm{e}}(t+\Delta t/2) - f_{\mathrm{w}}(t+\Delta t/2)}{h}. \tag{3.21}$$

The flux-function is now time averaged and is determined using the solution of the Riemann problem between adjacent cells. The local Riemann problem at the cell boundary where $x = x_{\mathrm{e}}$ is defined as

$$\text{PDE}: \quad \frac{\partial \varphi}{\partial t} + \frac{\partial \varphi}{\partial x} = 0; \tag{3.22a}$$

$$\text{IC}: \qquad \varphi(x_{\mathrm{e}}, t) = \begin{cases} \varphi_P(t) & \text{if } x < x_{\mathrm{e}} \\ \\ \varphi_{\mathrm{E}}(t) & \text{if } x > x_{\mathrm{e}}. \end{cases} \tag{3.22b}$$

By assuming that $\varphi\left(x, t^*\right)$ – a combined solution of the local Riemann problems at the cell boundaries – is the exact solution to the PDE in Eqs. (3.22), the following flux relations

can be substituted into the volume averaged Eq. (3.21):

$$\varphi_{\mathrm{e}}(t^*) = \mathrm{RP}\left[\varphi_P(t), \varphi_{\mathrm{E}}(t)\right]; \tag{3.23a}$$

$$f_{\mathrm{e}}(t + \Delta t/2) = \frac{1}{\Delta t}\int_t^{t+\Delta t} f\left(\varphi_{\mathrm{e}}(t^*)\right) \mathrm{d}t; \tag{3.23b}$$

$$f_{\mathrm{e}}^{\mathrm{God.}} = f_{\mathrm{e}}\left(\varphi_P(t), \varphi_{\mathrm{E}}(t), t + \Delta t/2\right). \tag{3.23c}$$

It is expected that the solution to the linear advection equation will be the undamped initial conditions (say φ_0) convected downstream. In particular, it is expected that a discontinuity separating two values (say φ_{W} and φ_{E}) will propagate a distance $u\Delta t$ downstream over timestep Δt. In other words, data to the left of this discontinuity in its new location will assume the value φ_{W} and data to the right φ_{E}, thus the solution to the Riemann problem (Eqs. 3.22) is

$$\varphi(x,t) = \varphi_0(x - u\Delta t) = \begin{cases} \varphi_{\mathrm{W}} & \text{if } x - u\Delta t < 0 \\ \\ \varphi_{\mathrm{E}} & \text{if } x - u\Delta t > 0, \end{cases} \tag{3.24}$$

and hence the Godenov flux can be written for the linear transport equation as

$$f^{\mathrm{God.}}\left(\varphi_{\mathrm{W}}, \varphi_{\mathrm{E}}\right) = u\frac{\varphi_{\mathrm{W}} + \varphi_{\mathrm{E}}}{2} - |u|\frac{\varphi_{\mathrm{E}} - \varphi_{\mathrm{W}}}{2}. \tag{3.25}$$

For positive u the inter-cell Godunov flux is therefore given by $f_{\mathrm{w}}^{\mathrm{God.}} = u\varphi_{\mathrm{W}}(t)$ and $f_{\mathrm{e}}^{\mathrm{God.}} = u\varphi_P(t)$, which when substituted into Eq. (3.21) yields the CIR scheme.

The Godunov scheme becomes exact as the CFL number approaches unity since the time integral of flux through the face of the element is such that the entire φ content of the element is transferred into the downwind neighbouring cell (and artificial diffusion $\Gamma_{\mathrm{CIR}} \to 0$). In this sense the first-order upwind scheme for $C = 1$ is simply the exact translation of the initial-conditions by h. As alluded to in Section 3.4 this is only the case when a forward Euler integration scheme is used. Using a sub-time-step or a Runge-Kutta method when the time gradient is e.g. constructed from the average of the t and $t + \Delta t$ derivatives, this is no longer the case since $C \neq 1$ for intermediate sub-steps.

3.6.2 First-Order Upwind

The first-order finite-volume scheme can be written for the linear advection equation giving a reconstruction/extrapolation (based on a zeroth-order polynomial - i.e. constant value)

at the cell faces for the φ face fields as follows:

$$\varphi_{\mathrm{e}} \approx \begin{cases} \varphi_{\mathrm{E}} & \text{if } u < 0 \\ \\ \varphi_P & \text{if } u > 0, \end{cases} \quad \text{and} \quad \varphi_{\mathrm{w}} \approx \begin{cases} \varphi_P & \text{if } u < 0 \\ \\ \varphi_{\mathrm{W}} & \text{if } u > 0, \end{cases} \tag{3.26 a,b}$$

which gives the fluxes:

$$f_{\mathrm{e}} \approx \begin{cases} u_{\mathrm{e}}\varphi_{\mathrm{E}} & \text{if } u_{\mathrm{e}} < 0 \\ \\ u_{\mathrm{e}}\varphi_P & \text{if } u_{\mathrm{e}} > 0, \end{cases} \quad \text{and} \quad f_{\mathrm{w}} \approx \begin{cases} u_{\mathrm{w}}\varphi_P & \text{if } u_{\mathrm{w}} < 0 \\ \\ u_{\mathrm{w}}\varphi_{\mathrm{W}} & \text{if } u_{\mathrm{w}} > 0. \end{cases} \tag{3.27 a,b}$$

Again, these values can be substituted into the right hand side of Eq. (3.15) with the assumption of constant u and one-dimensional cells ($A = 1$) yielding the semi-discrete upwind-difference approximation

$$\frac{\mathrm{d}\varphi_P}{\mathrm{d}t} = -\begin{cases} \dfrac{u}{h}\left(\varphi_{\mathrm{E}} - \varphi_P\right) & \text{if } u < 0 \\ \\ \dfrac{u}{h}\left(\varphi_P - \varphi_{\mathrm{W}}\right) & \text{if } u > 0. \end{cases} \tag{3.28}$$

The expressions (Eqs. 3.28) can be combined and folded into the right hand side of Eq. (3.15) resulting in a first-order upwind scheme for the linear advection equation,

$$\begin{aligned} \frac{\mathrm{d}\varphi_P}{\mathrm{d}t} \approx -\frac{1}{h}\Big[&\left(\max\left[u_{\mathrm{e}}, 0\right]\varphi_P + \min\left[u_{\mathrm{e}}, 0\right]\varphi_{\mathrm{E}}\right) \\ &-\left(\max\left[u_{\mathrm{w}}, 0\right]\varphi_{\mathrm{W}} + \min\left[u_{\mathrm{w}}, 0\right]\varphi_P\right)\Big]. \end{aligned} \tag{3.29}$$

Applying the von Neumann analysis, supposing constant $u > 0$ as with the central difference scheme above, the amplification factor (as defined in Appendix A.1.1) can be expressed

$$|G|^2 = 1 + 2C\left(C - 1\right)\left(1 - \cos\left(k_m h\right)\right), \tag{3.30}$$

and therefore the explicit first-order upwind scheme is conditionally stable subject to a (local) CFL number in the range $0 \leq C \leq 1$. By noting that the linear advection equation represents an undamped wave travelling with speed u, and that the exact solution has an amplification factor $|G| = 1$, this gives the diffusion error (amplitude error) of the scheme as according to the RHS of Eq. (3.30).

A Taylor expansion shows that the first term omitted is of order h,

$$\frac{\varphi_{\mathrm{E}} - \varphi_P}{h} = \frac{\mathrm{d}\varphi_P}{\mathrm{d}x} + \frac{h}{2!}\frac{\mathrm{d}^2\varphi_P}{\mathrm{d}x^2} + \ldots = \frac{\mathrm{d}\varphi_P}{\mathrm{d}x} + \mathcal{O}(h), \tag{3.31}$$

and therefore while the scheme is stable, it is only of first-order. Again, assuming a positive

and constant u, the modified equation for the first-order upwind scheme is obtained via further expansion of the Taylor terms required in a truncation error analysis, and is

$$\frac{\partial \varphi}{\partial t} + u\frac{\partial \varphi}{\partial x} = (1-C)\,\frac{uh}{2!}\frac{\partial^2 \varphi}{\partial x^2} + \mathcal{O}\left(h^2\right). \tag{3.32}$$

The Taylor expansions are about t and x_P and the subscripts have been dropped for clarity. The coefficient of the first term on the RHS is a non-physical dissipative term, comparable in effect to the diffusion coefficient Γ in Eq. (3.5) or the Newtonian viscosity in the Navier-Stokes equations; however, it is completely artificial and an artefact of the difference scheme. Therefore the principal error of the first-order nature of this upwind scheme is an apparent viscosity,

$$\Gamma_{\mathcal{O}(1)\mathrm{UW}} \equiv \Gamma_{\mathrm{CIR}} = \frac{1}{2}hu(1-C). \tag{3.33}$$

3.6.3 Second-Order Schemes

Higher-order upwind schemes may be obtained by expanding $\mathrm{d}\varphi/\mathrm{d}x$ as a Maclaurin series with respect to x in local coordinates about x_P. Various numbers of terms may be retained, and they can be represented in different ways: for example using naïve combinations of upwind and central-differences for the first and second derivatives yields the following approximations:

$$\left.\frac{\mathrm{d}\varphi}{\mathrm{d}x}\right|_{\mathrm{LUD}} = \frac{\Delta x^0}{0!}\left.\frac{\mathrm{d}\varphi}{\mathrm{d}x}\right|_{\mathrm{UW}} + \frac{\Delta x^1}{1!}\left.\frac{\mathrm{d}^2\varphi}{\mathrm{d}x^2}\right|_{\mathrm{CD}} + \mathcal{O}(h^2) \approx \frac{\varphi_{WW} - 4\varphi_{\mathrm{W}} + 3\varphi_P}{2h}. \tag{3.34}$$

The second derivative in Eq. (3.34) is obtained by applying a central-difference to the first-order gradients resulting from an upwind difference at x_P and a central-difference between x_{WW} and x_P for the gradient at x_{W}. This result can be re-factored as upwind biased linear extrapolations from the cell centred values of the P and W cells to the east and west cell faces, allowing the RHS of Eq. (3.34) to be interpreted as a first-order upwind estimate for the field values at the cell faces corrected with a second-order approximation of the upwind gradient, and gives the Linear Upwind Difference (LUD) scheme, e.g. for constant $u > 0$

$$\begin{aligned}\frac{\mathrm{d}\varphi_P}{\mathrm{d}t} &= -\frac{u}{h}\left[\left(\varphi_P + \frac{1}{2}\left(\varphi_P - \varphi_{\mathrm{W}}\right)\right) - \left(\varphi_{\mathrm{W}} + \frac{1}{2}\left(\varphi_{\mathrm{W}} - \varphi_{WW}\right)\right)\right]; \\ &= -\frac{1}{h}\left[\left(f_{\mathrm{e}}^{\mathrm{lo}} + f_{\mathrm{e}}^{\mathrm{hi}}\right) - \left(f_{\mathrm{w}}^{\mathrm{lo}} + f_{\mathrm{w}}^{\mathrm{hi}}\right)\right].\end{aligned} \tag{3.35}$$

It is is fact possible to construct a second-order scheme by any linear combination of the LUD and central-difference schemes. A particular example is the Quadratic Upwind Inter-

polation for Convective Kinematics (QUICK, Leonard, 1979) that is given by

$$\frac{\mathrm{d}\varphi_P}{\mathrm{d}t} = -\frac{u}{h}\left[\left(\varphi_P(t) + \frac{1}{8}\left(3\varphi_{\mathrm{E}} + 2\varphi_P(t) - \varphi_{\mathrm{W}}(t)\right)\right) - \left(\varphi_{\mathrm{W}}(t) + \frac{1}{8}\left(3\varphi_P + 2\varphi_{\mathrm{W}}(t) - \varphi_{WW}(t)\right)\right)\right]; \tag{3.36}$$

and uses an upstream weighted quadratic interpolation to give the face field values. A general expression for an upwind scheme of any order can be obtained by rewriting Eq. (3.29) as

$$\varphi_P(t + \Delta t) = \varphi_P(t) - \Delta t\left[u^+\varphi_x^- + u^-\varphi_x^+\right], \tag{3.37}$$

where the terms $u^+ = \max(u, 0)$, $u^- = \min(u, 0)$ and $\varphi_x^{\pm}$ are the derivatives up-winded in the appropriate direction – e.g. expressions of the type in Eq. (3.34), Eq. (3.35) or Eq. (3.36). When the expression is factorised as in Eq. (3.35) or Eq. (3.36), this is readily interpreted as a flux balance across the cell. As with the central-difference scheme, the second-order upwind schemes have a leading truncation error term of magnitude $\mathcal{O}(h^2)$ but poor stability characteristics.

In order to demonstrate the problems associated with first-order methods and second-order linear schemes it is instructive to consider a one-dimensional solution of the linear advection equations. Figure 3.2 demonstrates the headline results by showing the convection of a square or sinusoidal pulse initial disturbance through a periodically bounded domain using first-order upwind, second-order upwind (LUD) and a high-resolution scheme based on QUICK to calculate the face fields. The first-order scheme is clearly extremely diffusive. The second-order schemes with constant coefficients (LUD) show wiggles around discontinuities that pervade the entire domain, but are capable of tracking gradually varying distributions with only minor phase errors. The second-order method with non-constant coefficients (monotonic QUICK – discussed in the following section) tracks both discontinuous and continuous flow features very well, with minimum diffusion or phase errors. To obtain the non-linear scheme, a flux (or slope) limiter function is used.

3.7 Non-Linear/High-Resolution Schemes

3.7.1 Flux and Slope Limiters

Eq. (3.35) can be generalised for higher-order schemes based on an extension of a first-order upwind scheme by introducing the function $\psi(\theta)$ such that, for example, the LUD

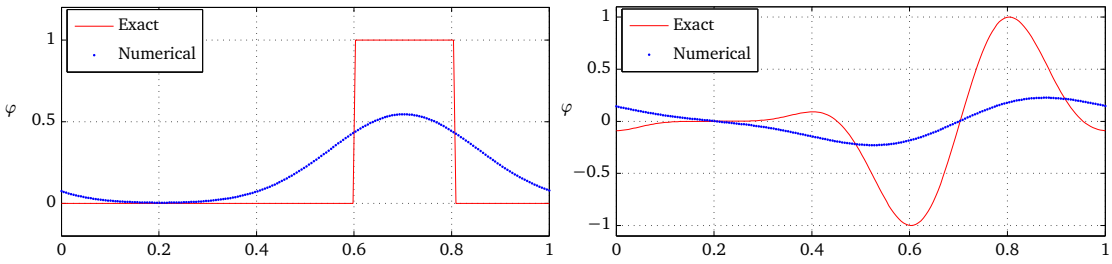

(a) First order upwind scheme

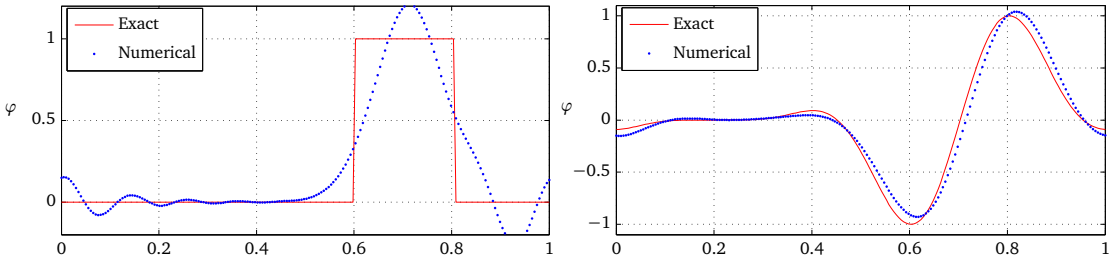

(b) LUD scheme

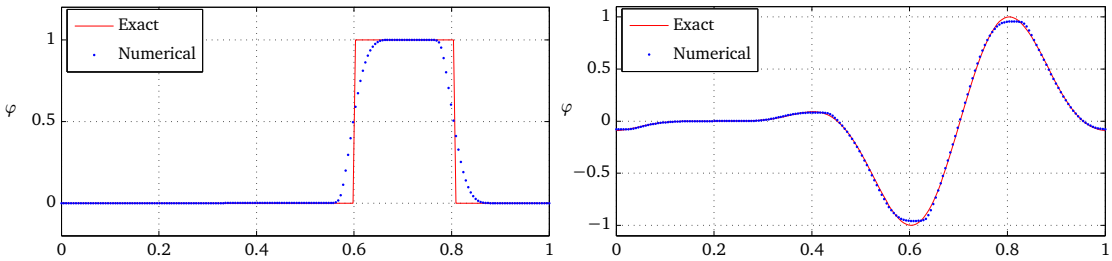

(c) QUICK (UMIST) scheme

Figure 3.2: One-dimensional finite-volume schemes. Headline performance characteristics of: (a) $\mathcal{O}(h, t^2)$ upwind scheme with piecewise constant reconstruction; (b) $\mathcal{O}(h^2, t^2)$ upwind scheme with piecewise linear reconstruction and no limiter; and (c) $\mathcal{O}(h^2, t^2)$ upwind scheme with piecewise quadratic reconstruction using a flux limiter.

scheme can be written

$$\frac{\mathrm{d}\varphi_P}{\mathrm{d}t} = -\frac{u}{h}\Bigg[\Big(\varphi_P(t) + \frac{1}{2}\psi\big(\theta_P(t)\big)\big(\varphi_{\mathrm{E}}(t) - \varphi_P(t)\big)\Big) - \Big(\varphi_{\mathrm{W}}(t) + \frac{1}{2}\psi\big(\theta_{\mathrm{W}}(t)\big)\Big(\varphi_P(t) - \varphi_{\mathrm{W}}(t)\big)\Big)\Bigg], \tag{3.38}$$

where

$$\theta_P(t) = \frac{\varphi_P(t) - \varphi_{\mathrm{W}}(t)}{\varphi_{\mathrm{E}}(t) - \varphi_P(t)} \qquad \text{and} \qquad \theta_{\mathrm{W}}(t) = \frac{\varphi_{\mathrm{W}}(t) - \varphi_{\mathrm{WW}}(t)}{\varphi_{\mathrm{P}}(t) - \varphi_{\mathrm{W}}(t)} \tag{3.39}$$

are the ratios of the gradients over successive cell interfaces in an upwind direction, and for the LUD scheme $\psi_{\mathrm{LUD}}(\theta) = \theta$. To obtain the first-order upwind scheme set $\psi(\theta) = 0$ and to obtain the central-difference scheme set $\psi(\theta) = 1$. In other words, ψ is a blending function that can result in a scheme that is an average between first-order upwind and various higher-order methods. The nature of the function $\psi(\theta)$ can be arbitrarily non-linear and chosen to result in some desired stability characteristics for the resulting scheme. For ψ that is linear or a sum of harmonic functions in θ, a linear scheme (e.g. first-order upwind, LUD, QUICK, etc.) is obtained, with all the associated issues. For non-constant ψ, the result is a scheme that can modify itself in a solution dependant manner. This results in schemes that are capable of resolving discontinuities at considerably better fidelity than linear schemes, so due to the non-linearity in this function, when the term "high-resolution" is applied to a scheme of this kind, it is synonymous with "non-linear."

3.7.1.1 Harten's TVD Theorem

For transient 1-D transport equations, Harten's theorem (Harten, 1983) gives the requirements for a scheme to be total variance diminishing (TVD), which follows on from the monotonicity requirement (Eq. 3.20) and states that for a scheme to be considered TVD

$$\mathrm{TV}(\varphi, t + \Delta t) \leq \mathrm{TV}(\varphi, t), \tag{3.40}$$

where

$$\mathrm{TV}(\varphi, t) = \lim_{\epsilon \to 0} \sup \frac{1}{\epsilon} \int_{-\infty}^{+\infty} \big|\varphi(x + \epsilon, t) - \varphi(x, t)\big| \, \mathrm{d}x, \tag{3.41}$$

or in discrete form over a domain of N cells

$$\mathrm{TV}(\varphi_P, t) = \sum_{i=1}^{N-1} \big|\varphi_{\mathrm{E}}(t) - \varphi_P(t)\big|. \tag{3.42}$$

This states that in time, maxima reduce, minima increase and no new extrema are created.

Writing Eq. (3.37) in terms of the high and low-order face fluxes and assuming for the sake of brevity $u > 0$, it becomes apparent that the function ψ can be made to act as a clutch, controlling the order of the difference scheme used depending on the output of the function $\psi(\theta)$:

$$\frac{\varphi_P(t+\Delta t)-\varphi_P(t)}{\Delta t} = -\frac{1}{h}\Bigg[\left(f_{\mathrm{e}}^{\mathrm{lo}} + \psi\left(\theta_P\right)\left(f_{\mathrm{e}}^{\mathrm{hi}} - f_{\mathrm{e}}^{\mathrm{lo}}\right)\right) - \left(f_{\mathrm{w}}^{\mathrm{lo}} + \psi\left(\theta_{\mathrm{W}}\right)\left(f_{\mathrm{w}}^{\mathrm{hi}} - f_{\mathrm{w}}^{\mathrm{lo}}\right)\right)\Bigg]. \tag{3.43}$$

Now if the low- and high-order fluxes are broken into coefficient form, for a general scheme whose stencil has l points to the left of P and r to the right

$$f_{e,w}^{\mathrm{lo}} = u\sum_{j=-l}^{r}\alpha_j\varphi_{P-j} \quad \text{and similarly} \quad f_{e,w}^{\mathrm{hi}} = u\sum_{j=-l}^{r}\beta_j\varphi_{P-j}, \tag{3.44 a,b}$$

the TVD flux term for the cell faces can be written as

$$f_{\mathrm{w}}^{\mathrm{TVD}} = u\left[\alpha_0 + \left(\beta_0-\alpha_0\right)\psi\left(\theta_{\mathrm{W}}\right)\right]\varphi_{\mathrm{W}} + u\left[\alpha_1 + \left(\beta_1-\alpha_1\right)\psi\left(\theta_{\mathrm{W}}\right)\right]\varphi_{\mathrm{WW}} + \ldots, \tag{3.45a}$$

$$f_{\mathrm{e}}^{\mathrm{TVD}} = u\left[\alpha_0 + \left(\beta_0-\alpha_0\right)\psi\left(\theta_P\right)\right]\varphi_P + u\left[\alpha_1 + \left(\beta_1-\alpha_1\right)\psi\left(\theta_P\right)\right]\varphi_{\mathrm{W}} + \ldots \tag{3.45b}$$

Defining a linear scheme as one where the coefficients α, β are constant – e.g. $\psi(\theta)$ is linear in θ – Harten (1983) has proven that monotonicity is preserved as long as the coefficients are positive or zero. For non-constant ψ the expressions (Eqs. 3.45) can be substituted into Eq. (3.43):

$$\varphi_P(t+\Delta t) = \varphi_P(t) - \left(A\Delta\varphi_P(t) - B\Delta\varphi_{\mathrm{W}}(t)\right); \tag{3.46a}$$

$$A = C\left[\alpha_0 + \left(\beta_0-\alpha_0\right)\psi\left(\theta_P\right)\right]; \tag{3.46b}$$

$$B = C\left[\alpha_1 + \left(\beta_1-\alpha_1\right)\psi\left(\theta_{\mathrm{W}}\right)\right]; \tag{3.46c}$$

where C is the Courant number, $\Delta\varphi_{\mathrm{W}} = \varphi_{\mathrm{W}} - \varphi_{\mathrm{WW}}$ and $\Delta\varphi_P = \varphi_P - \varphi_{\mathrm{W}}$.

Harten's theorem goes onto state that a non-linear scheme that satisfies the following inequalities is TVD:

$$A \geq 0; \tag{3.47a}$$

$$B \geq 0; \tag{3.47b}$$

$$0 \leq A + B \leq 1. \tag{3.47c}$$

In other words, when the function ψ is chosen, for the scheme to be TVD [i.e. satisfy Eq. (3.42)] the following conditions must hold:

- for the linear mode of a scheme the non-negativity condition must be met;
- for the non-linear mode of scheme, the conditions Eqs. (3.47) must additionally be met.

3.7.1.2 Flux Limiters and the TVD Diagram

Further to Harten's theorem, Sweby (1984) produced the necessary and sufficient conditions for a scheme to be TVD and second-order accurate, by parametrising it in terms of the flux limiter operand θ and the limiter operator ψ. The required $\theta - \psi$ relationship is:

- When $0 < \theta < 1$, for a TVD scheme $\psi(\theta) \leq 2\theta$;
- When $\theta \geq 1$, for a TVD scheme $\psi(\theta) \leq 2$;

  For $\mathcal{O}(2)$ accurate TVD schemes the admissible range of $\mathcal{O}(2)$ schemes is bounded by the central and LUD schemes [since $\mathcal{O}(2)$ schemes are made up of linear combination of LUD and central schemes]:

- When $0 < \theta < 1$, for a $\mathcal{O}(2)$ TVD scheme $\theta \leq \psi(\theta) \leq 1$: this allows limiters to dampen steep slopes;
- When $\theta \geq 1$, for an $\mathcal{O}(2)$ TVD scheme $1 \leq \psi(\theta) \leq \theta$: this allows limiters to steepen slopes to try and maintain discontinuities;
  finally Sweby states:
- For $\mathcal{O}(2)$ accurate TVD schemes $\psi(1) = 1$: away from steep gradients the $\mathcal{O}(2)$ scheme is used.

This gives rise to the Sweby TVD diagram, Fig. 3.3. The ratio θ of the cell averages is an indicator for how smooth the solution is near the cell interface. When the solution is smooth, then the ratio will tend towards 1 and therefore the (flux limiter) function ψ is chosen so as to retain the high-order components of the scheme, and to attenuate the scheme to the first-order mode when discontinuities are present. It does so by mixing the solutions due to first and high-order methods. The first-order upwind scheme could be written using $\psi(\theta) = 0$ for all θ, resulting in maximum limitation for all gradients and resulting in a particularly diffusive but still TVD scheme. The central-difference scheme is obtained for $\psi(\theta) = 1$ for all θ and is thus only TVD for $\theta > 0.5$, and is thus unusable.

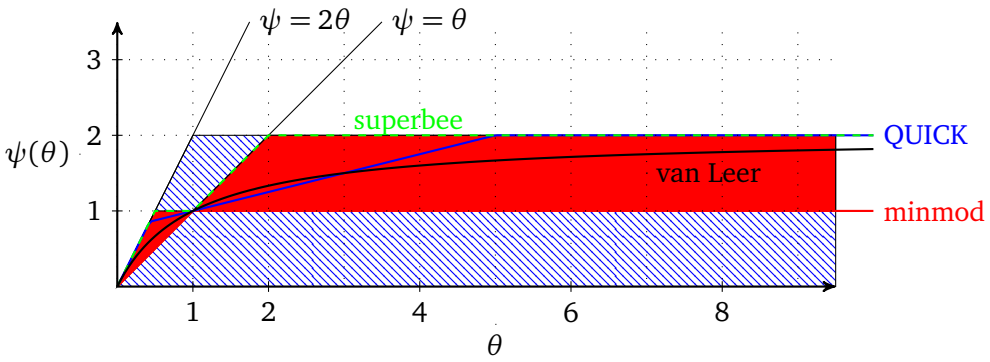

Figure 3.3: Admissible flux limiter region for TVD schemes. Hatched region $\mathcal{O}(1)$; hatched and shaded $\mathcal{O}(2)$.

Using flux-limiters, the limitations of Godenov's theorem are circumvented and the dissipation of first-order schemes can be reduced without introducing wiggles into the solution. The scheme is at best only first-order around discontinuities.

In this thesis, various classes of flux limiter functions are considered. All but one are symmetric, exhibiting the property

$$\frac{\psi(\theta)}{\theta} = \psi\left(\frac{1}{\theta}\right), \tag{3.48}$$

thus treating backwards and forwards facing slopes in the same manner. (In other words, the forwards and backwards gradients are interchangeable, and interface values calculated between cell P and E, $\varphi_{P,\mathrm{e}} = \varphi_{\mathrm{E,w}}$. This ensures that if initial data are symmetric, then the reconstruction and thus resulting solution will also be symmetric. It is not obvious whether this is an absolute requirement in time dependant flows with non-symmetric initial conditions. The formulation is most likely a necessity when these schemes are used to solve steady-state/equilibrium problems.) Flux-limiters can be characterised as either piecewise-linear (PL) where the limiters switches between different schemes to ensure bounded solutions and polynomial-ratio (PR), which are smooth. Examples of PL schemes are minmod and superbee. An example of a PR scheme is the van Leer limiter.

The flux-limiter returns a value between zero and two with values decreasing from one limiting the high-order method and damping overshoots by favouring the artificial viscosity of the low-order method, and values increasing from one steepening the effective slope by favouring the higher-order method. The more compressive – increased $\psi(\theta)$ for a given θ – a limiter is, the more aggressively "squared" the features in the solution results will become and the less diffusive it will be. A less compressive limiter is more diffusive, until the point where flow features will be excessively smeared. In either case, the resulting solution will be a poor approximation of the true solution and thus limiters at both extremes of the TVD region – as indicated by the lighter region in Fig. 3.3 – result in solution accuracy of only first-order. There are a staggering number of limiters – see Waterson and Deconinck (2007) for a summary – and only a sample are considered herein.

3.7.1.3 Sweby Φ-Limiters

A family of limiters known as the Sweby Φ-limiter is given by

$$\psi(\theta) = \max\left[0, \min\left(\Phi\theta, 1\right), \min\left(\theta, \Phi\right)\right], \tag{3.49}$$

for various $1 \leq \Phi \leq 2$. The most famous are due to Roe (1985).

minmod is obtained by setting $\Phi = 1$, which uses the maximum slope limiting permitted for a second-order scheme, which hence yields the most dissipative solutions around discontinuities for a second-order scheme.

superbee is obtained by setting $\Phi = 2$, which applies the maximum steepening permitted while remaining in the second-order region resulting in the most compressive (least dissipative) second-order limiter – to such an extent that slopes are artificially steepened and waves are characteristically "squared" (this means superbee is excellent for propagating a square pulse, but can be unrealistic otherwise).

3.7.1.4 Van Leer's PR Limiter

The scheme due to van Leer (1974) is one of many that strike a compromise between minmod and superbee on the Sweby diagram. It is a smooth limiter, based on modifications to the LUD-type second-order upwind scheme of Fromm (1968), and can be somewhat diffusive compared with schemes that allow more steepening. The expression for van Leer's limiter is

$$\psi(\theta) = \frac{\theta + \|\theta\|}{1 + \|\theta\|}. \tag{3.50}$$

3.7.1.5 PL-κ Limiters

A family of general piecewise linear (PL) limiters can be parameterised in terms of coefficients κ and M according to

$$\psi(\theta)_{\kappa,M} = \max\left[0, \min\left(M, \frac{1}{2}(1+\kappa)\,\theta + \frac{1}{2}(1-\kappa), 2\theta\right)\right]. \tag{3.51}$$

Koren The Koren (Koren, 1993) scheme becomes a third-order upwind scheme for smooth enough data. It is obtained from Eq. (3.51) by setting $\kappa = 1/3$ and $M = 2$.

3.7.1.6 Symmetric PL-κ Limiters

Similarly, a family of general symmetric piecewise linear limiters can be parameterised in terms of coefficients κ and M according to

$$\psi(\theta)_{\kappa,M} = \max\left[0, \min\left(M, \frac{1}{2}(1+\kappa)\,\theta + \frac{1}{2}(1-\kappa), \frac{1}{2}(1-\kappa)\,\theta + \frac{1}{2}(1+\kappa), 2\theta\right)\right]. \tag{3.52}$$

MUSCL A member of the Monotonic Upwind Scheme for Conservation Laws (MUSCL) family of schemes (van Leer, 1979) is a bounded version of the second-order upwind

(LUD/Fromm type) scheme obtained from Eq. (3.52) by setting $\kappa = 0$ and $M = 2$.

UMIST The Upstream Monotonic Interpolation for Scalar Transport (UMIST) scheme of Lien and Leschziner (1994) is a symmetric, second-order TVD implementation of the QUICK scheme, which has evolved from a sort of hybrid of QUICK and MUSCL. Again, this scheme strikes a compromise at moderate gradient ratios; however, it applies the maximum steepening permitted for ratios above 5. The UMIST scheme is obtained from Eq. (3.52) by setting $\kappa = \frac{1}{2}$ and $M = 2$.

3.7.1.7 Limiter Performance

The performance of these schemes is compared for flows carrying smooth and discontinuous initial φ data in Chapter 6.

3.8 A Diffusion Equation

In order to examine the diffusion term in isolation, consider the advection/diffusion equation but set the flow velocity to zero

$$\int_{\Delta t}\int_{\Omega} \frac{\partial \varphi}{\partial t}\, \mathrm{d}V\, \mathrm{d}t = \int_{\Delta t}\int_{\partial\Omega} \left(\Gamma \nabla \varphi\right) \cdot \mathrm{d}\boldsymbol{S}\, \mathrm{d}t. \tag{3.53}$$

Since the effects of diffusion are relatively minor in convection dominated flows (e.g. in real world flows at high Reynolds number, where $\Gamma \equiv \nu \ll 1$) and serves to smear the transport variable across the domain, and since the Laplacian is independent of direction, a relatively simplistic approximation to the gradients is sufficient for this term in the general transport equation. Considering the diffusion coefficient Γ as constant in time and space, Eq. (3.53) is written

$$\int \left(\Gamma \nabla \varphi\right) \cdot \mathrm{d}\boldsymbol{S} \equiv \Gamma \sum_{\text{faces}} \left[A_f \boldsymbol{n}_f \cdot (\nabla \varphi)_f \right]. \tag{3.54}$$

A central-difference approach is used to approximate the gradients at the cell faces, where the expressions required are for the gradients in

$$\boldsymbol{n} \cdot \nabla \varphi = \boldsymbol{n} \cdot \left[\frac{\partial \varphi_{\mathrm{e}}}{\partial x} \; \frac{\partial \varphi_{\mathrm{e}}}{\partial y} \; \frac{\partial \varphi_{\mathrm{e}}}{\partial z} \right], \tag{3.55}$$

and $\boldsymbol{n}$ has the values defined in Table 3.3. So, for example in the x-direction, a second-order central-difference gives

$$\frac{\partial \varphi_{\mathrm{e}}}{\partial x} = \frac{\varphi_{\mathrm{E}} - \varphi_P}{h} + \mathcal{O}(h^2) \quad \text{and} \quad \frac{\partial \varphi_{\mathrm{w}}}{\partial x} = \frac{\varphi_P - \varphi_{\mathrm{W}}}{h} + \mathcal{O}(h^2). \tag{3.56a,b}$$

Similarly, a fourth-order central scheme can be written

$$\frac{\partial \varphi_{\mathrm{e}}}{\partial x} = \frac{3}{4}\frac{\left(\varphi_{\mathrm{E}} - \varphi_P\right)}{h} + \frac{\varphi_{\mathrm{EE}} + \varphi_{\mathrm{E}} - \varphi_P - \varphi_{\mathrm{W}}}{12h} + \mathcal{O}(h^4) \quad \text{and}$$

$$\frac{\partial \varphi_{\mathrm{w}}}{\partial x} = \frac{3}{4}\frac{\left(\varphi_P - \varphi_{\mathrm{W}}\right)}{h} + \frac{\varphi_{\mathrm{E}} + \varphi_P - \varphi_{\mathrm{W}} - \varphi_{\mathrm{WW}}}{12h} + \mathcal{O}(h^4) \tag{3.57a}$$

The RHS of Eq. (3.53) can be written (using e.g. the second-order scheme) for one dimension as

$$\int_{\Delta t}\int_{\partial\Omega} \left(\Gamma \nabla \varphi\right) \cdot \mathrm{d}\boldsymbol{S}\, \mathrm{d}t \approx \Gamma \int_{\Delta t} \left[A_{\mathrm{e}} \left(\frac{\varphi_{\mathrm{E}} - \varphi_P}{h} \right) - A_{\mathrm{w}} \left(\frac{\varphi_P - \varphi_{\mathrm{W}}}{h} \right) \right] \mathrm{d}t. \tag{3.58}$$

The terms in the square brackets on the RHS are readily interpreted as the diffusive fluxes. The extension to two and three dimensions is via either an operator addition method – equivalent to adding terms for the other faces between the square brackets on the RHS of Eq. (3.58) – or an operator splitting method – where Eq. (3.58) is rotated to each dimension in sequence – as discussed in Section 3.4. The method proposed in this thesis uses the operator addition approach for the internal components of the diffusion operator, but operator splitting for convection directions.

Von Neumann stability analysis yields the following criteria for this scheme to be remain stable during time integration by a forward Euler method. Defining the von Neumann number (and VN condition) $\sigma = \Gamma \Delta t / h^2$ (cf. Courant number and CFL condition, see Merkle and Choi, 1988), the amplification factor is

$$G = 1 - 4\sigma \sin^2\left(\frac{kh}{2}\right), \tag{3.59}$$

and for the scheme to remain stable $\sigma < 1/2$. Therefore there is a time-step limitation $\Delta t < h^2/2\Gamma$. Fortunately, for convection dominated flows this limitation is considerably larger than that required by the CFL condition.

The volume integrated diffusion term can be written for the three vorticity transport equations, assuming a cell whose face normals are aligned to a Cartesian axis system, giving the following second-order operators for each of the i components as

$$\frac{\mathrm{d}\omega_i}{\mathrm{d}t} = L_{D_i} \approx \nu \left[\frac{\left(\omega_i\right)_{\mathrm{E}} - \left(\omega_i\right)_{\mathrm{W}}}{\Delta x^2} + \frac{\left(\omega_i\right)_{\mathrm{N}} - \left(\omega_i\right)_{\mathrm{S}}}{\Delta y^2} + \frac{\left(\omega_i\right)_{\mathrm{T}} - \left(\omega_i\right)_{\mathrm{B}}}{\Delta z^2} \right], \tag{3.60}$$

where the fourth-order scheme follows naturally.

The inclusion of the diffusion term in the current method is by application of these individual components simultaneously, such that the operator addition defines the final

three-dimensional operator

$$L_D(\boldsymbol{\omega}_P, t) = \left[L_{D_x}(\boldsymbol{\omega}_P, t) + L_{D_y}(\boldsymbol{\omega}_P, t) + L_{D_z}(\boldsymbol{\omega}_P, t) \right], \tag{3.61}$$

which is then used with the operator splitting approach along with the convection and stretching operators.

The performance of the diffusion approximation is examined in Chapter 6.

3.9 Tilting/Stretching Term

Unlike the advection/diffusion equation, the vorticity transport equations contain a non-linear coupling term that is responsible for modifying the orientation and rate of the "spin" of a vortex element due to the velocity field. It is essentially the change in vorticity caused by coupling velocity gradients in the fluid with conservation of angular momentum – the ballerina effect. At the most intuitive level, the magnitude of velocity induced by vortex filament will increase as it is stretched since the diameter will contract to conserve volume, and the angular velocity will increase to conserve angular momentum. It is also responsible for tilting the axis of a "filament".

Observing that gradients of the velocity field can be written as the second rank tensor

$$\nabla \boldsymbol{u} = \begin{pmatrix} \dfrac{\partial u}{\partial x} & \dfrac{\partial v}{\partial x} & \dfrac{\partial w}{\partial x} \\ \dfrac{\partial u}{\partial y} & \dfrac{\partial v}{\partial y} & \dfrac{\partial w}{\partial y} \\ \dfrac{\partial u}{\partial z} & \dfrac{\partial v}{\partial z} & \dfrac{\partial w}{\partial z} \end{pmatrix} \tag{3.62}$$

it is possible to write the inner product of the vorticity with the velocity gradient as

$$\boldsymbol{\omega} \cdot (\nabla \boldsymbol{u}) = \begin{bmatrix} \omega_x \\ \omega_y \\ \omega_z \end{bmatrix} \cdot \begin{bmatrix} \dfrac{\partial u}{\partial x} & \dfrac{\partial u}{\partial y} & \dfrac{\partial u}{\partial z} \\ \dfrac{\partial v}{\partial x} & \dfrac{\partial v}{\partial y} & \dfrac{\partial v}{\partial z} \\ \dfrac{\partial w}{\partial x} & \dfrac{\partial w}{\partial y} & \dfrac{\partial w}{\partial z} \end{bmatrix}, \tag{3.63}$$

so the i^{th} component of the stretching term can be written $\boldsymbol{\omega} \cdot \nabla u_i$. As an example, consider the x component of an inviscid version of Eq. (2.1c):

$$\frac{\mathrm{D}\omega_x}{\mathrm{D}t} = \omega_x \frac{\partial u}{\partial x} + \omega_y \frac{\partial u}{\partial y} + \omega_z \frac{\partial u}{\partial z}. \tag{3.64}$$

Applying Gauss's theorem to the volume integrated stretching term of the i^{th} component

of the vorticity transport equation,

$$\int_{\Omega} \boldsymbol{\omega} \cdot (\nabla u_i)\,\mathrm{d}V = \int_{\partial\Omega} \boldsymbol{\omega} \cdot (u_i\ \mathrm{d}\boldsymbol{S}) = \sum_{\text{faces}} \left[\boldsymbol{\omega}_f \cdot (u_f A_f \boldsymbol{n}_f)\right]. \tag{3.65}$$

In a slowly varying velocity field positive along the x-axis, i.e. $u > 0$, the velocity at each cell face would set up gradients over the cell. On the faces whose normal is not aligned with the x-axis (n, s, t, b) the velocity is tangential, and a vortex "spin" axis normal to that face would experience tilting due to the gradient causing the axis to change orientation; on the other faces (e and w), a "spin" axis that was normal to these faces would either be compressed or stretched due to the u velocity gradient. In the finite-volume framework, this allows the transfer of angular momentum between different "spin" orientations, effected in terms of the relative size of the components of the vorticity vector that essentially defines the "spin" axis. The magnitude of the vorticity vector is also changed, however, the creation or destruction of angular momentum is disallowed due to conservation, and (except for sources) the amount of vorticity in the domain remains constant due to the finite-volume method. In other words, this acts by allowing the transfer of components of vorticity between adjacent cells due to stretching in one cell being counteracted by shrinking in another and any change in direction of the vorticity preserves the magnitude.

The volume integrated stretching term can be written for the three vorticity transport equations, assuming a cubic cell aligned to a Cartesian axis system:

$$\frac{\mathrm{d}\omega_x}{\mathrm{d}t} \approx L_{\mathrm{Str}._x} = \frac{1}{\Delta x}\left[\left((u\omega_x)_{\mathrm{e}} - (u\omega_x)_{\mathrm{w}}\right) + \left(\left(u\omega_y\right)_{\mathrm{n}} - \left(u\omega_y\right)_{\mathrm{s}}\right) + \left((u\omega_z)_{\mathrm{t}} - (u\omega_z)_{\mathrm{b}}\right)\right]; \tag{3.66a}$$

$$\frac{\mathrm{d}\omega_y}{\mathrm{d}t} \approx L_{\mathrm{Str}._y} = \frac{1}{\Delta y}\left[\left((v\omega_x)_{\mathrm{e}} - (v\omega_x)_{\mathrm{w}}\right) + \left(\left(v\omega_y\right)_{\mathrm{n}} - \left(v\omega_y\right)_{\mathrm{s}}\right) + \left((v\omega_z)_{\mathrm{t}} - (v\omega_z)_{\mathrm{b}}\right)\right]; \tag{3.66b}$$

$$\frac{\mathrm{d}\omega_z}{\mathrm{d}t} \approx L_{\mathrm{Str}._z} = \frac{1}{\Delta z}\left[\left((w\omega_x)_{\mathrm{e}} - (w\omega_x)_{\mathrm{w}}\right) + \left(\left(w\omega_y\right)_{\mathrm{n}} - \left(w\omega_y\right)_{\mathrm{s}}\right) + \left((w\omega_z)_{\mathrm{t}} - (w\omega_z)_{\mathrm{b}}\right)\right]. \tag{3.66c}$$

An alternative means for calculating the stretch/compression term is based on treating $\boldsymbol{\omega} \cdot \nabla \boldsymbol{u}$ as a source term and integrating it as follows:

$$\mathrm{S}_{\boldsymbol{\omega}} = \boldsymbol{\omega} \cdot (\nabla \boldsymbol{u}) \rightarrow \int_{\Omega} \boldsymbol{\omega} \cdot (\nabla \boldsymbol{u})\ \mathrm{d}V \equiv \int_{\Omega} \mathrm{S}_{\boldsymbol{\omega}}\,\mathrm{d}V \approx \overline{\mathrm{S}}_{\boldsymbol{\omega}} = \overline{\boldsymbol{\omega} \cdot (\nabla \boldsymbol{u})}. \tag{3.67}$$

The overbar denotes the volume integral averaged quantities. In the present method this is performed using the pointwise values of the velocity gradients calculated at neighbouring

cells (the interaction list l in the parlance of the FMM calculation) as quadrature points for a Gauss-Lobatto cubature. The volume over which this integration is performed is 8 times that of a single cell, since the integration bounds are twice the cell spacing, but there is no explicit interpolation. The three componenents of this ($L_{\text{Str.}_x}$, $L_{\text{Str.}_y}$ and $L_{\text{Str.}_x}$) are then used in place of their finite volume equivalents. The difference in these methods is not analysed in this work, however Figs. 7.11 and 7.12 show their respective impact on a turbine simulation.

The inclusion of the stretching term in the current method is by the application of these individual components simultaneously, such that the operator addition defines the final three-dimensional operator,

$$L_{\text{Str.}}(\boldsymbol{\omega}_P, t) = \left[L_{\text{Str.}_x}(\boldsymbol{\omega}_P, t) + L_{\text{Str.}_y}(\boldsymbol{\omega}_P, t) + L_{\text{Str.}_z}(\boldsymbol{\omega}_P, t) \right], \tag{3.68}$$

which is then used with the operator splitting approach along with the convection and diffusion operators. The face values of vorticity are obtained by a central-difference between the neighbouring cells.

The performance of the tilting/stretching term is not examined individually in this thesis (see Concluding Remarks at the end of this chapter).

3.10 Splitting Method for the Vorticity Transport Equations

The method is applied as follows:

***x*-direction example** Flow velocities normal to the faces are obtained by interpolation between cell corner values of u to give u_{e} and u_{w}. Up-axis and down-axis ratios of cell gradients are obtained:

$$\theta_{\text{e}}^{+} = \frac{\varphi_P - \varphi_{\text{W}}}{\varphi_{\text{E}} - \varphi_P}; \quad \theta_{\text{e}}^{-} = \frac{\varphi_{\text{EE}} - \varphi_{\text{E}}}{\varphi_{\text{E}} - \varphi_P}; \tag{3.69a,b}$$

$$\theta_{\text{w}}^{+} = \frac{\varphi_P - \varphi_{\text{W}}}{\varphi_P - \varphi_{\text{W}}}; \quad \theta_{\text{w}}^{-} = \frac{\varphi_{\text{W}} - \varphi_{\text{WW}}}{\varphi_P - \varphi_{\text{W}}}. \tag{3.69c,d}$$

The convective fluxes through the cell faces are:

$$\begin{aligned} \text{East face:} \quad f_{\text{e}} = \max[u_{\text{e}}, 0] \left(\varphi_P + \frac{1}{2}\psi\left(\theta_{\text{e}}^{+}\right)\left(\varphi_{\text{E}} - \varphi_P\right) \right) \\ - \max[-u_{\text{e}}, 0] \left(\varphi_{\text{E}} - \frac{1}{2}\psi\left(\theta_{\text{e}}^{-}\right)\left(\varphi_{\text{E}} - \varphi_P\right) \right); \quad \text{and} \end{aligned} \tag{3.70a}$$

$$\text{West face:}\quad f_{\mathrm{w}} = \max[-u_{\mathrm{w}}, 0]\left(\varphi_P - \frac{1}{2}\psi\left(\theta_{\mathrm{w}}^{+}\right)\left(\varphi_P - \varphi_{\mathrm{W}}\right)\right) - \max[u_{\mathrm{w}}, 0]\left(\varphi_{\mathrm{W}} + \frac{1}{2}\psi\left(\theta_{\mathrm{w}}^{-}\right)\left(\varphi_P - \varphi_{\mathrm{W}}\right)\right). \tag{3.70b}$$

The diffusive flux through the cell faces is simply

$$\text{East face:}\quad d_{\mathrm{e}} = \Gamma\frac{\left(\varphi_{\mathrm{E}} - \varphi_P\right)}{h};\quad \text{and}$$

$$\text{West face:}\quad d_{\mathrm{w}} = \Gamma\frac{\left(\varphi_P - \varphi_{\mathrm{W}}\right)}{h}. \tag{3.71a}$$

The semi-discrete x-direction evolution with operator addition is therefore

$$\frac{\mathrm{d}\varphi_P}{\mathrm{d}t} = \frac{1}{h}\left[A_{\mathrm{e}}\left(d_{\mathrm{e}} - f_{\mathrm{e}}\right) - A_{\mathrm{w}}\left(d_{\mathrm{w}} - f_{\mathrm{w}}\right)\right], \tag{3.72}$$

and diffusion or convection operators are obtained by considering d or f in isolation.

Equivalent expressions exist for the y- and y-directions.

Splitting Method The steps for advancing the solution over Δt from t_0 are:

1. At $t = t_0$ perform x-convection sweep:
   (a) using $\varphi(t_0)$, calculate velocity field at cell corners and calculate face velocity fields by interpolation of corner velocities;
   (b) using φ_{WW}, φ_{W}, φ_P, φ_{E} and φ_{EE} calculate ratio of gradients $\theta^{\pm}$ over east and west faces using Eqs. (3.69a,b). Calculate flux-limiter function values $\psi(\theta^{\pm})$ at each face using one of Eqs. (3.49) to (3.52), etc.;
   (c) use face u velocity fields to calculate east and west face convective fluxes using Eqs. (3.70);
   (d) calculate time-derivatives due to the convection term and integrate over Δt to $t^{(x)}$;
2. At $t = t^{(x)}$ perform x-diffusion sweep:
   (a) using φ_{W} and φ_{E}, obtain diffusion face fluxes via Eqs. (3.71a);
   (b) calculate time-derivatives due to the diffusion term and integrate over Δt to $t^{(xx)}$. Retain $\varphi(t^{(xx)})$;
3. At $t = t_0$ perform y-diffusion sweep:
   (a) using φ_{S} and φ_{N}, obtain diffusion face fluxes via the rotated version of Eqs. (3.71a);

(b) calculate time-derivatives due to the diffusion term and integrate over Δt to $t^{(y)}$;

4. At $t = t^{(y)}$ perform y-convection sweep:

   (a) using $\varphi(t^{(y)})$, calculate velocity field at cell corners and calculate face velocity fields by interpolation of corner velocities;

   (b) using φ_{SS}, φ_{S}, φ_P, φ_{N} and φ_{NN} calculate ratio of gradients $\theta^{\pm}$ over east and west faces using Eqs. (3.69a,b). Calculate flux-limiter function values $\psi(\theta^{\pm})$ at each face using one of Eqs. (3.49) to (3.52), etc.;

   (c) use face v velocity fields to calculate north and south face convective fluxes using the rotated version of Eqs. (3.70);

   (d) calculate time-derivatives due to the convection term and integrate over Δt to $t^{(yy)}$;

5. Take the arithmetic mean of $\varphi(t^{(xx)})$ and $\varphi(t^{(yy)})$ to obtain $\varphi(t_0 + \Delta t)$.

The three-dimensional version follows naturally.

3.11 Conclusions

General Remarks and Chapter Summary This chapter has outlined the major developments in the finite-volume method, indicated where the FVM has been utilised for tidal devices and then developed a finite-volume scheme for the vorticity transport equations. In the preceding sections, a finite-volume discretisation for each of the convection, diffusion and tilting/stretching terms in the vorticity transport equations was presented. The performance of the convection component is crucial in preventing non-physical diffusion of the vorticity, and various methods for modelling the convection were discussed. Schemes where higher than first-order terms were retained are susceptible to unbounded error growth, and as such near discontinuities, a finite-volume scheme for the convection term can be at most first-order accurate. Higher-order schemes will introduce wiggles in the solution due, as analysis in Appendix A.1 shows, to introduction of a non-physical dispersive term. These wiggles emanate from under and overshoots in the solution. Unfortunately, analysis in Section 3.6.2 shows that the first-order upwind scheme suffers a severe limitation on retaining small-scale flow features, since it effectively introduces a non-physical dissipative term. This gives rise to the notion of a high resolution non-linear scheme, where the various coefficients of the neighbour weighting stencil are modified in

a solution dependant manner, such that away from strong solution gradients a second or higher-order scheme is employed, but near strong gradients a first-order scheme is used. This is accomplished by means of a flux-limiter function, which operates on the ratio of the solution gradients upwind and downwind of a cell interface. The raison d'être of the flux-limiters is stated by Sweby (1984):

> Given a basic scheme which preserves second-order accuracy in space and time, but which is unbounded, an appropriate limiter is introduced which diminishes the oscillation-provoking, anti-diffusive truncation error on the basis of the TVD constraint.

Where discontinuities are detected, the flux-limiter reduces or eliminates the contribution of higher-order terms to the convection discretisation. The form of the limiter functions is determined by the bounds on solution gradients according to Harten's theorem and as commonly expressed by the Sweby diagram – Fig. 3.3. This causes the solution to damp out any spurious oscillations such that it is total variance diminishing. When the solution is smooth (far from discontinuities) and $\theta \approx 1$ the flux limiter function will be near unity, allowing the minimum attenuation of the high-order method.

Impacts on this Thesis Section 3.4 presented operator-adding and operator-splitting which are used as a means of combining the appropriate schemes for convection, diffusion and stretching, as developed in Sections 3.6 to 3.9. A finite-volume over a time-step using the symmetric Strang operator-splitting method to combine the subcomponents allows a solution evolution that is second-order in time, and second-order in space (to the extent that the individual one-dimensional sweeps are). It also facilitates the inclusion of source terms. Finally, Section 3.10 explicitly spells out the complete method as used in this thesis for the finite-volume portion of the developed code, both in two and in three dimensions. This includes indication of how source terms and face velocities are calculated, and how the "external" finite-volume time-steps are advanced along with the "internal" boundary-element sub-time-steps.

References

Adams, N., Ranford, D. and Livingston, D. (2011). "Modelling and optimisation of tidal arrays." In "Proceedings of the 9th European Wave and Tidal Energy Conference (EWTEC2011)," Southampton, England.

Afgan, I., McNaughton, J., Rolfo, S., Apsley, D., Stallard, T. and Stansby, P. (2013). "Turbulent flow and loading on a tidal stream turbine by LES and RANS." *International Journal of Heat and Fluid Flow*.

ANSYS (2012). "FLUENT user guide." Tech. rep., ANSYS Inc.

ANSYS (2013). "ANSYS WINDMODELLER." Tech. rep., ANSYS Inc.

Bai, L., Spence, R.R.G. and Dudziak, G. (2009). "Investigation of the influence of array arrangement and spacing on tidal energy converter (TEC) performance using a 3-dimensional CFD model." In "Proceedings of the 8th European Wave and Tidal Energy Conference (EWTEC2009)," Uppsala, Sweden.

Batten, W.M.J., Harrison, M. and Bahaj, A.S. (2011). "The accuracy of the actuator disc-RANS approach for predicting the performance and far wake of a horizontal axis tidal stream turbine." In "Proceedings of the 9th European Wave and Tidal Energy Conference (EWTEC2011)," Southampton, England.

Belloni, C.S. and Willden, R.H. (2011). "Flow field and performance analysis of bidirectional and open-centre ducted tidal turbines." In "Proceedings of the 9th European Wave and Tidal Energy Conference (EWTEC2011)," Southampton, England.

Boris, J.P. and Book, D.L. (1973). "Flux-corrected transport I: SHASTA, a fluid transport algorithm that works." *Journal of Computational Physics*, **11**(1): pp. 38–69.

Calaf, M., Meneveau, C. and Meyers, J. (2010). "Large eddy simulation study of fully developed wind-turbine array boundary layers." *Physics of Fluids*, **22**(1).

Churchfield, M., Li, Y. and Moriarty, P. (2011). "A large-eddy simulation study of wake propagation and power production in an array of tidal-current turbines." In "Proceedings of the 9th European Wave and Tidal Energy Conference (EWTEC2011)," Southampton, England.

Clarke, J.A., Connor, G., Grant, A.D., Johnstone, C.M. and MacKenzie, D. (2007). "Design of a contra-rotating tidal power turbine and analysis of performance." In "Proceedings of the 7th European Wave and Tidal Energy Conference (EWTEC2007)," Porto, Portugal.

Consul, C. and Willden, R. (2009). "Influence of solidity on the performance of a cross-flow turbine." In "Proceedings of the 8th European Wave and Tidal Energy Conference (EWTEC2009)," Uppsala, Sweden.

Consul, C.A., Willden, R.H.J. and McIntosh, S.C. (2011). "An investigation of the influence of free surface effects on the hydrodynamic performance of marine cross-flow turbines." In "Proceedings of the 9th European Wave and Tidal Energy Conference (EWTEC2011)," Southampton, England.

Couch, S., Sun, X. and Bryden, I. (2005). "Modeling of energy extraction from tidal currents." In "Proceedings of the 6th European Wave and Tidal Energy Conference (EWTEC2005)," Glasgow, Scotland.

Courant, R., Friedrichs, K. and Lewy, H. (1928). "Über die partiellen Differenzengleichungen der mathematischen Physik." *Mathematische Annalen*, **100**(1): pp. 32–74.

Courant, R., Isaacson, E. and Rees, M. (1952). "On the solution of nonlinear hyperbolic differential equations by finite differences." *Communications on Pure and Applied Mathematics*, **5**(3): pp. 243–255.

Daly, T., Myers, L.E. and Bahaj, A.S. (2011). "Numerical analysis of the acceleration and wake effects resulting from changes in tidal turbine array position in a channel." In "Proceedings of the 9th European Wave and Tidal Energy Conference (EWTEC2011)," Southampton, England.

Engquist, B., Osher, S. and Somerville, R. (1985). *Large-Scale Computations in Fluid Mechanics*. No. 1 in Lectures in Applied Mathematics. American Mathematical Society.

Fromm, J.E. (1968). "A method for reducing dispersion in convective difference schemes." *Journal of Computational Physics*, **3**(2): pp. 176–189.

Godunov, S. (1959). "A difference scheme for numerical solution of discontinuous solution of hydrodynamic equations." *Matematicheskii Sbornik*, **47**: pp. 271–306.

Gretton, G. and Bruce, T. (2005). "Preliminary results from analytical and numerical models of a variable-pitch vertical-axis tidal current turbine." In "Proceedings of the 9th European Wave and Tidal Energy Conference (EWTEC2005)," Glasgow, Scotland.

Gretton, G.I. and Bruce, T. (2007). "Aspects of mathematical modelling of a prototype scale vertical-axis turbine." In A. Falcão (ed.), "Proceedings of the 7th European Wave and Tidal Energy Conference (EWTEC2007)," Porto, Portugal.

Gretton, G.I., Bruce, T. and Ingram, D.M. (2009). "Hydrodynamic modelling of a vertical axis tidal current turbine using CFD." In "Proceedings of the 8th European Wave and Tidal Energy Conference (EWTEC2009)," Uppsala, Sweden.

Gretton, G.I., Ingram, D.M. and Bryden, I.G. (2011). "Results from blade element momentum and RANS analyses of a practical full-scale horizontal axis tidal current turbines." In "Proceedings of the 9th European Wave and Tidal Energy Conference (EWTEC2011)," Southampton, England.

Harrison, M.E., Batten, W.M.J., Myers, L.E. and Bahaj, A.S. (2009). "A comparison between CFD simulations and experiments for predicting the far wake of horizontal axis tidal turbines." In "Proceedings of the 8th European Wave and Tidal Energy Conference (EWTEC2009)," Uppsala, Sweden.

Harten, A. (1983). "High resolution schemes for hyperbolic conservation laws." *Journal of Computational Physics*, **49**: pp. 357–393.

Hirsch, C. (1988). *Numerical Computation of Internal and External Flows (Volumes 1 & 2)*. John Wiley and Sons, Inc., New York, NY, USA.

James, S.C., Barco, J., Johnson, E., Lefantzi, S., and Roberts, J.D. (2011). "Flow sensitivity to marine hydrokinetic energy generation from currents using a hydrodynamic model." In "Proceedings of the 9th European Wave and Tidal Energy Conference (EWTEC2011)," Southampton, England.

Jimenez, A., Crespo, A., Migoya, E. and Garcia, J. (2007). "Advances in large-eddy simulation of a wind turbine wake." *Journal of Physics: Conference Series*, **75**(1): pp. 12–41.

Jo, C.H., Lee, K.H., Yim, J.Y. and Rho, Y.H. (2011). "Interaction effect analysis for tidal current power farm feasibility study applied to projects in Korea." In "Proceedings of the 9th European Wave and Tidal Energy Conference (EWTEC2011)," Southampton, England.

Jones, I., Staples, C., Wells, A., McSherry, R., Grimwade, J. and Mateus, A. (2011). "Numerical modelling of high energy tidal regions using three-dimensional CFD." In "Proceedings of the 9th European Wave and Tidal Energy Conference (EWTEC2011)," Southampton, England.

Kawaguti, M. (1953). "Numerical solution of the navier-stokes equations for the flow around a circular cylinder at reynolds number 40." *Journal of the Physical Society of Japan*, **8**(6): pp. 747–757.

Klaptocz, V., Rawlings, G., Nabavi, Y., Alidadi, M., Li, Y. and Calisal, S. (2007). "Numerical and experimental investigation of a ducted vertical axis tidal current turbine." In "Proceedings of the 7th European Wave and Tidal Energy Conference (EWTEC2007)," Porto, Portugal.

Kloos, G., Gonzalez, C.A. and Finnigan, T.D. (2009). "The bioSTREAM^{TM}tidal current energy converters." In "Proceedings of the 8th European Wave and Tidal Energy Conference (EWTEC2009)," Uppsala, Sweden.

Koren, B. (1993). "A robust upwind discretization method for advection, diffusion and source terms." In "Numerical methods for advection-diffusion problems," vol. 45 of *Notes on Numerical Fluid Mechanics*, pp. 117–138. Vieweg.

Leonard, B. (1979). "A stable and accurate convective modelling procedure based on quadratic upstream interpolation." *Computer Methods in Applied Mechanics and Engineering*, **19**(1): pp. 59–98.

LeVeque, R.J. (2002). *Finite Volume Methods for Hyperbolic Problems*. Cambridge texts in applied mathematics.

Lien, F.S. and Leschziner, M.A. (1994). "Upstream monotonic interpolation for scalar transport with application to complex turbulent flows." *International Journal for Numerical Methods in Fluids*, **19**(6): pp. 527–548.

Malki, R., Masters, I., Williams, A. and Croft, T. (2011). "The influence of tidal stream turbine spacing on performance." In "Proceedings of the 9th European Wave and Tidal Energy Conference (EWTEC2011)," Southampton, England.

Malki, R., Williams, A., Croft, T., Togneri, M. and Masters, I. (2013). "A coupled blade element momentum – computational fluid dynamics model for evaluating tidal stream turbine performance." *Applied Mathematical Modelling*, **37**(5): pp. 3006–3020.

Mason-Jones, A., O'Doherty, D., Morris, C., O'Doherty, T., Byrne, C., Prickett, P.W., Grosvenor, R.I., Owen, I., Tedds, S. and Poole, R. (2011). "Scaling of a prototype tidal stream turbine using non-dimensional parameters." In "Proceedings of the 9th European Wave and Tidal Energy Conference (EWTEC2011)," Southampton, England.

Masters, I., Malki, R., Williams, A.J. and Croft, T.N. (2013). "The influence of flow acceleration on tidal stream turbine wake dynamics: A numerical study using a coupled bem-cfd model." *Applied Mathematical Modelling*, **37**(16–17): pp. 7905–7918.

McIntosh, S.C., Fleming, C.F. and Willden, R.H. (2011). "Embedded RANS-BEM tidal turbine design." In "Proceedings of the 9th European Wave and Tidal Energy Conference (EWTEC2011)," Southampton, England.

McSherry, R., Grimwade, J., Jones, I., Mathias, S., Wells, A. and Mateus, A. (2011). "3D CFD modelling of tidal turbine performance with validation against laboratory experiments." In "Proceedings of the 9th European Wave and Tidal Energy Conference (EWTEC2011)," Southampton, England.

Merkle, C.L. and Choi, Y.H. (1988). "Computation of low-speed compressible flows with time-marching procedures." *International Journal for Numerical Methods in Engineering*, **25**(2): pp. 293–311.

O'Doherty, D., Mason-Jones, A., Morris, C., O'Doherty, T., Byrne, C., Prickett, P. and Grosvenor, R. (2011). "Interaction of marine turbines in close proximity." In "Proceedings of the 9th European Wave and Tidal Energy Conference (EWTEC2011)," Southampton, England.

O'Doherty, D., Mason-Jones, A., O'Doherty, T. and Byrne, C. (2009). "Considerations of improved tidal stream turbine performance using double rows of contra-rotating blades." In "Proceedings of the 8th European Wave and Tidal Energy Conference (EWTEC2009)," Uppsala, Sweden.

Roe, B. (1985). "Some contributions to the modeling of discontinuous flows." *Lecture Nores in Applied Mathematics*, **22**: pp. 163–193.

Ruopp, A., Ruprecht, A. and Riedelbauch, S. (2011). "Automatic blade optimisation of tidal current turbines using OpenFOAM." In "Proceedings of the 9th European Wave and Tidal Energy Conference (EWTEC2011)," Southampton, England.

Strang, G. (1968). "On the construction and comparison of difference schemes." *SIAM Journal on Numerical Analysis*, **5**(3): pp. 506–517.

Sweby, P.K. (1984). "High resolution schemes using flux limiters for hyperbolic conservation laws." *SIAM Journal on Numerical Analysis*, **21**(5): pp. 995–1011.

Thom, A. (1933). "The flow past circular cylinders at low speeds." *Proceedings of the Royal Society of London A: Containing Papers of a Mathematical and Physical Character*, **141**(854): pp. 651–669.

Toro, E.F. (1999). *Riemann Solvers and Numerical Methods for Fluid Dynamics: A Practical Introduction*. Springer, Berlin, 2nd edn.

Turnock, S.R., Phillips, A.B., Banks, J. and Nicholls-Lee, R. (2011). "Modelling tidal current turbine wakes using a coupled RANS-BEMT approach as a tool for analysing power capture of arrays of turbines." *Ocean Engineering*, **38**(11-12): pp. 1300–1307.

van Leer, B. (1974). "Towards the ultimate conservative difference scheme II: Monotonicity and conservation combined in a second-order scheme." *Journal of Computational Physics*, **14**(4): pp. 361–370.

van Leer, B. (1977). "Towards the ultimate conservative difference scheme III. upstream-centered finite-difference schemes for ideal compressible flow." *Journal of Computational Physics*, **23**(3): pp. 263–275.

van Leer, B. (1979). "Towards the ultimate conservative difference scheme V: A second-order sequel to Godunov's method." *Journal of Computational Physics*, **32**: pp. 101–136.

Versteeg, H.K. and Malalasekera, W. (2007). *An Introduction to Computational Fluid Dynamics: the Finite Volume Methods*. Pearson/Prentice Hall, New York, 2nd edn.

Waterson, N. and Deconinck, H. (2007). "Design principles for bounded higher-order convection schemes – a unified approach." *Journal of Computational Physics*, **224**(1): pp. 182–207.

4

Boundary-Element Methods for Marine Hydrodynamics

4.1 Introduction

The purpose of this chapter is to set out the means by which the method proposed in this thesis represents the geometric configuration of bodies which it is designed to model. Specifically, this chapter describes the means by which solid bodies are modelled and wakes are generated, allowing the method to apply to situations which are relevant from an engineering perspective in a manner which is physically realistic.

4.1.1 Relevance

This chapter is split into three sections: the first is a review of boundary-element methods; the next outlines theoretical topics concerning the governing equations; and the final section their practical implementation. The "inputs" to the chapter are the governing equations of fluid flow, and the Navier-Stokes equations, and the "output" is a description of the boundary-element method applied in this work.

In the theoretical section, the governing equations are rendered into a simplified form known as potential flow, and the justification for this approach is given, from both a physical and computational point of view. The applied section then provides a computational method for solving the equations.

4.2 A Review of Boundary-Element Methods

Boundary-Element Methods (BEMs) are amongst the longest serving practicable computational methods for numerical evaluation of engineering problems, so much so that there are numerous specialist journals (e.g. Engineering Analysis with Boundary Elements – five year impact factor 1.431), books (e.g. the venerable Katz and Plotkin, 2001) and review

papers (e.g. Johnson, Tinoco and Yu, 2005) on the methods. They have been used extensively in naval architecture for the design of ship hulls and propellers, and in aeronautical engineering were the tools of choice for the aerodynamic design of aircraft for almost forty years. Their ability to reduce the dimensionality of a problem from three to two dimensions (or two to one dimensions) greatly reduces the computer power required to arrive at an engineering solution, as long as the underlying assumptions are valid, of course. The speed to a solution allows BEMs to be used in highly iterative design work, for example aerofoil inverse design with optimisation algorithms where an aerofoil shape is sought for a given pressure distribution – the means by which the NREL S809 and S814 foils were obtained (Somers, 1997, 2004). Relatively recent developments in RANS and Eulerian solvers have somewhat diminished BEMs niche, however, the solution speed and a range of extensions have brought BEM capabilities which practical RANS/Eulerian CFD is only just beginning to better in certain engineering applications.

4.2.1 Premise

The essence of a boundary-element method is to render the flow using surfaces rather than by an Eulerian notion of continua. BEMs (for fluid dynamics and relevant to this thesis) rely on the linearising assumptions of potential flow, especially the concept of superposition. Early BEMs solved algebraic systems of analytical expressions for the velocity due to surface distributions of elemental potential flow solutions. More modern aero/hydrodynamic BEM approximates the governing integral equations using a potential based Green's function solution for Laplace's equation, and Gauss's theorem to render the volume integral equations into surface integrals. The surfaces are then discretised into panel elements, each of which has a distribution of unknown strength of a Green's function solution over it. Boundary conditions are then specified, and the unknown values are solved to satisfy the boundary conditions.

Every boundary-element method has the following constituents:

1. an integral form of the (linearised) equations governing fluid flow;
2. a discretisation of the surfaces of a geometric representation of a physical problem into panels;
3. one or more boundary conditions for each equation (i.e. each panel, or each panel corner), fulfilled by the distribution of singularities over each panel;
4. a method of supplying some physical meaning to the problem in order to isolate the unique and correct solution; and

5. a linear system of equations embodying these.

In addition to these requirements, each method needs a matrix solver – however, this is a general problem beyond the scope of this thesis.

Katz and Plotkin (2001) divide the historic evolution of BEM into three developmental stages. These track the theoretical evolution of the method and the availability of the computational ability to use the methods. In the first stage, the theoretical base was laid. The second stage charts the development of higher-order methods, involving linear/quadratic/etc. distributions of surface elements and associated curved panels. Availability of computer resources at this time was still limited to large corporations and government agencies. The third stage corresponds to the availability of desktop computers, and is characterised by a resurgence in the popularity, availability and development of low-order methods. At present, there appears to be a renaissance in the development of higher-order methods along with a fairly consistent evolution and use of the fast, reliable and relatively easy to implement low-order methods.

4.2.2 Relevant History

The work of Hess and Smith (1964) of Douglas Aircraft was instrumental in providing a logical and extensible groundwork for boundary-element methods and published the first practical method for three-dimensional computational work. Their method allowed calculation of the solutions for thick bodies by using a superposition of the contributions of the boundary-element sides to represent the influence of a surface distribution of sources on plane polygon panels (usually quadrilaterals) and solved for velocity using a Neumann boundary-condition. This limited calculation to non-lifting bodies since there was no means of generating a bound circulation and satisfying a Kutta condition, and so a common approach used a vortex-lattice-method on the camber-surface of the wing. Further developments in Hess (1972) utilised a distribution of dipoles and the inclusion of one or more wake elements to achieve lifting solutions. The major contribution of Hess and Smith was the development of the analytical expressions relating the distribution of the source and dipole distributions to the velocity perturbation potential at some distant point. Later work by Jensen (1988) (in Bertram, 2011) arrived at a “better” approximation for the source distribution on a panel which allows closed panels – the method of Hess and Smith required flat quadrilateral source panels rather than rectilinear panels and resulted in “gaps” in the meshed surface.

Morino and Kuo (1974) introduced a method for more complex bodies based on solving the boundary integral equations for perturbation potential rather than velocity. The

idea was to use a Dirichlet boundary-condition for the internal potential and a Neumann boundary-condition on the body surface. Maskew (1982) developed a method based on constant strength source and dipole on quadrilateral panel elements which evolved into the VSAERO package (see Maskew, 1987). Maskew presents two options for the internal potential – either zero internal potential, achieved by matching the surface normal flow, or zero internal flow – and finds that a zero internal potential results in more accurate results given a compromised panelling. In a comparison in Youngren, Bouchard and Coopersmith (1984) of the method of Hess and Smith and that of Morino and Kuo, it was found that the Morino and Kuo formulation was far less sensitive to the quality and size of the surface panels.

In Johnston (1980), the analytical solutions of the boundary-integral-equations for source and dipole panels are presented, along with far-field expressions based on multipole expansions. These expressions form the basis of almost all recent low-order methods.

4.2.3 Wakes and Lifting Flow

One of the fundamental descriptions of the generation of lift involves the concept that a circulation is set up around the lifting section. In boundary-element methods, this is coupled with the Kutta condition: the flow must leave the aerofoil/wing “smoothly” at the trailing edge in order to satisfy Helmholtz’ vortex laws and Kelvin’s theorem. In other words, a lift generating body must generate a wake. In computations using lifting lines, the “bowl" of one or more horseshoe vortices is attached to the chord-line of the wing/foil and their “legs” are extended infinitely far downstream. In more sophisticated methods, the space between the legs is segmented into a lattice of vortex rings or represented by panels over which an equivalent singularity element is spread (and a constant dipole singularity panel which extends infinitely far downstream is equivalent to the legs of the horseshoe vortex). In calculations where the lift is constant, e.g. an aircraft in cruise or an isolated turbine/hub configuration, the infinite length constant strength trailing vortex model is valid insofar as the underlying flow model can be. In time varying flows, the requirement of constant circulation in the domain necessitates shedding of appropriate circulation into the wake. From a boundary-element method point of view, this requires that the horseshoe vortex wake is segmented along the length of the vortices. This results in a vortex lattice representation of the wake, where the downstream circulation distribution approximates the rate of change of bound circulation on the wing, and the spanwise circulation distribution at each downstream location is a record of the wing spanwise circulation at the time it was shed.

There are three typical BEM methods for defining the geometry of the wake behind a lifting body:

1. fixed-wake model, where the location of wake elements is specified in advance of the calculation;

2. free-wake, where the evolution of the location of the wake elements proceeds in a Lagrangian manner according the local velocity; and

3. wake-relaxation models, which attempt to move a pre-defined wake into a physically realistic location.

4.2.4 Steady vs. Unsteady Panel Methods

In aerospace applications, the lift and (induced) drag characteristics of aircraft configurations was sought, normally for the particular parts of the flight envelope where the assumptions held, e.g. cruise. In naval work on propellers, the thrust delivered and the power requirements of propellers was sought. Both of these situations were essentially “steady” and symmetric. Unsteady BEM flow analysis is necessary when dealing with multi-body flows, for example ship propellers in the presence of rudders or hulls, and aircraft propellers near wings. In these scenarios, it is clearly not possible to iteratively relax the wake into a force-free location, since this location is time varying. Instead, it is normal to allow the wake to convect according to the force-free wake boundary conditions. The requirement to “grow” a wake, rather than relax an existing pre-allocated wake somewhat changes the nature of the method. In steady methods, such as fixed or quasi/full wake relaxation models, it is assumed that the wake panel patch strengths varies only in a radial or spanwise direction (as they are steady-state). A somewhat simplified matrix of influence coefficients is calculated for the wake panels and placed on the “known" RHS of the linear algebra. In time-marching methods this is not practical, and the influence is simply added to the RHS on an ad hoc basis. This means that it is then possible to treat the wake influence as an inflow velocity, rather than as a perturbation potential at the panel centroids, and this means that elements other than panels can be used in the wake.

Unsteady panel methods have been successfully implemented based on the Morino formulation for naval propellers by e.g. Hsin (1990), Kinnas, Hsin and Keenan (1991) and Hoshino (1993). After the early work, free-wake models seem to have fallen out of favour and fixed wake models are preferred, since free-wake models using panels – and even wake relaxation methods – suffer from issues due to the ill-posedness of the vortex wake problem. In sufficient time, instabilities develop in the shed wake resulting in “vortex-

spaghetti" (in the words of Snell, 1998). This is especially evident in methods where there is genuine unsteadiness in the motion of a propeller – for example heaving motion – or for propellers in yaw misalignment (see Politis, 2004, for both), or in the far-field of the helicopter wake in Gennaretti and Bernardini (2007).

4.2.5 Recent Developments and Relevant Work

Current work in BEMs used in hydrodynamics or aerodynamics is focussed on improving the models in several key areas:

- increasing accuracy by increasing the order of singularity elements – e.g. hyper-singular singularities (r^3 rather than r^2 decay as $r \to \infty$) using bi-linear (Politis, 2004; van Garrel, 2011) or bi-quadratic (Pyo, 1995; Topper, 2010) elements, and/or increasing the order of the mesh using e.g. cubic or NURB-splines etc. (Kim, Lee and Kerwin, 2007);

- increasing accuracy by reducing the errors due to the mesh – e.g. by better alignment/mapping in Kinnas (1996), or reduction of "bad" elements by orthogonal (Hsin, 1990), or quasi-orthogonal (Baltazar, 2008) meshing;

- increasing accuracy/application by using alternative wake models – e.g. wake-relaxation, free-wake, vortex wake in Willis (2006) or Maganga *et al.* (2008);

- increasing applicability by adding additional physics – e.g. cavitation in Vaz (2005), leading edge-separation in Baltazar (2008);

- modification of model to include panel-based vortex-shedding – e.g. Taylor and Vezza (1999) in two dimensions and Stock and Gharakhani (2010) in three dimensions; and

- extension and application of the method to unsteady, multi-body calculations, e.g. Liu, Colbourne and Chin (2005); Dixon *et al.* (2008).

Turnock (1997) describes a source/dipole method called PALISUPAN ('PARALLEL LIFTING SURFACE PANEL'). Nicholls-Lee, Turnock and Boyd (2011) used this along with FEA analysis to perform fluid-structure interaction analysis or turbine blades.

Vaz (2005) developed a low-order Morino formulation to investigate cavitation on lifting surfaces and ship propellers. The method predicts the inception and growth of a cavitation bubble by analysis of the pressure distribution. A surface transpiration method is then employed to simulate the change in surface geometry due to the cavitation bubble.

Willis (2006) uses a high-order method coupled to a vortex blob wake to simulate flow around aircraft configurations. The method uses a quadratic distribution of sources and dipoles on quadratic geometry, whose influence coefficients are computed by a FFT-type expansion. Vortex particles are shed into the wake to satisfy the Kutta condition.

Gennaretti and Bernardini (2007) use an unsteady panel method based on the Morino formulation to model the blade-vortex interactions of an advancing helicopter rotor system.

Vaz (2005) developed and Baltazar (2008) uses a low-order Morino formulation BEM for analysis of the flow around naval propellers. The analysis focusses on the predictive performance effects due to the type of wake model (rigid, semi-relaxed, fully relaxed) and the quality of the mesh, especially near the tip. This is later extended to tidal current turbines in Baltazar and Falcão de Campos (2011). Maganga *et al.* (2008) developed and Pinon *et al.* (2012) uses a panel method with a vortex particle based free wake to simulate flow around tidal turbines.

Topper (2010) developed a high-order, bi-quadratic basis function BEM method for analysis of the flow around tidal turbines, which included a free-surface. The method was able to model solitonic wave propagation with reasonable accuracy, however was unstable when lifting surfaces were modelled.

Kinnas *et al.* (2012) present a comparison between various boundary-element methods, including a vortex-lattice method (VLM), a lifting-line and a source/vortex panel method, with application to a tidal turbine rotor model.

4.2.6 Extensions Using Vortex Methods

Taylor and Vezza (1999) developed a two-dimensional BEM/particle method that uses a panel-based representation of the surface of interest (e.g. a foil or a bridge deck), where a linear distribution of vortex elements are shed along each panel during each time-step. The method has the ability to "re-absorb" particles which pass into the inner wake region from the outer. The method uses a random walk approximation to model the Newtonian viscosity and a quadtree/expansion-based fast velocity summation. Because of the relative efficiency in coupling with a two-dimensional/three degree-of-freedom fluid structure interaction model, the method is capable of modelling dynamic stall on aerofoils, and galloping bridge decks etc. which would be very difficult to model in three dimensions (see Taylor and Vezza, 2009).

McCombes (2006) developed a two-dimensional structural model of an oscillating foil type tidal energy converter which used an unsteady BEM with a vortex particle wake. The particles were modelled as Rankine vortices, and there was no diffusion model.

The method in Gharakhani, Sitaraman and Stock (2005) releases vortex particles from triangular BEM panel surfaces in a three-dimensional analogue to the model of Taylor and Vezza. In this way, the viscous nature of the boundary-layer is approximated in three-dimensions. The method has been applied to flow past a "discoid" at incidence (in Gharakhani and Stock, 2005). While this method appears a functioning extension to classical BEM, the method seems to suffer from Reynolds number limits due to increased computational overhead because of the number of particles required to capture small scale fluid phenomena and effectively model viscosity in high Re flow.

In viscous boundary-element methods Ploumhans *et al.* (2002) suggests achieving the no-slip condition via the following two boundary conditions for the three components of vorticity:

1. a Dirichlet condition for zero normal-to-surface vorticity component; and
2. a Neumann condition to cancel out the tangential velocity components at the wall for the two tangential vorticity components.

Koumoutsakos, Leonard and Pepin (1994) propose the use of a vortex sheet method in an extension of the idea of Lighthill (1963, in Cottet and Koumoutsakos, 2000) that by using a potential flow vortex sheet to enforce zero normal flow, then provide a vorticity diffusion "flux" into the domain to correct the error due to the sheet, a no-slip condition can be enforced.

4.2.7 Extensions Using RANS

There are various BEM-RANS or vortex-RANS hybrid methods. They stem from the inclination that while BEM or vortex methods are useful in describing long term wake evolution, they suffer in their limiting assumptions, are difficult to implement or are slow when used to predict the viscous near-field. To this end a RANS solver can be implemented as a "vortex-generator" for a BEM-type or vortex wake model.

Schmitz and Chattot (2006) extend the BEM model of a wind turbine by using Stokes' theorem in a RANS sub-domain in order to obtain approximately the bound circulation via a numerical integration round an aerofoil section, and thus the shed and trailed vorticity behind a rotor-blade. The method used a helicoidal vortex lattice to simulate the far-field wake. The method was coupled in both directions: the vorticity was transposed from the Eulerian to the Lagrangian domain, and the velocity field due to the Lagrangian domain was used to provide the boundary conditions to the Eulerian domain. It is not apparent exactly how the model is coupled – it appears that the use of an "infinite" vortex helix for

the Lagrangian wake results in a steady calculation, and that a number of iterations are required before integrated values (e.g. section C_d or rotor C_T) converge.

Whitehouse *et al.* (2007) use a RANS solution for the near-field, coupled to Brown's 'VORTICITY TRANSPORT MODEL' (VTM, Brown and Line, 2005) for the far-field in a hybrid method for rotor-system modelling. The idea is that the vorticity due to the viscous flow in the RANS domain is calculated on the boundaries of the RANS/VTM domains. At this point if it is convected back into the RANS domain it is subsumed – otherwise it evolves according to the vorticity transport equation in the VTM domain. The method is thus coupled in vorticity in both directions. The velocity due to the VTM domain is used as the "inflow" velocity in the RANS domain. It is not clear how the effects of the RANS domain on the velocity in the VTM domain are captured.

Stock and Gharakhani (2010) also use a hybrid method applied to a helicopter rotor, using a RANS solver for the near-field and vortex particles for the wake. This appears to be a similar arrangement to the hybrid method of Whitehouse *et al.*, except that a vortex blob method is employed in the wake.

4.2.8 Dirichlet vs. Neumann Boundary Conditions

Hoeijmakers (1992) lists the various pros and cons of Dirichlet and Neumann BCs for BEMs for aircraft aerodynamics and also the merits and demerits of high and low-order methods. In particular he remarks that although Neumann BCs appear more "forgiving" of irregular panel geometry, Dirichlet BCs are more accurate (for the same computing cost), better behaved and less storage intensive.

4.2.8.1 High vs. Low-Order Panel Methods

Two Dimensions Linear vortex panels (quadratic dipole panels) are better than constant vortex panel (linear dipole panels) because the self-influence of a constant strength vortex panel at its centroid is zero. This would potentially cause issues since the diagonal of the influence matrix would be zero. (Linear strength dipole panels [constant vortex panels] are also better than constant dipole panels, since these equate to a vortex at each edge of the panel, and thus the near-field off-surface velocity field will be somewhat – and artificially – perturbed.) There is an additional problem with the constant vortex panel scheme in that the (linear) Kutta condition requires an equal vortex distribution strength over the two trailing edge panels – this reduces the number of unknowns and results in an under-specified problem.

Three Dimensions Maskew (1982) found that for quadrilateral panels, a constant source/dipole method afforded similar accuracy, reduced cost and was more forgiving of sloppy panelling by comparison with contemporary higher-order methods. Hoeijmakers (1992) reported that the advantages of using low-order methods are significantly reduced complexity (in terms of design, programming and maintenance); a reduction in required levels of information for defining surfaces; and an increase in flexibility since no particular directional distribution is assumed. Of higher-order methods, Hoeijmakers states that the advantages are generally seen only as panel size tends to zero – in other words, an asymptotic tendency to higher accuracy results may not, all other things being equal, translate into a better accuracy than lower-order methods.

4.2.9 Effects of Mesh Quality

Low-order BEMs are observed to function "well enough" over most of a surface, even for a relatively "poor" mesh. There has, however, been some effort in attempting to reduce the errors by increasing the mesh quality for the solution: typically this is near discontinuities in one or both grid directions. Pyo (1995) reports that the predictive performance of the panel method is compromised towards a propeller tip, resulting in non-physical velocities and pressures (this can be seen in the tip pressure distributions for a naval propeller in shown in Fig. 9.1a). Hsin (1990) found that the prediction of surface velocities and thus pressure distributions near the tip of a propeller was improved by attempting to retain a degree of orthogonality to the mesh, even when the geometry is highly distorted. Methods where the grid is aligned to the flow are used by Kinnas, Hsin and Keenan (1991), and with quasi-orthogonal surface discretisation are developed by Baltazar (2008). These both result in some improvement to the pressure – and thus load – predictions.

For high-order methods, the ability to use third order b-splines allows a reduction in the number of panels. Kim, Lee and Kerwin (2007) use third order splines and surface distributions and report that while they are able to reduce the number of panels significantly compared to a low-order method, for field evaluations near a panel they must subdivide the panel and the evaluations must be performed numerically via quadrature rather than through analytical expressions for the surface integrals.

4.3 Theoretical Topics

Fluid flow can be described by the Navier-Stokes equations which can be reduced to a simpler form by making assumptions that the fluid being modelled is both inviscid and

irrotational. Using this subset of the flow physics, a model can be created which is both considerably simpler in terms of theory and less demanding in terms of required computational resource than attempting to model the Navier-Stokes equations in full. However, before proceeding, the validity of these assumptions must be tested.

4.3.1 Validity of an Assumption of Irrotational Flow.

An irrotational flow is obtained if it is possible to define a velocity field by the gradient of a scalar potential field. The necessary and sufficient conditions of this are

$$\boldsymbol{u} = \nabla\phi \quad \longleftrightarrow \quad \boldsymbol{\omega} = 0. \tag{4.1}$$

The LHS states that the velocity field is given by the gradient of a scalar field ϕ, the velocity potential. The RHS states that vorticity is zero, since the curl of the gradient of a "well-behaved" scalar field is zero. This obviously poses some issues, since vorticity (and hence circulation) are disallowed in the potential flow framework. Regions where the flow is not irrotational will be those where there is nonzero vorticity, i.e. where there are regions of circulation and regions with strong velocity gradients, for example in shear layers such as wakes and boundary layers.

According to Kelvin's circulation theorem, in a potential flow the total circulation in a domain must remain constant and thus – at least when considering a case where flow is impulsively started from rest – zero. Since this thesis is concerned with flows about hydrodynamic bodies generating lift, and given that one of the key models of the mechanisms of the generation of lifting force by a lifting body is the set-up of a circulation about that body, in order to satisfy Kelvin's theorem, circulation of opposite sign and equal magnitude must appear somewhere in the domain.

4.3.1.1 Helmholtz's Theorems

Helmholtz's theorems state that:

1. a vortex is of constant strength along its length;
2. a vortex cannot begin or end in a fluid;
3. an irrotational flow will remain so unless acted upon by some external influence, including under influence of a conservative body force, e.g. gravity.

Taking Kelvin's theorem along with Helmholtz's second and third theorems, circulation produced in the domain around, say, a hydrofoil must be in effect cancelled by circulation

which is created by and attached to the hydrofoil. Combining this with the real world physical observation of the trailing and shed vortices around wings, it becomes apparent that a potential flow domain where the flow is irrotational cannot – in theory – model lifting bodies. In order to circumvent this and arrive at a model which is useful, the problem being modelled is split into two separate domains, one of which contains the potential flow domain, the other the shed and trailing vorticity due to lift generation. In effect, the domain containing the vorticity/circulation is modelled separately to, but simultaneously with, the potential flow domain.

4.3.2 Validity of an Assumption of Inviscid Flow.

Recalling the continuity and momentum equations (Eqs. 1.2a and 1.2b) and following the dimensional analysis by Katz and Plotkin (2001), transformed versions of the Navier-Stokes equations can be written by creating dimensionless versions of all of the variables by dividing each by a reference quantity e.g. a characteristic length L, speed V, time T, or reference pressure p_0 such that the results are of magnitude $\mathcal{O}(1)$. These are then substituted into Eq. (1.2a) and Eq. (1.2b),

$$\nabla \cdot \overline{\boldsymbol{u}} = 0, \tag{4.2a}$$

$$\left(\frac{L}{TV}\right)\frac{\partial \overline{\boldsymbol{u}}}{\partial \overline{t}} + \overline{\boldsymbol{u}} \cdot \nabla \overline{\boldsymbol{u}} = -\left(\frac{p_0}{\rho V^2}\right)\nabla \overline{p} + \left(\frac{\nu}{VL}\right)\nabla^2 \overline{\boldsymbol{u}}, \tag{4.2b}$$

where the overbar, $\overline{[\ldots]}$, indicates that a term is dimensionless. Since these terms are of $\mathcal{O}(1)$, the groupings in parenthesis now indicate the relative magnitude of each term in the equation. The first bracketed term on the LHS is a time-constant, indicative of the level of time-dependence in the solution, and is often equivalent to the Strouhal number. The first bracketed term on the RHS is the Euler number, i.e. the ratio between pressure and inertia forces. The next term is the reciprocal of the Reynolds number, which is the ratio of inertial to viscous forces.

It can clearly be observed that for a high Reynolds number, the effects of viscosity can be neglected as long as the adjoining term $\nabla^2 \overline{\boldsymbol{u}}$ is not sufficiently greater than $\mathcal{O}(1)$ that taken together their magnitude is similar to the other terms. Situations where this might arise are at no-slip flow boundaries or in wakes where, due to strong velocity gradients $\mathcal{O}(\nabla^2 \boldsymbol{u}) \approx \mathcal{O}(\nu^{-1})$, the effects of viscosity are amplified i.e. in boundary layers. It is possible, therefore, to define conditions where viscosity cannot be neglected as those close to a body or otherwise in a shear layer, and those where it can be neglected as outside the

boundary layer and away from the body and wakes. For a high Reynolds number (but laminar) boundary layer across a flat plate of unit chord, the Blasius solution gives the final thickness $\delta = 4.91\sqrt{1/\mathrm{Re}}$, which is small relative to the chord length at high Reynolds numbers relevant to tidal power, i.e. $\mathcal{O}(\mathrm{Re}) > 10^5$, and these layers can be assumed infinitesimally thin.

However, as with all simplifications, there are some caveats. In an inviscid modelling framework, body surfaces are unable to support a no-slip condition and therefore there is no information on boundary layer development, growth, transition or separation. Without information on shear stress distribution, skin friction drag cannot be predicted, and without information on the evolution of the boundary layer, separation and thus stall cannot be predicted. Care must be undertaken using BEMs (even with corrections) in large perturbation cases where the simplified physics would be violated.

4.3.3 Modelling using a BEM

Before continuing, and as a brief synopsis of the preceding paragraphs, the main points bearing on this work regarding potential flow are:

1. The flow is divided into distinct and separate domains:
    - a viscous and rotational domain which encapsulates boundary layers on bodies and free shear layers in wakes, and thus contains all the vorticity in the modelling framework; and
    - an inviscid and irrotational potential flow domain.
2. At practical Reynolds numbers, the boundary layer thickness is very small with respect to a characteristic length scale, and is thus assumed infinitesimally thin.
3. There is no facility or inclusion in the reduced governing equations of the effects of turbulence since all rotating flow is confined to infinitesimally thin layers.
4. Similarly, there is no means of including (within the simplified physics of the reduced governing equations) the effects of separation and stall, since the infinitesimally thin rotational flow layers must conform to body surfaces.
5. These limitations still allow the BEM method to be applied to a large range of engineering flows.

The basis of the theoretical framework of the model is now described.

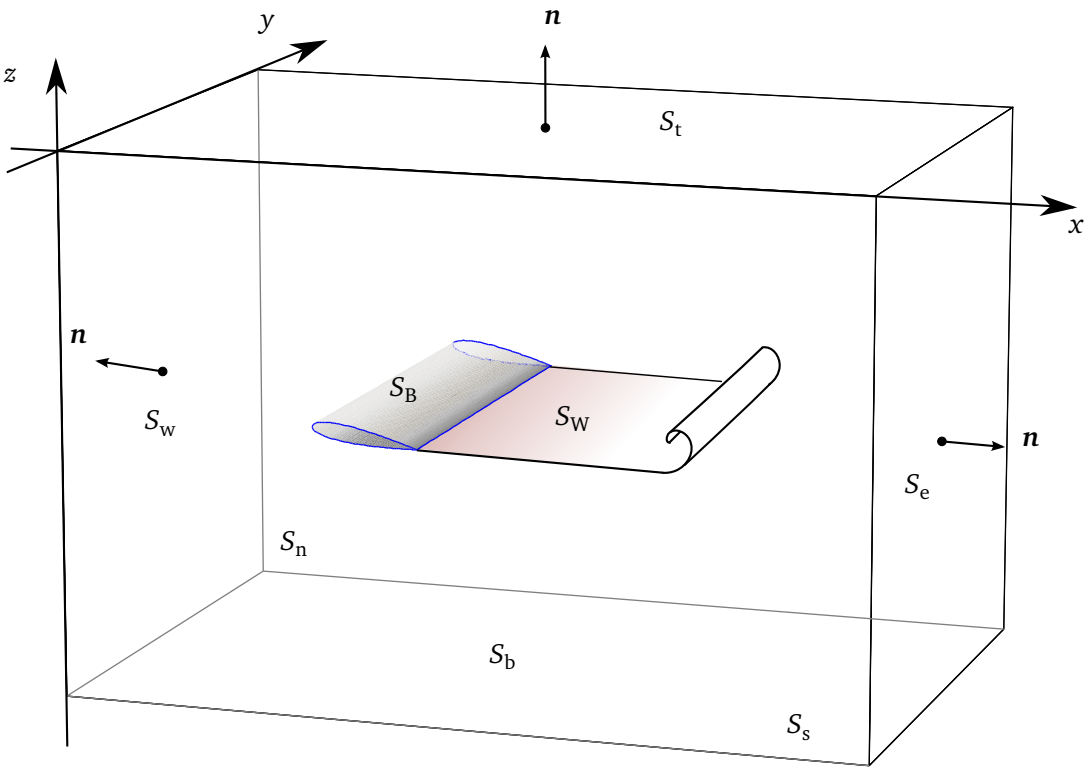

Figure 4.1: The BEM domain.

Table 4.1: Summary of velocities in the problem domain.

$\boldsymbol{u}_\infty$	Uniform freestream velocity field	
$\boldsymbol{u}_{\text{eff.}}(\boldsymbol{x})$	Effective velocity field due to non-uniform or rotational flows e.g. wakes or gusts	$\boldsymbol{x} \in \Omega$
$\boldsymbol{u}'(\boldsymbol{x}) = \nabla\phi(\boldsymbol{x})$	Perturbation velocity	$\boldsymbol{x} \in \Omega$
$\boldsymbol{u}_0(\boldsymbol{x}) = \boldsymbol{u}_\infty + \boldsymbol{u}_{\text{eff.}}(\boldsymbol{x}) + \boldsymbol{u}'(\boldsymbol{x})$	Overall velocity field	
$\boldsymbol{u}(\boldsymbol{x}) = \boldsymbol{u}_0(\boldsymbol{x}) - \boldsymbol{v}_{\text{kin.}}(\boldsymbol{x})$	Incident velocity at point on body	$\boldsymbol{x} \in \partial\Omega$
$\boldsymbol{v}_{\text{kin.}}(\boldsymbol{x}) = \dot{\boldsymbol{x}}_{\text{c.g.}} + \boldsymbol{\Omega} \times (\boldsymbol{x} - \boldsymbol{x}_{\text{c.g.}})$	Kinematic velocity at point on body	$\boldsymbol{x} \in \partial\Omega$

The Computational Domain Consider an arbitrarily shaped, simply connected domain which may be – but is not necessarily – bounded. Define any domain boundaries $S_{[\ldots]}$ such that, for example in Fig. 4.1 where the domain is a cuboid, the far-field surfaces are $S_\infty (= S_\mathrm{n} + S_\mathrm{s} + S_\mathrm{e} + S_\mathrm{w} + S_\mathrm{t} + S_\mathrm{b})$ and also near-field, body fitted solid boundary surfaces. These far-field surfaces are assumed to be sufficiently distant from any other bodies in the flow that they experience only freestream conditions. The computational domain contains all the fluid of interest and all other elements of the calculation, namely all bodies and connected wakes. Body surfaces are denoted S_B and wake surfaces S_W. A body fixed reference frame is set up such that the position of a point P in space $\boldsymbol{x}_P \left(x, y, z, t\right)$ in the global reference frame can be written as

$$\boldsymbol{x}_P = \boldsymbol{x}_{\mathrm{c.g.}} + \boldsymbol{r}, \tag{4.3}$$

Fixing point P to the body, when the body frame is translating with velocity $\dot{\boldsymbol{x}}_{\mathrm{c.g.}}$ and rotating with angular velocity $\boldsymbol{\Omega}$, the kinematic velocity of point P with respect to the global reference frame is given by

$$\dot{\boldsymbol{x}}_P = \dot{\boldsymbol{x}}_{\mathrm{c.g.}} + \boldsymbol{\Omega} \times \boldsymbol{r}. \tag{4.4}$$

Velocity Definitions Hereupon, the fluid velocity field is written as $\boldsymbol{u}$ and body point velocities as $\boldsymbol{v}$. The fluid is assumed to be incompressible and inviscid, and the flowfield is assumed irrotational except for infinitesimally thin regions on body surfaces and wakes. Define a freestream velocity $\boldsymbol{u}_\infty$ and pressure p_∞ which occur at S_∞, sufficiently far away from any disturbance (essentially at infinity) that they are not affected by the presence of bodies, and then assume they act throughout the domain as the background or base-line velocity and pressure fields. In the presence of rotational velocity field due to e.g. boundary-layers and wakes, an effective velocity field $\boldsymbol{u}_{\mathrm{eff.}}$ – which contains the induced velocities – is also introduced. When calculating $\boldsymbol{u}_0$, the flow velocity at a stationary point, $\boldsymbol{u}_{\mathrm{eff.}}$ is simply added to $\boldsymbol{u}_\infty$. In a moving reference frame whose origin is coincident and moving with a point $\boldsymbol{x}_P$ on the surface of a body, a total incident velocity $\boldsymbol{u}(\boldsymbol{x}_P)$ is obtained by subtraction of the kinematic velocity at the point $\boldsymbol{v}_{\mathrm{kin.}} = \dot{\boldsymbol{x}}_\mathrm{P}$ from the inflow velocity field $\boldsymbol{u}_0(\boldsymbol{x}_P)$ at that point. $\dot{\boldsymbol{x}}_{\mathrm{c.g.}}$ is the kinematic velocity of the centre of rotation (e.g. flexural axis, centre of gravity etc.) of the body and $\boldsymbol{r}$ is the displacement of $\boldsymbol{x}_P$ from $\boldsymbol{x}_{\mathrm{c.g.}}$.

4.3.4 Governing Equations of Unsteady Potential Flow

Defining a (total) potential Φ for irrotational flow such that along a path from an arbitrary distant point $\boldsymbol{x}_{P_\infty}$ to a field point $\boldsymbol{x}_P$

$$\Phi\left(\boldsymbol{x}_P\right) = \int_{P_\infty}^{P} u\,\mathrm{d}x + v\,\mathrm{d}y + w\,\mathrm{d}z, \tag{4.5}$$

the velocity $\boldsymbol{u}\left(\boldsymbol{x}_P\right) = \nabla\Phi\left(\boldsymbol{x}_P\right)$ and the potential equation

$$\nabla \cdot \rho \nabla \Phi = 0, \tag{4.6}$$

is obtained from the continuity equation, Eq. (1.2a). For incompressible flow this becomes Laplace's equation for the potential Φ:

$$\nabla^2 \Phi = 0. \tag{4.7}$$

For small perturbations write a scalar perturbation potential,

$$\phi = \Phi - \Phi_\infty, \tag{4.8}$$

where $\nabla\Phi = \boldsymbol{u}_\infty$ and thus the velocity field in the domain is calculated by the gradient of the velocity perturbation potential plus the freestream velocity,

$$\boldsymbol{u} = \nabla\Phi = \boldsymbol{u}_\infty + \nabla\phi. \tag{4.9}$$

Solutions to Laplace's equation are harmonic functions, and therefore they are can be linearly superposed.

4.3.4.1 Vorticity in the Domain

The definition of vorticity $\boldsymbol{\omega}$ is given in Eq. (2.1b) and a vector perturbation potential, $\boldsymbol{\Psi}$, can be introduced such that the velocity in the domain can be obtained by the curl of the vector potential field,

$$\boldsymbol{u} = \nabla \times \boldsymbol{\Psi}. \tag{4.10}$$

For a solenoidal vector potential field ($\nabla \cdot \boldsymbol{\Psi} = 0$, since the curl of the gradient of a divergence free vector field is zero), a vector Poisson equation is given by

$$\nabla^2 \boldsymbol{\Psi} = -\boldsymbol{\omega}, \tag{4.11}$$

and the vorticity can be written

$$\boldsymbol{\omega} = \nabla \times \boldsymbol{u} = \nabla \times (\nabla \times \boldsymbol{\Psi}). \tag{4.12}$$

The vector potential due to a volume distribution of vorticity in the domain Ω is given by

$$\boldsymbol{\Psi}\left(\boldsymbol{x}_P, t\right) = \frac{1}{4\pi} \int_{\Omega} \frac{\boldsymbol{\omega}}{\left|\boldsymbol{x}_P - \boldsymbol{x}\right|} \mathrm{d}V; \tag{4.13}$$

and taking the curl of $\boldsymbol{\Psi}$ gives the Biot-Savart law which defines the velocity induced by the distribution of vorticity in the domain,

$$\boldsymbol{u}\left(\boldsymbol{x}_P, t\right) = \nabla \times \boldsymbol{\Psi}\left(\boldsymbol{x}_P, t\right) = \nabla \times \frac{1}{4\pi} \int_{\Omega} \frac{\boldsymbol{\omega}}{\left|\boldsymbol{x}_P - \boldsymbol{x}\right|} \mathrm{d}V. \tag{4.14}$$

4.3.4.2 Pressure Relationship

Incompressible Navier-Stokes equations, Eq. (1.2b), reduce to the Euler equation as viscosity vanishes, and for irrotational flows the Euler equations can be integrated along a streamline, from a surface point into the far-field, to yield the unsteady Bernoulli equation,

$$\frac{\partial \phi}{\partial t} + \frac{p}{\rho} + \frac{|\boldsymbol{u}|^2}{2} + gz = \frac{p_\infty}{\rho} + \frac{\left|\boldsymbol{u}_\infty\right|^2}{2}. \tag{4.15}$$

4.3.5 Integral Equations

4.3.5.1 General Expression

The following section very briefly describes the mathematical framework for obtaining the potential at some point in a domain; the spatial gradients of which are the velocity. To begin with, note that the Laplacian is a linear differential operator and the properties of a particular isolated solution of the Laplacian is representative of all possible solutions of the Laplace equation. Assume the existence of a free-space Green's function solution for the Laplacian,

$$\nabla^2 G\left(\boldsymbol{x}, \boldsymbol{y}\right) = \delta(\boldsymbol{y} - \boldsymbol{x}), \tag{4.16}$$

where δ is the Dirac delta and the RHS is the expression for a point source of unit strength. Specify the Green's function as the fundamental solution to Eq. (4.16),

$$G\left(\boldsymbol{x}, \boldsymbol{y}\right) = -\frac{1}{\epsilon(\boldsymbol{x})} \cdot \frac{1}{r\left(\boldsymbol{x}, \boldsymbol{y}\right)}, \qquad r\left(\boldsymbol{x}, \boldsymbol{y}\right) = |\boldsymbol{r}| = \left|\boldsymbol{y} - \boldsymbol{x}\right|, \tag{4.17}$$

where $\boldsymbol{r}$ should be interpreted as the displacement of $\boldsymbol{y}$ from $\boldsymbol{x}$. The constant $\epsilon(\boldsymbol{x})$ is a result of volume (surface due to Gauss' theorem) integration of $\delta(\boldsymbol{y} - \boldsymbol{x})$ taken over a

sphere of vanishingly small radius centred on $\boldsymbol{x}$ and is given by

$$\epsilon(\boldsymbol{x}) = \begin{cases} 4\pi, & \boldsymbol{x} \in \Omega, \\ 2\pi, & \boldsymbol{x} \in \partial\Omega, \\ 0, & \boldsymbol{x} \text{ interior to } \partial\Omega. \end{cases} \tag{4.18}$$

The multiplier $\epsilon = 4\pi$ results from the entire spherical surface being considered; $\epsilon = 2\pi$ results from half the surface being occluded by the domain boundary $\partial\Omega$ e.g. on S_{B}. In two dimensions, these values are halved, since the surface is no longer a sphere but a circle.

Defining the potentials at two points the domain Ω as $\phi(\boldsymbol{x})$ and $\phi(\boldsymbol{y})$, Green's first identity for each of these two potentials is written

$$\int_{\Omega} \phi(\boldsymbol{x}) \nabla^2 \phi(\boldsymbol{y}) \, \mathrm{d}V = \int_{\partial\Omega} \left(\phi(\boldsymbol{x}) \left(\nabla\phi(\boldsymbol{y}) \cdot \mathrm{d}\boldsymbol{S} \right) \right) - \int_{\Omega} \nabla\phi(\boldsymbol{x}) \cdot \nabla\phi(\boldsymbol{y}) \, \mathrm{d}V, \tag{4.19a}$$

$$\int_{\Omega} \phi(\boldsymbol{y}) \nabla^2 \phi(\boldsymbol{x}) \, \mathrm{d}V = \int_{\partial\Omega} \left(\phi(\boldsymbol{y}) \left(\nabla\phi(\boldsymbol{x}) \cdot \mathrm{d}\boldsymbol{S} \right) \right) - \int_{\Omega} \nabla\phi(\boldsymbol{y}) \cdot \nabla\phi(\boldsymbol{x}) \, \mathrm{d}V. \tag{4.19b}$$

Subtracting Eq. (4.19a) from Eq. (4.19b) results in Green's second identity,

$$\int_{\Omega} \left(\phi(\boldsymbol{y}) \nabla^2 \phi(\boldsymbol{x}) - \phi(\boldsymbol{x}) \nabla^2 \phi(\boldsymbol{y}) \right) \mathrm{d}V = \int_{\partial\Omega} \left(\phi(\boldsymbol{y}) \nabla\phi(\boldsymbol{x}) - \phi(\boldsymbol{x}) \nabla\phi(\boldsymbol{y}) \right) \cdot \mathrm{d}\boldsymbol{S}, \tag{4.20}$$

which is a re-statement of Gauss' theorem, that the volume integral of the divergence of ϕ over the domain is obtained from the surface integral (of the flux) over the domain boundaries. Substitution of the Green's function G, which is dependant on both $\boldsymbol{x}$ and $\boldsymbol{y}$, for $\phi(\boldsymbol{x})$ gives

$$\begin{aligned} &\int_{\Omega} \left(\phi(\boldsymbol{y}) \delta(\boldsymbol{y} - \boldsymbol{x}) - G(\boldsymbol{x}, \boldsymbol{y}) \nabla^2 \phi(\boldsymbol{y}) \right) \mathrm{d}V = \\ &\int_{\partial\Omega} \left(\phi(\boldsymbol{y}) \nabla G(\boldsymbol{x}, \boldsymbol{y}) - G(\boldsymbol{x}, \boldsymbol{y}) \nabla\phi(\boldsymbol{y}) \right) \cdot \mathrm{d}\boldsymbol{S}. \end{aligned} \tag{4.21}$$

Noting that the Dirac delta function has the fundamental property

$$\int_{a-\varepsilon}^{a+\varepsilon} f(x) \delta(x - a) \, \mathrm{d}x = f(a) \text{for } \varepsilon > 0, \tag{4.22}$$

$\phi(\boldsymbol{x})$ is now a function of the distribution of distant potential $\phi(\boldsymbol{y})$. Recalling that Laplace's equation states $\nabla^2\phi = 0$, the perturbation potential at a point $\boldsymbol{x}$ can be written

$$\phi(\boldsymbol{x}) = \int_{\partial\Omega} \left(\phi(\boldsymbol{y}) \nabla G(\boldsymbol{x}, \boldsymbol{y}) - G(\boldsymbol{x}, \boldsymbol{y}) \nabla\phi(\boldsymbol{y}) \right) \cdot \mathrm{d}\boldsymbol{S}. \tag{4.23}$$

So, for a domain bounded by surfaces S_B and containing a wake sheet with surface S_W, $\phi(\boldsymbol{x})$ in the domain is dependant on both the distribution of potential on and the gradient of potential normal to the surfaces in and of the domain. Dropping the terms in parenthesis on the understanding that the integrals occur over remote points $\boldsymbol{y}$ and the Greens function is dependant on local field point $\boldsymbol{x}$ as well as the remote points, the potential due to a general, arbitrary surface is

$$\phi(\boldsymbol{x}) = \int_{\partial\Omega} \left[\phi_{\partial\Omega} \frac{\partial G}{\partial \boldsymbol{n}} - G \frac{\partial \phi_{\partial\Omega}}{\partial \boldsymbol{n}} \right] \mathrm{d}S. \tag{4.24}$$

Consider the general scenario whereby a submerged boundary exists with a given potential on either side of the surface as well as a given normal gradient on either side. This might occur if there were an "internal" potential within a solid body, see Fig. 4.2a for example, or perhaps either side of a wake surface, e.g. Fig. 4.2b. On the exterior and interior sides, denoted $(^+)$ and $(^-)$ respectively, the potential is $\phi^{+/-}$ and normal gradient $(\partial\phi/\partial\boldsymbol{n})^{+/-}$. On solid bodies $(\partial\phi/\partial\boldsymbol{n})$ is discontinuous, whereas on wakes it is continuous (since wakes cannot support a load). The influence of both sides of these surfaces is obtained by addition of Eq. (4.24) applied to each side, and therefore the boundary integral equation for ϕ can be expressed as

$$\phi(\boldsymbol{x}) = \int_{\partial\Omega} \left[\left(\phi^+ - \phi^-\right) \cdot \frac{\partial G}{\partial \boldsymbol{n}} - G \frac{\partial}{\partial \boldsymbol{n}} \left(\phi^+ - \phi^-\right) \right] \mathrm{d}S. \tag{4.25}$$

Defining a dipole strength μ as the difference between the external $(^+)$ and internal $(^-)$ potentials on a body surface, or the upper $(^+)$ and lower $(^-)$ wake potentials, and a source strength σ as the difference between the internal and external gradients in the direction of the normal,

$$-\mu = \phi^+ - \phi^- = \Delta\phi \tag{4.26a}$$

$$-\sigma = \frac{\partial \phi^+}{\partial n^+} - \frac{\partial \phi^-}{\partial n^-} = \frac{\partial \Delta\phi}{\partial n}, \tag{4.26b}$$

and substituting in the expression for the Green's function, Eq. (4.18), the boundary integral equation can be expressed in terms of these singularity strengths on body surfaces S_B and wake surfaces S_W:

$$\epsilon(\boldsymbol{x})\phi(\boldsymbol{x}) = \int_{S_B} \left[\mu \frac{\partial}{\partial \boldsymbol{n}} \left(\frac{1}{r}\right) - \sigma \frac{1}{r} \right] \mathrm{d}S + \int_{S_W} \mu \frac{\partial}{\partial \boldsymbol{n}} \left(\frac{1}{r}\right) \mathrm{d}S. \tag{4.27}$$

Eq. (4.27) is an expression for the potential at a field point in the domain or at a surface

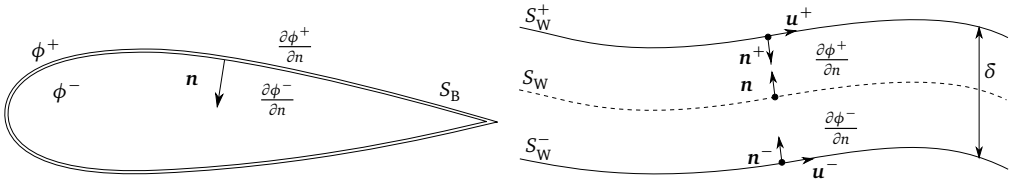

(a) Near a solid surface S_B **(b)** Near a wake surface S_W

Figure 4.2: Definitions of potential, velocity and normals. Solid boundaries (═), wake sheet (- - -) and displaced wake sheet (—)

point on the boundary of the domain due to the distribution of ϕ and $\partial\phi/\partial\boldsymbol{n}$ on the domain boundaries, expressed in terms of source and dipole distributions σ and μ. This is an expression for the solution of the boundary value problem, and what remains is to determine physically relevant values of ϕ and $\partial\phi/\partial\boldsymbol{n}$ under the constraints of the boundary conditions.

4.3.6 Boundary Conditions

The Laplace equation is an elliptical differential equation which results in a boundary-value problem. A wide variety of boundary conditions can be specified as follows. Normal mass flux can be specified directly by the Neumann condition

$$(\rho)\,\frac{\partial\phi}{\partial\boldsymbol{n}} = b_1. \tag{4.28}$$

The Dirichlet condition,

$$\phi = b_2, \tag{4.29}$$

simply specifies the potential directly. In the present work the discretised boundary surfaces (which approximate $\partial\Omega$) are denoted S, and grouped into three subsets:

1. body surfaces S_B which belong to bodies which are submerged in the flow and may generate lift;
2. wake surfaces S_W which belong to the wakes of lift generating bodies; and
3. far-field surfaces S_∞.

4.3.6.1 Solid Surfaces

On solid flow boundaries, for example the surface of e.g. submerged bodies, sea-beds or experimental facility walls, a kinematic boundary condition (KBC) is obtained by requiring zero flow normal to the body surface by setting b_1 to the local normal inflow velocity, i.e.

$$\text{KBC} \quad : \quad \frac{\partial\phi}{\partial n} = -(\boldsymbol{u}_0 - \boldsymbol{v}_k)\cdot\boldsymbol{n}. \tag{4.30}$$

This is the impermeability boundary condition, and $\boldsymbol{n}$ is the normal to surface S_B. This represents the most direct and physical boundary condition for a body surface.

4.3.6.2 Wake Surfaces

A body generating lift must shed a wake. In boundary-element methods, the wake is considered a continuous vortex sheet of zero thickness over which there is a jump discontinuity

in tangential velocity. The concentrated vorticity in these zero thickness surfaces allows circulation in an otherwise potential flow. There are two boundary conditions for the wake, a kinematic boundary condition (KBC) and a dynamic BC (DBC). The KBC states that the wake aligns itself with the velocity in the flow, that is the wake constitutes a streamline and as such there is no flow normal to the wake surface, although the wake surface at large is allowed to deflect by convection in a direction parallel to local wake surface normals. The DBC states that the wake evolves in a force-free manner, and therefore does not sustain a pressure difference between the upper and lower surfaces. To articulate these boundary conditions, the wake is notionally considered as having a constant, infinitesimal but nonzero thickness (say δ) and is thus composed of an upper and lower surface. The corresponding normals to these surfaces at a point on the actual wake surface are parallel to the wake normal, but they point from the displaced surfaces inwards towards the actual wake surface, and are equal and opposite. Since mass flux normal to the wake surface is disallowed – the kinematic boundary condition – the gradients of ϕ are equal and so δ is kept constant and the normals of the displaced surfaces $S_{\mathrm{W}}^{+/-}$ will remain parallel to those of the wake S_{W}.

The boundary conditions can be written for a point $\boldsymbol{x}_{\mathrm{wake}}$ on the wake surface as:

$$\mathrm{KBC}: \begin{cases} \boldsymbol{n} \cdot \Delta\left((\rho)\,\nabla\phi\right) & = 0 \qquad \therefore \\ \\ \boldsymbol{u}^{+}\left(\boldsymbol{x}_{\mathrm{wake}}\right) \cdot \boldsymbol{n}^{+} & = \boldsymbol{u}^{-}\left(\boldsymbol{x}_{\mathrm{wake}}\right) \cdot \boldsymbol{n}^{-} = \tilde{\boldsymbol{u}}\left(\boldsymbol{x}_{\mathrm{wake}}\right) \cdot \boldsymbol{n}; \end{cases} \tag{4.31a}$$

$$\mathrm{DBC}: p^{+}\left(\boldsymbol{x}_{\mathrm{wake}}\right) - p^{-}\left(\boldsymbol{x}_{\mathrm{wake}}\right) = \Delta p = 0; \tag{4.31b}$$

where Δ denotes a jump across the sheet, +/- denotes an evaluation of superscripted quantity an infinitesimally small distance from the surface in the +/- direction of the normal, and $\tilde{\boldsymbol{u}} = \frac{1}{2} \cdot (\boldsymbol{u}^{+} + \boldsymbol{u}^{-})$ is the arithmetic mean of the +/- velocities and is taken as the velocity of the point $\boldsymbol{x}_{\mathrm{wake}}$ on the sheet. (In theory, velocity at a point whose displacement is zero from a vortex sheet will be infinite due to the singularity in the Biot-Savart law). By applying the Bernoulli equation (Eq. 4.42) to each side of the sheet,

$$\frac{\partial \phi^{+}}{\partial t} + \frac{1}{2}\left|\boldsymbol{u}^{+}\right|^{2} + \frac{p^{+}}{\rho} = \frac{\partial \phi^{-}}{\partial t} + \frac{1}{2}\left|\boldsymbol{u}^{-}\right|^{2} + \frac{p^{-}}{\rho}, \tag{4.32}$$

then subtracting the RHS of Eq. (4.32) from the LHS,

$$\frac{\partial\left(\Delta\phi\right)}{\partial t} + \frac{\Delta p}{\rho} + \tilde{\boldsymbol{u}} \cdot \Delta \boldsymbol{u} = 0. \tag{4.33}$$

Recalling that $\boldsymbol{u}^{\pm} = \nabla\phi^{\pm}$ and applying the DBC, Eq. (4.33) can be simplified and written as the continuity equation for the wake sheet:

$$\frac{\partial\left(\Delta\phi\right)}{\partial t} + \tilde{\boldsymbol{u}} \cdot \nabla\left(\Delta\phi\right) \equiv \frac{\partial\mu}{\partial t} + \tilde{\boldsymbol{u}} \cdot \nabla\mu = 0. \tag{4.34}$$

In other words, the LHS of Eq. (4.34) can be written in terms of a dipole strength μ.

If the wake is in an equilibrium location (the DBC is satisfied) then there will be no normal velocity moving the wake surface, and the wake evolution equation can be re-written:

$$\frac{\partial\Delta\phi}{\partial t} + \boldsymbol{u} \cdot \nabla\left(\Delta\phi\right) = \frac{\partial\Delta\phi}{\partial t} + \boldsymbol{u} \cdot \boldsymbol{\tau}\frac{\partial\Delta\phi}{\partial\boldsymbol{\tau}} = 0 \tag{4.35}$$

Although the wake does indeed convect according to the velocity field, in actuality it convects along the instantaneous stream-surface which it defines itself, by the KBC and DBC. The advantage of this expression is that it is now obvious how the wake is connected to the shedding boundary surface, both in terms of BCs there, and also initial conditions – in other words if the strength is determined via $\Delta\phi_0$ and the position evolves along the separation streamline from the surface, then $\Delta\phi_0$ must be related to the trailing edge ϕ on the upper and lower surface, or rather equal to the section circulation, i.e. $-\Gamma = \Delta\phi_{\text{T.E.}}$, and the streamline evolves along the wake from the shedding surface.

4.3.6.3 Far-field Conditions

The disturbance due to the body and wake should decay far from the source of the disturbance:

$$|\boldsymbol{x}| \to \infty,\ \boldsymbol{u} \to \boldsymbol{u}_{\infty} \text{ and } \nabla\phi \to 0, \tag{4.36}$$

or equivalently:

$$\lim_{r\to\infty}\left(\nabla\phi - \boldsymbol{u}\right) = 0. \tag{4.37}$$

Similarly, when calculating the influence of the far-field, if the fluid is stationary, ϕ_{∞} is constant and $\nabla\phi = 0$ when calculating velocities, or indeed influences via Eq. (4.25).

4.3.6.4 The Morino Formulation

The method proposed herein uses the so-called Morino formulation for the boundary conditions (Morino and Kuo, 1974). A closed wetted body, considered as a boundary surface, divides the domain into "external" and an "internal" domains. Following the previous nomenclature, the wetted, external surface of the body is denoted $(+)$, and the unwetted internal surface $(-)$. The Morino formulation sets the perturbation potential in the internal domain uniformly equal to zero and then arrives at boundary conditions necessary to

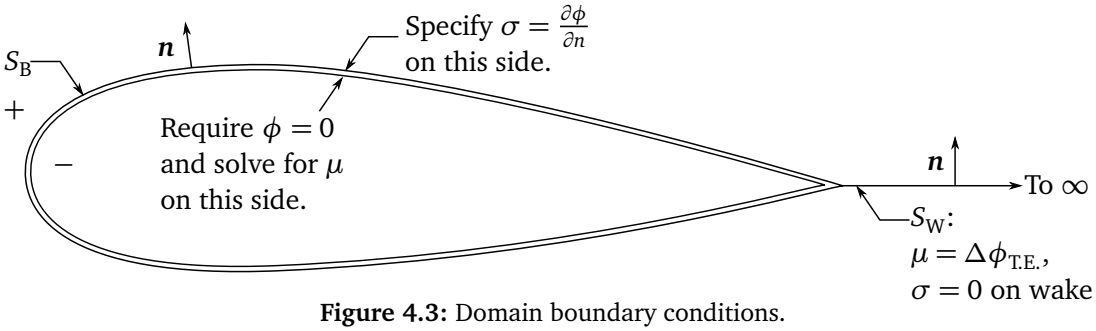

Figure 4.3: Domain boundary conditions.

adequately enforce e.g. the impermeability condition. To do this, the Morino formulation sets the source strength equal to the incident normal velocity, completely specifying the internal and external boundary conditions

$$\phi^- = 0 \tag{4.38a}$$

$$\sigma = \boldsymbol{u}_0^+ \cdot \boldsymbol{n}. \tag{4.38b}$$

(Recall the expression for the source strength [Eq. 4.26b], and note that the gradients of the zero internal potential are uniformly zero, i.e.

$$\frac{\partial \phi^-}{\partial n^-} = 0 \quad \text{therefore} \quad \sigma = -\frac{\partial \phi^+}{\partial n^+} = -\boldsymbol{u}'^+ \cdot \boldsymbol{n}. \tag{4.39}$$

Next, substitute into the external boundary condition the definition of the incident velocity, rewritten $\boldsymbol{u}' = \boldsymbol{u} - \boldsymbol{u}_0$, recovering

$$\sigma = \boldsymbol{u}_0 \cdot \boldsymbol{n} = -\boldsymbol{u}'^+ \cdot \boldsymbol{n} = \boldsymbol{u} - \boldsymbol{u}_0, \tag{4.40}$$

and so for zero resultant normal flow set $\sigma = \boldsymbol{u}_0^+ \cdot \boldsymbol{n}$.)

To use this method requires the application of the internal boundary condition. Since applying a distribution of sources over the surface of the body will (almost always) result in a nonzero internal potential, the Morino formulation (Morino and Kuo, 1974) uses a distribution of dipoles to correct the error due to the sources. In a practical method, the body surface is discretised into panels, and each panel has a source distribution placed on it according to the boundary conditions. Instead of sampling the internal potential throughout the body, a practical method samples it at the collocation point at each panel centroid to arrive at an approximation to the internal potential. Since the source strengths are known, it is possible to calculate the error in perturbation potential at each panel collocation point due to all other panels. Following Katz and Plotkin (2001) and writing an influence matrix of coefficients for the influence in ϕ at each panel collocation point due to a unit dipole on every panel, a system of linear algebraic equations can be obtained to calculate the unknown dipole strengths. Solving this removes the ϕ error at each panel. Since the normal gradient of a dipole distribution perturbation potential is zero, the dipole cancels out the source perturbation potential error without inducing an erroneous normal velocity.

4.3.7 Velocity, Pressure and Force Calculations

4.3.7.1 Velocity and Pressure

If the velocity potential ϕ is known at some field point $\boldsymbol{x}$, the fluid perturbation velocity at this point is obtained by taking $\nabla\phi$. If this point is on the surface of a body, gradients of the surface distribution of ϕ can be taken along local surface coordinates ζ and η to obtain the tangential flow velocities, or alternatively $\partial\phi/\partial n$ gives the velocity component normal to the surface (if present). Tangential velocities are combined in local axis with inflow velocities due to the influence of the freestream, wake and body kinematics such that:

$$\boldsymbol{u} = \left[\boldsymbol{u}_0 - \left(\dot{\boldsymbol{x}}_{\text{c.g.}} + \boldsymbol{\Omega} \times \left(\boldsymbol{x} - \boldsymbol{x}_{\text{c.g.}}\right)\right)\right] \cdot \begin{bmatrix} \zeta \\ \eta \\ n \end{bmatrix} + \begin{bmatrix} \frac{\partial\phi}{\partial\zeta} \\ \frac{\partial\phi}{\partial\eta} \\ \frac{\partial\phi}{\partial n} \end{bmatrix}. \tag{4.41}$$

Defining a reference velocity magnitude – such as that of the freestream velocity if the body is static, or the freestream plus kinematic terms if the device is in motion – the surface pressure coefficient distribution is written as a result of the Bernoulli equation,

$$C_p = 1 - \frac{1}{u_{\text{ref}}^2}\left(|\boldsymbol{u}|^2 - 2\frac{\partial\phi}{\partial t}\right). \tag{4.42}$$

4.3.7.2 Forces and Hydrodynamic Coefficients

Hydrodynamic forces and moments can be obtained by the integration of the pressure distribution over the surface of the submerged bodies. Force is calculated along the outward pointing normal of the body surface, while moments of this force are taken with respect to the axis of some convenient co-ordinate system

$$\boldsymbol{F} = \int_S p\boldsymbol{n}\,\mathrm{d}S \quad \text{and} \quad \boldsymbol{M} = \int_S p\boldsymbol{n} \times \boldsymbol{x}\,\mathrm{d}S. \tag{4.43}$$

The components of forces and moments on hydrodynamic bodies are traditionally non-dimensionalised into coefficient form using the force acting on some reference area (at a reference displacement for moments) due to the freestream pressure resulting from the freestream velocity magnitude u_∞,

$$C_{[x,y,z]} = \frac{F_{[x,y,z]}}{\frac{1}{2}\rho u_\infty^2 S} \quad \text{and} \quad C_{[m,n,q]} = \frac{M_{[x,y,z]}}{\frac{1}{2}\rho u_\infty^2 \left[x,y,z\right] S}. \tag{4.44}$$

For two-dimensional cases, the dimension z, force F_z and thus moments M_x and M_y and their corresponding coefficients do not exist. Also, the area S degenerates into a length. In

the three-dimensional case of a wing or hydrofoil-like body, the area S is the planform area (area projected onto a plane) of the wing and it is traditional to resolve the forces into lift and drag directions orthogonal to the nominal inflow velocity vector using the aerodynamic angles α for pitch. The lift and drag forces and their corresponding coefficients are

$$L = F_y \cos\alpha + F_x \sin\alpha \qquad \text{and} \qquad D = F_y \sin\alpha - F_x \cos\alpha \tag{4.45}$$

$$C_L = \frac{L}{\frac{1}{2}\rho u_\infty^2 S} \qquad \text{and} \qquad C_D = \frac{D}{\frac{1}{2}\rho u_\infty^2 S}. \tag{4.46}$$

Traditionally, when dealing with two-dimensional sectional forces and coefficients, the subscripts are written in lower-case e.g. C_l, C_d and C_m. There are also other conventions at work when dealing with e.g. cross-flow turbine blade coefficients in two dimensions, and these will be adopted on an ad hoc basis and are the blade element forces normal and tangential to the path of motion of the turbine blade (in Section 6.3.6).

In the case of turbines it is traditional to use the following performance metrics: power coefficient, thrust coefficient and tip-speed ratio; respectively

$$C_P = \frac{P}{\frac{1}{2}\rho u_\infty^3 S}, \qquad C_T = \frac{T}{\frac{1}{2}\rho u_\infty^2 S} \qquad \text{and} \qquad \lambda = \frac{\Omega R}{u_\infty}. \tag{4.47}$$

Power is non-dimensionalised by the available hydraulic power through a reference area, S, equivalent to that of the rotor. Thrust is non-dimensionalised by the hydrodynamic (rather than hydrostatic) pressure force acting over a surface equivalent to that of the rotor. In the case of an axial flow turbine, power is calculated using the torque about the axis of rotation, as obtained using Eq. (4.43), multiplied by the angular frequency. For a cross-flow turbine, the shaft torque also includes a component due to the transmission of the aerofoil pitching moment about the point of attachment along a notional "arm" of the rotor.

4.3.7.3 Unsteady Flow Considerations

Due to the Kutta condition and also the implications of conservation of angular momentum in Helmholtz's theorem, whenever the circulation on the blade changes so too must the wake. Given that the circulation on the blade results in the velocity distribution on the surface, there will also be some time dependency in the evolution of the surface velocity, and hence force on the surface. This gives rise to a local $\partial\gamma/\partial t$ term, which corresponds to the time derivative of the potential in the unsteady Bernoulli equation.

4.4 General Implementation

This section concerns the practical implementation of the governing equations described above. Preceding sections described a boundary value problem for the solution of the Laplace equation for flow about lifting and non-lifting bodies, and this section focusses on the the boundary surface distribution of ϕ so as to arrive at a practical approximation of this solution. Steps involved in this process are:

1. discretisation of body surfaces S_B and wake surfaces S_W into a computationally tractable form;

2. determination of the (unknown) boundary values of ϕ due to the boundary conditions; and

3. calculation of velocities and pressures in the domain/on body surfaces.

To accomplish Item 1, all surfaces present in the computation are subdivided into panels or elements. In the present method, these are taken as flat sub-surfaces, defined by their corner points: two in two dimensions, three or four in three dimensions. In three dimensions, panels are bounded by straight lines between their defining corners, and the surface bounded by these sides is an approximation of the actual surface of interest. Through the use of triangular elements, all surfaces are ensured completely gap-free.

Item 2 requires obtaining numerically the values of ϕ on the boundary surfaces. Laplace's equation is linear, and a solution can be obtained by superposition. This allows the solution ϕ at the centroid of one of the panels to be defined as the linear sum of the influence of all of the sub-panels on bodies and wakes. To each body panel is attached a distribution of sources, and if the panel is part of a lift generating body, a distribution of dipoles is also attached in order to generate a circulation. (Actually, in the proposed method all panels have both a source and a dipole distribution attached to them, even if $\mu = 0$. This is because without specifying the interior potential at all panels the problem would be ill posed and the coefficient matrix would be singular.) A distribution of dipoles is attached to each wake panel. The resulting potential at panel i can then be written

$$\phi_i = \sum_j^{n_\mathrm{body}} a_{i,j}\mu_j + \sum_k^{n_\mathrm{body}} b_{i,k}\sigma_k + \sum_l^{n_\mathrm{wake}} c_{i,l}\mu_l. \tag{4.48}$$

These equations are written for all panels with unknown ϕ – the body surface panels, since for wake surface panels $\Delta\phi$ is fixed when they are created – resulting in a linear system of equations for the unknowns ϕ_j and $\Delta\phi_k$. In the method implemented in this thesis,

the source values are set to the incident velocity, and thus $\boldsymbol{\sigma}$ is known. The body dipole strengths are then sought by solving the following system of equations:

$$\mathbf{A}\boldsymbol{\mu}_{\text{body}} = -\left(\mathbf{B}\boldsymbol{\sigma}_{\text{body}} + \mathbf{C}\boldsymbol{\mu}_{\text{wake}}\right). \tag{4.49}$$

Once Eq. (4.49) has been solved for the panel singularity strengths, the velocities and thus pressures and forces throughout the domain and on its surfaces can be calculated.

4.4.1 Two-Dimensional Panel Geometry and Velocity Calculation

A point generating a Newton potential of unit strength located at the origin of an arbitrary axis system $O_{x'y'}$ induces the following potential at some field point $\boldsymbol{x}_P$:

$$\phi_{\text{Newton}}\left(\boldsymbol{x}_P\right) = -\frac{\log\left(|\boldsymbol{x}'_P|^2 + \delta^2\right)}{4\pi}, \tag{4.50}$$

which is de-singularised with a smoothing parameter δ. The velocity due to a point vortex of strength $\boldsymbol{\Gamma} = \left[0, 0, \gamma\right]^T$, located at the same origin and calculated at the position $\boldsymbol{x}_P$ of some distant point P is equal in magnitude to, and tangential in direction to the gradient of the Newton potential field, yielding a modified form of the Biot-Savart law. Denoting the smoothed Biot-Savart kernel $\boldsymbol{K}_\delta = \nabla\phi_{\text{Newton}}\left(\boldsymbol{x}_P\right)$ the velocity is given by

$$\boldsymbol{u}'\left(\boldsymbol{x}_P\right) = \boldsymbol{K}_\delta \times \boldsymbol{\Gamma}, \tag{4.51a}$$

$$u'\left(\boldsymbol{x}'_P\right) = -\frac{\gamma}{2\pi} \cdot \frac{y'_P}{\left(|\boldsymbol{x}'_P|^2 + \delta^2\right)}, \tag{4.51b}$$

$$v'\left(\boldsymbol{x}'_P\right) = \frac{\gamma}{2\pi} \cdot \frac{x'_P}{\left(|\boldsymbol{x}'_P|^2 + \delta^2\right)}. \tag{4.51c}$$

For a linear strength vortex distribution along a panel lying on the x'-axis where the vortex strength is given by

$$\gamma\left(x'\right) = \gamma_1 + \frac{\partial\gamma}{\partial x'}\left(x' - x'_1\right), \tag{4.52}$$

the velocity at some distant point $\boldsymbol{x}'_P$ can be calculated using the integral of the Biot-Savart law along the panel,

$$u'\left(x'_P, y'_P\right) = \frac{1}{2\pi}\int_{x'_1}^{x'_2}\left(\gamma_1 + x'\frac{\partial\gamma}{\partial x'}\right) \cdot \frac{y'_P}{\left(x'_P - x'\right)^2 + y'^2_P}\,\mathrm{d}x', \tag{4.53a}$$

$$v'\left(x'_P, y'_P\right) = -\frac{1}{2\pi}\int_{x'_1}^{x'_2}\left(\gamma_1 + x'\frac{\partial\gamma}{\partial x'}\right) \cdot \frac{\left(x'_P - x'\right)}{\left(x'_P - x'\right)^2 + y'^2_P}\,\mathrm{d}x'. \tag{4.53b}$$

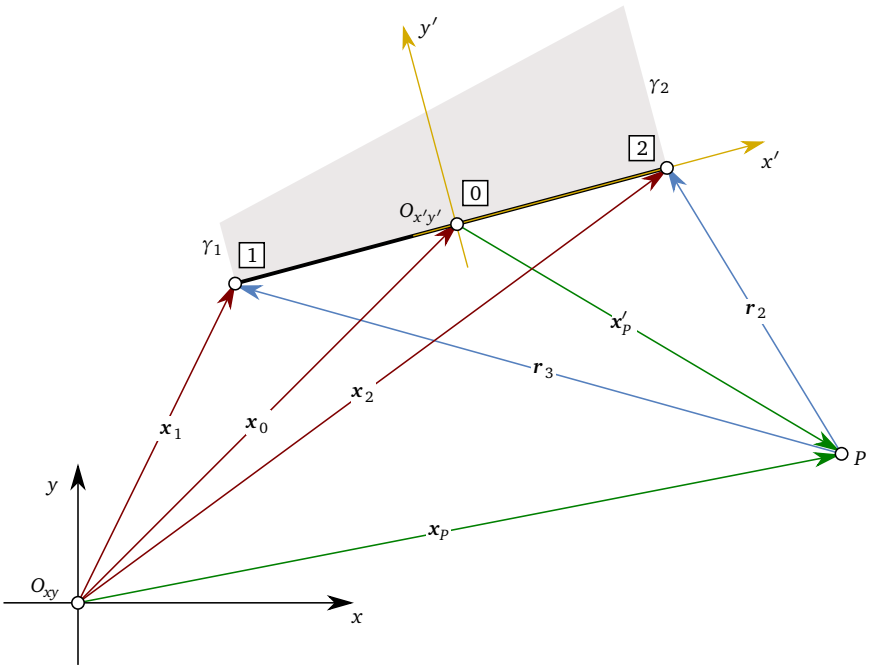

Figure 4.4: Straight line boundary-element geometry, including description of singularity distribution.

All evaluations are considered in local panel coordinates, and the meaning of the terms is illustrated in Fig. 4.4. Analytical expressions for the integrals have been made available by many authors, e.g. Johnston (1980) and Katz and Plotkin (2001), and can be calculated analytically by hand or using a computer symbolic mathematics tool (e.g. MATHEMATICA).

4.4.2 Three-Dimensional Panel Geometry and Potential Calculation

A source distribution of unit strength induces the following perturbation potential at $\boldsymbol{x}$:

$$\phi(\boldsymbol{x}) = -\frac{1}{2\pi}\int_{\partial S}\frac{1}{r}\,\mathrm{d}S_y, \tag{4.54}$$

and the perturbation potential induced by a surface distribution of dipoles of unit strength is given by

$$\phi(\boldsymbol{x}) = -\frac{1}{2\pi}\int_{\partial S}\frac{\partial}{\partial n_y}\,\mathrm{d}S_y = \frac{1}{2\pi}\int_{\partial S}\frac{\boldsymbol{n}\cdot\boldsymbol{r}}{r^3}\,\mathrm{d}S_y. \tag{4.55}$$

Again, analytical expressions for the integrals have been made available by many authors e.g. Johnston (1980) and Katz and Plotkin (2001).

4.4.2.1 Quadrilateral Panel Boundary-Element

Following Vaz (2005), consider a general flat panel in three dimensions – illustrated in Fig. 4.5 – whose corners $i = 1,\ldots,4$ are located at $\boldsymbol{x}_i$ and whose centroid is located at $\boldsymbol{x}_0$. Define a local coordinate system (ξ,η,n). The centroid of the panel is given by:

$$\boldsymbol{x}_0 = \frac{1}{4}\left[\boldsymbol{x}_1+\boldsymbol{x}_2+\boldsymbol{x}_3+\boldsymbol{x}_4\right]. \tag{4.56}$$

The local coordinate system is defined by the local tangent vectors and the normal,

$$\xi = \frac{\frac{1}{2}(\boldsymbol{x}_2+\boldsymbol{x}_3)-\boldsymbol{x}_0}{\left|\frac{1}{2}(\boldsymbol{x}_2+\boldsymbol{x}_3)-\boldsymbol{x}_0\right|},\ \boldsymbol{\eta} = \frac{\frac{1}{2}(\boldsymbol{x}_3+\boldsymbol{x}_4)-\boldsymbol{x}_0}{\left|\frac{1}{2}(\boldsymbol{x}_3+\boldsymbol{x}_4)-\boldsymbol{x}_0\right|}\ \text{and}\ \boldsymbol{n} = \frac{\xi\times\boldsymbol{\eta}}{\left|\xi\times\boldsymbol{\eta}\right|}, \tag{4.57}$$

which allows a transformation matrix and Jacobian such that the field point $\boldsymbol{x}_P$ may be rendered into and quadrature may be performed in local panel coordinates. Of use later is the area of the panel, given by

$$\Delta S = \frac{1}{2}\left|(\boldsymbol{x}_3-\boldsymbol{x}_1)\times(\boldsymbol{x}_4-\boldsymbol{x}_2)\right|. \tag{4.58}$$

Expressions for Eq. (4.54) and Eq. (4.55) can be established in local panel coordinates. The potential at a field point $\boldsymbol{x}_P$ due to a distribution of constant unit strength dipoles over

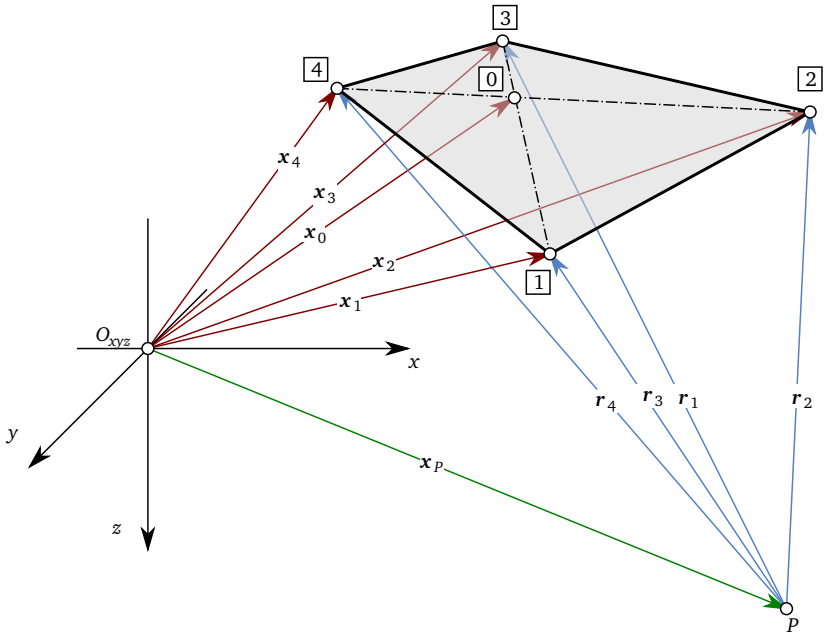

Figure 4.5: Quadrilateral boundary-element geometry.

the panel surface is given by

$$\phi_\mu(\boldsymbol{x}) = \int_{\Delta S} \frac{\partial}{\partial n}\left(\frac{1}{r(\boldsymbol{x},\boldsymbol{x}')}\right) \mathrm{d}S'. \tag{4.59}$$

The analytical expression of Eq. (4.59) is obtained in Johnston (1980):

$$\phi_\mu(\boldsymbol{x}) = \frac{1}{2\pi}\left(\theta_1 - \theta_2 + \theta_3 - \theta_4\right), \tag{4.60}$$

where the term in brackets is the contribution of the corner points to the solid angle subtended by the panel at point $\boldsymbol{x}$ projected onto the plane of the panel, calculated such that

$$\tan\theta_i = \frac{r_i \boldsymbol{r}_i \cdot \left(\boldsymbol{\xi}_i \times \boldsymbol{\eta}_i\right)}{\left(\boldsymbol{r}_i \times \boldsymbol{\xi}_i\right)\cdot\left(\boldsymbol{r}_i \times \boldsymbol{\eta}_i\right)}, \text{ where } -\pi \leq \theta \leq \pi. \tag{4.61}$$

When calculating θ, the intrinsic C++ function `atan2` is used, which naturally returns θ as the principal value in the range $(-\pi, \pi]$.

The potential at a field point $\boldsymbol{x}_P$ due to a distribution of constant unit strength sources over the panel surface is given by

$$\phi_\sigma(\boldsymbol{x}) = \int_{\Delta S} \frac{1}{r(\boldsymbol{x},\boldsymbol{x}')}\,\mathrm{d}S'. \tag{4.62}$$

The analytical expression of Eq. (4.62) is given according to Hess and Smith (1964) and Johnston (1980) as

$$\phi_\sigma(\boldsymbol{x}) = -\frac{1}{2\pi}\sum_i^4 \left[\frac{\boldsymbol{n}}{|\boldsymbol{d}_i|}\cdot\left(\boldsymbol{r}_i \times \boldsymbol{d}_i\right)\ln\left(\frac{|\boldsymbol{r}_i| + |\boldsymbol{r}_{i+1}| + 2|\boldsymbol{d}_i|}{|\boldsymbol{r}_i| + |\boldsymbol{r}_{i+1}| - 2|\boldsymbol{d}_i|}\right)\right] + (\boldsymbol{r_0}\cdot\boldsymbol{n})\,\phi_\mu(\boldsymbol{x}), \tag{4.63}$$

where the term in square brackets is the contribution of the corner points, $\boldsymbol{d}_i = \boldsymbol{x}_{i+1} - \boldsymbol{x}_i$, and the cyclic convention is applied.

Eq. (4.60) is only strictly correct for flat panels – quadrilateral panels are flat whereas a general panel may be twisted. In this circumstance there exist two options: split the panel into two or four triangular sub-panels, or define a more general hyperboloidal panel geometry. This work only considers the triangular panel.

4.4.2.2 Triangular Panel Boundary-Element

Triangular panels are always flat. Eq. (4.60) and Eq. (4.63) can be recycled for a triangular element simply by omission of the contribution of one of the corners. Consider a triangular panel in three dimensions – illustrated in Section 4.5 – whose corners $i = 1, 2, 3$ are located at $\boldsymbol{x}_i$ and whose centroid is located at $\boldsymbol{x}_0$. Again, defining a local coordinate system

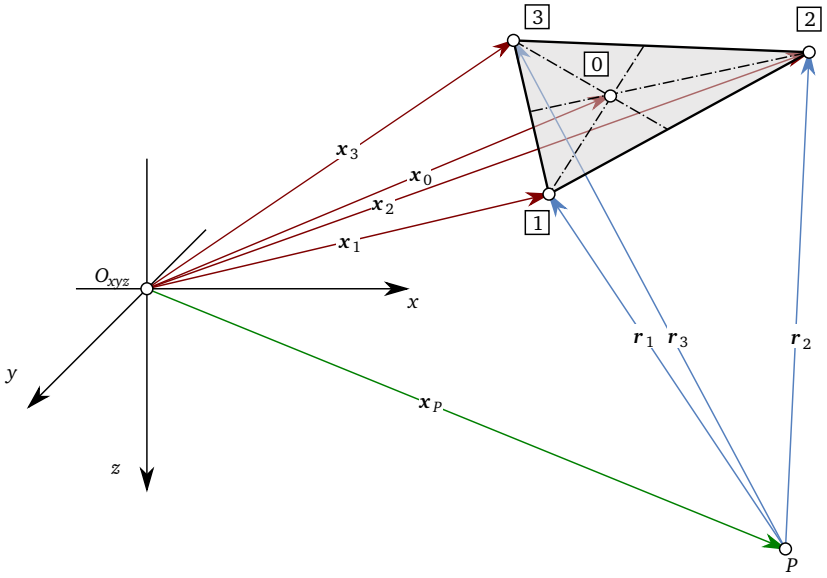

Figure 4.6: Triangular boundary-element geometry.

(ξ, η, n). The centroid of the panel is given by

$$\boldsymbol{x}_0 = \frac{1}{3}\left[\boldsymbol{x}_1 + \boldsymbol{x}_2 + \boldsymbol{x}_3\right]. \tag{4.64}$$

The potential at a field point $\boldsymbol{x}_P$ due to a distribution of constant unit strength dipoles over the triangular panel surface is given by

$$\phi_\mu(\boldsymbol{x}) = \frac{1}{2\pi}\left(\theta_1 - \theta_2 + \theta_3\right). \tag{4.65}$$

The corresponding expression for the potential induced by a constant unit strength distribution of sources over the triangular element is

$$\phi_\sigma(\boldsymbol{x}) = -\frac{1}{2\pi}\sum_i^3 \left[\frac{\boldsymbol{n}}{|\boldsymbol{d}_i|}\cdot(\boldsymbol{r}_i \times \boldsymbol{d}_i)\ln\left(\frac{|\boldsymbol{r}_i| + |\boldsymbol{r}_{i+1}| + 2|\boldsymbol{d}_i|}{|\boldsymbol{r}_i| + |\boldsymbol{r}_{i+1}| - 2|\boldsymbol{d}_i|}\right)\right] + (\boldsymbol{r_0}\cdot\boldsymbol{n})\,\phi_\mu(\boldsymbol{x}), \tag{4.66}$$

again observing the cyclic convention.

4.4.2.3 Far-field Evaluation

When the field point lies some considerable distance from the panel, it is often expedient in terms of calculation efficiency and accuracy to use an approximation of the panel based on a point singularity. The choice of distance at which the approximation is utilised is entirely arbitrary, however, Katz and Plotkin (2001) suggests $|\boldsymbol{r}_0|$ greater than 3-5 times the maximum diagonal of the panel, and Baltazar and Falcão de Campos (2008) follows Vaz (2005), using a far-field approximation for $|\boldsymbol{r}_0|$ greater than 6.5 times the maximum diagonal. In the present method, a means of obtaining a representative panel length is $h_{\text{equiv.}} = \sqrt{\text{area}}$, as given by Topper (2010). This is used to compensate for panels which may be somewhat skewed. A far-field approximation is employed when the target is greater than 7 times $h_{\text{equiv.}}$ from the sphere of radius half the maximum diagonal centred on the panel centroid. See also Section 5.2.4 for discussion on implementation in the FVM.

The potential due to a panel represented by a point source of unit strength is given by

$$\phi_\sigma(\boldsymbol{x}) = -\frac{\Delta S}{4\pi}\cdot\frac{1}{|\boldsymbol{r}_0|}, \tag{4.67}$$

and the potential due to a panel represented by point dipole of unit strength is given by

$$\phi_\mu(\boldsymbol{x}) = -\frac{\Delta S}{4\pi}\cdot\frac{\boldsymbol{n}\cdot\boldsymbol{r}_0}{|\boldsymbol{r}_0|^3}. \tag{4.68}$$

The panel area ΔS is calculated using Eq. (4.58).

4.5 Conclusions

General Remarks and Recap This chapter has presented a framework for the modelling of fluid flow around hydrodynamic bodies using a boundary-element method. The first part presented a brief survey of developments leading to the BEM employed in the method proposed herein. The major advantages of a BEM include the ability to model lifting bodies using methods which are both computationally unintensive and relatively insensitive to meshing quality by comparison with CFD. This is achieved by reducing the problem to a purely boundary-value problem rather than modelling it in an Eulerian manner. Low-order methods based on a Morino formulation are established as delivering robust models in the with low sensitivity to mesh quality and specification of boundary conditions. This is compromised in part by a requirement to use low-order panels which contain no intrinsic information on the surface distribution of potential above a first-order approximation. The principal advantage of the somewhat indirect Morino formulation – which specifies the perturbation potential rather than the velocity as in the traditional earlier methods – is that the number of unknowns is reduced from three velocity components to simply the perturbation potential. The simplified potential flow equations were examined for applicability to the modelling problem, and a theoretical basis for the model was described. Finally, the implementation of the boundary-element method was described.

Impacts on this Thesis The theoretical underpinnings of the boundary-element component of the method proposed in this thesis were presented. The expressions for the influence coefficients of the BEM linear algebra have been given, and the system of equations stated. Using this method, a body surface may be approximated using quad/triangular panels, and given a velocity inflow, the surface distribution of ϕ established. This is achieved by locally specifying no-through flow boundary conditions at each panel using a distribution of sources, and then solving for a distribution of dipoles to "correct" this by solving for zero internal ϕ. Once the surface distribution of dipoles is known, the surface velocity is given by $\nabla\phi \equiv \nabla\mu$ and the pressures can be calculated. The loads on a device may be calculated by this method.

To arrive at a unique solution to the linear algebra, a wake patch is generated in order to satisfy the Kelvin and Helmholtz theorems. The dipole panels are equivalent to vortex panels of the same strength but reduced order – i.e. instead of a constant distribution of vorticity over the panel, it is concentrated around the panel's periphery in filaments. These filaments are then converted into blobs and used as input to the finite-volume mesh.

References

Baltazar, J. (2008). *On The Modelling Of The Potential Flow About Wings And Marine Propellers Using A Boundary Element Methods*. Ph.D. thesis, Universidade Técnica De Lisboa Instituto Superior Técnico, Lisbon, Portugal.

Baltazar, J. and Falcão de Campos, J.A.C. (2011). "Hydrodynamic analysis of a horizontal axis marine current turbine with a boundary element method." *Journal of Offshore Mechanics and Arctic Engineering*, **133**(4).

Baltazar, J. and Falcão de Campos, J. (2008). "Hydrodynamic analysis of a horizontal axis marine current turbine with a boundary element method." In "Proceedings of the ASME 27th International Conference on Offshore Mechanics and Arctic Engineering," Estoril, Portugal.

Bertram, V. (2011). *Practical Ship Hydrodynamics*. Butterworth-Heinemann, 2nd edn.

Brown, R. and Line, A.J. (2005). "Efficient high-resolution wake modeling using the vorticity transport equations." *AIAA Journal*, **43**(7): pp. 1434–1443.

Cottet, G. and Koumoutsakos, P. (2000). *Vortex methods: theory and practice*. Cambridge University Press.

Dixon, K., Simao Ferreira, C., Hofemann, C., Van Bussel, G. and Van Kuik, G. (2008). "A 3D unsteady panel method for vertical axis wind turbines." In "Proceedings of the European Wind Energy Conference & Exhibition (EWEC2008)," .

Gennaretti, M. and Bernardini, G. (2007). "Novel Boundary Integral Formulation for Blade Vortex Interaction Aerodynamics of Helicopter Rotors." *AIAA Journal*, **45**: pp. 1169–1176.

Gharakhani, A., Sitaraman, J. and Stock, M.J. (2005). "A Lagrangian vortex method for simulating flow over 3-D objects." In "Proceedings of the 2005 ASME Fluids Engineering Division Summer Meeting and Exhibition (ASME FEDSM2005)," Houston, TX, US.

Gharakhani, A. and Stock, M.J. (2005). "3D vortex simulation of flow over a circular disk at an angle of attack." In "Proceedings of the 17th AIAA Computational Fluid Dynamics Conference," Toronto, Ontario Canada.

Hess, J. (1972). "Calculation of potential flow about arbitrary three-dimensional lifting bodies." Tech. rep., Douglas Aircraft Company, Long Beach, CA.

Hess, J. and Smith, A. (1964). "Calculation of nonlifting potential flow about arbitrary three dimensional bodies." *Journal of Ship Research*, **8**(2): pp. 22–44.

Hoeijmakers, H. (1992). "Panel methods for aerodynamic analysis and design." In "AGARD-R-783 - Special Course on Engineering Methods in Aerodynamic Analysis and Design of Aircraft," NATO Research and Technology Organisation.

Hoshino, T. (1993). "Hydrodynamic analysis of propellers in unsteady flow using a surface panel method." *Journal of the Society of Naval Architects of Japan*, (174): pp. 71–87.

Hsin, C.Y. (1990). *Development and analysis of panel methods for propellers in unsteady flow*. Ph.D. thesis, Massachusetts Institute of Technology. Dept. of Ocean Engineering.

Jensen, G. (1988). "Berechnung der stationären Potentialströmung um ein Schiff unter Berücksichtigung der nichtlinearen Randbedingung an der freien Wasseroberfläche." Tech. Rep. IfS-Report 484, University of Hamburg.

Johnson, F.T., Tinoco, E.N. and Yu, N.J. (2005). "Thirty years of development and application of CFD at Boeing Commercial Airplanes, Seattle." *Computers and Fluids*, **34**(10): pp. 1115–1151.

Johnston, F.T. (1980). "A general panel method for the analysis and design of arbitrary configurations in incompressible flows." Contractors Report CR 3079, NASA.

Katz, J. and Plotkin, A. (2001). *Low Speed Aerodynamics*. Cambridge University Press.

Kim, G.D., Lee, C.S. and Kerwin, J. (2007). "A b-spline based higher order panel method for analysis of steady flow around marine propellers." *Ocean Engineering*, **34**(14-15): pp. 2045–2060.

Kinnas, S. (1996). *Advances in Marine Hydrodynamics*, vol. 5 of *Advances in Fluid Mechanics*, chap. Theory and numerical methods for the hydrodynamic analysis of marine propulsors, pp. 279–322. Computational Mechanics Publications, Southampton, UK.

Kinnas, S., Hsin, C.Y. and Keenan, D. (1991). "A potential based panel method for the unsteady flow around open and ducted propellers." *Proceedings of the Eighteenth Symposium on Naval Hydrodynamics*, pp. 667–685.

Kinnas, S.A., Xu, W., Yu, Y.H. and He, L. (2012). "Computational methods for the design and prediction of performance of tidal turbines." *Journal of Offshore Mechanics and Arctic Engineering*, **134**(1).

Koumoutsakos, P., Leonard, A. and Pepin, F. (1994). "Boundary conditions for viscous vortex methods." *Journal of Computational Physics*, **113**(1): pp. 52–61.

Lighthill, M. (1963). *Laminar Boundary Layers*, chap. Introduction. Boundary Layer Theory, pp. 54–61. Oxford University Press.

Liu, P., Colbourne, B. and Chin, S. (2005). "A time-domain surface panel method for a flow interaction between a marine propeller and an ice blockage with variable proximity." *Journal of Naval Architecture and Marine Engineering*, **2**(1): pp. 15–20.

Maganga, F., Pinon, G., Germain, G. and Rivoalen, E. (2008). "Numerical simulation of the wake of marine current turbines with a particle method." In "Proceedings of the 10th World Renewable Energy Congress (WRECX)," Glasgow, Scotland.

Maskew, B. (1982). "Prediction of Subsonic Aerodynamic Characteristics: A Case for Low-Order Panel Methods." *Journal of Aircraft*, **19**(2): pp. 157–163.

Maskew, B. (1987). "Program VSAERO theory document: A computer program for calculating nonlinear aerodynamic characteristics of arbitrary configurations." Tech. Rep. NASA CR 4023, NASA.

McCombes, T. (2006). *Performance Evaluation Of Oscillating Hydrofoils When Used To Extract Energy From Tidal Currents*. Master's thesis, The University of Strathclyde.

Morino, L. and Kuo, C. (1974). "Subsonic potential aerodynamics for complex configurations- a general theory." *AIAA Journal*, **12**: pp. 191–197.

Nicholls-Lee, R., Turnock, S. and Boyd, S. (2011). "A method for analysing fluid structure interactions on a horizontal axis tidal turbine." In "Proceedings of the 9th European Wave and Tidal Energy Conference (EWTEC2011)," Southampton, England.

Pinon, G., Mycek, P., Germain, G. and Rivoalen, E. (2012). "Numerical simulation of the wake of marine current turbines with a particle method." *Renewable Energy*, **46**(0): pp. 111–126.

Ploumhans, P., Winckelmans, G., Salmon, J., Leonard, A. and Warren, M. (2002). "Vortex methods for direct numerical simulation of three-dimensional bluff body flows: Application to the sphere at Re=300, 500, and 1000." *Journal of Computational Physics*, **178**(2): pp. 427–463.

Politis, G.K. (2004). "Simulation of unsteady motion of a propeller in a fluid including free wake modeling." *Engineering Analysis with Boundary Elements*, **28**(6): pp. 633–653.

Pyo, S. (1995). *Numerical Modelling of Propeller Tip Flows With Wake Sheet Roll-up in Three Dimensions*. Ph.D. thesis, Masschusetts Institute of Technology.

Schmitz, S. and Chattot, J.J. (2006). "Characterization of three dimensional effects for the rotating and parked NREL Phase VI wind turbine." *Journal of Solar Energy Engineering (Transactions of the ASME)*, **128**(4): pp. 445–454.

Snell, H. (1998). "Review of the present status of rotor aerodynamics." *Wind Energy*, **1**(1): pp. 46–69.

Somers, D. (1997). "Design and experimental performance of the S809 airfoils." Tech. Rep. NREL/SR-440-6918, NREL.

Somers, D. (2004). "The S814 and S815 airfoils." Tech. Rep. NREL/SR-500-36292, NREL.

Stock, M.J. and Gharakhani, A. (2010). "Modeling rotor wakes with a hybrid OVERFLOW-vortex method on a GPU cluster." In "Proceedings of the 28th AIAA Applied Aerodynamics Conference," .

Taylor, I. and Vezza, M. (1999). "Calculation of the flow field around a square section cylinder undergoing forced transverse oscillations using a discrete vortex method." *Journal of Wind Engineering and Industrial Aerodynamics*, **82**(1-3): pp. 271–291.

Taylor, I. and Vezza, M. (2009). "A numerical investigation into the aerodynamic characteristics and aeroelastic stability of a footbridge." *Journal of Fluids and Structures*, **25**(1): pp. 155–177.

Topper, M. (2010). *Numerical Modelling of Flows Involving Submerged Bodies and Free Surfaces*. Ph.D. thesis, The University of Edinburgh.

Turnock, S. (1997). *Technical manual and user guide for the surface panel code:* PALISUPAN. No. 100 in Ship Science Reports. University of Southampton.

van Garrel, A. (2011). "Development of a wind turbine rotor flow panel method." Tech. rep., Energy Research Centre of the Netherlands (ECN).

Vaz, G. (2005). *Modelling of Sheet Cavitation on Hydrofoils and Marine Propellers using Boundary Element Methods*. Ph.D. thesis, Universidade Técnica De Lisboa Instituto Superior Técnico.

Whitehouse, G., Boschitsch, A., Quackenbush, T., Wachspress, D., and Brown, R. (2007). "Novel eulerian vorticity transport wake module for rotorcraft flow analysis." In "In Proceedings of the 63rd Annual Forum of the American Helicopter Society," Virginia Beach, USA.

Willis, D.J. (2006). *An Unsteady, Accelerated, High Order Panel Method with Vortex Particle Wakes*. Ph.D. thesis, Massachusetts Institute of Technology.

Youngren, H., Bouchard, E. and Coopersmith, R. (1984). *Quadrilateral Element Panel Method:* QUADPAN*; User's Manual Ver. 3.2*.

5

Method as Applied – Tying it all Together

5.1 Introduction

This chapter provides a brief description of how the computer program V3D was developed to implement the method proposed in this thesis.

5.1.1 Relevance

As discussed in Chapter 1, there is a particular difficulty in traditional CFD when modelling wake vorticity behind a turbine rotor-system. At the time of writing, the primary alternative to the primitive variable RANS or LES/DES approaches was either a boundary-element method based on a potential flow solution and modelling the wake as a number of panels, as in Baltazar and Falcão de Campos (2011), or a vorticity transport based approach to the Navier-Stokes equations, as used in Fletcher and Brown (2010) to model wind turbines. A principal shortcoming of these methods that this thesis addresses is that neither are capable on their own of modelling both the relatively low aspect ratio, high thickness blades of a tidal turbine and the wakes they generate. A secondary issue, and the rationale for developing the open-source V3D code described herein, was that the source code for most software packages (and in fact virtually every other) was unavailable for casual inspection.

The preceding chapters have outlined the major hydrodynamic considerations one must capture when simulating tidal turbines, and have discussed the methods used in the literature to model these. The conclusions of each chapter have outlined the relevance of the material to this thesis, however, the following is a précis of the rationale for the method described in this chapter.

- Blade-element/momentum theory remains the major design method for turbines and propellers, however, it is one-dimensional and steady state, and includes no real information on the evolution of device wakes. Significant modification and post hoc extension is required to mimic the physics of real flows.

- Computational fluid dynamics can (in theory) model most of the flow physics, although at considerable expense. CFD techniques can be used, however, to model elements of the flow, namely the wake, while a simplified method can be used to model flow at solid boundaries.

- Boundary-element methods (BEMs) suffer in how they model wakes – free wake modelling is typically problematic in that using vortex filament/panel models for wakes results in simulation instability in finite time; fixed and relaxing wake models do not predict complex wake evolution. BEMs do have a number of attractive attributes:

  - They can model thick, three-dimensional bodies using considerably lower computational resource than finite-volume CFD;
  - A boundary element mesh is considerably simpler to construct than the volumetric meshes required in finite-volume CFD;
  - BEMs perform satisfactorily in providing a realistic aero/hydrodynamic body for wake generation – as long as the underlying assumptions are understood the conditions of the methods inherent simplifications are not violated.

- The wake can be though of as separated shear layers, and can be simulated using a vortex model by transforming the Navier-Stokes equations into the velocity-vorticity form. Typical aero/hydrodynamic vortex models use Lagrangian particles to represent the wake, however, these require frequent re-initialisation in order to remain convergent, since their cores must overlap but the elements are free to move sufficiently far apart that this might not always be the case. Furthermore, calculations are generally applied on a mesh, for example calculating the gradients of the velocity and vorticity fields. An alternative is to lock the "particles" into the cell locations of a finite-volume mesh, and use the finite-volume framework to perform convection, diffusion and stretching calculations to evolve the flow. This has the advantages of being inherently – as long as the underlying methods are – stable and accurate in space and time, while also maintaining the core overlap required for convergence.

High accuracy finite-volume methods can be applied to the wake problem in isolation from the surface conformal boundary layer flow problem, and used to provide an Eulerian-Lagrangian method to model the location, strength and evolution of wake vorticity. This work thus uses a BEM as a vorticity source and the FVM as a physics engine to evolve the wake. They are coupled using vortex methods (such as interpolation kernels) and

there are a number of utilities, for example the fast-multipole method and octrees which allow inversion of the vorticity field back to the velocity field, and simplify book-keeping respectively.

The novelty of this thesis is thus restated as being the description of a method that allows the wake behind turbines or lifting bodies represented by a classical boundary-element method to be represented using a vorticity transport flow solver. No evidence of a turbine model utilising a coupled BEM/FVM has been found in the literature (of course it is noted that absence of evidence is not evidence of absence), and as such there is novelty in the method, form, implementation and use of the V3D code to model tidal turbines.

5.1.2 Justification of Methods

Ought really to include a reference to Fig. C.6 here.

Supplementary deliverables of this work are now enumerated:

1. A CFD code has been developed (from scratch) that contains and couples:
    - a Boundary-Element Method (panel code – BEM) for modelling the blade/bodies;
    - a Finite-Volume Method (flow solver – FVM) for wake modelling;
    - a Fast-Multipole Method (FMM) for recovering the velocity field;
    - the various ancillary methods and subroutines required in a fully unsteady three-dimensional CFD package, e.g. routines for basic mesh input/output, generating boundary and initial conditions and outputting and post-processing the resulting data.
2. Supporting data analysis methods and pre/post-processing packages have been developed (again from scratch):
    - a CAD based system using ANSYS GAMBIT (now deprecated as the University ANSYS licence no longer supports GAMBIT);
    - a custom GUI driven geometry processor and mesh generator to provide input data for the V3D model;
    - a custom GUI driven post-processing package to provide data reduction, interrogation and visualisation facilities.
3. The performance of the V3D code is analysed against published experimental and numerical data.

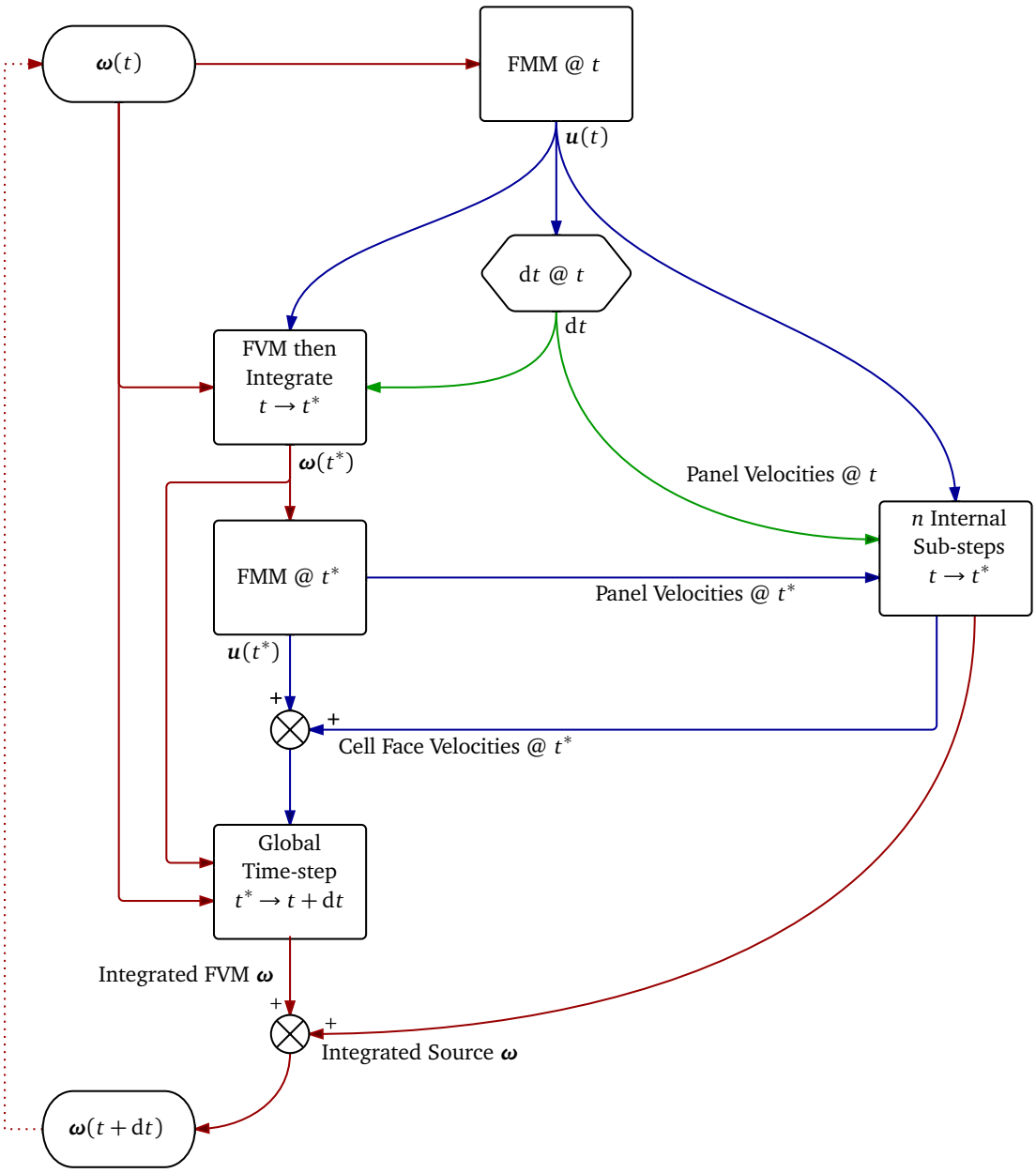

Figure 5.1: Flow chart of algorithm.

The core algorithm comprises a wrapper for the following methods that have been described in preceding chapters and implemented in a computer program:

- Boundary-Element Method: takes input in the form of velocity data at the centroid of the panels, produces output in the form of the surface distribution of singularity strengths on the body and wake panels.
- Finite-Volume Method: takes input in the form of approximations to velocity and vorticity fields, produces output in the form of the time derivatives of the vorticity field.
- Fast Multipole Method: takes input in the form of a vorticity field, produces an approximation to the velocity field.
- Domain Decomposition Method: takes input in the form of the vorticity field, outputs an approximation discretised on a mesh using octree/quadtree data structures.

The wrapper is responsible for overall book-keeping for the methods and also implements the time-integration, data read/write and other ancillary routines. Geometry preprocessing is performed in either the commercial package ANSYS GAMBIT or a custom graphical user interface implemented in MATLAB. These can be used to prepare a Neutral (.neu) file containing the coordinates, connectivity and boundary conditions of the BEM mesh, which is ingested into the program. Further information on simulation setup is provided through a text user interface (TUI) or via a Case (.cas) file.

Program Flow Chart After initialisation and data ingestion, the program computes the solution based on Fig. 5.1. The components in Fig. 5.1 are described in more detail in the following sections.

5.2 Analytical and Numerical Integration and Differentiation

This thesis uses methods which require the analytical and numerical evaluation of the integral and differential quantities associated with the velocity vector field. These are

- analytical integration of velocity perturbation potential (ϕ where $\boldsymbol{u} = \nabla\phi$) over two and three dimensional domains, transformed into the integral of source and dipole distributions over domain boundaries – this is discussed in Chapter 4;
- numerical integration of the Biot-Savart law in differential form for the inversion of the vorticity Poisson equation – discussed in Section 5.2.1;

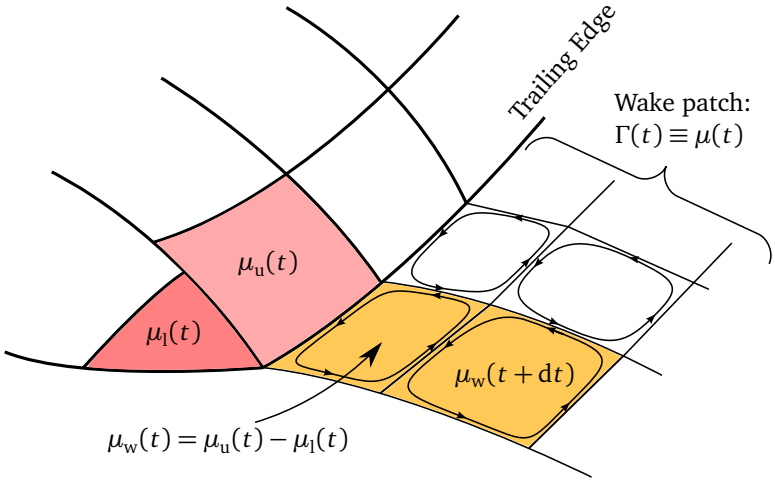

Figure 5.2: Wake panel patch generation.

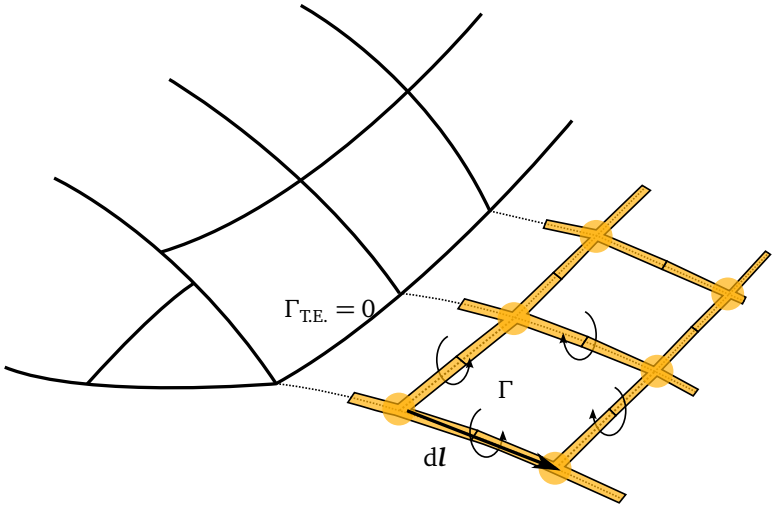

Figure 5.3: Conversion of wake panels of circulation Γ to vortex blobs of vorticity $\Gamma\ d\boldsymbol{l}$. Yellow shaded regions illustrate integration bounds for each blob.

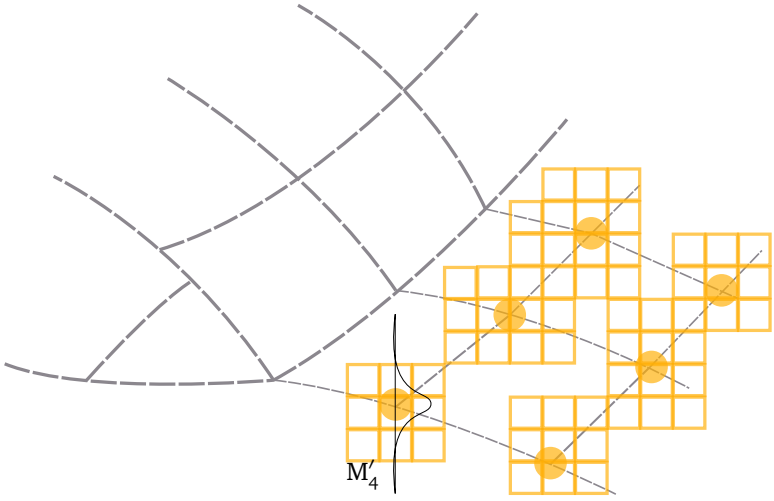

Figure 5.4: Interpolation of blobs onto underlying Cartesian mesh.

- calculating the gradients of the velocity field – discussed in Section 5.2.3; and
- calculating the gradients of ϕ to obtain a perturbation velocity field – discussed in Section 5.2.4.

5.2.1 A Practical Vortex Method Implementation

This section describes the approach adopted in the present method for managing the finite-volume mesh and recovering the velocities at the cell interfaces. The method utilises a hierarchical domain decomposition method, based on octrees/quadtrees for the book-keeping, and a FMM to recover the velocities in the domain due to a volume distribution of vorticity.

Recalling that the continuous vorticity distribution in the domain is approximated in the finite-volume method by n discrete vortex containing cells,

$$\boldsymbol{\omega}(\boldsymbol{x},t) \approx \boldsymbol{\omega}_\delta = \sum_i^n \boldsymbol{\Gamma}_i(t)\,\zeta_\delta\left(\boldsymbol{x}-\boldsymbol{x}_i\right). \tag{5.1}$$

The vorticity field is discretised into elements defined by the position of a discrete vortex of core radius δ and vorticity distribution ζ_δ at $\boldsymbol{x}_i$ and its circulation $\boldsymbol{\Gamma}_i = \boldsymbol{\omega}_i \Delta V$. These correspond to the finite-volume cells, and the value of the vorticity in each cell is free to change according to the evolution dictated by the finite-volume solution of the vorticity transport equations.

If the wake particle vorticity field is given by

$$\boldsymbol{\omega}(\boldsymbol{x}) = \sum_p \zeta_\sigma(\boldsymbol{x}-\boldsymbol{x}_p)\boldsymbol{\omega}_p, \tag{5.2}$$

then the mesh vorticity field is constructed from the wake "blob" strengths using the projection

$$\boldsymbol{\omega}(\boldsymbol{x}_m) = \frac{1}{h^3}\sum_p M_4'(\boldsymbol{x}_m-\boldsymbol{x}_p)\boldsymbol{\omega}_p. \tag{5.3}$$

Here $\boldsymbol{\omega}$ is the particle strength, ζ_σ is the smoothed cutoff function approximation to the Dirac delta, $\boldsymbol{x}_p$ and $\boldsymbol{x}_m$ are the particle and mesh locations, respectively, and there are p particles.

5.2.1.1 Domain Decomposition

The zonal decomposition employed herein follows Brown and Line (2005), and thus Cheng, Greengard and Rokhlin (1999), and the basic method of the quad/octree domain decomposition is as follows:

1. Create root voxel, enclosing entire domain allowing a certain latitude for expansion of the region of interest during calculation run;

2. Subdivide into quadrants/octants j;

3. For each $j = 1, \ldots, 4/8$, determine the number n_j of vorticity containing cells within j;

4. If n_j is below some arbitrary cutoff, or if the side length of j is equal to the side length of the finite-volume cell, stop. Otherwise goto 2.

This process automatically focusses the computational resource on regions containing vorticity, however, if it is required to obtain velocity field information at an arbitrary point outside the regions of interest, this can be achieved by inserting additional vorticity free voxels containing markers at any point in the FMM process.

To facilitate the domain decomposition, the following relationships are defined between voxels. For a voxel i at octree level m they are as follows:

- Parent – the voxel at level $(m-1)$ that i is an oct/quadrant of;
- Child – a voxel at level $(m+1)$ that i is the parent of;
- Neighbour – a voxel that is immediately adjacent (orthogonally speaking) to i;
- Interaction list – voxels that are immediately adjacent to i, both orthogonally and diagonally, including i. There are 9 in two dimensions and 27 in three dimensions;
- Colleagues – voxels at the level m whose parents are contained in the interaction list of the parent of i, but excluding those contained in the interaction list of i. There are 27 in two dimensions and 189 in three dimensions.

"Book-keeping" is especially straightforward with a quad/octree, since all connectivity information at each level is contained within the structure of the tree, which can be represented by the unique ID of each node. The position of a voxel within its parent is given by a binary translation from the location at west-south-bottom $[0,0,0]$ to east-north-top $[1,1,1]$. These translation coordinates are concatenated for each level of the tree, resulting in a binary address for the voxel. Each triple within the address gives the local *xyz* coordinates of each octant when multiplied by the octant side length. This binary address can be written in octal – the base-8 numbering system, denoted subscript 8 (base-4 could be used in two dimensions, however in the present method, a quadtree is considered as a "slice" of an octree) – giving a unique integer ID number for each node of the tree. If

each level m from the root is denoted by numbers increasing from $m = 0 \dots m_{\max}$, and each child branch/leaf within a node is numbered $0 \leq P_{10} \leq 7$ according to the decimal representation of the binary (base-2) translation vector, the unique ID for each element is given in octal by

$$\mathrm{ID}_8 = \sum_{m=0}^{m_{\max}} P_{10}(m) \times 8^m. \tag{5.4}$$

Conveniently this forms the address of the node whose ID it is, as well as the address of all the ancestral nodes in the tree and can thus be used to establish the xyz coordinates of the node and its ancestors. Any node in the tree can be checked quickly for existence or interrogated by following the directions to that node contained in its ID. Directions to neighbours of nodes can be found by ascertaining whether the neighbour shares the node's parent and if not by recursively checking the parent's neighbours in the same direction before dropping back down the tree. Once the tree is established, a hard link via a stored pointer to the node is created, so the displacement following method is only used when inserting new nodes or in obtaining the details of neighbouring nodes that are required when calculating the interaction lists.

The interaction list is determined using the immediate side and corner neighbours of a node. This is required at the leaf level, where the FVM cells reside so as to get the FVM cell neighbours, and also at higher levels in order to perform the FMM. The colleagues of node i are obtained by excluding the interaction list of node i from the list of the children of the interaction set of i's parent node. Figure 5.5 demonstrates the relationships in two dimensions, and the extension to three dimensions is straightforward.

5.2.1.2 Asymptotic Cost of FMM as Applied

Cheng, Greengard and Rokhlin (1999) calculated the cost of the FMM algorithm as

$$C_{\mathrm{FMM}} = 27ns + 2np^2 + 189\frac{n}{s}p^2 + 20\frac{n}{s}p^3, \tag{5.5}$$

for a dense distribution of n particles, s particles before division and p being the maximum level of expansion – this simplifies to $\mathcal{O}(n)$ if p is fixed. In order, the terms are due to the direct computation of colleagues (using e.g. Eq. 2.26), due to forming and evaluation of the local and multipole expansions at the leaf level, e.g. with expressions similar to Eqs. (2.34) and (5.23) and due to the remaining interactions at each level of the tree, such as Eqs. (2.35) and (2.38). The performance of the FMM can be evaluated in terms of the complexity of the algorithm. Consider the n-body problem evaluated directly: since this involves calculating pairwise interactions at each cell for every other cell, this entails

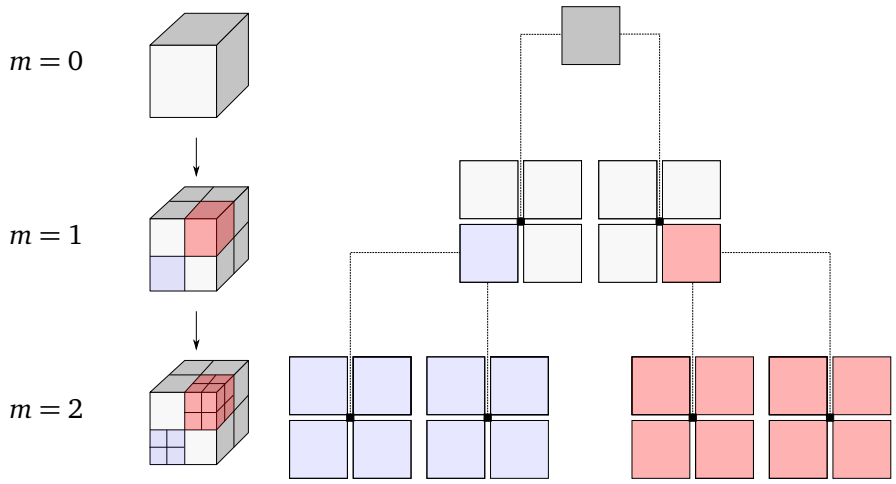

(a) Octree data structure

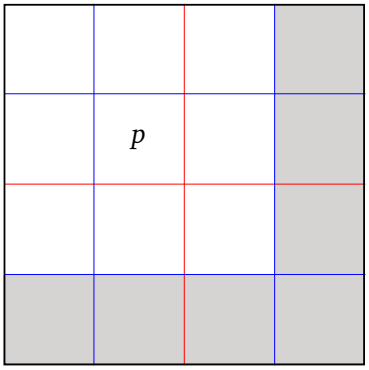

(b) Level $m-1$, $p = \text{parent}(i)$

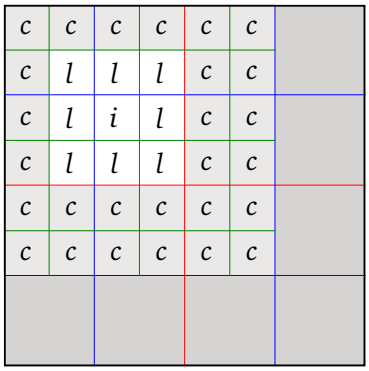

(c) Level m

Figure 5.5: Three-dimensional octree and two-dimensional quadtree relationships between parent p and child i, and between node i and colleagues c and interaction list l. Three-dimensional relationships follow naturally.

$\mathcal{O}\left(n^2\right)$ computational effort. The FMM method reduces this to $\mathcal{O}\left(n \log n\right)$ by using the domain decomposition to identify $\log n$ cells and thus perform $\log n$ calculations for each of the n cells by performing them only within the near-field (Yokota and Barba, 2011). The difference in the costs between the Cheng, Greengard and Rokhlin method and the method of Yokota and Barba is related to the ability to re-use the moment and velocity gradients at each level in the tree.

The cost of obtaining the moments of vorticity in D dimensions at a point due to a single vortex is

$$C_{\text{mom.}} = \mathcal{O}\left(p_{\text{max}}^{D+1}\right). \tag{5.6}$$

Since the moments at each node at each level m must comprise of the contributions of all the subordinate vortices, it is easy then to see that the cost of computing the cluster moments at each level directly in three dimensions is

$$C_{\text{mom.}} = \begin{cases} \mathcal{O}\left(p_{\text{max}}^3 n\right) & \text{for } m = m_{\text{max}} \text{ only,} \\ \mathcal{O}\left(p_{\text{max}}^3 n \log_8 n\right) & \text{for } 0 \leq m \leq m_{\text{max}}. \end{cases} \tag{5.7}$$

The cost for all levels is simply $m_{\text{max}} n \cdot p_{\text{max}}^4$. The logarithm is introduced since a dense tree will at each level have 8^m nodes, and this can be inverted to determine the number of levels required for their storage as $m_{\text{max}} = \log_8 n$. Therefore the logarithm multiplier decays to unity if the direct calculation is only applied to the leaf layer since the cost is associated with the parent node. Similarly, the cost of the binomial expansion is

$$C_{\text{binom.}} = \mathcal{O}\left(8 p_{\text{max}}^6 \log_8 \left(\frac{n}{8}\right)\right). \tag{5.8}$$

The cost of the moment calculation is thus $\mathcal{O}(n)$, reduced from $\mathcal{O}(n \log n)$ by the binomial sum. Obtaining the velocity field due to the multipole expansion at each branch from the colleagues incurs a similar cost

$$C_{\text{m.e.}} = \mathcal{O}\left(189 p_{\text{max}}^6 \log_8 \left(\frac{n}{8}\right)\right), \tag{5.9}$$

and the cost of translating the velocity field in a local expansion to the children tree nodes is

$$C_{\text{l.e.}} = \mathcal{O}\left(8 p_{\text{max}}^6 \log_8 \left(\frac{n}{8}\right)\right). \tag{5.10}$$

The cost of collapsing the velocity field to the cells at the highest level of the tree is

$$\mathcal{O}\left(8 p_{\text{max}}^3 n\right), \tag{5.11}$$

and the cost of collecting the velocities due to the colleagues at $m = m_{\max}$ is

$$\mathcal{O}(189n). \tag{5.12}$$

The order of precedence for an order-of-magnitude analysis is

$$\mathcal{O}(n^2) > \mathcal{O}(n \log n) > \mathcal{O}(n) > \mathcal{O}(\log n), \tag{5.13}$$

therefore, for constant p and observing that constants (i.e. $\log_8 8$), coefficient multipliers and the base of the logarithms are immaterial, the total cost of the FMM is therefore given by

$$C_{\text{FMM}} = \mathcal{O}(n) + \mathcal{O}\left(\log n\right) + \mathcal{O}\left(\log n\right) + \mathcal{O}(n) + \mathcal{O}(n) \equiv \mathcal{O}(n). \tag{5.14}$$

The actual computational cost of the implementation is examined below.

5.2.1.3 Observed Performance of the Octree/FMM Strategy

The FMM is tested in a number of manners to determine the performance of the algorithm. It should be noted that the FMM tested is for the point vortex method, i.e. the FMM version of Eq. (5.16c). The results of the FMM of a piecewise constant distribution in cubic cells (Eq. 5.17) have consistent accuracy and time requirements, but the time required to perform the direct calculation is such that it was not practical to gather sufficient data.

- The number of cells n and the order of expansion $p_{\max}$ are increased and the time to a solution measured and compared with the time taken for a direct calculation. This test is done on an arbitrary distribution of $1000 \leq n \leq 4\,000\,000$ vorticity containing cells is created in a cubic domain, and FMM velocities are calculated for $3 \leq p_{\max} \leq 8$. Figure 5.6 presents the wall clock times for these runs along with their equivalent direct calculation time. Also plotted are lines of gradient $\mathcal{O}(n)$ and $\mathcal{O}(n \log n)$ obtained by assuming the direct calculation time scales as $\mathcal{O}(n^2)$. From this diagram the "break-even" point of using various truncation levels of the FMM is obtained, at around 20 000 cells for the lowest practical accuracy $p_{\max} = 3$ and at around 300 000 cells for the highest accuracy considered in this test ($p_{\max} = 8$).

- n is fixed at approximately 100 000, and $p_{\max}$ is varied $3 \leq p_{\max} \leq 16$. A cubic volume with an arbitrary distribution of vorticity is discretised using 48 cells in each direction and the velocities are calculated using the FMM and direct calculations. Using the l^2 norm of the velocity error in the FMM, the relative error at each cell is obtained as

$$\varepsilon_{\text{rel.}} = \frac{|\boldsymbol{\varepsilon}|}{\left|\boldsymbol{u}_{\text{FMM}}\right|}. \tag{5.15}$$

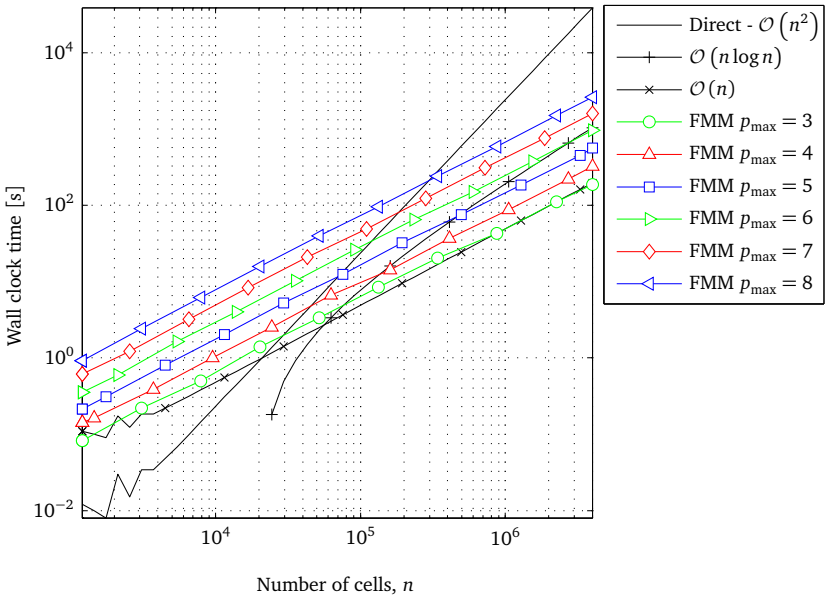

Figure 5.6: Wall clock times for increasing numbers of voxels and increasing FMM expansion order.

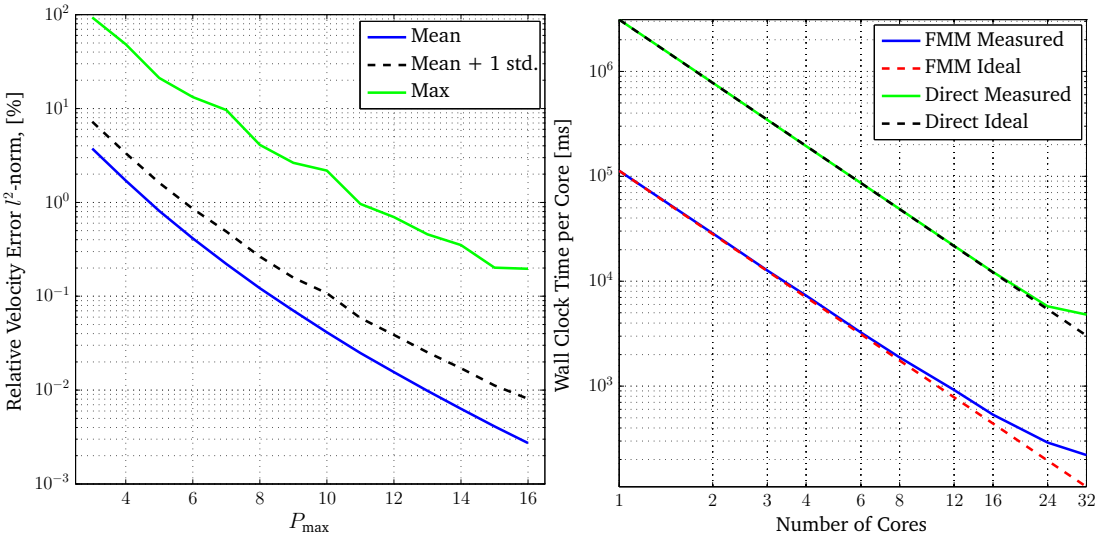

(a) Convergence with increasing expansion order

(b) CPU scaling

Figure 5.7: Performance of FMM with n =110 592 cells (48^3 – lowest possible of $n^3 \geq$100 000 with n even).

and the maximum, mean and standard deviations are plotted in Fig. 5.7a. The mean error drops rapidly from approximately 4 % as the expansion order is increased, and the standard deviation in the error – and thus the average spread in the errors – is consistently ± 0.3 to 0.6 of an order of magnitude around the mean. The maximum error, however, does not drop below 10 % until an expansion order of about 7.

- The order of the expansion is fixed at $p_{\max} = 8$ and the same distribution of vorticity is reused, however this time the number of processors available is varied between 1 and 32. Figure 5.7b plots the time required per CPU for a velocity field calculation via both Eq. (5.16c) and Eq. (5.17). Also plotted is the ideal scaling. It is clear that both methods scale almost ideally, except at higher CPU counts. While it is not apparent why this might be the case, obviously a combination of areas of non-parallelised code and inefficient parallelisation of the rest become bottlenecks as the number of processors increases. However, there is clearly a significant advantage to running on multi-processor machines, and the code scales well with almost the expected work distribution per core.

5.2.2 Volumetric Biot-Savart Expressions

The finite-volume method representation of vorticity in the domain which is used in the method proposed in this thesis is predicated on the pointwise representation of a piecewise constant distribution of vorticity, where each point represents a cubic volume. Recalling the Biot-Savart law in integral form, the velocity due to the distribution of vorticity over the domain is

$$4\pi \boldsymbol{u}(\boldsymbol{x}) = \sum_{i}^{\text{cells}} \int_{V} \boldsymbol{\omega}_i \times \nabla \left(\frac{1}{r} \right) \mathrm{d}V \tag{5.16a}$$

$$= \sum_{i}^{\text{cells}} \int_{V_i} \boldsymbol{\omega}_i \times \frac{\boldsymbol{r}}{r^3} \mathrm{d}V \tag{5.16b}$$

$$\approx \sum_{i}^{\text{cells}} \boldsymbol{\omega}_i \times \frac{\boldsymbol{r}}{r_\delta^3}. \tag{5.16c}$$

By using a smoothing term ($r \to r_\delta$) to regularise Eq. (5.16b), an approximation to the volume integral is obtained which can allow the use of the pointwise vorticity field representation. However, this does not result in an exact representation of either the vorticity field or the resultant velocity field when used in e.g. the FMM to calculate moments of the vorticity or in the direct calculation of velocities due to cell colleagues. The alternative

is to perform either a numerical or analytical evaluation of the integral then to sum the resulting velocities.

Suh (2000) provides expressions for the velocity due to a volume distribution of vorticity bounded by planar faces. In the context of this thesis (constant strength vorticity distribution), integrating Eq. (5.16a) by parts and recalling Green's second identity, the resulting velocity is obtained by

$$4\pi \boldsymbol{u}(\boldsymbol{x}) = \sum_{i}^{\text{cells}} \sum_{j}^{\text{faces}} \phi_{\sigma,j}(\boldsymbol{x}) \left(\boldsymbol{\omega}_i \times \boldsymbol{n}_j \right). \tag{5.17}$$

Here $\boldsymbol{n}$ denotes the unit normals of the cell faces and ϕ_σ is the velocity perturbation potential due to a distribution of sources of strength 4π or 2π (depending if $\boldsymbol{x}$ is a field or a face point) over the faces of the cell, calculated according to Eq. (4.63).

An alternative is to use Gaussian quadrature rules to perform a numerical cubature over the cell using the Biot-Savart expression for a point vortex, e.g. Eq. (5.16c). This method has the advantage that the quadrature points and weights can be used to provide the $\boldsymbol{x}$ and $\boldsymbol{\omega}$ input to the FMM, and that the nearfield evaluations for both the Biot-Savart law and its gradients can be calculated in advance at arbitrarily high degree, or exactly, and stored in memory for use at runtime. This reduces the cost of the FMM applied to Eq. (5.17) to that of the FMM applied to Eq. (5.16c). Obviously the analytical volume integration values of the velocity field are only approximated by the cubature: the quality of the approximation hinges on both the number of points and also the choice of the smoothing parameter (which is required due to the FMM). In Fig. 5.8, the smoothing parameter is chosen as $\delta^2 = 0.001$ and results obtained approximating the vorticity distribution at fairly low degrees are presented. The error decay is exceptionally quick, even when using only 4^3 cubature points, and there is no particular advantage to using more points except in the interior of the volume: the error of approximately 0.017% at $x = \pm 3$ is due to the smoothing parameter – when this is set to zero, the error decays to $\mathcal{O}(4 \times 10^{-6})$% after $x = \pm 3$, but the kernel is undifferentiable.

5.2.3 Velocity Field Gradients

If the FVM integrated source method is used for the stretch/compression term in the vorticity transport equation the gradients of the velocity field must be calculated. Fortunately this is relatively easy to accomplish analytically using the gradients of the Biot-Savart law, or by using the velocity field as it is calculated during the FMM. The gradients of the Biot-Savart law for a point vortex (as in Eq. 5.16c) are a second rank tensor calculated as follows. First

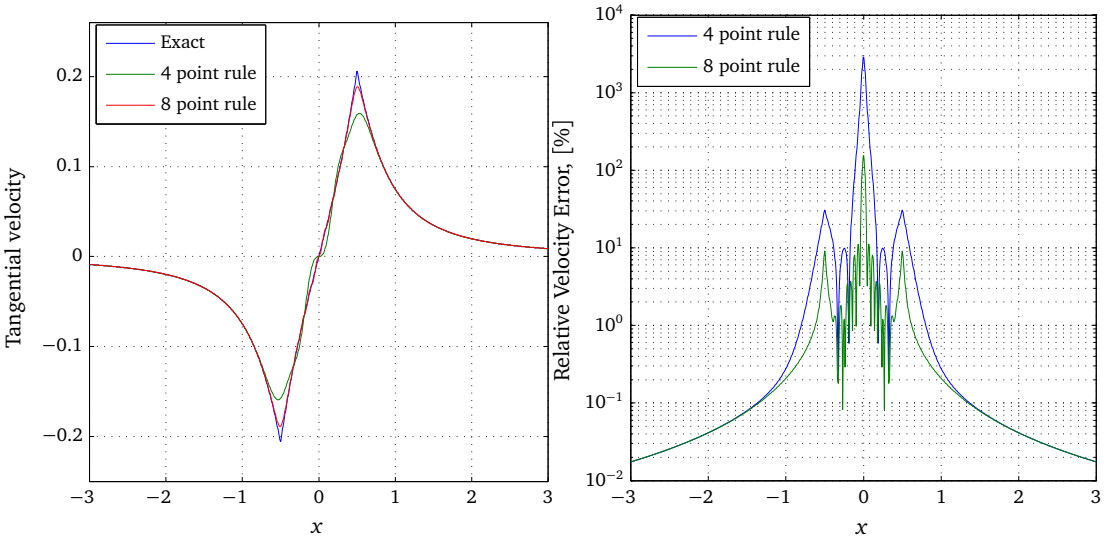

(a) Tangential velocity **(b)** Error in tangential velocity

Figure 5.8: Tangential velocity due to a distribution of vorticity in a unit cube centred at the origin computed using exact expression (Eq. 5.17) and cubature with 4^3 and 8^3 points with a Gaussian quadrature rule for location and weights. The relative error has decayed to below 0.02% by ± 3. In any case, FMM algorithm does not include the influence of any vorticity within this radius of the cell centre, switching instead to a direct evaluation of the analytical Biot-Savart expression.

the vector product rule for the numerator $\boldsymbol{\omega}(\boldsymbol{x}) \times \boldsymbol{r}(\boldsymbol{x}, \boldsymbol{y})$ results simply in the tensor cross product of a 3×3 identity matrix and the vorticity vector. This results in the f and f' terms required for a vector quotient rule:

$$\boldsymbol{f} = \boldsymbol{\omega}(\boldsymbol{x}) \times \boldsymbol{r}(\boldsymbol{x}, \boldsymbol{y}); \tag{5.18a}$$

$$\boldsymbol{f}' = \mathbf{I} \otimes \boldsymbol{\omega}(\boldsymbol{x}). \tag{5.18b}$$

The g and g' terms are simply

$$g = r_\delta^3; \tag{5.19a}$$

$$\boldsymbol{g}' = 3\boldsymbol{r}\, r_\delta^3. \tag{5.19b}$$

The velocity gradient tensor is thus given by

$$\nabla \boldsymbol{u}(\boldsymbol{x}) = \sum^{\text{cells}} \frac{\boldsymbol{f}' g - \boldsymbol{g}' \otimes \boldsymbol{f}}{g^2}. \tag{5.20}$$

The gradients of the volumetric form of the Biot-Savart law (Eq. 5.17) are even easier to derive (if not necessarily easier to compute). The product rule is applied noting that the cross product term is constant and the resulting tensor is

$$4\pi \nabla \boldsymbol{u}(\boldsymbol{x}) = \sum_j^{\text{faces}} \boldsymbol{u}_{\sigma,j}(\boldsymbol{x}) \otimes \left(\boldsymbol{\omega}_i \times \boldsymbol{n}_j \right), \tag{5.21}$$

where the term $\boldsymbol{u}_\sigma$ is the velocity induced due to the (unit) source distribution over the faces of the cell.

The fast-multipole velocity field tensors which are calculated during the downwards sweeps of the octree can also be used to obtain the velocity gradients due to more distant clusters of cells. The gradients of the velocity field at the centre of a velocity field expansion, $\boldsymbol{x}_c$, are simply the first orthogonal terms in Eq. (2.37):

$$\nabla \boldsymbol{u}(\boldsymbol{x}_c) = - \begin{bmatrix} D_x^{\boldsymbol{e}_x} \boldsymbol{u}(\boldsymbol{x}_c) & D_y^{\boldsymbol{e}_x} \boldsymbol{u}(\boldsymbol{x}_c) & D_z^{\boldsymbol{e}_x} \boldsymbol{u}(\boldsymbol{x}_c) \\ D_x^{\boldsymbol{e}_y} \boldsymbol{u}(\boldsymbol{x}_c) & D_y^{\boldsymbol{e}_y} \boldsymbol{u}(\boldsymbol{x}_c) & D_z^{\boldsymbol{e}_y} \boldsymbol{u}(\boldsymbol{x}_c) \\ D_x^{\boldsymbol{e}_z} \boldsymbol{u}(\boldsymbol{x}_c) & D_y^{\boldsymbol{e}_z} \boldsymbol{u}(\boldsymbol{x}_c) & D_z^{\boldsymbol{e}_z} \boldsymbol{u}(\boldsymbol{x}_c) \end{bmatrix}. \tag{5.22}$$

Gradients at a nearby location can be obtained in the same manner as the velocity (as in

Eq. 2.38):

$$\nabla \boldsymbol{u}(\boldsymbol{x}) = \sum_{\boldsymbol{k}=0}^{p} \frac{(\boldsymbol{x}-\boldsymbol{x}_c)}{(\boldsymbol{k})!} \begin{bmatrix} D_x^{\boldsymbol{k}+\boldsymbol{e}_x}\boldsymbol{u}(\boldsymbol{x}_c) & D_y^{\boldsymbol{k}+\boldsymbol{e}_x}\boldsymbol{u}(\boldsymbol{x}_c) & D_z^{\boldsymbol{k}+\boldsymbol{e}_x}\boldsymbol{u}(\boldsymbol{x}_c) \\ D_x^{\boldsymbol{k}+\boldsymbol{e}_y}\boldsymbol{u}(\boldsymbol{x}_c) & D_y^{\boldsymbol{k}+\boldsymbol{e}_y}\boldsymbol{u}(\boldsymbol{x}_c) & D_z^{\boldsymbol{k}+\boldsymbol{e}_y}\boldsymbol{u}(\boldsymbol{x}_c) \\ D_x^{\boldsymbol{k}+\boldsymbol{e}_z}\boldsymbol{u}(\boldsymbol{x}_c) & D_y^{\boldsymbol{k}+\boldsymbol{e}_z}\boldsymbol{u}(\boldsymbol{x}_c) & D_z^{\boldsymbol{k}+\boldsymbol{e}_z}\boldsymbol{u}(\boldsymbol{x}_c) \end{bmatrix}. \tag{5.23}$$

The terms $\boldsymbol{e}_i$ are the Cartesian basis vectors in the i^{th} direction (treated as integers and used as multi-indices).

5.2.4 Calculating gradients of ϕ

5.2.4.1 Calculating $\nabla\phi$

The perturbation velocity is given by spatial derivatives of ϕ. The expressions for the potential due to a panel can be differentiated analytically to yield expressions for the velocity they induce. However, this is a computationally expensive calculation: it is much more expedient to calculate then numerically differentiate ϕ, especially on the FVM mesh. To this end, a fourth-order central scheme is applied – similar to the diffusion scheme – to obtain $\partial\phi/\partial x$ on the east and west faces, $\partial\phi/\partial y$ on the north and south faces, and $\partial\phi/\partial z$ on the top and bottom faces of the FVM cells. The values of ϕ are calculated using both the exact and the multipole expansion expressions given in Section 4.4 depending on the distance to the target from the panel: once the distance is greater n times the panel's maximum diagonal, the multipole expression is used. Since, through experience, it has been determined that the panel sizes ought to be of the same order as that of the cells, it is possible to increase the speed of the velocity calculation as the distance increases by calculating ϕ at the centre of increasingly large clusters of cells. This is applied based on a rule that the node being evaluated be sufficiently distant from the panel as evaluated using the subtended angle over the node extents at the panel centroid $\theta = 2\tan^{-1}\left(\frac{1}{2n}\right)$, which approximates to $1/n$ for large n. In the method herein, for panels whose dimensions are of the order of the FVM cell size, $n \geq 7$ results in the use of the the farfield expressions for the children of nodes which are colleagues of the parent of the node in which the panel is located. The recursive hierarchy of colleagues is then utilised, as this maintains the restriction on θ.

The values of the perturbation potential at each level of the octree are then interpolated down into the children of the nodes and differentiated at the leaves (cells).

5.2.4.2 Calculating $\partial\phi/\partial t$

The time derivative of the velocity perturbation potential features in the unsteady Bernoulli equation which is used to generate the face pressures. A cubic-spline is use to generate the gradients using previously calculated values, i.e. using $\phi_{n-3}, \ldots, \phi_n$.

5.3 Implementation of a Finite-Volume Scheme for the Vorticity Transport Equations

The vorticity transport equations may now be discretised according to the rules and requirements of Chapter 3 for stability and accuracy. In the current method a sparse, octree based data structure is used to contain and manage the finite-volume cells. Due to the sparsity, access operators based on indices are not feasible, and so each cell is linked to its neighbours by a pointer. This being the case, it is of course logical to write all the finite-volume expressions using the compass notation, rather than with cell indexing. A second point is that the method uses only quadrilateral or cubic cells of unit volume – this reduces the complexity of the equations somewhat, allowing various terms (volume, area and distance terms) to cancel and factor out.

5.3.1 Two-dimensional Flows

In two dimensions, the vorticity transport equations are simply a single equation for transport closed with (in this thesis) a Biot-Savart inversion of the vorticity field for the velocity field. The method in this thesis can use a scheme that is first or up to second-order in space and first or second-order in time. Experience with the linear convection equation in two dimensions for rotating flows indicates that a second-order time integration is required. First or higher-order spatial discretisation uses the same equations, but with different limiter functions.

The transport equation is solved by splitting into two directional operations, one for the x-flux and one for the y, plus a diffusion operation for each. Operator splitting, based on the Symmetrically Weighted Strang Splitting, is used with a series of explicit forward Euler type sub-steps along with intermediate fields, which are then averaged, as described in the algorithm for the convection-diffusion and vorticity transport equations in Section 3.4. At each sub-time, the velocity field must be re-calculated to account for the changes in the vorticity field. The diffusive fluxes $d_{[\ldots]}$ and the convective fluxes $f_{[\ldots]}$ are calculated at the appropriate time-interval, as described in Sections 3.6 and 3.8. This is second-order in time and up to second-order in space.

5.3.2 Three-Dimensional Flows

In two dimensions, the vorticity transport equations is simply a single equation for transport, closed with a single equation for the velocity. In three dimensions, there are three equations, one for each component of the vorticity vector, and a tilting/stretching term that couples them. For three-dimensional flows in this thesis, only the alternate-dimension splitting method is used. This is for the pragmatic reason that it allows better control of sub-stepping associated with the boundary-element method portion of the process and requires fewer velocity evaluations.

5.4 Implementation of the Boundary-Element Method

Sections 4.3 and 4.4 have described all of the mathematics required to evaluate the boundary value problem. This Section describes the implementation in its current form, including the modifications required for the BEM section of the method to interface with the finite-volume section.

5.4.1 Unsteady Two-Dimensional Boundary-Element Methodology

5.4.1.1 Surface Discretisation

Boundary surface geometry in two dimensions is generally obtained from either lookup tables or equations describing shapes of interest, e.g. aerofoils. Coordinates are ingested into the program and scaled, translated and rotated as appropriate. An approximation of the surface, generated using straight line panels arranged such that points are clustered towards areas with high curvature or discontinuities, is made from the input coordinates and a collocation point is placed at the midpoint of each panel. A system of equations is then solved to enforce the boundary conditions on each panel.

Once the boundary conditions are satisfied, total velocities are calculated at a collocation point allowing the use of the unsteady Bernoulli equation to calculate the pressure coefficient,

$$C_p = 1 - \frac{u}{u_{\text{ref.}}} - \frac{2}{u_{\text{ref.}}} \cdot \frac{\partial \phi}{\partial t}. \tag{5.24}$$

The time derivative of ϕ is approximated using the data from previous time-steps. The velocity perturbation potential due to the panels is calculated by

$$\phi\left(x'_p, y'_p\right) = -\frac{1}{2\pi} \int_{x_1}^{x_2} \left(\gamma_1 + x \frac{\partial \gamma}{\partial x}\right) \arctan\left(\frac{y'_p}{x'_p - x}\right) \mathrm{d}x, \tag{5.25}$$

and the tangential velocity on each panel can be determined from the gradient $\frac{\partial \phi}{\partial x'}$ on each panel.

The system of equations is set up as follows. First a calculation is performed that obtains the velocity influence a distant panel j would have on the i^{th} panel collocation point. Once this has been obtained for all combinations of i and j, these influence coefficients are written as the influence matrix **A**. This can then be used to solve the linear system composed of equations of the form $\sum_j A_{i,j}\gamma_j = v_i'$ where the right hand side is the relative incident velocity parallel to the local y-axis of the i^{th} panel – i.e. enforcing a zero normal flow boundary condition.

5.4.1.2 Boundary Condition Calculation

At each time-step, a set of equations is solved such that the velocity at each panel collocation point is some particular value (zero normal velocity relative to the motion of the collocation point). A linear vortex element is placed on each panel, allowing the velocity due to the influence of the panels on themselves to be calculated, and the strength of the vortices is solved to satisfy the boundary condition on each panel.

5.4.1.3 BEM Sub-Time-Stepping and Wake Model

At each time-step, the circulation of all the panels is integrated to give the foil circulation, and a proto-vortex is created and shed into the wake at some distance (the distance travelled over a third of a sub-time-step) from the trailing edge. These vortices are allowed to convect downstream under the influence of the foil, the freestream and their own self induced velocities until the global time-step is advanced and they are interpolated onto the mesh.

5.4.2 Unsteady Three-Dimensional Boundary-Element Methodology

5.4.2.1 Surface Discretisation.

A geometry processing step results in an analytical expression, which is generally approximate, for the surface of interest. Normally, for such things as aerofoil shapes and hubs, look-up tables are interpolated on to provide the three-dimensional vector triples that will be used to generate surface fitted boundary-element meshes. By and large the surface mesh will be composed of quadrilateral elements except in regions where, for the sake of expediency in meshing, triangles are more appropriate – a particular example being in regions around sharp trailing edges. Since the expression for the perturbation potential influence

coefficient due to a source panel is only strictly correct for flat panels, and since the surface of a general body is not conveniently faceted, an element of discretion is required when deciding that a panel is sufficiently twisted that it should be replaced by two or more triangular sub-elements. In practice, this is accomplished automatically by insisting that the maximum angle between the normals at panel corners and at the collocation point is 15° before subdivision. In most practical cases this is sufficiently coarse a requirement that only in particularly curved or twisted examples is subdivision necessary in terms of solution correctness, and most definitely the disadvantages associated with both the additional storage overhead (i.e. non-structured mesh connectivity) and the higher complexity in surface differentiation are better treated by a gradual increase in the mesh density. There are of course certain irregular geometries where using a largely or wholly triangular mesh is expedient.

Corner points are scattered onto the surface as defined by the look-up tables or geometric equations, and an approximation to the surface is created by joining these with straight line elements to define the panels. Already a large amount of information on the curvature of the surface has been lost and the mesh density is chosen such that effects of the loss of this information is balanced against the computational overhead of increased mesh density. Each panel has a collocation point placed at its centroid, and the local coordinate system, transformation matrix and areas are calculated, along with other regularly used constants, such as the displacement of panel corners and neighbour collocation points taken in local panel coordinates.

5.4.2.2 Boundary Condition Calculation.

At each sub-time-step, the kinematic velocity is obtained at each panel centroid, along with the inflows due to the wake induced velocity and the freestream, and a surface distribution of sources is placed onto the panel so as to cancel out the local inflow. All the other panels in the domain will obviously render this cancelling as false. The influence of all the other panels in the domain is now sought – for those panels whose surface singularity distribution strength is already known, that is the source strength on body panels and the dipole strength on wake panels, the potential at the centroid of the panel of interest is calculated. A distribution of dipoles is placed over the panels such that there is zero potential inside the body, approximated at the “internal” face of each panel at the collocation points. Since the panel’s dipole strengths are all co-dependant, this gives rise to the system of equations

$$\mathbf{A}\boldsymbol{\mu}_{\text{body}} = \mathbf{B}\boldsymbol{\sigma}_{\text{body}} + \mathbf{C}\boldsymbol{\mu}_{\text{wake}}. \tag{5.26}$$

Here $\boldsymbol{\mu}_{\text{body}}$, $\boldsymbol{\sigma}_{\text{body}}$ and $\boldsymbol{\mu}_{\text{wake}}$ respectively denote the vector of unknown body panel dipole strengths, the vector of body panel sources (which contains the effects of freestream, kinematic and wake velocity inflow) and the vector of wake panel dipole strengths respectively.

A Kutta condition is required to ensure that the distribution of dipole strengths represents approximately a physical reality. In the current method, for simplicity a linear Kutta condition is applied, following Katz and Plotkin (2001). The requirement of the Kutta condition is related to the dynamic boundary conditions on the wake – that the wake sheet does not support a pressure differential – and in two dimensions is approximated by requiring equal velocity at the trailing-edge panel centroids. Attempting this in three dimensions is not possible without under-determining the system of equations. The alternative is to specify $\Delta\phi$ at the trailing edge, and this is accomplished by including the strength of a proto-wake panel, attached to the trailing-edge, in the unknown dipole strength vector in Eq. (5.27), which becomes

$$\mathbf{A}\boldsymbol{\mu}_{\text{body}} + \mathbf{D}\boldsymbol{\mu}_{\text{proto-wake}} = \mathbf{B}\boldsymbol{\sigma}_{\text{body}} + \mathbf{C}\boldsymbol{\mu}_{\text{wake}}. \tag{5.27}$$

From a practical perspective, it is specified that ϕ at the trailing-edge sums to zero, giving $\mu_{\text{proto-wake}} = \mu_{\text{upper}} - \mu_{\text{lower}}$, allowing the two influence matrices on the LHS to be rolled together and the proto-wake panels' strengths solved for implicitly.

5.4.2.3 BEM Sub-Time-Stepping and Wake Model

Once the system of equations has been solved and the distribution of dipoles is known, a new wake panel is generated downstream of – but attached to – the the proto-wake panel. The new wake panel inherits its circulation, which remains constant, from the dipole strength of its proto-wake panel, and its position from the velocity field and time-step duration. Subsequent time-steps will produce additional panels between this one and the proto-wake panel to form a patch. The panel is evolved in the velocity field due to the body, wakes and freestream, until it is destroyed after a suitable number of additional time-steps, when its circulation is converted into a number of vortex blobs.

Since wake panels occur along the length of the trailing edge, they evolve together as a patch. When the patch has reached a certain size, i.e. after n time-steps, vortex blobs are generated at the corner points of the patch, and the strength of these blobs is taken from the circulation strength and edge orientation of the four (two for edge blobs, one for corner) panels that share the corner, by summation of half the contribution of the comprising panel edges. An alternative is to generate blobs at m locations along each edge, for example at the mid-point, and split the contribution of each edge in this manner.

In either case, the vortex blobs locations and strengths are determined by the abscissae and weights of a Gauss-Lobatto quadrature rule (which is accurate for polynomials of to degree $2n-3$ for n points – since the vortex filament strength is constant, then minimally 2 points are required). These options are shown schematically in Fig. 5.3.

The influences of the three wake sub-models are dealt with separately: the patches are dealt with using the traditional BEM, i.e. via influence coefficients; the blobs are dealt with using a direct summation with the Biot-Savart law, and are included along with the FMM far-wake contribution in the inflow calculation when specifying the source strengths. It is also possible to specify inflow velocity due to the panel wakes as an alternative to the classic BEM approach, however, doing so results in a small but significant discontinuity between the proto-wake (evaluated by perturbation potential coefficient) and the first row of wake panels (whose velocity influence would be sought). This inflow continuity error results in a new starting vortex at each outer time-step, and so the Dirichlet rather than Neumann BCs are preferred for the wake patches.

5.5 Some General Points and Conclusions

Multi-body Simulations In many cases the objective of the simulation is to determine the effect of a body on another – in arrays for example, or coaxial rotor systems. In these cases, the model is constructed in the normal manner: the geometry data is ingested, the BEM mesh created and influence matrices calculated etc. The principle difference between this and a single body case is that, from the point of view of the boundary element method, single body cases are effectively steady-state, even where the body is moving. In a multi-body case, if two bodies are moving such that they are both not translating together and rotating about a shared point, then the displacement between points on their surfaces will change in time. This requires the influence coefficients be calculated at each time-step, and this can prove potentially very expensive.

Recap This chapter has outlined the method of this thesis – and in particular the means by which the sub-components of the model are connected. The algorithm for time-stepping the various models has been presented, the means by which the BEM and FVM parts of the code are connected has been illustrated and the performance of the fast-multipole method used for velocity recovery has been demonstrated.

Impacts on this Thesis The model proposed in this thesis is now fully described, and some of the various sub-components have been demonstrated. What remains is to present

results from a barrage of tests on the model, proceeding from simple to complex cases and finally demonstrating the method applied in real world scenarios.

References

Baltazar, J. and Falcão de Campos, J.A.C. (2011). "Hydrodynamic analysis of a horizontal axis marine current turbine with a boundary element method." *Journal of Offshore Mechanics and Arctic Engineering*, **133**(4).

Brown, R. and Line, A.J. (2005). "Efficient high-resolution wake modeling using the vorticity transport equations." *AIAA Journal*, **43**(7): pp. 1434–1443.

Cheng, H., Greengard, L. and Rokhlin, V. (1999). "A fast adaptive multipole algorithm in three dimensions." *Journal of Computational Physics*, **155**(2): pp. 468–498.

Fletcher, T.M. and Brown, R.E. (2010). "Simulation of wind turbine wake interaction using the vorticity transport model." *Wind Energy*, **13**(7): pp. 587–602.

Katz, J. and Plotkin, A. (2001). *Low Speed Aerodynamics*. Cambridge University Press.

Suh, J.C. (2000). "The evaluation of the Biot-Savart integral." *Journal of Engineering Mathematics*, **37**: pp. 375–395.

Yokota, R. and Barba, L. (2011). "Comparing the treecode with FMM on GPUs for vortex particle simulations of a leapfrogging vortex rings." *Computers and Fluids*, **45**(1): pp. 155–161.

6

Unit Tests and Proof-of-Concept Studies in One and Two Dimensions

6.1 Introduction

The purpose of this chapter is to examine the performance of the various methods described in Chapters 2 to 5 for the discretisation of the vorticity transport equations and modelling immersed bodies. A series of tests of increasing complexity is deployed, with a view to reducing the number of factors by the time a three-dimensional method is reached so as to arrive at a baseline set of parameters for performing tests in three dimensions.

6.1.1 Relevance

The objectives of the tests are:

One-dimensional flow To ascertain the minimum time and spatial resolution required to preserve flow features over physical time scales. Accomplished by testing the performance of:

1. Finite-volume discretisation schemes for convection using the linear advection equation;
2. FVM schemes for the diffusion equation;
3. Time advancement schemes for both.

Two-dimensional flow To verify that the minimum requirements from one dimensional flow correspond, and additionally to test the combined vorticity transport wake/boundary-element method. Accomplished by testing the performance of:

1. Finite-volume discretisation schemes for convection using the linear advection equation;

2. Operator addition and operator splitting schemes for the same;
3. Application of FVM scheme to the vorticity-transport equation in the absence of a BEM;
4. Application of the combined vorticity FVM/BEM method to two-dimensional test cases.

The results of the tests are:

Quantitative metrics

- the errors between the computed and analytical solutions, expressed as a relative error;
- the errors between different spatial and temporal resolutions expressed in terms of the *grid convergence index*;

Qualitative metrics

- effects of the various schemes on the ability to capture and adequately represent the shape and distribution of the solution;
- the ability of the scheme to remain stable, and remain TVD.

The factors of the tests in this chapter for the finite-volume part of the method applied to the general transport equations are:

- temporal and spatial resolutions (i.e. CFL and von Neumann conditions);
- temporal and spatial accuracy (i.e. order of accuracy of integration);
- effects of the choice of flux-limiter function (minmod, superbee, . . .);
- effects of approach to combining operators (i.e. adding or splitting);

The tests are performed such that, while incrementally increasing complexity in the solution, the number of factors tested is reduced. Tests performed in one dimension will examine, in the absence of a spatially varying velocity field and with flow aligned to the cell faces, the performance of finite-volume schemes for advection and diffusion at various spatial and temporal resolutions and the effects on solution accuracy of higher than first-order integration strategies. Tests in two dimensions focus on the ability to adequately model flow which is not aligned to the cell faces, and in particular rotating flow. Tests will be performed on the general transport and vorticity transport equations. Finally, tests in two dimensions which couple the finite-volume and boundary-element methods will be performed as a proof-of-concept for the method of this thesis.

6.2 One-Dimensional Flow Cases

6.2.1 Diffusion Test Cases

Description. In order to test the performance of the diffusion discretisation scheme, consider the time evolution of the general transport equations in absence of a velocity field by evaluating the diffusion equation,

$$\frac{\partial \varphi}{\partial t} = \Gamma \frac{\partial^2 \varphi}{\partial x^2}, \tag{6.1}$$

in the domain $x \in [-1, 1] \times t \in [t_0, t]$. Here Γ is a diffusion coefficient.

Problem Definition. Since the pure diffusion equation is parabolic, boundary conditions must be specified at all domain boundaries. Defining a Gaussian distribution of φ centred at x_c on an "infinite" domain at time t_0 by

$$\varphi\left(x, t_0\right) = \exp\left(-\frac{\left(x - x_c\right)^2}{4\Gamma t_0}\right), \tag{6.2}$$

and allowing it to diffuse, the time evolution of the distribution is given analytically by

$$\varphi\left(x, t\right) = \sqrt{\left(\frac{t}{t_0}\right)} \exp\left(-\frac{\left(x - x_c\right)^2}{4\Gamma t_0}\right). \tag{6.3}$$

This is used to provide the time varying spatial boundary conditions for the ends of the truncated (i.e. finite) domain. It is thus possible to determine the adequacy of the diffusion discretisation in time and space by comparison of results obtained using numerical methods throughout the domain with those given analytically using Eq. (6.3).

Details of Numerical Experiments Numerical experiments are performed setting an arbitrary diffusion coefficient $\Gamma = 1$ (see following paragraph), and with domain discretisations of 50, 100 and 200 cells with time-steps corresponding to von Neumann numbers $\sigma = 1/2$, $1/4$ and $1/8$. The nonzero starting time is chosen such that the width of the bottom of the pulse (which varies with $\sqrt{\Gamma t}$) is sufficiently resolved, having a width of approximately 1 giving the minimum number of cells as approximately 26 (i.e. the number of cells between the two cells where $\varphi(x) \approx 1.5 \times 10^{-2}$) for a domain of 50 cells.

Numerical Results Since the evolution and initial conditions are dependant on starting time t_0, results are presented at a non-dimensional time $\tau = t/t_0$ which effectively decouples the effect of different viscosity coefficients from the time required to reach a particular stage of solution evolution, e.g. $\varphi(\Gamma_1, \tau) = \varphi(\Gamma_2, \tau)$ for positive and different Γ_1 and Γ_2.

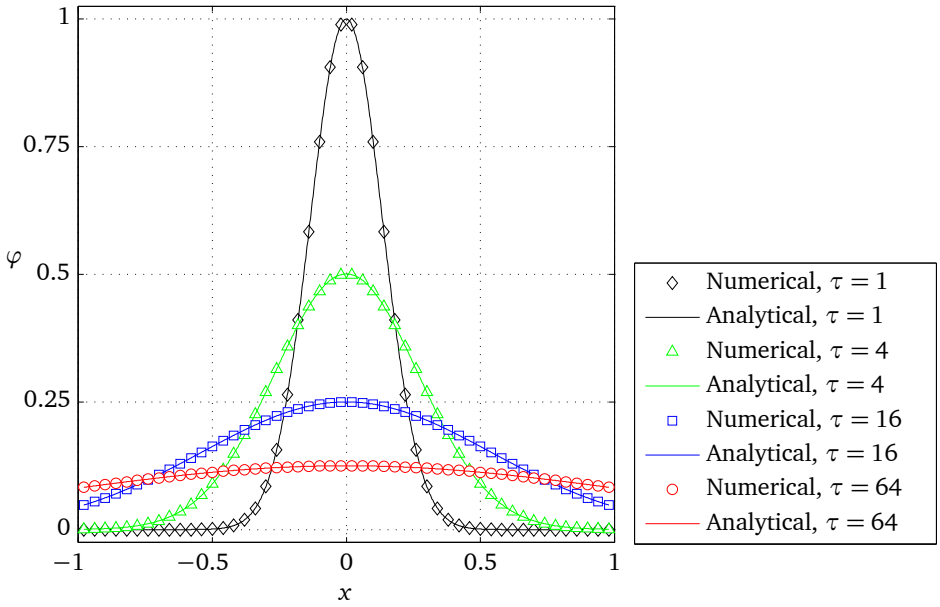

Figure 6.1: Euler integrated one-dimensional diffusion only test case. Initial conditions ($\tau = 1$) and results at $\tau = 4$, $\tau = 16$ and $\tau = 16$ for a domain of 50 cells.

Table 6.1: Grid convergence study for diffusion equation using finite-volume with $\mathcal{O}(\Delta t)$ (a,b) and $\mathcal{O}(\Delta t^2)$ (c,d) time-stepping. Norms of errors for decreasing von Neumann number (σ) taken at non-dimensional times $\tau = 8$.

	φ error l^1 norm						GCI %		
σ	Coarse	Medium	Fine	Continuum	R	p	m-c	f-m	ratio
1/4	4.23×10^{-5}	1.04×10^{-5}	2.58×10^{-6}	4×10^{-8}	0.2	2.0	1.3×10^{-3}	3.2×10^{-4}	1.0
1/8	1.12×10^{-5}	2.72×10^{-6}	6.71×10^{-7}	2×10^{-8}	0.2	2.0	3.4×10^{-4}	8.2×10^{-5}	1.0
1/16	3.80×10^{-5}	9.28×10^{-6}	2.30×10^{-6}	5×10^{-8}	0.2	2.0	1.2×10^{-3}	2.8×10^{-4}	1.0

(a) Error norms due to an Euler integrated $\mathcal{O}(h^2)$ scheme.

1/4	1.06×10^{-4}	2.61×10^{-5}	6.49×10^{-6}	6×10^{-8}	0.2	2.0	3.3×10^{-3}	8.0×10^{-4}	1.0
1/8	5.30×10^{-5}	1.31×10^{-5}	3.24×10^{-6}	3×10^{-8}	0.2	2.0	1.6×10^{-3}	4.0×10^{-4}	1.0
1/16	2.64×10^{-5}	6.53×10^{-6}	1.62×10^{-6}	6×10^{-9}	0.2	2.0	8.2×10^{-4}	2.0×10^{-4}	1.0

(b) Error norms due to an Euler integrated $\mathcal{O}(h^4)$ scheme

1/4	6.52×10^{-5}	1.59×10^{-5}	3.92×10^{-6}	1×10^{-7}	0.2	2.0	2.0×10^{-3}	4.8×10^{-4}	1.0
1/8	6.49×10^{-5}	1.59×10^{-5}	3.92×10^{-6}	8×10^{-8}	0.2	2.0	2.0×10^{-3}	4.8×10^{-4}	1.0
1/16	6.49×10^{-5}	1.59×10^{-5}	3.92×10^{-6}	8×10^{-8}	0.2	2.0	2.0×10^{-3}	4.8×10^{-4}	1.0

(c) Error norms due to an $\mathcal{O}(\Delta t^2)$ integrated $\mathcal{O}(h^2)$ scheme.

1/4	6.11×10^{-7}	3.81×10^{-8}	2.37×10^{-9}	2×10^{-12}	0.1	4.0	4.8×10^{-6}	3.0×10^{-7}	1.0
1/8	3.60×10^{-7}	2.23×10^{-8}	1.39×10^{-9}	5×10^{-12}	0.1	4.0	2.8×10^{-6}	1.7×10^{-7}	1.0
1/16	2.97×10^{-7}	1.84×10^{-8}	1.15×10^{-9}	4×10^{-12}	0.1	4.0	2.3×10^{-6}	1.4×10^{-7}	1.0

(d) Error norms due to an $\mathcal{O}(\Delta t^2)$ integrated $\mathcal{O}(h^4)$ scheme.

The variables of interest in this test are: the minimum resolution (found to be 26 cells); the order of time integration ($\mathcal{O}(\Delta t)$ Euler or $\mathcal{O}(\Delta t^2)$ Runge-Kutta); the order of the approximation to the face derivatives is limited to $\mathcal{O}(h^2)$ central differences or $\mathcal{O}(h^4)$ central difference.

Some indicative snapshots of the results at various solution times are presented in Fig. 6.1, and Table 6.1 contains a grid convergence study of results at $\tau = 8$. The key outcomes are that in tests using either Euler or Heun integration, l^1 and l^∞ convergence for low-order spatial schemes matches that expected, whereas fourth-order spatial convergence is only achieved with second-order time-stepping. Similarly, expected first- and second-order temporal convergence is only obtained when using the fourth-order difference scheme: otherwise results are either oscillatory when using the Euler scheme, or converge very slowly with the Runge-Kutta scheme. Either way, the grid convergence metrics of the low-order scheme combinations are not sufficiently powerful to indicate that anything other than a fourth-order in space, second-order in time scheme should be used, especially given the minimal overhead associated with using the higher order scheme. What these results demonstrate is that the error in the approximation to the diffusion equation is very small, diminishes in time, and can be reduced slightly by decreasing the von Neumann number σ. Given that $\Gamma = 1$ for these tests, but in "real life" flows is replaced by a kinematic viscosity ν between 1×10^{-6} to $2 \times 10^{-6}\,\mathrm{m^2\,s^{-1}}$ for water, in linear advection and vorticity transport simulations, errors due to e.g. artificial diffusion will tend to swamp these small errors.

6.2.2 Advection

Description. Presented here are results from a series of studies of the finite-volume discretisation of the advection equation in one dimension. By solving the linear convection equation in the absence of diffusion, any dissipation will be entirely artificial and an artefact of the method. Two cases are examined: a sinusoidal pulse, and a series of discontinuous waves. The smooth wave allows most schemes to be examined, and (expected) phase errors in schemes which would be unusable near discontinuities can be checked. It also allows testing whether the time-marching and spatial schemes converge at the formally stated rate. The discontinuous waves allow the performance and characteristics of the flux limiters to be examined.

Problem Definition. The problem is to obtain the solution at increasing times of

$$\frac{\partial \varphi}{\partial t} + u\nabla\varphi = 0, \tag{6.4}$$

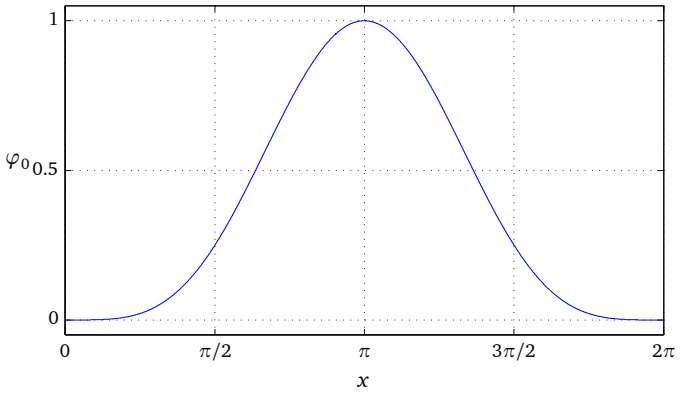

(a) Smooth initial data

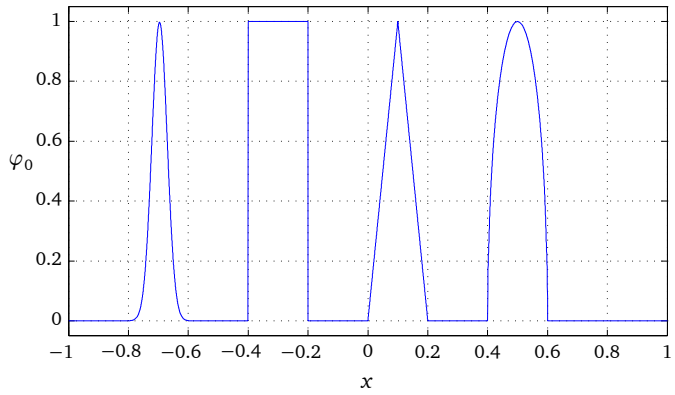

(b) Discontinuous initial data

Figure 6.2: One-dimensional advection only test case initial conditions.

subject to various initial conditions. These are chosen to be a sinusoidal pulse whose form is simply

$$\varphi_0(x) = \sin^4 x, \tag{6.5}$$

over the periodic bounded domain $-2\pi \leq x < 2\pi$, and a tight series of 4 discontinuous waves over periodic $-1 \leq x < 1$. The waves are defined by the initial conditions:

$$\varphi_0(x) = \begin{cases} \frac{1}{6}(F(x,\beta,z-\delta) + F(x,\beta,z+\delta) + 4F(x,\beta,z)) & \text{if } -0.9 \leq x \leq -0.7, \\ 1 & \text{if } -0.5 \leq x \leq -0.3, \\ 1 - |10(x-0.1)| & \text{if } -1 \leq x \leq 0.1, \\ \frac{1}{6}(G(x,\alpha,a-\delta) + G(x,\alpha,a+\delta) + 4G(x,\alpha,a)) & \text{if } 0.3 \leq x \leq 0.5, \\ 0 & \text{otherwise;} \end{cases} \tag{6.6a}$$

$$F(x,\beta,z) = \mathrm{e}^{-\beta(x-z)^2}, \quad G(x,\alpha,a) = \sqrt{\max(1-\alpha^2(x-a)^2, 0)}; \tag{6.6b}$$

namely a Gaussian, a square wave, a triangular peak and a half-ellipse. The constants $a = 0.5$, $z = -0.7$, $\delta = 0.005$, $\alpha = 10$ and $\beta = \frac{\log 2}{36\delta^2}$. The sinusoidal pulse provides a demonstration of the schemes with a relatively smooth signal whereas the discontinuous wave provides the counterexample.

The problem set-up shown in Fig. 6.2a and Fig. 6.2b is a domain of length 100, 200 of 400 cells, with a velocity $u = 1.0$ from left to right. Above 100 cells resolution (in images at this scale) there is no observable difference in the general appearance of the initial-conditions, and most images show the lowest resolution results for clarity. Time-stepping was performed at a range of Courant numbers: 1/2, 1/4 and 1/8. The tests were performed for sufficient time-steps to allow a number of cycles of the signal.

Numerical Results: Smooth Initial Conditions Figure 3.2 shows a representative subset of the results for the first-order and non-limited second-order schemes. Figures 6.3 to 6.4 shows an excerpt of the results taken for the smooth initial conditions. Table C.1 shows the results of a grid convergence study on the calculated l^1 and l^∞ norms of the errors obtained over a sweep of space resolutions. The l^1 norm of the error is the global error metric and represents the average error per cell. The l^∞ norm is the maximum error. A solution can be convergent in one and not the other due to some combination of compensating errors – for example by having very localised but strong errors in an otherwise large and accurately rendered solution, as occurs in high resolution superbee cases. For this reason it only makes sense to consider the error norms for the smooth solution, since small deviations in the discontinuous solution can result in disproportionately large error values. Table C.3

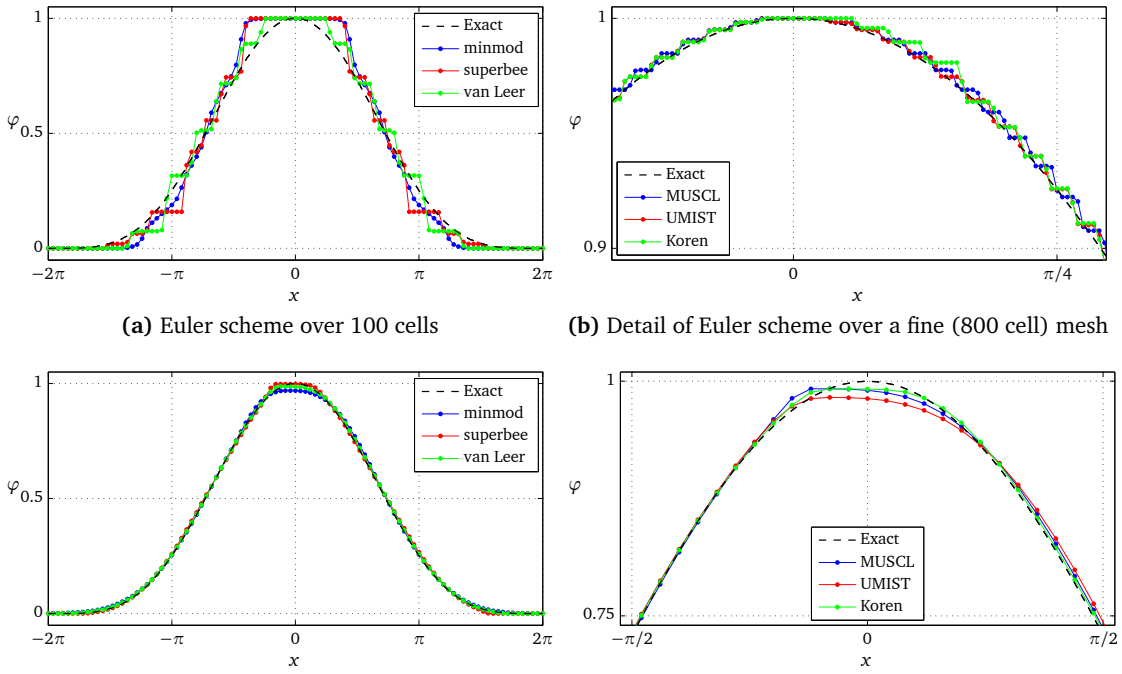

(a) Euler scheme over 100 cells

(b) Detail of Euler scheme over a fine (800 cell) mesh

(c) Heun's method over 100 cells

(d) Detail of Heun's method over a 100 cell mesh

Figure 6.3: Comparison of representative schemes using first- and second-order integrators for continuous initial conditions ($\varphi_0 = \sin^4 x$).

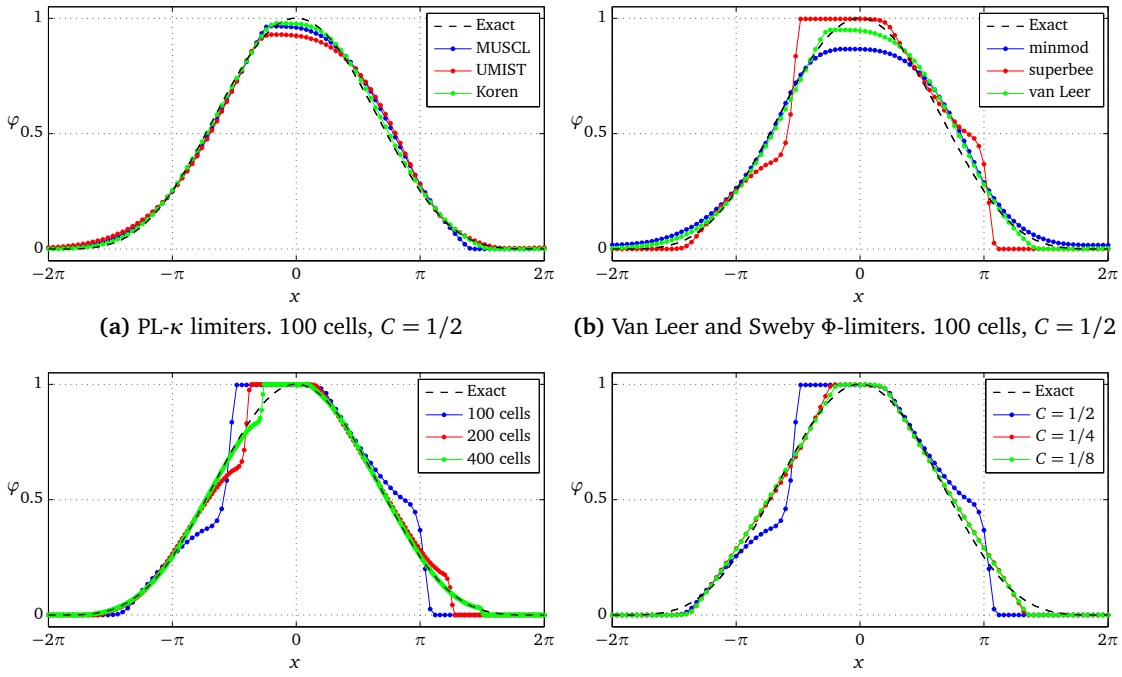

(a) PL-κ limiters. 100 cells, $C = 1/2$

(b) Van Leer and Sweby Φ-limiters. 100 cells, $C = 1/2$

(c) superbee over various meshes. $C = 1/2$

(d) superbee at various Courant numbers

Figure 6.4: Comparison of schemes using second-order time integrators for continuous initial conditions ($\varphi_0 = \sin^4 x$).

contains a convergence study for decreasing time-step applied over a 400 cell mesh. The results presented here are the residuals between different refinement levels, rather than the error between the computed and expected results as before. This allows the convergence behaviour in Δt to be examined independently of the accuracy predicted result – i.e. answer whether the results become more precise.

The first-order upwind scheme is extremely dissipative, as expected, and should be considered unusable. Also as expected, higher than first-order schemes are completely unstable when using Euler integration, and produce under/overshoots as well as leading/lagging the true solution with Heun's method, rendering them unusable.

Euler integration results in steepening of slopes, eventually resulting in "squared" waves with all flux limited schemes – see Fig. 6.3a – even when extremely high numbers of cells are used – e.g. Fig. 6.3b. This can be ameliorated somewhat by decreasing the Courant number, however this only serves to reduce the rate at which the squaring-off occurs and in time Euler integrated results will become unusable.

Heun's second-order Runge-Kutta method reduces or eliminates this effect, resulting in considerably smoother solutions which match those expected significantly better – see Fig. 6.4 – and results are now more dependant on the flux limiter function used. Initially, after one revolution, all flux limited schemes render the solution relatively smoothly and with good accuracy. However, after ten revolutions, compared to the van Leer and PL$-\kappa$ limiters, minmod demonstrates relatively diffusive behaviour, and superbee steepens and compresses the signal to such an extent that at all time and space resolutions examined it is completely distorted: superbee is not usable, and minmod use requires careful consideration.

The grid convergence metrics in Table C.1 bear this out: after 10 revolutions and as the mesh density increases, the superbee limiter l^1 error norm is not convergent ($R > 1$ indicating monotonic divergence), even though the l^∞ error is. This is because although the maximum error is decreasing, the average error per cell is growing as the gap between the real and computed solutions increases.

The order of convergence is broadly as expected for the symmetric limiters, at least for the short time simulations. After 10 revolutions, there is some drift in convergence order, especially for l^1 norms and in particular, minmod suffers. The implication is that increasing resolution results in less overall reduction in errors throughout the domain – evidenced by the continuum error magnitudes and the GCIs – than using the more convergent Koren limiter.

According to the grid convergence metrics, the Koren limiter shows the least drift in

apparent convergence over time, maintaining approximately $\mathcal{O}(h^{2.5})$ accuracy in both l^1- and l^∞ norms of the error and the lowest errors in each test. This is slightly lower than the expected convergence rate of $\mathcal{O}(h^3)$ but slightly higher than the other limiters.

Grid convergence studies at low/moderate spatial resolutions (100-400 cells) result in convergence at approximately the formal order of the spatial schemes but slightly higher for the temporal schemes. At increasing spatial resolution, convergence studies on the time-step length show that at moderate Courant number, $1/8 \leq C \leq 1/2$, the errors converge very quickly – at higher than the formal rate – and it is only at much lower Δt, i.e. $1/32 \leq C \leq 1/8$, that the formal (second) order of Heun's method is recovered. The implication is that at low grid resolutions the errors are primarily composed of truncation errors in space, and it is only at the finer resolutions that these diminish enough to isolate the errors due to the time integration scheme.

Numerical Results: Discontinuous Initial Conditions Analysis of the results with discontinuous initial data is somewhat more challenging, since it is not particularly insightful to compare numerical with exact and computed results in a l^1 or l^∞ sense since very small deviations in the solutions (e.g. small phase differences) can result in very large amplitude errors, especially around sharp corners. Rather, the quantitative metrics will be the solution value sampled at $x = 0$, i.e. at the midpoint of the triangular wave, and also the integrated value of φ in $-0.5 \leq x \leq -0.3$, which corresponds to the area underneath the square wave. The correct values of these are 1.0 and 0.2 respectively. Considering the triangular peak will demonstrate how much "rounding-off" has occurred due to an inability to retain a sharp wave even if a somewhat compressed nub of the triangle remains; the integration under the square wave will indicate the relative diffusiveness of the scheme by demonstrating how much φ has dissipated out of this region.

Qualitative metrics are simply the appearance of the results. Of particular importance, given the performance of superbee in the smooth ICs tests, is the ability of the model to maintain square waves without overly sharpening the rounded waves.

A sweep over 200, 400 and 800 cells reveals that superbee is still performing relatively poorly, with obvious errors in the advancing face and that the minmod scheme is the most diffusive, with almost all information about the distribution of φ lost after 10 revolutions. Since these represent the two extremes of the second-order limiters, these results are to be expected. Grid convergence metrics confirm the poor performance of minmod, even over short durations, and both van Leer and UMIST also appear relatively diffusive over long terms, with van Leer performing slightly worse in the discontinuous case than the MUSCL scheme. The most satisfactory results are therefore obtained using MUSCL and

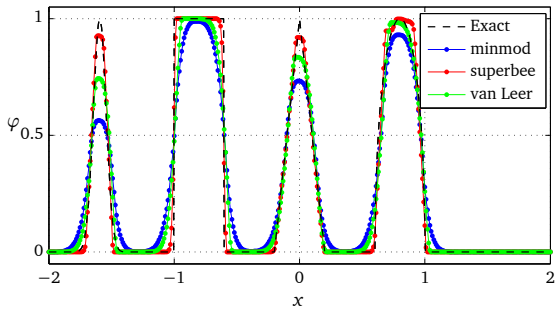

(a) Van Leer and Sweby Φ-limiters. 1 revolution, 400 cells, $C = 1/8$

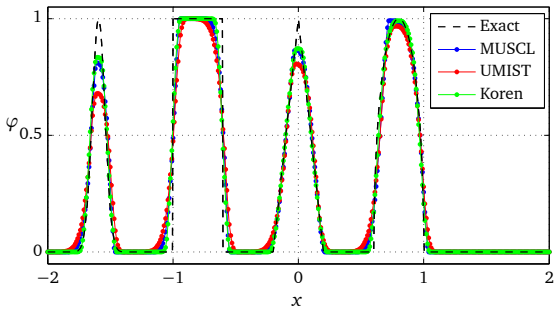

(b) PL-κ limiters. 1 revolution, 400 cells, $C = 1/8$

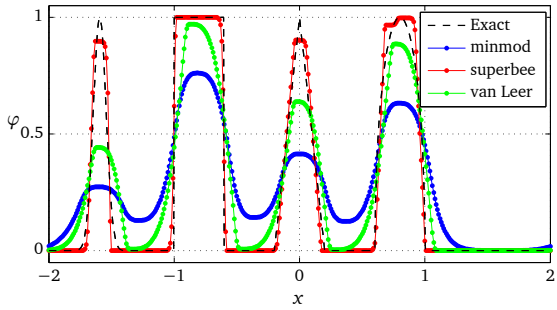

(c) Van Leer and Sweby Φ-limiters. 10 revolutions, 400 cells, $C = 1/8$

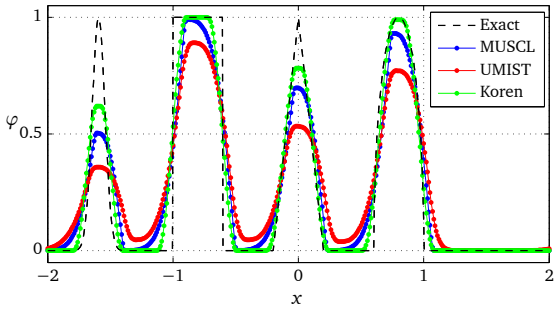

(d) PL-κ limiters. 10 revolutions, 400 cells, $C = 1/8$

Figure 6.5: Comparison of schemes using second-order time integrators for discontinuous initial conditions.

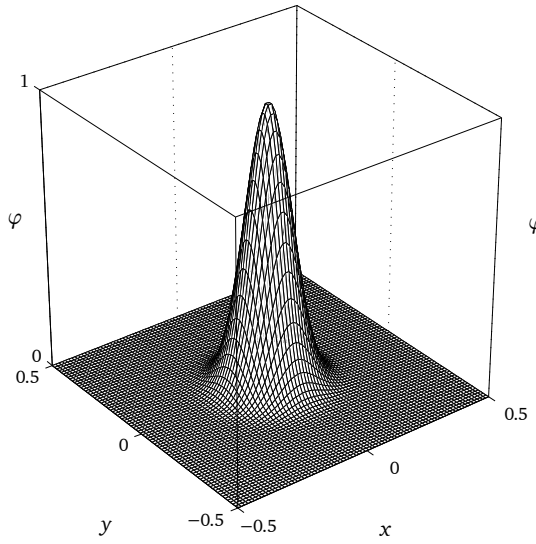

(a) Translational flow

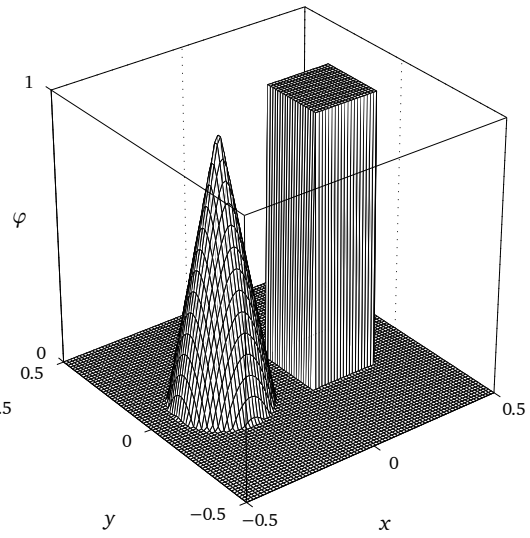

(b) Rotational flow

Figure 6.6: Surface plots of initial conditions of scalar function $\varphi(x, y, t_0)$ for two-dimensional test cases.

Koren schemes, which appear convergent at the expected rate. Of the pair, although there is not much to pick between them, Koren offers the best resolution of discontinuities, as is apparent in Fig. 6.5.

Conclusions which can be drawn from these results are:

- discount minmod as it is too diffusive;
- discount superbee as it is too compressive;
- discount UMIST as it performs worse than the other limiters at these resolutions and over long timescales;
- Koren performs better in resolving discontinuities than van Leer and MUSCL;
- MUSCL performs very slightly better than van Leer; however
- van Leer performs quite satisfactorily and has the advantage that it requires evaluation of a single algebraic function [floating point $\texttt{abs}(\theta)$] and is thus the least computationally expensive to use.

6.3 Two-Dimensional Flow Cases

6.3.1 Advection

To test the performance of the schemes with general transport equation in two dimensions, test cases involving the convection of a continuous and discontinuous initial conditions (in this case a Gaussian blob and a triangular/square wave distribution respectively) are considered. The first is a diagonal flow test case (flow parallel to a particular axis being essentially one-dimensional) and the second is a rotating flow case. Initial conditions for the diagonal flow case are shown in Fig. 6.6a and for the rotating flow case in Fig. 6.6b, and the particulars are described below.

6.3.1.1 Unit Test 1: Diagonal Flow

Description. This test examines the performance of the finite-volume aspect of the code in modelling the (linear) advection of a Gaussian blob in the absence of shear. A scalar blob is advected in a diagonal flow over a periodically bounded domain using the various integration schemes described in Chapter 3 which were identified in Section 6.2 as the most promising. Since the true solution to this test after an integral number of periods is the un-deformed initial conditions, this test represents a simple means of analysis.

Relevance. This test allows a comparison of both the advection discretisation schemes and the time-stepping schemes in the simplest truly two-dimensional test case. Confidence is gained that the methods are convergent, and experience in the spatial and temporal resolutions required to resolve flow-features is acquired.

Problem Definition. Consider a square domain of unit side length, with periodic boundary conditions in both directions and a velocity field throughout of $u = v = 1.0$ which convects a scalar φ.

Initial conditions are given by a discretisation of the Gaussian blob

$$\varphi\left(x, y\right) = \frac{h^2}{4\pi} \exp\left(\frac{r^2}{2c^2}\right), \tag{6.7}$$

centred on the origin, where h is the mesh spacing (uniform in both x and y directions), r is the radius of $\left(x, y\right)$ about the origin and $c = 0.075$. Figure 6.6a shows a surface plot of the initial conditions.

Since the flow is periodic and φ is inert, the scalar field after each period can be compared with the initial conditions to determine the error.

Details of Numerical Experiments The initial condition scalar is binned into the FVM mesh, and the Gaussian blob is truncated (by setting the cell values to zero) when $r^2 > 0.125$. As the factors of interest are the integration schemes, spatial mesh densities are used which double with each test, with tests performed using 101, 201 and 401 cells along the sides of the domain. This corresponds to 71, 141 and 281 cells across the diameter of the blob, respectively. (The extra cell is used to enable the value of $\varphi(0, 0)$ to be taken directly rather than by interpolation.) Time-step lengths are specified using Courant numbers of 0.5, 0.25 and 0.125 (in both the x and y directions).

For the finite-volume schemes, tests consider the second order upwind schemes obtained using the van Leer, MUSCL and Koren limiters (as one-dimensional tests showed the Sweby Φ-limiters unusable, and a small advantage in using the MUSCL over the UMIST quadratic schemes).

For time integration, operator addition using Heun's second-order Runge-Kutta scheme and the time-stepping obtained using second-order operator splitting in alternating-dimension (AD) and symmetrically weighted sequential splitting (SWSS) forms are considered.

Numerical Results A subset of the numerical results is presented in Fig. 6.7. These are run at a Courant number of $C = 1/4$ in each dimension and are taken after 5 solution

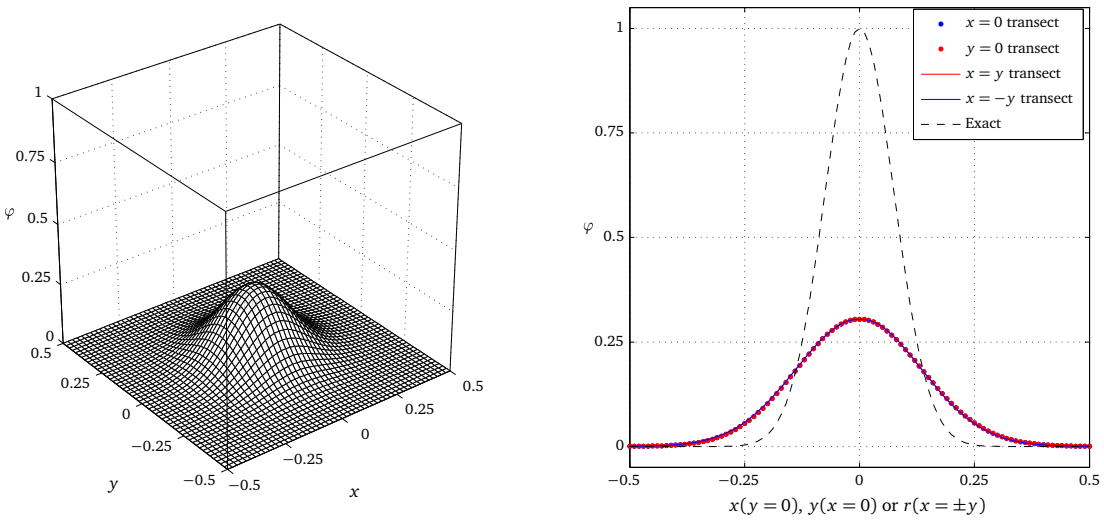

(a) Operator addition, Heun integration

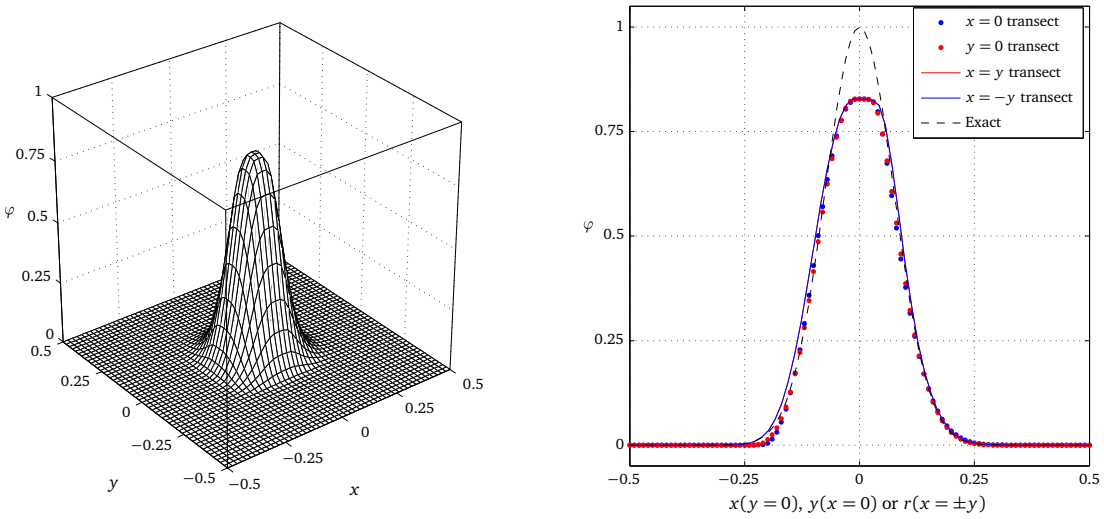

(b) Alternate dimension operator splitting

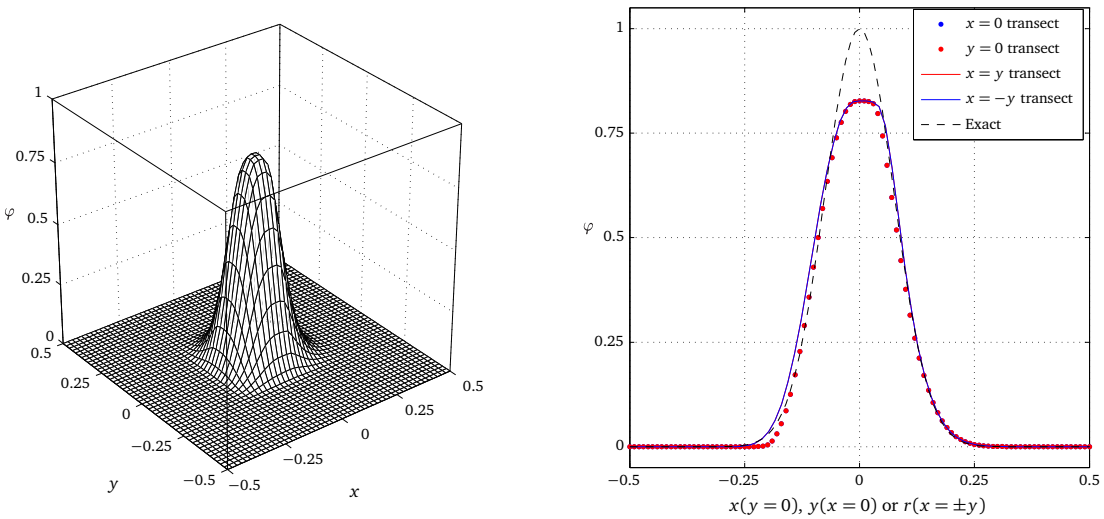

(c) Symmetrically weighted sequential splitting

revolutions from the lowest resolution grids. This is in order to draw out major differences between each scheme which are obscured from view at higher resolutions. A cursory visual inspection reveals that the most striking disparity between the methods is between the Heun integrated operator addition and the second-order splitting schemes. This is perhaps expected since the operator adding methodology is known to be only first-order accurate in time, even when using a second-order time integrator, since it updates the cell average φ due to the information contained in neighbouring cells without taking into account that contained in its diagonal neighbours. (In other words, in the naïve implementation of the semi-discrete version of Eq. 3.10 using Heun's multistep second-order Runge-Kutta method in two dimensions, the second-order cross-derivatives in the Taylor expansion of $\varphi(t+\Delta t)$ have not been modelled. These are also neglected in the forward Euler method. While the individual dimensional integrations are second-order – as minimally required due to the results in Section 6.2 – globally the method is only first-order in h and these errors swamp the potential savings due to more accurate time-stepping.)

The difference between the second-order schemes is much less obvious, with a subtle asymmetry in the distribution of φ on the faces of the blob visible in the alternate dimension scheme, as expected due to its non-symmetrical application of operators. Aside from this, the apparent accuracy of the second-order methods is visually very similar. A grid convergence study is given for the splitting schemes in Table 6.2. The metrics for these studies are the l^1 norms of the error between the computed and exact solution, obtained at successive grid refinement levels as well as the height of the φ peak at the origin. The results demonstrate the expected second-order h convergence on the true solution according to the l^1 norms of the error, and while approximation of the peak height is also convergent, it is at a slightly lower rate.

Figure C.1 shows cell values over the domain for low and high resolution cases, taken after five revolutions, using each method. These, along with the diagonal transects in Fig. 6.7 give an indication of the quality of the reproduction of the circular distribution in the initial condition.

Discussion The obvious result of these tests is that the second-order time-stepping via operator addition is insufficient as, in this instance, the method becomes excessively diffu-

---

Figure 6.7*(facing page)*: Diagonal flow test case on a 101×101 cell square mesh using (a) operator addition via Heun's method, (b) Strang splitting and (c) symmetrically weighted sequential splitting. Surface plots (left) showing every second cell; solution transects (right) showing results along major and minor diagonals, and x and y axes. Results are taken after 5 revolutions, Koren limiter, $u = v = 1$, $C_{\max} = 1/4$.

Table 6.2: Grid convergence study for two-dimensional diagonal convection of a Gaussian blob using second-order alternate dimension (a) and symmetrically weighted sequential splitting (b) schemes with various limiters. Results taken after five solution revolutions, with Courant numbers in each direction $C = 1/4$ and $u = v = 1$.

		(i) φ error l^1 norm or (ii) φ at $(0,0)$						GCI %		
Scheme		Coarse	Medium	Fine	Continuum	R	p	m-c	f-m	ratio
van Leer	(i)	4.95×10^{-3}	1.43×10^{-3}	4.07×10^{-4}	-1×10^{-5}	0.3	1.8	0.2	0.05	1.0
	(ii)	7.53×10^{-1}	9.01×10^{-1}	9.63×10^{-1}	1	0.4	1.3	10	6	0.9
MUSCL	(i)	3.90×10^{-3}	1.08×10^{-3}	3.18×10^{-4}	3×10^{-5}	0.3	1.9	0.1	0.04	1.0
	(ii)	8.29×10^{-1}	9.40×10^{-1}	9.78×10^{-1}	1	0.3	1.6	8	3	1.0
Koren	(i)	3.07×10^{-3}	7.68×10^{-4}	2.18×10^{-4}	4×10^{-5}	0.2	2.1	0.09	0.02	1.0
	(ii)	8.28×10^{-1}	9.41×10^{-1}	9.79×10^{-1}	1	0.3	1.5	8	3	1.0

(a) Convergence metrics for $\mathcal{O}(\Delta t^2)$ AD splitting

van Leer	(i)	4.25×10^{-3}	1.21×10^{-3}	3.39×10^{-4}	-1×10^{-5}	0.3	1.8	0.2	0.04	1.0
	(ii)	7.62×10^{-1}	9.05×10^{-1}	9.64×10^{-1}	1	0.4	1.3	10	5	0.9
MUSCL	(i)	3.20×10^{-3}	8.26×10^{-4}	2.35×10^{-4}	4×10^{-5}	0.2	2.0	0.1	0.02	1.0
	(ii)	8.39×10^{-1}	9.46×10^{-1}	9.81×10^{-1}	1	0.3	1.6	7	2	1.0
Koren	(i)	3.35×10^{-3}	8.78×10^{-4}	2.51×10^{-4}	4×10^{-5}	0.3	2.0	0.1	0.03	1.0
	(ii)	8.27×10^{-1}	9.39×10^{-1}	9.78×10^{-1}	1	0.4	1.5	8	3	1.0

(b) Convergence metrics for $\mathcal{O}(\Delta t^2)$ SWSS splitting

sive by comparison with the spatially higher-order schemes. The splitting schemes perform considerably better and, whilst only utilising Euler sub-stepping and thus being formally first-order accurate in time, display second-order error l^1 convergence in space (see Table 6.2). The very slight difference between the alternate-dimension and symmetric splitting schemes is only apparent by examining graphically the distribution of φ on the faces of the Gaussian pulse. The cost of the symmetric distribution is an additional application of the convection scheme and this introduces additional artificial diffusion. Given the similarity in magnitude between the errors, the very close agreement in both the distribution of φ in Fig. C.1, and the fine grid values of the grid convergence metrics, it is likely that the slight accuracy penalty in not obtaining truly symmetrical results is so small that it would be swamped by errors introduced elsewhere, and offset by the computational cost savings.

6.3.1.2 Unit Test 2: Rotational Flow

Description. This test also examines the performance the finite-volume aspect of the code in modelling the (linear) advection of an initial scalar field, theoretically in the absence of shear. A scalar field is advected in a rotating flow in a periodically bounded domain using the various integration schemes described in Chapter 3. Again, because the scalar field evolves under a solid-body rotation and the true solution to this test after an integer number of periods is the un-deformed initial conditions, this test represents a simple route for analysis of the schemes.

Previous Results This test follows very slightly modified case particulars as described by (LeVeque, 2002, §20.8.2).

Relevance. This test allows a comparison of both the advection discretisation schemes and the time-stepping schemes in a more complicated two-dimensional test case where local cell velocities – and hence Courant numbers – are different. Confidence is gained that the methods are convergent, and experience is gained in the spatial and temporal resolutions required to resolve features in a rotating flow.

Problem Definition. Consider a square domain of unit side length, with periodic boundary conditions in both directions and a velocity field throughout defined by the divergence free velocity field obtained from the stream function $\psi\left(x,y\right)=x^2+y^2$:

$$u\left(x,y\right)=2y; \tag{6.8a}$$

$$v\left(x,y\right)=-2x. \tag{6.8b}$$

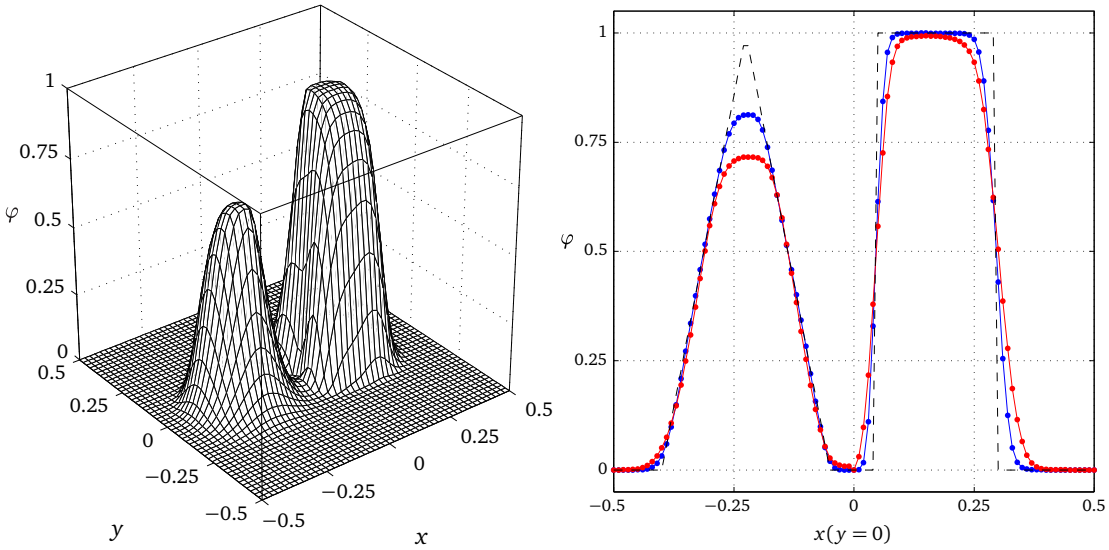

(a) 101 × 101 cells

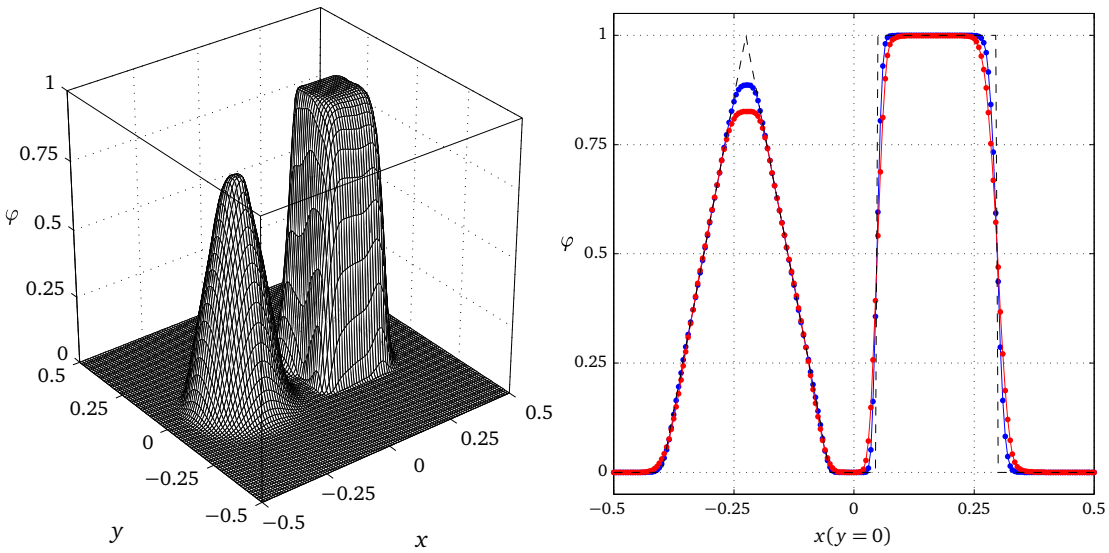

(b) 201 × 201 cells

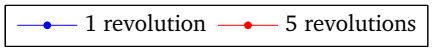

Figure 6.8: Rotating flow test case on 101 × 101 (top) and 201 × 201 (bottom) cell square meshes using symmetrically weighted sequential splitting and the van Leer scheme. Surface plots (left) showing every second cell with results sampled after 5 revolutions; solution transects (right) showing results along and x axes, taken after 1 and 5 revolutions. Velocity field obtained from stream function $\psi(x, y) = x^2 + y^2$, $C_{\max} = 1/4$.

Initial conditions are given by a discretisation of the scalar field

$$\varphi(x,y) = \begin{cases} 1 & \text{if } 0.05 < x < 0.3 \text{ and } -0.125 < y < 0.125, \\ 1 - \dfrac{r}{0.175} & \text{if } r \equiv \sqrt{(x+0.225)^2 + y^2} < 0.175, \\ 0 & \text{otherwise.} \end{cases} \tag{6.9}$$

This describes a uniformly zero scalar field, except in offset square and conical regions where – respectively – φ is set uniformly to, and linearly grows to unity. The mesh spacing h is uniform in both x and y directions. Figure 6.6b shows a surface plot of the initial conditions.

Details of Numerical Experiments. The initial condition scalar distribution is binned into the FVM mesh. Spatial resolutions are the same as for the diagonal flow test case, as are the same (maximum in this case) Courant numbers. The details of the schemes and analysis are as defined previously.

Numerical Results A subset of results is presented in Figs. 6.8, C.2 and C.3. Surface plots for the φ distributions are given in illustrative cases using the van Leer and Koren limiters. Visually, the main difference appears to be something of a rounding off of the sharp corner on the downstream face of the square block when using the van Leer scheme at all resolutions, see Fig. 6.8 in particular. However, overall performance is very good, and in line with results obtained in the diagonal flow cases – it required five solution revolutions to distinguish between results, and even then only the low resolution cases deviated sufficiently to display graphically.

Discussion These results demonstrate the method can model rotating flows in the absence of shear while maintaining the integrity of the distribution of transported variables. This might actually not be so important in vortex flows, since these will tend to be semi-self organising in that the distribution will naturally tend to axi-symmetrification or vortex street/Helmholtz instability type arrangements in viscous and even “shear-free” (read inviscid Lagrangian) flows.

6.3.2 Relaxation of a Perturbed Monopole into a Tripole Attractor

Description. The evolution of a vortex monopole perturbed by a quadrupole is used here as a unit study to examine the performance of the finite-volume and the fast-multipole methods in the absence of a turbine blade model. Modifying a base Gaussian vortex blob with a quadrupole perturbation results in the vorticity fields shown in Figure 6.9.

Previous Results. This section follows a series of tests performed in Rossi, Lingevitch and Bernoff (1997) and later in Barba (2004). Rossi, Lingevitch and Bernoff uses the test as a means of demonstrating a non-linear vortex blob model which uses both particle splitting and core spreading. Barba tests against their results in a proof-of-concept study of her method which places vortex particles in a regular lattice. The idea is that for above a certain perturbation magnitude the vortex quadrupole will relax into a quasi-steady, rotating tripole, whereas for perturbations below this threshold, the system will decay into an axisymmetric monopole.

Relevance. The two major processes governing the evolution of two-dimensional turbulent flow are vortex axisymmetrisation, where complex structures decay into an axisymmetric state, and vortex merging, which occurs when vortices of the same sign approach sufficiently close that a substantial amount of their core vorticity is shared and they form a single vortex core. Both mechanisms are at work in this example, and this test also highlights on a third mechanism, Taylor dispersion, whereby vorticity is sheared out from the core following streamlines along the "spiral-arms" and the rate of dissipation due to viscous diffusion is enhanced. Therefore the relevance of this example to the present work is in demonstrating that it is capable of capturing these non-linear, viscous flow phenomena, both spatially and temporally.

Problem Definition. Initial conditions are a vorticity field decomposed into a "base" vorticity ω_0 comprising a Gaussian vortex monopole and a "perturbation" vorticity ω' consisting of a Gaussian quadrupole. The amplitude δ of the perturbation is such that the system will, in sufficient time, relax into quasi-steady tripole rotating around the system centroid, and in the cases described herein $\delta = 0.25$. The initial conditions for the vorticity fields

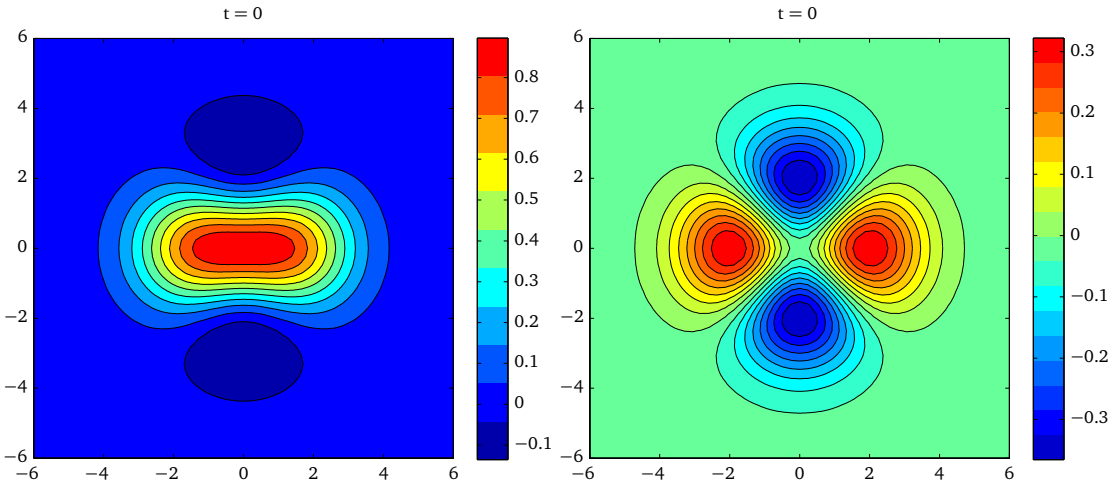

(a) Total vorticity field $\omega_0(\boldsymbol{x},0)$ **(b)** Perturbation vorticity field $\omega'(\boldsymbol{x},0)$

Figure 6.9: Initial conditions for perturbed monopole test case.

are given by:

$$\omega_0(\boldsymbol{x},0) = \frac{1}{4\pi}|\boldsymbol{x}|^2 \exp\left(\frac{-|\boldsymbol{x}|^2}{4}\right) \tag{6.10a}$$

$$\omega'(\boldsymbol{x},0) = \frac{\delta}{4\pi}|\boldsymbol{x}|^2 \exp\left(\frac{-|\boldsymbol{x}|^2}{4}\right)\cos(2\theta) \tag{6.10b}$$

where $\theta = \arg(\boldsymbol{x})$. The vorticity fields are shown in Figure 6.9. Viscous calculations have been performed at a $\mathrm{Re} = 10^4$ where $\mathrm{Re} = \frac{\omega_0}{\nu}$ resulting in a diffusion coefficient of $\Gamma = \frac{1}{\mathrm{Re}}$.

Details of Numerical Experiments Eq. (6.10) is used to generate the field at mesh point $\boldsymbol{x}$. The initial condition vorticity field is scaled and interpolated into a quasi-two-dimensional "quadtree" mesh (actually just a single plane of cells in an octree mesh). Following Barba (2004) the initial field is truncated at a radius of 6 around the origin, however cells generated later are permitted outwith this boundary. The mesh density is determined by the scaling parameter, set such that there are 120 cells along the initial radius resulting in an initial 240×240 cell domain. In these tests the symmetrically weighted sequential splitting scheme (Section 3.10) is used with a non-symmetric Koren flux limiter (Eq. 3.51, with $\kappa = 1/3$ and $M = 2$). Flux due to diffusion is calculated by fourth-order central-differences (Eq. 3.57a) at each cell interface and the diffusion coefficient is determined by setting the Reynolds number as $\mathrm{Re} = \frac{\sum \omega_0}{\nu}$. Time-stepping is accomplished internally by Euler sub-steps, and as such the calculation should generally be better than first-order in space and time. Velocity recovery is via the fast-multipole method with $p_{\max} = 8$, and using the two-dimensional Biot-Savart kernel with the kernel smoothing parameter chosen such that the core size results in the maximum velocity occurring at the neighbouring cell centres. Data is recorded at every 1 second of simulation time over a run duration of 1500 s. The time-step lengths, and the total number of time-steps are determined by the maximum local CFL conditions ($C_{\max} < 0.25$) and are time-variant, but by the end of the run Δt had converged to ≈ 0.08s for $\mathrm{Re} = 10^4$ and 19 486 time-steps had taken 7065 s wall clock time using 8 cores of an Intel Xeon 2.93 GHz CPU.

Numerical Results Contours of the total and perturbation vorticity fields are shown in Fig. C.4 and Fig. C.5 respectively. Contour plots of perturbation vorticity from the present method and the literature are presented for intermediate time-steps in Fig. 6.10. These show good qualitative agreement with Barba (2004) and Rossi, Lingevitch and Bernoff (1997), both in terms of rotation angle and general shape, although the present method

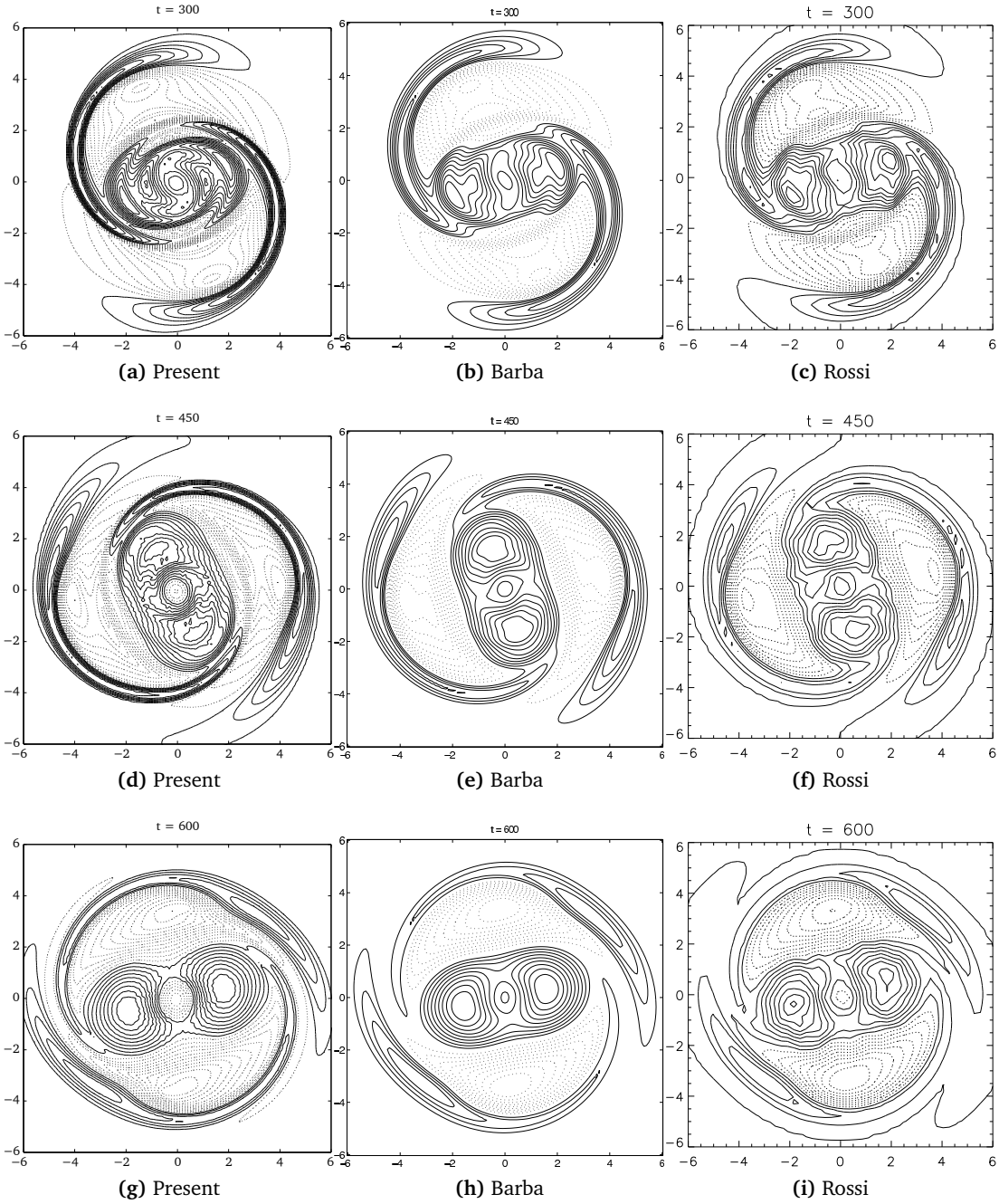

(a) Present **(b)** Barba **(c)** Rossi

(d) Present **(e)** Barba **(f)** Rossi

(g) Present **(h)** Barba **(i)** Rossi

Figure 6.10: Perturbation vorticity, $\mathrm{Re} = 10^4, \delta = 0.25$. Following the literature, solid lines correspond to positive vorticity, dashed to negative, and there are 20 equally spaced contours. Figures from Rossi, Lingevitch and Bernoff (1997) and Barba (2004) reproduced with permission.

resolves significantly finer detail than both of the other results, especially at lower time-steps.

A particular data reduction strategy considers the time evolution of the angular velocity (Ω) of the vortex structure. This analysis follows the method of Rossi, Lingevitch and Bernoff (1997) which calculates this numerically, since no analytical solution is available. Since the zeroth and first moments of vorticity are conserved by the numerical method due to its formulation and thus cannot provide any globally integrated information on the time evolution of the vorticity field, Ω is determined from using the time history of the second moments. Calculating the second moments in polar coordinates as

$$m_{xx}(t) = \iint x^2 \omega(r,\theta,t)\, r \,\mathrm{d}r \,\mathrm{d}\theta; \tag{6.11a}$$

$$m_{xy}(t) = \iint xy\, \omega(r,\theta,t)\, r \,\mathrm{d}r \,\mathrm{d}\theta; \tag{6.11b}$$

$$m_{yy}(t) = \iint y^2 \omega(r,\theta,t)\, r \,\mathrm{d}r \,\mathrm{d}\theta; \tag{6.11c}$$

the angular velocity can be obtained from the inversion of the equation of motion

$$\begin{bmatrix} m_{xx}(t) & 2m_{xy}(t) & m_{yy}(t) \\ m_{xy}(t) & m_{yy}(t) - m_{xx}(t) & -m_{xy}(t) \\ m_{yy}(t) & -2m_{xy}(t) & m_{xx}(t) \end{bmatrix} \begin{bmatrix} \cos^2(\Omega\Delta t) \\ \sin(\Omega\Delta t)\cos(\Omega\Delta t) \\ \sin^2(\Omega\Delta t) \end{bmatrix} = \begin{bmatrix} m_{xx}(t+\Delta t) \\ m_{xy}(t+\Delta t) \\ m_{yy}(t+\Delta t) \end{bmatrix}, \tag{6.12}$$

which is a linear system and easily solved for the trigonometric terms, which are then manipulated to give the local value of Ω as

$$\Omega = \frac{1}{\Delta t} \tan^{-1} \left[\frac{\sin(\Omega\Delta t)\cos(\Omega\Delta t)}{\cos^2(\Omega\Delta t)} \right]. \tag{6.13}$$

The evolution of Ω determined for the present method is plotted in Fig. 6.11 along with that from Rossi, Lingevitch and Bernoff (1997). The present method can be seen to under/overshoot the reference results very slightly, however the overall shape and magnitude of the curve is as expected. It may be argued that the results obtained from the present method are, given that they have been obtained using a very high resolution discretisation, the more accurate, however it might be that the current method accentuates the peaks and troughs because the growth in velocity with vorticity concentration is slightly higher when using the Biot-Savart rather than the gradients of a Gaussian kernel.

Discussion. A single run of the tripole attractor case has been presented, for a single mesh density, model setup and so on. During the preceding sections, experience has been

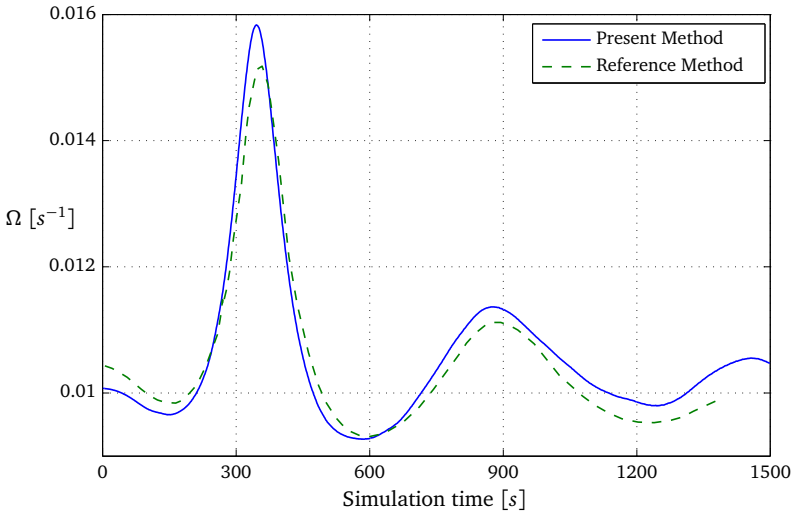

Figure 6.11: Relaxing tripole global metrics: slow evolution of angular velocity. Comparison of results obtained using the method proposed in this thesis, and those in Rossi, Lingevitch and Bernoff (1997).

gained in the selection of these parameters that an informed judgement on their selection and appropriateness could be reached, and with those selected the results are entirely satisfactory. Thus, from the massive parameter space, a selection of model configurations has been drawn which produces results which match those from the literature.

Qualitative analysis by comparison with published results is positive, and this is bolstered by a fairly good quantitative match with global performance metrics. Confidence has been gained in the ability of the coupled fast-multipole/finite-volume solver to accurately model a simple test case.

6.3.3 Static Hydrofoil

Description. This section reports tests on an impulsively started hydrofoil at various static angles of attack. This will test the combined boundary-element method, finite-volume and fast-multipole method coupling since the aerofoil will be at a nonzero incidence, generate lift and thus a wake. The foil section used is a NACA 0015 profile and is examined over a range of pre-stall angles of attack chosen such that the majority of the chord would be in the attached regime in viscous flow.

Relevance. The ability to correctly calculate the static section lift coefficient is essential before progression to more complex scenarios. Furthermore it is important that the lift develops in time in a manner which is consistent with the development and convection of the starting vortex.

Problem Definition. Initial conditions are zero vorticity throughout the domain. A NACA 0015 aerofoil section, represented by panels with a linear vortex distribution, is pitched to an angle of attack, and subjected to a uniform freestream inflow parallel to the x-axis of 1.0 chord-length per second. Circulation is generated around the foil and a starting vortex is shed and convected downstream. The time varying pressure coefficients are recorded and integrated to provide the lift coefficient history, as influenced by the starting vortex.

Details of Numerical Experiments The foil section is discretised into panels in a cosine arrangement (reduced spacing near leading and trailing edge) with 32, 64 and 128 panels in the low resolution case, and 1024, 2048 and 4096 panels in the high resolution case. The number of FVM cells is such that the density along the chord-length matches the panel count. (The high resolution cases use the low resolution FVM cell density.) The influence coefficient matrix is calculated according to Section 5.4.1. A minimum sub-step length of 0.001 s is chosen for the BEM, with a maximum allowable number of sub-steps before

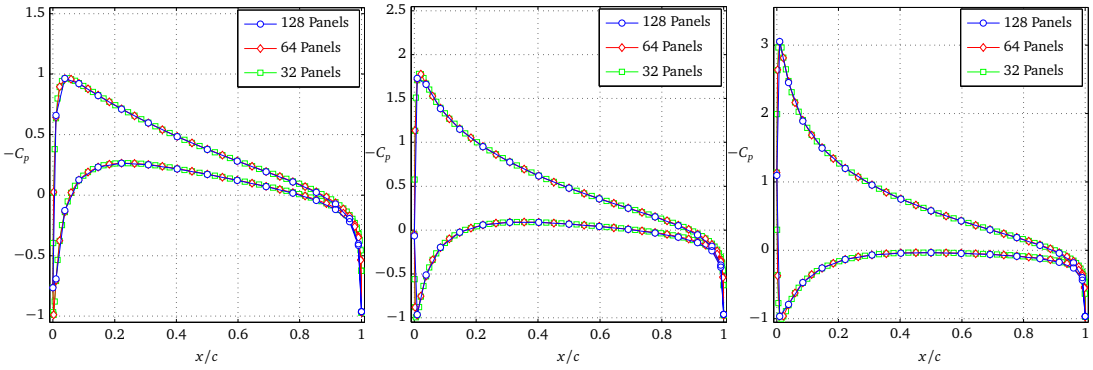

(a) $\alpha = 2.5°$ **(b)** $\alpha = 5°$ **(c)** $\alpha = 7.5°$

Table 6.3: Grid convergence metrics for flow past a two-dimensional NACA 0015 hydrofoil using section lift coefficients. Incidence α ranges from 2.5° to 7.5°.

	Section C_l						GCI %		
	Coarse	Medium	Fine	Continuum	R	p	m-c	f-m	ratio
Lower resolution cases									
Eq. (6.14a)	0.299	0.304	0.306	0.308	0.483	1.051	1.97	0.944	1.01
Eq. (6.14b)	0.308	0.308	0.308	0.309	0.254	1.978	0.104	0.0265	1
Higher resolution cases									
Eq. (6.14a)	0.308	0.308	0.308	0.309	0.499	1.002	0.0598	0.0299	1
Eq. (6.14b)	0.309	0.309	0.309	0.309	0.244	2.036	9.31×10^{-5}	2.27×10^{-5}	1

(a) $\alpha = 2.5°$

Lower resolution cases									
Eq. (6.14a)	0.596	0.607	0.612	0.616	0.482	1.052	2.01	0.962	1.01
Eq. (6.14b)	0.614	0.616	0.616	0.616	0.254	1.978	0.104	0.0265	1
Higher resolution cases									
Eq. (6.14a)	0.616	0.616	0.616	0.616	0.499	1.002	0.061	0.0305	1
Eq. (6.14b)	0.616	0.616	0.616	0.616	0.244	2.035	9.32×10^{-5}	2.27×10^{-5}	1

(b) $\alpha = 5.0°$

Lower resolution cases									
Eq. (6.14a)	0.892	0.908	0.916	0.923	0.482	1.053	2.08	0.993	1.01
Eq. (6.14b)	0.920	0.922	0.923	0.923	0.254	1.978	0.104	0.0265	1
Higher resolution cases									
Eq. (6.14a)	0.922	0.923	0.923	0.923	0.499	1.002	0.0629	0.0314	1
Eq. (6.14b)	0.923	0.923	0.923	0.923	0.244	2.035	9.32×10^{-5}	2.27×10^{-5}	1

(c) $\alpha = 7.5°$

increasing the global time-step set to 10. Data is recorded at each sub-time-step and output every one second of simulation time.

Numerical Results Section pressure coefficients are presented in Section 6.3.4 for incidences of 2.5, 5 and 7.5 degrees using the BEM meshes with 32, 64 and 128 panels. From these pressure distributions, and also from the distribution of Γ around the aerofoil, section lift coefficients can be calculated and compared: lift is calculated according to

$$C_l = \frac{F_y \cos\alpha + F_x \sin\alpha}{q} \tag{6.14a}$$

$$C_l = \frac{\rho u_\infty \Gamma}{q} \tag{6.14b}$$

where $q = \frac{1}{2}\rho u_\infty^2 c$ and bound circulation $\Gamma = \oint_{\text{foil}} \gamma \, \mathrm{d}S$. These are presented in Table 6.3, along with the convergence metrics for these cases.

Discussion. It is apparent from the convergence study that the circulatory lift coefficient is considerably less sensitive in h than the pressure lift coefficient. This is borne out by conducting a second series of tests in which a series of very high chordwise panel counts are used to probe the asymptotic region further: the deviation between the pressure and the circulatory lift is observed to have reduced considerably, with the pressure lift coefficient tending towards the circulatory lift coefficient. Pressure coefficients are visually convergent and agree well with results from the literature. Wake vorticity images in Fig. 6.13 show that the wake circulation is visually convergent, demonstrating the same overall geometric distribution and overall strength – obviously the less diffusive quality and thus greater detail in the higher resolution cases stands out.

6.3.4 Static Hydrofoil with BVI

Description. This section considers an impulsively started hydrofoil which is allowed to develop lift and arrive at a steady-state before experiencing a perturbation to the inflow velocity due to proximity to a vortex which is convected past it. This will again test the coupling between the BEM and FVM/FMM aspects of the code, specifically in terms of the response of the hydrofoil forces to the perturbation, and also the effect of the hydrofoil on the the vortex. The NACA 0015 aerofoil from the previous test is reused and initiate a vortex some distance upstream of the foil, but positioned in such a manner that it would eventually impact the foil. The vortex is then allowed to convect towards the foil.

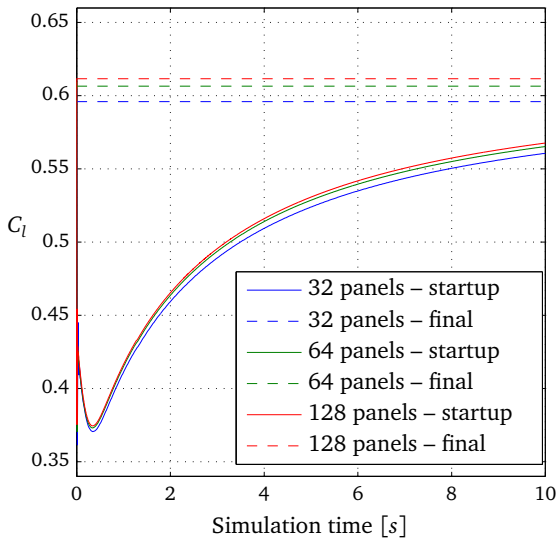

Figure 6.12: Lift coefficient startup time history for static hydrofoil obtained at various resolutions as indicated. Also shown is the final value for each resolution. $\alpha = 5°$.

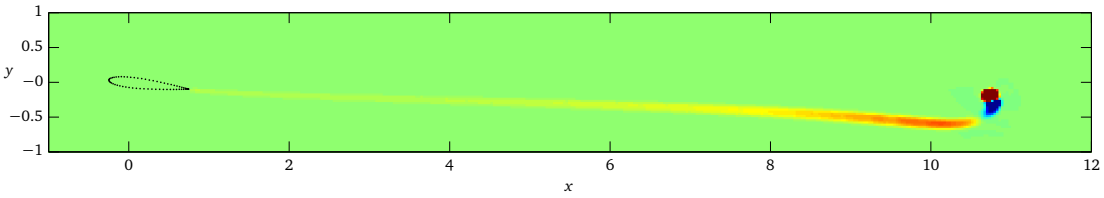

(a) 32 panel resolution

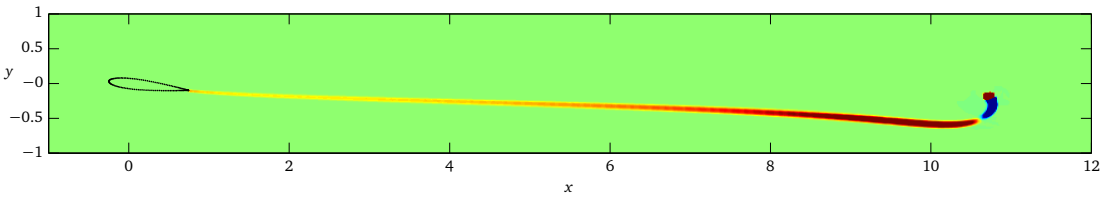

(b) 64 panel resolution

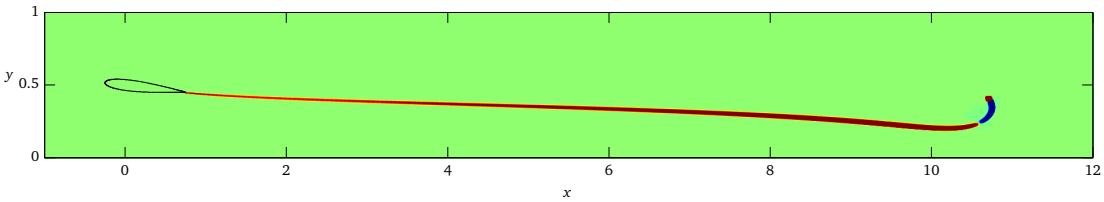

(c) 128 panel resolution

Figure 6.13: Images of domain vorticity for the static hydrofoil with simulations run at resolutions as indicated. Results obtained after 10 seconds simulation time. $u = 1$ chord-length/second, $\alpha = 7.5°$. Red colour denotes positive (about out-of-page z-axis) vorticity and blue negative. Colour axis is saturated.

Relevance. The objective of this test is to establish that the BEM is affecting the flow-field correctly, in particular that the vortex is deformed and carried round the hydrofoil, rather than pass through the boundary-elements into the interior of the foil. The boundary-element method does not apply a boundary-condition to the finite-volume cells per se, but relies on the modification to the velocity field due to the BEM to enforce the no penetration boundary condition. This test will establish whether it is possible to proceed under the assumption that the BEM boundary conditions are sufficient, and if so provide insight into the required resolution for both the BEM and FVM. If the test is failed, the method will not adequately provide insight into the blade-vortex-interaction effects which are routinely encountered during normal operation of cross-flow turbines, and further will cast into doubt the ability of the method to work as desired in three dimensions for e.g. coaxial and array configurations of axial-flow turbines.

Problem Definition. Initial conditions are zero vorticity throughout the domain, except at a location 10 chord-lengths upstream of the foil where a vortex is placed at $y = 0$. The vorticity distribution is given by a Lamb-Oseen vortex or radius $r = 0.4c$ and magnitude $\Gamma = 0.8$:

$$\omega(\theta, r) = -2\Gamma \frac{J_1(kr)}{J_0(ka)} \sin(\theta), \tag{6.15}$$

where J_0 and J_1 are the regular spherical Bessel functions of zeroth and first-order, respectively.

The NACA 0015 foil is generated using straight line panels with a linear vortex distribution attached to each, and is set to a geometric angle of attack of zero degrees to the x-axis. A uniform freestream velocity is specified at 1 chord-length per second and circulation is generated around the foil, with resultant wake vortices are convected due to the freestream and the influence of the passing vortex.

Details of Numerical Experiments Aside from the initial vorticity in the domain, the details of the setup are as for the static hydrofoil, above.

Numerical Results Figure 6.14 presents images of the vorticity in the domain taken at five second intervals. These show the approach to, impingement and wake interaction associated with the vortex as it convects downstream. Figure 6.15 shows the detail of the blade-vortex interaction: the vortex is initially deformed by the proximity of the blade, before being bisected. Since the vortex induces an angle of attack at the foil, this generates a circulation at the blade, and this deflects the vortex slightly above the foil centreline. As the foil penetrates the vortex, it is wrapped around the leading edge with the bulk of the

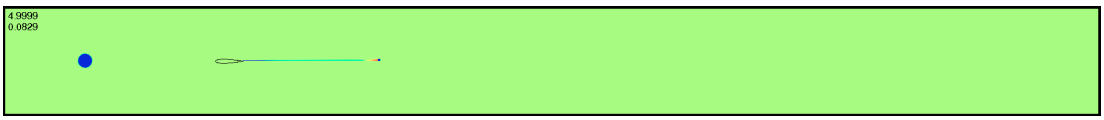

(a) $t = 5\,\mathrm{s}$

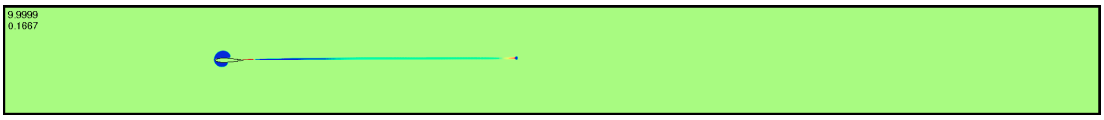

(b) $t = 10\,\mathrm{s}$

(c) $t = 15\,\mathrm{s}$

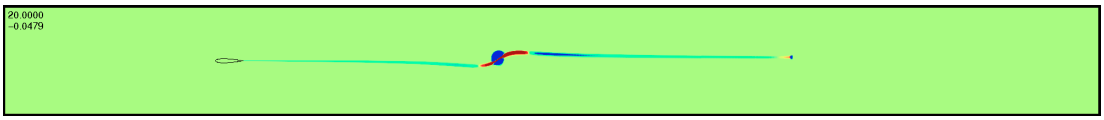

(d) $t = 20\,\mathrm{s}$

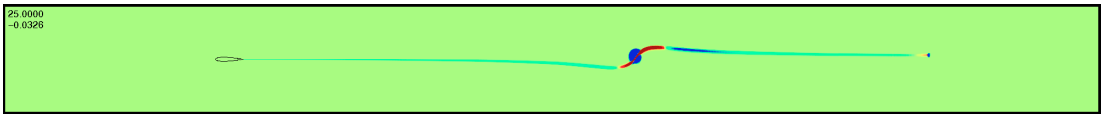

(e) $t = 25\,\mathrm{s}$

Figure 6.14: Vorticity field for static hydrofoil interacting with a vortex initiated on foil centreline 10 chord-lengths upstream. Red colour denotes positive (about out-of-page z-axis) vorticity and blue negative. Colour axis is saturated.

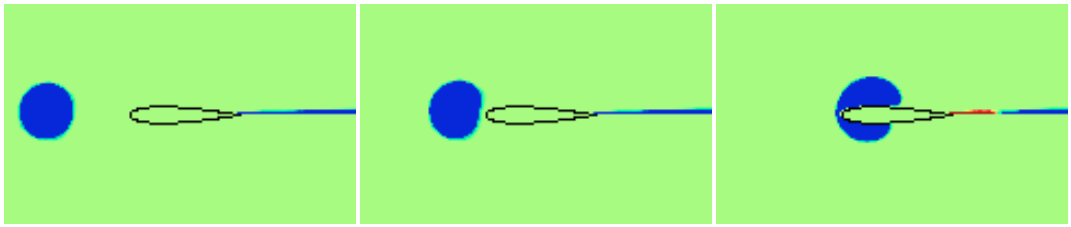

(a) $t = 9.0\,\mathrm{s}$ **(b)** $t = 9.5\,\mathrm{s}$ **(c)** $t = 10.0\,\mathrm{s}$

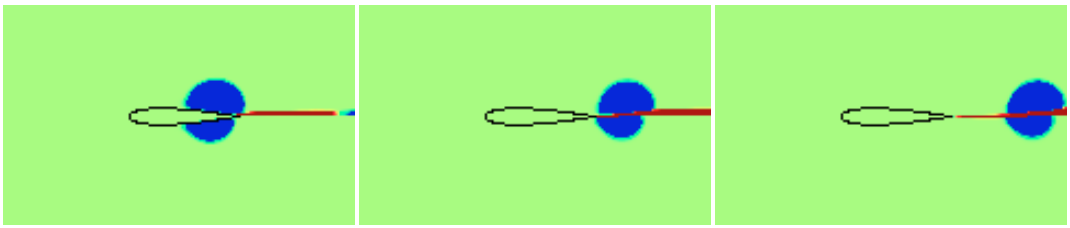

(d) $t = 10.5\,\mathrm{s}$ **(e)** $t = 11\,\mathrm{s}$ **(f)** $t = 11.5\,\mathrm{s}$

Figure 6.15: Detail of vorticity field for static hydrofoil interacting with a vortex initiated on foil centreline 10 chord-lengths upstream. Red colour denotes positive (about out-of-page z-axis) vorticity and blue negative. Colour axis is saturated.

vortex passing over the upper surface. Since the foil's lower surface flow is retarded and the upper surface flow is increased due to the rotation of the vortex, the two sections do not arrive at the trailing edge simultaneously, and the vortex is somewhat deformed as it separates from the blade. The process of axisymmetrisation restores its roundness to some extend as it convects away, however there is a continuous and moderate interaction with the wake of the foil.

Figure C.6 shows the evolution of the FVM domain for a similar test to that described here. The relevance of this image is that it shows the structure of the FVM mesh and the octree, demonstrating the way in which they combine to form an adaptive, solution dependant, Lagrangian/Eulerian model.

Discussion. The main point which this experiment serves to highlight is that the no-penetration boundary condition from the boundary-element method can be satisfactorily applied in the finite-volume – as long as the boundary mesh is sufficiently high resolution that there is almost a one-to-one matching between the BEM and FVM mesh densities. While this is easily attainable in two-dimensional problems, it might be too onerous a stipulation in three-dimensional cases.

6.3.5 Oscillating Hydrofoil

Description. The following outlines a series of tests performed using the BEM, FMM and Eulerian FV wake models applied to the simple case of forced pitch oscillation of a very thin, symmetrical foil. The results from the numerical method are compared with the predictions made by the so-called "quasi-static" lift equation (QSLE) which yields an expression for the quasi-static lift (coefficient). The QSLE is written in terms of circulatory and non-circulatory lift:

$$l_{\text{q-s.}} = l_{\text{circ.}} + l_{\text{non-circ.}}. \tag{6.16}$$

The numbers generated by the QSLE do not take into account in any way the influence of the wake, however they do allow the disentanglement of the contributions to the overall lift of the kinematic and added mass components. This allows comparison of the output from the present model with and without the wake and an added mass correction factor to determine whether the results are consistent with theory, and if not ascertain in which part of the model the inconsistencies arise.

Consider a thin aerofoil, chord c, whose static lift curve slope is known from thin aerofoil theory to be 2π per radian. The foil is pitched about a point, position x_{f} from the leading edge. The circulatory lift force on this foil when it is pitching comes from an in-

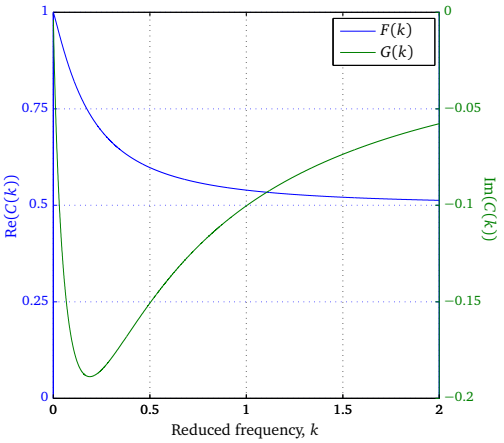

(a) Real and imaginary parts of $C(k)$

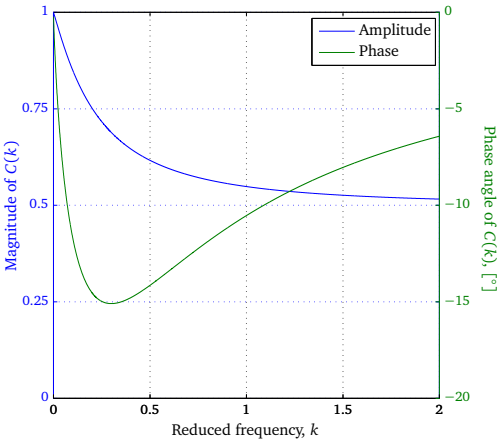

(b) Amplitude multiplier and phase difference

Figure 6.16: Theodorsen's lift deficiency function.

stantaneous static component plus an effective camber due to the variation of kinematic velocity along the foil

$$l_{\text{circ.}} = q2\pi \left(\alpha(t) + \frac{1}{u} \left(\frac{3c}{4} - x_{\text{f}} \right) \dot{\alpha}(t) \right), \tag{6.17}$$

where $q = \frac{1}{2}\rho u^2 c$ is the force due to dynamic pressure acting on the chord "area" and the remainder of the term is thus the quasi-static (circulatory) lift coefficient. Because any foil motion cannot occur in isolation from some motion of the surrounding fluid, there is a force on the foil due to the displacement of the fluid, and this is known – from its use in equations of motion as an apparent increase in system mass – as the "added mass". This term comes from the work done to move a circle of (dense) fluid the same diameter as the chord of the foil and is

$$l_{\text{non-circ.}}(t) = \pi \left(\frac{c}{2} \right)^2 \rho \left(U\dot{\alpha}(t) - \left(x_{\text{f}} - \frac{c}{2} \right) \ddot{\alpha}(t) \right). \tag{6.18}$$

The two components of the lift allow the de-coupling of the circulatory lift, which is related to the vorticity in the domain, from the added-mass lift, which is the result of reactive forces acting on the blade due to the acceleration of the fluid around the blade. The model proposed in this thesis does not explicitly account for added-mass, since there is no way to include it in the potential flow side of the model other than via an empirical correction. Results presented herein have not been corrected – except in Fig. 6.19 – and are thus for the circulatory component only.

The use of these forms of the lift equations enables the modelling of various components of the overall lift to be verified. For example, if the foil is undergoing a sinusoidal pitch forcing, the apparent camber due to the pitch rate term in Eq. (6.17) increases the lift coefficient above the expected static lift coefficient while the foil is pitching. This results in a quasi-static lift which with a component $-\pi/2$ out of phase whose magnitude is dependent on the frequency. At nonzero frequencies this manifests in a sinusoidal increase in lift, maximal while the foil pitch rate is greatest, and so the lift appears to lead the forcing and be a greater magnitude than expected. In the boundary element model this effect is due to the increasing kinematic velocities acting on panels at various increasing radii of rotation, and thus the effect of their pressures: if the inflow vectors are aligned, the foil would appear to have an artificial camber.

If the foil is undergoing motion which results in continuous changes in circulation, then a continuous wake will be shed in order to satisfy Kelvin's theorem, and this wake will result in deviations from the QSLE predictions, since there will be time-deviations in inflow angle of attack from the quasi-static pitch regime. This was characterised and analysed by

Theodorsen (1935), who found an expression valid for the infinitesimal sinusoidal motion of a flat plate with a planar wake. By using the quasi-steady lift equation, and the corrections for the wake, it is possible to determine whether the boundary-element component and the inflow component are working as expected.

Previous Results. The Theodorsen Lift-Deficiency Function ("Theodorsen's function") is an analytical correction, exact in the limit of zero amplitude sinusoidal motion, for the circulatory component of the QSLE. It acts by attenuating the circulatory lift amplitude and changing its phase in a frequency dependant manner. Theodorsen's function is written as

$$C(k) = F(k) + \mathrm{i}G(k), \tag{6.19}$$

where $k = \dfrac{\omega c}{2u}$ is the reduced frequency, and $F(k)$ and $G(k)$ are defined in terms of Bessel functions as

$$F(k) = \frac{J_1(k)(J_1(k) + Y_0(k)) + Y_1(k)(Y_1(k) - J_0(k))}{(J_1(k) + Y_0(k))^2 + (Y_1(k) - J_0(k))^2} \tag{6.20a}$$

$$G(k) = -\frac{J_0(k)J_1(k) + Y_0(k)Y_1(k)}{(J_1(k) + Y_0(k))^2 + (Y_1(k) - J_0(k))^2}. \tag{6.20b}$$

The value of the real and imaginary parts of $C(k)$ can be plotted (Fig. 6.16 for $k < 2$) and the QSLE can be modified to the "Unsteady Lift Equation" (USLE):

$$l_{\text{u.}} = C(k) l_{\text{circ.}} + l_{\text{non-circ.}}. \tag{6.21}$$

In order to apply Theodorsen's function, the foil lift must be considered as an imaginary number. The foil is fixed in plunge and the pitch forcing function is written as

$$\alpha(t) = \alpha_0 + \alpha_1 \mathrm{e}^{\mathrm{i}(\omega t)}, \tag{6.22}$$

with Eqs. (6.17) and (6.18) following naturally.

Relevance. Theodorsen's function is correct in the limit of zero amplitude oscillation, and as such a convergence of numerical experimental results to the prediction is expected. This provides a simple and expedient means of determining the quality of fully unsteady load prediction, taking into account both the kinematics of the foil and the influence of the wake in a simple test situation. It allows a means for identifying the various contributions to the overall predicted lift and determining how consistent they are with predictions. The components which come into play during this test are: wake induced downwash; kinematic

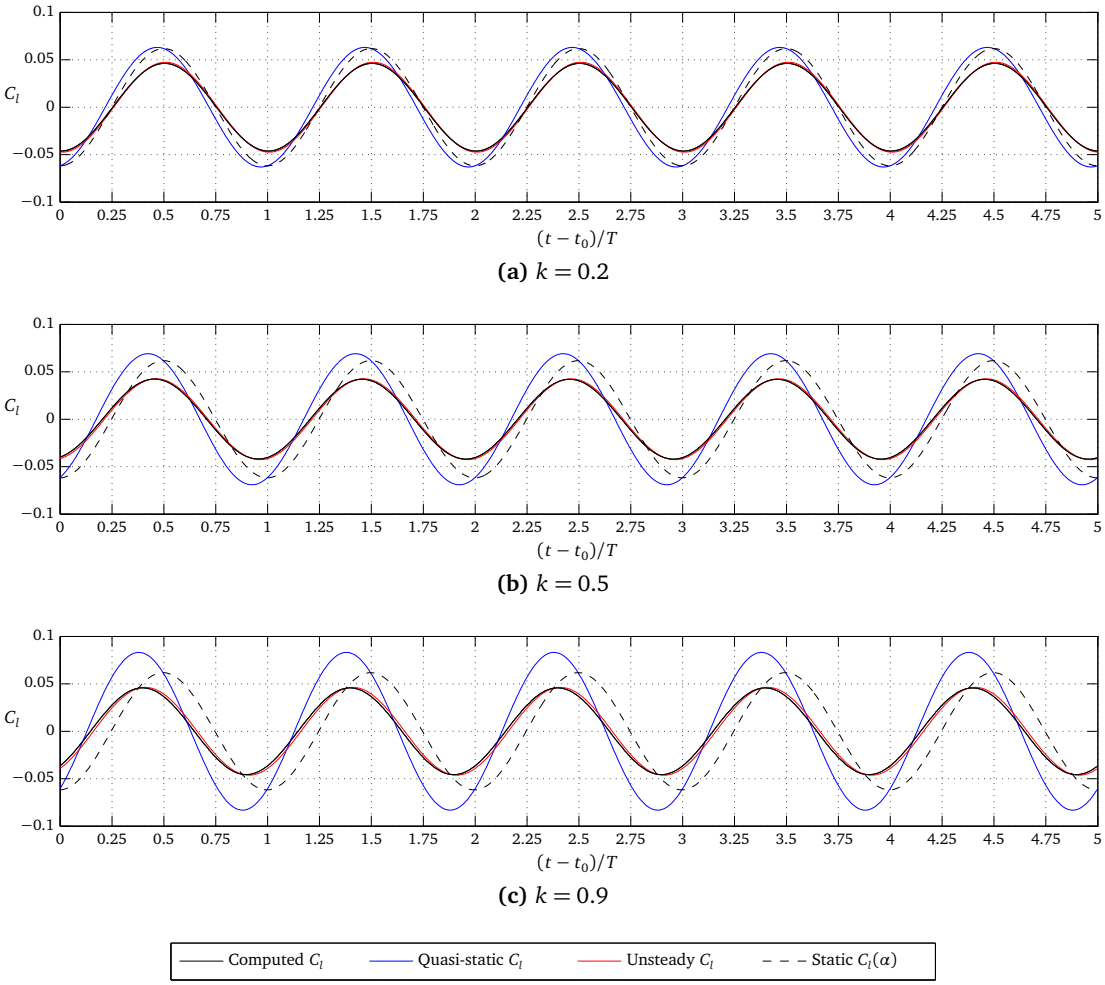

(a) $k = 0.2$

(b) $k = 0.5$

(c) $k = 0.9$

Figure 6.17: Oscillatory lift histories for various reduced frequencies. Plots show instantaneous static, quasi-static, unsteady and calculated lift coefficients for the last five of 25 oscillations. Results obtained with 32 panels on upper and lower surfaces of the blade, and 32 finite-volume elements along the blade chord. $u/c = 1\,\mathrm{s}^{-1}$, $\alpha_1 = 0.5°$.

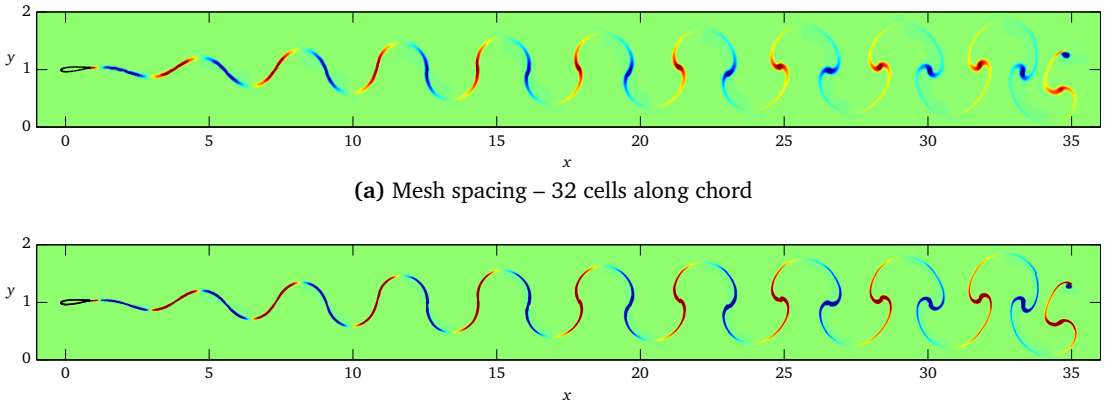

(a) Mesh spacing – 32 cells along chord

(b) Mesh spacing – 64 cells along chord

Figure 6.18: Illustrative vorticity fields for oscillating foils at different resolutions for reduced frequency $k = 0.9$. Peak amplitude of oscillation is $\alpha_1 = 5°$ – this is to allow wake to deform quickly and is considerably higher than the amplitude used in the cases described in the main text.

camber effects due to pitching and effects of time derivatives of velocity perturbation potential in the unsteady Bernoulli equation (Eq. 4.42). This is a classic aerodynamics problem, with significance in the rotorcraft and (especially cross-flow) turbine communities, and has thus amassed a considerable attendant body of work. Theoretical and experimental work have primarily been created to study dynamic stall, e.g. McCroskey (1982), Piziali (1994), Hoo, Do and Pan (2005), and more relevantly as means of improving models of cross-flow turbines, e.g. Deglaire *et al.* (2009) or Gretton, Ingram and Bryden (2011).

Problem Definition. The aerofoil is instantiated in a domain devoid of vorticity at $t = 0$, and is set to pitch about its quarter-chord according to forcing function $\alpha = \alpha_0 + \alpha_1 \sin(\omega t)$. Fluid flow is modelled following the x-axis at a rate of one chord-length per second; the viscosity is set to zero in these tests as the Reynolds number should tend to infinity (although there is of course artificial diffusion). The x and y forces on the foil are recorded at each time-step of the boundary element method. This is obtained from the pressure distribution calculated according to the unsteady Bernoulli equation. The instantaneous foil lift coefficient is resolved out of these and the geometric angle of attack.

Details of Numerical Experiments Based on experience with static hydrofoils, a panel density of 32 cells is chosen with the FVM mesh density such that there is effectively one cell per panel. As in previous hydrofoil tests, a cosine arrangement of panels clusters them towards the leading and trailing edges. The FVM setup is as previous tests: the Koren limiter is used with an SWSS time advancement, with a maximum allowable time-step length determined by $C_{\max} \leq 0.25$ in each dimension as well as a CFL-like condition on the internal sub-stepping for boundary-element panels such that they cannot cross an entire FVM cell during a single outer time-step. Since the motion of the foil is confined to low pitch deviations, in general it is found that the limiting factor is the FVM time-step, and as such only a single internal sub-step is normally required.

The pitch amplitude $\alpha_1 = 0.5^\circ$ and the static pitch offset $\alpha_0 = 0$ are selected, and a sweep of reduced frequencies between 0.2 and 2.0 is undertaken.

Results. Figure 6.17 shows a representative subset of time-series obtained using the two-dimensional form of the model proposed in this thesis. These plots show a time history of the lift coefficient, taken at $k = 0.2$, 0.5 and 0.9, for an aerofoil pitching about its quarter-chord with a peak amplitude of 0.5°. Figure 6.18 shows the vorticity field obtained at two mesh densities and demonstrates plot convergence in the wake model – n.b. these plots are generated with a higher amplitude pitch oscillation in order to demonstrate the wake

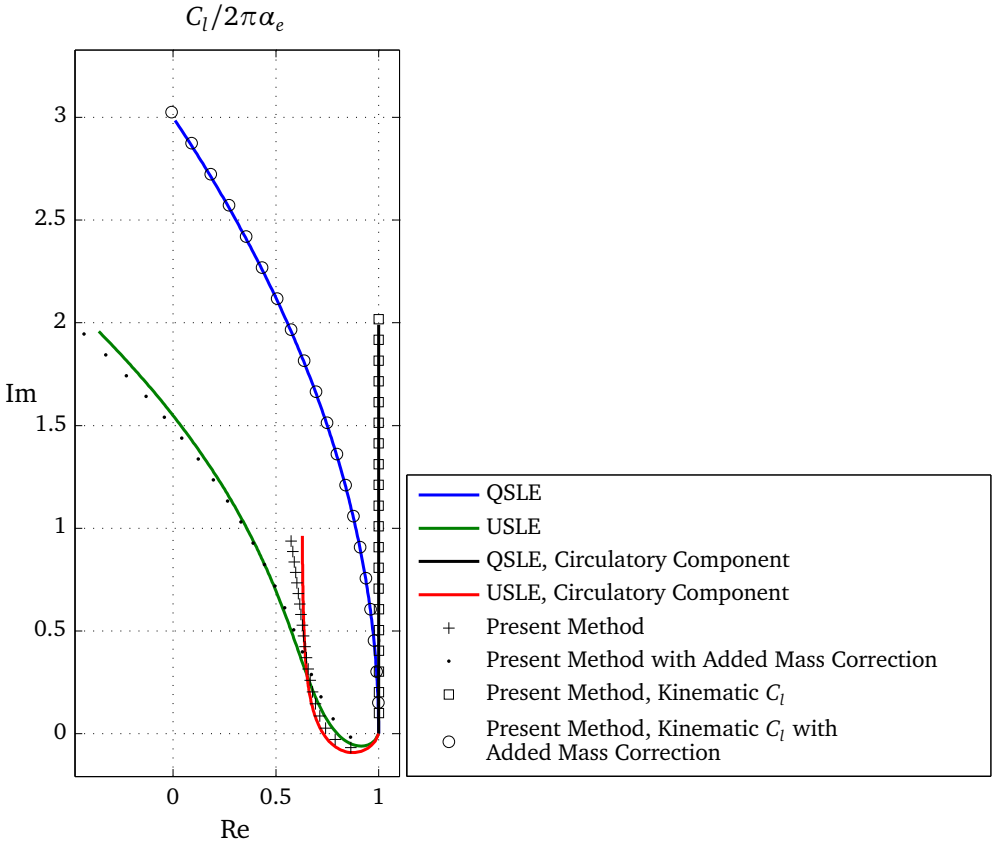

Figure 6.19: Loci of real and imaginary components of unsteady lift on an oscillating thin aerofoil as a function of reduced frequency. Comparison of analytical and numerical results. Numerical results reduced frequency increasing in equal increments of 0.1 from 0.1 to 2.0 outwards from $(1, i0)$.

deformation in a plot of a sensible size.

For these plots to make sense in the context of Theodorsen's function, the forcing functions and lift responses must be reconciled with their imaginary counterparts as part of general functions in complex exponential form. However, when obtaining data from experiments or numerical simulation, what is obtained, although actually entirely sensible time domain representations of the time histories obtained by using the function $\alpha = \alpha_0 \cos(\omega t)$ as the forcing function, are only part of the complex signals,

$$\left[A_0 \left(\cos\left(\omega t + \varphi\right) + \mathrm{i}\sin\left(\omega t + \varphi\right)\right)\right], \tag{6.23}$$

and could equally be the real or imaginary part.

A data reduction can be performed using the recorded numerical experimental results as well as the expected QSLE data generated using the pitch forcing function. Since general output data have an unknown start time and phase, it is not possible to use the preceding equations and simply "plug in the numbers". From the simulation, two time series are recorded. By obtaining the phase between these, and their difference in magnitude, their proximity to the analytical solution can be determined. Since each of the two data series are sinusoidal and assumed to be representable by a convergent Fourier series, the coefficients a and b of

$$l(t) = \frac{a_0}{2} + a_1 \cos(\omega t) + b_1 \sin(\omega t) + a_2 \cos(2\omega t) + b_2 \sin(2\omega t), \tag{6.24}$$

are solved for, and then the phases φ and amplitudes A of each signal are given by

$$\varphi = \tan^{-1}\left(\frac{a_1}{b_1}\right) \tag{6.25a}$$

$$A = \sqrt{a_1^2 + b_1^2}. \tag{6.25b}$$

The phase difference between the signals is thus $\varphi = \varphi_2 - \varphi_1$ and the ratio of amplitudes $R = A_2/A_1$. Following McCroskey (1982) is possible, therefore, to present a far more condensed form of these results using the ratio R of magnitudes between of the computed time-series to the static lift along with the phase angle φ between the pitch forcing and the lift response to plot an Argand diagram:

$$R\angle\varphi = \frac{C_l(t)}{C_{l_\alpha}\alpha(t)} = \frac{C_{l1}}{C_{l_\alpha}\alpha_1} \cdot [\cos\left(\varphi\right) + \mathrm{i}\sin\left(\varphi\right)]. \tag{6.26}$$

C_{l_α} is the static lift curve slope.

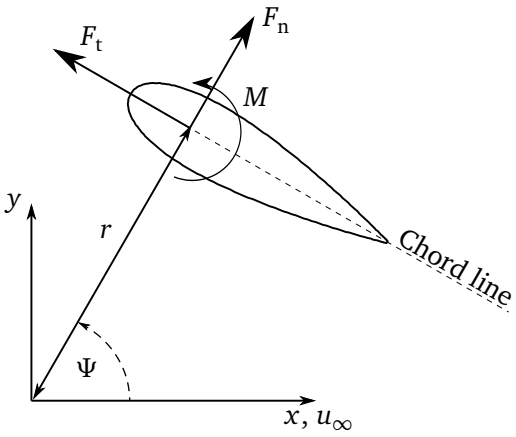

Parameter	Value
Radius, r	1.25 m
Blade Chord, c	0.2 m
Blade Section	NACA 0024
Freestream Velocity, u_∞	2.5 m s^{-1}
Number of Blades N	3
Solidity ($\sigma = Nc/2r$)	0.24
Typical Re	$\mathcal{O}(10^6)$

Figure 6.20 & Table 6.4: Blade element forces and moments, coordinate definitions, and case particulars for cross-flow turbine simulation.

Discussion. The loci of the real and imaginary parts of the ratio of lift coefficients – including theoretical and numerical results – are plotted in the Argand diagram in Fig. 6.19. All lines start at $1 + \mathrm{i}0$ and the symbols show $0 \leqslant k \leqslant 2$ in increments of 0.1. This plots results obtained theoretically as solid lines, and those obtained using the present method with varying corrections using symbols. The square symbols denote uncorrected results obtained using the present method without including the influence of the wake – e.g. these are the kinematic components of the lift coefficients. Circles indicate the same results but with an added mass correction factor (via Eq. 6.18). It is obvious that these results track the predictions of the QSLE quite well, and that, therefore, the kinematic velocities, pressures and forces are calculated in a consistent and correct manner.

Points and pluses are used to show the results of the present method including the inflow due to the wake, with and without an added-mass correction. The main result here is that the method captures the gross trends in the unsteady lift phase and magnitudes fairly well. The errors could be due to one or both of phase and magnitude errors. By observing the time histories in Fig. 6.17 it is apparent that (in these and various other cases) the predicted phase angle is out, and the computed C_l leads the analytical C_l – at least for the reduced frequencies shown here. This tends to rotate the points and pluses such that the lag is reduced for $k < 0.1454$ – where the line cuts the real axis – and the lead is increased above this. By comparing the ratio of amplitudes in the predicted and computed results it is apparent that the discrepancy between predicted and calculated results in Fig. 6.19 is (primarily – there is some deviation in amplitude ratios, especially at the lower k) due to rotation of the points because of phase errors.

6.3.6 Cross-flow Turbine

Description This section outlines briefly tests performed using the proposed method on a cross-flow turbine configuration. These results have been presented in detail in Johnson, Gretton and McCombes (2010) and the following is a description of the contribution to this paper made by the author of this thesis.

The case concerns the cross-flow turbine concept described in Salter and Taylor (2007) and modelled using CFD in Gretton and Bruce (2007) and Gretton, Bruce and Ingram (2009). The particulars of the turbine concept and test case are listed in Table 6.4.

Previous Results The turbine concept has been modelled in detail using CFD and a blade-element/momentum theory model, both presented in Gretton, Bruce and Ingram (2009). For the purposes of this section, these are taken to be the definitive performance measure-

ments for this device. The turbine was also modelled using a discrete vortex model, with a comparison of the results generated using the method proposed in this thesis, the CFD of Gretton, Bruce and Ingram (2009) and these results presented as part of Johnson, Gretton and McCombes (2010).

Relevance This cross-flow turbine cases is particularly difficult to model since it requires resolution of multiple blades moving through a strongly time-varying flowfield. From the perspective of the proposed model, as a test case it draws on the various performance tests conducted to this point, and extends them by adding additional bodies. Cross-flow devices are the only turbines which can effectively be analysed in two dimensions and this case represents a good study for the method modelling a practical, real-life configuration.

Problem Definition. The details of the test case are given in Fig. 6.20 and Table 6.4 and follow that modelled in the previous work. The three blades of the turbine are initialised in a domain containing zero vorticity and rotate about their shared circumference. Newtonian viscosity is set to zero so Reynolds number is tending to infinity – even though the chord Reynolds number of the blades in real flows is of the order of 10^6.

The blade forces aligned with the global axis system are computed and output at each time-step. The results obtained are processed into coefficient form and presented along with results obtained using ANSYS CFX and a blade-element/momentum theory method.

Details of Numerical Experiments The blade was resolved using 50 panels on the upper and lower surfaces with a reduced number of cells (25) along its length, resulting in 250 cells across the rotor diameter – this number was eventually discovered to provide the best compromise between resolution and computational cost.

The FVM model is set up as before, except the MUSCL limiter was employed although it is expected that results obtained with other PL-κ limiters would be similar. A maximum Courant number of 0.25 was enforced in each dimension, and a pseudo-CFL condition applied to the blade was used to determine the maximum length of the internal sub-step.

Results Results are generated over a sweep of tip-speed-ratios from $2 \leq \lambda \leq 3.6$ in increments of 0.2. The resultant forces are resolved tangential and normal to the blade chord, which is itself perpendicular to the radius and tangential to the circumference of rotation, and a moment about the quarter-chord, denoted (following the notation of Strickland, 1975):

$$F_{\mathrm{n}}^{+} = \frac{F_{\mathrm{n}}}{\frac{1}{2}\rho u_{\infty}^{2} c} \; ; \qquad F_{\mathrm{t}}^{+} = \frac{F_{\mathrm{t}}}{\frac{1}{2}\rho u_{\infty}^{2} c} \; ; \qquad M^{+} = \frac{M_{c/4}}{\frac{1}{2}\rho u_{\infty}^{2} c^{2}}. \tag{6.27a,b,c}$$

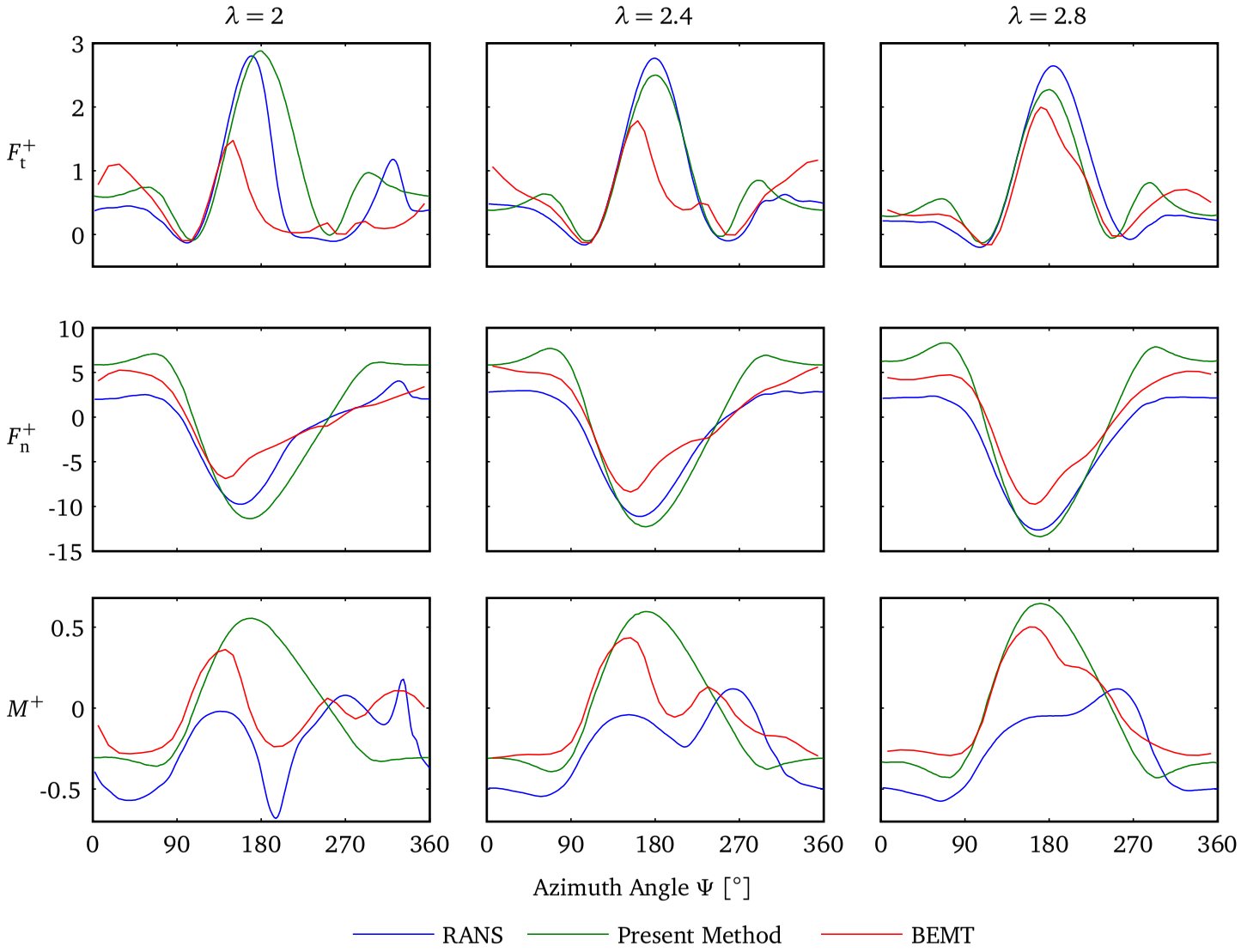
λ = 2
λ = 2.4
λ = 2.8
F_t^+
F_n^+
M^+
3
2
1
0
10
5
0
-5
-10
-15
0.5
0
-0.5
0
90
180
270
360
Azimuth Angle Ψ [°]
RANS
Present Method
BEMT

The instantaneous power of the turbine is a result of the shaft torque, which is composed primarily of the tangential component of the resultant force on the blades, plus a small foil pitching moment contribution:

$$Q^+ = F_\mathrm{t}^+ + M^+ \frac{c}{r} \,. \tag{6.28}$$

Performance indicators for the turbine are given in terms of the time-averaged shaft torque, power and thrust coefficients:

$$C_Q = \overline{Q^+}\sigma \;; \qquad C_P = C_Q\lambda \;; \qquad C_T = \frac{\sigma}{2\pi}\int_0^{2\pi} \left[F_\mathrm{t}^+ \sin\Psi + F_\mathrm{n}^+ \cos\Psi\right] \mathrm{d}\Psi. \tag{6.29a,b,c}$$

A subset of the processed data is displayed in Fig. 6.21 for low tip-speed ratios. It is immediately apparent that the low TSR results are dominated by viscous effects. This is demonstrated by the RANS solution – and the BEMT solution to an extent – in the F_t^+ trace. After $\Psi = 90°$, where the geometric and kinematic incidence is at its lowest, both solutions initially follow the inviscid solution. The tangential force traces increase to a peak, then drop off, either due to stall in the RANS and BEMT methods, or a decreasing angle of attack in V3D. The RANS solution continues to a peak incidence before stalling which is considerably higher than that predicted using the BEMT code, which is reliant on static stall data. The inviscid solution of the present method does not stall, and as such continues to a higher peak tangential force, and falls away with incidence, rather than entering the stalled regime. A similar story can be said of the higher TSR tangential force traces, although as λ increases, the excursions of geometric angle of attack are reduced, and the influence of stall on the force traces is diminished simply because the blade is spending less of the cycle in stall. This leads to the tendency of the RANS and BEMT results towards the inviscid results to an extent, although it can be seen that the inviscid trace still underpredicts the tangential force somewhat. This is put down to the effects of stall delay which is captured by neither the BEMT nor the V3D methods.

A similar result can be seen in the moment coefficient traces: the BEMT and the RANS solution especially is dominated by moment stall, which is completely absent from the V3D results. Both the RANS and BEMT results show a characteristic dip in moment (just after $\Psi = 180°$, i.e. the middle of the upstream blade pass) where after the angle of attack exceeds the moment stall angle then begins to recover, but with a reduced resultant inflow velocity. Again, as the TSR increases, the viscous effects become less severe, and the BEMT

Figure 6.21*(facing page)*: Non-dimensionalised forces and moments on the blade, taken after the 60$^{\text{th}}$ revolution. Comparison of results obtained using the methods indicated. Taken from Johnson, Gretton and McCombes (2010), with permission.

results in particular tend towards the attached regime and thus the inviscid results.

The normal force coefficients determine the thrust reactive loading on the device, and are a result, primarily, of the lift force on the blades, but resolved in a direction which is not useful for power generation. As such, their adequate prediction is closely related to the ability of the models to accurately predict the lift on the blades. The significant result here is that the V3D model is, due to its inability to model stall, overpredicting the normal force magnitude on both the up and downstream passes of the blade for the lower TSRs, and overpredicting the downstream pass for the higher TSRs. This has the net effect of increasing the time-average of the dominant component of the thrust coefficient, and thus increase the predicted average thrust of the rotor, even though the the agreement between the models for the upstream passes is quite good.

Discussion The F_{n}^{+} trace represents to some extent the the history of energy removed from the flow: if, during the upstream pass, a blade is in stall, it will have left more momentum in the flow to remove during the downstream pass. Conversely, if the blade is not stalling – as in the inviscid case – it would be expected that there is a significant momentum deficit over the azimuths corresponding to the downstream pass. This is captured in the BEMT code by the induction factors (and to an extent by the streamtube spreading), and in the RANS code by the direct modelling of the physical mechanisms. In the V3D code it is represented primarily by the influence of the wake, although there is some interaction between the boundary-condition specification and thus circulation on each blade, but this is very small. The implication is therefore that if the model is measuring higher forces on the downstream segment than should be expected these correspond to an exceptionally high thrust coefficient, and if the only mechanism for modelling the momentum deficit is the wake, then there must be an error in either the wake model or the post-processing (this is not unlikely – the transformations required to get the data output from the code into the various forms presented herein are numerous and fraught with potential to introduce "user" errors).

6.4 Conclusions

General Remarks and Recap This chapter has presented cases used to identify and quantify the performance characteristics of the model developed herein. Individual components of the finite-volume scheme have been tested for accuracy, consistency and convergence, and the factor space available in setting up a useful model has been reduced considerably by identification of the optimal, and elimination of sub-optimal finite-volume modelling

schemes. Experience has been gained in appropriate parameters for e.g. time-step length and mesh scaling also, as well as in expected convergence rates.

More involved test cases used the combined finite-volume and fast-multipole methods to construct a vorticity transport solver. This was tested against a scenario from the literature and found to perform well.

Since an engineering model is the goal of this thesis, the next phase involved looking at flows around aerofoils. The results were convergent and as physically realistic as could be expected from the model.

An oscillating foil was presented as a means of comparing predicted and analytical results, and barring some minor discrepancies, the unsteady lift predicted by the proposed method matches satisfactorily that predicted using Theodorsen's method.

Finally, application of the model to a cross-flow turbine revealed the limitations of the model when used to simulate useful engineering flows. In particular, its inability to capture stall severely hampers its applicability at low tip-speed ratios, however as TSR increased, the results improved (as expected).

The oscillating foil and crossflow turbine tests are out of chronological order as reported here: the oscillating foil tests were an attempt to understand better the nature of the problems in the crossflow turbine model. These were specifically related to the importance of dynamic stall (not examined) and unsteady lift, and also the impact of the wake model. Time constraints, and the prioritisation of the three-dimensional aspect of the method, prevented full examination of these factors.

Impacts on this Thesis

- The finite-volume solution to the diffusion equation is best tackled with a fourth-order method as this significantly reduces error for minimum overhead;
- Second-order spatial schemes are mandatory as is second-order time-stepping;
- The van Leer and PL-κ (MUSCL/Koren) limiters offer the "best" performance, and the van Leer is most efficient;
- Splitting schemes provide best accuracy in two-dimensional flows over operator addition, and there is little to choose between the alternate dimensions and symmetrical schemes;
- Results presented for flows in the absence of bodies are promising;

- Results for static foils show a good convergence and expected evolution of the flow, including blade/vortex interaction;
- Results for oscillating foil show satisfactory convergence on analytical results;
- Results for a cross-flow turbine draw out the shortcomings of the model in cases dominated by stall and separation, but are otherwise promising, considering their difficulty.

References

Barba, L.A. (2004). *Vortex Method for computing high-Reynolds number flows: Increased accuracy with a fully mesh-less formulation*. Ph.D. thesis, California Institute of Technology.

Deglaire, P., Engblom, S., Ågren, O. and Bernhoff, H. (2009). "Analytical solutions for a single blade in vertical axis turbine motion in two-dimensions." *European Journal of Mechanics - B/Fluids*, **28**(4): pp. 506–520.

Gretton, G.I. and Bruce, T. (2007). "Aspects of mathematical modelling of a prototype scale vertical-axis turbine." In A. Falcão (ed.), "Proceedings of the 7th European Wave and Tidal Energy Conference (EWTEC2007)," Porto, Portugal.

Gretton, G.I., Bruce, T. and Ingram, D.M. (2009). "Hydrodynamic modelling of a vertical axis tidal current turbine using CFD." In "Proceedings of the 8th European Wave and Tidal Energy Conference (EWTEC2009)," Uppsala, Sweden.

Gretton, G.I., Ingram, D.M. and Bryden, I.G. (2011). "Results from blade element momentum and RANS analyses of a practical full-scale horizontal axis tidal current turbines." In "Proceedings of the 9th European Wave and Tidal Energy Conference (EWTEC2011)," Southampton, England.

Hoo, E., Do, K. and Pan, J. (2005). "An investigation on the lift force of a wing pitching in dynamic stall for a comfort control vessel." *Journal of Fluids and Structures*, **21**(8): pp. 707–730.

Johnson, P., Gretton, G. and McCombes, T. (2010). "Numerical modelling of cross-flow turbines: a direct comparison of four prediciton techniques." In "Proceedings of the 3rd International Conference on Ocean Energy (ICOE2010)," Bilbao, Spain.

LeVeque, R.J. (2002). *Finite Volume Methods for Hyperbolic Problems*. Cambridge texts in applied mathematics.

McCroskey, W.J. (1982). "Unsteady airfoils." *Annual Review of Fluid Mechanics*, **14**(1): pp. 285–311.

Piziali, R.A. (1994). "2-D and 3-D oscillating wing aerodynamics for a range of angles of attack including stall." Tech. Rep. NASA-TM-4632, NASA.

Rossi, L.F., Lingevitch, J.F. and Bernoff, A.J. (1997). "Quasi-steady monopole and tripole attractors for relaxing vortices." *Physics of Fluids*, **9**(8): pp. 2329–2338.

Salter, S. and Taylor, J. (2007). "Vertical-axis tidal-current generators and the Pentland Firth." *Proceedings of the Institution of Mechanical Engineers, Part A: Journal of Power and Energy*, **221**(2): pp. 181–199.

Strickland, J. (1975). “The Darrieus turbine: A performance prediction model using multiple streamtubes.” Tech. Rep. SAND75-0431, Sandia National Laboratory.

Theodorsen, T. (1935). “General theory of aerodynamic instability and the mechanism of flutter.” Tech. Rep. Report No. 496, NACA.

7

Proof-of-Concept Studies in Three Dimensions

7.1 Introduction

This chapter presents a series of investigations undertaken to test the various aspects of the method in three dimensions, in particular coupled and decoupled tests of the boundary-element method (BEM) and the combined finite-volume method (FVM) / fast-multipole method (FMM) wake model.

7.1.1 Relevance

The objectives of this chapter are to ascertain if the model is consistent and convergent, in both global and a sub-model unit test senses, and whether the results are a reasonable approximation of reality. Where there are convergence issues, or the model is grossly inaccurate, the causes of this are examined with a view of determining the limits of applicability of the model. The confidence envelope will be reduced from that obtained based on purely theoretical considerations, since the tests reported have been selected as those in which the model should in theory perform well.

The results presented are for cases of modelling:

- flow past a non-lifting sphere, with comparison to theory;
- flow past a static hydrofoil, with comparison to experiment;
- flow past a wind turbine rotor, with comparison to experiment;
- flow past a tidal turbine rotor, with an inter-model comparison.

In each case, results obtained at various discretisation resolutions are examined using the method described in Appendix A.3 for convergence characteristics, and a Richardson extrapolated result is presented.

7.2 Non-lifting Bodies

7.2.1 Sphere

This section outlines a test of the BEM part of the code about a non-lifting – i.e. static – sphere. As it is non-lifting, there is no circulation and thus no wake generated, and this test will therefore not utilise the FVM and associated portions of the code. The purpose of this test is to gain confidence the method and ascertain the convergence behaviour, and thus the required meshing levels, of the three-dimensional BEM aspect of the method.

The meshes are a latitude/longitude surface of revolution, a cubed-sphere type quadrilateral mesh via a gnomonic equiangular central projection, and also a fully triangulated approximation to the sphere surface obtained by recursive subdivision of a platonic solid.

Description Results are generated for the flow past a sphere of unit radius for increasing mesh densities, using three meshing strategies. The first is simply generated by using a surface of revolution, or mapping the position of the corners of a rectangular patch onto a sphere. This is intuitively the first option as it is straightforwards to implement and can easily be refined by increasing the number of lines of latitude or longitude. At the poles the mesh density becomes "infinite," as the spacing between lines of latitude becomes zero, potentially producing erroneous results due high aspect ratio triangular panels. This gives rise to the combined effects of high mesh density gradients and issues in effectively implementing a finite-difference scheme to obtain approximations to surface gradients.

The second mesh is obtained by using a gnomonic projection of a tessellated cube onto the surface of the sphere. This results in six patches which are individually rectangular in computational space. The advantages of this form of mesh is that it is more uniform over the poles and, in general, simple finite-difference approaches can be employed to obtain surface gradients. At patch boundaries, especially corners where three patches meet, there is a discontinuity in computational space necessitating a more elaborate method to obtain the gradients.

The third mesh is a triangular tessellation of the surface. This is obtained by a symmetric, recursive subdivision of the edges defining an initial platonic solid (an icosahedron), and projection of the vertices obtained after the final subdivision onto the sphere surface. Due to the nature this mesh, it is not possible to use methods associated with the regular quad meshes for gradient calculation, and more elaborate finite-difference calculations must be performed.

Results are presented for various mesh densities using the three meshing strategies.

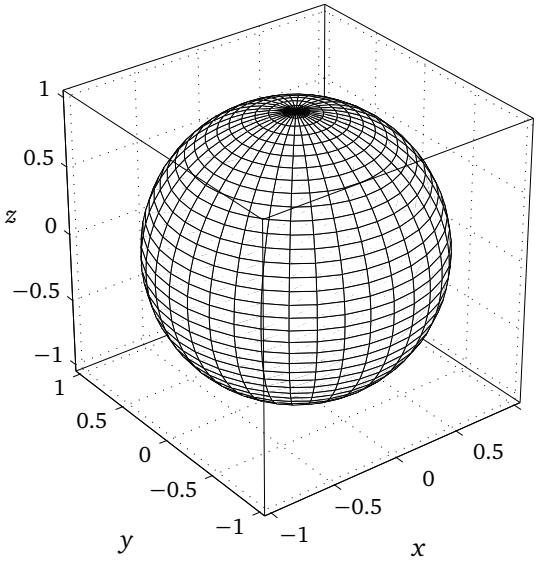

(a) Quad mesh by revolution

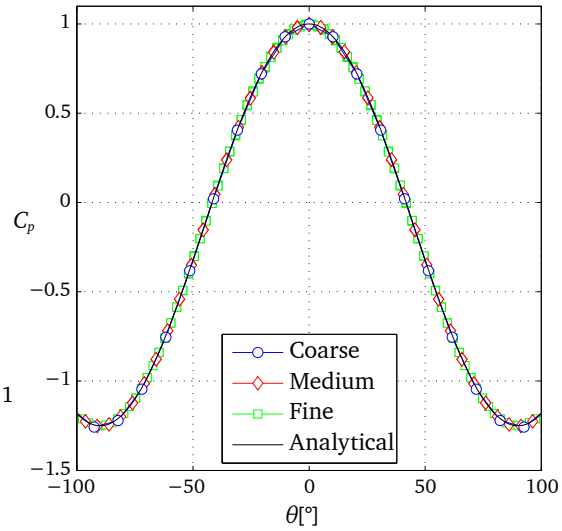

(b) Quad mesh by revolution – Pressure Coefficient

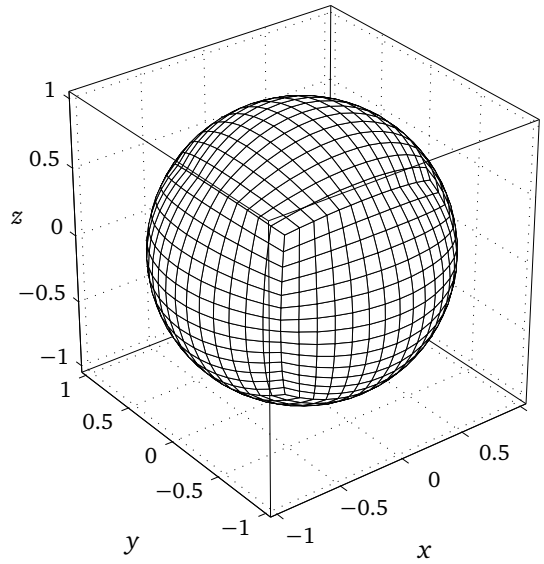

(c) Quad patch mesh

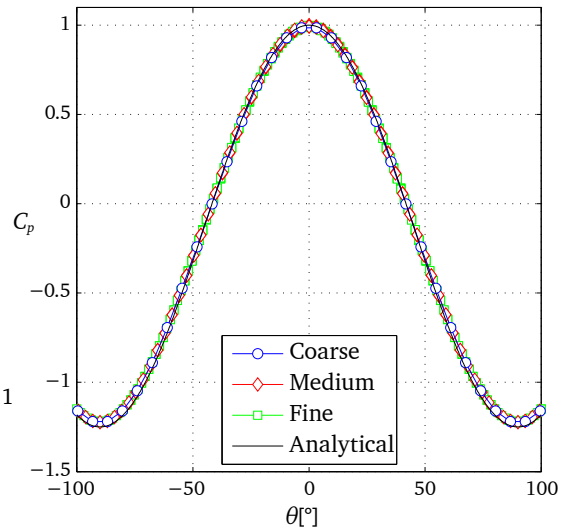

(d) Quad patch mesh – Pressure Coefficient

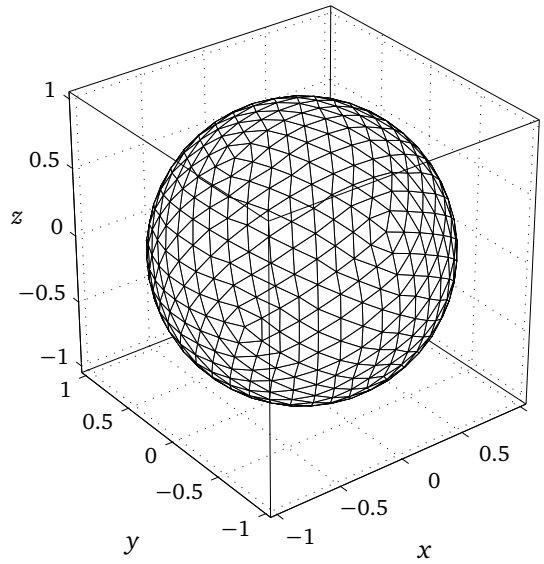

(e) Tri mesh

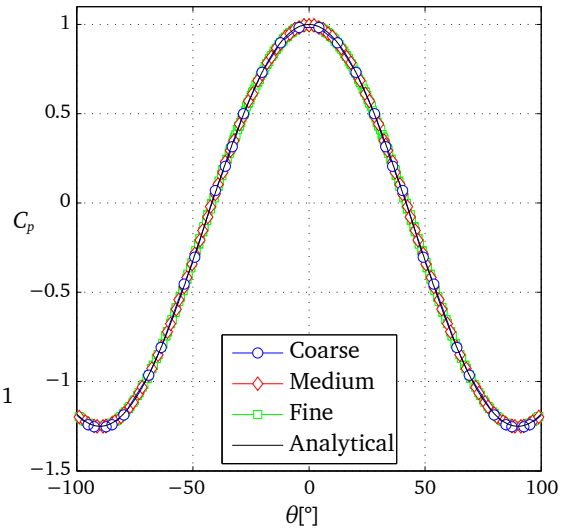

(f) Tri mesh – Pressure Coefficient

Distribution of potential on the sphere are compared to theory – this removes artefacts introduced by post-processing – as well as the distribution of pressure coefficient.

Previous Results Potential flow about a sphere is well known, and there exist analytical expressions for the distribution of potential, velocity and pressure. The perturbation potential in the domain due to flow past a sphere of radius R, with surface normal is $\boldsymbol{n}$, follows from the solution of a non-permeable dipole of the same radius:

$$\phi(r) = u_\infty \left(R + \frac{r^3}{2R^2} \right) \cos\theta. \tag{7.1}$$

The velocity, and thus the pressure coefficient, is obtained by differentiating the perturbation potential on the sphere ($r = R$) circumferentially

$$V = -\frac{3}{2} V_\infty \sin\theta; \tag{7.2a}$$

$$C_p = 1 - \frac{9}{4} \sin^2\theta. \tag{7.2b}$$

To obtain an arbitrary great circle on the sphere, rather than the one which lies on the xy-plane, the polar angle of a point of interest is used to generate a transformation matrix:

$$\Psi = \tan^{-1}\left(\frac{z}{y}\right), \quad \begin{bmatrix} x' \\ y' \\ z' \end{bmatrix} = \begin{bmatrix} 1 & 0 & 0 \\ 0 & \cos\Psi & \sin\Psi \\ 0 & -\sin\Psi & \cos\Psi \end{bmatrix} \begin{bmatrix} x \\ y \\ z \end{bmatrix} \quad \text{and so} \quad \theta = \tan^{-1}\left(\frac{y'}{x'}\right). \tag{7.3}$$

Relevance This test focusses on the ability of the method to generate a good result for ϕ given varying quality approximations to the surface geometry, and thus the ability to effectively recover a reasonably accurate surface pressure distribution. The simplicity of the geometry allows fairly easy grid convergence tests to be performed, and the availability of analytical solutions allows both methodological and post-processing errors to be quantified.

Problem Definition A spherical mesh of unit radius is generated using one of the three meshing strategies listed above. Initial conditions are zero vorticity throughout the domain

---

Figure 7.1*(facing page)*: (a, c, e) Boundary element meshing strategies for a unit sphere. Mesh counts are 1296, 1350 and 1280 for quad revolution, quad patch and tri panel meshes respectively. (b, d, f) Pressure coefficients obtained for θ around z-axis (i.e. $\Psi = 0$).

(which will remain zero as the sphere is non-lifting) and a freestream potential $\phi_\infty = u_\infty x$ results in an inflow velocity positive in a direction parallel to the x-axis. A surface distribution of sources is placed on the sphere, and the distribution of dipoles required to enforce zero potential inside the sphere is obtained. For this test, and as in all further cases none of the far-field formulae – Eqs. (4.67) and (4.68) – for surface panels are used when generating the influence coefficient matrices (their use is reserved for computing farfield velocities by numerical differentiation).

Since it is not possible to discriminate between errors introduced during pre-processing, processing and post-processing in a post hoc analysis of the results – that is, it is not possible to disentangle the errors due to the method from those due to pre-processing, and similarly, those due to post-processing from those of the method (and hence also pre-processing) – in an attempt to get a handle on the the causality and error cascade, analysis is performed at all three stages. The quality of surface representation afforded by each of the three meshing strategies is considered first. Next an analysis of the quality of the distribution of ϕ – the "raw" data produced by the code – is undertaken. Errors due to the post-processing step are isolated by considering the accuracy of the gradient calculation. Finally, the surface pressure distribution – the "processed" result which includes the effects of all errors – is examined.

Details of Numerical Experiments The BEM grid is refined. Because of the nature of the grid generation of the triangular mesh, it is only possible to generate tri meshes between integer refinement levels 2 and 5 before the number of panels becomes too large for the available memory on the test computer since influence coefficient matrices occupy size of each element (8 B for a double precision [64 bit – no tests were performed at 32 bit] floating-point number) multiplied by the number of panels squared, and there are two matrices. It was obviously easier to control the element counts on the quadrilateral grids.

To begin, the quality of the mesh is evaluated by analysing the degree of sphericalness. All panels are composed of chords of the sphere, and points along the chords deviate from the sphere surface except at their defining mesh vertices which lie exactly on the surface of the sphere. The exact location of the panel centroid is defined as that obtained in spherical coordinates by using the average azimuth and elevation angles of the corner points at a radius of exactly unity, whereas the method herein uses a collocation point at the centroid of the panel defined by the corner points in Cartesian coordinates. The following two pre-processor error metrics are thus obtained at the panel collocation points which are coincident with the element centroids:

Table 7.1: Geometric, processing and post-processing error convergence for a non-lifting sphere. Quad mesh by revolution: $N_{\text{elem.}} = [m \times m]$ panels; quad mesh by patching: $N_{\text{elem.}} = 6 \times [n \times n]$ panels; tri mesh by recursion: $N_{\text{elem.}} = 5 \times 4^r$ panels at r recursion levels.

Mesh	Refinement	$N_{\text{elem.}}$	$h_{\text{equiv.}}$	$\|\epsilon_R\|_\infty$	$\|\epsilon_{\boldsymbol{n}}\|_\infty$	$\|\epsilon_\phi\|_\infty$	$\|\epsilon_{C_p}\|_\infty$
Rev.	$m = 35$	1225	0.0286	5.0286×10^{-3}	1.4547×10^{-2}	6.5415×10^{-3}	2.2572×10^{-2}
	$m = 71$	5041	0.0141	1.2233×10^{-3}	7.3252×10^{-3}	3.4698×10^{-3}	5.5013×10^{-3}
	$m = 142$	20164	0.0070	3.0586×10^{-4}	3.6811×10^{-3}	1.7928×10^{-3}	1.3751×10^{-3}
Patch	$n = 14$	1176	0.0292	3.1292×10^{-3}	1.9065×10^{-3}	9.9175×10^{-3}	3.7190×10^{-2}
	$n = 29$	5046	0.0141	7.3302×10^{-4}	4.5283×10^{-4}	9.3902×10^{-3}	3.6093×10^{-2}
	$n = 58$	20184	0.0070	1.8331×10^{-4}	1.1422×10^{-4}	9.2039×10^{-3}	3.5812×10^{-2}
Tri.	$r = 4$	1280	0.0280	4.5284×10^{-3}	1.0718×10^{-2}	4.4430×10^{-3}	2.1750×10^{-2}
	$r = 5$	5120	0.0140	1.1379×10^{-3}	5.4236×10^{-3}	2.4478×10^{-3}	9.5708×10^{-3}
	$r = 6$	20480	0.0070	2.8484×10^{-4}	2.7198×10^{-3}	1.2668×10^{-3}	4.3053×10^{-3}

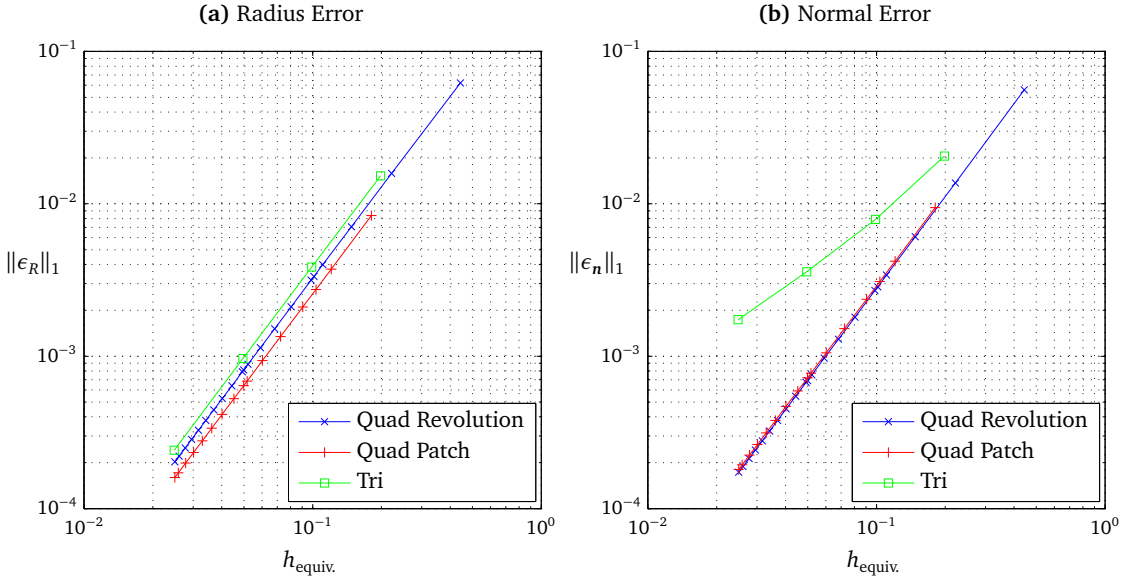

Figure 7.2: Grid convergence study for flow past a non-lifting sphere. The radius errors in all cases converge quadratically with mesh spacing h, as would be expected since the error in centroid location is related to the displacement along two chords; the normal errors for the quads converge quadratically, but the triangles converge linearly with h.

- **radius error:** the linear deviation of the centroid from the surface of the sphere, measured radially – this indicates how close the collocation point is to representing a point on the sphere even if it does not lie on the panel centroid;

- **normal error:** the angular deviation of the normal at the centroid from the position vector to the centroid obtained by averaging the vertex points in spherical coordinates – this indicates how good the collocation point and panel are at representing an infinitesimal surface element of the sphere.

The errors due to processing are all rolled into the single result (ϕ) which is the metric. The error in the results due to the method is defined as simply the difference between the expected and calculated ϕ at the panel collocation points. This is the only result which can obtained from the method without further post-processing and is obviously a combination of discretisation and process errors.

In the code as it is applied, an assumption is made that the general panel will be a quad element with eight distinct neighbours. A pre-processing step determines the four side and four corner neighbours of each panel, and these are later used to perform gradient calculations using finite-difference operators applied in local panel coordinates. This simplifies matters greatly in cases where rectangular patches have been mapped onto body surfaces, e.g. wings or turbine blades. If the situation arises where, for example, a panel side neighbour is the same element as its corner neighbour, the local co-ordinate system on the panel is no longer smooth, and there will be an error in the computed result. This is always true for triangular elements. In these cases, and all tests described in this section, the surface gradients are obtained using a least-squares gradient reconstruction which encompasses all panels within a 10° arc of the collocation point of the panel at which the gradient is being sought.

Post-processing errors arise due to the approximation of the surface gradients. This test uses a least squares approximation, and the number of neighbouring points considered thus varies with the mesh density.

Numerical Results The error in process variable, denoted ε_ϕ, is obtained by comparison against the analytical solution, Eq. (7.1). This can be obtained for all panels by considering the angle θ between the (analytical) sphere normal at the (analytical) panel centroid and the inflow velocity vector. Again, the l^2-norms of the errors are computed for each mesh case.

Post-processing errors associated with the gradient reconstruction can easily be examined by application of the least-squares coefficient matrix to the solution vector, and

	Error l^1-norms						GCI %		
Mesh	Coarse	Medium	Fine	Continuous	R	p	m-c	f-m	ratio
Rev	3.011×10^{-3}	7.332×10^{-4}	1.834×10^{-4}	8.527×10^{-6}	0.241	2.05	8.73×10^{-2}	2.187×10^{-2}	0.963
Patch	2.737×10^{-3}	6.387×10^{-4}	1.597×10^{-4}	1.807×10^{-5}	0.228	2.13	7.05×10^{-2}	1.771×10^{-2}	0.909
Tri	3.810×10^{-3}	9.545×10^{-4}	2.388×10^{-4}	-6.799×10^{-7}	0.251	2.00	1.20×10^{-1}	2.994×10^{-2}	1.001

(a) Radius errors $\epsilon = \dfrac{|\boldsymbol{r}_{\text{colloc.-pt.}} - \boldsymbol{r}_{\text{sphere}}|}{|\boldsymbol{r}_{\text{sphere}}|}$ [1].

Rev	3.377×10^{-3}	8.284×10^{-4}	2.076×10^{-4}	7.646×10^{-6}	0.244	2.04	9.89×10^{-2}	2.500×10^{-2}	0.963
Patch	1.378×10^{-3}	3.212×10^{-4}	8.030×10^{-5}	9.198×10^{-6}	0.228	2.13	3.54×10^{-2}	8.889×10^{-3}	0.909
Tri	6.457×10^{-3}	3.225×10^{-3}	1.612×10^{-3}	5.462×10^{-6}	0.499	1.00	4.04×10^{-1}	2.011×10^{-1}	1.002

(b) Normal errors $\epsilon = \arccos\left(\dfrac{\boldsymbol{n}_{\text{colloc.-pt.}} \cdot \boldsymbol{r}_{\text{sphere}}}{|\boldsymbol{n}_{\text{colloc.-pt.}}||\boldsymbol{r}_{\text{sphere}}|}\right)$ [rad].

Rev	4.963×10^{-4}	1.216×10^{-4}	3.050×10^{-5}	1.226×10^{-6}	0.243	2.04	1.45×10^{-2}	3.659×10^{-3}	0.963
Patch	4.816×10^{-3}	4.977×10^{-3}	4.996×10^{-3}	4.999×10^{-3}	0.121	3.04	2.46×10^{-3}	3.370×10^{-4}	0.886
Tri	1.369×10^{-3}	7.287×10^{-4}	3.747×10^{-4}	-6.256×10^{-5}	0.553	0.86	9.90×10^{-2}	5.468×10^{-2}	1.000

(c) Perturbation potential errors $\epsilon = \phi_{\text{colloc.-pt.}} - \dfrac{3}{2} u_\infty r \cos\theta$ [$\text{m}^2\,\text{s}^{-1}$].

Rev	8.028×10^{-3}	1.941×10^{-3}	4.846×10^{-4}	2.676×10^{-5}	0.239	2.06	2.31×10^{-1}	5.725×10^{-2}	0.964
Patch	2.051×10^{-2}	2.023×10^{-2}	2.027×10^{-2}	–	−0.150	–	–	–	–
Tri	7.039×10^{-3}	2.516×10^{-3}	1.069×10^{-3}	3.884×10^{-4}	0.320	1.64	2.67×10^{-1}	8.518×10^{-2}	1.001

(d) Pressure coefficient errors $\epsilon = C_p - \left(1 - \dfrac{9}{4}\sin^2\theta\right)$ [1].

comparing the computed and input solutions. The error in pressure coefficient is obtained by comparison of the post-processed pressure distribution and contains the effects of the errors due to all preceding steps including the least-squares error.

Table 7.1 details the grids considered and lists the errors obtained, Table 7.2 show the results of a convergence study on the result errors. The radius and normal error norms are plotted in Fig. 7.2. Figure D.1 in Appendix D plots the distributions of pressure coefficients and errors in velocity potential over the sphere surfaces.

Discussion The results are very promising. Convergence rates of geometric quantities is apparently related to the equivalent area of the panels, except in the case of the normal errors in the tri-mesh, which converge with the panel equivalent length. Errors in ϕ converge in both the quad-rev and tri-mesh cases, but for some unknown reason it does not seem possible to get convergence on zero error from the quad-patches. It is not apparent why this should be: both radius and normal errors converge on zero and it was not possible to identify the cause of this. The main contender for the error is most likely a "user" error in post-processing, since there is not an obvious reason why this meshing strategy should be ineffective. (It remains to say that the values predicted using the quad-patch meshing are still fairly close in agreement with the analytical solutions: it is only by comparison with the other methods that the errors are significant.) As a result, the pressure coefficient was non-convergent for the quad-patches, converged at a $\mathcal{O}(h^2)$ rate for the quad by revolution mesh, and at a considerably slower rate for the triangular mesh.

What is interesting is the distribution of errors in all mesh cases. For the quad-revolution case both geometric, ϕ and pressure errors are focussed at the poles where the quadrilaterals deteriorate into high aspect-ratio triangles. For the quad-patch, the geometric errors increase towards the interior of the patches, and correlate strongly with the area of the panels. For the mesh quality, panels with high skew are focussed at the seams between the patches, and concentrate especially at the points where three patches meet – fortunately this does not appear to influence the processing, and is not carried over into the post-processing, since the least-squares surface gradient reconstruction does not consider which patch a panel belongs to. The ϕ errors start uniformly high on the upwind ($x < 0$) face , and their value drops symmetrically then changes sign and increases as $x > 0$, with a band of zero error around the longitude lying on the $x = 0$ plane. The triangular mesh error distribution is by far the most intriguing, showing triangular and pentagonal clusters of

Table 7.2*(facing page)*: Grid convergence study for three-dimensional flow about a non-lifting sphere. $u_\infty = 1$, $r = 1$, θ around transformed z'-axis.

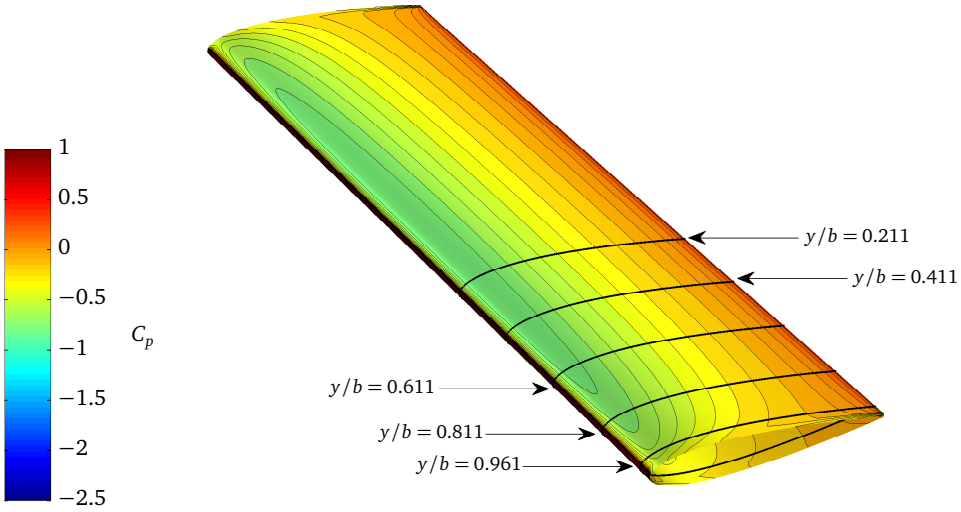

Figure 7.3: Case A1 pressure distribution. C_p over three-dimensional ($AR = 4$) NACA 0015 hydrofoil at α =2.5°, resolved over 64 cells (BEM mesh 64 × 64).

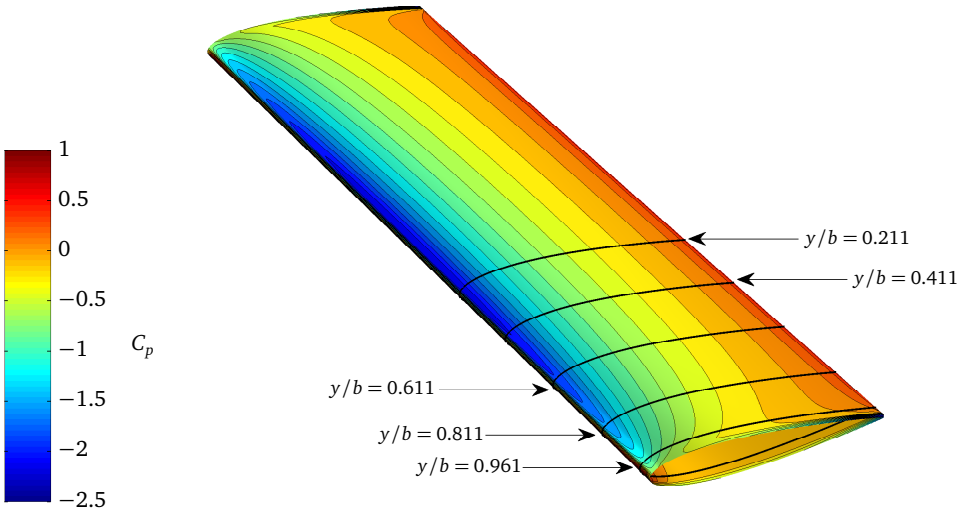

Figure 7.4: Case A2 pressure distribution. C_p over three-dimensional ($AR = 4$) NACA 0015 hydrofoil at α =8.5°, resolved over 64 FVM cells (BEM mesh 64 × 64).

Case	Source	Aspect-ratio	Angle of Incidence	Reynolds number
A1	Falcão de Campos (1988)	4.0	2.5°	1.72×10^6
A2	Falcão de Campos (1988)	4.0	8.5°	1.73×10^6
B	McAlister and Takahashi (1991)	6.6	12°	2.0×10^6

Table 7.3: Case particulars for three-dimensional hydrofoils.

triangles in a recursive arrangement. It is not clear why the errors are in this configuration, although it is logical that the geometric errors follow the area of the panels (and the panel equivalent lengths) directly, and the normal error is probably a good surrogate indicator of how far the panels are from being equilateral. This is corroborated to some extent by comparison of the distribution of the skew (computed using the circumcircle method), although in panels with zero skew there is still both radius and normal error. The distribution of ϕ error in the triangular mesh exhibits a similar hierarchical triangular chequerboarding pattern, however in this case, there is an underlying quadrilateral/hexagonal pattern also, and it does not appear that the distribution of ϕ errors is related to the radius error nor the normal error and is apparently insensitive to the very small fluctuations in skew.

In all cases, the overall distribution of the pressure coefficient follows the analytical solution satisfactorily.

7.3 Lifting Bodies

7.3.1 Static Hydrofoil

Description This section compares the predictions of the FVM/BEM code obtained in three dimensions for rectangular hydrofoil/wing geometry based on a NACA 0015 aerofoil section. Results are generated for mesh densities beginning at what could be considered "the bare minimum" to obtain (semi) usable results for minimum computational effort, and scale up mesh densities through a practical medium to an absolute maximum given available computational resource. The results are compared with one-another to demonstrate convergence, and final results are compared to those obtained from the literature.

The objective of this section is to use the simplest coupled three-dimensional flow scenario to demonstrate the convergent behaviour of the method, obtain confidence that predictions are capable of representing experimental data, and so determine the practical mesh requirements to obtain reasonable results.

Previous Results The results obtained numerically are compared with experimental data from the literature, specifically the cavitation tunnel results in Falcão de Campos (1988) for a hydrofoil and those from a wind tunnel in McAlister and Takahashi (1991) for a symmetric half-wing. These data allow comparison of surface pressures with results obtained for a low aspect-ratio wings, $AR = 4,6$, which will demonstrate three-dimensional effects (the cavitation tunnel data are also obtained using water as the working fluid).

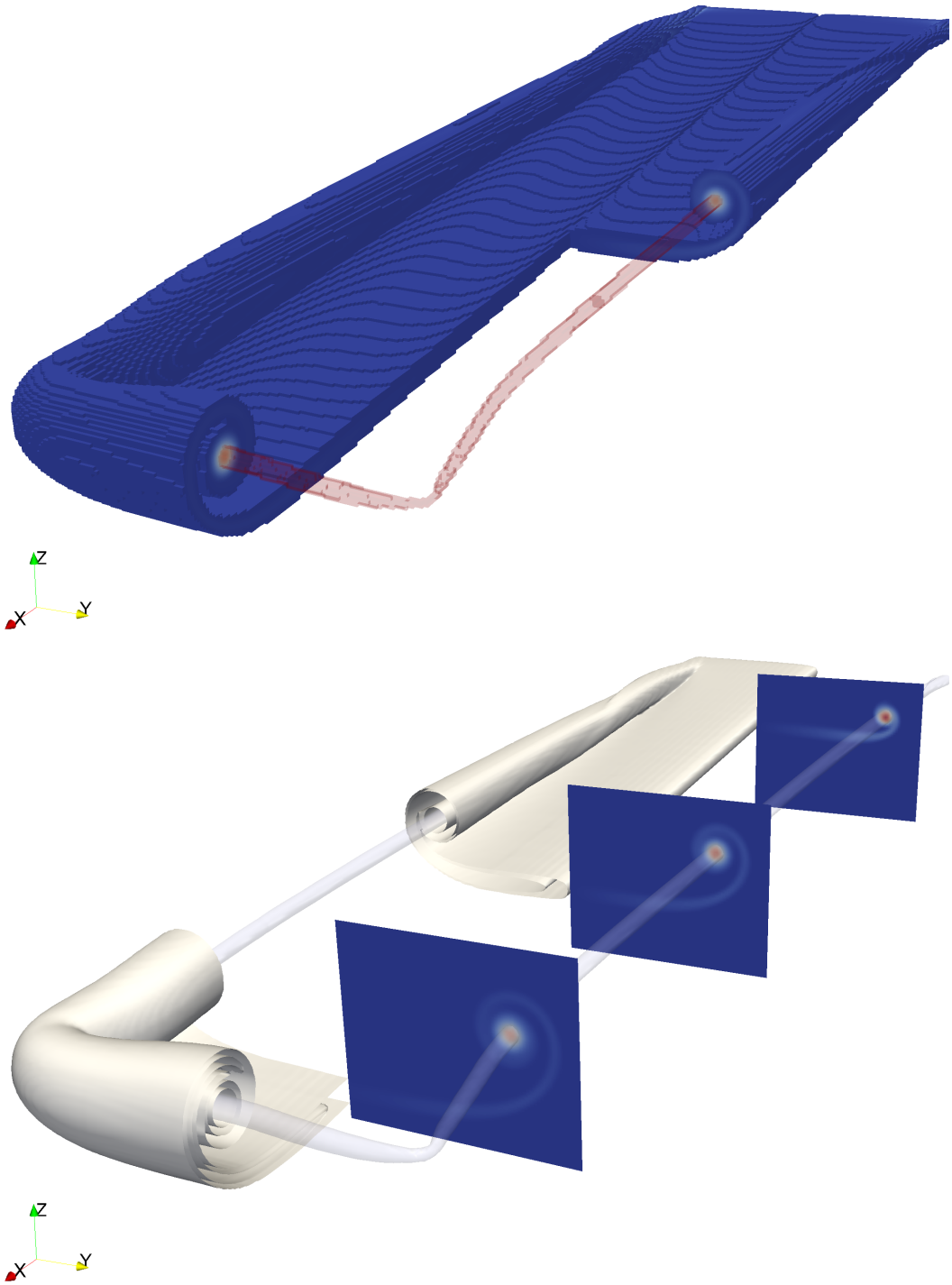

Figure 7.5: Vorticity isosurface images of the hydrofoil wake detail, taken at $t = 16c/u_\infty$. Contours of $|\boldsymbol{\omega}| = [0.01, 0.1, 1]\,\text{sec}^{-1}$ (white) to show sheet rollup and indication of active cells in blue in to domain as seen in tree. Core illustrated in red (above) and cornflower (below) taken at $|\boldsymbol{\omega}| = 5\,\text{sec}^{-1}$.

Relevance Static wings generating lift will also generate a vortex wake sheet which rolls up into coherent outboard "trailing" vortices separated by inboard "shed" vorticity. The tip vortices will induce downwash on the surface of the wing, which diminishes towards the centre-span, reducing the effective angle of attack and thus decreasing lift. This will be manifest in the pressure distribution on the surfaces of the wing. As the tip vortices leave the wing their axes will collimate, they will entrain vorticity shed inboard and their vorticity will be convected downstream.

This test focusses on the ability of the model to generate a good approximation of the wake, and thus effectively recover a reasonably accurate surface pressure distribution, especially in the span-wise direction. The relevance of this example is thus in demonstrating an effective coupling between the Boundary Element and the Finite Volume aspects of the code. Obviously, failure to generate adequate results in a simple, static test case severely hamper the applicability of the method when applied to more complex or moving geometry.

Problem Definition In all three-dimensional hydrofoil/wing cases the problem is posed as follows. Initial conditions are zero vorticity throughout the domain. A wing, composed of NACA 0015 aerofoil sections, is considered using a BEM mesh providing a surface approximation consisting of flat quadrilateral elements. This geometry is then translated forward a distance $c/4$ and rotated about the y-axis to the desired angle of attack. A freestream velocity $\boldsymbol{u}_\infty$ is specified as $2.5\,\mathrm{m\,s^{-1}}$ along the x-axis, and finite-volume kinematic viscosity ν is obtained such that the chord Reynolds numbers are as given in Table 7.3.

Details of Numerical Experiments Initial tests consider the implications of the density of the surface mesh, and an Eulerian mesh density approximately equal to the number of panels along the hydrofoil span is chosen, such that there are no empty cells when binning the vortons. Boundary mesh generation parameters: Gaussian chord bell spacing parameter $\sigma^2 = 7$, span bell parameter $\sigma^2 = 16$, where the meaning of σ is given by in the equation for mesh spacing:

$$\delta x = \frac{1}{\sigma \cdot \sqrt{2\pi}} \exp\left(-100 \frac{\left(x - \frac{1}{2}\right)^2}{2\sigma^2} \right). \tag{7.4}$$

Table 7.4: Grid convergence metrics for flow past a three-dimensional hydrofoil cases A1 and A2 using three-dimensional lift coefficients.

	Wing C_L						GCI %		
	Coarse	Medium	Fine	Continuum	R	p	m-c	f-m	ratio
				α =2.5°					
Eq. (7.5a)	0.1667	0.1669	0.1672	0.1681	0.812	0.73	0.86	0.70	1.00
Eq. (7.5b)	0.1687	0.1689	0.1691	0.1701	0.811	0.73	0.83	0.67	1.00
				α =8.5°					
Eq. (7.5a)	0.5649	0.5657	0.5663	0.5694	0.823	0.68	0.82	0.67	1.00
Eq. (7.5b)	0.5727	0.5736	0.5743	0.5774	0.811	0.73	0.83	0.67	1.00

Table 7.5: Grid convergence study for case A1 and A2 using local section lift coefficients.

(a) C_l grid convergence metrics for flow past a 3-D hydrofoil, $\alpha = 2.5°$

	$C_l\,(y/b)$						GCI %		
y/b	Coarse	Medium	Fine	Continuum	R	p	m-c	f-m	ratio
0.211	0.197	0.198	0.199	0.201	0.781	0.86	1.75	1.36	1.00
0.411	0.188	0.189	0.189	0.191	0.786	0.84	1.74	1.36	1.00
0.611	0.169	0.169	0.170	0.172	0.798	0.78	1.74	1.38	1.00
0.811	0.131	0.131	0.131	0.133	0.851	0.56	1.93	1.64	1.00
0.961	0.072	0.072	0.071	0.071	0.381	3.35	0.49	0.19	1.00

(b) C_l grid convergence metrics for flow past a 3-D hydrofoil, $\alpha = 8.5°$

	$C_l\,(y/b)$						GCI %		
y/b	Coarse	Medium	Fine	Continuum	R	p	m-c	f-m	ratio
0.211	0.665	0.668	0.670	0.677	0.781	0.86	1.75	1.36	1.00
0.411	0.633	0.636	0.638	0.645	0.786	0.84	1.74	1.36	1.00
0.611	0.569	0.571	0.572	0.579	0.798	0.78	1.74	1.39	1.00
0.811	0.441	0.442	0.443	0.449	0.850	0.56	1.93	1.64	1.00
0.961	0.246	0.245	0.245	0.243	0.675	1.37	0.94	0.64	1.00

In order to determine the convergence (or otherwise) of the solution, the lift coefficient is used as a data reduction variable and computed via the following two methods,

$$C_L = \frac{2}{u_\infty S} \int_{-b/2}^{b/2} \Delta\phi\,(y)\,\mathrm{d}y \qquad \text{and} \tag{7.5a}$$

$$C_L = \frac{2}{\rho u_\infty^2 S} \sum_{\text{Panels}} \Big(\Delta F_z \cos\alpha - \Delta F_x \sin\alpha \Big). \tag{7.5b}$$

Eq. (7.5a) is the lift obtained by the Kutta-Jukowski theorem, Eq. (7.5b) that obtained by summing the calculated force contributions of all the panels. To determine the cause of convergence difficulties, the local convergence along the span is also examined, using the local section C_l.

In order to obtain a reasonable spread of results, a refinement factor of 2 is used such that after obtaining the finest mesh that can reasonably be computed, successive meshes have half the chord and span-wise resolution of the mesh preceding to eventually obtain the following grids: 16×16, 32×32, and 64×64, representing the number of panels on each of the top and bottom surfaces in the chordwise direction, and the number of panels in the spanwise direction.

Numerical Results For the first test a refinement on the FVM and BEM grids is performed. Since the CFL condition is used to determine the time-step length in an ad hoc, solution dependant manner, it is not possible to de-couple the global time-step and mesh sizes for refinement study. Similarly, since the FVM mesh density is linked directly to the BEM mesh density so as to avoid empty cells when binning the wake vorticity, the number of degrees of freedom is limited to simply the BEM mesh density (acknowledging that as this increases, the FVM mesh density increases and the global - external - time-step reduces). The simulation duration and the FMM expansion order are taken as 20 seconds and 8 respectively.

To evaluate visually the effect of increasing the mesh density, chord-wise pressure coefficient (C_p) distributions are calculated and compared at the following span-wise stations $y/b = \{0.211, 0.411, 0.611, 0.811 \text{ and } 0.961\}$. The experimental results due to Falcão de Campos (1988) are then superimposed for comparison. The pressure coefficients are obtained on the blade surfaces, interpolated to the required spanwise stations and plotted in Figs. D.2 and D.3 in Appendix D along with the spanwise distribution of circulation for each mesh density.

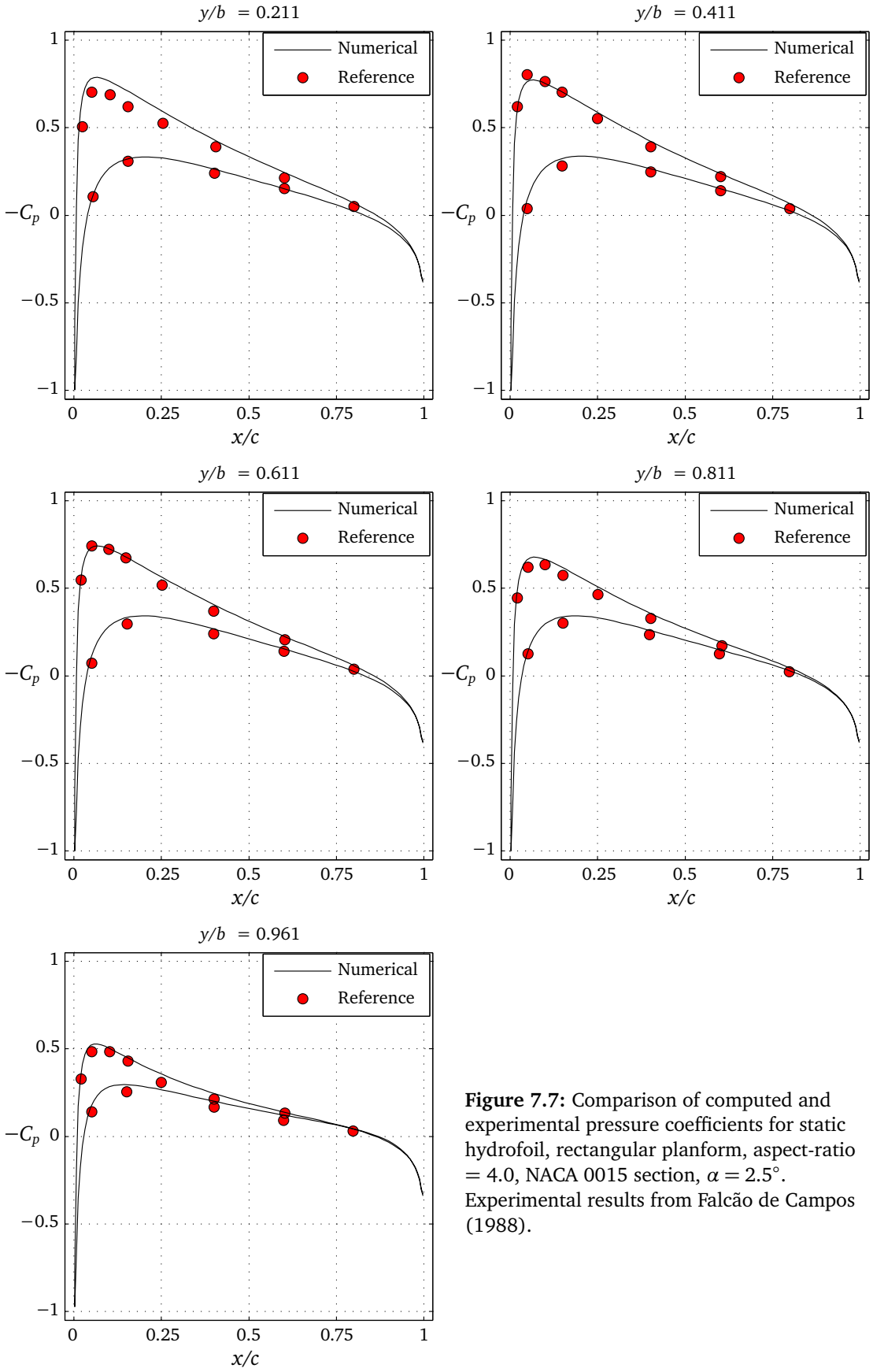

Figure 7.7: Comparison of computed and experimental pressure coefficients for static hydrofoil, rectangular planform, aspect-ratio = 4.0, NACA 0015 section, $\alpha = 2.5°$. Experimental results from Falcão de Campos (1988).

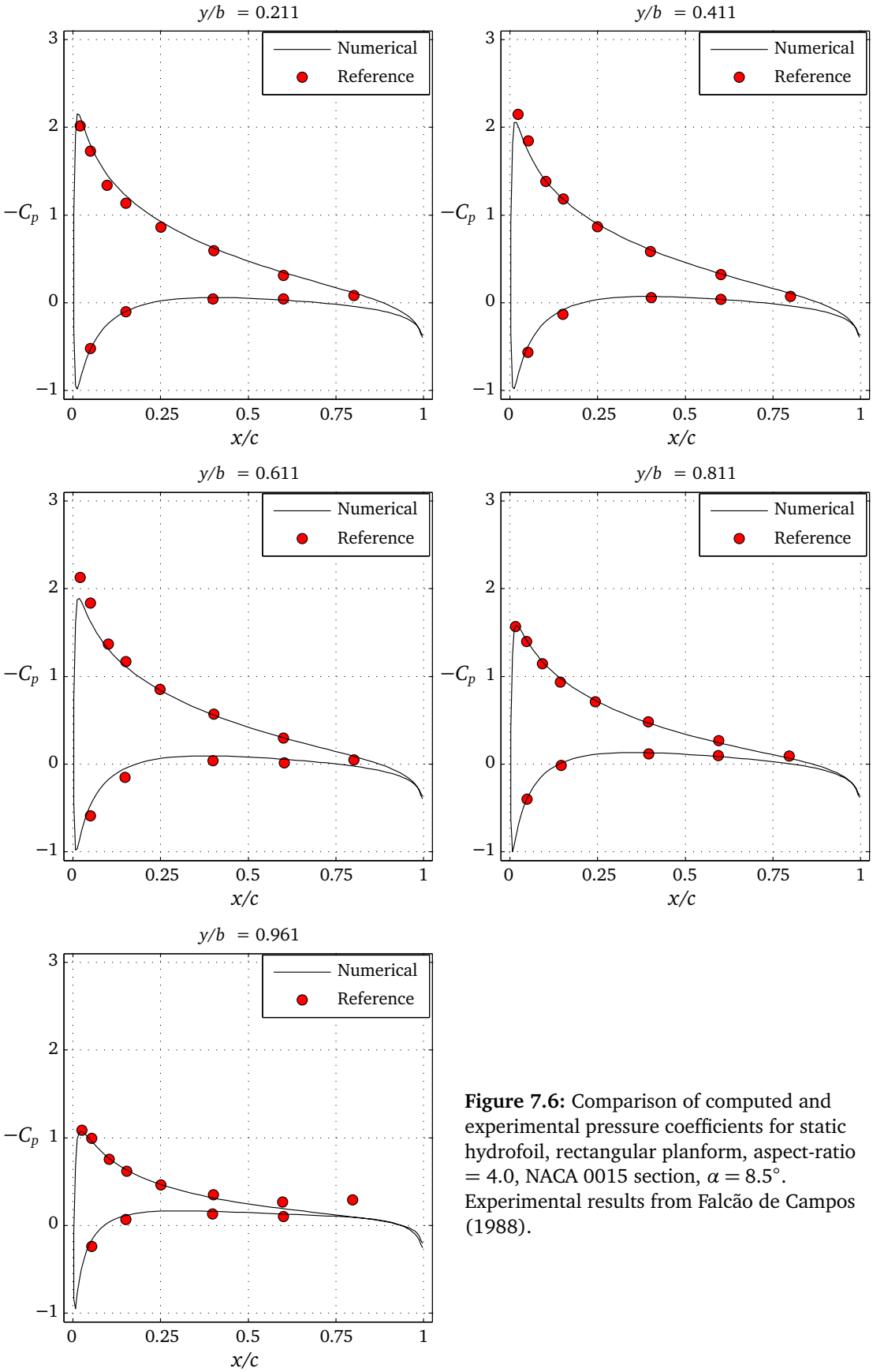

Figure 7.6: Comparison of computed and experimental pressure coefficients for static hydrofoil, rectangular planform, aspect-ratio = 4.0, NACA 0015 section, $\alpha = 8.5°$. Experimental results from Falcão de Campos (1988).

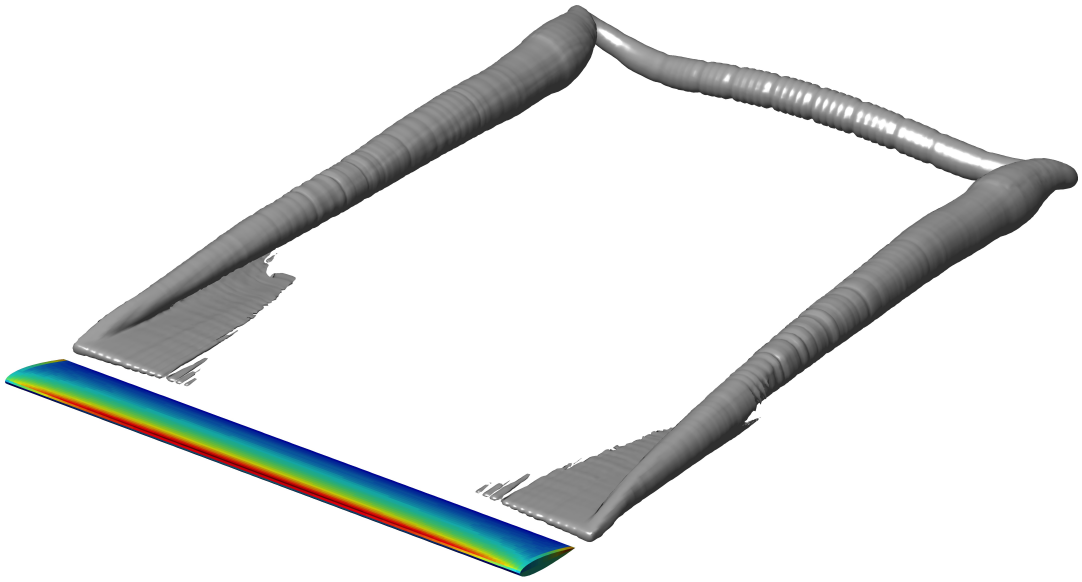

Figure 7.8: Vorticity l^2 isosurfaces for case B wing after time $u_\infty t/c = 7$.

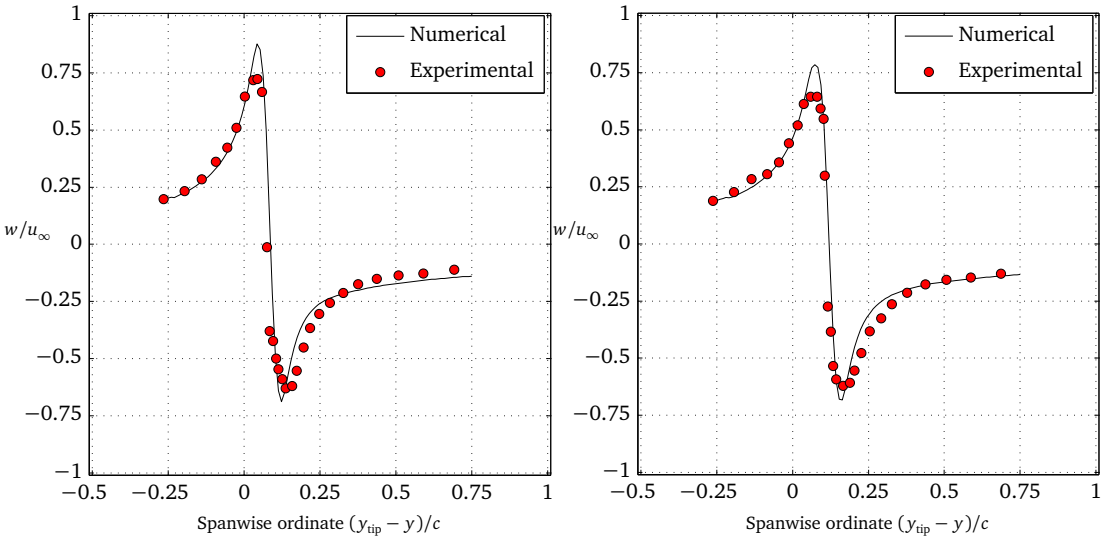

(a) $(x - x_{TE})/c = 1$

(b) $(x - x_{TE})/c = 2$

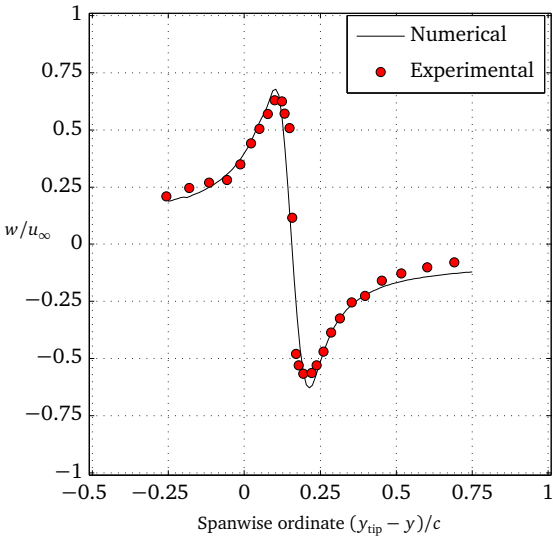

(c) $(x - x_{TE})/c = 4$

Figure 7.9: Comparison of computed and experimental vertical (w) velocities in the wake of a static hydrofoil, rectangular planform, aspect-ratio = 6.6, NACA 0015 section, $\alpha = 12°$. Experimental results from McAlister and Takahashi (1991).

At each station, the pressure distribution is integrated to yield the local sectional lift coefficient, and these are presented in Tables 7.5a and 7.5b. The wing three-dimensional lift coefficient is also calculated for each mesh, using the two methods outlined above, and presented in Table 7.4.

Figure 7.5 shows a cutaway of the active cells in the domain and vorticity isosurfaces for the wake, taken from the high resolution case after $t = 16c/u_\infty$ seconds. Similarly, Fig. D.4 in Appendix D shows the high and also the low and intermediate resolution wake isosurfaces obtained for the time $t = 33c/u_\infty$ seconds.

The numerical results calculated at the highest mesh resolution are compared with experimental results of Falcão de Campos (1988), obtained using the Large Cavitation Tunnel facility at MARIN. These are presented in Figs. 7.6 and 7.7 for cases A1 and A2 respectively. Pressure coefficients are presented at the same span-wise ordinates as per the verification process above, along with experimental results of the same.

Figure 7.9 shows a series of velocity transects of the wake behind the higher aspect-ratio foil in case B. The vertical velocity is plotted at one, two and four chordlengths downstream from the trailing edge and compared with the experimental data presented in McAlister and Takahashi (1991). These were obtained using a 64×64 panel mesh after 20 seconds simulation time.

Discussion and Conclusions Results presented for the static foil cases show reasonable convergence – not quite at a rate of unity, but close – except near the tip. Looking at Figs. D.2 and D.3, it is apparent that in each case the 16×16 panel mesh is insufficient towards the tip. This gives rise to a non-plot-convergent lift contribution towards the tip at low resolutions. This does not really come across in the grid-convergence tables: the integrated section lift is approximately the same as in the medium and fine resolutions, but the mechanism by which it is generated is different. The low resolution case has both higher suction and lower pressure at $y/b = 0.961$. Assuming that there are no “user" errors in the method, the obvious contenders for explanation of this are:

- that the tip vortex is not interpolated to sufficiently high a resolution;
- errors in computing the surface velocity gradients (done here using central differences inboard of sharp edges between adjoining sections of the mesh, forward/backward differences at sharp edged interfaces); and
- interpolation errors due to the distribution of panels towards the tip.

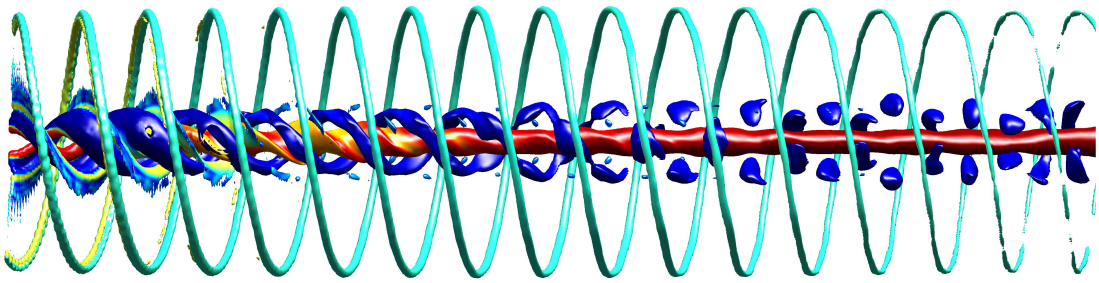

Figure 7.10: Computational results for NREL rotor resolved over 72 FVM cells (BEM mesh 32×32). Tip-speed ratio $\lambda = 5.4$, simulation time is $2\pi\Omega t = 10$ revs. Isosurface of vorticity magnitude $|\boldsymbol{\omega}| = 4.0$, coloured by axial vorticity ω_x.

Figure 7.11: NREL wake vorticity with stretching term calculated via the FVM.

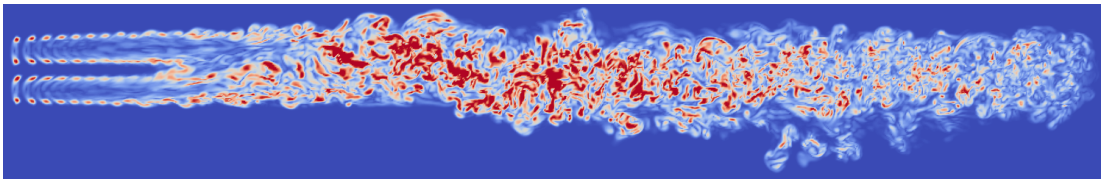

Figure 7.12: NREL wake vorticity with stretching term calculated via the FMM.

Table 7.6: Grid convergence study for the NREL Phase VI turbine rotor at $\lambda = 5.41$ using local section lift coefficients. Coarse mesh is 16×16 panels, medium is 32×32 and fine 64×64.

	$C_l\,(r/R)$						GCI %		
r/R	Coarse	Medium	Fine	Continuum	R	p	m-c	f-m	ratio
0.3	0.727	0.756	0.768	0.779	0.447	1.16	3.81	1.68	1.02
0.47	0.827	0.857	0.872	0.887	0.496	1.01	4.41	2.15	1.02
0.63	0.816	0.844	0.857	0.867	0.445	1.17	3.31	1.45	1.01
0.8	0.734	0.757	0.766	0.772	0.401	1.32	2.53	1.00	1.01
0.95	0.557	0.546	0.543	0.541	0.342	1.55	1.28	0.44	0.99

A series of experiments using clusters of mesh points towards the tip indicate that the resolution of ϕ and also the numerical differentiation are the source of a very small component of the overall error. By running simulations at considerably higher FVM mesh densities, and by comparison with results from "pure" BEM-panel wakes – of both free and fixed-wake geometries – it is concluded that the error is a result of incorrect inflow due to incorrect wake geometry representation, since the errors reduce in the free-wake panel only model. Running higher FVM cell count along the span than the number of panels increases the number of empty cells – this results in a non-overlapping vorticity field due to empty cells.

The topology of the wake is examined in Figs. 7.5, 7.8, 7.9 and D.4. Visual inspection indicates that the three-dimensional wake development, in particular the rollup is modelled well. The concentrated cores of tip vorticity are tracked downstream until meeting the starting vortex, which is preserved for some considerable time. Figure D.4 shows that the distribution of vorticity appears visually convergent, and that the vorticity is preserved even for the very low resolution meshes. Also visible in Fig. D.4 is the difference in the vorticity field immediately after the trailing edge: the low resolution case both lacks the fine detail and has considerably higher vortex core diameters – accounting in part for the disparity in results discussed previously.

The strength of the tip vortices appears to be commensurate with the predicted three-dimensional lift coefficient, as confirmed by comparison of the circulatory and pressure lift coefficients, and this is confirmed by examining the wake velocity transects for the Case B aerofoil. In Fig. 7.9 the proposed method appears to predict both the strength and the location of the outboard vorticity, and in particular the cores, quite well – there is some marginal disagreement with experiment for the inboard vortex sheet strength. This might be due to the use in McAlister and Takahashi (1991) of a wall bounded semi-span rather than an isolated wing as in the present method – an interesting comparison would be to model this case including the wind-tunnel walls – however the results are encouraging.

7.3.2 NREL Phase VI Wind Turbine

Description This Section presents a comparison with a turbine rotor. The NREL Phase VI NASA Ames wind tunnel tests are significant since they are one of a very small number of sources of published and reviewed pressure coefficient data for a turbine rotor experiment. What is more remarkable is that, like the MEXICO experiment, the turbine experiment was performed at full scale, and thus the results are for full scale Reynolds numbers.

Results are generated at a range of mesh densities, seeking to obtain indication of the

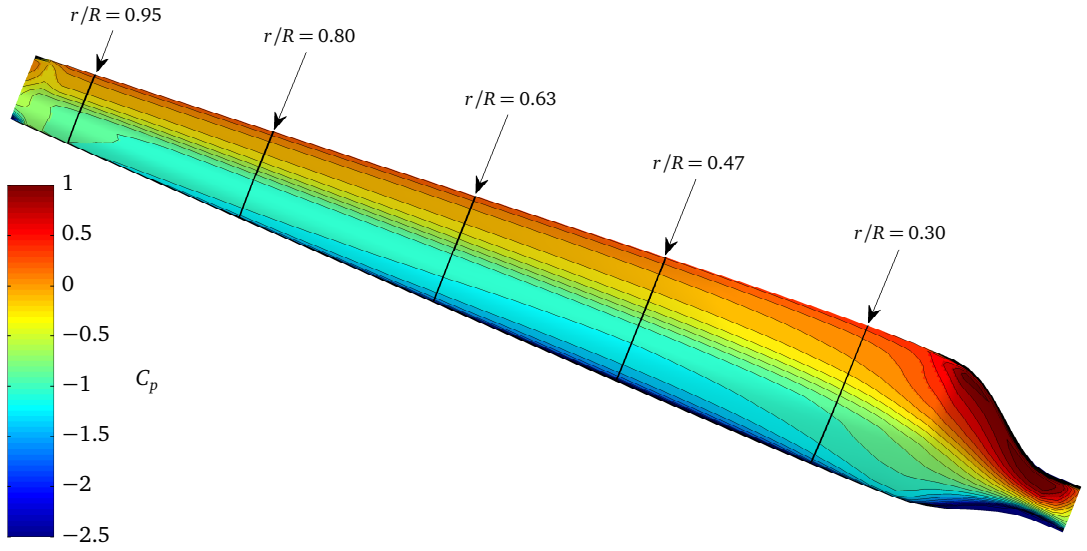

Figure 7.13: Pressure coefficient on suction side of blade of the NREL rotor resolved over 72 FVM cells (BEM mesh 32×32). Tip-speed ratio $\lambda = 5.4$, simulation time is $2\pi\Omega t = 5$ revs.

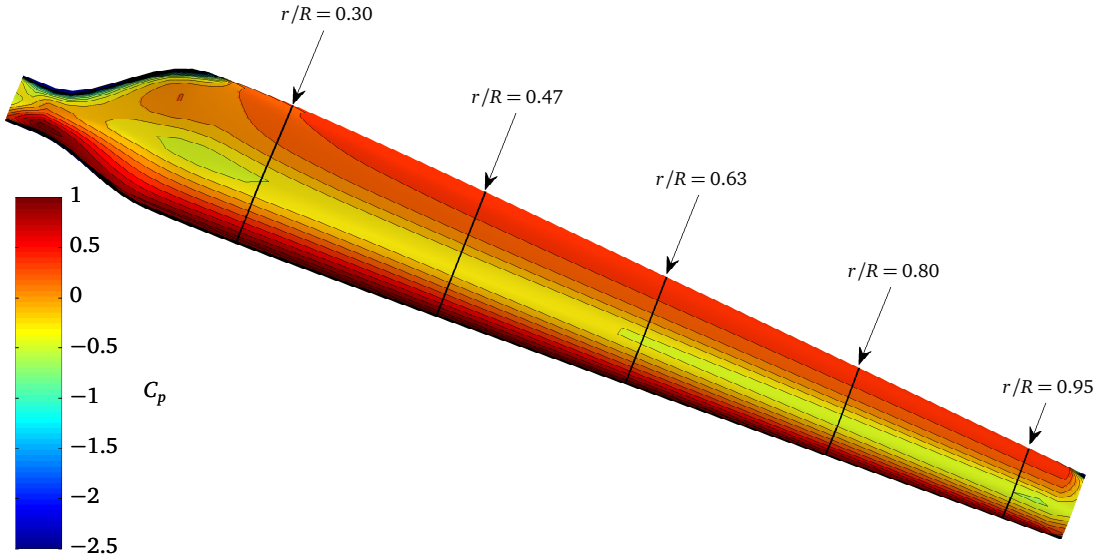

Figure 7.14: Pressure coefficient on pressure side of blade of the NREL rotor resolved over 72 FVM cells (BEM mesh 32×32). Tip-speed ratio $\lambda = 5.4$, simulation time is $2\pi\Omega t = 5$ revs.

lowest usable mesh density, a practical "day-to-day" mesh density and also the highest reasonable given our computational facilities.

The tests performed are a joint BEM and FVM mesh refinement study at $\lambda = 5.4$ and comparison with experimental pressure coefficient data obtained from the literature.

Relevance The objectives of this section are to demonstrate the convergent behaviour of the method when used to model rotating systems, obtain confidence that predictions are capable of representing experimental data, and determine the practical mesh requirements to obtain reasonable results.

Problem Definition Calculations are performed here on only an axial flow case without taking consideration of the nacelle, tower or wind tunnel walls. The details of the experiments are given in Simms *et al.* (2001). The rotor consists of 2 blades, composed of NREL S809 aerofoil sections, twisted and tapered according to Hand *et al.* (2001), and as given in Table D.1. Each blade is constructed using a BEM mesh providing a surface approximation consisting of quadrilateral elements. The blades are translated and rotated into their initial positions, set to a tip twist angle of 3° with zero cone. The machine is a constant speed device, and is modelled according to run S070000 at 71.9 RPM, so a freestream velocity u_∞ of $7\,\mathrm{m\,s^{-1}}$ along the x-axis results in the tip-speed ratio $\lambda = 5.41$.

Details of Numerical Experiments Initial conditions are zero vorticity throughout the domain. The dynamic viscosity is set as $1.769 \times 10^{-5}\,\mathrm{Pa\,s}$ with ρ=$1.246\,\mathrm{kg\,m^{-3}}$, resulting in a chord Reynolds number of 2×10^5 at the root and 9.7×10^5 at the tip. The kinematic viscosity is set appropriately in the finite-volume method.

Blade mesh densities of 16×16, 32×32, and 64×64 panels are generated, again with a bell-shaped distribution of points with $\sigma = 7$ in the chordwise direction. In the spanwise direction the distribution is constant, except around the root cutout.

Numerical Results Results are obtained for $\lambda = 5.4$ using the coarse, medium and fine meshes to generate pressure coefficient plots at the radial stations $r/R = \{0.3, 0.47, 0.63, 0.8 \text{ and } 0.95\}$. For all radii the experimental results from the NREL UAE Hand *et al.* (2001); Sørensen, Michelsen and Schreck (2002) are superimposed for comparison. The local section lift coefficients (due to the pressure distribution) are also calculated at these radii.

The pressure coefficients are calculated on the blade surfaces, interpolated to the required radial stations and plotted in Fig. D.6 along with the radial distribution of circulation for each mesh density. What is clear by visual inspection at each radius is the apparent

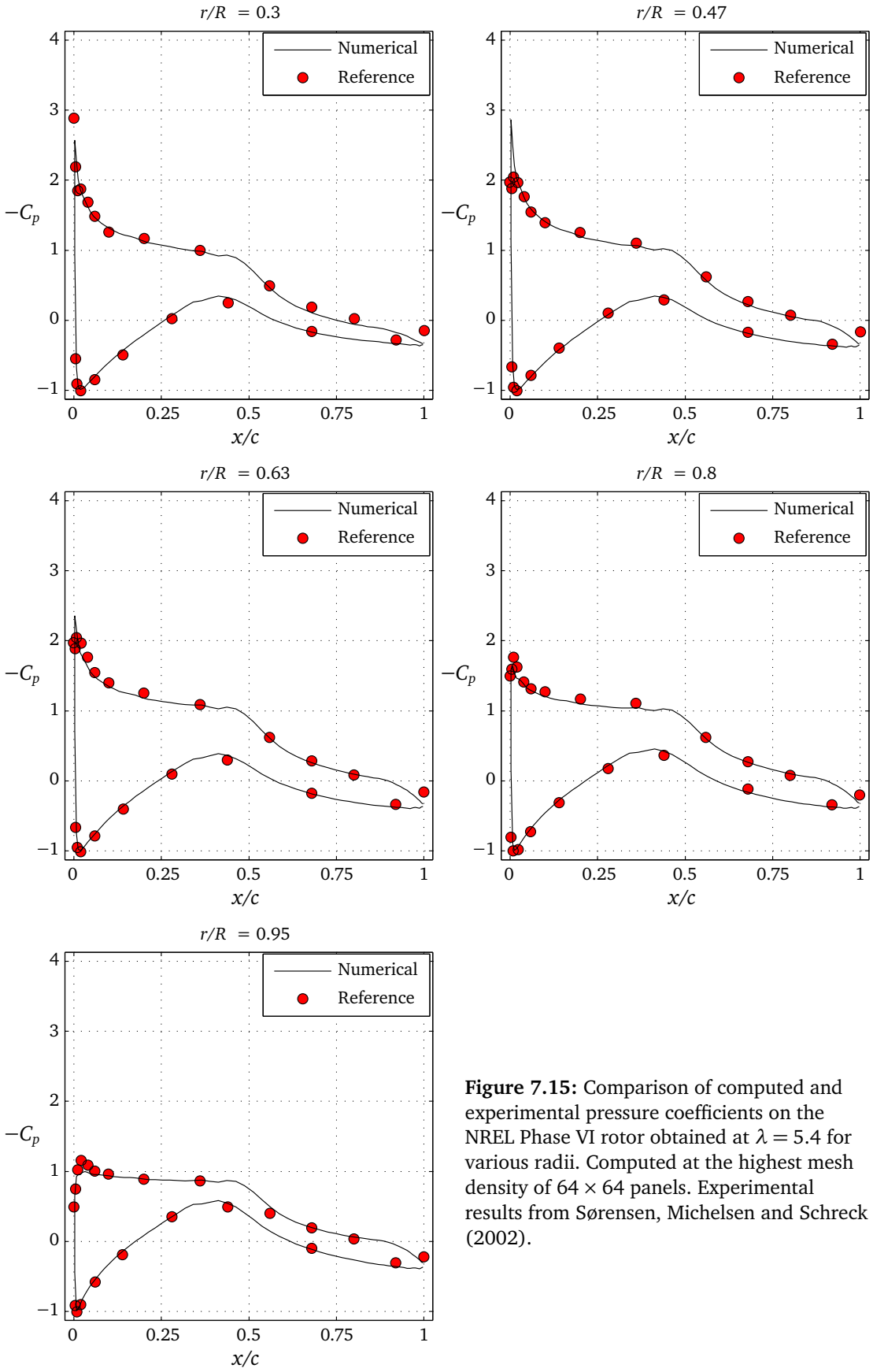

Figure 7.15: Comparison of computed and experimental pressure coefficients on the NREL Phase VI rotor obtained at $\lambda = 5.4$ for various radii. Computed at the highest mesh density of 64×64 panels. Experimental results from Sørensen, Michelsen and Schreck (2002).

proximity of the pressure distributions as calculated with each mesh. Save for a tendency to predict progressively lower suction peaks and closer approximations to zero trailing edge pressure difference, there is not much to split the results.

At each station, the pressure distribution is integrated to yield the local section lift coefficient, and these are presented in Table 7.6. The processed data bears out the similarity in the different solutions. All radius C_l are convergent in the asymptotic region ($R \approx 1$), and all exhibit a fine mesh uncertainty (GCI) in the order of a few percent.

The circulation distribution per unit span for each mesh is also drawn in Fig. D.6, normalised against the kinematic velocity at the tip. A dashed line at $r/R = 0.25$ indicates where the root cutout begins, and a "hump" in circulation can be seen inboard of this radius, due to a combination of the low radius and also recovering lift on the aerofoil sections inboard of the cutout (in reality, the blade blends into a cylindrical section at the root, whereas in the model it comprises an S809 section at the correct thickness). The circulation demonstrates plot convergence, with a narrowing gap between the coarse/medium, and medium/fine mesh results.

Figure 7.15 plots the results from the NREL UAE, taken from Sørensen, Michelsen and Schreck (2002), against those calculated at the highest mesh density using the present method. Save deviations towards the trailing edge, results for each radius map well onto the experimental data, although the upper surface suction peaks at the leading edge do seem to be over-predicted at $r/R = 0.47 - 0.63$, although there remains the possibility that the pressure tappings in the experiment were not concurrent with the suction peaks. Wake vorticity isosurfaces are presented in Figs. 7.10 and 7.16. The effects of the differing stretch/compression models (as discussed in Section 3.9) are presented in Figs. 7.11 and 7.12 where it is apparent that the higher-order method (using the FMM velocity field) results in much smaller flow-features than the linear method.

Discussion The major error in this test appears at the trailing edge, where all meshes produce a down-turned upper surface pressure coefficient distribution with a very small drop in lower surface pressure towards the trailing edge. In Sørensen, Michelsen and Schreck (2002), a RANS code produced results with a distinctly up-turned pressure coefficient towards the TE on the lower surface, and far less of a downturn on the upper. This appears to match the experimental data better than the present method, and is possibly down to conceptual errors – incorrect specification of the TE wake angle – or theoretical errors – separation towards the TE not being captured in the present method.

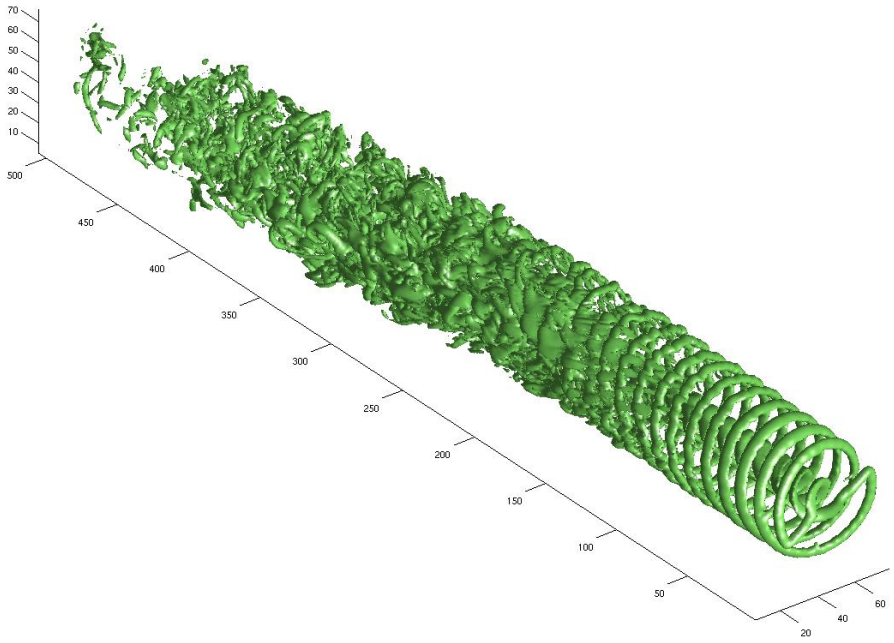

Figure 7.16: Wake vorticity l^2 isosurface for the NREL Phase VI Turbine after 10 s at $\lambda = 5.4$.

Figure 7.17: Mesh densities for Southampton rotor cases.

Case	BEM mesh density	# FVM cells across rotor	FVM cell size h	Scale factor
Coarse	16×16	40	2 cm	50
Medium	32×32	80	1 cm	100
Fine	64×64	160	0.5 cm	200

Figure 7.18: Grid convergence study for the Southampton turbine rotor at $\lambda = 6$ using local section lift coefficients. Coarse mesh is 16×16 panels, medium is 32×32 and fine 64×64.

	$C_l\,(r/R)$						GCI %		
r/R	Coarse	Medium	Fine	Continuum	R	p	m-c	f-m	ratio
0.25	1.195	1.258	1.286	1.307	0.434	1.20	4.81	2.05	1.02
0.4	1.079	1.129	1.153	1.175	0.480	1.06	5.09	2.39	1.02
0.600	0.994	1.043	1.070	1.106	0.565	0.82	7.55	4.16	1.03
0.900	0.842	0.881	0.901	0.923	0.524	0.93	6.01	3.08	1.02
0.990	0.648	0.610	0.568	–	1.132	–	–	–	–

7.3.3 Southampton Rotor

Description These are the first tests performed on a horizontal axis tidal turbine rotor. The Southampton Rotor experiments were performed in a circulating water channel and towing tank and, due to the scale of the rotor, pressure distribution data was not captured along with the more global parameters ($C_P - \lambda$ and $C_T - \lambda$ data for example). An inter-model comparison is thus used for the pressure data.

This section presents a comparison of the section pressure distributions obtained using the present method with those from Baltazar and Falcão de Campos (2008, 2011) and a comparison of global performance metrics with those obtained experimentally by Bahaj, Batten and McCann (2007).

The following tests are performed:

- For $\lambda = 6$:
  - BEM and FVM mesh refinement study. Surface loads, flow velocities and wake topologies are compared at three refinement levels.
  - Inter model comparison with numerical pressure coefficient data obtained from the literature.
- Generation of $C_P - \lambda$ and $C_T - \lambda$ curves and comparison with experimentally obtained performance characteristics drawn from the literature.

Previous Results Numerical results obtained with the present method are compared with the experimentally obtained global performance metrics from Bahaj, Batten and McCann (2007) and also the numerically obtained pressure coefficient data from Baltazar and Falcão de Campos (2008, 2011).

Relevance These tests, like those of the NREL rotor above, demonstrate the ability of the model to capture many of the flow physics pertinent to turbine performance at design tip-speed ratios (TSRs). The Southampton Turbine rotor is established as a standard benchmark test, and has been used with, for example, panel codes in Liu (2010); Baltazar and Falcão de Campos (2011); Kinnas *et al.* (2012), or CFD codes in Bai, Spence and Dudziak (2009); McSherry *et al.* (2011); Afgan *et al.* (2013).

Problem Definition The meshing strategies for the BEM and FVM meshes are detailed in Fig. 7.17. The key objective in coupling the BEM and FVM is that there are no cells which are left empty as vorticity is binned from the BEM. Given that the length of the blade is

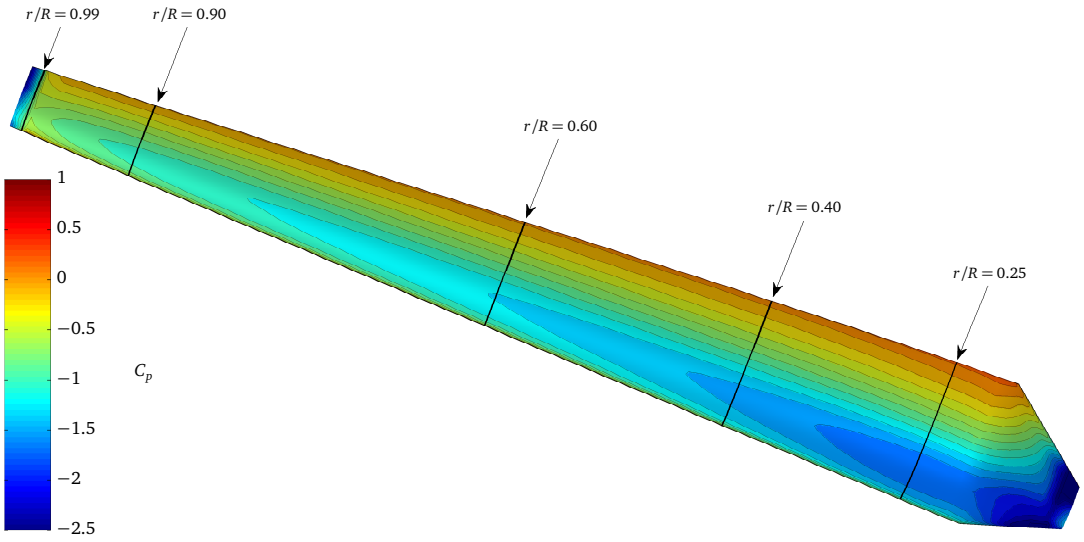

Figure 7.19: Pressure coefficient on suction side of blade of the Southampton rotor resolved over 150 FVM cells (BEM mesh 64×64). Tip-speed ratio $\lambda = 6$, simulation time is $t = 5$ seconds.

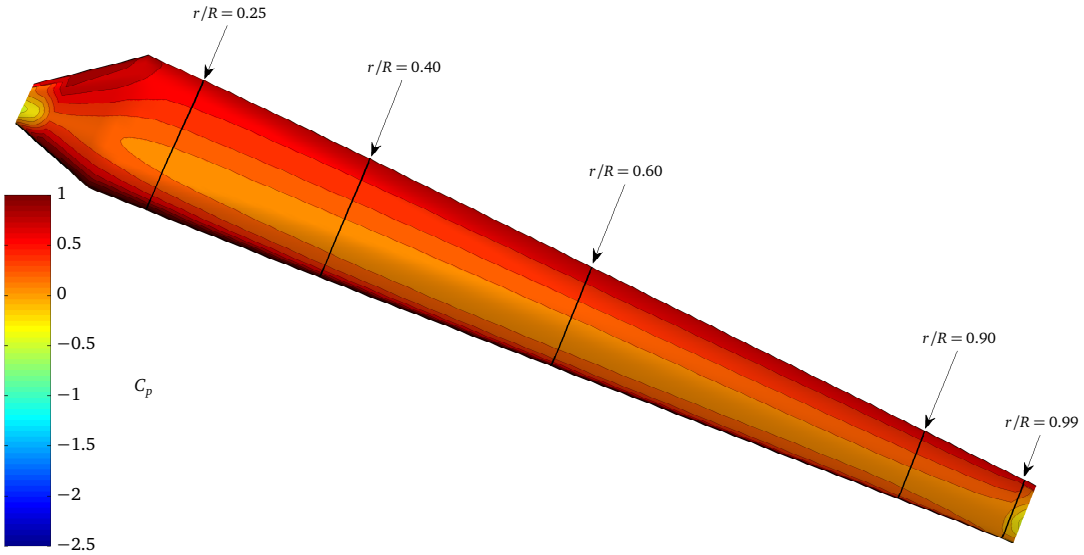

Figure 7.20: Pressure coefficient on pressure side of blade of the Southampton rotor resolved over 150 FVM cells (BEM mesh 64×64). Tip-speed ratio $\lambda = 6$, simulation time is $t = 5$ seconds.

0.32 m from cutout to tip, then the number of cells is 2.5 the number of panels and the scale factor is 1.25 the number of cells. This means in general each panel will binned into 1-2 cells.

Details of Numerical Experiments Initial conditions are again zero vorticity throughout the domain. The Southampton Rotor comprises three blades, each composed of a distribution of NACA 63-8xx sections ranging in thickness from 24 % at the root to 12.6 % at the tip with linear twist and cubic thickness distribution, as described in Bahaj, Batten and McCann (2007). The rotor geometry is created using NACA 63-8xx sections obtained by interpolating between the coordinates data for 12 %, 15 %, 18 % and 24 % thick aerofoils to the appropriate thickness. These sections are then twisted about the quarter-chord and tapered according the the blade specifications given in Bahaj, Batten and McCann (2007). No information is provided regarding the geometry of the transition piece at the root of the blade, and as such an approximate root section is postulated, tapering linearly from $c/R = (0.3 \times 0.125)$ to 0.125 between 12.5 % and 20 % radius.

The blades are translated and rotated into their initial positions, and are adjusted to a 5° set angle, measured as the pitch at the tip. A freestream velocity of $u_\infty = 1.5\ \mathrm{m\,s^{-1}}$ is specified along the positive x-axis, and a kinematic viscosity ν is obtained such that at the standard mean chord ($c_{\mathrm{SMC}} = 0.0854\,\mathrm{m}$, at $R = 0.25\,\mathrm{m}$), the Reynolds number is $\mathrm{Re}_{\mathrm{SMC}} = \mathcal{O}(10^5)$.

BEM meshes at 16×16 (coarse), 32×32 (medium) and 64×64 (fine) chord and span-wise interval counts in order to ascertain the convergence behaviour of global and local parameters. The BEM mesh density follows the NREL and NACA 0015 hydrofoil bell-shaped distributions. The FVM mesh density is set such that there are no empty cells across the rotor at initialisation resulting in in 40, 80 and 160 cells across the rotor diameter.

Results and Discussion For the first test, data obtained for $\lambda = 6.0$ using the coarse, medium and fine meshes is used to generate pressure coefficient plots at the radial stations $r/R = \{0.25, 0.4, 0.6, 0.9 \text{ and } 0.99\}$. For the outermost three radii numerical results obtained by Baltazar and Falcão de Campos (2008, 2011) are superimposed for comparison. The local section lift coefficients (due to the pressure distribution) are also calculated at these radii.

The pressure coefficients are calculated on the blade surfaces, interpolated to the required radial stations and plotted in Fig. D.9 along with the radial distribution of circulation for each mesh density. Points which are immediately apparent are that the plots are very close together, and that in all cases the code struggles to find a solution which equates

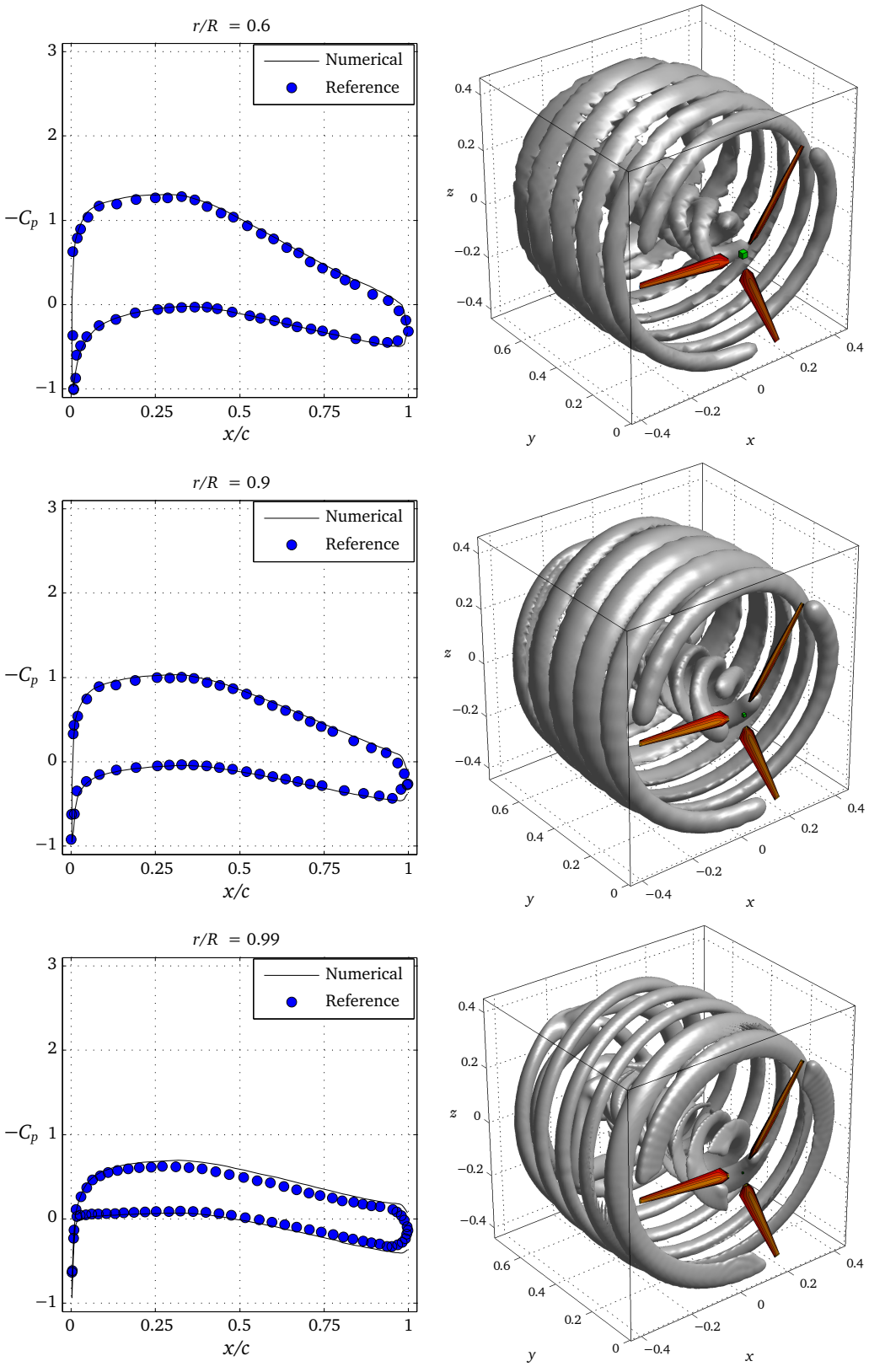
r/R = 0.6
Numerical
Reference
−Cp
x/c
r/R = 0.9
Numerical
Reference
−Cp
x/c
r/R = 0.99
Numerical
Reference
−Cp
x/c
z
y
x

the upper and lower trailing edge pressures. At each station, the pressure distribution is integrated to yield the local section lift coefficient, and these are presented in Fig. 7.18. In each case, bar the furthest outboard, the grids are drawn such that the solution is in the asymptotic range of convergence, as indicated by the small individual GCI values, and the proximity of their convergence ratio to unity. As for the outboard section, the GCI ratio is greater than one, and indicative of at best oscillatory convergence, if the solution is indeed converging. Experience with the NREL case, and that of the static hydrofoils, along with judgement based on observation of the C_p distributions in Fig. D.9, suggests that this behaviour is due to a combination of the proximity of tip vortex (and its nearly singular manifestation in the proto-wake), the reduction in resolution causing the $r/R = 0.99$ section to potentially be inboard of only a single panel and thus affected by both interpolation difficulties, and the reduction in order of the surface gradient reconstruction due to the change from central to forward/backward differencing at the surface boundaries.

The circulation distribution per unit span for each mesh is also drawn in Fig. D.9, normalised against the kinematic velocity of the span-wise station. A dashed line at $r/R = 0.2$ indicates where the root cutout begins, and a sharp drop-off in circulation can be seen inboard of this radius. What is striking is - as with the pressure coefficients - circulation appears to converge well; in general, there is less clear air between the medium and finest meshes than the coarse and medium. This will have obvious knock-on effects since it is the time and space rates of change in radial circulation which give the wake its strength, and is indicative that the wake strengths are convergent.

Figure 7.21 plots the pressure coefficient obtained at the highest resolution using the present method superimposed on the results presented in Baltazar and Falcão de Campos (2011), calculated using a "pure" boundary element method with a panelled wake whose shape is determined by relaxation and whose strength, along with that of the body panels, is calculated via an iterative pressure Kutta condition. Results plotted at $r/R = 0.6$ and $r/R = 0.9$ seem to agree very well, with major deviations visible only towards the trailing edge where the linear Kutta condition employed in the present method fails to guarantee zero pressure jump at the trailing edge. However, given the overall agreement in both shape and magnitude, and the limited percentage of chord where this effect is manifest, these are amongst the more trivial errors in the present method. Towards the tip there is

---

Figure 7.21*(facing page)*: LHS: Comparison of computed and experimental pressure coefficients for the Southampton rotor at $t = 10$ seconds. RHS: Vorticity $l^2 = 6.0$ isosurfaces for the Southampton rotor at increasing BEM and FVM mesh densities at $t = 0.9$ seconds – a green cube at the origin indicates the FVM cell size. Mesh densities are 16×16 (top); 32×32 (middle); 64×64 (bottom) with FVM cell spacings respectively of 2 cm, 1 cm and 5 mm. All $\lambda = 6$.

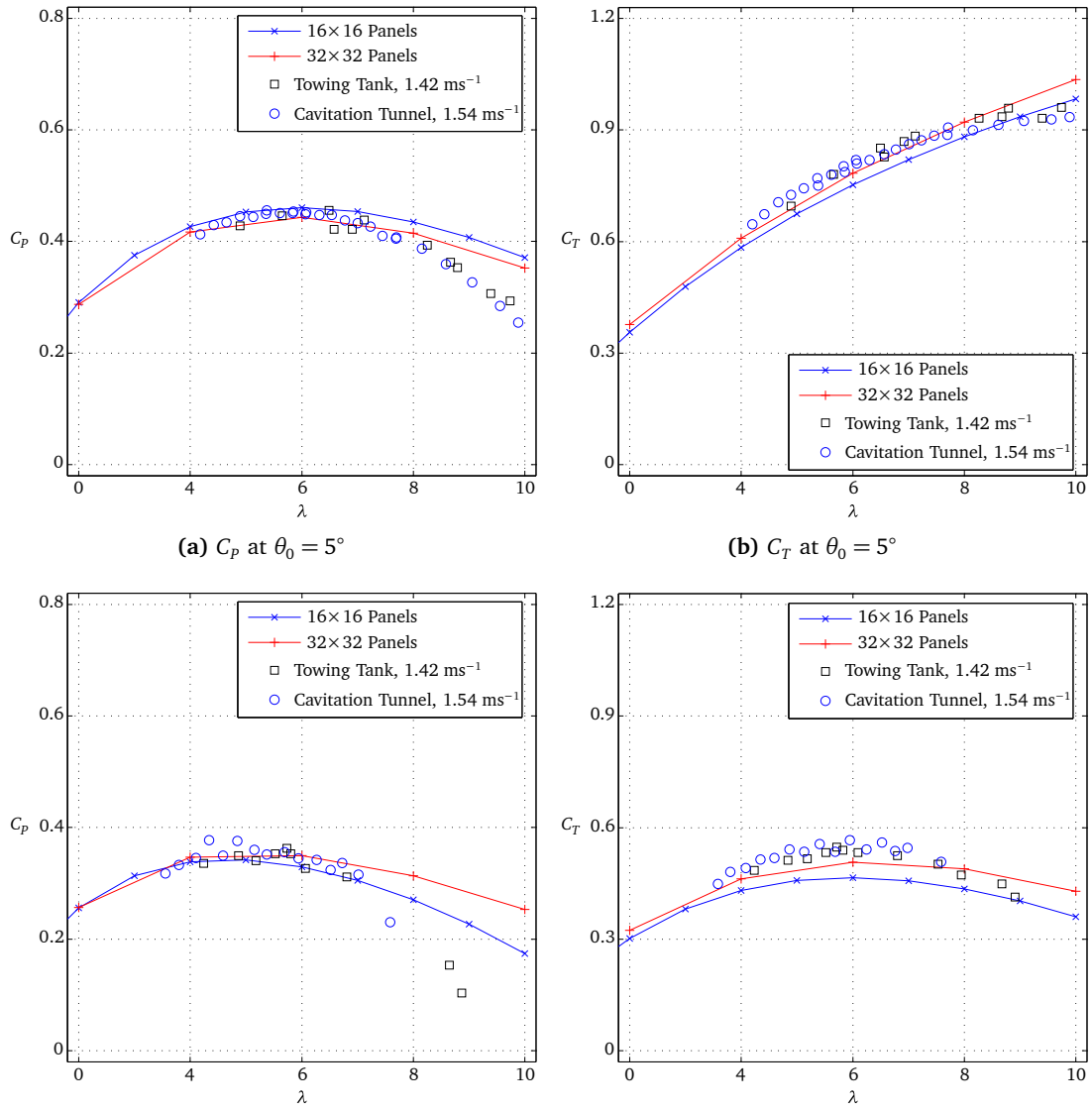

(a) C_P at $\theta_0 = 5°$

(b) C_T at $\theta_0 = 5°$

(c) C_P at $\theta_0 = 10°$

(d) C_T at $\theta_0 = 10°$

Figure 7.22: Comparison of computed and experimental thrust and power coefficients for the Southampton rotor with varying boundary element mesh densities, obtained at a range of λ. Experimental results from Bahaj, Batten and McCann (2007).

poorer agreement in magnitude, with a lower minimum and higher maximum pressures on the 30% to 90% section of the chord. The convergence observed in Fig. D.9 at the tip seems to suggest that a higher mesh resolution could reduce these disparities somewhat, however, the computational cost of running the finest mesh case here precludes further study of this at present.

Figure 7.22 compares the power and thrust coefficients results with experimental results presented in Bahaj, Batten and McCann (2007) for two blade pitch settings. Since the number of time-steps required for a given simulation duration is determined by the CFL number, and this is related by the FVM mesh density to the BEM mesh density, as the BEM mesh is doubled, the wall clock time required to perform the case increases rapidly. This being the case, results are not presented at the finest resolution: for the medium mesh, results are obtained at TSRs of 2-10 in intervals of 2. For the coarsest mesh, all integer TSRs from 1 to 10 are computed. The power and thrust coefficients for hub pitch angles of $\theta_0 = 5^\circ$ and $\theta_0 = 10^\circ$, calculated over the range of λ superimposed onto the experimental results from towing tank and cavitation tunnel tests presented in Bahaj, Batten and McCann (2007).

As can be seen, in both the power coefficient plots, the results obtained using the proposed method are comparable at each mesh density, and show reasonable agreement with experimental results for TSRs from 4 to the design λ of 6.0. For TSRs below 4, the inability of the present model to capture separation and stall will severely hamper the ability of the model to capture the drop-off in power due to these effects – viscosity will tend to increase the drag and reduce the lift, effects which will decrease power and increase thrust.

7.4 Conclusions

General Remarks and Recap This chapter has described a series of tests performed on the boundary-element method and combined BEM/finite-volume vorticity flow solver proposed in this thesis. The tests have been a three-dimensional extension of those conducted in Chapter 6. Experience has been gained in boundary-element meshing strategies, and in the required resolutions to produce an accurate and convergent solution to flows around lifting and non-lifting bodies.

The non-lifting cases provided insight into the most appropriate surface meshing strategies, and influence of the level of accuracy of the boundary-element mesh on the computed solution.

Basic lifting body flows were the solution of flow around a rectangular hydrofoil or

wing. The results obtained for these were found to be convergent – as long as the locations where samples were taken were sufficiently resolved. A meshing density of 32 panels in the spanwise direction was found to be the practical minimum – with 16 cells the finite-volume distribution of vorticity towards the tip was found to be too coarse and produced too low a pressure on both the suction and pressure sides. The inboard lift coefficients in two- and three-dimensions were shown to be convergent.

References

Afgan, I., McNaughton, J., Rolfo, S., Apsley, D., Stallard, T. and Stansby, P. (2013). "Turbulent flow and loading on a tidal stream turbine by LES and RANS." *International Journal of Heat and Fluid Flow*.

Bahaj, A., Batten, W. and McCann, G. (2007). "Experimental verifications of numerical predictions for the hydrodynamic performance of horizontal axis marine current turbines." *Renewable Energy*, **32**(15): pp. 2479–2490.

Bai, L., Spence, R.R.G. and Dudziak, G. (2009). "Investigation of the influence of array arrangement and spacing on tidal energy converter (TEC) performance using a 3-dimensional CFD model." In "Proceedings of the 8th European Wave and Tidal Energy Conference (EWTEC2009)," Uppsala, Sweden.

Baltazar, J. and Falcão de Campos, J.A.C. (2011). "Hydrodynamic analysis of a horizontal axis marine current turbine with a boundary element method." *Journal of Offshore Mechanics and Arctic Engineering*, **133**(4).

Baltazar, J. and Falcão de Campos, J. (2008). "Hydrodynamic analysis of a horizontal axis marine current turbine with a boundary element method." In "Proceedings of the ASME 27th International Conference on Offshore Mechanics and Arctic Engineering," Estoril, Portugal.

Falcão de Campos, J.A.C. (1988). "Experimental and theoretical investigation of the tip vortices associated with elliptical and rectangular wings." Tech. rep., MARIN.

Hand, M.M., Simms, D.A., Fingersh, L.J., Jager, D.W., Cotrell, J.R., Schreck, S. and Larwood, S.M. (2001). "Unsteady Aerodynamics Experiment Phase VI: Wind Tunnel Test Configurations and Available Data Campaigns." Tech. Rep. NREL/TP-500-29955, NREL.

Kinnas, S.A., Xu, W., Yu, Y.H. and He, L. (2012). "Computational methods for the design and prediction of performance of tidal turbines." *Journal of Offshore Mechanics and Arctic Engineering*, **134**(1).

Liu, P. (2010). "A computational hydrodynamics method for horizontal axis turbine - panel method modeling migration from propulsion to turbine energy." *Energy*, **35**(7): pp. 2843–2851.

McAlister, K.W. and Takahashi, R.K. (1991). "NACA 0015 wing pressure and trailing vortex measurements." Tech. Rep. NASA-TP-3151, NASA.

McSherry, R., Grimwade, J., Jones, I., Mathias, S., Wells, A. and Mateus, A. (2011). "3D CFD modelling of tidal turbine performance with validation against laboratory experiments." In "Proceedings of the 9th European Wave and Tidal Energy Conference (EWTEC2011)," Southampton, England.

Simms, D., Schreck, S., Hand, M. and Fingersh, L.J. (2001). "NREL Unsteady Aerodynamics Experiment in the NASA-Ames wind tunnel: A comparison of predictions to measurements." Tech. Rep. NREL/TP-500-29494, NREL.

Sørensen, N.N., Michelsen, J.A. and Schreck, S. (2002). "Navier-Stokes predictions of the NREL Phase VI rotor in the NASA Ames 80 ft x 120 ft wind tunnel." *Wind Energy*, **5**: pp. 151–169.

8

Fully Unsteady Three-Dimensional Example Cases

8.1 Introduction

Excluding the oscillating foil and cross-flow turbine examples in previous chapters, all of the cases described thus far tend to a notionally steady state, even if the model proposed is always three-dimensional and always unsteady. The upshot of this is that if the the code was behaving in a quasi-iterative mode, starting transients in monitored quantities may eventually be eliminated and a steady value reached. Even the oscillating foil and cross-flow turbines were periodic problems, where the oscillations in a quantity might eventually settle towards phase converged values.

This chapter addresses cases which will not tend to a steady-state solution, and in which time-averaged results must occasionally be presented. Since the method described herein is fully unsteady, these cases represent those which should become the bread and butter work for the developed code. The aim in this chapter is therefore to demonstrate three-dimensional, transient solutions to some exemplar problems, and to seek the limits of applicability of the method.

During the course of this research, these cases have been written up into McCombes, Johnstone and Grant (2010a,b) for Section 8.2, and McCombes, Johnstone and Grant (2011) for Section 8.3.

8.2 Array Layout Optimisation

This section presents results from the proposed model applied to the calculations required for turbine arrays. Traditional computational fluid dynamics based on primitive variable Reynolds-averaged Navier-Stokes solutions are typically unable to preserve the wakes of tidal turbines sufficiently far downstream to be practical in ascertaining the unsteady loads

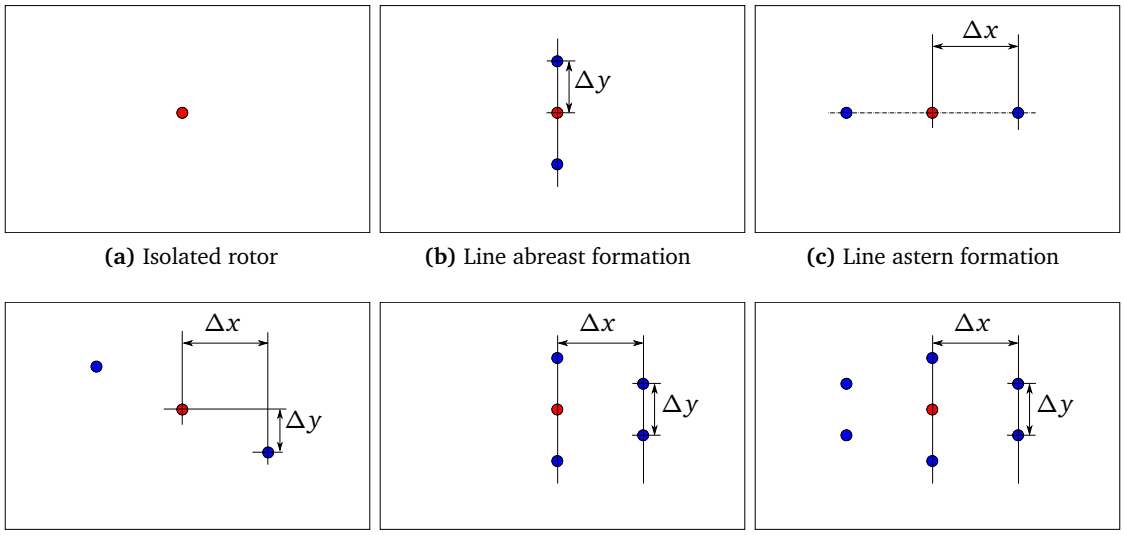

(a) Isolated rotor **(b)** Line abreast formation **(c)** Line astern formation

(d) Echelon formation **(e)** 3-2/W formation **(f)** 2-3-2/hex formation

Figure 8.1: Basic “first-generation" array configurations. Inflow is left-to-right and the red dot is the “central” turbine.

Table 8.1: Baseline and deviation in power coefficient C_P and thrust coefficient C_T for the central rotor. Square brackets, [...], indicate corresponding changes in power from Bai, Spence and Dudziak (2009).

Configuration		Spacing (diam.)		C_P		C_T	
		Δx	Δy	Value (1)	± (%)	Value (1)	± (%)
Isolated rotor		–	–	0.4251	–	0.8617	–
Line astern	A	5	–	0.4068	-4.3	0.9031	+4.8
	B	10	–	0.4535	+6.6902	0.8634	+0.2022
Line abreast	A	–	1.5	0.4175	-1.78	0.8486	-1.52
	B	–	3	0.4535	+6.6902 [+7.0]	0.8634	+0.2022
Echelon	A	5	1.5	0.4270	+0.44	0.8613	-0.05
	B	10	3	0.4242	-0.2	0.8556	-0.71
3-2/W formation		10	3	0.4539	+6.6750 [+6.4]	0.8635	+0.2146
2-3-2/hexagonal		10	3	0.4209	-0.9766 [-1.4]	0.8695	+0.9067

on devices in arrays. The method proposed in this thesis was specifically designed for these types of calculations. The Navier-Stokes equations are solved in a vorticity-velocity form, using an octree based arbitrary-Lagrangian-Eulerian mesh which copes with the strong distortions in spatial resolution required to track the wake vorticity, and a high-resolution finite-volume scheme with fairly compressive limiters to prevent artificial dissipation.

Results are presented for small groups of devices in generic array configurations, demonstrating the implications of different degrees of device overshadowing at the various ranges likely to be encountered in a practical array setting.

8.2.1 Introduction

The key questions bound to be asked of developers during the array deployment process are those related to device spacing. Maximally efficient exploitation of an available resource is balanced against the requirements and limitations of the site – and developer – and will manifest itself as a trade-off between the number of devices that can be installed at a particular site (and the return on investment of these) and the power output and longevity of individual devices. A simplified hydrodynamic subsystem associated with an array of turbine devices operating as an array can be split into the incident sea-state and device interactions. The incident sea-state includes some quantifiable and defined measure of turbulence, velocity profiles and wave-current-interactions, but is devoid of any array effects. This is overlaid with the inter-device influences in terms of interacting pressure fields and wake induced loadings. The purpose of this section is to identify some of these array effects and their impact on power generation and device loadings.

8.2.2 Array Configurations

Some potential array layouts are selected, chosen to be as representative as possible. Array configurations analysed are: line abreast, line astern and echelon formations of three devices; and a W-shaped 3-2 array of five, and a hexagonal 2-3-2 array of seven devices. These are compared to a single device. These exemplar arrangements seek to provide results relevant to developers aiming for initial small array deployment, and also pertain directly to the intermediate stages during installation of large arrays. Results are presented in steady axial flow conditions (i.e. normal working conditions). Table 8.1 and Fig. 8.1 describe the six cases presented.

The array layouts described in Fig. 8.1 have been modelled using a generic three-bladed turbine based on that of Bahaj, Batten and McCann (2007) whose details are to be found in Table D.3 in Appendix D. These results are compared to the performance of an isolated

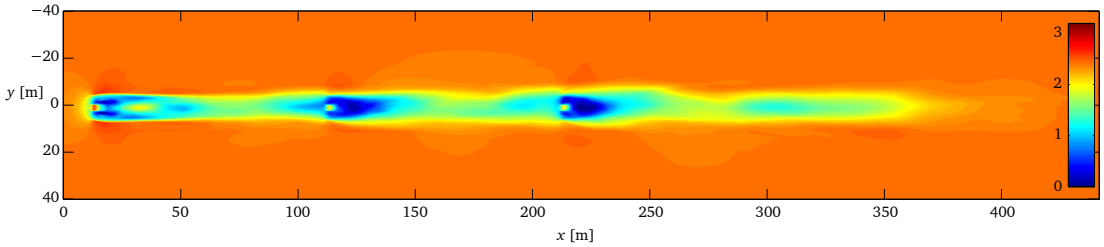

(a) Line astern time averaged velocity

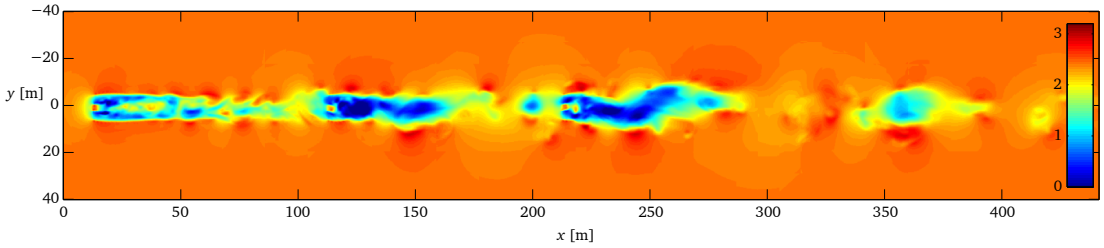

(b) Line astern instantaneous velocity

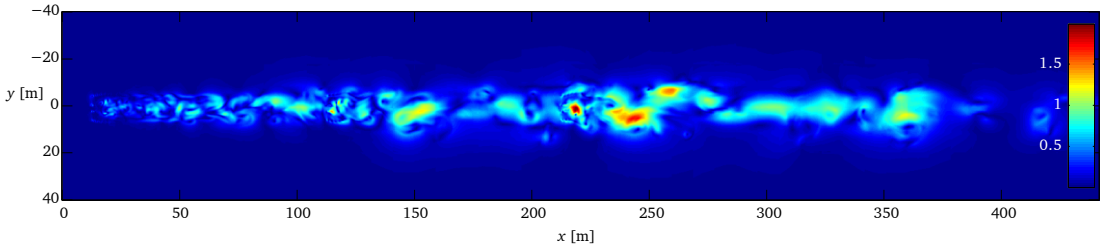

(c) Line astern instantaneous kinetic energy

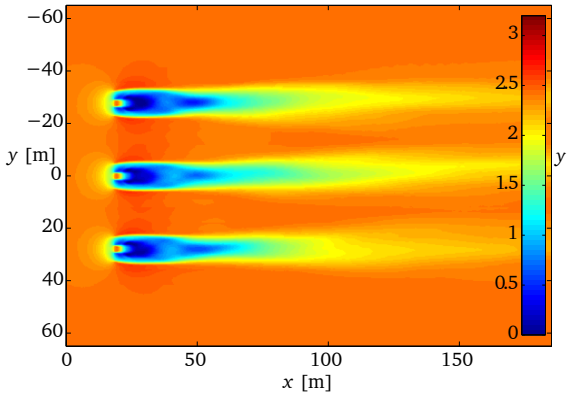

(d) Line abreast time averaged velocity

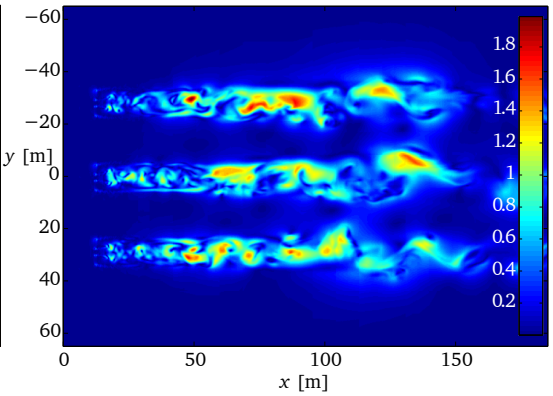

(e) Line abreast instantaneous kinetic energy

Figure 8.2: Time averaged and instantaneous u (axial) velocity contours and instantaneous kinetic energy contours for array configurations as indicated. $u_\infty = 2.5\,\mathrm{m\,s^{-1}}$.

turbine. The turbine radius has been scaled to 5 m, and it is operating at a tip-speed ratio of 6 with a tip twist angle of 5°, which for an isolated rotor simulation corresponds to a calculated thrust coefficient $C_T = 0.85$ and a power coefficient $C_P = 0.43$. Simulations were performed with 70 cells across the rotor, equating to 32 spanwise panels along each blade, for 200 seconds simulation time.

8.2.3 Results

A slice is taken through an area around the turbines and the velocity is computed at the cells. Since the domain does not naturally form a rectangular section (as it tracks the wake in a Lagrangian manner) this process artificially creates cells in empty regions on the octree. When the velocity gradient fields are collapsed here, the result is a somewhat more blocky velocity field compared to the relatively smooth fields due to higher cell concentrations in the more highly resolved sub-volumes of the domain. Figures 8.2 and 8.4 shows the axial velocity component (u) for the five configurations time averaged over 40 seconds after approximately 160 seconds simulation time. The sampling rate was every second, and in retrospect should have been higher; it was not anticipated how strongly the wakes would interact after the first instabilities occurred and there was high energy, large-scale motion.

Velocity deficit is obvious in the wake, and wake recovery to about 80 % of freestream can be seen to have occurred within 10 rotor diameters for the isolated and abreast configurations. When turbines are arranged in staggered fences, as in the 3-2/W and 2-3-2/hex configurations, wake recovery appears strongly influenced by the acceleration of fluid around downstream turbines resulting in a narrower wake with a much stronger shear layer at the wake boundary: the beginnings of this can be seen in the wake of the central turbine of line abreast formation.

Figures 8.2 and 8.4 show slices, parallel to the axes of the turbines, through the velocity fields associated with a subset of the array configurations. Instantaneous velocity fields show the breakdown of the individual turbine wake from coherent structures into a stochastic turbulent wake, and this is time averaged in order to determine the overall momentum deficit. Figures 8.2c and 8.2e show the distribution of large-scale kinetic energy associated with the breakdown of the wakes for the same configurations at the final timestep. Table 8.1 presents the performance coefficients for the central turbines and Table 8.2 for the three turbines in each of the 6 cases considered, comparing against those for an isolated turbine.

A number of the deviations are considerably less than a single percent, and it could

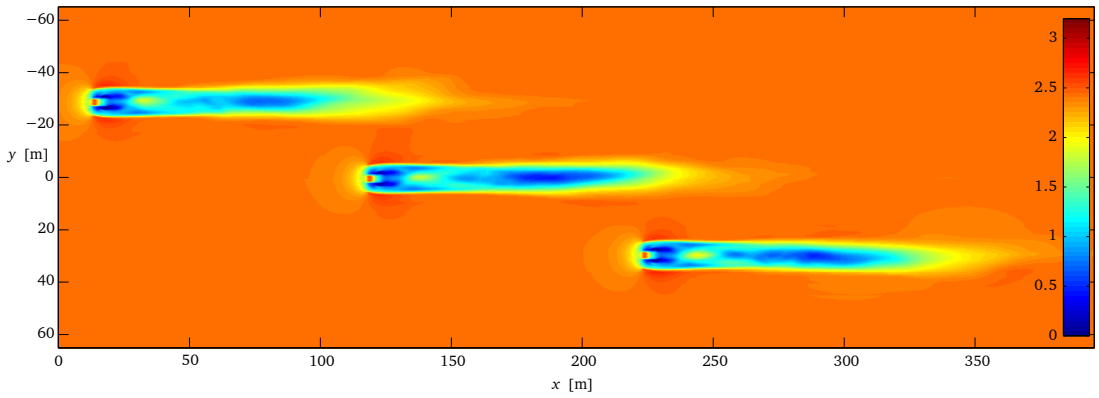

(a) Echelon formation

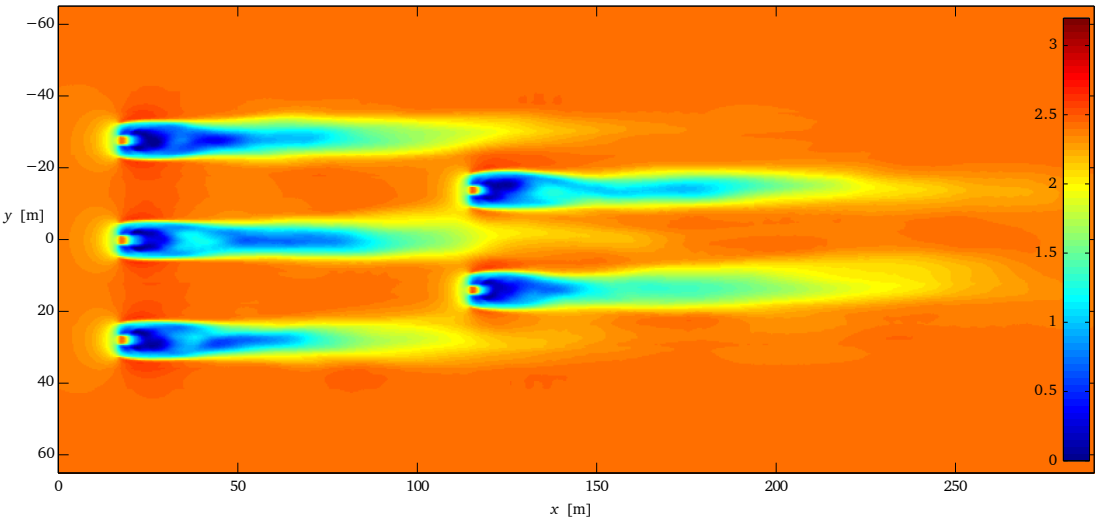

(b) 3-2/W formation

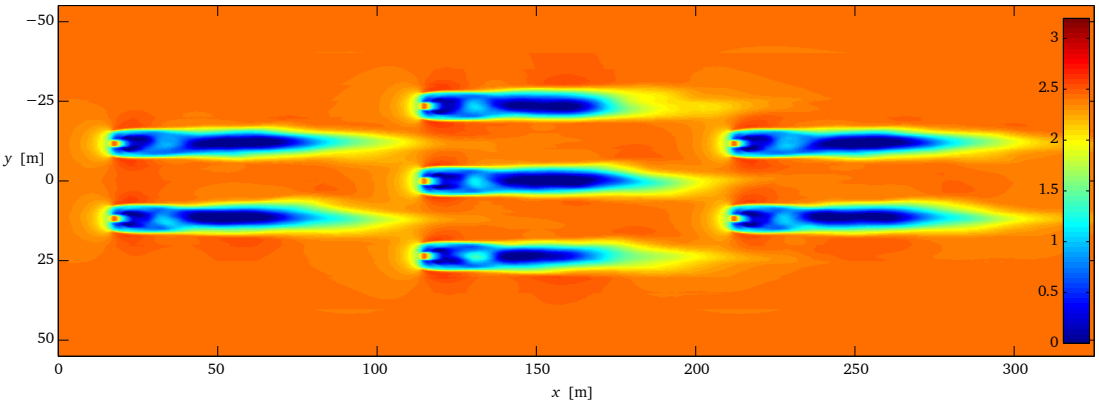

(c) 2-3-2/hex formation

Figure 8.3: Time averaged u (axial) velocity contours for array configurations as indicated. $\lambda = 6$, inflow $u_\infty = 2.5\,\mathrm{m\,s^{-1}}$.

be argued that these are numerical scatter, which for the purposes of this chapter can potentially be ignored. Further analysis into these would entail grid dependency checks.

The results for the line astern cases are most telling; and the strong, compounded roll-off of C_P is readily explained by examination of Fig. 8.2a. The drop in thrust coefficient for the furthest downstream turbine is associated with the reduction in power generation.

A comparison between the line abreast cases reveals that where the turbines are very close together, there is a negative impact. Wake vorticity isosurfaces reveal significant interaction between the wakes, to the point where they essentially merge within 10 diameters from the rotor fence. Figure 8.5b shows a vorticity isosurface of the wake, demonstrating the level of interaction and convolution. Given the relatively high loading, it remains for further work to uncover whether the same penalties would apply under different loading regimes. The results from line abreast, case B, begin to indicate that a positive benefit can be attained by arranging turbines into a fence configuration, but taken alongside those from case A, caution must be exercised in order to find the optimum spacing, which is likely to be operating condition specific.

The echelon configurations both show negligible impact, however the snapshots in Fig. 8.4a and Fig. 8.4b demonstrate that unsteady wake interactions do exist, and it remains to determine the nature and degree of these impacts although Fig. 8.5c seems to suggest that the wake interaction draws momentum (thus carrying the wake) of the first, then second turbines slightly towards those downstream. This may partly explain the deviations in power coefficient. Comparing the quasi-steady time averaged results and the unsteady snapshots shows the degree to which coherent wake structures have broken down by the time they reach rotors far downstream. The kinetic energy k (using kinetic energy in the same manner as with turbulent kinetic energy, although here not referring to sub-grid scale modelling, $k = \left(\overline{(u')^2} + \overline{(v')^2} + \overline{(w')^2}\right)/2$, where the over-bar and prime indicate time-averaging operator and fluctuations from RMS values respectively) plots demonstrate a sort of "inverse" energy cascade, where large, semi-random, self-organising high-energy structures evolve from the numerous, smaller structures emitted in the vortex wake of the rotor. These then begin to dissipate energy as vorticity is diffused out into the grid. The k peaks in the line astern case B are especially significant, indicating that the model predicts that large amounts of energy are being wasted in the wake. There is also evidence of this in Fig. 8.5a, which shows vorticity isosurfaces for the line astern case A, with significant wake mixing aft of the downstream rotors amplifying the instability and growth of these large eddies.

Power and thrust coefficients are presented in Tables 8.1 and 8.2. Accelerating flow

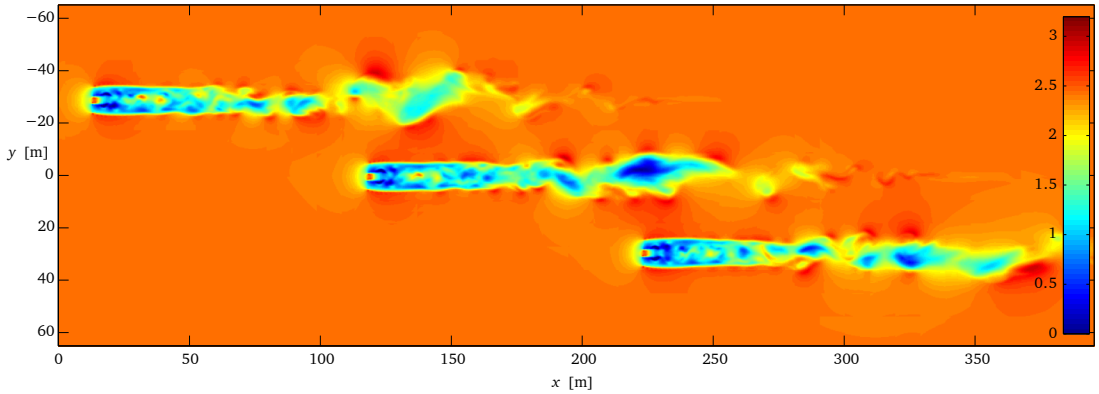

(a) Velocity

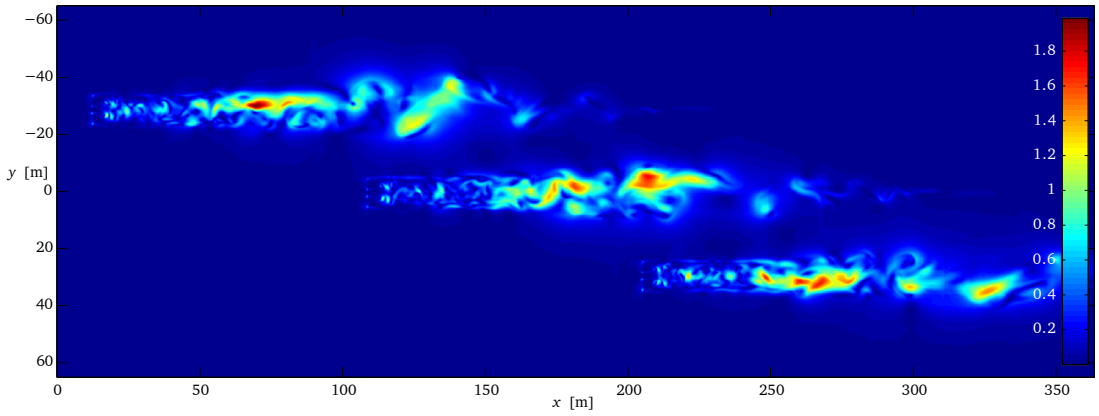

(b) Kinetic energy

Figure 8.4: Instantaneous u (axial) velocity contours and kinetic energy contours for array configurations as indicated. $u_\infty = 2.5\,\mathrm{m\,s^{-1}}$.

Table 8.2: Performance metrics for turbine array devices. Order is left → right for turbines from $[-x,-y] \rightarrow [+x,+y]$. Red dot in Fig. 8.1 corresponds to middle columns.

Configuration		$C_P \pm (\%)$			$C_T \pm (\%)$		
Line astern	A	0.0	−4.3	20.68	0.0	4.8	−1.98
	B	0.0	−8.74	−15.74	0.0	3.0	−0.2
Line abreast	A	−1.89	−1.78	−1.89	−1.03	−1.52	−0.93
	B	0.7	0.2	0.4	1.81	1.23	1.75
Echelon	A	0.08	0.44	0.66	−0.24	−0.05	−0.47
	B	−0.45	−0.2	−0.3	0.0	−0.71	−0.2

around the central turbine does seem to affect power and thrust by some small percentage, as does operation in a wake, especially for the downstream devices in a line astern formation. The temporal nature of this deviation requires further investigation to determine the relative proportions due to transient circulatory and constant momentum effects.

8.2.4 Conclusions

Output from analysis of a family of array configurations shows the interplay between velocity fields and wake recovery. This is especially evident when considering fences of devices, and the provisional results seem to indicate that although the overall high deficit (near wake) region is larger in an array, recovery of the far wake occurs faster as momentum is entrained into the wake from the accelerated flow around downstream turbines.

Calculated power output from turbines bracketed between cross-stream neighbours is enhanced due to flow acceleration and it is anticipated that this will be exaggerated when real life flow constraints are included in the model. Turbines operating downstream and inline with neighbours suffer from increased thrust, due to cross-stream neighbours, and reduced power output due to up-stream turbines.

The code proposed in this thesis has been designed to be fully time-resolved and three-dimensional. While the results presented have mainly been essentially two-dimensional snapshots that have been time-averaged, future work could address the unsteady and three-dimensional aspects of the results dataset not touched on here. The code performs well with simple cases such as isolated rotors being entirely soluble on a modest specification desktop. The 2-3-2/hexagonal array, however, was especially computationally demanding, with the calculation of influence coefficients and solution of a very large system of equations required at each time-step. The code was run on the University of Strathclyde's new HPC and scales well in shared memory.

8.3 Coaxial Rotor Configuration

8.3.1 Introduction

The flowfield of a coaxial is significantly more complex than a single rotor, and since the downstream rotor operates in the wake of the upstream one, special considerations must be taken when attempting to model this device class. This section describes the comparison of the method developed in this thesis with a new blade-element model for coaxial, contra-rotating tidal turbines, and the comparison of this model with an existing BEMT model. Since there is a paucity of coaxial turbine analysis in the literature this section seeks to

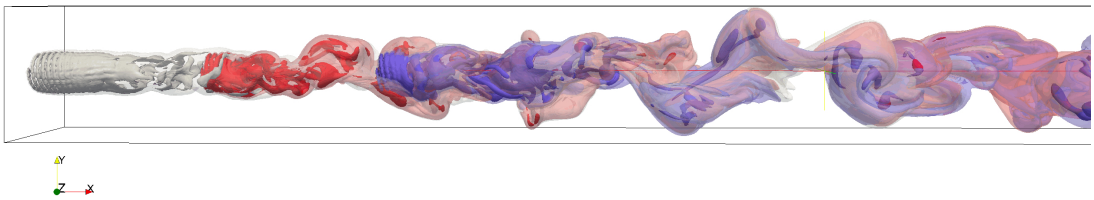

(a) Line astern formation

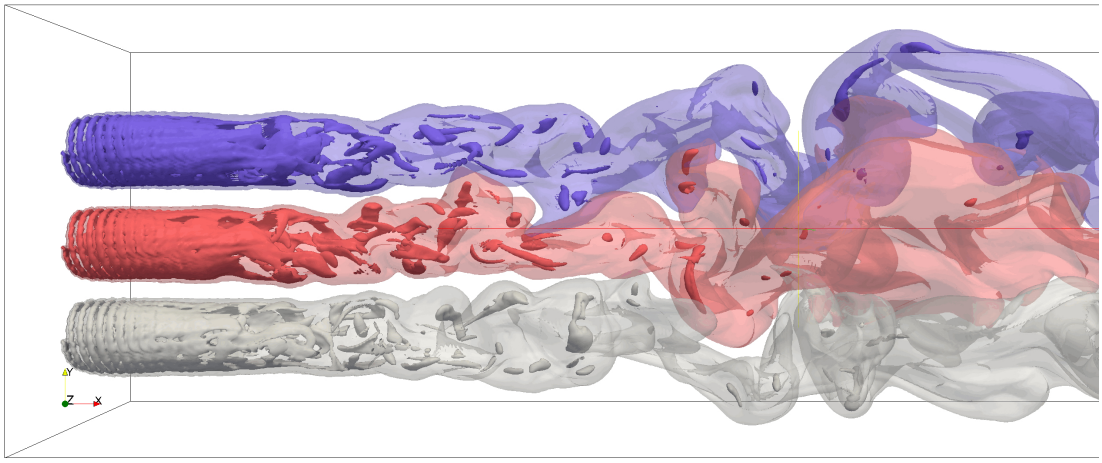

(b) Line abreast formation

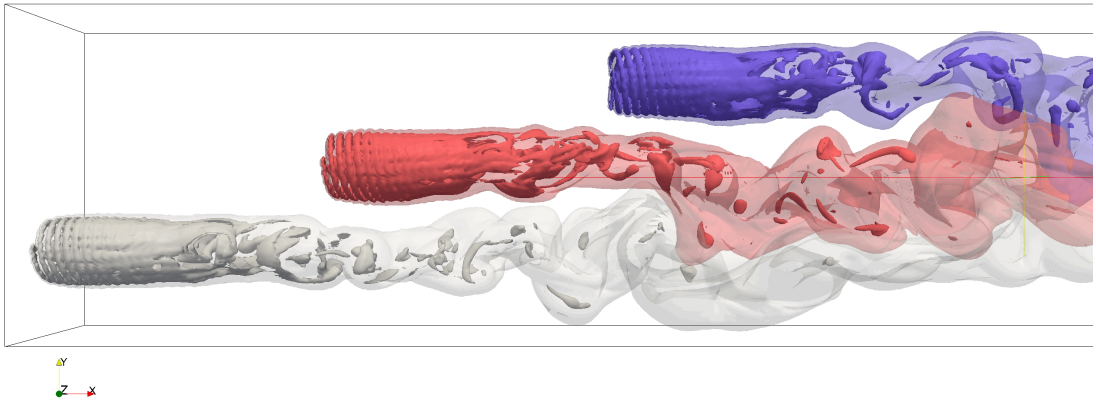

(c) Echelon formation

Figure 8.5: Vorticity l^2 isosurfaces of wakes generated due to basic “first-generation" array configurations. $\lambda = 6$, inflow $u_\infty = 2.5\,\mathrm{m\,s^{-1}}$, left-to-right.

develop further the analytical methods in Clarke *et al.* (2005) and compare them with the numerical approaches developed in McCombes, Johnstone and Grant (2009).

The models described in this section are as follows: two blade element models, each using a different conceptualisation of the problem are presented, and compared to the method of this thesis. The first BEMT model is a re-deployment of one from the literature (Clarke *et al.*, 2005); the second has been developed recently. The advantages of a blade-element/momentum model are the relative speed and robustness of the model. However, these models are severely hampered by approximations and assumptions required by their formulation, most notably the effects of time or azimuth averaging.

Coaxial rotors form the basis of the Nautricity CoRMaT turbines. The most often cited advantages of a coaxial rotor configurations are that there is a possible moderate increase in power output for a given inflow area, by recovering swirl momentum losses from the upstream rotor and thus it is possible to balance each rotor torque without the use of bulky superstructure. The CoRMaT turbine has been described in Clarke *et al.* (2007a) and as such only the data required to repeat the work herein are presented. The concept, as modelled here, has 2 contra-rotating rotors, of 3 (upstream – R1) and 4 (downstream – R2) blades and a submersible, direct-drive generator housed in an elliptically ended cylindrical nacelle. Each blade has an NREL S814 aerofoil section, and the blade geometry is given in Table D.2.

This sections presents and compares preliminary results from the codes for the upstream rotor in isolation, and also the dual rotor configuration. Global performance parameters are presented and the relative merits of each code are discussed.

8.3.2 Method

8.3.2.1 A Coaxial Blade-Element/Momentum Theory

For a conventional single-rotor turbine, simple blade element theory equates forces on the blade and on the fluid stream through the equations

$$\begin{aligned} \mathrm{d}F &= 4\pi r \rho u_\infty^2 a\,(1-a)\,\mathrm{d}r \\ &= \pi\rho\sigma v \left[C_l\Omega\left(1+a'\right) + C_d u_\infty (1-a)\right] r\mathrm{d}r \end{aligned} \tag{8.1}$$

for the axial, and

$$\begin{aligned} \mathrm{d}S &= 4\pi r^2 u_\infty (1-a)\,a'\Omega\mathrm{d}r \\ &= \rho w\sigma \left[C_l u_\infty (1-a) - C_d\Omega r\left(1+a'\right)\right] r\mathrm{d}r \end{aligned} \tag{8.2}$$

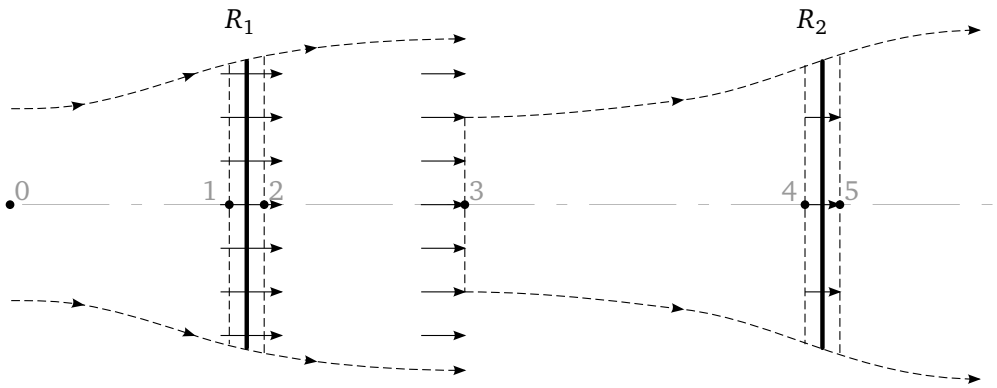

Figure 8.6: Control volumes used in a blade-element/momentum theory methods for coaxial turbines.

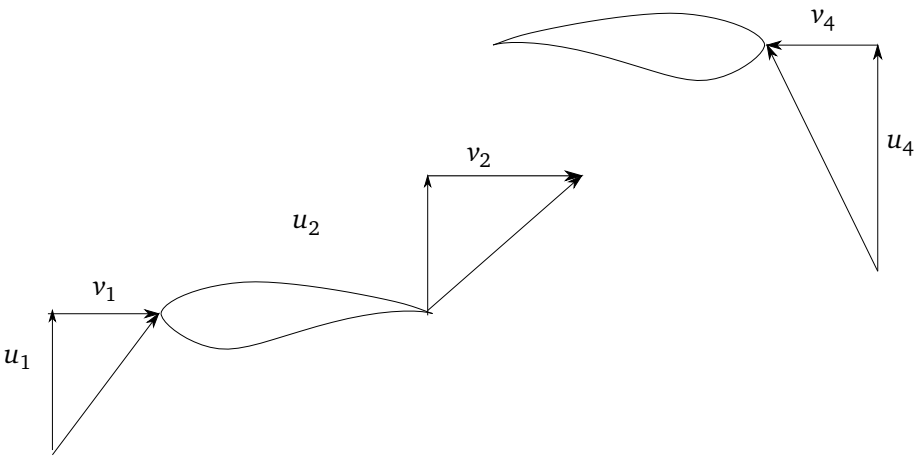

Figure 8.7: Velocity triangles used in blade element momentum theory methods for coaxial turbines.

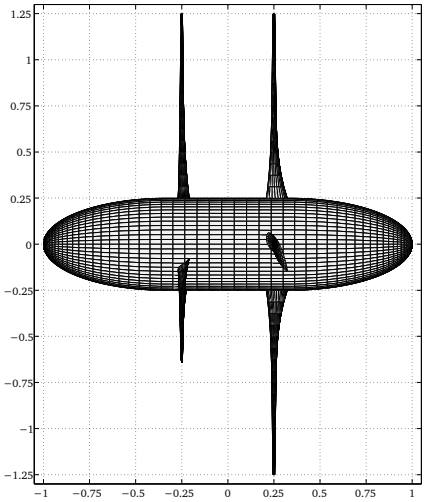

(a) Side elevation showing coaxial blade spacing

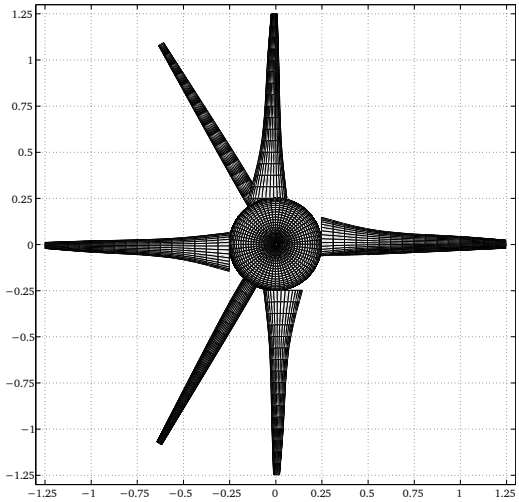

(b) Rear elevation showing the "square–cut" root sections of the rear rotor as required for stability

Figure 8.8: Boundary-element mesh used with the V3D code.

for the tangential components. These equations are solved by an iterative process to produce converged values of the axial and tangential induction factors, a and a', after which the velocity vectors may be evaluated. Performance predictions for the complete rotor are obtained from a summation over all blade elements, making an appropriate allowance for blade tip losses (in this case by the Prandtl method). A momentum theory for a coaxial turbine can be obtained by considering the rotors as either operating in the same plane (as in Clarke *et al.*, 2007b) or with the downstream rotor operating in the fully developed wake of the upstream rotor. In the co-incident case, the conditions up and downstream of both rotors are the same, and the rotor systems are considered to act as a single actuator disc.

A Simple New Method A simple BEMT for a coaxial considers the downstream rotor to operate in the fully developed wake of the upstream rotor as illustrated in Fig. 8.6. Assuming that the wake is fully developed is theoretically convenient, since it allows the blade element calculations to proceed sequentially rather than simultaneously as the wake velocity in the upstream calculation is not affected by the downstream rotor. The upstream rotor's stream-tube expansion is complete, and the downstream rotor inflow velocity can thus be determined at each blade element, using conservation of mass and angular momentum in the wake.

The velocity triangles for the rotors are shown in Fig. 8.7 and the velocity component subscript numbering corresponds to the regions indicated in Fig. 8.6. In accordance with standard BEMT, the inflow and outflow velocities at a blade element on rotor 1 can be written as:

$$u_1 = u_2 = u_0\left(1 - a_{\mathrm{R1}}\right) \tag{8.3a}$$

$$v_1 = \Omega_{\mathrm{R1}} r_{\mathrm{R1}}\left(1 + a'_{\mathrm{R1}}\right) \tag{8.3b}$$

$$v_2 = 2a'_{\mathrm{R1}}\Omega_{\mathrm{R1}} r_{\mathrm{R1}} \tag{8.3c}$$

$$u_3 = u_0\left(1 - 2a_{\mathrm{R1}}\right) \tag{8.3d}$$

where Eq. (8.3a) and Eq. (8.3b) are the inflow velocity components, the axial component of the outflow is the same as the inflow, and Eq. (8.3c) gives the tangential component. The stream-tube axial component of the fully developed wake due rotor 1 is given by Eq. (8.3d). This allows use of basic conservation of momentum principles to calculate the blade element wake expansion and the moment of inertia for an annulus to calculate the new wake tangential velocity, v_3.

Once v_3 has been obtained, the inflow conditions for rotor 2 are known, and the second

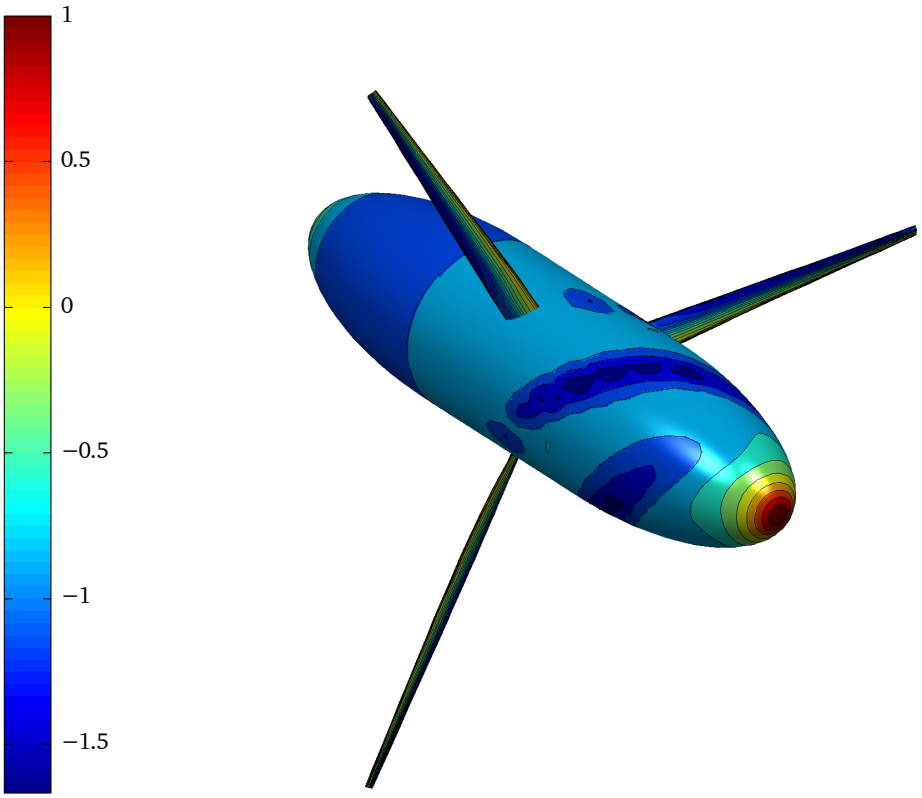

(a) Single rotor (R1) configuration

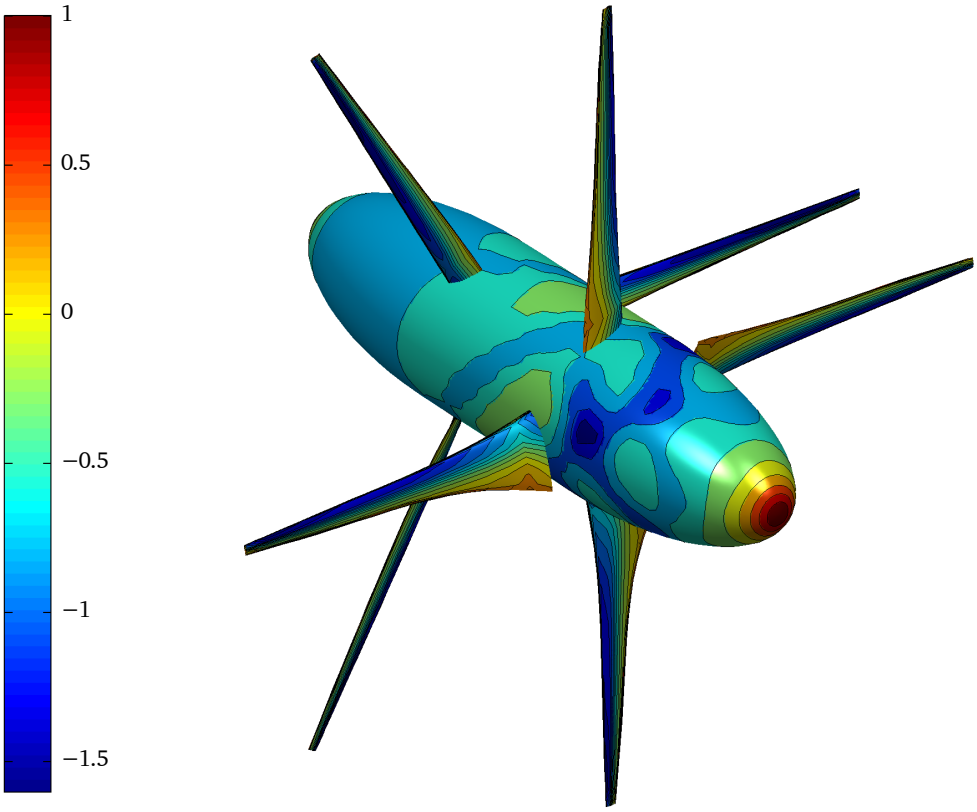

(b) Dual rotor configuration

Figure 8.9: Pressure coefficient contours on turbine blades and nacelles.

rotor calculation can commence using the following inflow velocity components:

$$u_4 = f\left(u_3\right)\left(1 - a_{\mathrm{R2}}\right) \tag{8.4a}$$

$$v_4 = \left(\Omega_2 r_{\mathrm{R2}} - g\left(v_3\right)\right)\left(1 + a'_{\mathrm{R2}}\right) \tag{8.4b}$$

Since the stream-tube expansion at rotor 2 is not known in advance of the calculation, the process commences by setting $a_{\mathrm{R2}} = a'_{\mathrm{R2}} = 0$ such that $f\left(u_3\right) = u_3$ and $g\left(v_3\right) = v_3$ allowing an initial estimate of the induction factors to be obtained. After this and successive iterations, the stream-tube expansion at rotor 2 is calculated using conservation of momentum to obtain the new inflow conditions and $f\left(u_3\right)$ in Eq. (8.4a) and $g\left(v_3\right)$ in Eq. (8.4b) is updated.

8.3.3 Results

8.3.3.1 Single Rotor in Isolation

In order to incrementally gain confidence in the predictive capabilities of the models, simulations are performed on single rotor systems operating in isolation. Using the rotor 1 geometry given in Table D.2 in Appendix D for the CoRMaT rotors, blade element results were obtained using all the BEMT codes, and these were compared with the output of V3D. In all cases a V3D boundary-element mesh density of 32×32 has been used, and there are 50 cells across the rotor. The mesh geometry was very similar to that displayed in Fig. 8.8, but with R2 removed and the rotor centred on the hub.

Since BEMT can yield global rotor performance metrics, Fig. 8.10 shows the $C_P - \lambda$ characteristics of this rotor as predicted using BEMT with viscous aerofoil data from Somers (1997). The codes are obviously very much in agreement. The code used in case B is now reconfigured to use inviscid $C_l - \alpha$ data obtained for the NREL S814 aerofoil via the X-FOIL computer program (Drela and Giles, 1987). Inviscid data are used since the boundary conditions for the V3D code are also inviscid. This means that separation and stall will not be present, and is an acceptable compromise at the operating point where it is expected that the majority of the flow will be attached. However, in off-design conditions it is expected that there be some significant divergence between predictions. When comparing the V3D results to the BEMT results with inviscid section data, close agreement in global performance parameters – such as power coefficient – is expected and observed. The viscous and inviscid results tend to very close agreement as tip-speed ratio increases from around 6 (and hence local angles of attack drop such that very little or none of the rotor are out-with the quasi-linear portion of the $C_l - \alpha$ curve). Pressure coefficients

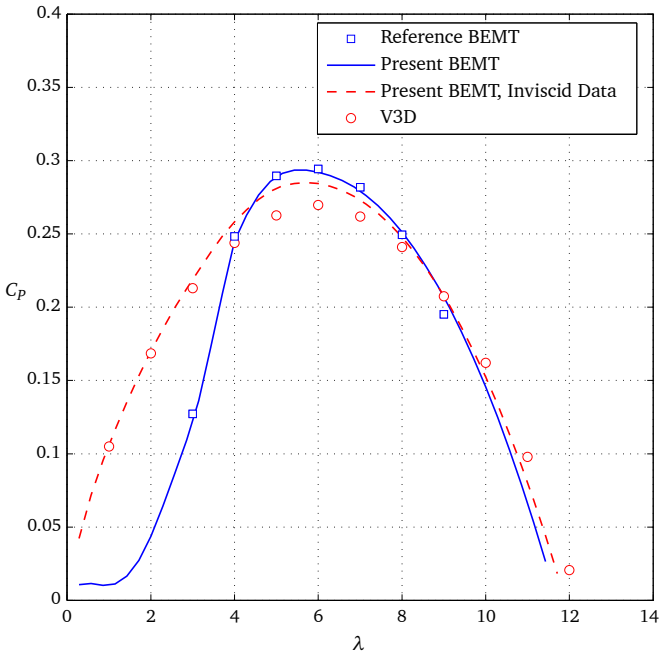

Figure 8.10: $C_P - \lambda$ curves for Rotor 1.

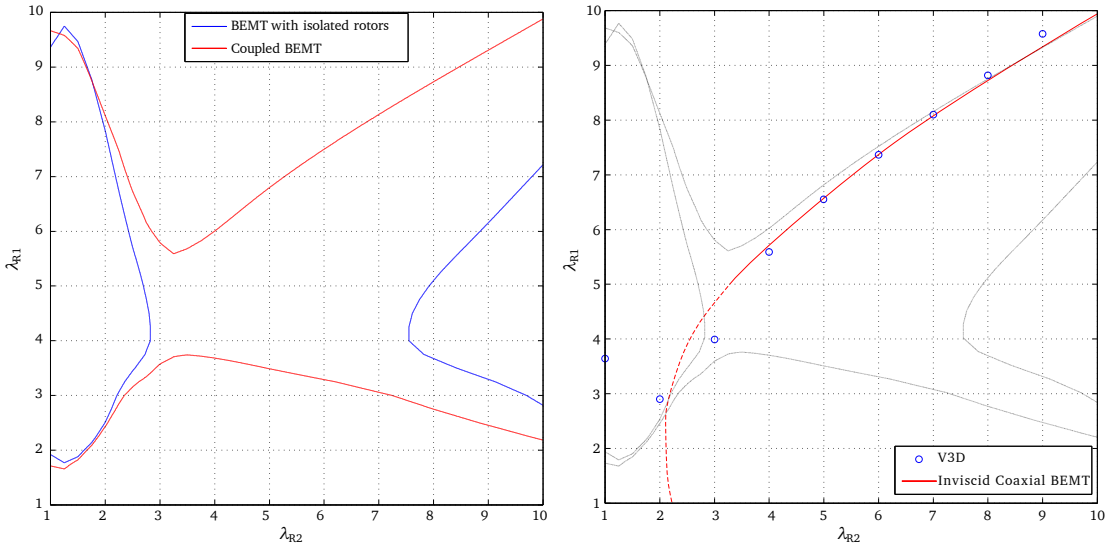

(a) BEMT **(b)** Inviscid BEMT and V3D

Figure 8.11: Zero torque contour on λ_{R1}-λ_{R2} plane.

for the single rotor system are presented in Fig. 8.9a.

8.3.3.2 Dual Rotor Configurations

The models are now changed to the dual rotor configuration. In the case of the BEMT models, this requires specifying the blade data in Table D.2; for the V3D code, a mesh is generated such as that in Fig. 8.8. In all cases, a V3D boundary-element mesh density of 32×32 has been used, and there are 50 cells across the rotor.

The principle objective with a contra-rotating turbine is to ensure that the total torque sums to zero. Therefore, a trim calculation has been performed using the blade element code in case B mode, and also using V3D (case A was not analysed, since it is an algebraic constraint for the code to return a torque balanced result). Figure 8.11a and Fig. 8.11b show the zero torque contour over the range of TSRs for both rotors, referenced against the inflow to rotor 1. Figure 8.11a indicates the importance of considering the rotor as a swirl coupled system as opposed to operating in isolation – i.e. the red line has the $f\left(u_4\right)$ and $g\left(v_4\right)$ modifications in Eq. (8.4a) and Eq. (8.4b), whereas the blue line only has $f\left(u_4\right)$. The approximately "saddle"–shaped divot in between the red lines (where R1 begins to exceed R2s torque) is completely absent if the rotors are considered in isolation. In other words, the R2 will always be predicted to have a higher torque than R1 between $\lambda \approx 3$ and $\lambda \approx 7.5$. When the swirl component is considered, however, the reduction in relative velocity onto the downstream blade element considerably reduces the torque on R2, allowing a much larger TSR range to be used with both rotors operating at or near optimum λ. Fig. 8.12.

Figure 8.11b now superimposes on the viscous BEMT results, inviscid BEMT and predictions. Immediately apparent is that the and BEMT results converge with the inviscid results as the TSR on both rotors increases. However, in situations where either of the rotors is experiencing low TSR, then there is a substantial lack of agreement in shape and value. The lower region of the red line has been marked with dashes – in this region it was difficult to obtain converged BEMT results using the method of case B. With a *heavy* under-relaxation on the iteration, results were obtained, however they were especially sensitive and the results have been smoothed. At TSRs below approximately 4, the level of agreement between the BEMT results diminishes somewhat. It is not clear whether this is an issue with the BEMT code coupling methodology, since convergence is somewhat hampered, or with the code experiencing particularly un-physical local forces. It is clear, however, that in its current incarnation, the code can only reasonably be expected to produce good results at high TSRs. Pressure coefficients for the coaxial rotor system are presented in Fig. 8.9b and

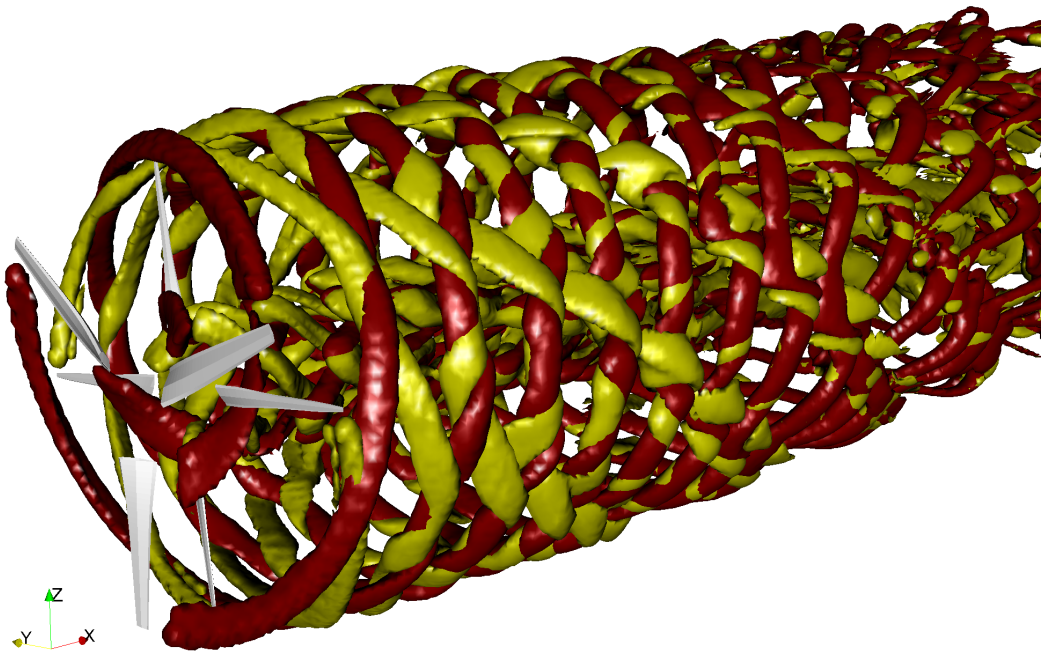

Figure 8.12: Vorticity l^2 isosurfaces for twin rotor configuration at $\lambda_{R1} = \lambda_{R2} = 4$.

wake vorticity isosurfaces in

8.3.3.3 Conclusion

This paper has presented results for single and double rotor configurations of the contra-rotating coaxial CoRMaT rotor, using a BEMT model from the literature, and another developed recently. These results have been compared to results obtained from the Navier-Stokes code which models wake vorticity. Results obtained agree well between the BEMT models themselves, and with the model when using inviscid input data. Results for single and dual rotor systems converge at high TSRs, since there will be lower prevalence of stall on the rotor. Future work will concentrate on reducing this disparity by further improving the code's ability to model viscous flows.

References

Bahaj, A., Batten, W. and McCann, G. (2007). "Experimental verifications of numerical predictions for the hydrodynamic performance of horizontal axis marine current turbines." *Renewable Energy*, **32**(15): pp. 2479–2490.

Bai, L., Spence, R.R.G. and Dudziak, G. (2009). "Investigation of the influence of array arrangement and spacing on tidal energy converter (TEC) performance using a 3-dimensional CFD model." In "Proceedings of the 8th European Wave and Tidal Energy Conference (EWTEC2009)," Uppsala, Sweden.

Clarke, J., Connor, G., Grant, A. and Johnstone, C. (2007a). "Design and testing of a contra-rotating tidal current turbine." *Proceedings of the Institution of Mechanical Engineers, Part A: Journal of Power and Energy*, **221**(2): pp. 171–179.

Clarke, J.A., Connor, G., Grant, A.D. and Johnstone, C.M. (2005). "Design and initial testing of a contra-rotating tidal power turbine." In "Proceedings of the 6th European Wave and Tidal Energy Conference (EWTEC2005)," Glasgow, Scotland.

Clarke, J.A., Connor, G., Grant, A.D., Johnstone, C.M. and MacKenzie, D. (2007b). "Design of a contra-rotating tidal power turbine and analysis of performance." In "Proceedings of the 7th European Wave and Tidal Energy Conference (EWTEC2007)," Porto, Portugal.

Drela, M. and Giles, M. (1987). "Viscous-inviscid analysis of transonic and low Reynolds number airfoils." *AIAA Journal*, **25**(10): pp. 1347–1355.

McCombes, T., Johnstone, C. and Grant, A. (2009). "Wake modelling for marine current turbines." In "Proceedings of the 8th European Wave and Tidal Energy Conference (EWTEC2009)," Uppsala, Sweden.

McCombes, T., Johnstone, C. and Grant, A. (2010a). "Unsteady wake modelling for arrays of tidal current turbines." In "Proceedings of the 11th World Renewable Energy Congress (WREC2010)," Abu Dhabi, UAE.

McCombes, T., Johnstone, C. and Grant, A. (2010b). "Wake modelling for marine current turbines." In "Proceedings of the 3rd International Conference on Ocean Energy (ICOE2010)," Bilbao, Spain.

McCombes, T., Johnstone, C. and Grant, A. (2011). "Navier-Stokes modelling for contra-rotating tidal turbines." In "Proceedings of the 9th European Wave and Tidal Energy Conference (EWTEC2011)," Southampton, England.

Somers, D. (1997). "Design and experimental performance of the S809 airfoils." Tech. Rep. NREL/SR-440-6918, NREL.

9

Perspectives, Future Work and Conclusions

The aim of this thesis has been to develop a method for modelling tidal turbines, and in particular to capture the evolution and impact of their wakes. The outcome of this work is the description and application of a method which provides a combination of boundary-element and vorticity transport flow solvers. The novelty of this work resides in the theoretical coupling methodology for these modelling strategies, the translation into a flow solver, and the practical application of the solver to real world cases. Using the method described herein, the distribution of pressures over three-dimensional representations of hydrodynamic systems can be obtained, and in particular those operating in the wake of upstream devices, in a manner, speed and efficiency which was hitherto not feasible using available software. The distinct advantages of the method are, therefore, the preservation of the wake and the ability to recover surface pressure and thus forces and moments acting over a body. Prior to commencement of the work described herein, there was no means of producing the data that this method allows, especially one which was publicly available and open-source.

This chapter now recaps the work presented in this thesis, before developing some global conclusions. Suggestions for future research are then proposed.

9.1 Summary

Chapter 1 introduced the topic of tidal power with an indication of the potential of the UK and Scottish waters and the rationale for research on tidal power devices. The various tidal power concepts were introduced along with prominent examples of their kind, and some comments were made on the possible efficiency of these devices. The key observations are that there is a significant resource available and no established means of exploiting it. Successful development of the sector hinges on overcoming significant R&D challenges in designing multi-device arrays, and this thesis focusses on advancing research

on a particular aspect; namely inter-device spacing due to wake interactions. The principal modelling strategies were discussed. Blade Element/Momentum Theory – whilst well adopted, simple to understand and implement and computationally efficient – provides only a one-dimensional solution with no real information about time varying forces or wake development. Panel codes or boundary-element methods are able to provide two- and three-dimensional solutions including flow fields and surface pressure distributions, but are hampered by a poor representation of the wake development. This leads to either prescriptive fixed/relaxing wake models which require either a priori knowledge of wake layout or iterate on wake position, or free-wake models which eventually result in “vortex spaghetti”. A discussion on RANS CFD for tidal turbines is deferred until Chapter 3, however, the principal shortcoming – namely artificial diffusion of the wake – is identified. The objectives and outline of the thesis are enumerated.

Chapter 2 introduced the concept of a vortex model, and described the evolution and application of what is fast becoming a very capable means of modelling unsteady, multi-scale flows. The methods from the literature most pertinent to this thesis were expanded, and the zonal decomposition, and the fast-multipole method as utilised were described.

Chapter 3 identified “traditional" finite-volume models used in tidal turbine computational analysis and presented a finite-volume method for the vorticity transport equations. The core concern was the adequate modelling of the convection term, since poor handling of this leads to an overly diffusive result. Naïvely attempting to remedy this using a higher-order scheme will result in an unstable solution advancement. Methods which would preserve discontinuities and suppress solution wiggles were presented and discussed, as were the means of producing a two- or three-dimensional version of the method.

Chapter 4 developed the boundary-element method for this work. A description of the historical development and theoretical underpinnings of the method was followed by a practical implementation for both two- and three-dimensional flows.

Chapter 5 described the method of this thesis: a boundary-element method using a vorticity-transport wake model in two and three dimensions. The means by which the methods were coupled was described. Emphasis was placed on creating a good approximation of the vorticity field using a distribution of particles obtained from a “traditional” boundary-element wake patch.

Chapter 6 presented proof-of-concept studies in two dimensions. These ranged from solving a vortex flow in the absence of the boundary-element model, through the simplest coupled vorticity-transport/BEM models of a static then oscillating aerofoil, and finally a preliminary application to a cross-flow tidal turbine.

Chapter 7 presented proof-of-concept and unit tests in three dimensions. Starting with a simple test of the BEM using flow around a non-lifting sphere then describing static hydrofoils followed by a wind turbine and a tidal turbine, the predictive performance of the method was examined.

Chapter 8 presents fully unsteady three-dimensional test cases, namely simulations of arrays of devices, and of a coaxial rotor system.

9.2 Contributions

The main contribution of this work is a novel numerical method combining a finite-volume vorticity-transport flow solver and a boundary-element method. Application of the method has demonstrated that it is convergent and has the ability to satisfactorily match experimental results in a number of cases. In particular, this is apparently the first model which uses a two- or three-dimensional solid body BEM to provide the vorticity source for a FVM vorticity solver – previous models utilised either the combination of a lifting-line with particle or FVM wake, or a BEM with either a panel or particle wake. This model combines the advantages of a vorticity based finite-volume wake model (Lagrangian wake tracking focusing resources where required, overlapping vortex cores eliminates the re-meshing requirements of particle methods and a simple hierarchical domain decomposition) with the ability to model "solid" lifting-body rotor-systems and thus obtain surface pressure distributions. This facilitates long-duration wake simulations with multiple lifting bodies at a resolution which is unavailable using traditional BEM or FVM methods.

A method for coupling the finite-volume wake model and the low-order boundary-element model based on sound vortex-methods practices has been presented and tested. While this is not the same as stating that the method has been validated, it implies that with further development the method could be used as a predictive tool, subject to further and rigorous calibration, verification and validation studies. The model has been demonstrated to match experimental results for three-dimensional flows with some degree of alacrity as long as the primary constraints on the modelled physics are not violated. While this effectively limits the model to considering on, or close to on-design condition studies without the requirement of some degree of interpretation in the results, the level of match in the results does indicate that there is merit in the modelling strategy and that further development is a worthwhile investment.

Since a large part of the work for this thesis was spent in verifying the performance of the individual parts of the code, substantive contributions also exist in the components of the model. The code developed during this work has a functioning fast-multipole

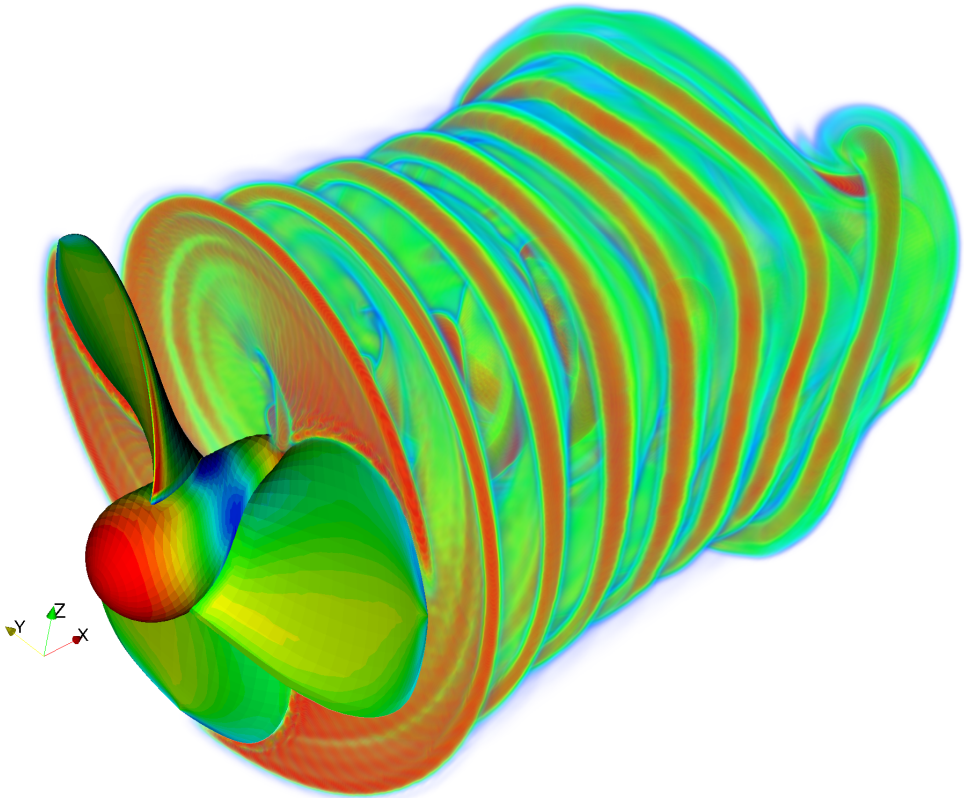

(a) Wake vorticity and surface pressure distributions associated with flow around a marine propeller. Surface geometry based on DTRC 4119 propeller described in Jessup (1989). Advance ratio $J = 0.833$.

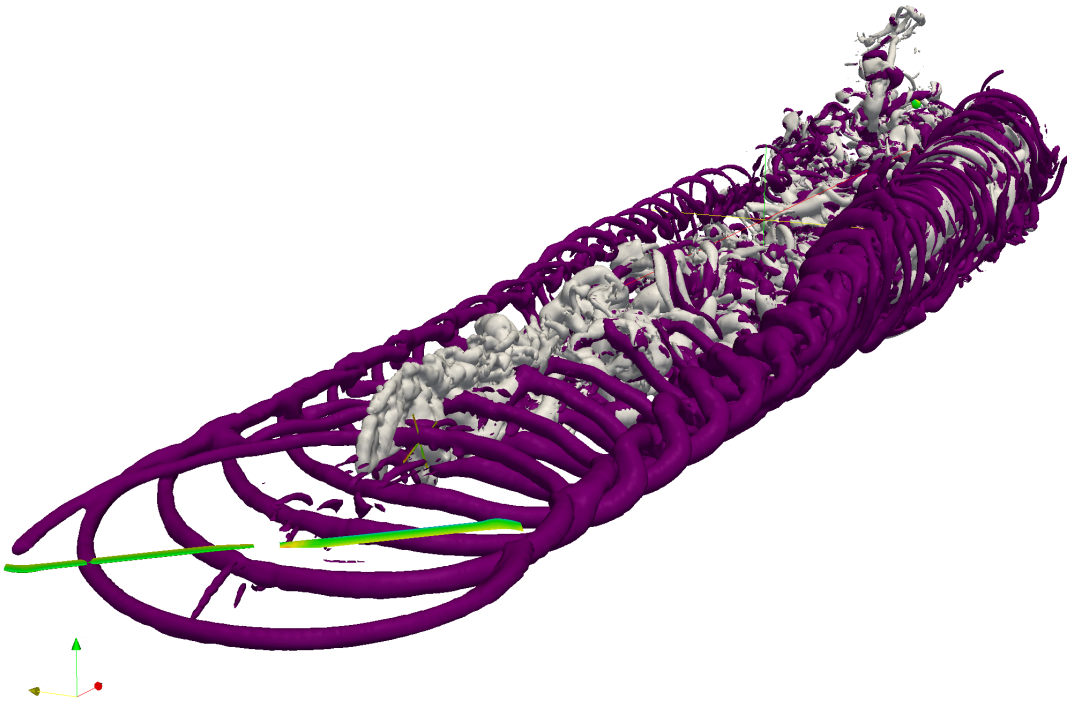

(b) Wake vorticity isosurfaces and surface pressure distributions associated with flow around a helicopter rotor. Surface geometry based on a 2 blade BERP tipped Puma rotor. Advance ratio $\mu = 0.177$, angle of attack $\alpha = -3^{\circ}$, sideslip $\beta = -6.84^{\circ}$, no cyclic/collective pitch.

Figure 9.1: Example applications of V3D flow-solver.

method for velocity recovery from a vorticity field, functioning two- and three-dimensional boundary-element models and a functioning unsteady three-dimensional finite-volume framework. It is not inconceivable that these would be of value to researchers in the field of marine renewables as well as those in aerospace, naval architecture and in pure vortex modelling. By disabling portions of the code, substantial aspects of previous methods from the literature could be verified; for example replacing the boundary-element source with a lifting-line results in a reasonable (if somewhat coarse) approximation of the VTM code of Brown and Line (2005). Disabling the wake interpolation steps results in an approximate version of the method of Maganga *et al.* (2008) while disabling the panel to particle (and also wake interpolation/binning) results in an approximate, free-wake version of the model in Baltazar and Falcão de Campos (2008). Of course, in each of these cases there are major differences in approach and implementation, however the underlying mathematics are substantively equivalent.

9.2.1 Potential Applications

In addition to the core objectives of the model – simulating flows associated with tidal turbines – given the provenance of the underlying components the flow solver naturally lends itself to modelling the wakes associated with rotor-systems and lifting body configurations from the the worlds of aerospace and marine engineering.

Example applications are presented in Figs. 9.1a and 9.1b with details in the captions. The method is able to model thrust producing bodies such as marine propellers, and multi-body simulations such as those due to helicopter main and tail rotor interactions.

9.3 Future Work *or Shortcomings of the Model*

There are a number of obvious opportunities for increasing the capability of the model developed during this work. For various reasons, mainly computational and as a result of time constraints, certain obvious modifications have not been included. Others have not been included as they would require substantial revision of the method and thus major recoding.

9.3.1 Fast Multipole Method

In the time it has taken for this work to be completed, a number of open-source FMM implementations have become available which may fit the requirements of the model. The code produced by Lindsay and Krasny (2001) has been available throughout, but does not

implement an octree nor a coefficient recycling method as applied herein. Furthermore, it does not provide an integration over cubic cells nor a means of recovering the velocity gradients as required and developed herein. Newer methods, such as those by the research group of Lorena Barba (see `http://lorenabarba.com`), contain MPI implementations which would allow the use of the larger HPC facilities which are becoming available, and the work of Stock and Gharakhani (2010) uses a shared memory GPU implementation of the FMM leveraging the processing power of a high number of single-precision processing units on a graphics card (but this is not open-source). If issues of ownership were resolved, the use of an external FMM module would have sped-up code development considerably and reduced the testing burden commensurately. The following sections outline some issues which a revision or alternative to the FMM might overcome.

9.3.1.1 Computational Cost and Technical Difficulty in Implementation

Complexity The FMM as implemented has been done in the simplest manner feasible. Implementing the method entails some technical difficulty as it requires the use of large and complex data structures which have a time varying complexity correlating to the evolution of the spatial distribution of vorticity. It was not conceivable to implement an efficient version of this method in a high-level language such as MATLAB due to the lack of class-support and the general performance issues encountered when using an interpreted language (although recent versions do support classes, and various MATLAB scripts were used to prototype the FMM algorithm). The memory requirements of the method as implemented are also an issue since the memory required to store the cluster moments and velocity field derivatives is allocated for each node. This results in a memory bound hard limit to the maximum growth in number of cells for a given problem.

It is possible that a more elegant solution for obtaining the velocity via a FMM can be implemented, from either or both of a mathematical or a computational point of view. The implications are that with a reduced FMM overhead for the same computational cost, larger meshes can be used and more flow physics resolved or higher-orders of multipole expansions could be taken increasing accuracy of the velocity field. A combination, using MPI and efficient programming, would allow extremely large domains to be modelled as there is no upper limit on the number of octree elements. Alternatively, use could be made of one of the parallelised Poisson solvers – although this would reduce the adaptability somewhat. Through experience gained modelling individual turbines, the rotor wake occupies a relatively compact region which could be enclosed in a temporary cuboidal volume, and boundary conditions could be calculated on this with relative low additional overhead by

e.g. the FMM. This is not readily applicable to large and sparse domains, such as those around arrays of turbines.

9.3.1.2 Extensions to Current Form

An interesting way of improving the performance of the model would be to modify the FMM method and associated data-structures to include the influence of the boundary-element model. This could be accomplished in a number of ways: the multipole and local expansions of the BEM elements (source and dipole panels) could be piggy-backed onto the velocity field sweeps, or the source/dipole panels could be replaced by vortex panels which could be included in the FMM directly – this would appear to be the best method, as it could be extended to include shedding of boundary layer vorticity from the panels enabling a viscous solution.

9.3.2 Boundary-Element Method

The BEM aspect of this methodology belongs to a class of analysis methods which have elements of a "black-art" about them. This implies that there is often significant (experienced) user-interaction required in order to tailor a simulation to a particular situation. This is no different to using traditional CFD, and is not necessarily a major criticism of low-order potential flow solutions per se, just that a large amount of variability in the results could be eliminated by improving the model in a number of ways.

9.3.2.1 Theoretical Limitations

The obvious theoretical limitation is that of potential flow. Without viscosity, body surface integrated drag calculations can only contain pressure drag. This is sufficient in many of the cases presented herein, where devices are operating such that their blades etc. are at a high lift/drag ratio. In off-design conditions drag starts to play a major role.

In addition to drag, the absence of a boundary layer prevents the model from representing dynamic stall (or any form of stall, in fact) which is a major contributor to the unsteady loads on an aero/hydrodynamic surface operating in an unsteady flowfield – an axial flow turbine in yaw for example, or the blade of an cross-flow turbine.

The assumptions of a constant distribution over the singularity elements has proved to be a major hindrance to the successful use of this model. This is because the wake generation relies on the distribution of the dipoles along the Kutta-condition panels at the trailing edge to give the wake patches their strengths. It is known that a dipole distribution of a particular order gives rise to a vortex distribution an order lower (see Katz and Plotkin,

2001), and thus in the present implementation a constant dipole distribution over the wake panels translates to a discontinuous vortex distribution, with vortices at only the panel edges. This has serious implications when the panel edge vortices are split and binned into the FVM mesh, as if the wake panel is sufficiently large there will be empty FVM cells and thus a non-smooth (lumpy) vorticity field. To avoid this, the internal BEM time-step and the spanwise/radial distribution of panels has been such that no wake panel is so long or wide as to bracket a cell. This is a major time-step limitation since a relatively coarse FVM mesh must be used, with cells at the same scale as the BEM panels, and the number of BEM time-steps must be fairly large to avoid the additional FMM calls required if the FVM time-step were reduced.

Additional points concerning a constant distribution of singularity elements are:

- that the panels must be flat for an exact solution of the analytical expressions for the influence coefficients;
- the no-penetration boundary condition is only satisfied at a single location on the panel surface; and
- that the gradient of the panel dipole strengths must be calculated using finite-differences, introducing a source of error.

These issues would all be dealt with by using a higher-order distribution of singularities, for example NURBS panel geometry with bi-linear or bi-quadratic elements. In the wake, it would be possible to generate a linear vortex sheet which could be interpolated easily and binned very effectively over a number of FVM cells. The number of cells could be increased and the BEM time-step could be matched with the FVM time-step (but still subject to the penetration CFL-like condition at the BEM mesh region of highest velocity to prevent FVM vorticity skipping “inside” the BEM volume). Curved panels would map to complex body surfaces better, requiring fewer panels overall. The no-normal flow boundary condition could be satisfied at a number of points over the panel (the additional matrix solution overhead is trivial if the matrix can be solved in shared memory) and the gradients of the higher-order singularity distributions can be determined implicitly using the polynomial coefficients and the geometric definitions of the panel.

9.3.2.2 Implementation Limitations

Computational limitations of the present BEM are performing the linear algebra, which becomes very expensive for large matrices, and the calculation of the velocity field due to the BEM. Neither of these problems are intractable: the matrix solver could be changed to

an MPI implementation and the velocity field could be calculated using FMM methods (as described above).

A final point is that the present implementation of a linear Kutta condition is not capable of achieving zero trailing edge pressure jump on any but hyper-convergent cases (static aerofoils, for example) and this is especially noticeable on the Southampton turbine blades discussed in Section 7.3.3. This is due to the inability in three dimensions of specifying both tangential direction velocity components simultaneously without under-determining the system of equations. An iterative pressure Kutta condition can reduce this to a tolerance, but at significant computational overhead.

9.4 Avenues for Future Work

Other obvious routes for improving the model involve increasing its ability to model the flow physics more completely.

9.4.1 Viscous Boundary Conditions

Viscous boundary conditions can be implemented in a vortex method using a number of frameworks: a BEM vortex method can shed Lagrangian vortices to satisfy the no-slip (and no penetration) conditions, or a purely finite-volume vortex method boundary condition can diffuse vorticity into the adjoining cells to satisfy the same. Lagrangian vortices can be binned in the same manner as in the present method and the wake modelled using the cubic finite-volume manner.

Quasi-viscous BEM boundary conditions can be applied in a number of manners, for example using a method known as “surface-transpiration” which uses the pressure distribution over the surface as input to a boundary layer calculation. The surface geometry is then modified so that the BEM panels no longer approximate the surface of the device, but include some thickness of the boundary layer. This method is not really applicable to anything but attached flows, and it is hard to imagine how it would be implemented in three dimensions as the boundary layer equations are essentially one-dimensional. However, if a technique was obtained, it could be added to the present method with only minimal modification, but at some considerable computational overhead as the influence coefficient matrices would have to be calculated and solved numerous times per time-step. The surface transpiration method has found regular use in two-dimensional codes with considerable success, for example the famous X-FOIL aerofoil analysis tool (Drela and Giles, 1987). In three-dimensional methods, an analogous approach is taken in modelling cavi-

tation bubbles (Vaz, 2005).

An alternative is to model the effects of flow separation by allowing a second wake to be shed from the BEM mesh. This simulates the effects of leading edge separation at stall, however there is a requirement for an a priori specification of the LE separation line, which is probably taken from experiment rather than physics. Researchers have used this method for ship propellers and tidal turbines, for example Baltazar and Falcão de Campos (2008). As with the surface transpiration method, this is simply a post-fix rather than a change in physics, but unlike the transpiration method the implementation of this method would not require additional iterations per sub-step, and an implementation using the present method would be relatively simple.

9.4.1.1 snappyHexMesh Method

Assuming that the analytical and numerical expressions for the Biot-Savart integral can be obtained for arbitrary polyhedra, then the OpenFOAM meshing tool snappyHexMesh (or similar) could be used to mesh complex geometries. The tool provides a surface approximation by cutting hexahedral elements, whilst maintaining a hex-core. The hex-core could be discarded and the surface representation retained, and influence coefficients specifying either zero normal flux, or no-slip calculated resulting in a large system of equations for the boundary conditions. The hex-core could then be reinstated using the solution dependant octree algorithm as vorticity is transferred out of the split cells. It is difficult to imagine how this method would be applied for deforming geometries or those with components moving relative to one-another.

9.4.1.2 Cartesian-Cut-Cell Method

Again assuming that the Biot-Savart integral can be efficiently evaluated over arbitrary volumes, an alternative would be the Cartesian-cut-cell method. In this method, the entire domain is considered as Cartesian cells (cubes), and the surface of the geometry is tracked through the domain as a front. Where a cell is intersected by the surface, it is cut. If the geometry is complex in a manner which means that a cell is intersected by more than one surface, the cells can be refined until a cell has a single intersecting face of between three and six vertices. Boundary conditions are then applied at the surface and the solution advanced. Cut-cell approaches have been applied to vortex methods in two dimensions in Stallard (2005). Limitations are likely to include the presence of shards – these increase the number of elements and may reduce the accuracy of the cubature.

Table 9.1: Computational and Experimental Parameters For Test Cases

Experimental Parameters			
Gravitational Acceleration	g	$9.81\,\mathrm{m\,s^{-2}}$	
Mean Water Depth	d	$2.245\,\mathrm{m}$	
Wave Height	a	$0.15\,\mathrm{m}$	
Fluid Density	ρ_{H_2O}	$999\,\mathrm{kg\,m^{-3}}$	
Blade Density	ρ_{Al}	$2700\,\mathrm{kg\,m^{-3}}$	
Turbine Hub Immersion Depth	d_{hub}	$0.25\,\mathrm{m}$	
Turbine Radius	R	$0.175\,\mathrm{m}$	
Tip Speed Ratio	λ	3.66	
Carriage Tow Speed	U	$1.0\,\mathrm{m\,s^{-1}}$	
Computational Parameters			
Panel Density	$n_{chord} \times n_{span}$	32×32	
FVM Cell Density	$n_{cell}/2R$	75	
Case Particulars			
		Case A	Case B
Wave Period	T_z	2 s	1 s
Wave Steepness	ka	8.7°	29.2°

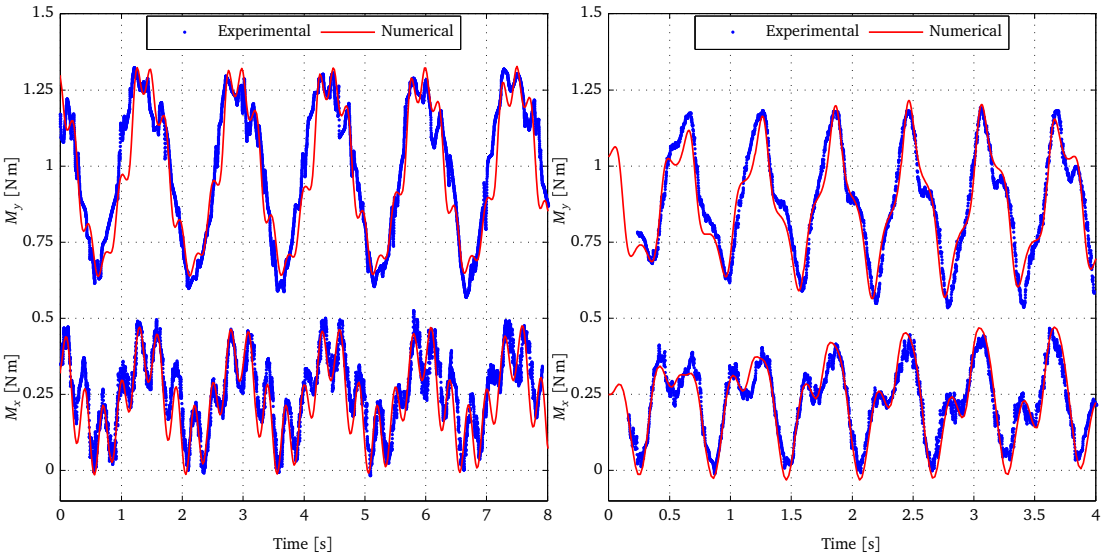

(a) Case A **(b)** Case B

Figure 9.2: Blade root bending moments. M_x and M_y are moments in- and out-of-plane, respectively.

9.4.2 Multiphase Flow: Waves, Free Surfaces and Cavitation

Multiphase flows for tidal devices encompass surface effects due to both the free-surface interface between the ocean and the air, but also the surface of cavitation bubbles. Both can be treated using either (or both of) the BEM method or the FVM method.

9.4.2.1 A Wave Theory Formulation

In research project work stemming from this thesis, McCombes, Johnstone and Grant (2013) present a combined wave theory/V3D model applied to cases from the literature, in particular the towing tank tests discussed in Barltrop *et al.* (2006). These cases have seen use in the tidal community in validating various numerical models, e.g. in Buckland, Masters and Orme (2011). The tests were carried out in the University of Strathclyde's Kelvin Hydrodynamics Lab 77 m × 4.6 m × 2.4 m towing tank, and for the purpose of the computational tests the parameters in Table 9.1 have been assumed. The turbine under consideration is a three-bladed axial flow type with linear chord and cubic twist distributions where the aerofoil section is uniformly NREL S814 – full details are given in Barltrop *et al.* (2006) where it is also noted that the results of their linear wave theory model break down due to the shape of the waves in the tow tank, so the 5^{th} order wave theory according to Skjelbreia and Hendrickson (1960) has been used in an attempt to capture the non-linear effects associated with steep waves.

Results are presented for the in- and out-of-plane bending moments encountered by one of the turbine blades, denoted M_x and M_y respectively. A significant component of the in-plane bending moment is due to the mass/buoyancy of the blade. The correction factor for this is calculated using the moment of the apparent immersed weight due to the mass distribution in the aluminium blades:

$$M_{x,\text{self}} = A_{\text{S814}} \left(\rho_{\text{H}_2\text{O}} - \rho_{\text{Al}} \right) g \cos\left(\psi\right) \int_{\text{root}}^{\text{tip}} c(r) r \, \mathrm{d}r. \tag{9.1}$$

Here A_{S814} is the area of the NREL S814 aerofoil of unit chord, $c(r)$ is the radial chord distribution, and ψ is the azimuthal position of the rotor blade.

Figure 9.2a shows the root bending moments for Case A, and Figure 9.2b shows those for Case B. It should be noted that the time axis represents neither simulation time nor experimental run time, and is merely an indicator of duration of the events in the time history: in all cases the experimental and numerical times have been aligned so the traces somewhat coincide. There is a slow evolution in the location and magnitude of the secondary peaks. It is expected that if longer simulations were run, or the blade azimuth were

adjusted prior to start-up, then segments of the simulation time histories could be selected such that the various peaks and shoulders coincide more satisfactorily with those in the experimental data. However, it is apparent that the hybrid V3D/wave theory model results broadly match those from Barltrop *et al.* (2006) in both frequencies and magnitudes for both wave frequencies, as well as in the evolution of the slowly varying phases. These results are very preliminary, and further work is underway to identify the key mechanisms behind the major discrepancies, in particular the role of viscous effects in the loading on the rotor.

9.4.2.2 BEM Formulation

BEM formulations for free-surfaces are a key naval architecture tool used in modelling vessels such as ships or floating wave power devices. The free-surface is considered a boundary and as such discretised into a number of panels. The difference between a solid boundary and the free-surface boundary is that the free-surface is allowed to deform according to the dynamics of the simulation. Tools in common use include WAMIT and ANSYS AQWA. Work by Topper (2010) used a high-order panel method to model the flow around devices in the vicinity of a free-surface.

Cavitation could also be captured in a similar manner using BEMs. In a method related to the surface transpiration method as well as the leading edge separation method, partial cavitation bubbles can be grown in areas of low pressure either by producing a layer of panels above the surface at a height given by the bubble thickness, or transpiring the boundary surface for the bubble thickness. Super-cavitation can be captured by additionally shedding “cavitation” panels (or other Lagrangian markers) which are deleted when the local pressure increases above vapour pressure. These methods would not require significant work to implement within the framework of the method of this thesis.

9.4.2.3 FVM Formulation

Multiphase finite-volume methods exist using various methods. Obvious methods either track the interface and move the cell boundaries in surface intersecting cells to conform to the free-surface, or fill each cell with a scalar parameter representing the proportion of the cell occupied by fluid. Multiphase flow could be modelled within the current method by using either method, however, a boundary condition would have to be applied at the interface to prevent vorticity from the liquid domain crossing into the air domain.

9.5 Conclusions

The primary conclusions of this work are as follows:

1. Off-the-shelf CFD methods do not adequately capture the full evolution of the wake behind a turbine, known to influence the power capture in arrays of devices.

2. A finite-volume/boundary-element method for modelling the flow around two- and three-dimensional bodies has been presented. The best results for modelling the convection equation is seen to be a symmetrically weighted sequential splitting scheme (although the slightly cheaper alternating dimensions scheme might be a better compromise when the cost of implementation is considered). This is solved with a non-linear, high resolution flux-limited finite-volume integration, and in particular using one of the PL-κ limiters such as Koren or MUSCL results in the lowest artificial diffusion whilst optimally preserving the shape of the distribution of transported variables in two- and three-dimensional flows.

3. Two-dimensional test cases have been presented and used as proof-of-concept studies for the full model. Flow in the absence of bodies was analysed with the relaxation of a perturbed monopole. The distribution of vorticity in time was seen to match well with previous numerical results, as too did the integrated quantities, in this case angular momentum. Confidence is thus gained in the method when applied to purely vortex flows.

4. The outcome of static two-dimensional BEM tests using aerofoil sections is that the method is able to model the flow around static bodies reliably and matches existing data in both pressure and integrated quantities. Unsteady two-dimensional cases involving an oscillating hydrofoil compute the lift amplitude and phase errors predicted using classical theories relatively well. Further analysis is required in order to establish fully the causes of discrepancies, however, by splitting the recovered force into that due to the kinematics and that due to the wake, it is seen that the kinematic terms match very well, and so errors must be due to the wake model.

5. Similarly, results published on two-dimensional modelling of a cross-flow turbine predict blade forces reasonably well, although the physics breaks down and major errors can be seen during stalled flow conditions. At high tip-speed ratios the match is more convincing. The same applies in evaluating integrated quantities – the quality of low tip-speed ratio results is questionable, with considerable overpredicton in force due to absence of stall. Thrust is also significantly overpredicted – as with

the oscillating foil this appears to be an issue with the wake model. The conclusion here is that stall modelling is essential when simulating cross-flow turbines, and unless there is a modification to the BEM utilised, predictions made using the current method, especially for low TSRs, are unreliable. Further work is required before confidence that the model performs adequately in two-dimensions is gained, however, movement is in the right direction.

6. Three-dimensional test cases for flows around a non-lifting sphere demonstrate that the method is convergent in surface meshing, and able to predict correctly the pressure distribution on three-dimensional surfaces. This implies that both the boundary-element method (including the geometry pre-processing) and the post-processing are functioning as expected.

7. Results from the flow around a three-dimensional lifting hydrofoil show strong convergence, both graphically for pressure distributions, and through a grid dependency study for integrated quantities. The output shows a good match with experimental results, both in terms of the surface pressures, and also the wake velocity field. Confidence is gained that the combined three-dimensional boundary-element method with a finite-volume vorticity flow solver for the wake is a viable modelling strategy.

8. Results from the final three-dimensional proof-of-concept studies presented show the pressure distribution predicted over the surface of a wind and tidal turbine. The wind turbine results are convergent, both graphically and in terms of a grid convergence study on local lift coefficient, and match experimental data very well. The same can also be said for the tidal turbine convergence results, however, experimental data is not available for the pressure distribution, but results from an inter-model comparison are very favourable. Contrary to the cross-flow turbine, the results obtained using the model to simulate high TSR cases do not match experimental data particularly well, and while experimental data from very low TSR cases is unavailable, for $4 < \lambda < 7$ the model performs satisfactorily.

9. Considering Item 5 and Item 8, it is concluded that the modelling method is acceptable as long as the physics limitations are strictly observed. This somewhat limits the method in application to off-design conditions and necessitates further work, as described previously. However, in on-design conditions the model performs well and can thus be used to make optimisations to devices in order to wring out the last few performance percentage points at the design condition.

10. Since the publication of the method of this thesis in McCombes, Johnstone and Grant (2011), the V3D code and ancillary routines have been developed and used in research projects, some of which have been described herein. The ethos of the Energy Systems Research unit and it's parent, the Department of Aerospace and Mechanical Engineering at the University of Strathclyde, is strongly pro open source, and as such the V3D and supporting programs is available in its entirety by contacting the author, or via the Energy Systems Research Unit at `http://www.strath.ac.uk/esru/`.

References

Baltazar, J. and Falcão de Campos, J. (2008). "Hydrodynamic analysis of a horizontal axis marine current turbine with a boundary element method." In "Proceedings of the ASME 27th International Conference on Offshore Mechanics and Arctic Engineering," Estoril, Portugal.

Barltrop, N., Varyani, K.S., Grant, A., Clelland, D. and Pham, X. (2006). "Wave-current interactions in marine current turbines." *Proceedings of the Institution of Mechanical Engineers, Part M: Journal of Engineering for the Maritime Environment*, **220**(4): pp. 195–203.

Brown, R. and Line, A.J. (2005). "Efficient high-resolution wake modeling using the vorticity transport equations." *AIAA Journal*, **43**(7): pp. 1434–1443.

Buckland, H.C., Masters, I. and Orme, J. (2011). "Wave implementation in blade element momentum theory for modelling tidal stream turbines." In "Proceedings of the 19th UK Conference of the Association for Computational Mechanics in Engineering," Edinburgh, Scotland.

Drela, M. and Giles, M. (1987). "Viscous-inviscid analysis of transonic and low Reynolds number airfoils." *AIAA Journal*, **25**(10): pp. 1347–1355.

Jessup, S.D. (1989). *An experimental Investigation of viscous aspects of propller blade flow*. Ph.D. thesis, The Catholic University of America.

Katz, J. and Plotkin, A. (2001). *Low Speed Aerodynamics*. Cambridge University Press.

Lindsay, K. and Krasny, R. (2001). "A particle method and adaptive treecode for vortex sheet motion in three-dimensional flow." *Journal of Computational Physics*, **172**(2): pp. 879–907.

Maganga, F., Pinon, G., Germain, G. and Rivoalen, E. (2008). "Numerical simulation of the wake of marine current turbines with a particle method." In "Proceedings of the 10th World Renewable Energy Congress (WRECX)," Glasgow, Scotland.

McCombes, T., Johnstone, C. and Grant, A. (2011). "Unsteady wake modelling for tidal current turbines." *IET Renewable Power Generation*, **5**(4): pp. 299–310.

McCombes, T., Johnstone, C. and Grant, A. (2013). "SUPERGEN Marine Research: Modelling Wave Induced Flow Effects on Tidal Turbines." In "Proceedings of the 10th European Wave and Tidal Energy Conference (EWTEC2011)," Åalborg, Denmark.

Skjelbreia, L. and Hendrickson, J. (1960). "Fifth order gravity wave theory." *Coastal Engineering Proceedings*, **1**(7): p. 10.

Stallard, T.J. (2005). *Simulation of Unsteady Viscous Flow-Structure Interaction*. Ph.D. thesis, The University of Oxford.

Stock, M.J. and Gharakhani, A. (2010). "Modeling rotor wakes with a hybrid OVERFLOW-vortex method on a GPU cluster." In "Proceedings of the 28th AIAA Applied Aerodynamics Conference," .

Topper, M. (2010). *Numerical Modelling of Flows Involving Submerged Bodies and Free Surfaces*. Ph.D. thesis, The University of Edinburgh.

Vaz, G. (2005). *Modelling of Sheet Cavitation on Hydrofoils and Marine Propellers using Boundary Element Methods*. Ph.D. thesis, Universidade Técnica De Lisboa Instituto Superior Técnico.

A

Comments on Stability, Errors, Verification and Validation

A.1 Error Analysis – Example Application to the Central-Difference Scheme

The formal solution accuracy of the central-difference approximation is determined by considering the relationship between the discrete approximation and exact derivatives. Considering the terms in the brackets on the RHS of Eq. (3.19), a Taylor expansion in x about x_P gives the following series which yield exact values for ϕ while the number of terms is infinite:

$$\phi_{\mathrm{E}} = \phi_P + h\frac{\mathrm{d}\phi_P}{\mathrm{d}x} + \frac{h^2}{2!}\frac{\mathrm{d}^2\phi_P}{\mathrm{d}x^2} + \frac{h^3}{3!}\frac{d^3\phi_P}{\mathrm{d}x^3} + \textit{higher-order terms}. \tag{A.1}$$

A similar expression can be obtained for ϕ_{W}. Substituting these into the central-difference of Eq. (3.19) and rearranging results in

$$\frac{\phi_{\mathrm{E}} - \phi_{\mathrm{W}}}{2h} = \frac{\mathrm{d}\phi_P}{\mathrm{d}x} + \frac{h^2}{3!}\frac{d^3\phi_P}{\mathrm{d}x^3} + \textit{higher-order terms} = \frac{\mathrm{d}\phi_P}{\mathrm{d}x} + \mathcal{O}\left(h^2\right). \tag{A.2}$$

In other words, the approximation employed has a local truncation error at x_P of $\mathcal{O}(h^2)$ – the remainder after the exact derivative on the RHS – and as a scheme it is described as *second-order* accurate in h which means that the solution converges with h^2. Obviously the higher the order of accuracy, the lower the truncation errors, since as $h \to 0$ then $\mathcal{O}(h^{n+1}) < \mathcal{O}(h^n)$.

The PDE which is actually solved when a numerical solution is sought for Eq. (3.13) is known as the *modified equation* (Toro, 1999; Cebeci *et al.*, 2005) which can be written for the central-scheme as

$$\frac{\partial\phi}{\partial t} + u\frac{\partial\phi}{\partial x} = -\frac{uh^2}{3!}\frac{\partial^3\phi}{\partial x^3}, \tag{A.3}$$

where it is taken as read that the Taylor expansions are about $t = t_0$ and x_P and the indices are dropped for clarity. The third derivative on the RHS is a non-physical dispersive term, resulting in phase shifts acting on the various wave-numbers obtained via von Neumann analysis.

A.1.1 von Neumann Stability Analysis

The von Neumann stability analysis can be used to demonstrate the inappropriateness of the central-difference scheme when applied to the model equation, and thus justify using more complex alternatives. Consider Eq. (3.13) written using the discretisation given in

Eq. (3.19) for the right hand side and a forwards Euler step for the time derivative

$$\frac{\phi_P(t+\Delta t)-\phi_P(t)}{\Delta t}=\frac{u}{h}\left[\frac{\phi_{\mathrm{E}}(t)-\phi_{\mathrm{W}}(t)}{2}\right]. \tag{A.4}$$

Now substitute the numerically computed approximate values of ϕ with the exact solution plus truncation and rounding errors such that $\phi_P(t)=\phi_P\prime(t)+\epsilon_P(t)$ and so on, and noting that the error must satisfy Eq. (A.4) given that the exact value does, the result is an error equation

$$\frac{\epsilon_P(t+\Delta t)-\epsilon_P(t)}{\Delta t}=\frac{u}{h}\left[\frac{\epsilon_{\mathrm{E}}(t)-\epsilon_{\mathrm{W}}(t)}{2}\right]. \tag{A.5}$$

Apply a Fourier expansion to Eq. (A.5) on the periodically bounded domain $x\in[0,L]$ subdivided into N cells of width h so that the error

$$\epsilon(x)=\sum_{m=1}^{N/2}A_m\mathrm{e}^{\mathrm{i}k_m x}, \tag{A.6}$$

where A_m is the amplitude of the m^{th} wave whose wave-number is k_m. The term $\mathrm{i}=\sqrt{-1}$. Assuming that the amplitude of the errors will vary exponentially in time yields the following (where α is a constant):

$$\epsilon(x_P,t)=\sum_{m=1}^{N/2}\mathrm{e}^{\alpha t}\mathrm{e}^{\mathrm{i}k_m x_P}; \tag{A.7}$$

and so on for $x_{\mathrm{E,W}}$ and $t, t+\Delta t$. The expansion is linear, whereby the behaviour of a single Fourier component is representative of the system as a whole, and so a single component can be isolated such that the error equation may, after some manipulation, be written

$$\mathrm{e}^{\alpha\Delta t}=1+\frac{u\Delta t}{h}\left[\frac{\mathrm{e}^{\mathrm{i}k_m h}-\mathrm{e}^{-\mathrm{i}k_m h}}{2}\right]=1+\mathrm{i}C\sin\left(k_m h\right), \tag{A.8}$$

where $C=\dfrac{u\Delta t}{h}$ is the Courant number (Courant, Friedrichs and Lewy, 1928). Define an amplification factor G for cell P as the ratio of successive error values in time:

$$G=\frac{\epsilon(t+\Delta t)}{\epsilon(t)}=\frac{\mathrm{e}^{\alpha(t+\Delta t)}\mathrm{e}^{\mathrm{i}k_m x_P}}{\mathrm{e}^{\alpha t}\mathrm{e}^{\mathrm{i}k_m x_P}}=\mathrm{e}^{\alpha\Delta t}. \tag{A.9}$$

The condition required for stability is that the magnitude of G is less than unity. Since $\left|\sin\left(k_m h\right)\right|>0$ for all resolvable k_m (that is $k_m=\dfrac{\pi}{Nh}$ where $N\in\mathbb{N}_1$, corresponding to waves whose half-wavelength is between the cell length h and the domain length L), the central-difference scheme is unconditionally unstable. Thus while central-differencing is second-order accurate, it is unusable due to its instability.

A.2 Definitions of Integrated Quantities, Errors and Norms

For evaluating average quantities over the domain (typically errors, e.g. between calculated and expected values f and f^{ex}), unless otherwise indicated, this thesis uses the following length/area/volume weighted l^{k} norms for N computational elements i of length, area or

volume Ω_i:

$$\|f - f^{\text{ex}}\|_{l^k} = \sqrt[k]{\frac{\sum_i^N \Omega_i \left(f_i - f_i^{\text{ex}}\right)^k}{\sum^N \Omega_i}} \tag{A.10}$$

which, if the grid is uniform, becomes

$$\|f - f^{\text{ex}}\|_{l^k} = \sqrt[k]{\frac{\sum_i^N \left(f_i - f_i^{\text{ex}}\right)^k}{N}}. \tag{A.11}$$

The ∞ norm, $\|f - f^{\text{ex}}\|_{l^\infty} = \max\left\{|f_1 - f_1^{\text{ex}}|, \ldots, |f_N - f_N^{\text{ex}}|\right\}/N$.

A.3 Validation and Verification

There is often confusion or muddling between terms "validation" and "verification" (V&V) when used with respect to CFD simulations. There are also sometimes ambiguities with regard to V&V as to whether they are with respect to the model or the solution. For the purposes of this thesis, the terms are used as defined formally in the AIAA Guide for the Verification and Validation of Computational Fluid Dynamics Simulations (AIAA, 1998).

> **Validation:** *The process of determining the degree to which a model is an accurate representation of the real world from the perspective of the intended uses of the model;*
>
> **Verification:** *The process of determining that a model implementation accurately represents the developer's conceptual description of the model and the solution to the model.*

They are succinctly captured by:

> **Validation:** *Solving the right equations;*
>
> **Verification:** *Solving the equations right.*

Assuming that the method works and "solves the right equations", the main sources of error in a CFD simulation are insufficient resolution (spatial and temporal), lack of iterative convergence, computer round-off errors and programmer errors. This thesis only explicitly addresses the resolution errors.

A.3.1 Verification

The parts of this thesis concerned with preliminary verification of the method described herein follow the process outlined in Celik (2008) which now forms part of the ASME Journal of Fluids Engineering Editorial Policy Statement on the Control of Numerical Accuracy, (Roache, Ghia and White, 1986).[1] The process for analysing the level of convergence in the specific case of a (1-3 dimensional) geometric mesh is used as an example here, however it is easily translated into higher dimensional mesh with time as an "axis". The method can also be used to determine the degree of convergence in a time-dependant simulation in

[1] The concatenated version of these two references is available online at `http://journaltool.asme.org/Templates/JFENumAccuracy.pdf`.

which the deviation in some integrated metric is expected to decay in time. Examples of this might be either attaining steady lift for an aerofoil, a diminishing difference in successive lift amplitudes for an oscillating hydrofoil obtained in a phase-locked manner or the time-average of momentum flux through a domain boundary.

To test the convergence of a method, one generates a mesh at the highest feasible resolution given an allowable computational cost, subject to the constraint that it is desirable to be able to effectively halve the resolution, ideally twice, in each dimension. However, given that a general mesh is unstructured, and mesh density might be anisotropic, a representative interval size $h_{\text{equiv.}}$ is defined based on the geometry of the problem, e.g. $h_{\text{equiv.}} = 1/\sqrt{(N)}$ for the 2-D mesh (which might be a boundary mesh in 3-D) of N elements. Once the meshes have been generated, the code is run and results collated and tabulated according to the requirement that representative measurements are obtained from each mesh which can either be integrated quantities or point measurements taken at the same mesh location at each resolution.

The objective of the remainder of the process is to determine the level of grid dependence in the solution. The means of achieving this are to first test that the samples are drawn from a process which is convergent in $h_{\text{equiv.}}$, specifically asymptote smoothly towards an "exact" (if not the correct) solution as $h_{\text{equiv.}} \to 0$. If they are the next stage assumes they can be fit to a convergent power series which equates the estimated solution to the exact solution plus an error

$$f'(\boldsymbol{x}, t, h_{\text{equiv.}}) = f_{\text{exact}}(\boldsymbol{x}, t) + \sum_{i=1}^{q} C_i(\boldsymbol{x}, t) h_{\text{equiv.}}^i + \mathcal{O}(h^{q+1}), \tag{A.12}$$

with coefficients $c_i(\boldsymbol{x}, t) = 0$ for all $0 < i < p$ in a method of order $p < q$. Dropping the higher-order terms and taking logarithms of either side of Equation A.12 obtains the expression for the error:

$$\log(\epsilon) = \log(f'(\boldsymbol{x}, t, h_{\text{equiv.}}) - f_{\text{exact}}(\boldsymbol{x}, t)) = \log(c_p) + p \log(h_{\text{equiv.}}), \tag{A.13}$$

from which the order of convergence p may be obtained, as long as the constancy of c_p is maintained (hence the requirement of samples being drawn from the asymptotic range). Since, ideally, multiple samples are available drawn from different resolutions, successive power series expansions can be combined to eliminate the low-order error terms. This process is combined with the *Richardson Extrapolation*, and forms the core of a Grid Convergence Study whose result is a high-order estimate of the continuum value of the solution for zero mesh spacing. The practical implementation is as follows:

1. Tabulate the $n(=3)$ results for f obtained at e.g. $h_{\text{equiv.}} = (1/N, 1/2N, 1/4N)$;

2. Compute the *grid refinement ratio*, r, between each pair of samples using

$$r_m(n) = h_{\text{equiv.}}(n+1)/h_{\text{equiv.}}(n). \tag{A.14}$$

3. If r is constant, an estimate of the order of convergence, p is obtained according to the three samples

$$p = \frac{\log\left[\dfrac{f(3) - f(2)}{f(2) - f(1)}\right]}{\log(r(1))}. \tag{A.15}$$

4. If r is not constant, i.e. the mesh is non-uniform, then use the estimate of the order

of convergence, p, in Eq. (A.15) as a starting guess in an iterative procedure for p

$$p = \frac{\log\left[\dfrac{f(3)-f(2)}{f(2)-f(1)}\right]+q}{\log(r(1))}; \quad \text{with} \tag{A.16}$$

$$q = \log\left(\frac{r(1)^p - s}{r(2)^p - s}\right); \quad \text{and} \tag{A.17}$$

$$s = \text{sign}\left(\frac{f(3)-f(2)}{f(2)-f(1)}\right).$$

For non-uniform grids, Roache (1998) states that good results from this analysis depend on grid refinement ratios $r > 1.3$.

5. Perform the Richardson extrapolation to estimate a continuum value of f

$$f_{\text{exact}} = f(1) + \frac{f(1)-f(2)}{r(1)^p - 1}. \tag{A.18}$$

6. Calculate the *grid convergence index*, GCI, for each grid using a factor of safety of $F_s = 1.25$ (for three samples)

$$\text{GCI}(n) = \frac{F_s}{r(n)^p - 1}\frac{\left|f(n+1)-f(n)\right|}{f(n)}. \tag{A.19}$$

7. Examine whether the data are drawn from the asymptotic region:

$$R(n) = r(n)^p \frac{GCI(n)}{GCI(n+1)}. \tag{A.20}$$

The various terms r, p, R etc. parameterise the degree of convergence of the solution. The grid convergence parameter R indicates whether the solution is convergent. A value in the range $0 < |R| < 1$ is indicative of convergence, otherwise divergence, of solution. The behaviour of the solution can also be determined: a value $R > 0$ is indicative of monotonic, otherwise oscillatory, behaviour in solution convergence. The GCI is an indication of the percent "error" between the sample and the asymptotic value, and a large GCI indicates that the sample is drawn from results away from the asymptotic range and would change significantly if the mesh were refined. A quick check as to whether the solutions are drawn from the asymptotic range is obtained by checking that $GCI_{23} = r^p GCI_{12}$ (rather, by checking that the ratio of the LHS and RHS is close to unity).

Using this method, it is possible to perform convergence analysis in the absence of the exact solution, and present results as an uncertainty statement. In the case of $F_s = 1.25$, the safety factor provides a confidence bound of 95% and the GCI provides the interval. Therefore for results obtained in this thesis and presented in this manner, the following statement holds:

> Converged solution, e.g. C_P, C_T, η, ..., lies in the interval $f(1)(1 \pm GCI)$, with a 95% confidence level.

A.3.2 Validation

There are formal validation processes, and verification forms part of of it. While the work herein does not implement any formal validation process, it broadly follows that suggested by NPARC, comprising:

1. **Examine iterative convergence** This involves examining the degree of solution change between subsequent results in an iterative method. A typical example is obtaining the velocity/pressure coupling in the solution of the primitive variable RANS equations. The method employed herein has no such iteration, and as such this is not considered in this work.

2. **Check consistence in solution** This is the somewhat subjective analysis which determines whether the results obtained appear to be physically consistent.

3. **Examine grid convergence in time and space** Examine the effects of increasing the mesh density. See Appendix A.3.1, above.

4. **Compare results with (experimental/analytical) data** This involves plotting computed results with those from the literature. These can be drawn from either experiment of analytical solutions. The AIAA Guide for the Verification and Validation of Computational Fluid Dynamics Simulations (AIAA, 1998) delineates between the various levels of validation experiment. They are interpreted herein as

    - **unit tests** tests on components of the model, and comparison with simple, exact results as used herein, or with simple experimental cases which are highly controlled with extensive, high quality measurements;
    - **benchmark cases** tests in which two components are coupled in the simplest manner;
    - **subsystem cases** tests in which sub-configurations are compared;
    - **complete systems** as in full scale wind tunnel tests where there are significant uncertainties in measurements, it is unfeasible to collect all desired data and there are complex, full scale fluid dynamics phenomena present. While these provide the best "real world" data for comparison, matching simulation results to these may only be done once experience is gained at simpler levels and it is ensured that compensating errors which may inspire over-confidence in simulation performance have been eliminated.

5. **Examine uncertainties** Examine whether there are conceptual issues in the choice and implementation of the mathematical model. This can be examined by substituting alternative models, for example different turbulence models, or differing flux limiters as in the case of this thesis.

References

AIAA (1998). "AIAA Guide for the Verification and Validation of Computational Fluid Dynamics Simulations."

Cebeci, T., Shao, J.P., Kafyeke, F. and Laurendeau, E. (2005). *Computational fluid dynamics for engineers: from panel to Navier-Stokes methods with computer programs*. Springer, Berlin, 1st edn.

Celik, I.B. (2008). "Procedure for estimation and reporting of uncertainty due to discretization in CFD applications." *Journal of Fluids Engineering*, **130**(7): 078001.

Courant, R., Friedrichs, K. and Lewy, H. (1928). "Über die partiellen Differenzengleichungen der mathematischen Physik." *Mathematische Annalen*, **100**(1): pp. 32–74.

Roache, P.J., Ghia, K.N. and White, F.M. (1986). "Editorial policy statement on the control of numerical accuracy." *Journal of Fluids Engineering*, **108**(1): pp. 2–2.

Roache, P. (1998). *Verification and Validation in Computational Science and Engineering*. Hermosa Publishers, New Mexico.

Toro, E.F. (1999). *Riemann Solvers and Numerical Methods for Fluid Dynamics: A Practical Introduction*. Springer, Berlin, 2nd edn.

B

Obtaining, Building and Running the Code

This appendix briefly outlines how to obtain, build and run the code. It describes the usage of the text and graphical user interfaces of the V3D and pre-processor tools, respectively.

B.1 Obtaining & Compiling the Latest Version of the Code

The release version of this code can be obtained from the Department of Mechanical and Aerospace Engineering at the University of Strathclyde.

B.1.1 Dependencies

The dependencies of this code are:

- GNU Make
- Either the GNU GCC g++ (v.>4.4.x) or SunCC (v.>12) compilers;
- A linker e.g. the GCC linker works for both g++ and sunCC.

The following libraries:

- matio: MAT File I/O Library – v.1.5.0 (tested on linux and OSX Mountain Lion – configure using the "`--without-hdf5`" flag)
- libpng: PNG Reference Library – deprecated
- ncurses: The Ncurses (new curses) library
- pngwriter: An easy to use C++ graphics library - deprecated
- libz: A Massively Spiffy Yet Delicately Unobtrusive Compression Library
- libmath: Basic mathematics functions
- GSL: GNU Scientific Library

some form of:

- lapack: Linear Algebra PACKage
- blas: Basic Linear Algebra Subprograms
- ATLAS: Automatically Tuned Linear Algebra Software (To compile ATLAS, obtain ATLAS and Netlib Lapack source. The following configure command seems to work reasonably well when run from the `build` directory on a 3 GHz machine:

```
../configure -b 64 -Fa alg -fPIC --shared -D c \
-DPentiumCPS=3000  -Si latune 1 --prefix=/usr/local \
--with-netlib-lapack-tarfile=/path/to/lapack-3.4.2.tgz
```

- gfortran libraries if Fortran variants of blas are used.

B.1.2 Building

After cd'ing into the `Combined` directory, the V3D code can be compiled using the included makefile and default (GCC) compiler. Optional flags in parenthesis. The `-j` option uses multi-threaded building:

```
make (-j)
```

It may be necessary to specify the `OSTYPE` environmental variable if the output of

```
echo $OSTYPE
```

is blank. On Mac OSX (Mountain) Lion issue the following command after logging into a shell:

```
export OSTYPE=darwin10.0
```

Previous OSX versions (tested on Leopard/Snow Leopard) issue:

```
export OSTYPE=darwin9.0
```

Linux variants (tested on openSuSE 10/11/12, various Red Hats, Scientific Linux 6 and CentOS release 5.9) issue:

```
export OSTYPE=linux
```

Cleaning

```
make clean
```

will remove binaries and executables ready for re-compiling.

Option flags To use Oracle compilers:

```
make CC=sunCC
```

To build to run in non-multithreaded (non-openMP) mode:

```
make OMP_FLAG=
```

this works with both GCC and sunCC. To build in debug mode (not optimised) but still multi-threaded (unless empty `OMP_FLAG` is used):

```
make debug (OMP_FLAG=) (-j)
```

B.2 Preprocessor

A MATLAB based Graphical User Interface (GUI) is available in the `./GUI` directory. Use this to generate boundary element meshes for use with this code. The GUI can be used by changing to the `./GUI` directory in MATLAB (or adding to the path) and issuing the command:

```
preproctab
```

from the MATLAB command line. Figure B.1 (below) shows the GUI process.

B.3 Running

Build output is an executable binary named "`main`" which is found in the `Combined` base directory. Run using the following command

```
./main
```

A Text User Interface (TUI) will guide you through the problem specification. Alternatively to the TUI, a case file might be used. Examples are included in the `./case_files` folder. Run

```
./main < case_files/nrel.cas
```

for example.

B.3.1 Text User Interface

Engine Initialisation & Setup:

- Verbose Menu Mode?
- Enter FMM maximum expansion order, $p_{\max}$
- Enter FMM smoothing parameter/radius, δ
- Enter scale factor for model
  This is the inverse of the size of the FVM cells, i.e. if 25, then one FVM cell is a 4 cm *cube.*
- Enter number of quadrature points to use during multipole expansions
- Enter M_4' interpolation radius, measured in cells
- Enter number of sub-time-steps to be approximated per FVM step n_{ss}
  The FVM CFL condition allows a relatively long global time-step by comparison with the kinematic CFL-like condition applied to the BEM mesh.
- Enter period of data output
  Output data will be written to file after a time very close to this period elapses – it is only approximate to avoid artificially shortening time-steps

- Enter fraction of time-step for proto-wake length, ΔS
  There is an argument, presented in Katz and Plotkin (2001) for favouring a shorter proto-wake size, between 0.25 and 0.33 of a time-step.
- Select flux limiter:
  0. First order upwind
  1. minmod
  2. superbee
  3. van Leer
  4. Koren (3rd order)
  5. MUSCL (TVD LUD/Fromm)
  6. UMIST (TVD QUICK)
  7. CADA (Čada and Torrilhon, 2009, implemented but not used herein)
  8. MC (van Leer, 1977, implemented but not used herein)
  9. CWENO MUSCL (Kurganov and Tadmor, 2000, implemented but not used herein)
- Use wave model?
  If selected
  - Enter wave period in seconds
  - Enter wave height in metres
  - Enter water depth in metres
  - Preferred wave theory?
    Either a linear or cnoidal wave theory (Skjelbreia and Hendrickson, 1960) may be selected.
- Enter number of bodies
  This is the number of separate *bodies in the simulation. Neutral files can contain one or more bodies, and multiple Neutral files can be read*
- Enter body to use for specifying # revs or use time
  If body n selected
  - Enter number of revs for body n

  otherwise
  - Enter simulation duration in seconds
- Prefer to specify degrees or radians for attitudes?
- Prefer to specify TSR plus axis or rates?
  If rates selected
  - Prefer to specify rates RPM, Hz, or $\mathrm{rad\,s^{-1}}$?
- Enter freestream velocity $\{u_\infty, v_\infty, w_\infty\}$
- Enter fluid density in $\mathrm{kg\,m^{-3}}$

- Enter fluid viscosity in Pa s
  If viscosity is zero, then no viscous calculation is performed. If $\mu > 0$
  - If performing a viscous calculation, use isotropic (13 point stencil), or anisotropic scheme (27 point stencil)?
    The anisotropic scheme is implemented, but not used in this thesis.
- Use iterative pressure Kutta condition?
  This is implemented in beta form in code, but not used in this thesis.
- Make an input log file?
  If selected, text is generated which can be used to avoid having to manually navigate this menu.

Body Setup – For each body:

- Enter input neutral file
- Enter geometry scale factor
- Mirror/flip input geometry?
  If selected
  - Mirror using yz, xz or xy plane?
- Use either translation/rotation/both for proto-wake?
- Number of panels to produce before conversion to vortex particles?
  Size of panel buffer wake.
- Minimum distance before binning particle into octree?
- Enter displacement of neutral file origin in global frame
- Enter body CG position (i.e. centre of rotation) $\left\{x_{\text{c.g.}}, y_{\text{c.g.}}, z_{\text{c.g.}}\right\}$
- Enter body CG translational velocity $\left\{v_x, v_y, v_z\right\}$
- Enter body attitude $\{\psi, \theta, \phi\}$ in [units selected previously]

If TSR plus radius was selected as preference for specifying body rates then

- Enter tip-speed ratio, λ
- Enter rotation axis unit vector
- Enter radius in metres

Otherwise

- Enter body rotational velocity $\{p, q, r\}$ in [units selected previously]

At this point, the simulation commences.

References

Čada, M. and Torrilhon, M. (2009). "Compact third-order limiter functions for finite volume methods." *Journal of Computational Physics*, **228**(11): pp. 4118–4145.

Katz, J. and Plotkin, A. (2001). *Low Speed Aerodynamics*. Cambridge University Press.

Kurganov, A. and Tadmor, E. (2000). "New high-resolution central schemes for nonlinear conservation laws and convection-diffusion equations." *Journal of Computational Physics*, **160**: pp. 241–282.

Skjelbreia, L. and Hendrickson, J. (1960). "Fifth order gravity wave theory." *Coastal Engineering Proceedings*, **1**(7): p. 10.

van Leer, B. (1977). "Towards the ultimate conservative difference scheme III. upstream-centered finite-difference schemes for ideal compressible flow." *Journal of Computational Physics*, **23**(3): pp. 263–275.

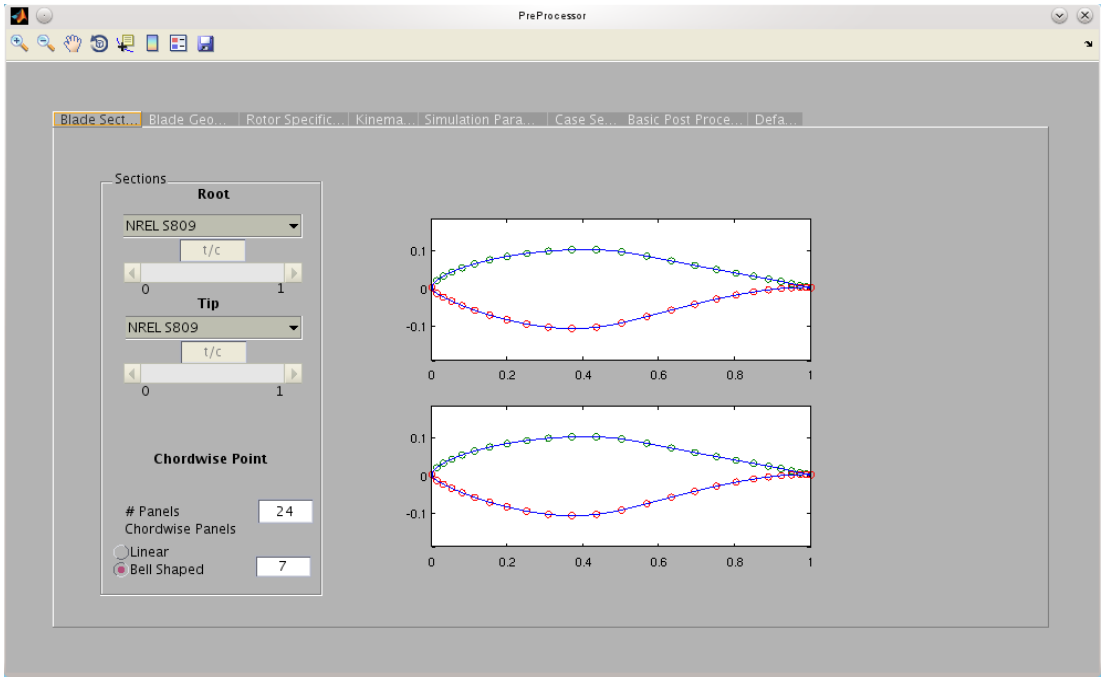

(a) Aerofoil and chordwise point density parameterisation. Either a linear chordwise array of panels can be selected, or they can be clustered according the the "bell" parameter – see Eq. (7.4).

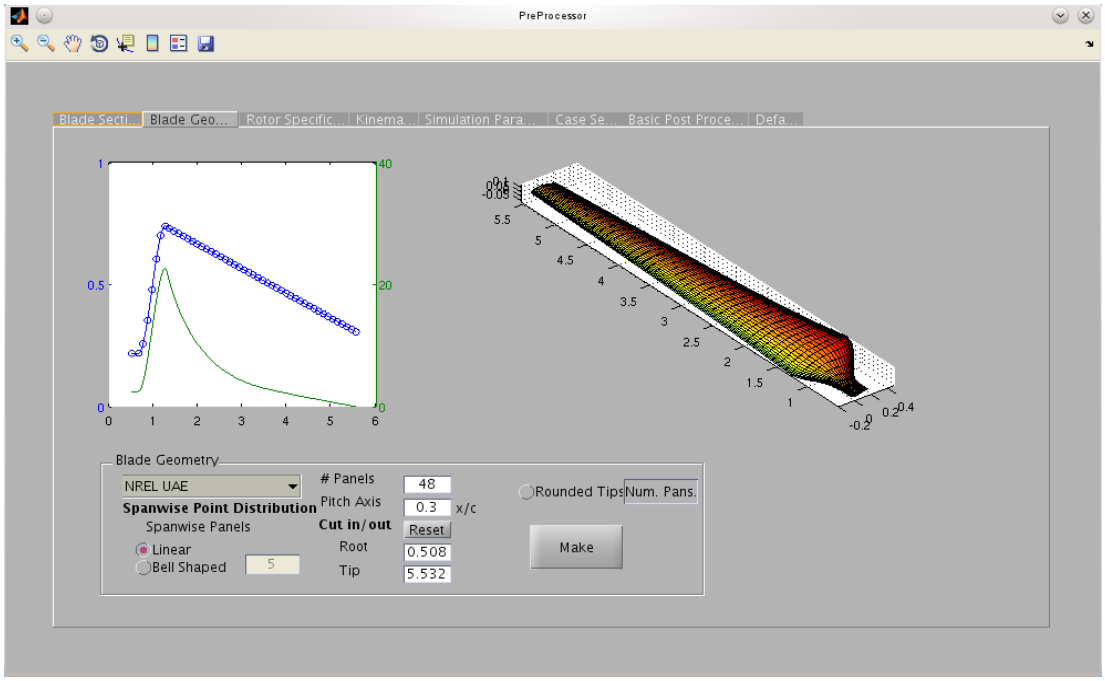

(b) Blade and spanwise point density parameterisation. Again, linear or clustered point distributions can be chosen, along with the ability to adjust the chordwise location of the pitch axis and the root and tip cut-outs. The "Rounded Tips" button allows alternative tip shape to be used.

Figure B.1: Elements of the GUI for generation of the geometry .neu file for for V3D simulations.

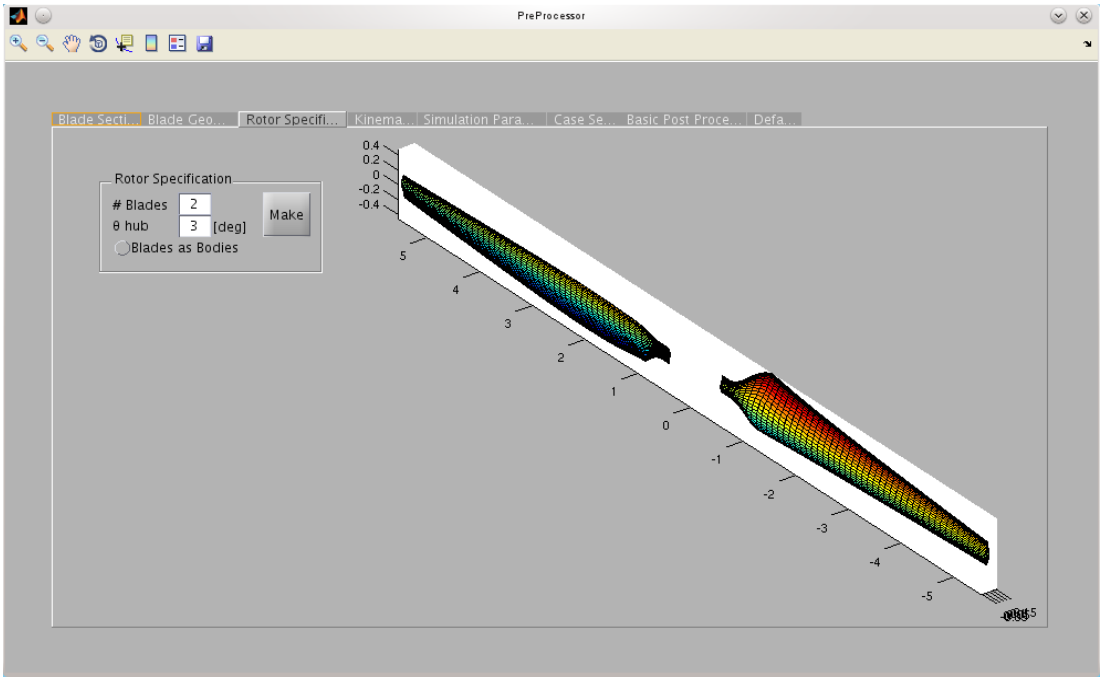

(c) Rotor setup. Number of blades and the hub collective pitch setting are set here. If “Blades as Bodies" is selected, then each blade is output in the Neutral file as an independent body. This allows blades to be moved independently of one-another, for example under cyclic pitch control, or for the vorticity from each blade to be isolated in order to examine e.g. blade-vortex interactions. Default rotation is about initial coincident global/local z-axis – this can be changed on the next tab by setting the rotor Euler angle $\theta = -\pi/2$ such that rotation is about the global x-axis.

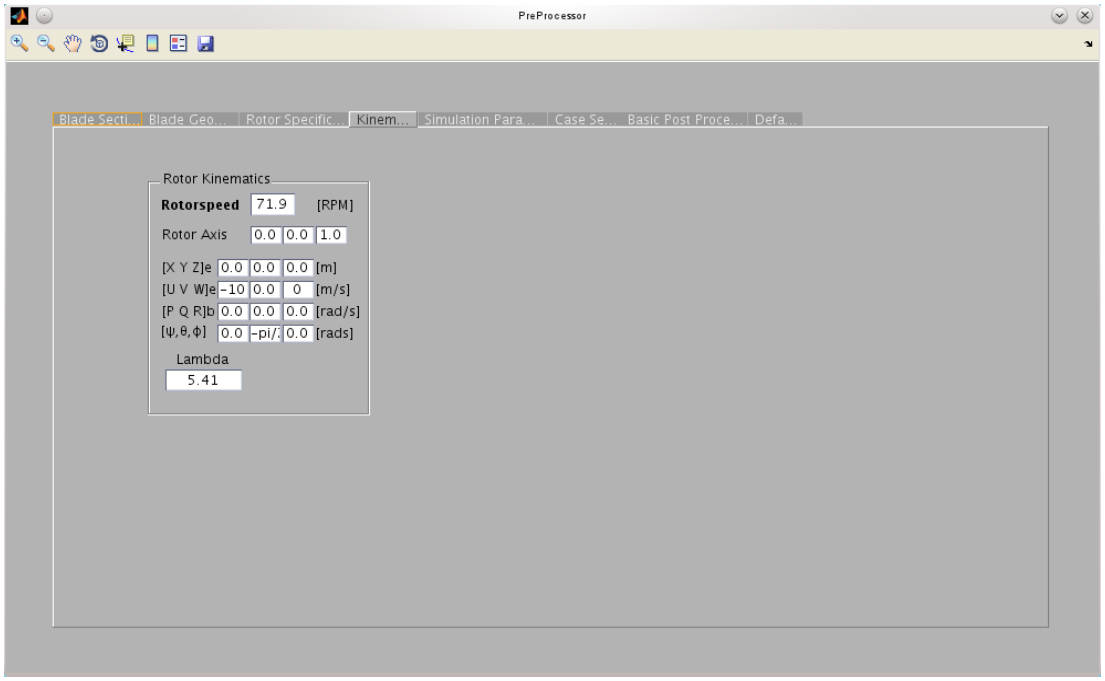

(d) Rotor kinematics: Rotorspeed, axis of rotation, location in global axis, velocity in earth axis, body rates and Euler angles are set here, and λ is specified. This panel is not fully implemented at the time of writing and these parameters being specified in the TUI, although the Euler angles are useful for setting up the rotor in the previous tab.

Figure B.1: (continued) Elements of the GUI for generation of the geometry .neu file for for V3D simulations.

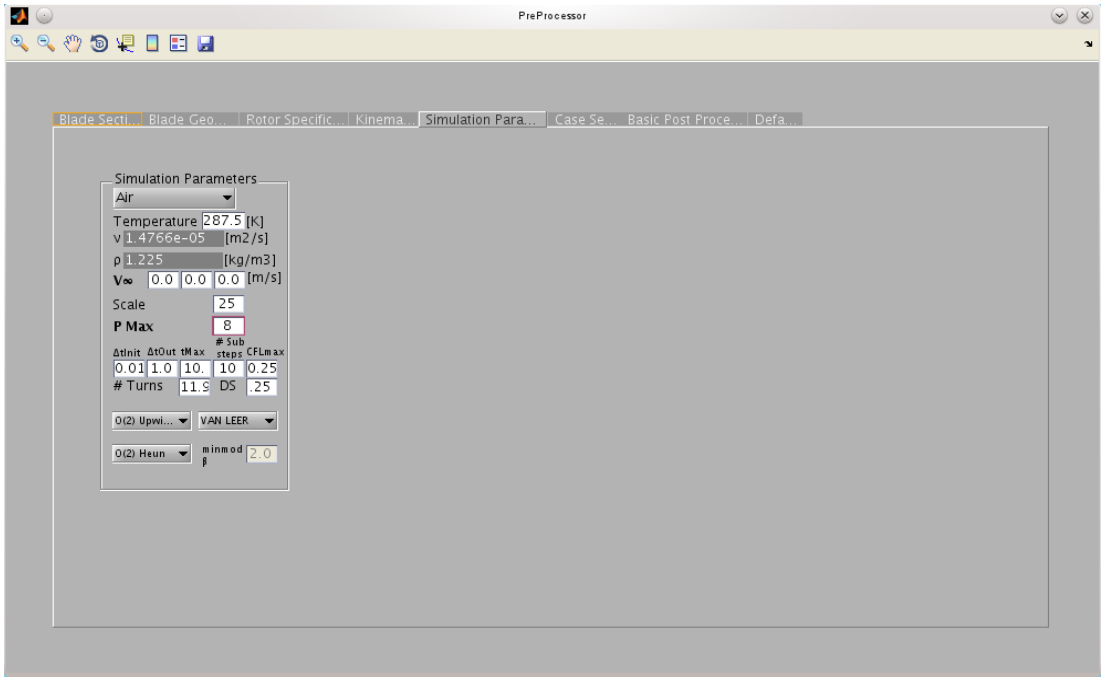

(e) Simulation parameters: Dropdown for selecting working fluid – options are air, fresh and saltwater. Specifying temperature, the density and viscosity are set automatically according to Sutherland's formula for an ideal gas (air) or ITTC Proceedure 7.5-02-01-03 for fresh and saltwater. Freestream velocity vector is specified here – this is included in velocities for all cell faces. The scale parameter is the reciprocal of the cell size – setting it to 25 equates to a 4 cm cell. $p_{\max}$ is the FMM truncation order. Initial time-step, time-step to write output, max time and number of sub-steps are set, followed by the maximum allowable cell CFL number. The number of turns is calculated and the proto-wake length (DS) is specified as a fraction of the time-step. The solver characteristics are available via pull-down menus, and if the MUSCL scheme is used, the minmod β parameter is set. This panel is not fully implemented at the time of writing, and the inputs it specifies are addressed via the TUI.

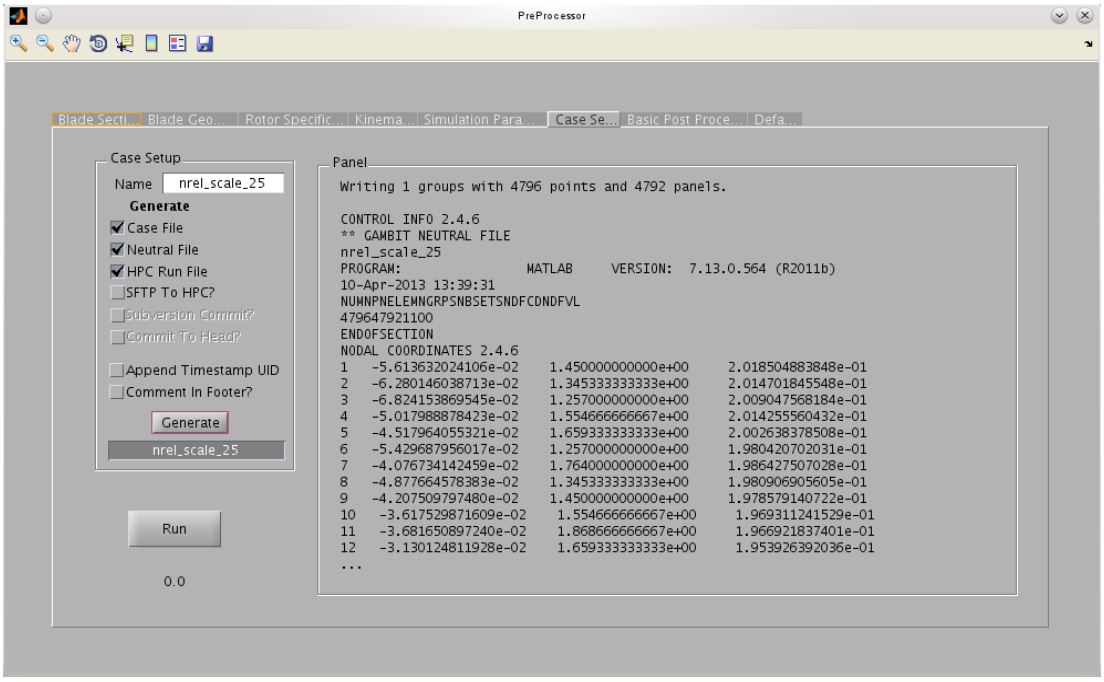

(f) Case setup – specify output name for case, Neutral and HPC runfile. Chose to upload to HPC then generate Neutral file. The header of the generated file is shown in the Panel window. On Posix OSes, the "RUN" button begins the simulation with the generated files.

Figure B.1: (continued) Elements of the GUI for generation of the geometry .neu file for for V3D simulations.

C

Supplementary Material for Chapter 6

Table C.1: Grid convergence study for the 1-D advection equation using finite-volume with various schemes using second-order time-stepping. Norms of errors for Courant number $C = 0.125$ taken after 1 (a) and 10 (b) solution revolutions. Smooth ICs, $u = 1$.

		φ error norms						GCI %		
Scheme		Coarse	Medium	Fine	Continuum	R	p	m-c	f-m	Ratio
minmod	l^1	5.80×10^{-3}	1.64×10^{-3}	4.46×10^{-4}	-4×10^{-5}	0.3	1.8	0.2	0.06	1.0
	l^∞	3.14×10^{-2}	1.32×10^{-2}	5.40×10^{-3}	-4×10^{-4}	0.4	1.2	2	0.7	1.0
superbee	l^1	4.51×10^{-3}	1.31×10^{-3}	3.55×10^{-4}	-5×10^{-5}	0.3	1.7	0.2	0.05	1.0
	l^∞	2.46×10^{-2}	1.13×10^{-2}	4.83×10^{-3}	-1×10^{-3}	0.5	1.0	2	0.8	1.0
van Leer	l^1	2.40×10^{-3}	6.18×10^{-4}	1.54×10^{-4}	-9×10^{-6}	0.3	1.9	0.08	0.02	1.0
	l^∞	1.39×10^{-2}	5.21×10^{-3}	1.97×10^{-3}	4×10^{-5}	0.4	1.4	0.6	0.2	1.0
MUSCL	l^1	1.91×10^{-3}	5.13×10^{-4}	1.32×10^{-4}	-1×10^{-5}	0.3	1.9	0.07	0.02	1.0
	l^∞	8.55×10^{-3}	4.26×10^{-3}	1.80×10^{-3}	-2×10^{-3}	0.6	0.8	0.7	0.4	1.0
UMIST	l^1	2.97×10^{-3}	8.19×10^{-4}	2.16×10^{-4}	-2×10^{-5}	0.3	1.8	0.1	0.03	1.0
	l^∞	1.84×10^{-2}	7.66×10^{-3}	3.13×10^{-3}	-2×10^{-4}	0.4	1.3	0.4	1	1.0
Koren	l^1	5.75×10^{-4}	1.10×10^{-4}	2.08×10^{-5}	-3×10^{-7}	0.2	2.4	0.01	0.003	1.0
	l^∞	7.86×10^{-3}	2.62×10^{-3}	8.64×10^{-4}	-2×10^{-5}	0.3	1.6	0.3	0.1	1.0

(a) Error norms after 1 revolution

minmod	l^1	3.62×10^{-2}	1.31×10^{-2}	3.89×10^{-3}	-2×10^{-3}	0.4	1.3	2	0.8	1.0
	l^∞	1.35×10^{-1}	5.88×10^{-2}	2.50×10^{-2}	-2×10^{-3}	0.4	1.2	8	3	1.0
superbee	l^1	1.50×10^{-2}	9.42×10^{-3}	3.09×10^{-3}	6×10^{-2}	1	-0.2	-6	-7	1.0
	l^∞	5.62×10^{-2}	3.61×10^{-2}	2.07×10^{-2}	-3×10^{-2}	0.8	0.4	8	6	1.0
van Leer	l^1	1.65×10^{-2}	4.89×10^{-3}	1.32×10^{-3}	-2×10^{-4}	0.3	1.7	0.6	0.2	1.0
	l^∞	5.03×10^{-2}	1.95×10^{-2}	8.22×10^{-3}	2×10^{-3}	0.4	1.4	2	0.8	1.0
MUSCL	l^1	1.43×10^{-2}	4.39×10^{-3}	1.22×10^{-3}	-3×10^{-4}	0.3	1.6	0.6	0.2	1.0
	l^∞	3.56×10^{-2}	1.74×10^{-2}	8.05×10^{-3}	-2×10^{-3}	0.5	1.0	2	1	1.0
UMIST	l^1	2.19×10^{-2}	7.28×10^{-3}	2.02×10^{-3}	-9×10^{-4}	0.4	1.5	1	0.4	1.0
	l^∞	8.03×10^{-2}	3.52×10^{-2}	1.47×10^{-2}	-2×10^{-3}	0.5	1.1	2	5	1.0
Koren	l^1	2.64×10^{-3}	4.90×10^{-4}	9.46×10^{-5}	5×10^{-6}	0.2	2.4	0.06	0.01	1.0
	l^∞	2.12×10^{-2}	6.52×10^{-3}	2.05×10^{-3}	8×10^{-5}	0.3	1.7	0.8	0.2	1.0

(b) Error norms after 10 revolutions

Table C.2: Grid convergence study for the 1-D advection equation using the finite-volume method with various schemes and $\mathcal{O}(\Delta t^2)$ Runge-Kutta time-stepping. Grid metrics are the value of φ at $x = 0$ (true value is 1.0), and the integral of φ between $x = -0.5$ and $x = -0.3$ (true value is 0.2). Data obtained at Courant number $C = 0.125$.

		(a): $\varphi(0)$; and (b): $\int_{-0.5}^{-0.3} \varphi(x)\,\mathrm{d}x$						GCI %		
Scheme		Coarse	Medium	Fine	Continuum	R	p	m-c	f-m	Ratio
minmod	(a)	0.559	0.732	0.836	0.988	0.595	0.748	43.6	22.8	0.876
	(b)	0.159	0.175	0.184	0.199	0.614	0.704	17.3	10.1	0.949
superbee	(a)	0.853	0.919	0.956	1.005	0.567	0.819	11.7	6.4	0.961
	(b)	0.190	0.195	0.197	0.200	0.498	1.006	3.13	1.54	0.988
van Leer	(a)	0.707	0.833	0.897	0.963	0.510	0.971	19.7	9.31	0.928
	(b)	0.174	0.184	0.190	0.200	0.608	0.718	10.8	6.33	0.967
MUSCL	(a)	0.765	0.863	0.915	0.975	0.532	0.911	16.1	8.09	0.943
	(b)	0.177	0.186	0.191	0.199	0.611	0.712	9.32	5.53	0.972
UMIST	(a)	0.664	0.804	0.875	0.949	0.509	0.975	22.6	10.6	0.918
	(b)	0.168	0.180	0.187	0.200	0.631	0.665	13.8	8.38	0.961
Koren	(a)	0.779	0.871	0.924	0.999	0.583	0.778	18.4	10.1	0.942
	(b)	0.180	0.188	0.193	0.200	0.582	0.780	7.73	4.39	0.975

(a) Results obtained after 1 revolution

minmod	(a)	0.285	0.415	0.610	0.029	1.506	−0.591	−116	−119	0.68
	(b)	0.101	0.139	0.165	0.218	0.676	0.566	70.9	40.5	0.845
superbee	(a)	0.813	0.901	0.950	1.007	0.542	0.884	14.6	7.5	0.949
	(b)	0.190	0.195	0.197	0.200	0.495	1.014	3.11	1.52	0.988
van Leer	(a)	0.419	0.638	0.803	1.319	0.757	0.401	134	80.3	0.794
	(b)	0.140	0.167	0.179	0.190	0.471	1.087	17.8	7.77	0.93
MUSCL	(a)	0.490	0.697	0.831	1.080	0.649	0.623	68.7	37.4	0.838
	(b)	0.150	0.169	0.180	0.197	0.592	0.757	20.7	11.5	0.937
UMIST	(a)	0.343	0.533	0.717	7.654	0.974	0.038	1670	1210	0.743
	(b)	0.121	0.155	0.172	0.188	0.490	1.030	26.3	11.6	0.903
Koren	(a)	0.573	0.782	0.875	0.949	0.444	1.172	26.6	10.6	0.894
	(b)	0.165	0.179	0.188	0.199	0.577	0.792	13.8	7.6	0.956

(b) Results obtained after 10 revolutions

Table C.3: Time-step convergence study for the advection equation using various schemes and second-order time-stepping. Norms of residuals between Courant number $C = 1/n$ for $n = 2, 4, 8$ and 16. Results sampled after 10 solution revolutions. Smooth ICs, $u = 1$.

		φ residual norms						GCI %		
Scheme		Coarse	Medium	Fine	Continuous	R	p	m-c	f-m	Ratio
minmod	l^1	4.75×10^{-4}	1.14×10^{-4}	2.84×10^{-5}	2×10^{-6}	0.2	2.1	0.01	0.003	1.0
	l^∞	3.53×10^{-5}	8.33×10^{-6}	2.06×10^{-6}	2×10^{-7}	0.2	2.1	0.001	0.0002	1.0
superbee	l^1	3.47×10^{-3}	1.28×10^{-4}	2.32×10^{-5}	2×10^{-5}	0.03	5.0	0.01	0.0004	1.0
	l^∞	5.53×10^{-4}	1.60×10^{-5}	1.65×10^{-6}	1×10^{-6}	0.03	5.2	0.002	5×10^{-5}	1.0
van Leer	l^1	4.21×10^{-4}	1.05×10^{-4}	2.61×10^{-5}	-2×10^{-7}	0.2	2.0	0.01	0.003	1.0
	l^∞	2.85×10^{-5}	7.07×10^{-6}	1.75×10^{-6}	-2×10^{-9}	0.2	2.0	0.0009	0.0002	1.0
MUSCL	l^1	4.37×10^{-4}	1.10×10^{-4}	2.74×10^{-5}	-6×10^{-7}	0.3	2.0	0.01	0.003	1.0
	l^∞	2.97×10^{-5}	7.50×10^{-6}	1.85×10^{-6}	-8×10^{-8}	0.3	2.0	0.0009	0.0002	1.0
UMIST	l^1	4.53×10^{-4}	1.16×10^{-4}	2.90×10^{-5}	-1×10^{-6}	0.3	2.0	0.01	0.004	1.0
	l^∞	3.26×10^{-5}	8.32×10^{-6}	2.07×10^{-6}	-9×10^{-8}	0.3	2.0	0.001	0.0003	1.0
Koren	l^1	4.45×10^{-4}	1.11×10^{-4}	2.83×10^{-5}	9×10^{-7}	0.2	2.0	0.01	0.003	1.0
	l^∞	3.24×10^{-5}	8.51×10^{-6}	2.16×10^{-6}	-1×10^{-7}	0.3	1.9	0.001	0.0003	1.0

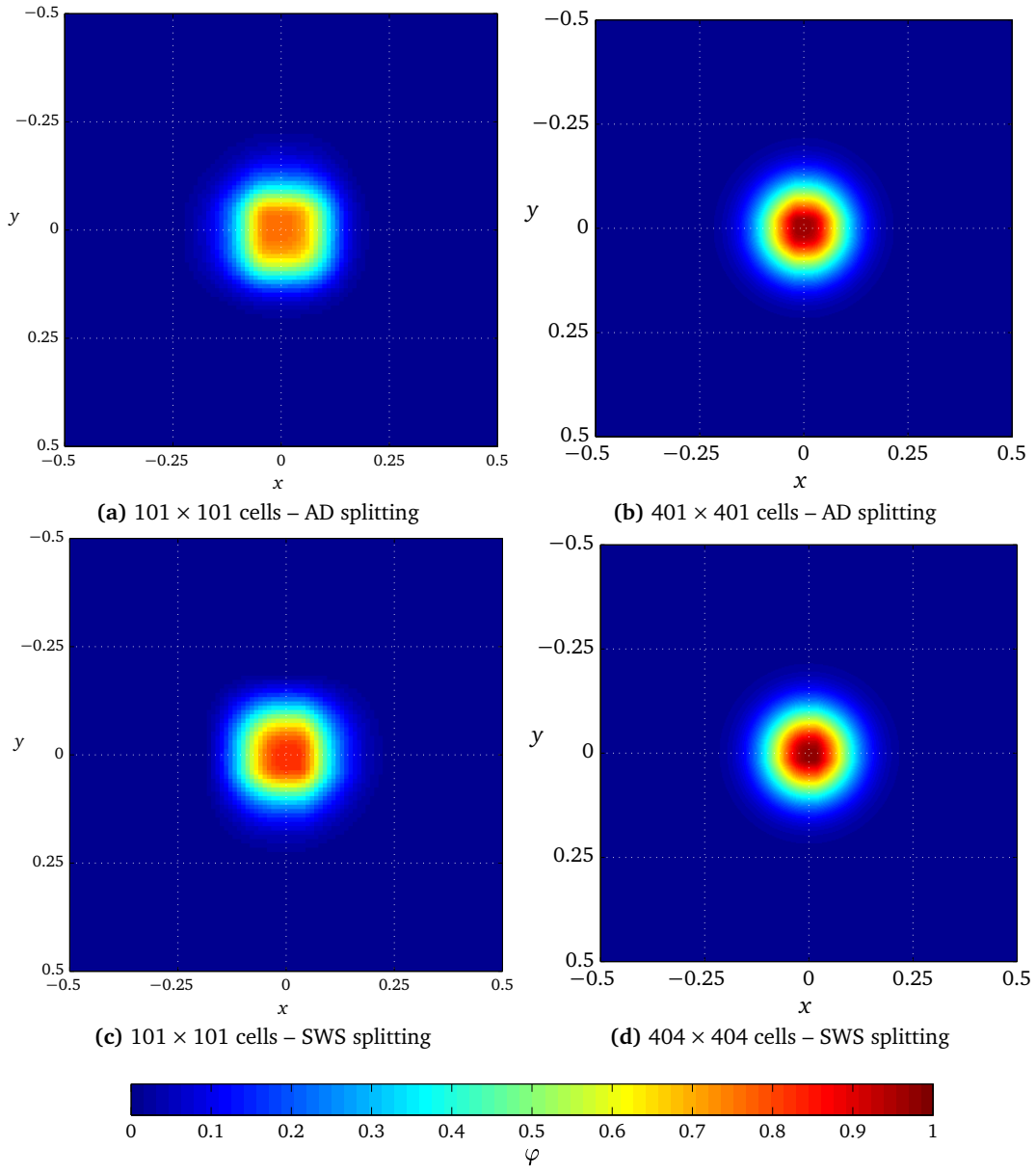

(a) 101 × 101 cells – AD splitting

(b) 401 × 401 cells – AD splitting

(c) 101 × 101 cells – SWS splitting

(d) 404 × 404 cells – SWS splitting

Figure C.1: Diagonal flow test case on 101 × 101 and 401 × 401 cell square meshes using alternate dimension and symmetrically weighted sequential splitting. Results are taken after 5 revolutions, $u = v = 1$, $C_{\max} = 1/4$.

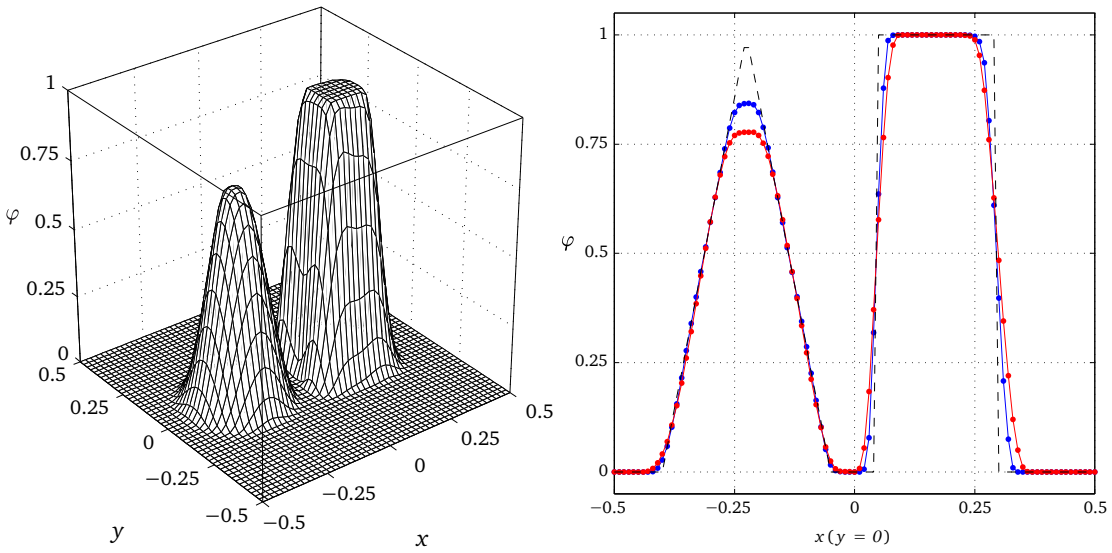

(a) 101 × 101 cells

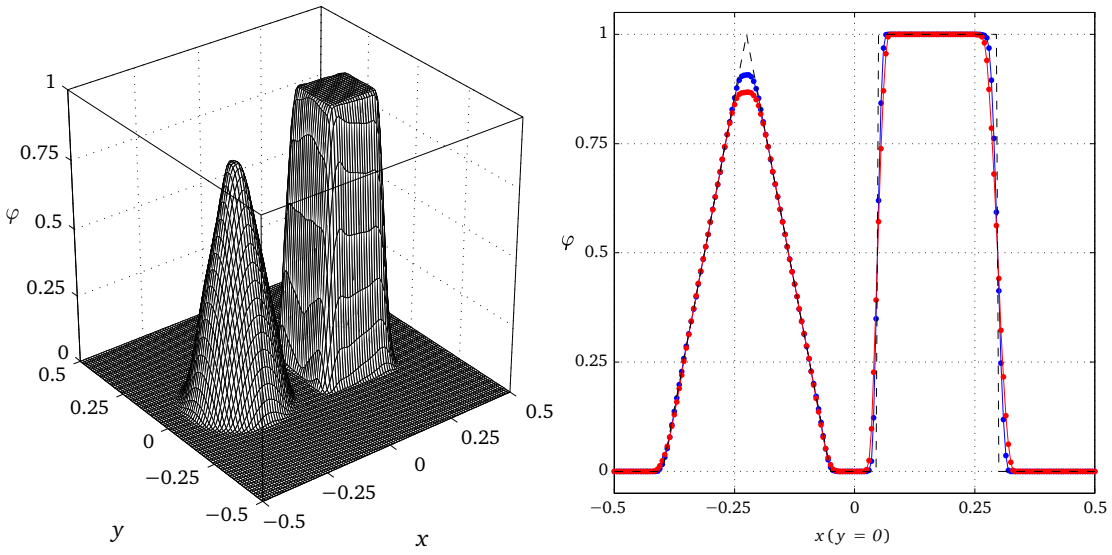

(b) 201 × 201 cells

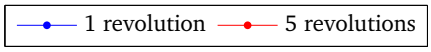

Figure C.2: Rotating flow test case on 101 × 101 (top) and 201 × 201 (bottom) cell square meshes using symmetrically weighted sequential splitting and the Koren scheme. Surface plots (left) showing every second cell with results sampled after 5 revolutions; solution transects (right) showing results along and x axes, taken after 1 and 5 revolutions. Velocity field obtained from stream function $\psi\left(x,y\right)=x^2+y^2$ $C_{\max}=1/4$.

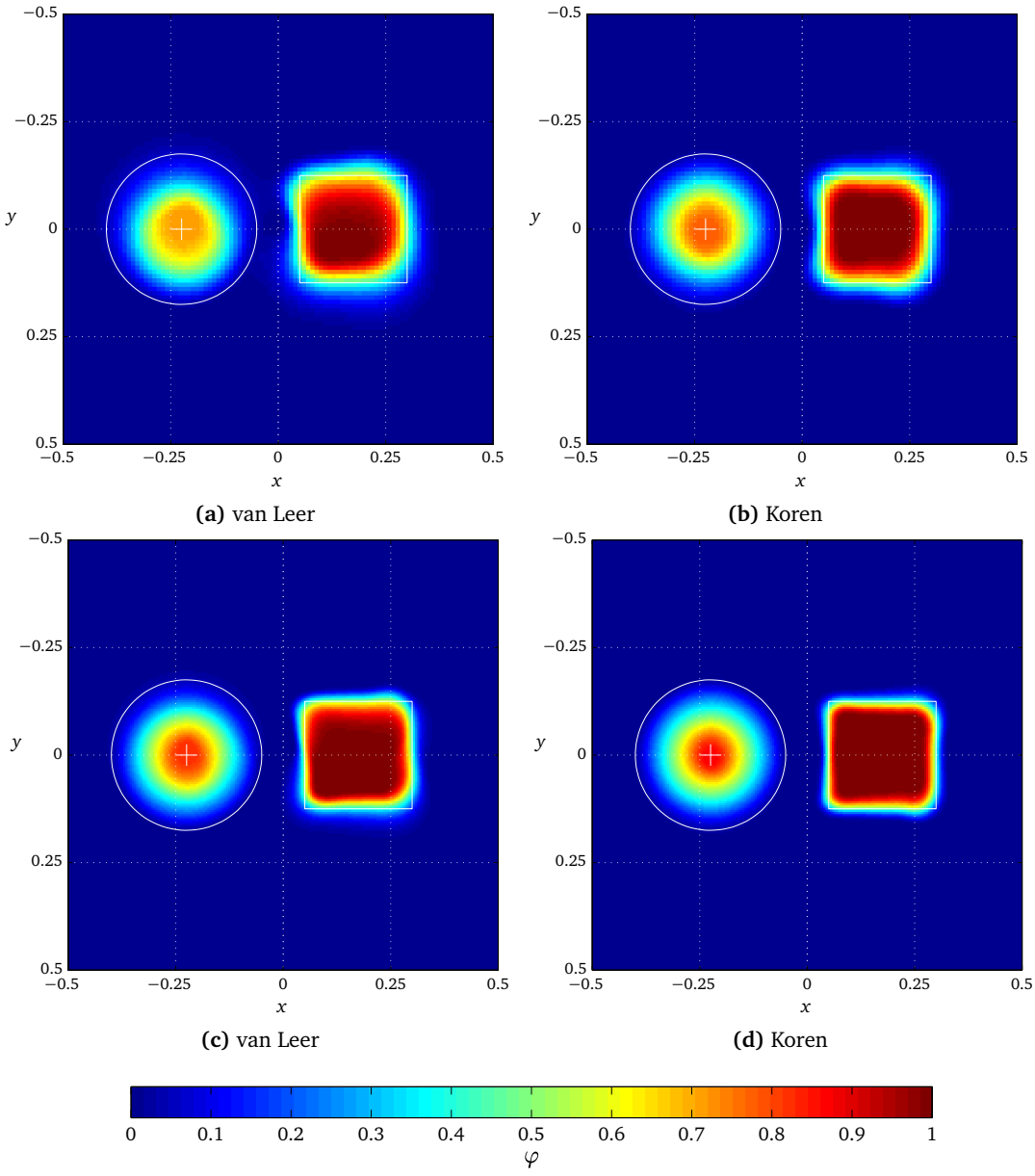

(a) van Leer **(b)** Koren

(c) van Leer **(d)** Koren

Figure C.3: Rotating flow test case on 101×101 (top) and 201×201 (bottom) cell square meshes using symmetrically weighted sequential splitting and limited schemes as indicated. Cell value plots showing results sampled after 5 revolutions. White circle, centred on cross at $(-0.025, 0)$, indicates bounds and peak location of cone; white square indicates bounds of block. Velocity field obtained from stream function $\psi\left(x, y\right) = x^2 + y^2$, $C_{\max} = 1/4$.

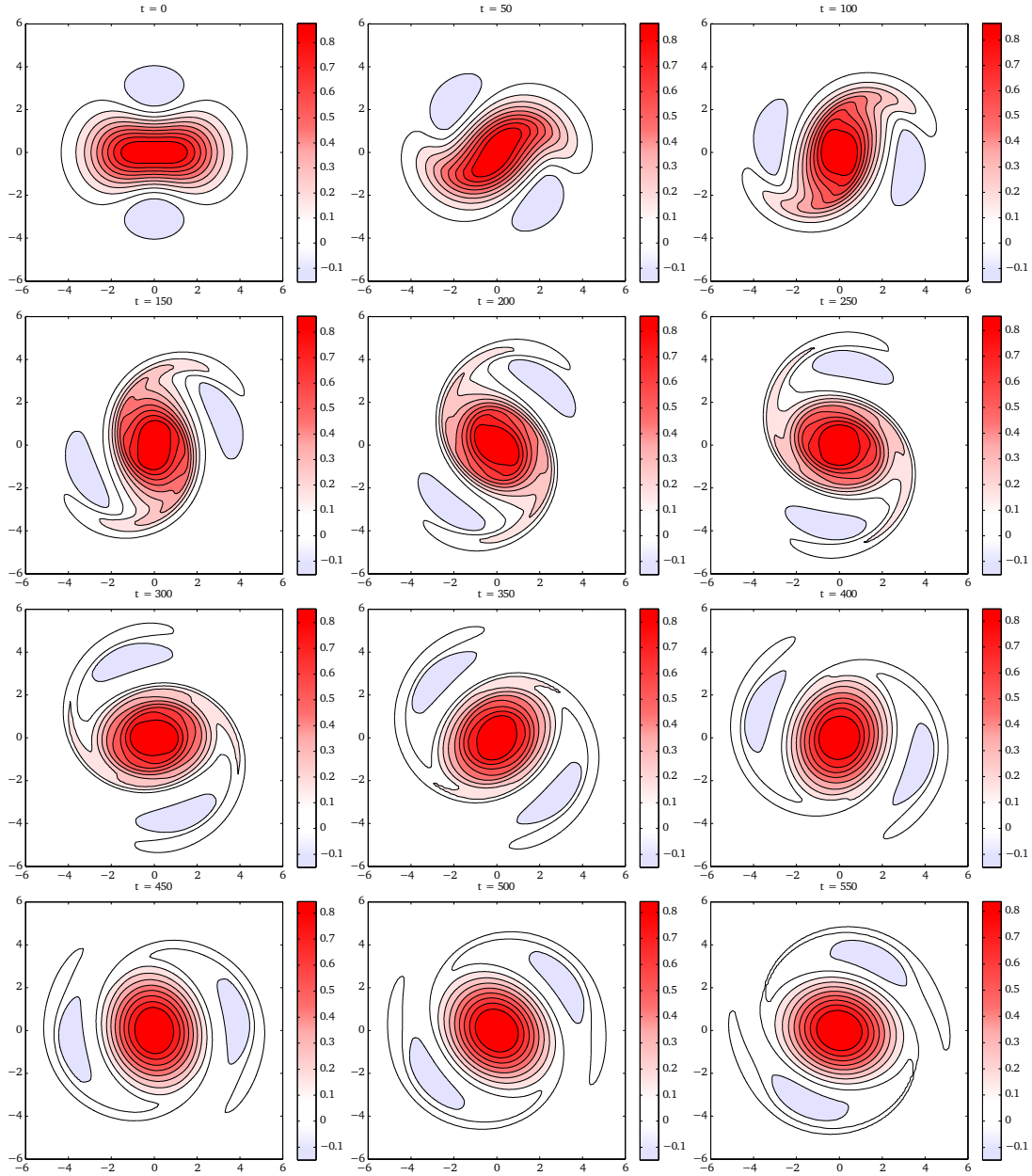

Figure C.4: Total vorticity field contours for a perturbed monopole relaxing into a tripole attractor. Normalised by maximum of base vorticity field ICs ω_0.

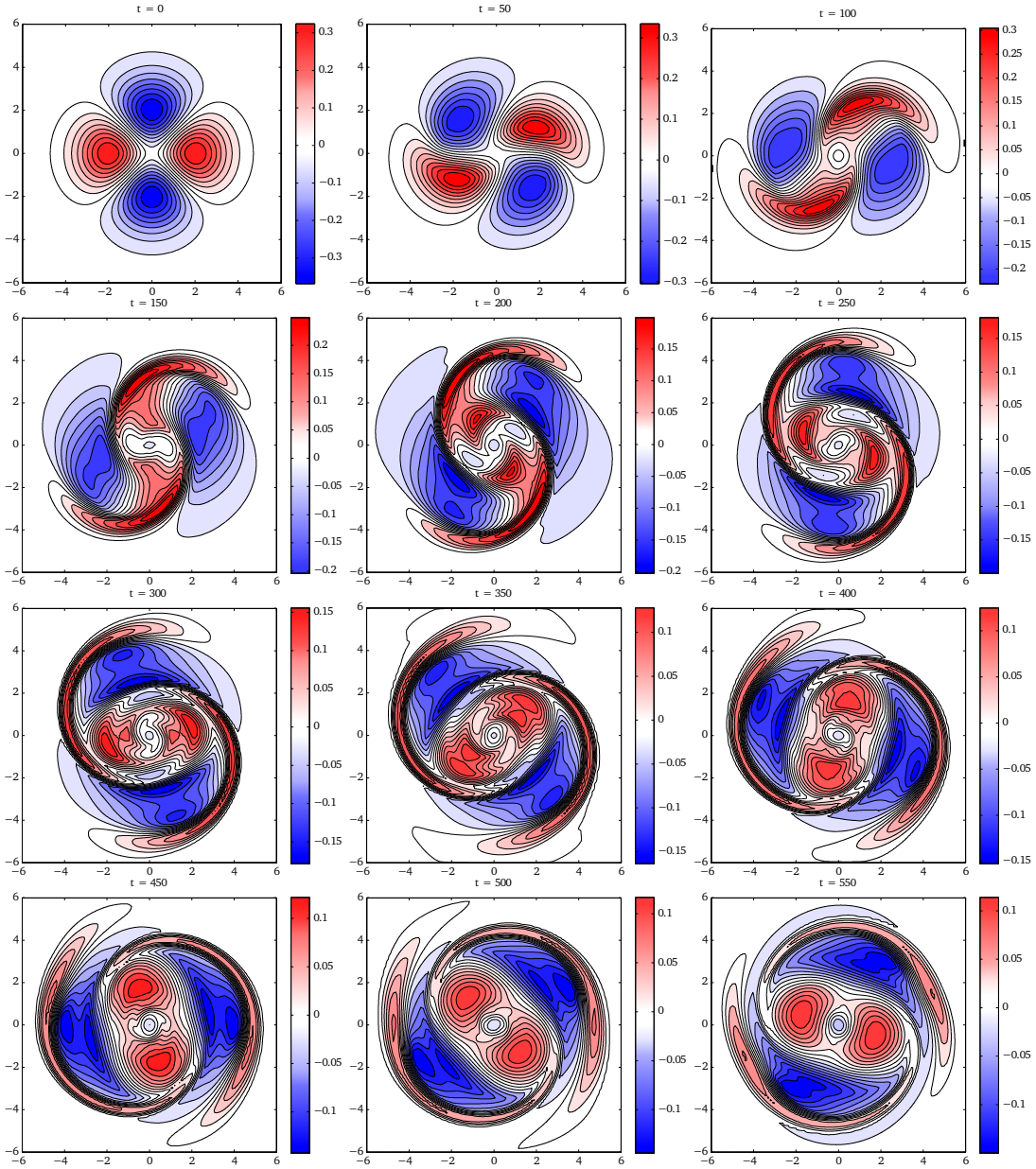

Figure C.5: Perturbation vorticity field contours for a perturbed monopole relaxing into a tripole attractor. Normalised by maximum of base vorticity field ICs ω_0.

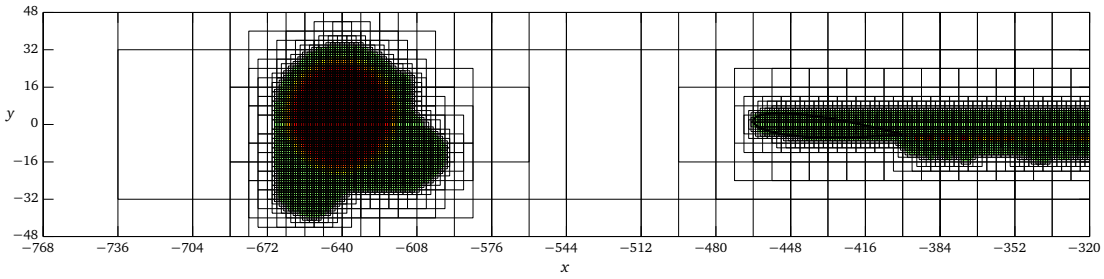

(a) $t = 7\,\mathrm{s}$

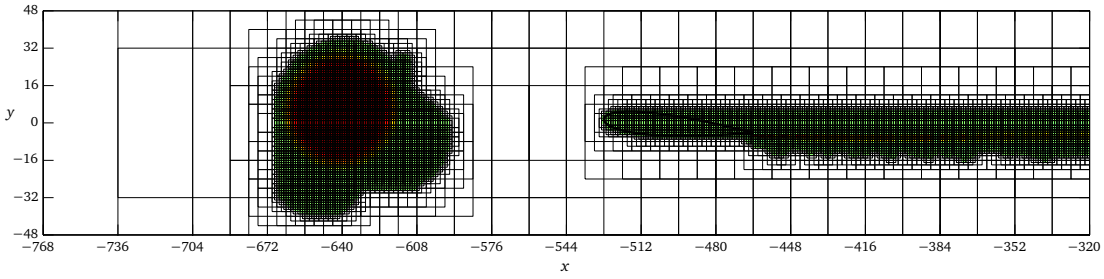

(b) $t = 8\,\mathrm{s}$

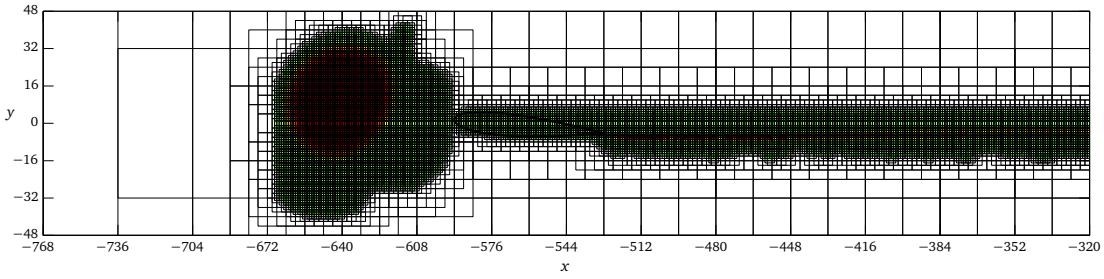

(c) $t = 9\,\mathrm{s}$

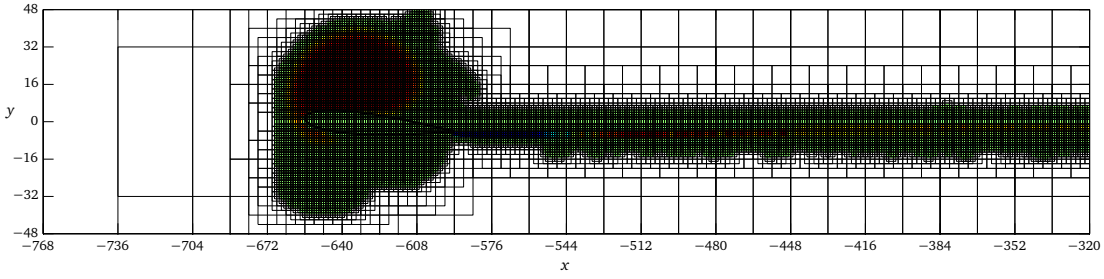

(d) $t = 10\,\mathrm{s}$

Figure C.6: The FVM mesh associated with the evolution of a BVI vorticity field similar to that examined in Section 6.3.4. Each smallest subdivision contains 4 FVM cells. Blue colour denotes negative (about out-of-page z-axis) vorticity and red positive. White denotes zero vorticity thus zero cells. Colour axis is saturated and the axis labels count number of cells in the x and y directions – the scale factor was 64 cells along the chord. Continued...

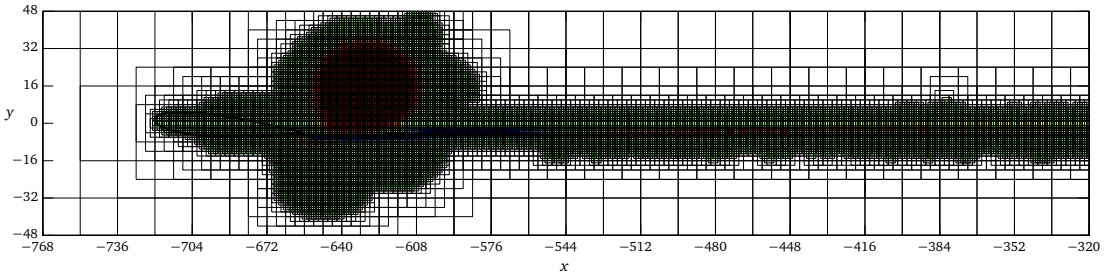

(e) $t = 11\,\mathrm{s}$

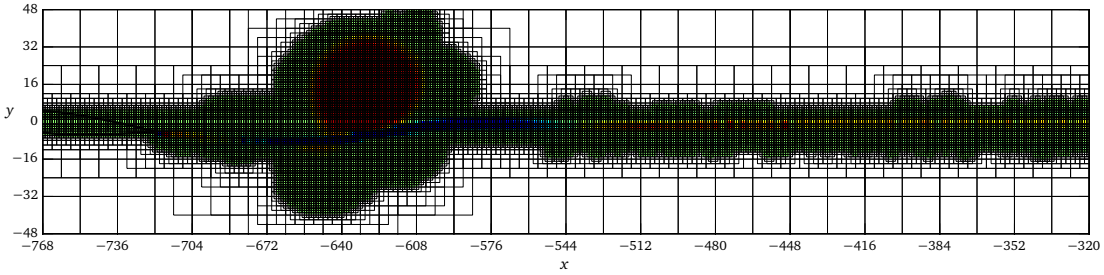

(f) $t = 12\,\mathrm{s}$

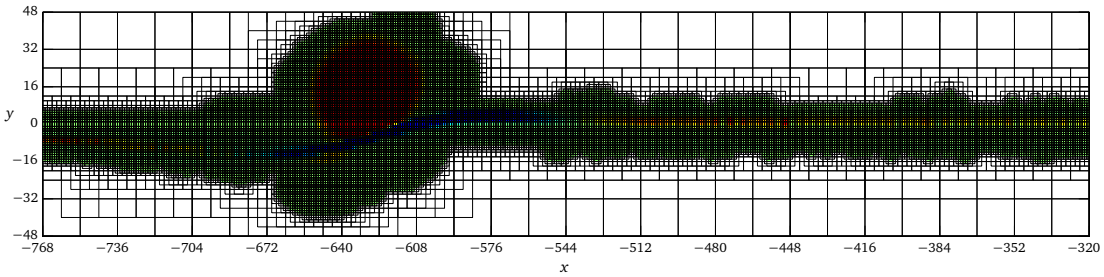

(g) $t = 13\,\mathrm{s}$

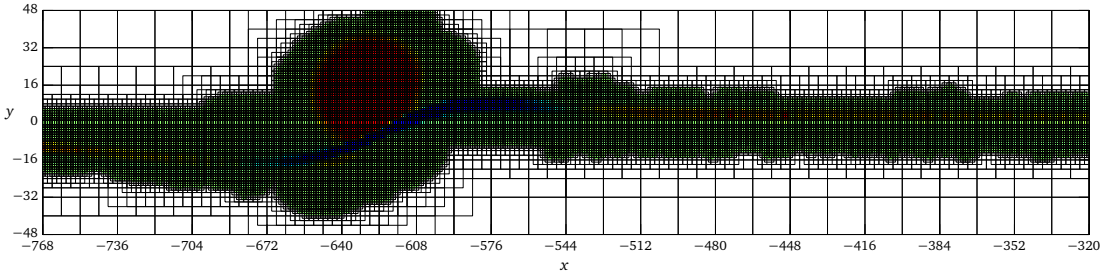

(h) $t = 14\,\mathrm{s}$

Figure C.6: Concluded.

D

Supplementary Material for Chapter 7

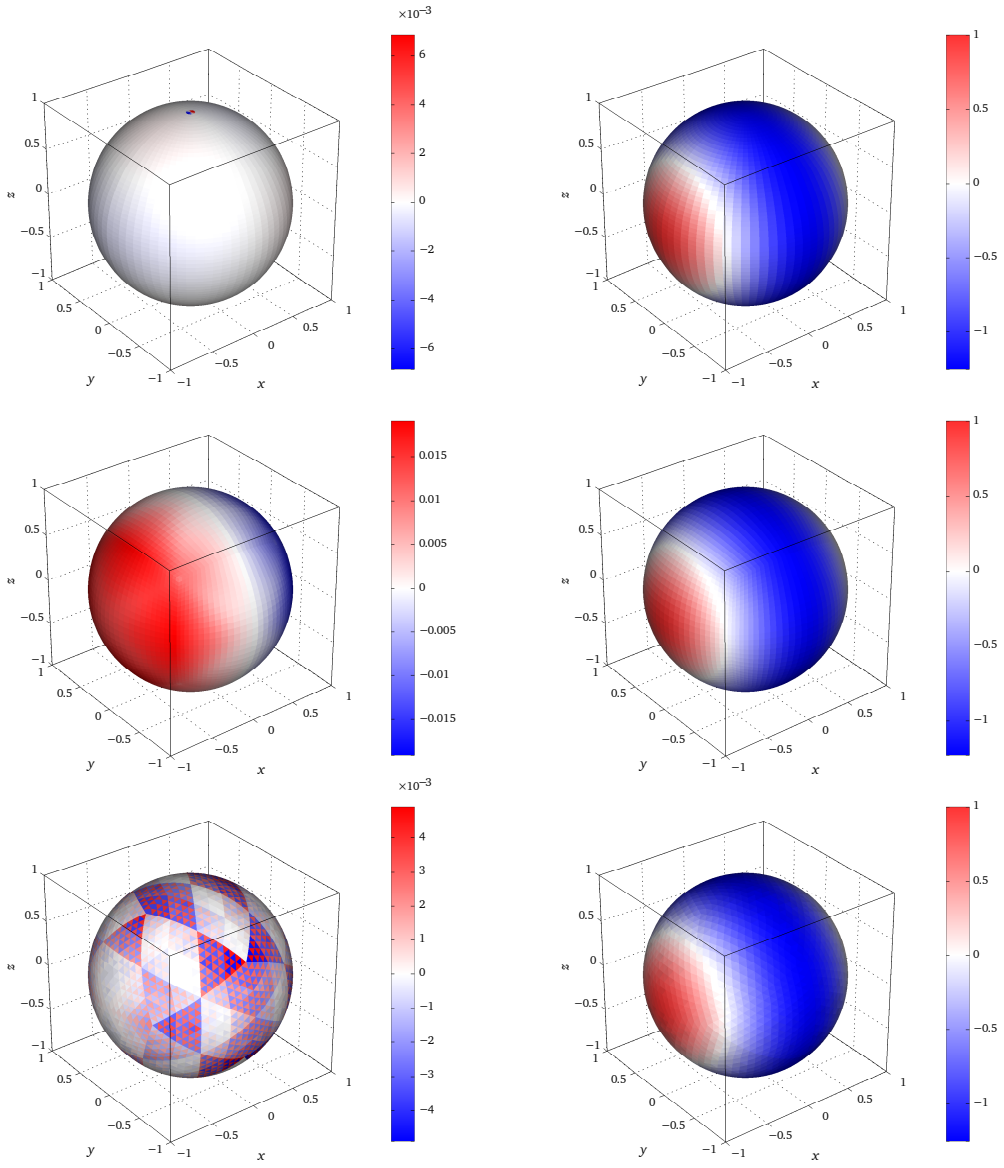

Figure D.1: Distribution of C_p (right) and errors in ϕ (left) due to flow around a sphere. Number of panels: quadrilateral elements due to revolution – 5184 (top); quadrilateral elements due to patches – 5046 (middle); triangular elements due to looping subdivision – 5120 (bottom).

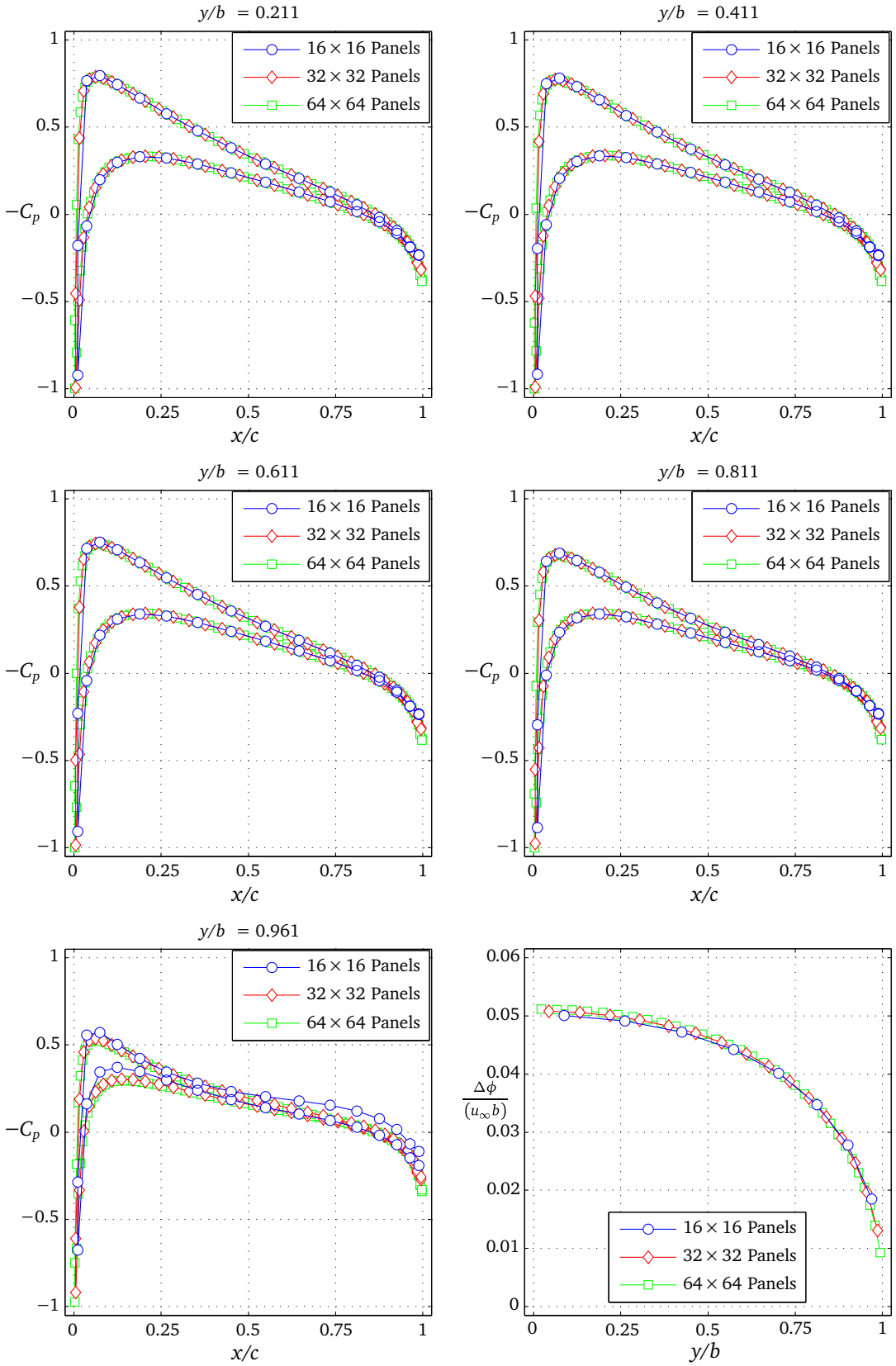

Figure D.2: Comparison of computed chordwise pressure coefficients and spanwise circulation distribution for static hydrofoil at varying boundary-element mesh densities. Rectangular planform, aspect-ratio = 4, NACA 0015 section, $\alpha = 2.5°$

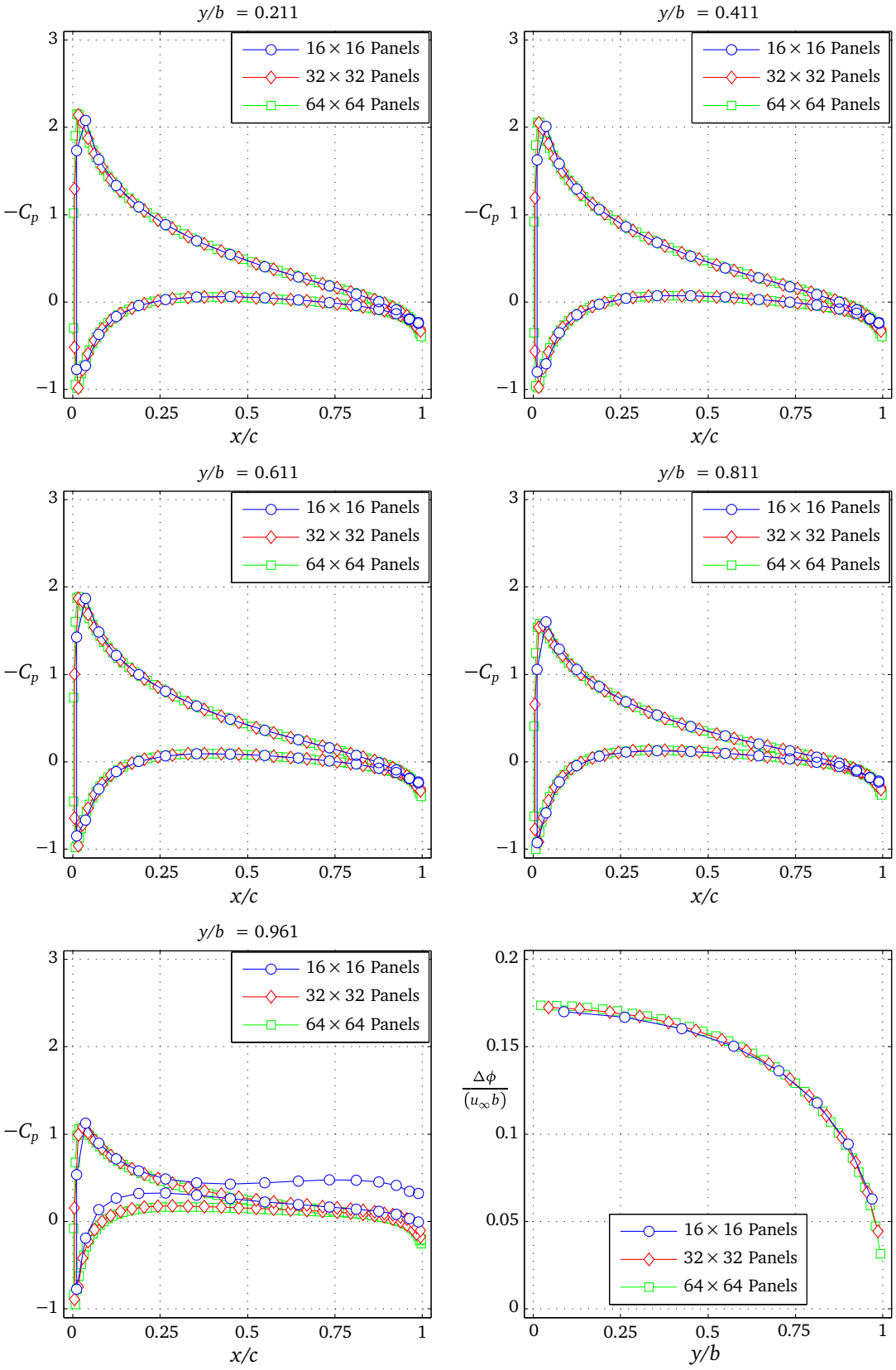

Figure D.3: Comparison of computed chordwise pressure coefficients and spanwise circulation distribution for static hydrofoil at varying boundary-element mesh densities, rectangular planform aspect-ratio = 4, NACA 0015 section, $\alpha = 8.5°$

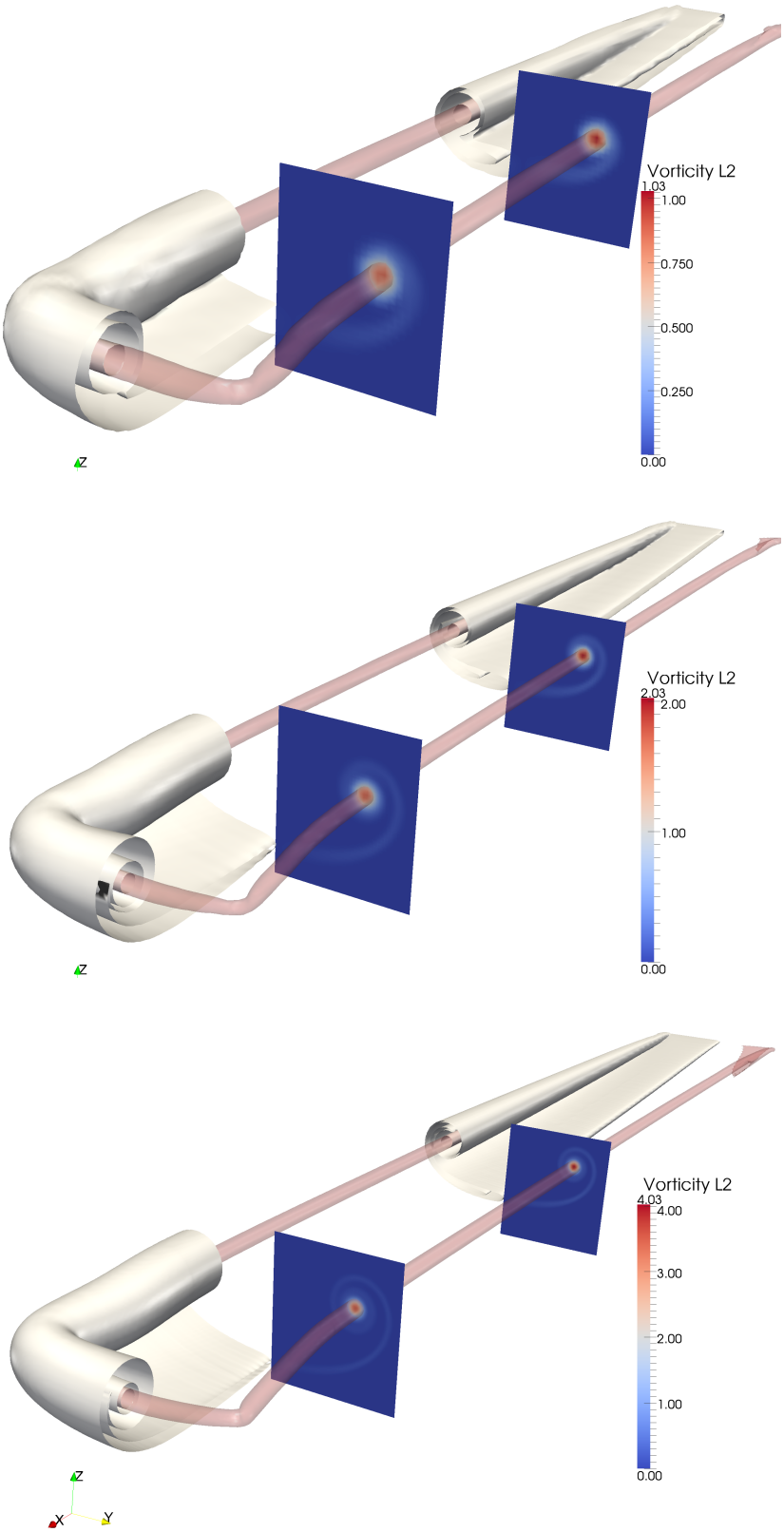

Figure D.4: Vorticity isosurface images of the hydrofoil wake detail, taken at $t = 33c/U_\infty$. Contours of $|\boldsymbol{\omega}| = [0.01, 0.1, 1]\,\text{sec}^{-1}$ (white) to show sheet rollup and indication of active cells in blue in to domain as seen in tree. Core illustrated in red (above) and cornflower (below) taken at $|\boldsymbol{\omega}| = 5\,\text{sec}^{-1}$. Top 16×16 panels; middle: 32×32 panels; bottom: 64×64 panels.

Table D.1: Blade geometries for the 2 bladed NREL Phase VI wind turbine rotor. Nominal radius is 5.029 m, with an extension piece taking it to 5.532 m. Blade twist is measured at the $r/R = 0.75$ station on the 5.03 m blade, and is positive towards feather. Tabulated values are for zero twist at $r/R = 0.75$ with $\theta = 2.5°$ towards stall at the tip. The blade section is a continuous NREL S809 aerofoil (see Fig. D.7), with constant thickness, except at the hub transition piece where it blends into a circular section. Taken from the description in Appendix A of Hand, M.M., Simms, D.A., Fingersh, L.J., Jager, D.W., Cotrell, J.R., Schreck, S. and Larwood, S.M. (2001). "Unsteady Aerodynamics Experiment Phase VI: Wind Tunnel Test Configurations and Available Data Campaigns." Tech. Rep. NREL/TP-500-29955, NREL.

R [m]	$r/5.532\,\mathrm{m}$	$r/5.029\,\mathrm{m}$	$c(r)$ [m]	$\theta(r)$ [°]	$t(r)$ [% $c(r)$]	Twist Axis [% $c(r)$]
0.000	0.000	0.000	–	–	–	–
0.508	0.092	0.101	0.218	0.000	100.00	50.0
0.660	0.120	0.131	0.218	0.000	100.00	50.0
0.883	0.160	0.176	0.183	0.000	100.00	50.0
1.008	0.183	0.200	0.349	6.700	46.70	35.9
1.067	0.193	0.212	0.442	9.900	34.84	33.5
1.133	0.205	0.225	0.544	13.400	28.31	31.9
1.257	0.227	0.250	0.738	20.040	20.87	30.0
1.343	0.243	0.267	0.728	18.074	20.95	30.0
1.510	0.273	0.300	0.711	14.292	20.95	30.0
1.648	0.298	0.328	0.697	11.909	20.95	30.0
1.952	0.353	0.388	0.666	7.979	20.95	30.0
2.257	0.408	0.449	0.636	5.308	20.95	30.0
2.343	0.424	0.466	0.627	4.715	20.95	30.0
2.562	0.463	0.509	0.605	3.425	20.95	30.0
2.867	0.518	0.570	0.574	2.083	20.95	30.0
3.172	0.573	0.631	0.543	1.150	20.95	30.0
3.185	0.576	0.633	0.542	1.115	20.95	30.0
3.476	0.628	0.691	0.512	0.494	20.95	30.0
3.781	0.683	0.752	0.482	−0.015	20.95	30.0
4.023	0.727	0.800	0.457	−0.381	20.95	30.0
4.086	0.739	0.812	0.451	−0.475	20.95	30.0
4.391	0.794	0.873	0.420	−0.920	20.95	30.0
4.696	0.849	0.934	0.389	−1.352	20.95	30.0
4.780	0.864	0.950	0.381	−1.469	20.95	30.0
5.000	0.904	0.994	0.358	−1.775	20.95	30.0
5.305	0.959	1.055	0.328	−2.191	20.95	30.0
5.532	1.000	1.100	0.305	−2.500	20.95	30.0

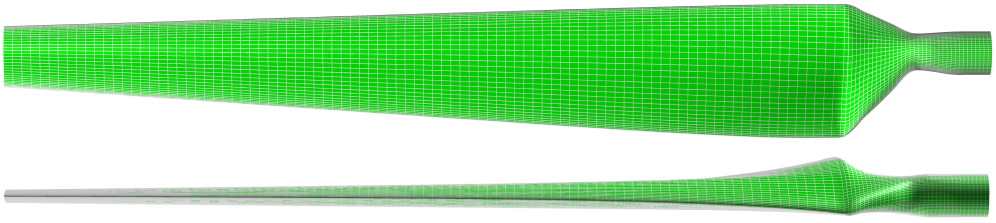

Figure D.5: NREL Phase VI blade mesh, showing transition piece approximation.

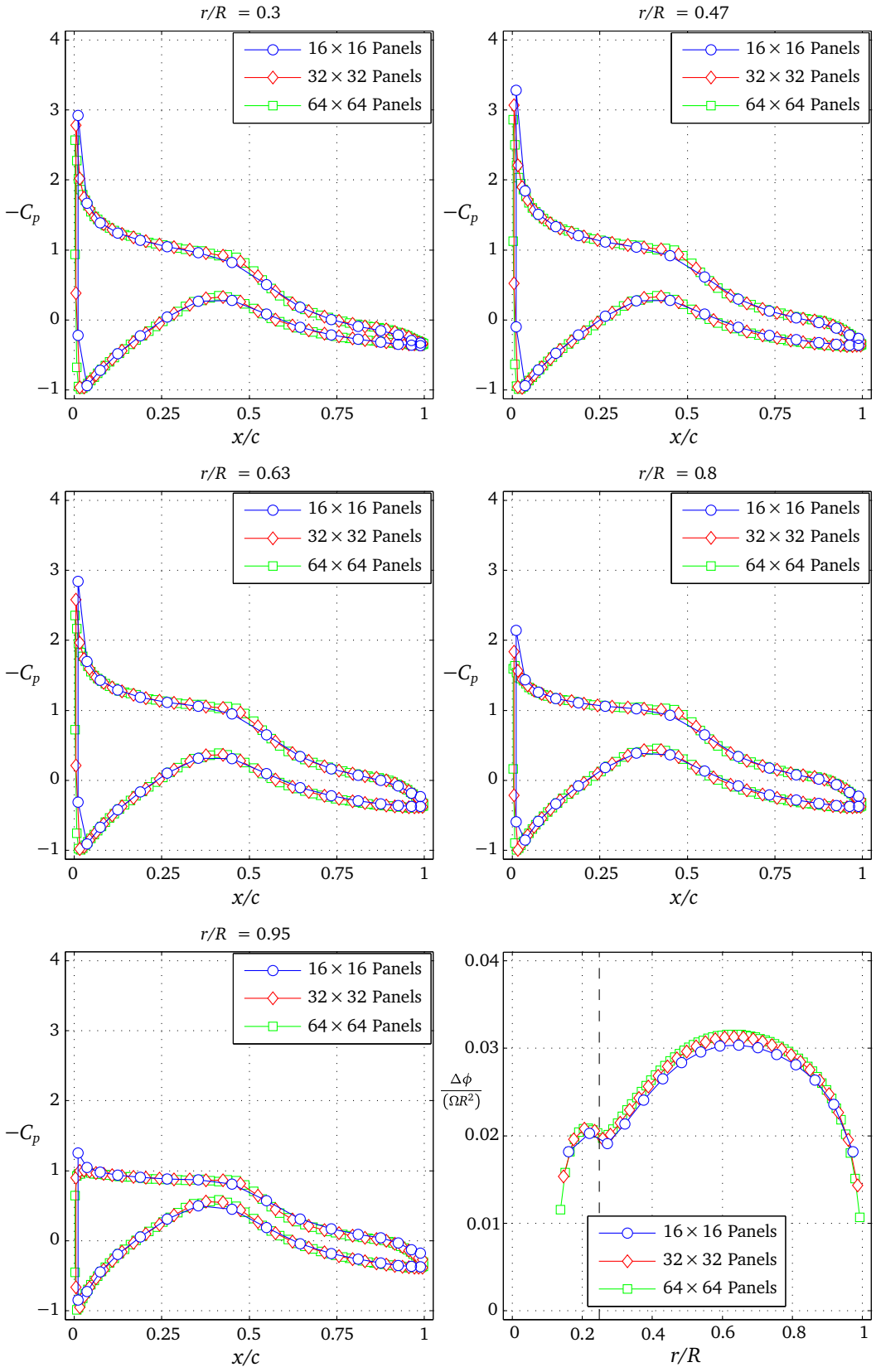

Figure D.6: Comparison of computed chordwise pressure coefficients and spanwise circulation distribution for the NREL Phase VI rotor with varying boundary-element mesh densities, obtained at $\lambda = 5.41$.

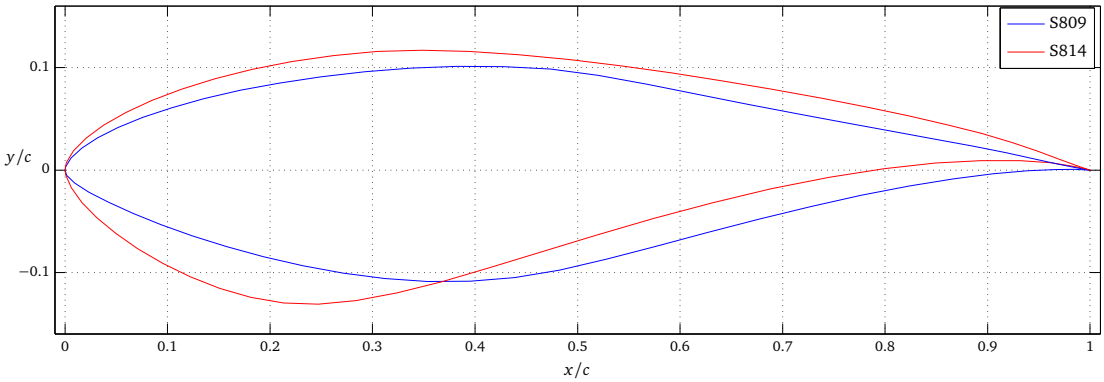

Figure D.7: Plot of NREL S-Series aerofoil coordinates relevant to this thesis.

Table D.2: Blade geometries for the Nautricity CoRMaT turbine rotors. To obtain constant solidity between each rotor, the upstream rotor has 3 blades and the downstream has 4 blades. Radius is 1.25 m and the blade twist is measured at the blade tip. The blade section is an NREL S814 aerofoil, with constant thickness. Taken from the description in Clarke, J.A., Connor, G., Grant, A.D. and Johnstone, C.M. (2005). "Design and initial testing of a contra-rotating tidal power turbine." In "Proceedings of the 6th European Wave and Tidal Energy Conference (EWTEC2005)," Glasgow, Scotland.

r/R	$c_1(r)/R$	$\theta_1(r)[^\circ]$	$c_2(r)/R$	$\theta_2(r)[^\circ]$
0.20	0.0800	35.5	0.1864	26.4
0.24	0.0772	30.7	0.1648	23.3
0.28	0.0744	26.6	0.1444	20.5
0.32	0.0716	23.2	0.1268	18.0
0.36	0.0688	20.3	0.1112	15.8
0.40	0.0660	18.0	0.0984	13.8
0.44	0.0632	16.0	0.0872	12.0
0.48	0.0604	14.3	0.0800	10.6
0.52	0.0576	12.9	0.0736	9.6
0.56	0.0548	11.7	0.0684	8.7
0.60	0.0520	10.7	0.0640	8.0
0.64	0.0492	9.8	0.0608	7.4
0.68	0.0464	9.0	0.0580	6.9
0.72	0.0436	8.3	0.0548	6.4
0.76	0.0408	7.6	0.0516	5.8
0.80	0.0380	7.0	0.0484	5.3
0.84	0.0352	6.4	0.0444	4.6
0.88	0.0324	5.9	0.0400	4.0
0.92	0.0296	5.5	0.0352	3.4
0.96	0.0268	5.1	0.0304	2.8
1.00	0.0240	4.9	0.0256	2.2

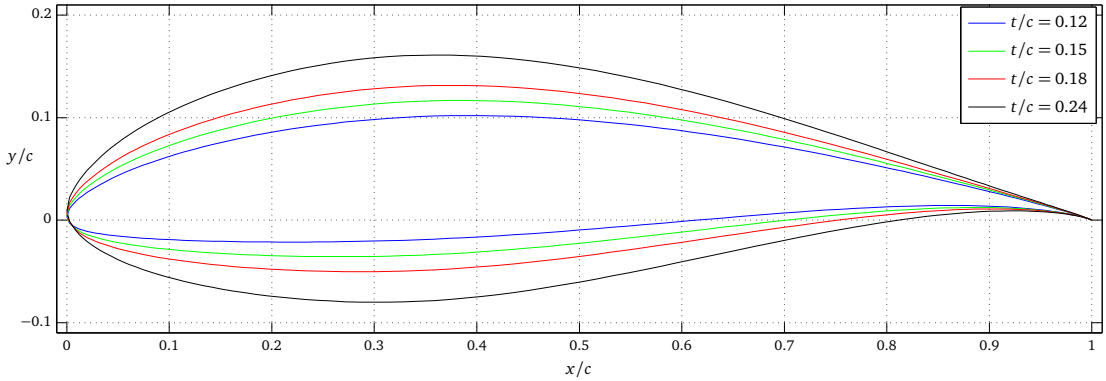

Figure D.8: Plot of NACA 63-8xx family aerofoil coordinates for thicknesses of 12 % to 24 %.

Table D.3: Blade geometry for the Southampton turbine rotor. The rotor has 3 blades, a 40 mm radius and the blade twist is measured at the blade tip. The blade section is based on a NACA 63-8xx aerofoil, with the thickness given in column 4 as a fraction of the chord. Taken from the description in Bahaj, A., Batten, W. and McCann, G. (2007). "Experimental verifications of numerical predictions for the hydrodynamic performance of horizontal axis marine current turbines." *Renewable Energy*, **32**(15): pp. 2479–2490.

r/R	$c(r)/R$	$\theta(r)[^\circ]$	$t/c(r)[\%]$
0.2	0.1250	15.0	24.0
0.3	0.1156	9.5	20.7
0.4	0.1063	6.1	18.7
0.5	0.0969	3.9	17.6
0.6	0.0875	2.4	16.6
0.7	0.0781	1.5	15.6
0.8	0.0688	0.9	14.6
0.9	0.0594	0.4	13.6
1.0	0.0500	0.0	12.6

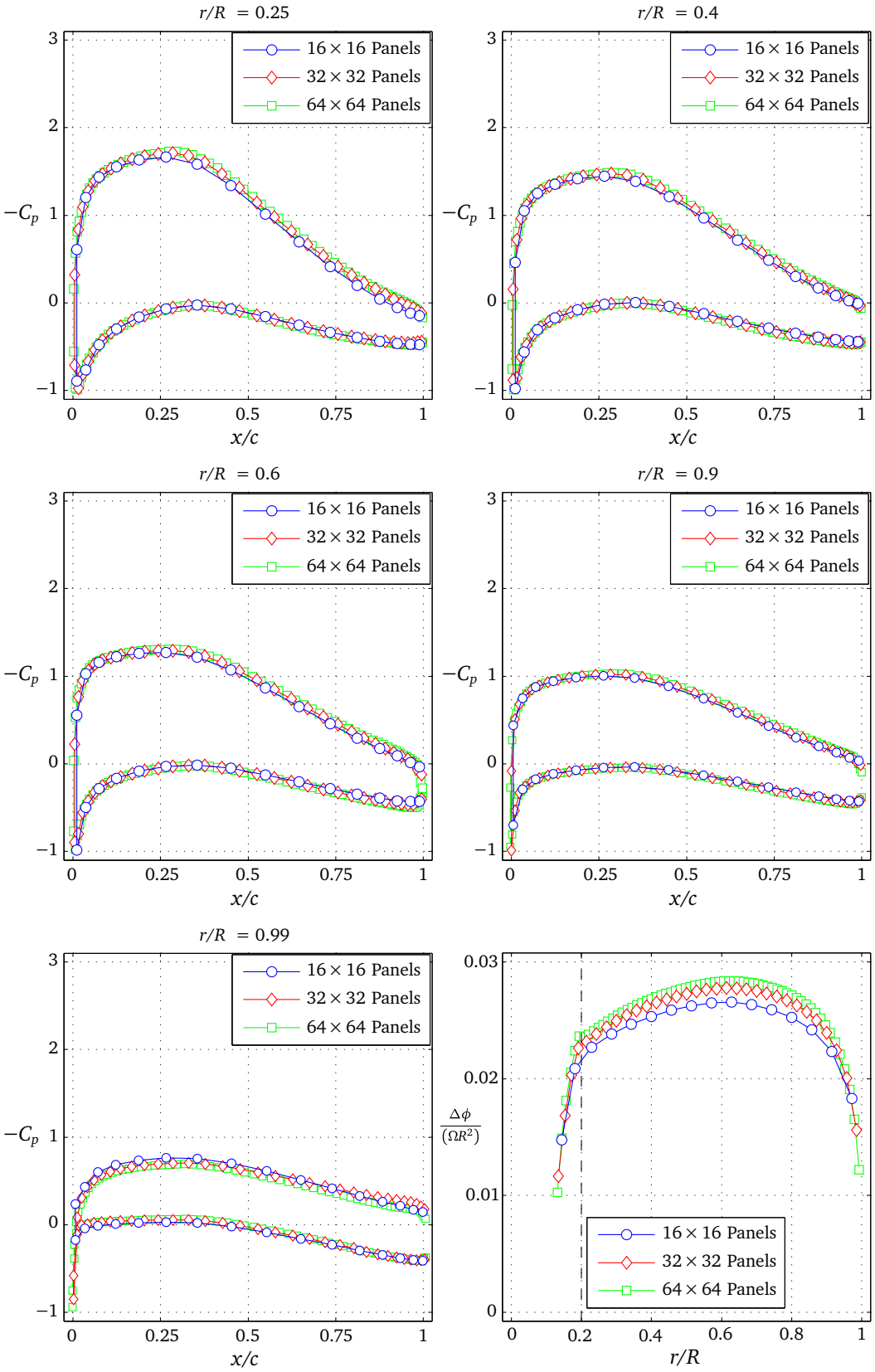

Figure D.9: Comparison of computed chordwise pressure coefficients and spanwise circulation distribution for the Southampton rotor with varying boundary-element mesh densities, obtained at $\lambda = 6$.

sin é